Design and control methods for high-accuracy variable reluctance actuators

by

Ian MacKenzie

Submitted to the Department of Mechanical Engineering
in partial fulfillment of the requirements for the degree of

Doctor of Philosophy in Mechanical Engineering

at the

MASSACHUSETTS INSTITUTE OF TECHNOLOGY

February 2015 [June 2015]

Signature redacted

Author .....
Department of Mechanical Engineering
February 13, 2015

Signature redacted

Certified by .....
David L. Trumper
Professor of Mechanical Engineering
Thesis Supervisor

Signature redacted

Accepted by .....
David E. Hardt
Chairman, Department Committee on Graduate Theses

Design and control methods for high-accuracy variable reluctance actuators

by

Ian MacKenzie

Submitted to the Department of Mechanical Engineering
on February 13, 2015, in partial fulfillment of the
requirements for the degree of
Doctor of Philosophy in Mechanical Engineering

Abstract

This thesis presents the design and control techniques of a variable reluctance actuator for driving a reticle motion stage in photolithography scanners. The primary thesis contributions include the design and experimental demonstration of a magnetic flux controller that uses a sense coil measurement, the design and experimental demonstration of a novel method to estimate actuator hysteresis in real-time, and the development of an actuator model that incorporates the effects of eddy currents.

The reticle stage in a scanning lithography machine requires high accelerations combined with sub-nanometer position accuracy. Reluctance actuators are capable of providing high force densities (force per moving mass) and lower power values relative to the present state-of-the-art Lorentz actuators that are used to drive the reticle stage. However, reluctance actuators are highly nonlinear with both current and air gap. They also display other nonlinear behavior from hysteresis and eddy currents. Linearizing the reluctance actuator is required for the high force accuracy required in the scanning stage.

In this thesis, we present a way to linearize the reluctance actuator with flux control using a sense coil as the feedback measurement. Because the sense coil is AC-coupled, we design a low-frequency estimate of the magnetic flux based upon the actuator current and air gap measurements. We combine the low-frequency estimate with the sense coil measurement using a complementary filter pair that provides an estimate of the flux from DC to frequencies of several kHz. For the low-frequency estimate, we develop a novel method for estimating the actuator hysteresis in real-time. For this flux estimator, we use an observer to model the actuator flux which treats the changing air gap as a disturbance to the plant model. The use of an observer allows the identification of a single-variable hysteresis model of actuator current rather than a two-variable hysteresis model of current and air gap. We also introduce a novel way for expressing the actuator hysteresis, whereby we incorporate the linearizing effect of the air gap directly into a Preisach hysteresis model via a change of variables. We demonstrate experimentally that this method is numerically stable in the presence of a dynamically changing gap, in contrast to some alternative

methods.

We designed and built a reluctance actuator prototype and 1-DoF motion testbed to demonstrate the accuracy of the actuator models and control techniques. We experimentally demonstrated that we can achieve a flux control bandwidth of 4 kHz that is capable of reducing the stiffness of the reluctance actuator to less than 0.012 N/µm for frequencies up to 100 Hz. This results in a force error of less than 0.03% of the full-scale force for a 10 µm air gap disturbance at this frequency. We also demonstrate that the actuator hysteresis model is capable of estimating the actuator flux accurately in the presence of dynamic gap disturbances of at least 35 µm peak-to-peak and with a static offset from the nominal air gap of at least 50 µm.

Thesis Supervisor: David L. Trumper
Title: Professor of Mechanical Engineering

Acknowledgments

I would first and foremost like to thank my advisor David Trumper for his guidance, encouragement, and patience throughout my graduate years. I have learned a great deal from him and have very much enjoyed working with him. He has imparted to me not only his extensive knowledge of mechatronics, but also how to communicate more effectively and how best to situate my research within the big picture.

I would also like to thank the members of my thesis committee. All of them offered invaluable feedback and support. Professor Jeffrey Lang took a keen interest in my project and helped me to debug experimental problems and to clarify my thinking. I learned electromagnetics from Professor Markus Zahn, without which knowledge my thesis would have been impossible. He also offered much-appreciated encouragement. Professor Martin Culpepper provided advice for improving my experimental testbed, and helped me to broaden my thinking by always encouraging me to think of other applications for my research. All of my committee members were always willing to be available and were eager to see me succeed.

In addition to my committee members, I would like to thank Professor Noel Perkins, my Master's advisor at the University of Michigan. He stimulated my interest in research and encouraged me to apply to MIT.

I would like to thank ASML for their collaboration and financial support. Steve Roux first introduced me to this project during a summer internship and enthusiastically supported its continuation. I would also like to thank Chris Ward and Mark Schuster, both of whom offered valuable feedback. I thank Charlie Griffin and Mark Hill for their help in setting up my experimental testbed at ASML. I also thank ASML for the employment opportunity they gave me in the middle of my PhD.

I also extend my thanks to Fred Sommerhalter, who built the reluctance actuator prototypes for my thesis. He also worked with us in finalizing the prototype design, where his motor expertise proved invaluable.

My labmates have helped make my time at MIT gratifying. Darya Amin-Shahidi collaborated with me on parts of my thesis and was an excellent sounding board for

discussing research ideas. Mohammad Nejad was always willing to offer his design and manufacturing expertise and was never shy about correcting my English. The Persian hegemony formed by Darya and Mohammad helped prevent the lab from descending into chaos. I also enjoyed collaborating with Roberto Meléndez who helped me machine parts and assisted me in preparing for my thesis defense. Jun Young Yoon was always willing to take the time to assist me in various endeavors, whether it was setting up an experiment or printing my thesis for me in my absence. The ongoing 'feud' between Roberto and Jun Young provided endless free entertainment to the lab. I enjoyed working with Aaron Gawlik on an earlier project and debating whether Michigan hockey or Minnesota hockey was better (Michigan, of course). I enjoyed frequent brainstorming sessions and philosophical discussions with Dean Ljubicic, even if on the latter he remains inexplicably unconvinced. I am also grateful to his family for feeding a poor graduate student on numerous occasions. Kevin Miu helped me navigate the idiosyncrasies of MIT, more often than not with a healthy dose of sarcasm included. Dan Kluk helped persuade me to join Professor Trumper's lab, and perhaps just as important, taught me all I know about craft beer. I also thank Lei Zhou, Minkyun Noh, Phillip Daniels, and Joe Church for their support. I also thank Laura Zanganjori for her administrative help and her friendly demeanor.

I cannot fully express my gratitude to my parents, who in addition to humoring me by smiling and nodding whenever I talk about my research, have freely given me their love and support throughout my life and have taught me responsibility and strong moral principles. Growing up, my siblings often provided the opportunity for applying these moral principles, despite frequent reluctance on my part to take advantage of these opportunities. For that, I both thank and apologize to my siblings.

Finally, I thank God, who as Creator and Sustainer of the natural world has provided the raw material for my scientific endeavors, and who as the Logos, the Source of all order and rationality, has made it possible for me to discover nature's truths. As C.S. Lewis wrote, "God never meant man to be a purely spiritual creature... We may think this rather crude and unspiritual. God does not... He likes matter. He invented it."

Contents

List of Figures

List of Tables

Chapter 1

Introduction

In the semiconductor industry, photolithography is a critical part of the process used to produce integrated circuits (IC's). In a state-of-the-art photolithography scanner, the reticle stage must accelerate at tens of g's while maintaining sub-nanometer position accuracy. As the industry continues to advance to higher throughputs and smaller feature sizes, the required accelerations must increase and the required position accuracy must improve. The present state-of-the-art Lorentz-force actuators used to drive the reticle stage will be unable to achieve these higher accelerations. Thus, a new actuation technology must be developed. In this thesis, we explore the alternative technology of reluctance actuators. Reluctance actuators can achieve much higher force densities (force-to-moving-mass ratio) than Lorentz actuators at small air gaps. Reluctance actuators, however, are significantly more nonlinear than Lorentz actuators, and so present a challenge in achieving the required position accuracy. This thesis examines how to model and control a reluctance actuator in order sufficiently to linearize it for photolithography applications. In this chapter, we first provide a background of the problem and then present prior art for linearizing reluctance actuators for lithography. We then give an overview of the thesis and summarize the primary contributions.

1.1 Background

In a lithography machine, the desired IC pattern is optically transferred onto a silicon wafer via a 'reticle' mask that contains a slit for exposing light on the wafer. A simplified diagram of the photolithography scanner is shown in Figure 1-1. Both the silicon wafer and the reticle are scanned back and forth relative to each other so that the entire silicon wafer can be patterned. The wafer stage is alternately scanned in y and stepped in x. The reticle stage is scanned in y and is coordinated with the wafer movement. A scan profile consists of acceleration and deacceleration phases at the beginning and end of the scan. In the middle of the scan is a constant velocity phase during which the wafer exposure occurs. More details on the operation of a lithography machine can be found in [18].

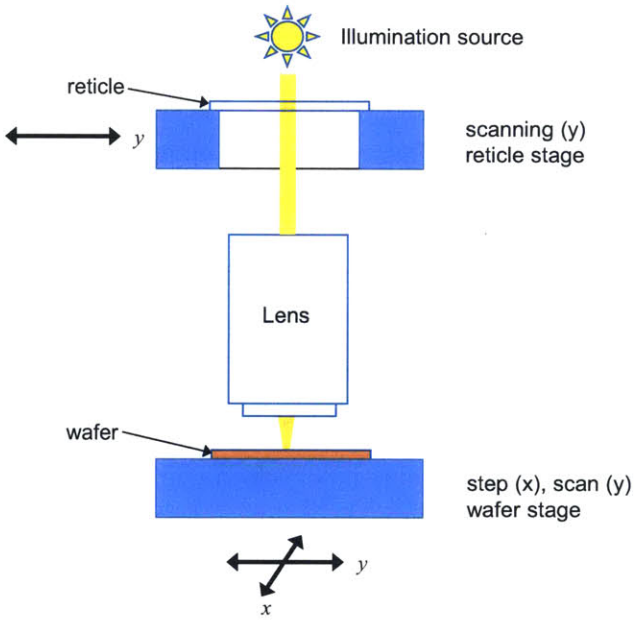

Figure 1-1: Diagram of lithography scanner.

Figure 1-2 shows a one-degree-of-freedom (DoF) model of a reticle stage (the wafer stage is similar). It consists of a long-stroke stage for coarse positioning and a short-stroke stage for fine positioning. The short-stroke stage is magnetically levitated in all six DoF and is servoed to the desired position referenced from an isolated metrology frame (y_{SS}). The long-stroke stage follows the short-stroke stage by attempting to

maintain a constant y_{diff}. Lorentz actuators are currently used for the short-stroke actuation (F_{SS}). Because the features printed on the IC can be as small as tens of nanometers, the position accuracy of the reticle and wafer during exposure must be accurate to a few nanometers or better. The servo bandwidth is limited by stage dynamics, so the majority of the position accuracy comes from the force feedforward accuracy, which must be better than 99.9% accurate for a typical trajectory. Complicating issues is the long-stroke tracking error, which introduces force disturbances into the short-stroke stage owing to the non-zero stiffness of the actuator. The maximum allowable actuator stiffness is $0.0001F_{\max}$ N/µm for a typical long-stroke peak tracking error of 10 µm, where $F_{\max}$ is the maximum force output of the actuator.

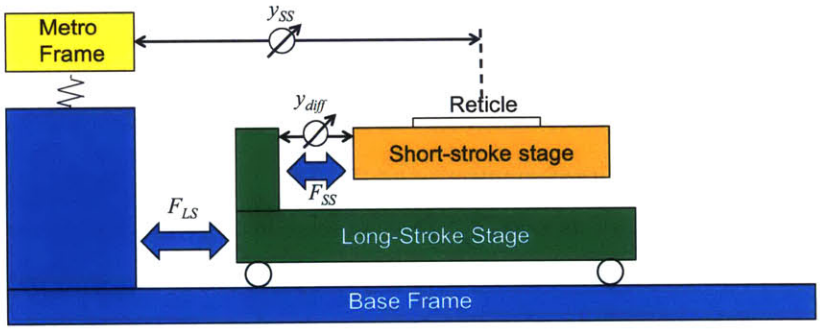

Figure 1-2: 1-DoF model of reticle stage.

To obtain higher throughputs, the reticle and wafer stages must be operated at higher speeds and accelerations. These higher accelerations require higher forces or lower moving masses. Presently, Lorentz actuators are near their limit in the acceleration they can achieve. For the scale of air gaps envisioned between actuator stator and payload (~1 mm), reluctance actuators can generate equivalent forces to a Lorentz actuator but with a much smaller actuator moving mass, or alternatively, they can generate much higher forces with an equivalent actuator moving mass.

Reluctance actuators come with a host of challenges not present in a Lorentz actuator, however. Chief among these is the reluctance actuator nonlinearity. Lorentz actuators generate a force that is approximately linear with current and have approximately zero stiffness in the driving direction. These features are conducive to achieving the high accuracy required for the reticle and wafer stages. Reluctance

actuators, in contrast, generate a force that is quadratic with current and display a large negative stiffness. Moreover, they exhibit hysteresis and can also be affected by eddy currents. These features must be properly compensated for in order for reluctance actuators to achieve the required force accuracy. The main focus of this thesis is developing ways to model and control the reluctance actuator to force-linearize it for use with a photolithography scanner. The work has been a collaboration with ASML, the world's leader in semiconductor lithography machines.

1.2 Prior Art

Reluctance actuators are used in a variety of precision engineering applications, most notably as magnetic bearings [37]. To the best of our knowledge, however, the lithography application is the only one in which reluctance actuators have been investigated for achieving high dynamic force accuracy (99.9% or better) and very low stiffness. In the following subsections, we review the solutions for linearizing reluctance actuators for use in lithography scanners in the available scholarly literature and patent literature. The prior art references can be categorized into two groups according to their approach to linearizing the actuator: actuator configuration (e.g., physical geometry, alternate ways to drive the actuator) and control. These two approaches are often complementary, i.e., they can be used together.

1.2.1 Actuator Configuration

In [42], Hol of ASML designed a reluctance actuator with a target surface that extends beyond the surface spanned by the stator pole faces. The target is also called the mover or armature. A sketch of the actuator is shown in Figure 1-3. The driving direction is along the y-axis. A current is driven through the coils (340.1 and 340.2) to generate a magnetic flux in the air gaps (390). This flux generates a force (F) on the target (310). The target surface (312) has a greater length (L1) in the x-direction than the length (L2) spanned by the stator (320) pole faces. Likewise, in the z-direction, the target surface has a greater length (L3) than the pole face dimension

(L4). Such a configuration makes the reluctance actuator less sensitive to relative motions between the stator and target in the x- and z-directions.

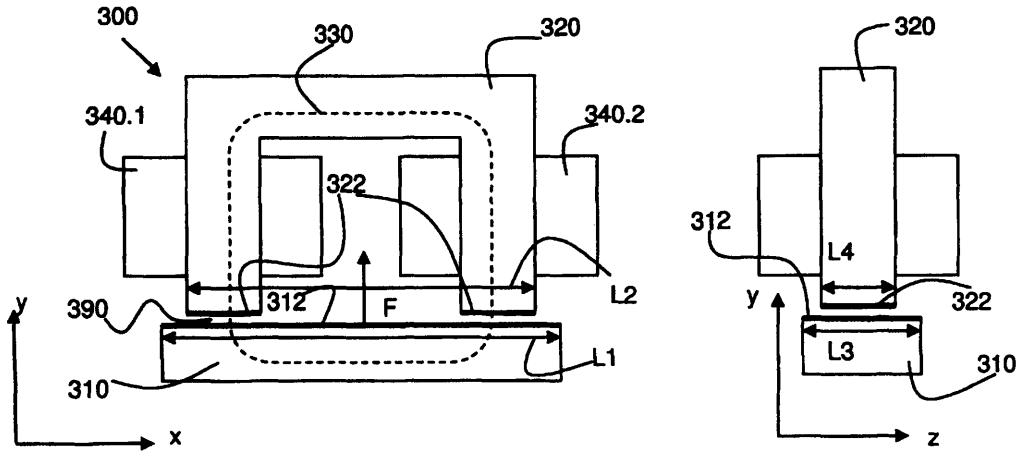

Figure 1-3: Schematic diagram of ASML's extended target design invented by Hol. Figure is taken from US Patent 8,687,171 [42].

Hol also designed a 2-DoF reluctance actuator in [41] that can generate a controllable torque in addition to a controllable force. As shown in Figure 1-4, the stator consists of three coils, where the center coil (CL3) is split into two independent coils (CL31 and CL32), and each of these is connected to one of the outer coils (CL1 and CL2). In this way, two independent currents (I_1 and I_2) can be used to control both a force in the z-direction and a torque about the y-axis. A reluctance actuator can be subject to parasitic torques that can compromise accuracy. This is especially true of reluctance actuators with three or more poles. We discuss this phenomenon in further detail in Section 2.6.2. This design therefore provides a method for counteracting these parasitic torques.

In [67], Ono of Nikon designed a reluctance actuator with a curved target. This is shown in Figure 1-5. The target is intended to have a stator on either side of it to make a bi-directional actuator (one stator can generate only an attractive force). Because the air gap flux is normal to the curved surface, the force generated by this flux will result in reduced parasitic torques about the target's longitudinal axis

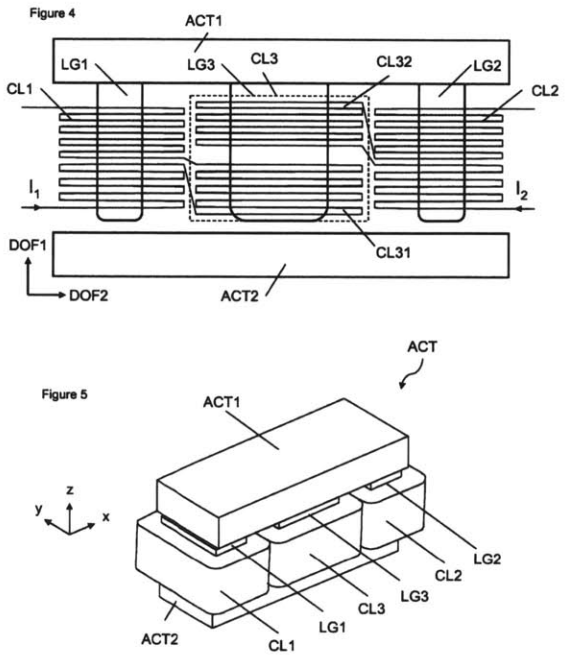

Figure 1-4: Schematic diagram of ASML's 2-DoF actuator design invented by Hol showing the coil wiring (top) and 3-D view of the actuator (bottom). Figure is taken from US Patent 8,472,010 [41].

that arise from misalignments or relative motion between the stator and target. One disadvantage of this design, however, is that the actuator will not be as efficient in generating force because the effective air gap is larger and because the flux normal to the target surface is not perfectly parallel to the driving direction.

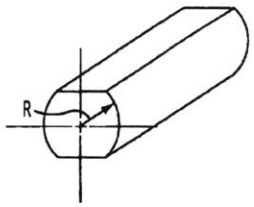

Figure 1-5: Schematic diagram of Nikon's reluctance actuator design invented by Ono showing curved target. Figure is taken from US Patent 6,906,334 [67].

Yuan of Nikon developed a way to drive two reluctance actuators as a single unit in order to simplify the control [82]. Figure 1-6 shows a precision stage (120) driven

by reluctance actuators (121 and 122). Reluctance actuators are typically operated with some bias force F_0 to avoid the theoretically infinite amplifier slew rates that would be required at zero force. We discuss this in Chapter 2. The net force F on the stage is $F_2 - F_1$. Then, to generate a force F to the right, the force F_2 generated by the right actuator (122) is increased to $F_0 + F/2$ and the force F_1 generated by the left actuator (121) is decreased to $F_0 - F/2$, where $F \leq 2F_0$. If the actuators are operated in tandem in this way, the maximum force achievable is $F = 2F_0$ because reluctance actuators can only generate attractive forces. Thus, to generate large forces, F_0 must be increased. However, with a large bias force the average power dissipation increases significantly. Yuan circumvents this problem by using a small bias force during the exposure (constant velocity) phase of the scan profile when the net force required is small, but then increasing the bias force during the acceleration phases when the required forces are large. In this way the large bias force is present during only portions of the scan, and he is able to operate the actuator pair as a single unit while minimizing power dissipation.

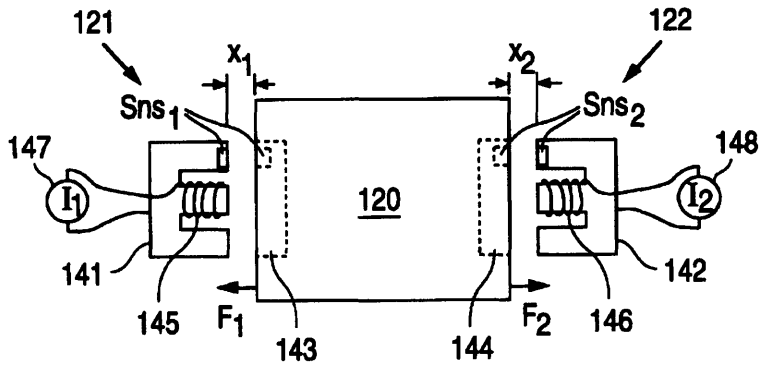

Figure 1-6: Schematic diagram of precision stage actuated with two reluctance actuators as a single unit. Figure is taken from US Patent 6,130,517 [82].

1.2.2 Control

Control of a reluctance actuator for force-linearization can be subdivided into two categories: model-based feedforward control and feedback control. In model-based

feedforward control, the desired force is used as the input to an inverse model of the actuator force. The inverse model then outputs a drive signal to the actuator (a current, for example). If the inverse model is accurate, the actuator will output a force that matches the desired force. In feedback control, a signal such as the air gap flux is sensed and controlled with a high-bandwidth control loop. These two categories are not mutually exclusive and can be used together.

Butler of ASML suggests in [19] a control scheme that uses both reluctance actuators and Lorentz actuators. The reluctance actuators are used for the feedforward force and the Lorentz actuators are used for the feedback force. Since the feedback force dominates during the constant-velocity exposure phase of the scan profile, the Lorentz actuators generate the actuation when the position accuracy is more critical. The feedforward force dominates during the acceleration phases of the scan, so the reluctance actuators provide a more efficient way of transmitting the force during the large-force portions of the scan. The idea then is that this scheme reduces the need for the reluctance actuator to be highly accurate. However, since the position control bandwidth of the stage is limited, the feedforward force accuracy must still be very good to meet the position accuracy requirement at the start of exposure. Another downside of this method is that the volume needed to accommodate both reluctance actuators and Lorentz actuators is limited.

During a summer internship I had at ASML in 2008, Steve Roux, Mike Carter, and I conceived a reluctance actuator with force feedback control. We filed for a patent application, which was published in 2013 [75]. In this design, a force sensing element is connected to the stator or target so that the actuator force can be directly controlled with a high-bandwidth force control loop. With an ideal force sensor, this is an attractive solution since force is the variable we are ultimately trying to control. However, real force sensors are problematic because they cannot distinguish between applied force and inertial forces, so stage accelerations will introduce errors into the force sensing. Another concept introduced in this patent is the idea of servoing the fine-positioning stage to different actuator air gaps during different phases of the scan profile. For example, in the schematic of Figure 1-7, a fine-positioning stage (3) is

actuated in the scan axis (x) by reluctance actuators (6 and 7). While accelerating in the +x-direction, actuator 7 is generating the force. During this acceleration phase, the actuator 7 air gap is made smaller and the air gap 6 is made larger. While accelerating in the -x-direction, actuator 6 is generating the force. During this phase, the actuator 6 air gap is made smaller and the air gap 7 is made larger. In this way, we can make better use of the improved actuator efficiency at small air gaps without necessarily having to tighten assembly tolerances.

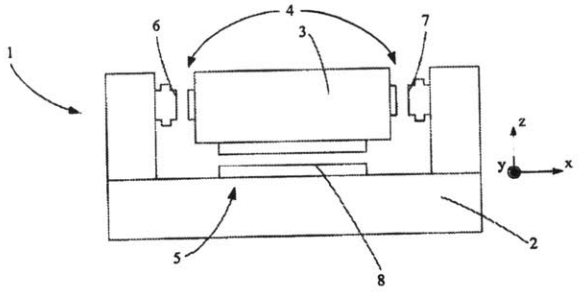

Figure 1-7: Schematic diagram of short-stroke stage actuated by two reluctance actautors. Figure is taken from US Patent 8,553,205 [75].

Hsin of Nikon describes a force feedback controller in [43] that utilizes an adaptive gain adjustment so that the loop gain remains relatively constant even during large gap disturbances. This allows for improved performance and stability over a large range of gaps. On a prototype actuator, a consistent loop crossover frequency of $\sim$60 Hz is demonstrated over a range of 800 µm. In contrast, without the adaptive gain adjustment, the loop crossover frequency shifts between 25-60 Hz depending on the gap, leading to deteriorated performance.

In [49], Katalenić uses a Hall sensor and sense coil for flux control using state feedback. A sense coil wound around one of the pole faces measures $d\lambda/dt$ and is used for a high-bandwidth inner loop, where λ is the total flux linked by the coil. A Hall sensor placed on one of the pole faces measures the flux density and is used for a low-bandwidth outer loop. Combining the sense coil and Hall sensor in this way provides for innovative way to take advantage of the benefits each sensor offers: the superior noise performance of the sense coil at high frequencies is realized, while the

Hall sensor compensates for the sense coil's inability to measure DC flux. With this method, a maximum force error less than 0.1 N was demonstrated for a 200 N force pulse on a 1-DoF testbed with a constant air gap. The main downside of this method is that the Hall sensor takes up volume in the air gap, which limits how small the air gap can be made, and thus limits the actuator efficiency.

Katalenić also describes a method that uses an inverse hysteresis model to control the actuator force via feedforward. The desired force and air gap measurement are first sent to a lookup table (LUT), which outputs an intermediate variable X. This intermediate variable is sent to an inverse hysteresis operator, which then outputs a commanded current. A high-bandwidth current loop then controls the actuator current to track the commanded current. If the inversion is accurate, the resulting current will produce the desired force. The variable X does not have any physical significance and is chosen based on constraints set by the form of the inverse hysteresis model. This method performs well at a constant air gap for a slowly varying desired force, exhibiting a maximum force error of less than 0.1 N for a force profile with a 240 N maximum force. The author cautions that because of the hysteresis model's simplicity, it is limited in its local memory, which limits this method's accuracy for more complex inputs, such as those resulting from a gap disturbance. Moreover, for this method to be sufficiently accurate for lithography applications, the air gap must be known to better than 250 nm.

There are a number of patents in the literature that develop inverse models for feedforward control. In [83], a standard model for a reluctance actuator current-force relationship is inverted to improve the linearity. In [22], additional parameters are added to the inverse model and then fine-tuned during calibration to generate a better fit. In [40], an automatic calibration algorithm uses an adaptive controller to fine-tune the inverse model that can also account for angular misalignments. These examples also make use of feedback linearization, whereby the gap measurement is fedback into the inverse model so that the gap dependency can be accounted for in the model. One thing these methods lack, however, is that they do not model the actuator saturation or hysteresis. This limits the achievable accuracy.

1.3 Thesis Overview

In this thesis, we focus on modeling and controlling the reluctance actuator for force-linearization. After considering various alternatives for controlling the actuator, we found flux control to be the best solution for our application. We focus on flux control using a sense coil for the feedback measurement because of its simplicity, its superior noise characteristics, and because it can be used without affecting the operating air gap, unlike other flux sensor alternatives. Because a sense coil is AC-coupled to the actuator flux, however, we cannot use it for control at DC. To generate a flux estimate for control at DC, we develop an actuator real-time hysteresis model based on the current and gap measurements, which are measurements already available in the lithography scanner. By combining this model with the sense coil measurement, we are able to design a flux controller for force-linearization of the actuator. With this flux controller, we test the force accuracy of the reluctance actuator on a 1-DoF air bearing stage and experimentally demonstrate a stiffness well below $0.04\,\mathrm{N/\mu m}$, which is equivalent to the specification of $0.0001F_{\max}$ N/µm for our prototype.

1.3.1 Reluctance Actuator Design

In Chapter 2, we present a detailed design and analysis overview of a reluctance actuator. A 2-D illustration of a three-pole reluctance actuator showing the primary flux path for one half of the actuator is shown in Figure 1-8. By producing a reluctance force normal to the actuator pole faces and by operating at small air gaps, a reluctance actuator is able to generate much higher force densities (force per unit mover mass) than a Lorentz actuator, allowing a reluctance-actuator-driven stage to achieve higher accelerations and servo bandwidths. The primary reluctance actuator nonlinearities that make accurate force control a challenge are also presented in Chapter 2. We address potential actuator configurations and control topologies that can be used to linearize the reluctance actuator.

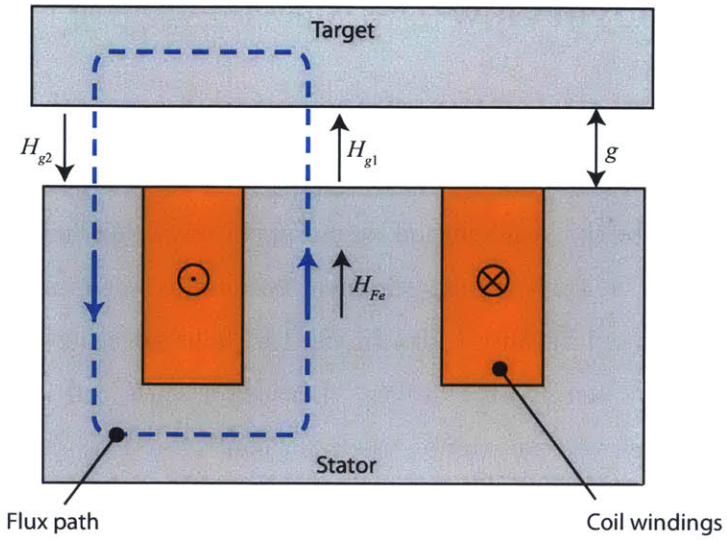

Figure 1-8: Three-pole reluctance actuator.

1.3.2 Reluctance Actuator Modeling

A key contribution of this thesis is the development of an accurate nonlinear model of the reluctance actuator that can be used for real-time force control. This model must be able accurately to capture the ferromagnetic hysteresis, saturation, and gap dependency of the reluctance actuator. In Chapter 3, we present the Preisach hysteresis model, which we use as the building block for our actuator model. We present two alternative ways to implement the Preisach model. We also present an alternative hysteresis model, the Chua model, which provides a simpler but less accurate way to model ferromagnetic hysteresis. In Chapter 4 and Chapter 5, we incorporate the Preisach hysteresis model into a lumped-parameter reluctance actuator model that is based on the analysis that was presented in Chapter 2. Using simulations of this model, we investigate the effects of hysteresis, gap disturbances, and eddy currents on force accuracy. We also develop theory for predicting errors from these sources.

We develop a model that can be used for real-time flux estimation in Chapter 6. We present a novel way of modeling the actuator using a 'sheared' model of the actuator hysteresis, whereby we incorporate the linearizing effect of the air gap directly into the hysteresis model. We term this model the sheared hysteresis model (SHM).

We then integrate this model into an observer that treats the changing air gap as a disturbance, which allows us to make use of a single-variable (one input) hysteresis model to estimate the flux. We simulate the SHM with observer and show that it is numerically stable in the presence of dynamic gap changes and that it captures the actuator behavior into saturation.

In Chapter 7, we extend the actuator lumped parameter model with additional elements using magnetic circuit techniques and flux tube methods to model the air gap fringing fields. This augmented model can be combined with the hysteresis model if additional accuracy is desired.

1.3.3 Reluctance Actuator and 1-DoF Testbed

A photograph of the prototype reluctance actuator stator is shown in Figure 1-9. A CAD model of both the stator and target is shown in Figure 1-10. The actuator stator consists of a ferromagnetic core comprised of two nickel-iron (NiFe) cut-cores adjacent to each other and a coil wound around the center pole. The target is a NiFe I-bar. A shielded sense coil is wound around the center pole face of the core for flux sensing. In the CAD models, this is shown as a printed circuit board (PCB), which is another possible way to implement a sense coil. In the photograph, the stator is shown mounted on load cells so that we can measure the actuator force output.

Figure 1-11 is a photograph of the 1-DoF air bearing testbed. The motion stage uses a linear air bearing with position measurement and feedback via a high-resolution linear encoder. The linear encoder is also used to provide an estimate of the reluctance actuator air gap. On one end of the motion stage is the reluctance actuator. On the other end of the motion stage is a voice coil actuator, used for nulling the reluctance actuator force and for applying position disturbances to the reluctance actuator. Using this motion stage, we test our reluctance actuator flux controller and use the load cells to measure the force accuracy. The detailed design of the reluctance actuator prototype and motion stage is described in Chapter 8.

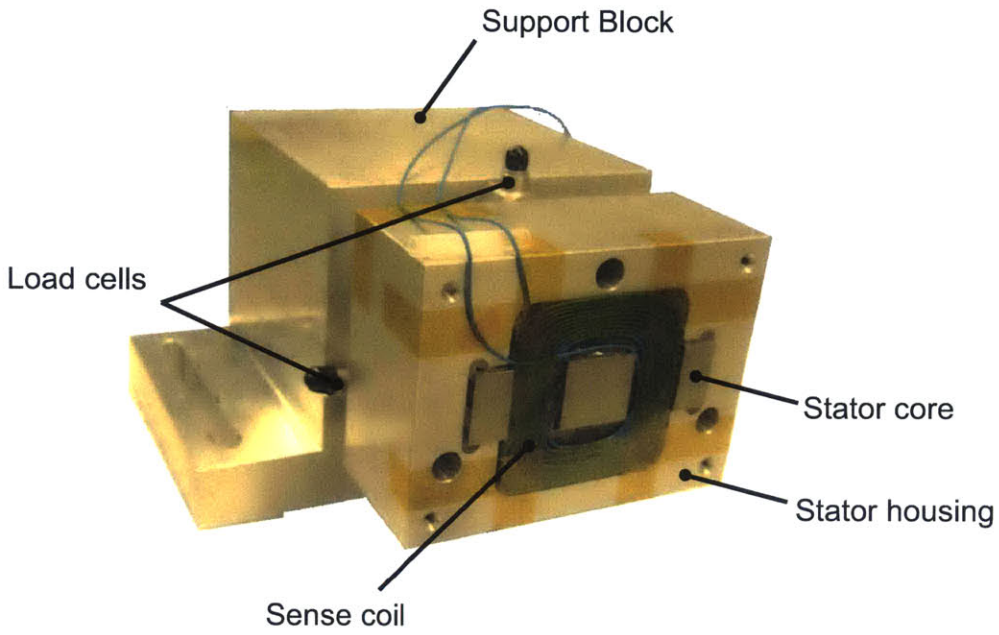

Figure 1-9: Reluctance actuator stator prototype.

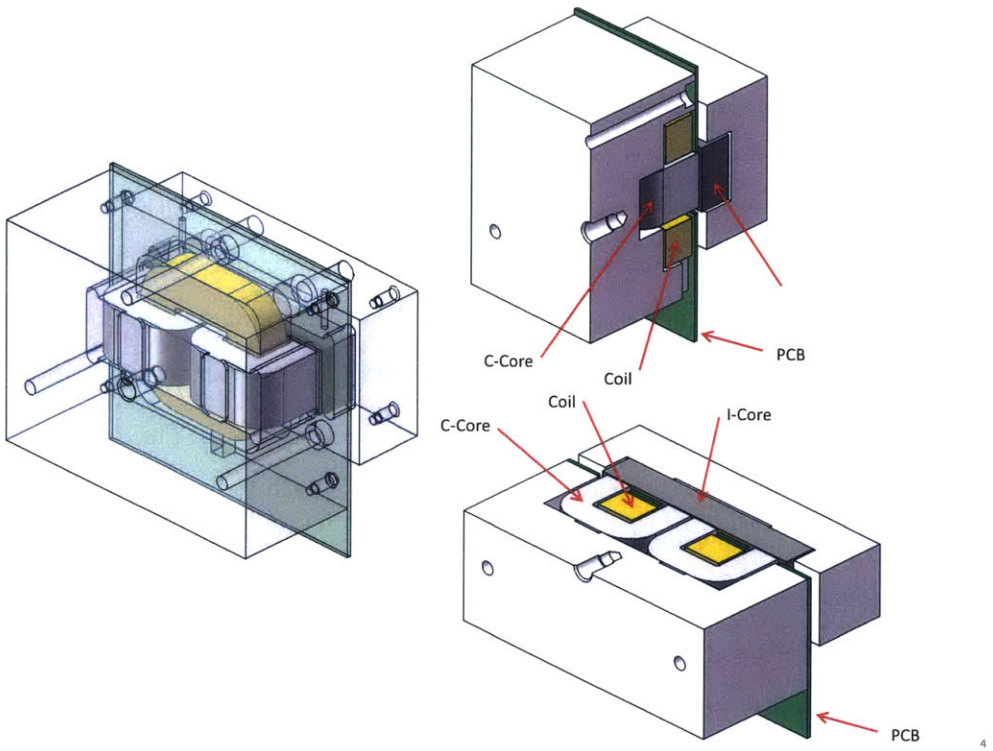

Figure 1-10: CAD model of reluctance actuator.

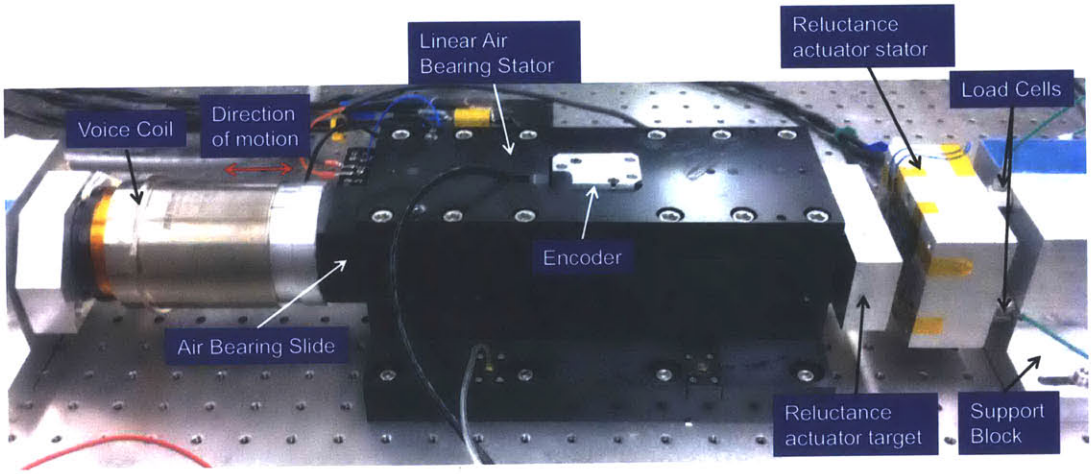

Figure 1-11: Photograph of 1-DoF testbed.

1.3.4 Loop-Widening Investigation

Chapter 9 discusses a loop-widening phenomenon we discovered on the reluctance actuator prototype: the actuator flux as measured by the sense coil shows a phase lag with respect to the measured actuator current that increases with frequency. This loop widening manifests itself at frequencies below 10 Hz, which is too low for eddy currents to account for it. Figure 1-12 demonstrates the loop-widening behavior by plotting the measured actuator flux density (B) against the measured current (I) for different frequencies. This makes accurate force control via flux feedback more difficult because the phase lag in the measured flux does not appear in the measured force. At the time of writing this thesis, our investigation into the cause of the loop widening remains inconclusive, and we therefore recommend further investigation.

1.3.5 Experimental Results

Finally, we present experimental results for the SHM and the flux controller on the 1-DoF testbed in Chapter 10. We demonstrate good agreement between the real-time SHM observer flux estimate and the sense coil flux estimate. Figure 1-13 shows the SHM estimate compared with the sense coil estimate when the actuator is driven with a voltage sine wave at a nominal air gap of 530 µm and a 35 µm peak-to-peak

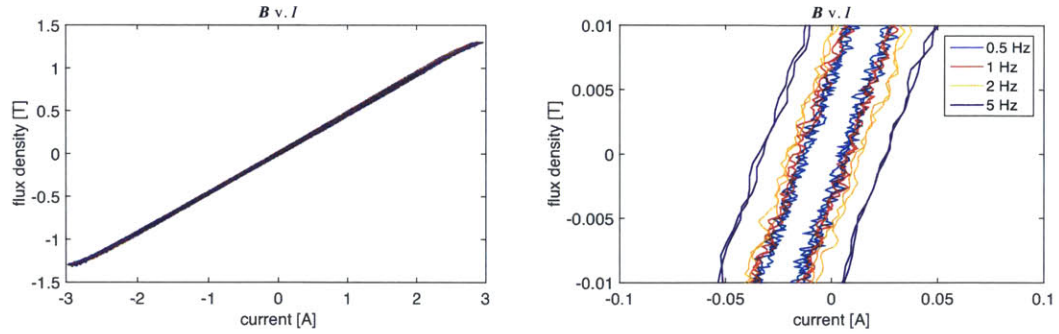

Figure 1-12: LEFT: *B-I* data measured on reluctance actuator demonstrating loop-widening phenomenon; RIGHT: zoomed in near origin.

dynamic gap disturbance is applied.

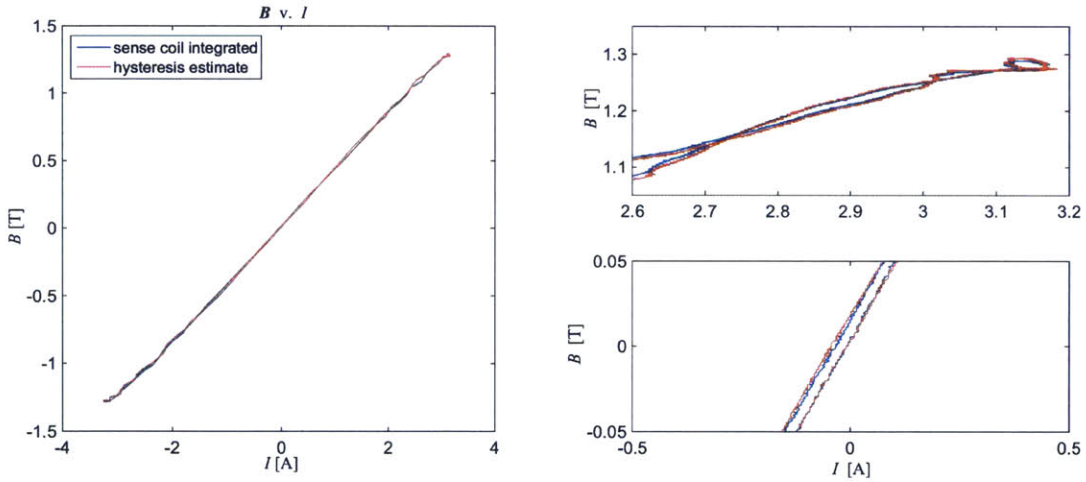

Figure 1-13: LEFT: SHM observer real-time flux estimate compared to sense coil measurement with 35 µm p-p gap disturbance about nominal gap of 530 µm; TOP RIGHT: zoomed in at saturation; BOTTOM RIGHT: zoomed in at origin.

Another key contribution of this thesis is designing a flux controller for the reluctance actuator that utilizes a sense coil for the feedback measurement. A sense coil allows us to measure the actuator flux without compromising the air gap. Because a sense coil measures the flux rate of change, the resulting signal must be integrated to obtain a flux measurement. The upshot is that the sense coil cannot measure at true DC. We have therefore designed a hybrid flux estimation scheme that combines the sense coil measurement with the SHM estimate that is valid at DC. The hybrid estimation scheme uses a complementary filter pair structure such that the flux estimate

relies on the sense coil for high frequencies and relies on the SHM at low frequencies. Using this hybrid estimation scheme, we achieve a 4 kHz crossover frequency for the flux controller on the reluctance actuator prototype. Combining the flux feedback with force-flux-gap model inversion control, we demonstrate a maximum stiffness of 0.012 N/μm at a bias force of 35 N for frequencies up to 100 Hz, well below the maximum allowable stiffness of 0.04 N/μm. The measured stiffness frequency responses for nominal forces of 5 N and 35 N are shown in Figure 1-14.

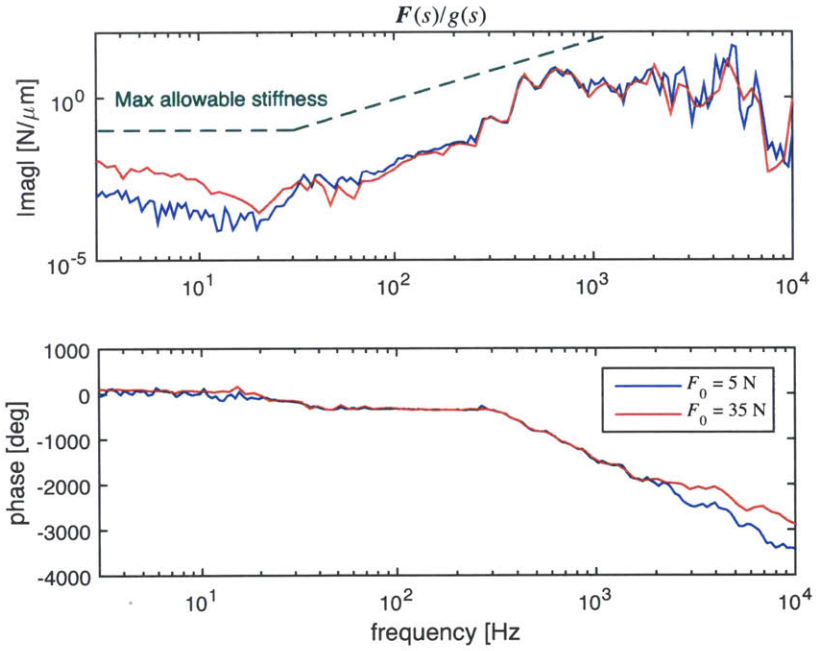

Figure 1-14: Measured frequency responses of flux-controlled reluctance actuator stiffness.

Chapter 2

Reluctance Actuator Design

In this chapter, we present a general design overview of reluctance actuators for high-precision applications. First, we develop the basic electromagnetic theory behind the reluctance actuator operation. We also present the electromagnetic theory for Lorentz actuator operation. We then contrast the reluctance actuator with the Lorentz actuator and demonstrate how a reluctance actuator can achieve much higher force densities for the range of operating gaps typical in the industry.

Next, we give an overview of the different core materials that can be used for a reluctance actuator and the trade-off between hysteresis and saturation flux density that typically exists among these materials. We then discuss the primary nonlinearities of a reluctance actuator that present challenges to high-precision control, chief among these being nonlinear stiffness, magnetic hysteresis and saturation, eddy currents, fringing fields, and the nonlinear force-flux relationship. We consider how to linearize a reluctance actuator through actuator configuration, i.e., through geometric or physical modifications to the basic actuator structure or by driving the actuator in different ways. We then consider how to linearize a reluctance actuator through various combinations of feedforward control and feedback control, the advantages and disadvantages of each controller topology, and the different types of sensors available for feedback control. We also discuss other controller methods such as feedback linearization and iterative learning control. Finally, we discuss alternate reluctance actuator configurations beyond the basic 'U'-core or 'E'-core configuration. These

include a double-sided reluctance actuator that is capable of generating bi-directional force, multi-Degree-of-Freedom actuators that can generate forces in multiple degrees of freedom (DoF), and multi-pole actuators that can generate the same force with lower moving mass.

2.1 Electromagnetic Fundamentals

In this section, we analyze the electromagnetic theory of the reluctance actuator and Lorentz actuator from first principles. We then compare the force generated by the two classes of actuators and show that the reluctance actuator is capable of generating much higher force densities (force per unit mass) than the Lorentz actuator.

2.1.1 Reluctance Actuator Electromagnetics

The reluctance actuator can be analyzed using Maxwell's equations as presented for example in [39]. Figure 2-1 is an illustration of a three-pole reluctance actuator showing the primary magnetic flux path for one half of the actuator. Here, NI is the number of amp-turns in the actuator coil, g is the length of the air gap, H_{g_1} and H_{g_2} are the magnetic field intensities in the two air gaps of the primary flux path, and H_{Fe} is the magnetic field intensity in the ferromagnetic core and target (also called the mover). In this analysis we assume symmetry, i.e., the air gap is uniform. We also assume uniform flux density in the steel, which is of uniform cross-section. We also analyze the actuator as a 2-D structure with depth d into the paper.

Air Gap Magnetic Flux Density

We first solve for the magnetic flux density in the air gap. This flux is found by applying Ampere's Law, Gauss's Law, and the material constitutive relationships.

Ampere's law in integral form is

$$\oint_C \mathbf{H} \cdot d\boldsymbol{l} = \iint_S \mathbf{J} \cdot d\mathbf{S}. \tag{2.1}$$

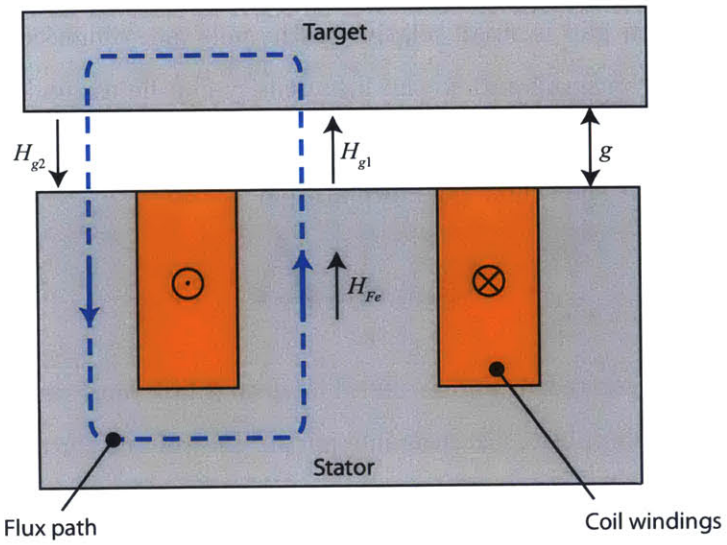

Figure 2-1: Flux path for a three-pole reluctance actuator

This states that the line integral of the magnetic field intensity (**H**) around a closed contour is equal to the surface integral of the current density (**J**) passing through the contour. For the flux path being considered in our reluctance actuator example, this simplifies to

$$H_{Fe}l_{Fe} + H_{g_1}g + H_{g_2}g = NI. \tag{2.2}$$

The variable l_{Fe} is the length of that portion of the flux path in the core and target. In this analysis, H_{g_1} and H_{g_2} are approximated as being constant in the gap. This is a reasonable assumption if the gap is small relative to leakage paths and if it is small relative to the pole-face dimensions. These conditions will obtain if the actuator is designed properly. Similarly, H_{Fe} may have local variations, but for a first-order analysis we consider its average value in order to represent the ferromagnetic portion of flux path as a single lumped parameter.

Gauss's Law is

$$\oiint_S \mathbf{B} \cdot d\mathbf{S} = 0. \tag{2.3}$$

This states that the closed surface integral of the magnetic flux density **B** must always be zero. In other words, the flux entering a volume must be equal to the flux that exits.

If the actuator air gap is small relative to the pole face dimensions, the amount of fringing flux will be small and so the flux density can be assumed to be uniform within the air gap. This assumption in conjunction with (2.3) can be applied to the reluctance actuator at the center pole face air gap as

$$B_c A_c = B_{g_1} A_{g_1}. \tag{2.4}$$

Equation (2.4) is illustrated in Figure 2-2. The dotted box represents the volume to which Gauss's Law is applied. Entering one part of the volume through the pole face area A_c is the core flux density B_c. Exiting the volume on the target side is the air gap flux density B_{g_1} through air gap area A_{g_1}.

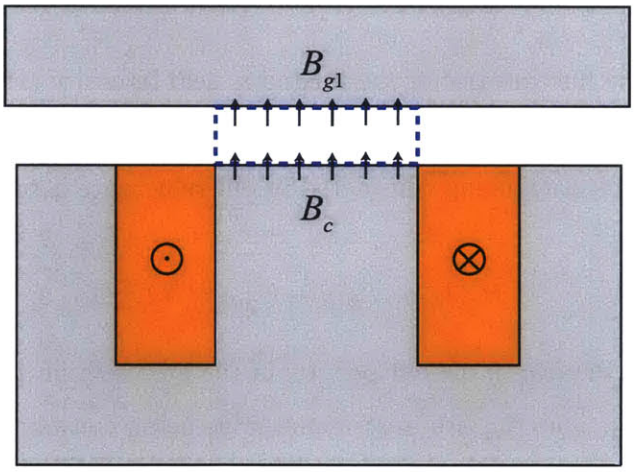

Figure 2-2: Gauss's Law applied to the center pole face air gap.

Since we have stipulated that fringing fields in the air gap are small, the flux that enters the volume through area A_c will leave through a nearly identical area, i.e., $A_{g_1} \approx A_c$. Equation (2.3) then reduces to $B_{g_1} = B_c$.

A similar analysis can be applied to the left-side air gap in the flux path. If the left and right pole faces are sized appropriately to be half the area of the center pole face, then the flux density in the left air gap will be equal to the flux density in the center air gap, that is, $B_{g_2} = B_{g_1} \triangleq B_g$.

The next step is to relate the magnetic field intensity to the magnetic flux density.

The flux density in the air gap is related to the field intensity through the permeability of free space, μ_0. The flux density in the core and target material is related to the field intensity in a nonlinear manner, but for a first-order analysis, this relationship can be approximated as linear by assuming a constant material permeability μ. These constitutive relationships are

$$B_g = \mu_0 H_g, \tag{2.5}$$

$$B_c = \mu H_{Fe}. \tag{2.6}$$

These relationships can be substituted into (2.2). Recalling that $B_c = B_g \triangleq B$, this results in

$$\frac{B}{\mu} l_{Fe} + \frac{B}{\mu_0} 2g = NI. \tag{2.7}$$

The core permeability, μ, is typically at least a thousand times greater than μ_0 when operating away from the saturation region of the material. If the reluctance actuator is designed correctly, the first term in (2.7) will be much smaller than the second term and can be ignored for the purposes of a first-order approximation (i.e., $\frac{2g}{\mu_0} >> \frac{l_{Fe}}{\mu}$). If we solve for B we deduce

$$B = \frac{\mu_0 NI}{2g}. \tag{2.8}$$

Thus, for a first-order approximation, the air gap magnetic flux density is proportional to current and inversely proportional to the gap.

If we desire a more accurate approximation for the gap flux density, we can include the core permeability in our calculation. Instead of ignoring the first term in (2.7), we can replace μ by $\mu_r \mu_0$, where μ_r is the relative permeability of the core material. If we then solve again for B, we arrive at

$$B = \frac{\mu_0 NI}{\frac{1}{\mu_r} l_{Fe} + 2g}. \tag{2.9}$$

As μ_r approaches infinity, (2.9) reduces to (2.8). The relationship can be further refined by replacing the constant μ_r by a single-valued function of H or B, e.g. $\mu_r = \mu_r(B)$, to account for the nonlinear permeability. Use of such a function permits

(2.9) to take into account saturation; however, it also requires iteration to solve. The nonlinear permeability function does not take into account hysteresis, fringing fields, or leakage flux. It also does not take into account any local field variations within the core or target material.

Reluctance Actuator Force

The force on the target can be derived from Maxwell's Stress Tensor[1] for example following the approach given in [90]. A magnetoquasistatic (MQS) field produces a stress tensor with components T_{ij} on a surface. The subscript i denotes the direction of the stress and the subscript j denotes the direction of the surface normal vector. Ignoring magnetostriction, this stress is given by

$$T_{ij} = \mu H_i H_j - \frac{1}{2}\delta_{ij}\mu H^2, \tag{2.10}$$

where H_i and H_j are the magnetic field intensities in the i- and j-directions, respectively, and δ_{ij} is the Kronecker delta, defined as 0 when $i \neq j$ and 1 when $i = j$, and H is the magnitude of the magnetic field. In Cartesian coordinates, the force in the i-direction on a body enclosed by a surface S is expressed as

$$F_i = \oint_S \left(T_{ix} + T_{iy} + T_{iz}\right) dS. \tag{2.11}$$

The key to using the Maxwell Stress Tensor effectively is to choose an appropriate surface over which to integrate. In the case of the reluctance actuator being discussed, we choose a surface shown by the dotted lines in Figure 2-3.

The flux passing through surfaces 2, 3, and 4 will be zero since we have ignored fringing and leakage flux in this analysis (if considering three dimensions, this is also true of the front and back surfaces), so these surfaces will not contribute to the integral in (2.11). This leaves surface 1 as the only surface contributing to the force evaluation. Along this surface, the flux density is normal to the surface, and thus the

[1]Other methods, such as energy methods, can also be used to derive the force

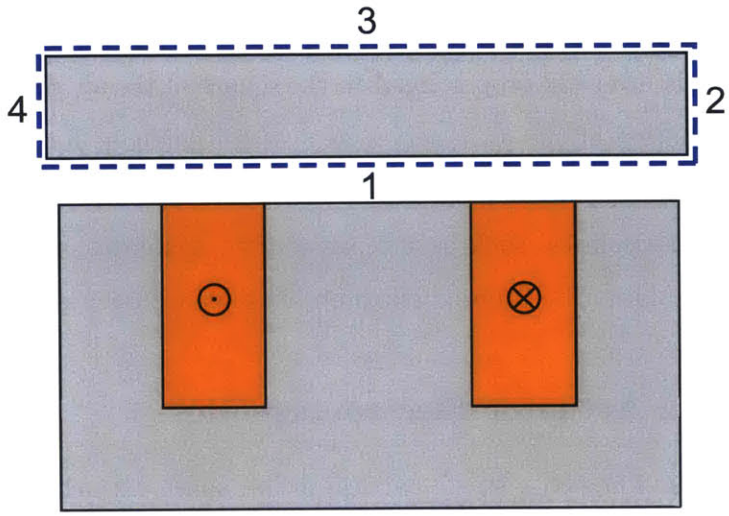

Figure 2-3: Maxwell surface for calculating the magnetic force on the mover.

force from the Maxwell stress tensor reduces to

$$F = \frac{1}{2\mu_0} \int_S B_n^2 dS. \tag{2.12}$$

In other words, the force generated from the flux passing through surface 1 is the square of the flux density normal to that surface (B_n) integrated over the surface.

In our simplified model, flux only passes through surface 1 at locations directly above the stator pole faces. Since the flux density can be approximated as being uniform at these locations, (2.12) simplifies to

$$F = \frac{1}{2\mu_0}(B^2 A_L + B^2 A_C + B^2 A_R) = \frac{B^2 A}{2\mu_0}. \tag{2.13}$$

Here A_L, A_C, and A_R are the left pole face area, center pole face area, and right pole face area, respectively. The total pole face area is denoted by A, which is the sum of A_L, A_C, and A_R.

Substituting (2.8) into (2.13), we arrive at

$$F = \frac{\mu_0 A N^2 I^2}{8g^2}. \tag{2.14}$$

The force is proportional to the total pole face area and is proportional to the square of the current. It is inversely proportional to the square of the air gap.

This approximation of the force serves as a useful guideline for a first iteration in the reluctance actuator design process. Because this analysis neglects many non-linearities and non-idealities, such as flux saturation, hysteresis, fringing flux, and leakage flux, it should not be counted on to obtain high-accuracy predictions.

2.1.2 Lorentz Actuator Electromagnetics

The electromagnetic force on a single particle in free space with charge q moving at velocity $\mathbf{v}$ in the presence of an electric field $\mathbf{E}$ and a magnetic flux density $\mathbf{B}$ is [39]

$$\mathbf{F} = q\left(\mathbf{E} + \mathbf{v} \times \mathbf{B}\right). \tag{2.15}$$

This force is known as the Lorentz force. It can be used to derive the force on a current-carrying wire of length l immersed in a field with flux density $\mathbf{B}$ [91] (see Figure 2-4) as

$$\mathbf{F} = \mathbf{I}l \times \mathbf{B}, \tag{2.16}$$

where $\mathbf{I}$ is the current carried by the wire and we assume charge neutrality in the conductor. This result can be applied to a group of N conductors immersed in the same magnetic flux density and each carrying the same current in the same direction. The total force on the conductors is

$$\mathbf{F} = N\mathbf{I}l \times \mathbf{B}. \tag{2.17}$$

A Lorentz actuator operates on this principle. A coil is placed in a uniform magnetic field generated by permanent magnets. When the coil is energized, the current interacts with the magnetic field to produce a force on the coil. An equal and opposite reaction force is generated on the permanent magnet structure.

The cross-section of one possible configuration of a Lorentz actuator is shown in Figure 2-5. A positive current generates a force on the coil in the positive y-direction.

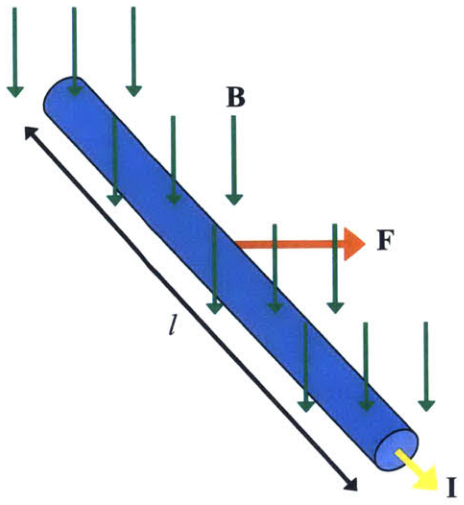

Figure 2-4: The Lorentz force on a current-carrying conductor immersed in an external magnetic flux density **B**.

In a typical application, the permanent magnet structure is attached to the moving stage, so the force on the stage is therefore in the negative y-direction. The motor constant of the actuator can be derived from (2.17) as $K = 2NlB_g$. Here N is the number of turns in the coil and l is the length of the coil (in the x-direction) within the magnetic field. Both sides of the coil interact with the magnetic field, which accounts for the factor of two. B_g is the magnetic flux density in the air gap between the permanent magnets.

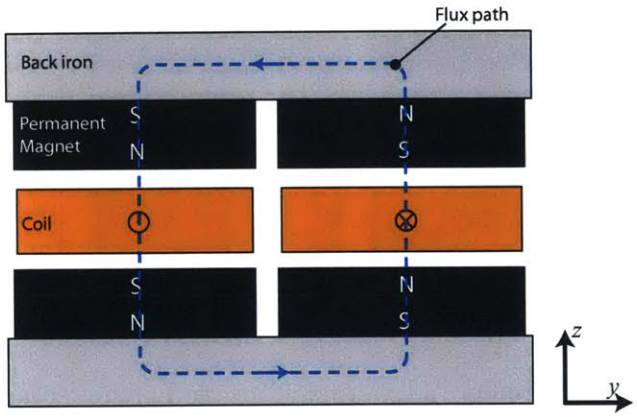

Figure 2-5: Cross-section of a Lorentz actuator.

As was done with the reluctance actuator analysis, we can apply Ampere's Law

(2.1) and Gauss's Law (2.3) to the Lorentz actuator to derive the flux density in the air gap. If we apply Ampere's Law to the flux path shown in Figure 2-6, we get

$$2H_m t + 2H_g g = 0, \tag{2.18}$$

where H_m is the magnetic field intensity in the permanent magnets, H_g is the field intensity in the air gaps between the permanent magnets, and t and g are twice the height of one permanent magnet and the height of the air gap, respectively. The magnetic field intensity in the back iron is assumed to be negligible because of its high permeability. The permanent magnets are assumed to be identical to one another and any additional magnetic field generated by the self-inductance of the coil is assumed to be negligible (valid for a first-order analysis in which we ignore inductance). The magnetic field intensities are assumed to be uniform within the permanent magnets and within the air gap. The Ampere loop is chosen to intersect the center of either side of the coil. This way the Ampere loop includes a number of amp-turns in the $+x$-direction identical to the number of amp-turns in the $-x$-direction and the right-hand side of Ampere's law is zero.

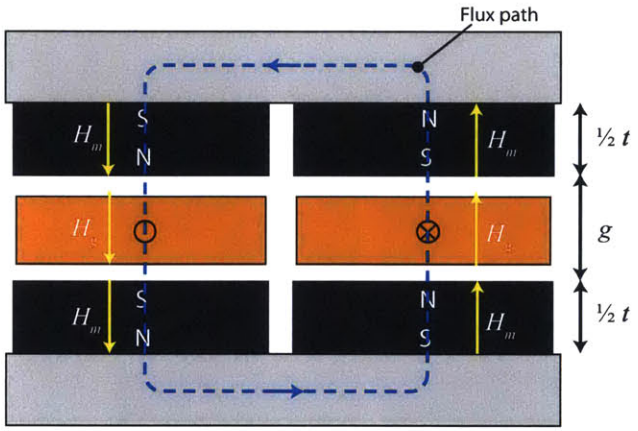

Figure 2-6: Ampere's law applied to the Lorentz actuator.

We then apply the constitutive laws relating the air gap and magnet flux densities to their respective field intensities. In the case of the air gap, we use the relationship

in (2.5). In the case of the permanent magnet, we have [39]

$$B_m = \mu_0 \left(H_m + M \right), \tag{2.19}$$

where M is the magnetization of the magnet, which is assumed z-directed. Substituting (2.5) and (2.19) into (2.17), we obtain

$$\begin{aligned} 2\left(\frac{B_m}{\mu_0} - M\right) t + 2\frac{B_g}{\mu_0} g &= 0, \\ 2B_m t + 2B_g g &= 2\mu_0 M t, \\ 2B_m t + 2B_g g &= 2B_r t. \end{aligned} \tag{2.20}$$

In the last line, $\mu_0 M$ has been replaced with B_r, the remanence flux density of the permanent magnet.

By the same reasoning employed in analyzing the reluctance actuator magnetics, we find that $B_g = B_m$ via Gauss's Law, i.e., the flux density in the air gap (B_g) is equal to the flux density in the permanent magnet (B_m). This assumes that fringing flux and leakage flux from the magnets are negligible. This is a very crude assumption for the given magnetic structure, but leads to a simple result for understanding actuator scaling. We can now solve for B_g as

$$B_g = \frac{t}{t+g} B_r. \tag{2.21}$$

Here B_g is equal to the remanence flux density of the permanent magnet multiplied by an attenuation factor of $t/(t+g)$, the ratio of total magnet thickness (t) to total magnet thickness plus air gap ($t+g$).

From (2.17), we can solve for the Lorentz actuator force in terms of the permanent

magnet remanence and given actuator parameters as

$$F = \left(\frac{t}{t+g}\right) 2NlB_r I. \tag{2.22}$$

The motor constant is thus $K = \frac{2t}{t+g} NlB_r$.

2.1.3 Comparison between Reluctance Actuator and Lorentz Actuator

In this section we compare the normal stress generated by the reluctance actuator to the shear stress generated by the Lorentz actuator. The stresses generated by the two actuators can be understood by referring to Figure 2-7.

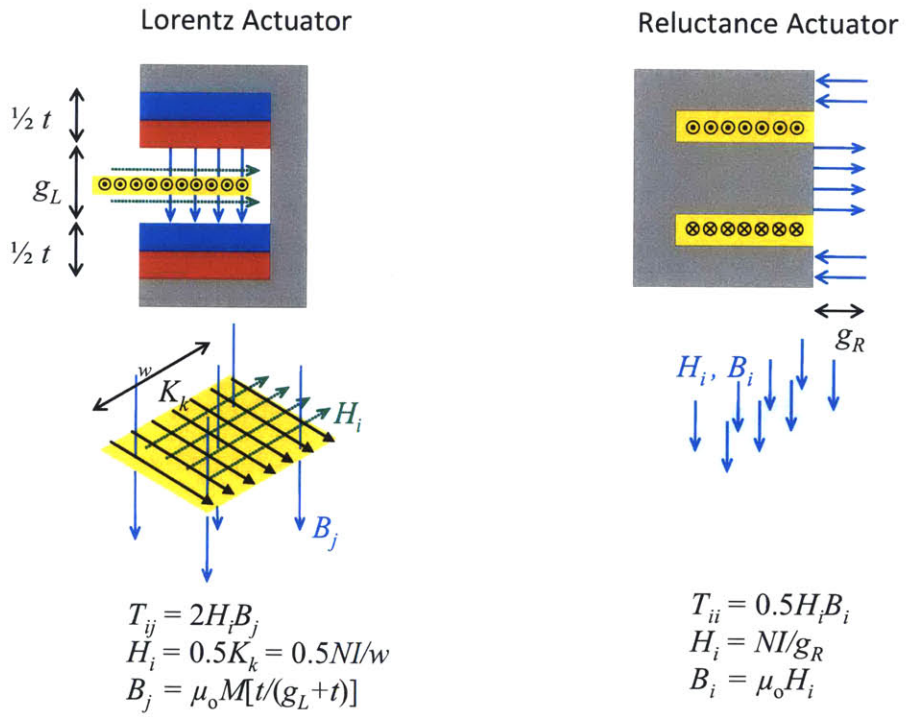

Figure 2-7: Force density comparison between a Lorentz actuator (left) and a reluctance actuator (right)

In the left illustration T_{ij} is the expression for the stress on the Lorentz actuator coil as derived from the Maxwell stress tensor (see (2.10)). The stresses on both the

upper and lower surface of the coil are identical, so they have been combined, giving rise to the factor of two. The relevant magnetic field intensity (H_i) and magnetic flux density (B_j) that produce the stress are orthogonal, creating a shear stress on the coil. If the coil current is approximated as a sheet current denoted by K_k, then H_i on either side of the coil has a magnitude equal to $0.5K_k$. This result can be derived from applying Ampere's Law to an interface with a sheet current [91]. The sheet current K_k is equal to the number of amp-turns (NI) in the coil divided by the coil width, w. The magnetic flux density produced by the permanent magnets (shown in blue and red, where blue represents the magnet north pole and red represents the magnet south pole) was derived in (2.21) and is proportional to the ratio of the magnet height to the magnet height plus air gap ($t/(t+g_L)$) . It is also proportional to the magnet remanence ($\mu_0 M$). We write T_{ij} for the Lorentz actuator as

$$\begin{aligned} T_{ij} &= \left(\frac{t}{g_L+t}\right)\frac{\mu_0 MNI}{w}, \\ T_{ij} &= \left(\frac{t}{g_L+t}\right)\frac{\mu_0 MJA_w}{w}. \end{aligned} \tag{2.23}$$

In the second line, we have replaced NI with JA_w, where J is the coil current density and A_w is the coil window area. If the gap between the coil and the permanent magnets is small relative to g_L, we can approximate A_w as $g_L w$. Then (2.23) becomes

$$T_{ij,L} = \left(\frac{t}{g_L+t}\right)\mu_0 MJg_L. \tag{2.24}$$

In the right illustration T_{ii} denotes the Maxwell stress for the reluctance actuator. In contrast to the Lorentz actuator, the stress is a normal stress rather than a shear stress. The magnetic field intensity (H_i) in the air gap is proportional to the amp-turns and inversely proportional to the air gap (g_R). This can be derived from (2.2) by noting that H_{Fe} is approximately zero. The magnetic flux density B_i is proportional

to H_i. We can write T_{ii} for the reluctance actuator as

$$T_{ii} = \frac{\mu_0 N^2 I^2}{2g_R^2},$$

$$T_{ii} = \frac{\mu_0 J^2 A_w^2}{2g_R^2}. \tag{2.25}$$

If we compare (2.25) with (2.24), we can note several things. First, the stress produced by the reluctance actuator increases quadratically with J, while the stress produced by the Lorentz actuator increases only linearly with J. At high current densities then, we can generate higher force slew rates (change of force with respect to current) with a reluctance actuator than we can with a Lorentz actuator. Second, by reducing the reluctance actuator air gap, we can increase the stress generated by the reluctance actuator, since T_{ii} is inversely proportional to g_R^2. This dimension is limited only by assembly and crash tolerances in a typical application, so can be made quite small (on the order of 1 mm). Third, for the reluctance actuator, the motion is in the same axis as g_R, so T_{ii} will change with displacement, i.e., it will have a non-zero stiffness. In contrast, the motion of the Lorentz actuator is orthogonal to g_L, so the Lorentz actuator will have zero stiffness based on this analysis.

Thermal constraints limit the maximum current density that can be achieved in a Lorentz or reluctance actuator. For a Lorentz actuator, in order to increase the T_{ij} for a given maximum current density, we must increase t or g_L. However, increasing t will increase the moving mass. We can instead increase g_L, but if the ratio of g_L/t becomes too large, the analysis from Section 2.1.2 will not remain valid, as the flux from the magnets will no longer couple with the coil. For a reluctance actuator, (2.25) indicates that once we have reached the thermal constraints that limit J, we can simply increase A_w in order to increase T_{ii}. Eventually however, we will be limited by the saturation flux density of the material. From (2.13), if we set $B = B_s$, where B_s is the saturation flux density, and note that $T_{ii} = F/A$, then we can write the maximum T_{ii} as

$$\max(T_{ii}) = \frac{2B_s^2}{\mu_0}. \tag{2.26}$$

Thus, for a reluctance actuator, the saturation flux density sets a hard limit to the achievable T_{ii}.

2.2 Core Materials

To design a reluctance actuator properly, an appropriate ferromagnetic material must be selected for the reluctance actuator core and target. The key parameters for selecting a core material are saturation flux density (B_s), coercivity (H_c), permeability (μ), and electrical conductivity (σ).

Saturation flux density is the maximum magnetic flux density that the material can sustain. Higher saturation flux density permits higher maximum force capability for the same actuator size, or alternatively, lower actuator mass for the same maximum force capability.

Coercivity is a measure of how wide the hysteresis loop is. It is defined as the magnitude of magnetic field necessary to drive the flux density of the material to zero from saturation [15]. Alternatively, it is sometimes defined as the field necessary to drive the magnetization to zero from saturation. For soft magnetic materials, these two definitions result in values that are nearly identical. On the B-H major loop, this will correspond to the magnitude of H where B is zero. Higher coercivity results in larger force errors (if the hysteresis is left uncompensated) and increased core losses. Figure 2-8 indicates B_s and H_c on the major hysteresis loop. The remanence flux density, B_r, is also shown.

Permeability is the magnetic analog to conductivity in an electrical medium. It is defined as the ratio of flux density to field strength ($\mu = B/H$) [15] and is a nonlinear function for soft magnetic materials. Higher permeability leads to lower magnetic potential drop in the core and target material and thus to a more efficient actuator (see (2.9)). As such, a higher permeability material will lead to higher force for the same number of amp-turns and the same air gap.

Electrical conductivity coupled with permeability determine the extent of eddy currents in the material. Eddy currents increase with increased electrical conductivity

and permeability and degrade the actuator's performance at higher frequencies.

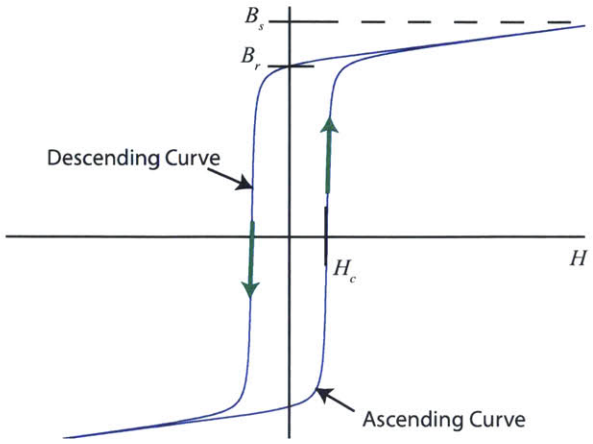

Figure 2-8: The coercivity (H_c), saturation flux density (B_s), and remanence (B_r) are indicated on the major hysteresis loop.

In general, there is a trade-off between a material's saturation flux density and its coercivity. A material with high saturation flux density will usually have a higher coercivity, and thus a wider hysteresis loop. Table 2.1[2] lists the coercivity and saturation flux density values for some typical materials. In the rest of this section, we take 49% NiFe as our baseline for comparison, because this is the material we used for the prototype actuators we designed (see Chapter 8).

Table 2.1: Comparison of key parameters for several core materials

Material	**Coercivity (A/m)**	**Saturation flux density (T)**
50% Ni-50% Fe	9.6	1.6
49% Ni-49% Fe	4.0	1.5
49% Co-49% Fe	14.4	2.3
3% Si-97% Fe	31.8	2.0
Nanocrystalline	0.6	1.2

The CoFe material has the highest saturation flux density. Because of the squared dependency of force with flux, CoFe can achieve a significantly higher maximum force

[2]The information on coercivity and saturation flux density values was obtained from Magnetic Metals [57]

than some of the alternatives. For example, a roughly 50% increase in saturation flux density over 49% NiFe will result in a 130% increase in maximum force capability for the same pole face area. CoFe therefore has the highest potential for high force-to-mass ratio, which makes it an attractive choice for high force density applications.

The next best alternative for achieving high force capability is SiFe. SiFe has a high saturation flux density that will result in an 80% improvement in force capability over 49% NiFe, and it provides a lower cost alternative to CoFe. SiFe is used for many motor applications and can be obtained at a much lower price than CoFe (it is also less expensive than NiFe).

Nanocrystalline material has the lowest coercivity of all the materials listed. This will result in much lower errors from hysteresis. One of the errors associated with hysteresis is the residual force error, defined as the force offset that results upon increasing the current to saturation levels and then reducing it back to zero. In Chapter 4, we show this error to increase with H_c^2 (see (4.13)). As a result of this squared dependency, Nanocrystalline material will have a residual force error of only 3% of 49% NiFe for actuators of the same size. However, due to saturation limits, it will only reach 50% of the maximum force capability of 49% NiFe.

2.3 Actuator Nonlinearities

A reluctance actuator is subject to nonlinear behaviors not present in a Lorentz actuator. These nonlinearites must be compensated for when used in high-precision applications. In this section we give a brief overview of some of these nonlinearities.

2.3.1 Force-flux Relationship

The nonlinearity most immediately apparent is the squared dependency of force on flux (2.13). One consequence of this is that a reluctance actuator is a uni-directional force actuator, i.e., it can generate force in only one direction. This is one downside of a reluctance actuator compared to a Lorentz actuator, which can generate both positive and negative forces. Another consequence of the squared dependency is that

the slope of the F-B curve is zero at $B = 0$, so to command a non-zero dF/dt at $B = 0$ requires infinite dB/dt, i.e., an infinite slew rate on the actuator drive current. Thus, reluctance actuators are usually operated with some bias level.

2.3.2 Hysteresis and Saturation

The B-H curve of a ferromagnetic material exhibits hysteresis and saturation. This is translated into the B-I (flux-current) domain and into the F-I (force-current) domain, where the effect of hysteresis is amplified because of the squared dependency. See Figure 2-8 for a B-H curve with hysteresis and saturation. Saturation can be compensated using a nonlinear lookup table between current and force. Hysteresis is more difficult to linearize when controlling only the current since it is a complex function of the drive current and past history. Some possibilities for linearizing hysteresis are discussed in Section 2.5.

2.3.3 Eddy Currents

Faraday's Law tells us that a changing flux will generate eddy currents in an electrically-conductive material. Via Ampere's Law, these eddy currents will in turn generate a counteracting magnetic flux, degrading actuator performance. Eddy currents are challenging to model and contribute to the non-ideal behavior of the actuator. Eddy currents are not accounted for in (2.2), because there we only considered the actuator coil current and neglected any potential eddy currents in the ferromagnetic core.

2.3.4 Gap Dependency

From (2.14), a nonlinear dependency on gap is evident. Because of the inverse dependency, a negative stiffness results in the actuator. In contrast, a Lorentz actuator has zero-stiffness in its driving direction. This is ideal for a system in which the long-stroke stage does not perfectly track the short-stroke stage: tracking errors will not translate to force disturbances on the short-stroke stage. With a reluctance actuator, tracking errors result in force disturbances if the negative stiffness is not compensated.

2.3.5 Fringing Flux

If the air gap flux is controlled directly (e.g., via a Hall-effect sensor), some of the nonlinearities discussed in the foregoing sections are mitigated. Since there is no hysteretic relationship between force and flux, the saturation and hysteresis nonlinearities are linearized by accurate flux control. Likewise, from (2.13), we see there is no gap dependency between force and flux.

However, owing to fringing fields in the air gap (which our first-order analysis neglected), the relationship between force and measured flux will have some dependency on gap. As the gap changes, the uniformity of the air gap flux changes (for example, as the gap increases, the flux will spread out more), and the relationship between force and measured flux changes. Equation (2.12) is still true, but it no longer reduces to (2.13) if the field is not uniform.

2.4 Linearization via Actuator Configuration

For precision applications, it is necessary to develop methods that linearize the actuator. These methods can be divided into two general categories: actuator configuration and actuator control. This section will address actuator configuration. Actuator configuration can refer to physical or geometric modifications to the actuator itself. It can also refer to alternate ways of driving the actuator.

2.4.1 Current-Biased Linearization

One way to improve the linearity of a reluctance actuator is to use current-biased linearization. In this method, two reluctance actuator stators are placed on either side of the mover (Figure 2-9). I_1 and I_2 are the excitation currents in the left and right stators, respectively, and g_1 and g_2 are the left and right operating air gaps, respectively. If the air gaps are equal, then $g_1 = g_2 \triangleq g_0$, and following an analysis

similar to that in Section 2.1.1, we can solve for the actuating force on the target as

$$F = \frac{C}{g_0^2} I_0 \tilde{I}, \tag{2.27}$$

where C is a constant that depends on geometry and number of turns, I_0 is the bias current defined as $(I_1 + I_2)/2$, and $\tilde{I}$ is the current difference between the two stators, defined as $(I_1 - I_2)/2$. For a more detailed analysis, see [56], Section 2.2.

Note that the squared dependency of force on current from (2.14) has been eliminated. If I_0 and g_0 are kept constant, we have a force actuator that is linear with current.

However, for scanning lithography applications, the presence of gap disturbances means that the constant gap assumption cannot be maintained. As a result, (2.27) will no longer be accurate. Moreover, hysteresis, saturation, and eddy currents remain unaddressed. Finally, to make full use of the reluctance actuator force capability in this configuration, the bias current must be set to a high value. This will result in high power-dissipation levels even when generating zero net force or when at standstill.

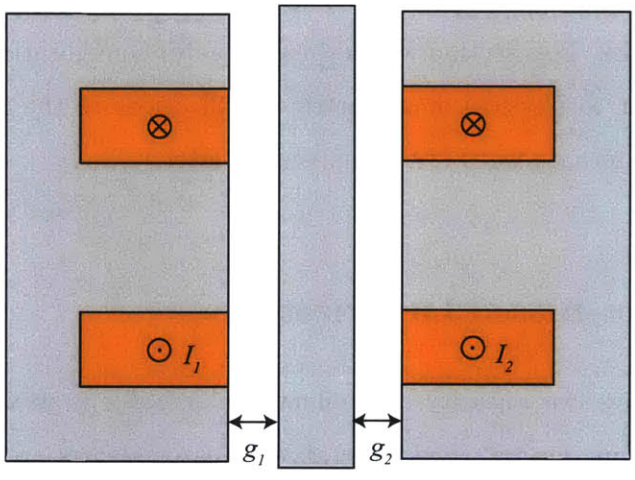

Figure 2-9: A current-biased reluctance actuator.

2.4.2 Flux-Biased Linearization with a Permanent Magnet

Another way to improve actuator linearity is by using a permanent magnet to bias the flux. There are a number of ways to implement such a scheme. One such way is shown in Figure 2-10 as presented in [56]. The force generated by this actuator is derived in [56] and is given by

$$F = \frac{A}{\mu_0} B_0 \left(\frac{\mu_0 NI}{g_0} + \frac{2g}{g_0} B_0 \right). \tag{2.28}$$

Here, A is the area of the mover normal to the direction of motion, B_0 is the DC bias flux generated by the permanent magnet, NI is the total number of amp-turns in the two stator coils, g_0 is the air gap when the mover is centered, and g is the deviation of the air gap from this nominal position (i.e., the gap between the target and stator on the left side is $g_L = g_0 + g$ and the gap on the right side is $g_R = g_0 - g$). The advantage of this actuator is that the force is now linear with both current and gap. While the stiffness is still finite and negative in sign owing to the gap dependency, a linear gap dependency is more manageable than the inverse quadratic dependency in a standard reluctance actuator topology. Unlike the current-biased linearization scheme, the linearity of the flux-biased actuator does not depend on the mover being centered. This approach is also more efficient since the bias flux is generated by a permanent magnet rather than by a bias current.

One downside of this flux-biased topology is that there is also a negative stiffness in the direction of permanent magnet magnetization (orthogonal to the motion direction). In the fast-tool servo application described in [56], this is not a problem because the mover is constrained by a rubber bearing. In a lithography tool however, the short-stroke chuck is magnetically levitated in all six degrees of freedom and so this negative stiffness could cause significant servo errors in the non-scanning axes.

Another related problem is that B_0 only remains constant insofar as the gap between the mover and the permanent magnet remains constant. Again, in [56], this problem is solved by means of the rubber bearing. In a lithography tool, there is no such lateral constraint.

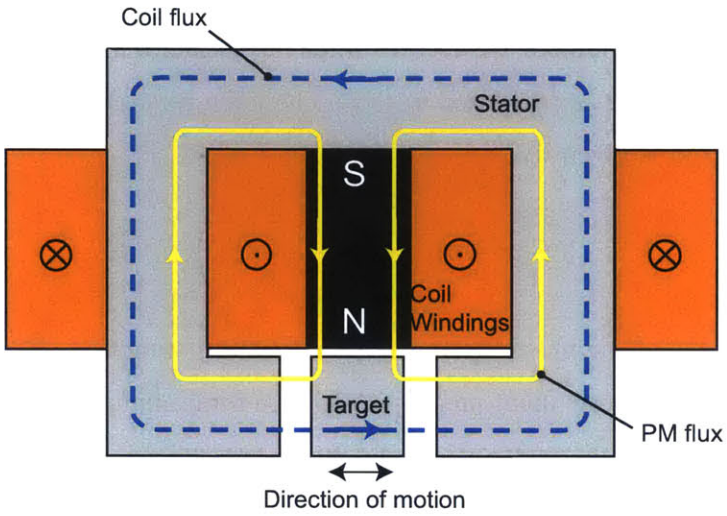

Figure 2-10: The flux-biased actuator with a permanent magnet generating the bias flux. Design presented by Lu [56].

One possible solution to the first problem is to orient the flux-biased actuators such that the permanent magnet magnetization is in the direction of gravity. This would allow for the permanent magnets to double as gravity compensators. Lithography tools already use permanent magnets in their gravity compensators, so this could be an effective way to achieve high linearity in the scan axis while using the permanent magnet stiffness in the vertical axis to its advantage. Nonlinearities such as hysteresis and saturation still remain because the analysis used to derive (2.28) does not take these into account.

2.4.3 Flux-Biased Linearization with an Electromagnet

A variation on the permanent magnet flux-biased actuator is to replace the permanent magnet with an electromagnet that generates the bias flux. See Figure 2-11. The two coils are driven in common-mode (CM) to generate the bias flux and are driven in differential-mode (DM) to generate the driving force on the target. The advantage here is that the DC current could be set to zero during wafer exposure so that the

negative stiffness orthogonal to the drive axis would be eliminated during this part of the scan. However, there are several disadvantages. The actuator would be less efficient since a current rather than a permanent magnet is being used to drive the DC flux. The gap between the DC electromagnet and the mover (x) would have to be significantly larger than the air gaps in the scanning direction (g_L and g_R) so that AC flux would not couple into the DC path. Since the gap between the DC electromagnet and mover would therefore be relatively large, driving the DC coil would result in larger power losses. A further complexity is managing the 'switching off' period of the DC electromagnet during exposure, which cannot be done instantaneously owing to the coil inductance and amplifier slew rate.

Alternatively, the center electromagnet could be kept active during the entire scan and used for actuating one of the non-scanning axes. This would allow for a compact 2-DoF actuator; however, the linearity of the actuator in the scan direction is lost and the control becomes more complicated because the force in the scanning axis is now dependent on both the central coil current and the outer coil currents.

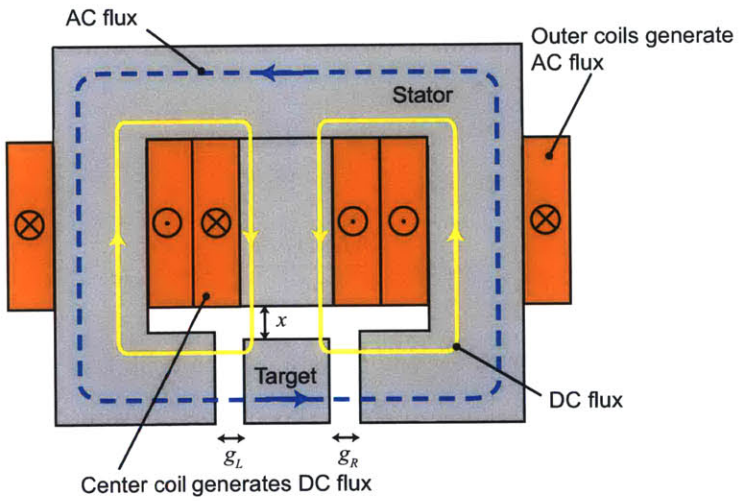

Figure 2-11: A flux-biased actuator with an electromagnet generating the bias flux.

2.4.4 Operating Regime

Intelligent choice of operating regime can lead to improved linearity for reluctance actuators. One way to do this is by operating away from the saturation region. This results in a more well-behaved actuator, as the actuator will approximately have the same permeability throughout the entire operating regime, and the $F \propto I^2$ relationship will therefore remain approximately valid. The hysteresis nonlinearity can also be reduced by operating away from saturation.

In high-acceleration applications in which achieving a low moving mass is critical, operating away from saturation is not an ideal solution because we are not taking full advantage of the force capabilities of the reluctance actuator: the mover mass will need to be made larger to generate the required force.

Another way to improve the actuator linearity is by increasing the nominal operating air gap. Consider again (2.7), rewritten here as

$$H_{Fe} l_{Fe} + \frac{B}{\mu_0} 2g = NI, \tag{2.29}$$

where we have substituted (2.5) for H_{g1} and H_{g2}. If we denote the applied magnetic field in the core as $H_a = NI/l_{Fe}$ and the ratio of total air gap length to mean ferromagnetic path length as $n = 2g/l_{Fe}$, then we can write (2.29) as

$$H_{Fe} + \frac{nB}{\mu_0} = H_a,$$

$$H_{Fe} + \frac{nB(H_{Fe})}{\mu_0} = H_a. \tag{2.30}$$

In the second line we have shown B as a function of H_{Fe} explicitly. We want to determine the B-H_a relationship from the material hysteresis curve. We plot the B-H_{Fe} material hysteresis curve in Figure 2-12, where it is indicated by the blue curve. If the air gap were zero, the B-H_{Fe} relationship would be identical to the B-H_a relationship. In this case, $H_a = H_{Fe}$, which can be seen by setting $n = 0$ in (2.30). To determine H_a when the air gap is not zero, we take the H_{Fe} values from

the material hysteresis curve and add the quantity nB/μ_0 to it, where $B = B(H_{Fe})$. The result is shown by the dotted green curve in the figure. The original hysteresis loop is 'sheared' by the amount nB/μ_0, thereby making the B-H_a relationship more linear. Note that the larger the ratio n (larger air gap), the greater the amount of shearing and linearization that occurs.

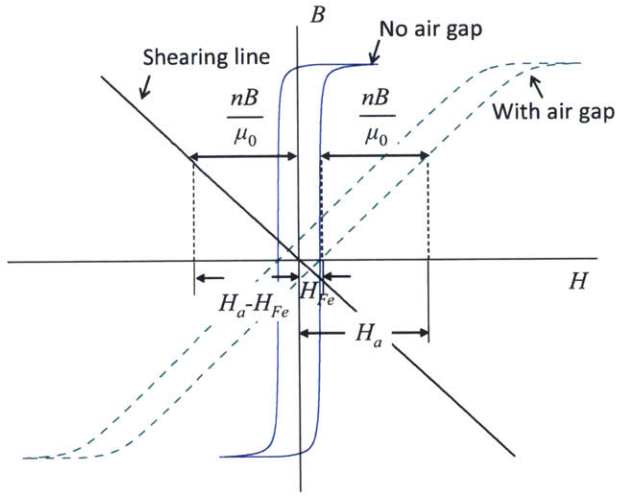

Figure 2-12: An actuator air gap causes the hysteresis loop to shear.

The linearization that results from shearing occurs because the linear air gap reluctance is large compared to the nonlinear material reluctance, and so the air gap magnetic field H_g dominates over H_{Fe}. Therefore, a change in the applied magnetic field H_a will generate a change in B that has a greater linear component to it when an air gap is present.

A further advantage to increasing the nominal operating gap is that gap disturbances have less effect on the force output, i.e., the magnitude of the stiffness is reduced. The downside of increasing the nominal operating gap is that more current is required to achieve a given force, thus dissipating more power. As can be seen from Figure 2-7, the normal stress is inversely proportional to the square of the air gap. Moreover, because a larger air gap will result in a less-uniform flux density in the air gap (i.e., more fringing), the B^2 relationship results in a further lower total force, and the target will need to be enlarged to achieve the same maximum force.

2.4.5 Target Geometry

Various modifications to the target geometry can improve the linearity of the actuator. Here we address two possible modifications.

One simple way to improve the performance of a reluctance actuator is by oversizing the target area relative to the stator pole face area in the off-drive-axis dimensions (x- and z-dimensions). An oversized target in the x-direction is shown in the left side of Figure 2-13. In this way, the actuator is made less sensitive to off-axis relative movement between the stator and target. To a first-order approximation, an oversized target will not generate any change in driving force from a relative motion in the x-axis or z-axis. The penalty paid is increased mover mass. In contrast, a target that is not oversized will result in changes in driving force when relative motion occurs. The reason for this is that in the oversized case, the air gap flux in the left and right air gaps travels through the same target area even when the target moves relative to the stator, whereas in the non-oversized case, the air gap flux in the left and right air gaps travel through a target area that varies as the target moves relative to the stator.

One method to reduce the sensitivity to changing fringing fields as the gap changes is to design the target with 'teeth' the same size as the stator pole faces. See the right-side illustration in Figure 2-13. Since fringing fields now have a larger air gap to traverse, and thus a higher reluctance to overcome, the fringing fields will be reduced. More of the field will be concentrated in the tooth. However, in contrast to the oversized-target design, the actuator force will become much more sensitive to relative off-axis motion between stator and target, and for this reason, this is not a strong candidate for lithography machines, which require 6-axis motion.

2.4.6 Laminating the Stator Core and Target

In an application that requires high-force accuracy over a broad frequency range, it is critical to laminate the core and target material. A solid chunk of steel used as the core or target material will result in internal eddy currents that will degrade the

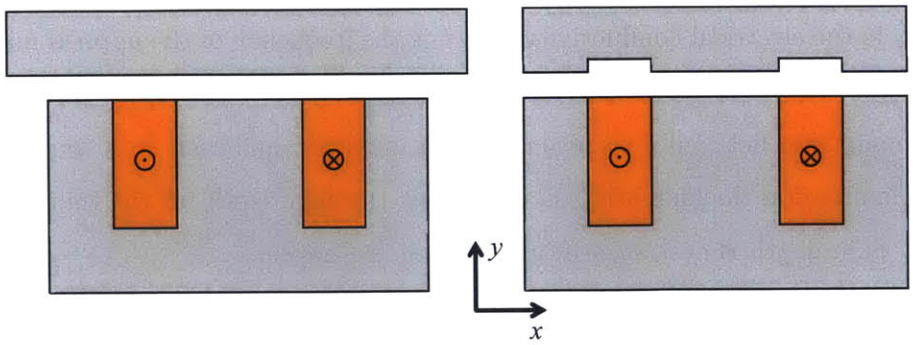

Figure 2-13: LEFT: reluctance actuator with oversized target. RIGHT: target with teeth.

accuracy and performance of the actuator. Moreover, the presence of eddy currents will increase the core losses.

The standard way to reduce eddy currents is to assemble the stator core and target with thin strips of permeable lamination material separated by insulating material. The thinner the lamination, the more effective it will be at breaking up eddy currents. An important parameter regarding laminations is the stacking factor: the ratio of permeable material thickness within a stack of laminations to the total stack thickness (which includes permeable material plus insulating material). As the laminations are made thinner, a higher proportion of the total thickness is taken up by insulation. This reduces the effective area for generating force.

A typical lamination thickness is 0.004" (~100 μm). Magnetic Metals lists the stacking factor for this lamination thickness as 90%. For comparison, a thinner lamination of 0.001" (~25 μm) has a stacking factor of only 75-83%, which will result in a noticeable force reduction for the same area. A key parameter for selecting lamination thickness is the skin depth. The skin depth is a measure of how far an applied magnetic field will penetrate a ferromagnetic material at a given frequency [39]. It is defined as the distance from the surface of the conductive material at which the flux density has decreased to $1/e$ of its surface value. The skin depth δ is given by

$$\delta = 2\sqrt{\frac{\pi}{\mu_r \mu_0 \sigma_e f}}, \tag{2.31}$$

where σ_e is the electrical conductivity and f is the frequency of the applied magnetic field signal. The skin depth is inversely proportional the square root of frequency. For the magnetic field fully to penetrate the magnetic material, it is important to select a lamination thickness that is well below the skin depth for the frequencies of interest. Skin depth is described in more detail in Chapter 5.

When designing a reluctance actuator with laminations, one consideration to take into account is how to orient the laminations. One option is to use stamped laminations in the shape of a 'U' or an 'E' and stack them on top of one other until the desired stator core height is achieved. Figure 2-14 shows an illustration of this. This is a standard method for building transformers. The target is assembled in a similar manner, but using a simple rectangular I-shape lamination rather than U-laminations or E-laminations. One downside of this is that anisotropic material cannot be correctly oriented in all of the flux path.

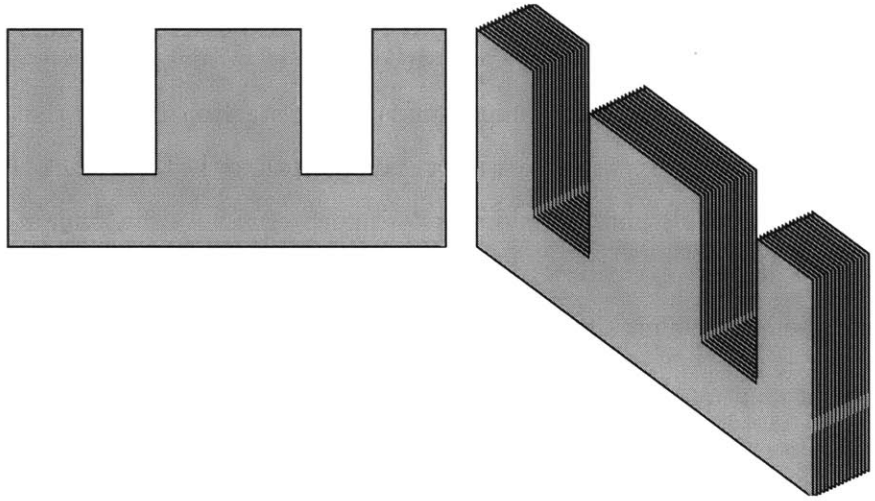

Figure 2-14: LEFT: a single E-lamination. RIGHT: an E-lamination stack.

Another option is to use tape-wound cut-cores. In this method, a thin strip of the core material is wound around a bobbin until the desired pole-face width is achieved. The resulting core is then cut in the center to make a 'U'-shaped actuator core. Two cut-cores can be placed side-by-side to make a three-pole actuator, see Figure 2-15. The target is assembled in a similar way, except that instead of cutting the tape-wound core in the center to form two U-cores, cuts are made at either end and the

resulting middle straight sections are used.

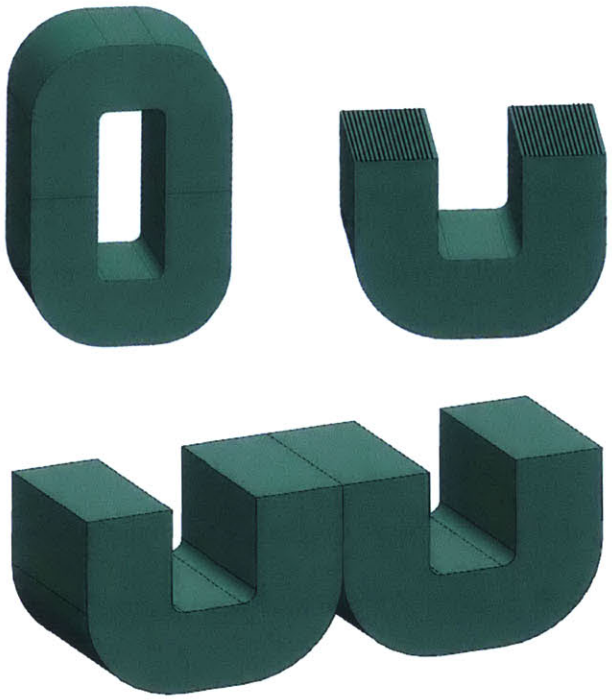

Figure 2-15: TOP LEFT: a tape-wound core with cuts in the center. TOP RIGHT: a tape-wound cut-core showing the lamination orientation. BOTTOM: two cut-cores placed side-by-side to form a three-pole actuator stator core.

In a cut-core actuator, the laminations are oriented differently from an actuator made from a stack of stamped laminations. In contrast to a U-core stack or an E-core stack, the grain orientation of the laminations is in the same orientation as the magnetic flux throughout the entire cut-core actuator. This results in higher core permeability (better for efficiency) and a smoother transition into the saturation region (better for control) [54].

Instead of laminated cores, an alternative way to reduce eddy currents is to use powder pressed iron cores. A powdered core consists of many small iron particles with polymer coatings pressed together. Because of the insulation between adjacent particles, these cores are very effective at breaking up eddy currents. However, the insulation acts as distributed air gaps within the core, which results in a much higher effective core reluctance. The permeability of the core is much lower than with a

laminated stack or with a laminated cut-core, resulting in lower efficiency and reduced force generation.

2.5 Linearization via Control

A reluctance actuator can also be linearized through control. In this section, we present some basic control strategies using standard feedforward and feedback techniques. We then present an overview of various potential sensors for feedback control. Finally, we present some advanced control methods that can be used further to enhance performance.

2.5.1 Standard Feedforward and Feedback Control

A combination of model-based feedforward control and local sensor-based feedback control can be used to linearize the reluctance actuator. The specific controller topology chosen depends on the sensors available for feedback and the required accuracy. Below we present several different potential controller topologies for a reluctance actuator that use combinations of feedforward control and feedback control. As a baseline, we assume that the reluctance actuator will have accurate current sensing, as this is also required for control of Lorentz actuators. Figures 2-16 and 2-17 show the block diagrams of various controller configurations.

Controller Topology with Current Sensing

Figure 2-16A shows a block diagram of a controller topology for a reluctance actuator in which only the current is sensed. Here F_d, B_d, and I_d are the desired actuator force, desired flux density, and desired current, respectively. Variables F, B, and I are the actual force, flux density, and current, respectively. The dotted blue box shows the current feedback loop. If the current feedback loop is sufficiently high bandwidth, the blue box can be approximated as a unity gain between I_d and I. In this topology, feedforward is necessary to invert the $F(B, g)$ and $B(I, g)$ relationships. The most basic form of feedforward in this case is to invert (2.8) or (eq:

flux density w core permeability) for $I(B_d, g_0)$ and (2.13) for $B(F_d, g_0)$, where g_0 is the nominal operating gap. A more accurate implementation is to use 1-D lookup tables based on real data rather than *a priori* analytic equations for the $I(B_d, g_0)$ and $B(F_d, g_0)$ functions. Alternatively, one can fit analytic functions to real data and then use these analytic functions for feedforward. These two latter options allow for magnetic saturation to be taken into account. Augmenting the $I(B_d, g_0)$ with an inverse hysteresis function can also improve the feedforward accuracy.

The dotted green box in the figure shows an additional feedforward path, which can be used to enhance performance further. Ideally, $FF_I = P_I^{-1}$, where P_I is the part of the actuator plant enclosed by the current feedback loop. Here, P_I represents the relationship between actuator drive voltage and actuator current, or, in linearized form, $P_I(s) = 1/(Ls + R)$, where L is the actuator inductance and R is the actuator resistance.

Two main challenges present themselves with a controller scheme that includes only a current sensor. The first is that because the $B(I, g)$ and $F(B, g)$ relationships depend on gap, the controller will suffer from large innacuracies if the changing gap is not taken into account. The second is that the complexity of the $I(B_d, g_0)$ relationship makes accurate modeling a challenge, particularly the modeling of magnetic hysteresis. When the controller must operate at high bandwidth, the computation time available for computing the output of a complex hysteretic model is much reduced. Additional phase lag between current and flux can also arise from eddy currents, making the $I(B_d, g)$ relationship a dynamic (and nonlinear) one, and thus further increasing the complexity.

Controller Topology with Current Sensing and Gap Sensing

Given that the operating gap will change dynamically by tens of micrometers during scanning, a controller that uses only current sensing will likely be unable to meet the required accuracy specifications. One way to rectify this is by adding a gap measurement. Figure 2-16B shows a block diagram of controller topology for a reluctance actuator in which the current and gap are both sensed. With the gap known, more

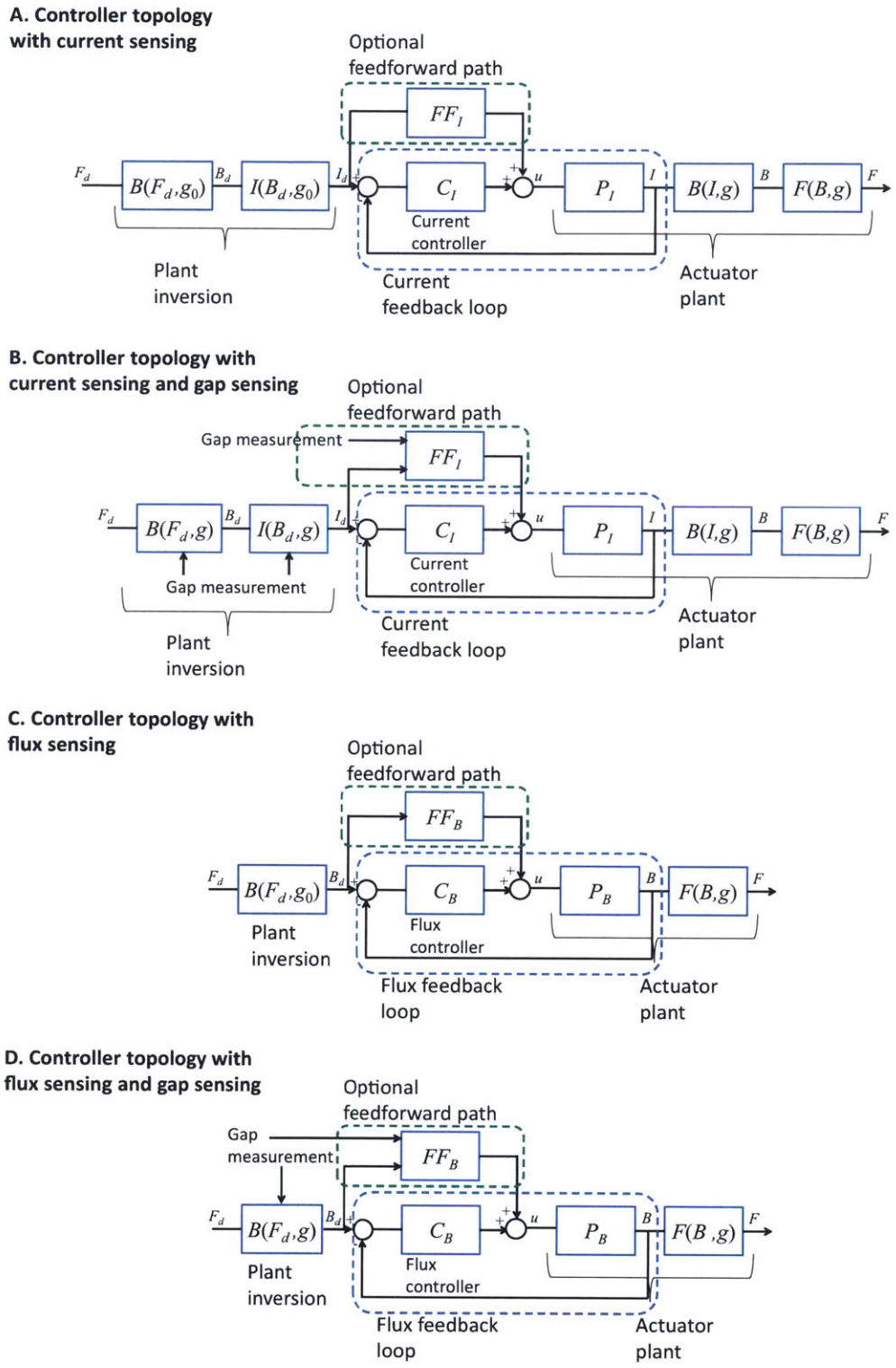

Figure 2-16: Block diagrams for four reluctance actuator control strategies.

E. Controller topology with flux sensing and current sensing

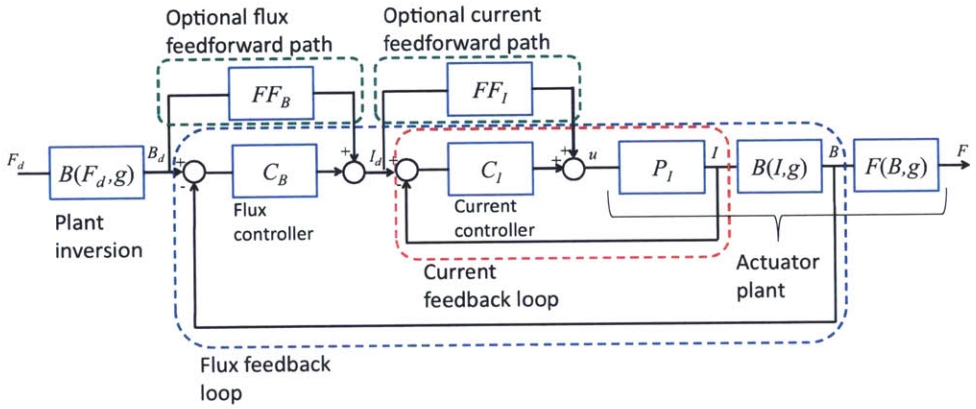

F. Controller topology with force sensing

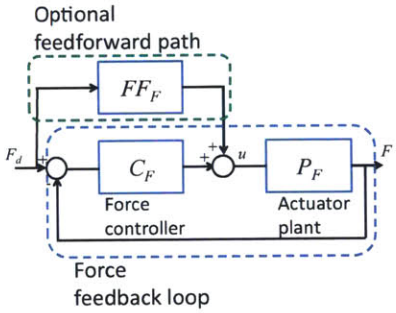

G. Controller topology with force sensing and current sensing

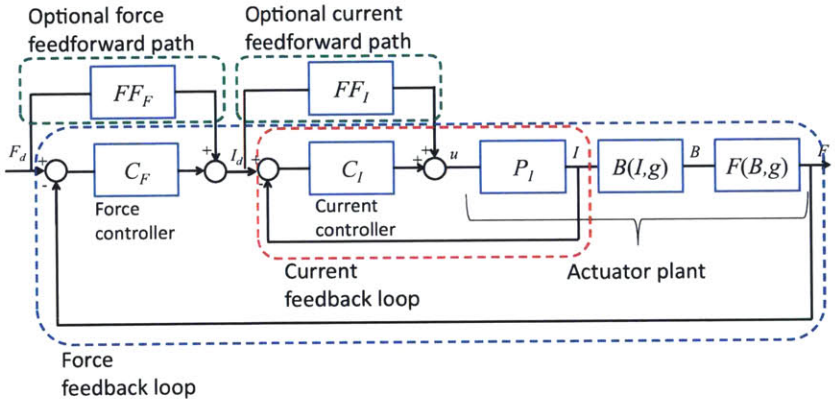

Figure 2-17: Block diagrams for three additional reluctance actuator control strategies.

accurate 2-D lookup tables can be implemented for the $I(B_d, g)$ and $B(F_d, g)$ functions. An inverse hysteresis model that depends both on desired flux density and operating gap can also be implemented for improved accuracy.

In a scanning lithography tool, measurements from differential sensors between the long-stroke stage and short-stroke stage are already available and can be used to estimate the gap. Since these sensors are not located in the reluctance actuator gap, it is necessary to transform these measurements into a local actuator coordinate system.

The price paid for adding a gap measurement is the increased complexity of the feedforward models. The lookup tables become 2-D lookup tables instead of 1-D lookup tables, and the inverse hysteresis model likewise becomes multivariable-dependent. The feedforward is also subject to errors arising from inaccuracies in the gap measurement: these include measurement delay, imperfect coordinate transformation, sensor nonlinearity, sensor noise, and the effect of flexible-body dynamics between the sensor location and the actuator air gap.

Controller Topology with Flux Sensing

If a flux sensor is used, the feedforward model becomes much simpler. This configuration is depicted in Figure 2-16C. If the flux feedback controller is sufficiently high-bandwidth, the blue box can be approximated as a unity gain between B_d and B. If the flux loop is sufficiently accurate and the relationship between force and flux has minimal dependency on gap, it is now only necessary to implement a $B(F_d, g_0)$ feedforward function. The $I(B_d, g)$ feedforward function and inverse hysteresis function are no longer necessary since B_d is achieved via a high-bandwidth feedback loop around the flux sensor (shown by the dotted blue box), although these can still be implemented in the optional feedforward path (dotted green box) if further performance enhancements are desired.

The flux controller will also tend automatically to correct for any flux reduction arising from eddy currents. The upshot is that the $B(F_d, g_0)$ inverse relationship required can be modeled as a static relationship even if eddy currents are present,

and thus will be easier to model accurately than the $I(B_d, g)$ relationship, which may require a frequency-dependent model in order to compensate for eddy currents.

Because of fringing field effects on force, a gap measurement is likely still needed for high-accuracy control even with flux feedback. Figure 2-16D is a configuration in which both the flux and the gap are sensed. However, unlike with the $I(B_d, g)$ relationship, this gap dependency is a second-order effect, so that the gap measurement accuracy and resolution needed for high-accuracy control with a flux sensor will be much reduced.

A third flux feedback configuration is shown in Figure 2-17E. In this configuration, the current is sensed as well. This allows us to include an inner high-bandwidth current feedback loop (dotted red box). If the bandwidth of this inner loop is sufficiently higher than the flux-controller bandwidth, the red box can be approximated as a unity gain between I_d and I from the perspective of the flux controller. This permits simpler controller design and higher bandwidth of the flux loop. The current controller will provide additional phase that compensates for the actuator inductance. In this way, the only phase loss that the flux controller has to compensate for is the phase loss from hysteresis and the phase loss from eddy currents. The phase loss from hysteresis will be minimal because of the linearizing effect of the operating gap, and the phase loss from eddy currents should also be minimal up to very high frequencies if the actuator is designed properly. A gap measurement (not shown) can also be included in this controller topology. Optional feedforward paths for both the flux and current can be included for improved performance.

Controller Topology with Force Sensing

Another type of controller topology includes a force feedback loop as shown in Figure 2-17F. If the force feedback loop is sufficiently high bandwidth and accurate, no additional feedforward is necessary. In terms of controller complexity, this topology is the simplest. Note also that no gap measurement is required in this scheme. The main drawback of this topology is the non-trivial challenge of implementing an accurate force sensor. One of the biggest challenges with force sensing is that the

acceleration of the actuator introduces an error into the force measurement. Another challenge is that the force sensor introduces a compliance into the mechanical force loop, which compromises bandwidth and increases the gap disturbance magnitude. A third challenge is that since the reluctance actuator can only generate force in one direction, the controller must be designed so as not to command a signal that results in a negative flux.

This controller configuration is augmented with a high-bandwidth current control loop in the topology of Figure 2-17G. This current control loop serves the same purpose that the current control loop in the flux feedback topology in Figure 2-17E served: it linearizes the plant as seen by the force controller and thus permits higher loop bandwidths and simpler controller designs. Other configurations not shown are also possible. For example, instead of a minor high-bandwidth current loop, we could include a minor high-bandwidth flux loop. Alternatively, we could include two minor loops, the innermost loop for the current and a second minor loop for the flux.

2.5.2 Sensors for Feedback Control

One of the key decisions in the design of a reluctance actuator is selecting an appropriate sensor for feedback control and choosing a location for this sensor. Evaluating different sensor options is based on various considerations such as the effect on actuator and stage dynamics, the effect on operating air gap, the relationship between sensor output and actuator force, sensor noise, sensor bandwidth, and sensor reliability. In this section, we will address sensors that can provide estimates of the actuator flux or actuator force. We do not cover current sensors here, since accurate current sensing is assumed to be already available owing to its use with present state-of-the-art Lorentz actuators. The types of possible sensors can be grouped according the following classification scheme: 1) flux sensors; 2) force sensors; 3) acceleration sensors; and 4) a combination of force sensors and acceleration sensors.

Flux Sensing

A sensor to measure magnetic flux density in the reluctance actuator air gap is required if the flux feedback topology shown in Figure 2-16C is chosen as the control scheme. There are several advantages to flux sensing over the alternatives. The measured signal is bipolar in the case of a Hall-effect sensor or a sense coil, i.e., a negative actuator flux results in a negative sensor output. This means that the sensor can distinguish between first- and fourth-quadrant operating regimes and the controller can transition through the zero-flux point without being subjected to problems arising from switching. That said, it is likely that the reluctance actuator will be operated with a bias force and will be driven only in the positive flux region, so the sensor bipolarity may be a moot point: because of the squared relationship of force with flux, there is no need to operate in the negative flux region. The sensor location and fixturing will likely have an insignificant effect on system dynamics, both in terms of stiffness and added mass. Another advantage is that stage acceleration will not affect the sensor measurement.

The main drawback of flux sensing is that the relationship between measured flux and actuator force must be modeled accurately in order to achieve accurate force control. This relationship, whether modeled analytically or implemented as a lookup table, will likely depend on operating gap and possibly on rotation of the mover relative to the stator.

Flux sensors can be categorized as either DC sensors or AC sensors.

(a) *DC Flux Sensors*: DC sensors include Hall effect sensors, magnetoresistive (MR) sensors, and giant magnetoresistive (GMR) sensors. All have the capability of measuring magnetic flux density at DC. This capability for direct flux measurement is its primary advantage over a sense coil, which is AC-coupled.

There are several disadvantages to direct-measurement sensors. One disadvantage is that the measurement is local: rather than measuring the average flux density over the entire pole face area, the measurement is taken at only a small fraction of the total pole face area. Since the flux density distribution over the

pole face will not be perfectly uniform, such a measurement will result in greater sensitivity of the actuator force-to-measured-flux relationship to changes in the flux distribution due to gap variation or off-axis relative motion between the stator and mover. The force-to-measured-flux relationship will also be more sensitive to local variations in saturation of the magnetic material. One way to reduce this effect is by using multiple sensors distributed across the surface of the pole face, but this comes at the cost of higher reliability risk, additional A/D channels, additional wires, and additional computation. Another difficulty to direct-measurement sensors is that the sensor's placement is typically in a high-risk location (on the pole face). This also limits the minimum air gap achievable and thus reduces the maximum force density capability of the actuator. One way to retain a small working gap is to recess the sensor in the pole face, but this reduces the flux measured by the sensor relative to the flux in the air gap.

(i) *Hall-Effect Sensors*: One possibility for sensor-based feedback control is to incorporate a Hall-effect sensor into the actuator operating gap. Figure 2-18 illustrates a reluctance actuator with a Hall-effect sensor. The Hall voltage, v_H, is proportional to both the current input to the sensor and the magnetic flux density transverse to the sensor [91]. This voltage is then the feedback variable used to compare against the desired flux density. One downside of a Hall-effect sensor is that it is an active sensor: electronics are necessary to provide a constant current to the Hall cell. Hall-effect sensors also typically have inferior noise characteristics and have higher temperature sensitivity compared to a sense coil.

(ii) *MR and GMR Sensors*: MR sensors are based on the property of magnetoresistance that some materials exhibit. Magnetoresistance is the phenomenon whereby a material's electrical resistance changes in response to an applied magnetic field. GMR sensors exhibit the same phenomenon, but show a much larger percentage change in resistance for the same mag-

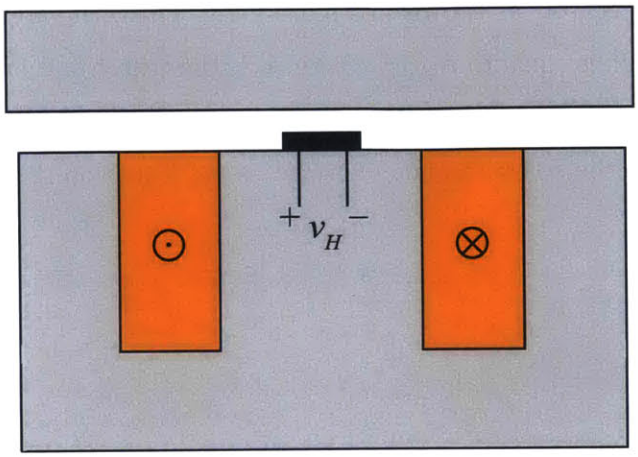

Figure 2-18: A reluctance actuator with a Hall-effect sensor in the air gap.

netic field. Like Hall-effect sensors, these sensors require a current or voltage source. The sensing resistors are usually configured as a Wheatstone bridge. Downsides of MR and GMR sensors are that they typically have a low linear range, they exhibit hysteresis, and they are usually unipolar, i.e., one cannot distinguish between positive and negative magnetic fields.

(b) *AC Flux Sensors (Sense Coil)*: A sense coil works by application of Faraday's Law [39], shown here as

$$\oint_C \mathbf{E} \cdot d\boldsymbol{l} = -\frac{d}{dt} \iint_S \mathbf{B} \cdot d\mathbf{S}. \tag{2.32}$$

This states that the line integral of the electric field around a closed contour is equal to the negative rate of change of the surface integral of the magnetic flux density passing through the contour. Equation (2.32) can be simplified to

$$\oint_C \mathbf{E} \cdot d\boldsymbol{l} = -\frac{d\bar{B}}{dt} A, \tag{2.33}$$

where A is the area of the surface and $\bar{B}$ is the mean flux density normal to the

surface.

Suppose that a coil with N_S turns is wound around the center pole face of the reluctance actuator, as shown in Figure 2-19. Then, the area A that the flux passes through is equal to $N_S A_p$, where A_p is the center pole face area. The left-hand side of (2.33) is simply the negative of the electrical potential, or voltage [39], between the coil terminals, denoted as v_S. Equation (2.33) now becomes

$$v_S = N_S A_p \frac{d\bar{B}}{dt}. \tag{2.34}$$

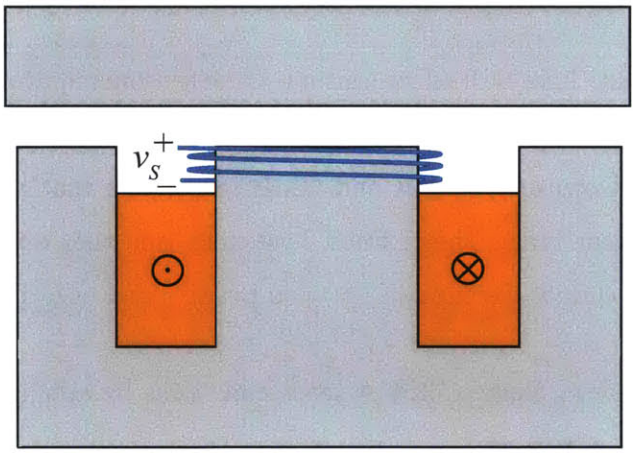

Figure 2-19: A reluctance actuator with a sense coil wound around the center pole face.

Solving for $\bar{B}$, we write

$$\bar{B} = \frac{1}{N_S A_p} \int v_S dt. \tag{2.35}$$

The average flux density passing through the area enclosed by the sense coil is proportional to the integral of the sense coil voltage.

A sense coil measurement offers several advantages over a direct-flux measurement. It is a more global measurement: since it is wound around the pole face, the voltage at the terminals of the sense coil will be proportional to the *aver-*

age flux rate of change through the pole face. This results in lower sensitivity of the force-to-measured-flux relationship to gap variations, to off-axis relative motion between stator and target, and to local variations in saturation. Another advantage is that a sense coil usually has better noise characteristics than a Hall-effect sensor. A third advantage is that it is a simple passive sensor: it only requires two leads to the coil output, whereas a Hall-effect sensor or MR sensor requires additional electronics. Electronics may be needed to perform the required integration, but this can be done remotely. Finally, a sense coil does not take up real estate in the air gap, permitting the design of a more efficient actuator and protecting the sensor from damage should a crash occur.

The main disadvantage of a sense coil is that it does not provide a true DC measurement. This results in drift when integrating the signal and poses a significant challenge to obtaining an accurate estimate of the DC flux. One potential way to circumvent this problem is to estimate the DC flux from the actuator current measurement. However, modeling the hysteresis between the current and flux density is a challenge in its own right.

(c) *Hybrid Configuration*: A hybrid measurement scheme takes advantage of the positive aspects of both a DC sensor and sense coil. One can use a Hall-effect sensor for DC and low-frequency measurements and use a sense coil for high-frequency measurements. Katalenić in [49] demonstrates one method for implementing such a configuration.

There are three main disadvantages with this arrangement. First, extra sensors result in extra wires and extra channels and more reliability concerns. Second, combining the two measurements into one flux estimate is not necessarily straightforward since the two sensors will have different calibrations. The signal processing consequently becomes more complex. Finally, we lose one of the benefits of using a sense coil only: the air gap must be made large enough to accommodate the DC sensor, thereby reducing the maximum force density capability of the actuator.

Force Sensing

Force sensing is an alternative to flux sensing. It is required if the force feedback configuration shown in Figure 2-16D is used. With force sensing, load cells (or strain gauges mounted to flexures) measure a force proportional to their displacement. Force sensing allows for direct sensing and control of the variable of interest, rather than having to design a feedback loop around an intermediate variable such as flux. One advantage this presents is that the need accurately to model the nonlinear relationship between flux and force and gap is eliminated. Another advantage over flux sensing is that one force sensor is capable of measuring the total actuator force, whereas one flux sensor is only capable of measuring the flux in one air gap, despite the force being dependent on the flux in *each* air gap. A final advantage to force sensing is that a load cell will not be located in the air gap, unlike a Hall-effect sensor or MR sensor.

There are notable downsides to force sensing, however. Because of the fundamental $F \propto B^2$ relationship, the sensor is unipolar, i.e., the sensor cannot distinguish the direction of flux. This can result in controller difficulties around the zero-flux point. Another potential problem with a force sensor is that it adds another stiffness element in the force loop, which can lead to deteriorated system dynamics. A third problem with force sensing is that load cells will not measure the true applied force because the inertial force from the stage acceleration introduces an error into the measurement. Compensating for this error is the most challenging difficulty with force sensing. Finally, an actuator mechanical design that incorporates load cells and is properly constrained presents challenges more complex than those associated with flux sensing. As with flux sensors, force sensors can be categorized as DC force sensors or AC force sensors.

(a) *DC Force Sensors (Strain Gauge Load Cells)*: Strain gauges provide a DC force measurement, and thus have a similar advantage over piezo-based load cells (which are AC-coupled) to a Hall-effect sensor over a sense coil. Strain gauges, however, have much lower stiffness than piezo-based force sensors, and this can adversely affect the actuator or stage dynamics. Another downside of strain

gauges is that they are sensitive to temperature. Strain gauge packages that compensate for temperature are available, but they dissipate additional power.

A strain gauge measures deflection by measuring the change in electrical resistance of a material undergoing mechanical strain. This resistance change is usually measured using a Wheatstone bridge. In a strain-gauge load cell, the strain gauge is attached to some structure (such as a flexure) that deforms linearly with load. The force can then be computed from Hooke's Law.

Figure 2-20 shows one potential actuator configuration that incorporates strain-gauge sensors mounted to flexures on the target side. The use of two strain gauges permits the measurement of actuator force and one actuator moment. One side of each flexure is attached to the target. The other side of each flexure is shown connected to ground. In a real lithography machine, this connection would be to the short-stroke stage instead.

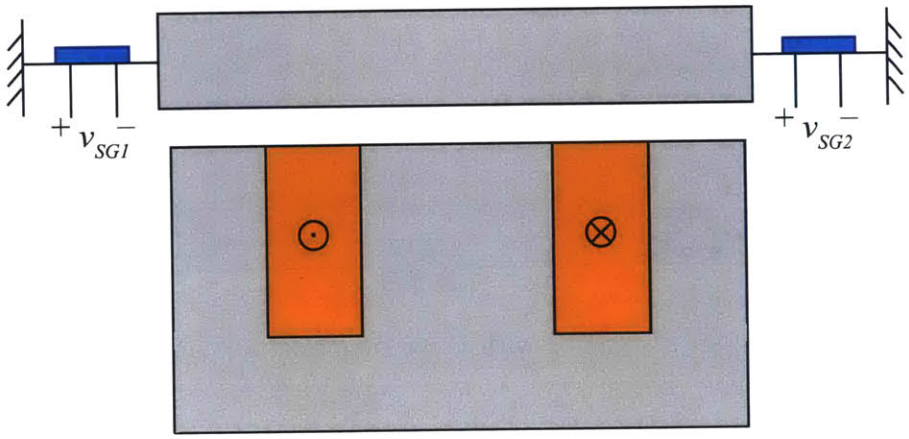

Figure 2-20: A reluctance actuator with strain guages mounted to flexures attached to the target.

(b) *AC Force Sensors (Piezoelectric Load Cells)*: Piezoelectric load cells offer the advantage of having high stiffness and large dynamic range.

Piezoelectric materials accumulate electrical charge when stress is applied to

the material. A charge amplifier measures this charge and converts it to a voltage proportional to the applied load. Such a piezo-based force sensor cannot measure true static loads because the charge accumulated from a static load will gradually dissipate.

Figure 2-21 shows one potential actuator configuration that incorporates three piezoelectric load cells mounted to the stator side. In a scanning stage, the other sides of the load cells would be connected to the long-stroke stage (not shown in the figure). The three load cell outputs can be tied together so that the voltage output of the charge amplifier is proportional to the sum of the loads applied to each piezo cell. Alternatively, separate charge amplifiers can measure the charge from each piezo cell independently, which would allow the measurement of actuator force and two actuator moments.

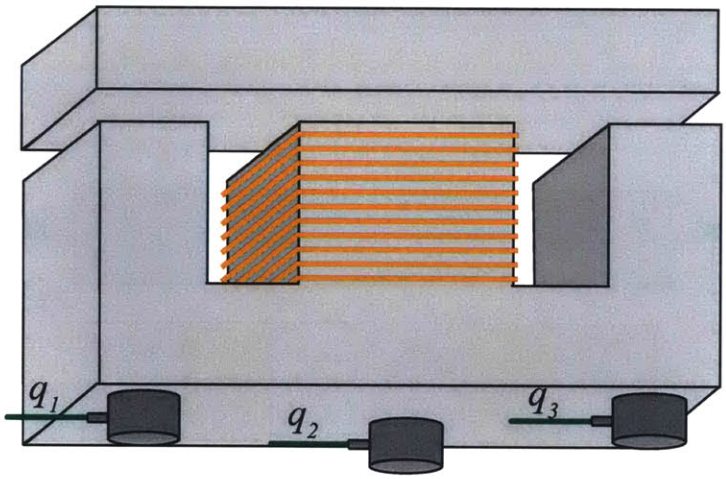

Figure 2-21: A reluctance actuator with three piezoelectric load cells connected to the stator.

Acceleration Sensing

Acceleration sensing is an alternative to force sensing. Instead of measuring the force directly using force sensors, the force can be estimated from the stage acceleration. The force on the stage is proportional to the stage acceleration. This includes components proportional to the snap and jerk (and higher-order derivatives) because of the

flexible-body dynamics of the stage. These components would have to be estimated, possibly in a feedforward manner.

Accelerometers are small and can be mounted easily to the stage with very little added mass. An added advantage is that an accelerometer will not affect the actuator operating gap. Figure 2-22 shows an actuator with an accelerometer attached to the target.

The most obvious liability of using an accelerometer for sensing is the one already noted: it provides only an indirect measurement of the force. A second downside is that the accelerometer must be attached to the short-stroke stage rather than to the long-stroke stage to obtain a reasonable estimate of the force. The upshot is the concomitant risks of disturbances from the additional wires and chuck distortion from accelerometer power dissipation.

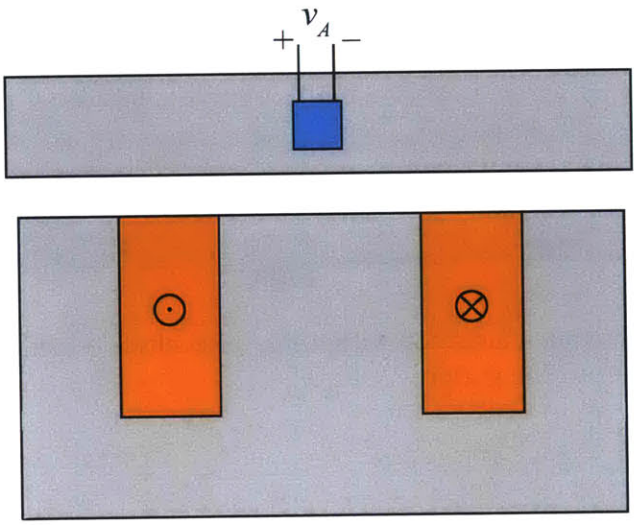

Figure 2-22: A reluctance actuator with an accelerometer attached to the target.

Force + Acceleration Sensing

Figure 2-23 shows an actuator with an accelerometer and three piezoelectric load cells mounted to the stator. By using both force sensors and accelerometers, some of the problems involved in using only one or the other method can be remedied.

An accelerometer permits compensation for the acceleration error due to force sensing alone. Force sensing provides a direct measurement of the force, rather than relying on force estimation required of acceleration sensing alone. Moreover, all the sensors can be located on the stator, which is not feasible with acceleration sensing alone.

The drawbacks of combined force and acceleration sensing include having to incorporate additional sensors and having to calibrate and combine different measurements into an accurate force estimate. As with force sensing alone or acceleration sensing alone, a combined force and acceleration measurement is a unipolar measurement.

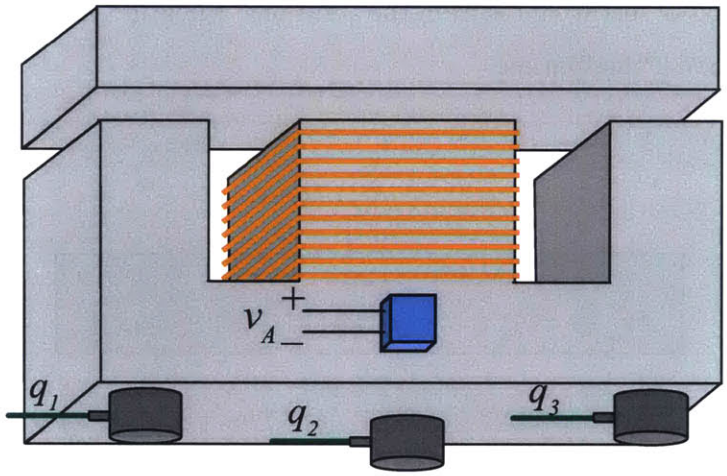

Figure 2-23: A reluctance actuator with three piezoelectric load cells and one accelerometer mounted to the stator.

2.5.3 Advanced Control Techniques

Beyond standard feedforward and feedback control, other control techniques can be used further to improve actuator performance. In this section, we will briefly describe two of these: feedback linearization and iterative learning control (ILC). These techniques are used in conjunction with standard feedback and feedforward techniques rather than in lieu of them.

Feedback Linearization

With feedback linearization, a nonlinear system is transformed into an equivalent linear system by feeding back a measured variable as an input to the transformation. This transformation permits the use of standard linear feedback control techniques. For example, suppose $y = P(v, x)$ is the nonlinear plant we are trying to control, and we have access to a measurement of x. If P is invertible, then preceding the plant with its inverse $P^{-1}(y, x)$ will yield the linear system $P^{-1}P = 1$. Figure 2-24 demonstrates the concept. The measurement x is fed back into the transformation $v = P^{-1}(u, x)$. Since $v = P^{-1}(u, x)$ and $y = P(v, x)$, then $y = P\left(P^{-1}(u, x), x\right)$, and the control signal u equals the output y. The controller C can be designed using linear control techniques since the effective plant is now equal to 1.

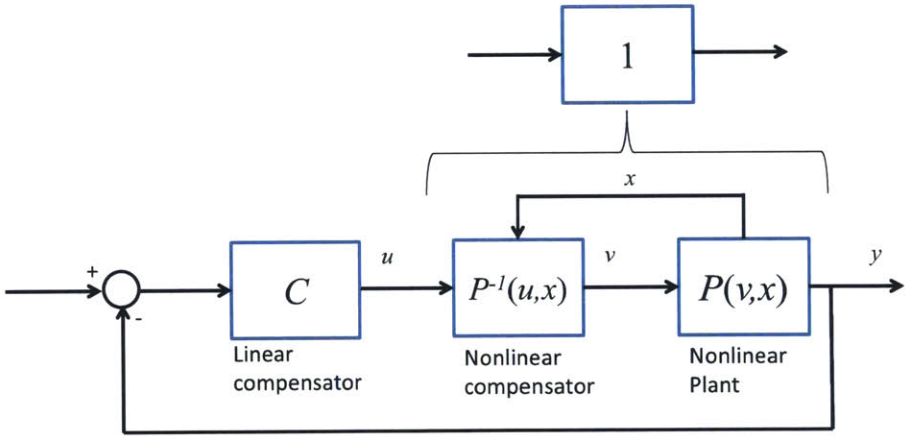

Figure 2-24: Block diagram of a controller with feedback linearization.

For some classes of nonlinear systems, feedback linearization is straightforward and can easily be implemented in software or an FPGA. A possible implementation of feedback linearization for a reluctance actuator controller is shown in Figure 2-25. Here the actuator flux density is being controlled via feedback, using the topology shown in the dotted blue box in Figure 2-16C. Figure 2-25 has an extra $I(B, g)$ block in the loop compared to the loop in Figure 2-16C. This is the nonlinear controller that transforms the nonlinear system into a linear one. Note that because B depends on the gap, a gap measurement input or gap estimate input is necessary for accurate

feedback linearization. If $I(B, g)$ is a perfect inverse of $B(I, g)$, the plant as seen by the linear controller is equal to 1.

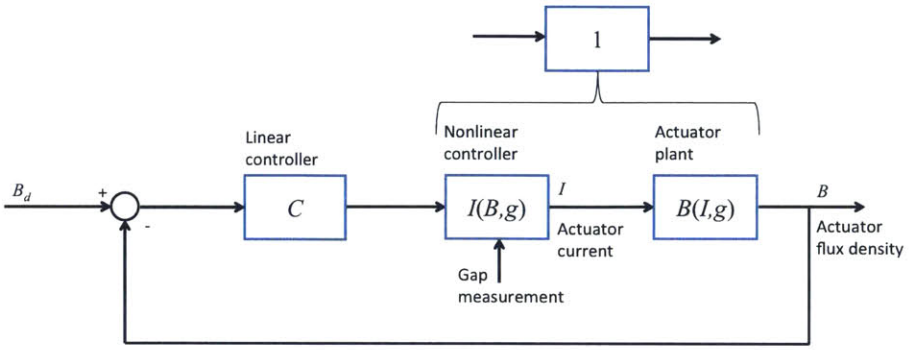

Figure 2-25: Feedback linearization for a reluctance actuator.

For a reluctance actuator flux control, feedback linearization offers the potential for effective control authority at both low flux levels and high flux levels near saturation. Without feedback linearization, feedback control authority degrades at saturation because the loop gain decreases.

The downsides of feedback linearization are the same as those for feedforward: it requires an accurate plant model and is sensitive to changes in the plant. Details regarding feedback linearization as applied to electromagnetic actuators can be found in [56, 85, 84].

Iterative learning control

Iterative learning control (ILC) is a technique that can be applied to systems with repeating trajectories. Each time a trajectory is completed (called a trial or iteration), ILC stores and uses information from that trial and previous trials to improve the tracking performance for the next trial. ILC does this by effectively learning the input required to drive the tracking error toward zero; as such, it changes the feedforward signal from trial to trial. It can be thought of as a feedback controller in the iteration domain: feedback after each trial is used to change the feedforward signal.

Figure 2-26 is a block diagram of the standard ILC topology [73]. The error sequence during the k^{th} iteration, e_k, is passed through the learning controller L

and then added to the k^{th} iteration feedforward input sequence, u_k. After passing the resulting combination through a 'robustness' filter Q, the result is stored as the feedforward input sequence for the $k+1$ iteration, u_{k+1}.

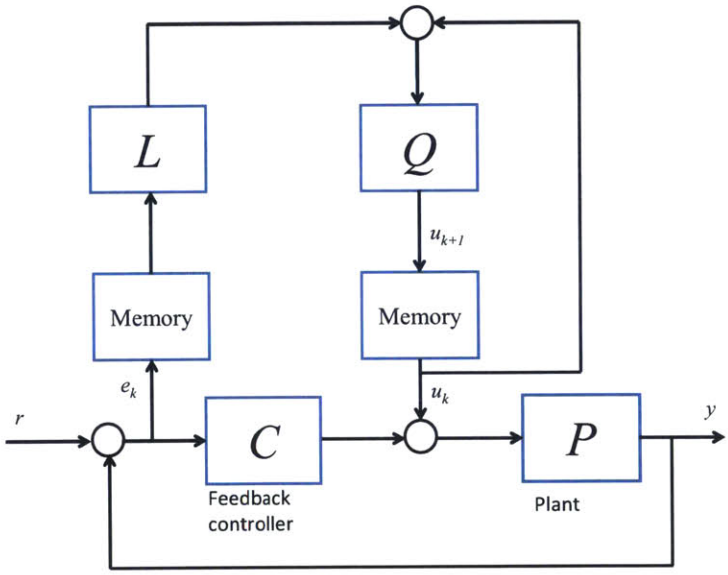

Figure 2-26: Standard ILC configuration.

Assuming $Q = 1$ for the moment, u_{k+1} can be written as

$$u_{k+1} = \left(I - \frac{LP}{1+CP}\right) u_k + \frac{L}{1+CP} r. \tag{2.36}$$

The optimal L is then given by the inverse of the process sensitivity function, $L = (1 + CP)/P$. Then $u_{k+1} = P^{-1}r$ and the output will perfectly track the desired reference. However, $P/(1 + CP)$ is often not invertible over the entire frequency band. In such cases, L is designed to approximate the inverse of the process sensitivity function as well as possible. To ensure convergence of the sequence of inputs, u_k, the criterion that must be satisfied is

$$\left\| I - \frac{L(s)P(s)}{1+C(s)P(s)} \right\| < 1 \tag{2.37}$$

for any $s = j\omega$. To ensure that this requirement is satisfied at all frequencies, a

robustness filter Q is added, such that the stability criterion now becomes

$$\left\| Q(s) \left(I - \frac{L(s)P(s)}{1 + C(s)P(s)} \right) \right\| < 1 \tag{2.38}$$

for any $s = j\omega$. The robustness filter Q is a low-pass filter with unity gain at frequencies below the cutoff. Designing Q this way ensures that at frequencies below the cutoff, the performance of the learning controller will be unaffected.

ILC thus offers a straightforward way to improve the feedforward accuracy from one iteration to the next. At frequencies below the crossover of the standard feedback loop, the gain of the optimal learning controller is dominated by the feedback controller gain rather than the plant gain, so modeling the plant perfectly is less critical than in the case of standard feedforward with no learning. ILC can also adapt to changes in the plant over time. However, it cannot adapt to non-repeating disturbances. Further details on standard ILC can be found in [34, 73].

Other variations of ILC can be found in the literature. These include lifted ILC [34, 73], current-iteration ILC versus past-iteration ILC [89, 17], and PD- and PID-type ILC [63, 17]. Two good survey papers on ILC are [2, 17].

In this section, we have presented a brief overview of various control techniques that can be applied to a reluctance actuator. In the next section we will shift our focus from reluctance actuator control to variations on the basic reluctance actuator configuration.

2.6 Alternate Actuator Configurations

Thus far in this chapter we have analyzed the reluctance actuator with a three-pole stator. The most basic types of electromagnetic actuators include a single soft-magnetic stator in the form of a 'U'-core (two poles) or an 'E'-core (three poles) with one independent actuator coil. A number of variations upon this building block exist. In this section we will consider a few of them.

2.6.1 Double-sided Actuator

A double-sided actuator, also described as a 'push-pull' pair, consists of a stator on either side of the target. Such a configuration is shown in Figure 2-9. The primary advantage with a push-pull pair is that the actuator module is bipolar: it can generate force in both the positive and negative directions.

Figure 2-27 shows a chuck with 'pull-only' reluctance actuators and a chuck with push-pull actuator pairs. The boxes marked 'x' and 'z' represent the x-Lorentz actuators and z-Lorentz actuators, respectively. With the pull-only configuration, the entire y-force during acceleration is applied at only one end of the chuck. With the push-pull configuration, the y-force can be distributed evenly among all four y-actuators. This results in the y-force distribution being symmetric about the x-axis. This leads to less distortion of the chuck and and is less likely to excite problematic modes. An additional advantage is that the total target mass can be reduced since each target in a push-pull configuration must only be capable of generating half the force that a target in a pull-only configuration must generate.

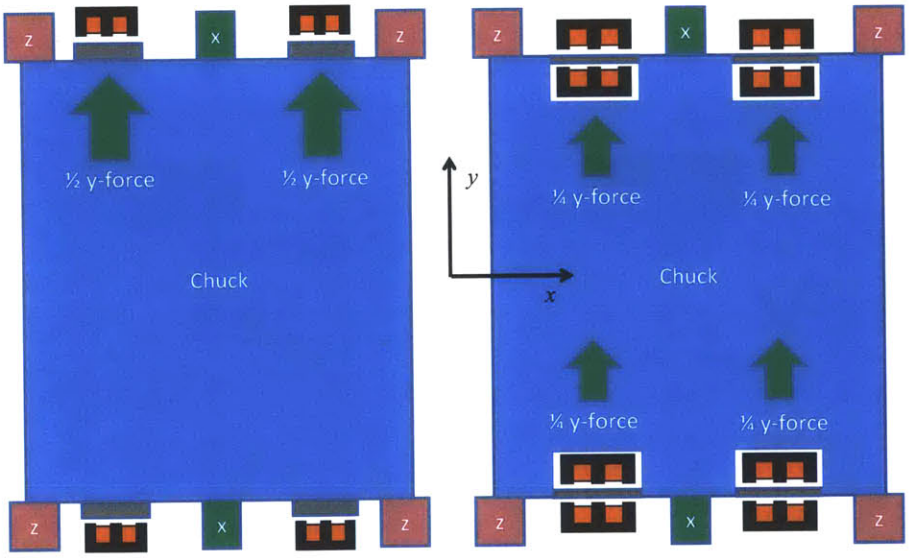

Figure 2-27: LEFT: chuck configuration with one-sided (pull-only) actuators. RIGHT: chuck configuration with double-sided (push-pull) actuators.

The major downside of a push-pull chuck configuration is that the chuck design

and long-stroke stage design become much more complex since the actuators interlock. Designing the reluctance actuators to operate at small air gaps is also more challenging because we now have to be concerned with tolerance stackups on both sides of the target. Moreover, with a pull-only actuator, the target can be designed such that it functions as the crash stop itself, for example by being preloaded with a soft spring against a hard stop. In this way, during normal operation, the target has a rigid connection because the spring pushes it against the hard stop and the stator generates force on the target in the same direction as the spring. However, in the case of a crash, the target gets pushed against the soft spring, which will help absorb the energy from the impact and protect the glass chuck from damage. Such a configuration is shown in Figure 2-28. Alternatively, the hard stop and preload spring could be located on the stator side. This concept has the potential to allow smaller operating gaps than would be permitted otherwise since we do not have to allow additional air gap for crash distance. In contrast, with a push-pull actuator pair, designing the target itself to be the crash stop is less feasible since the target must be rigid in both directions (although it may be possible to design the stators as crash stops). This means that the air gap must be larger to avoid the stator hitting the target in the case of a crash.

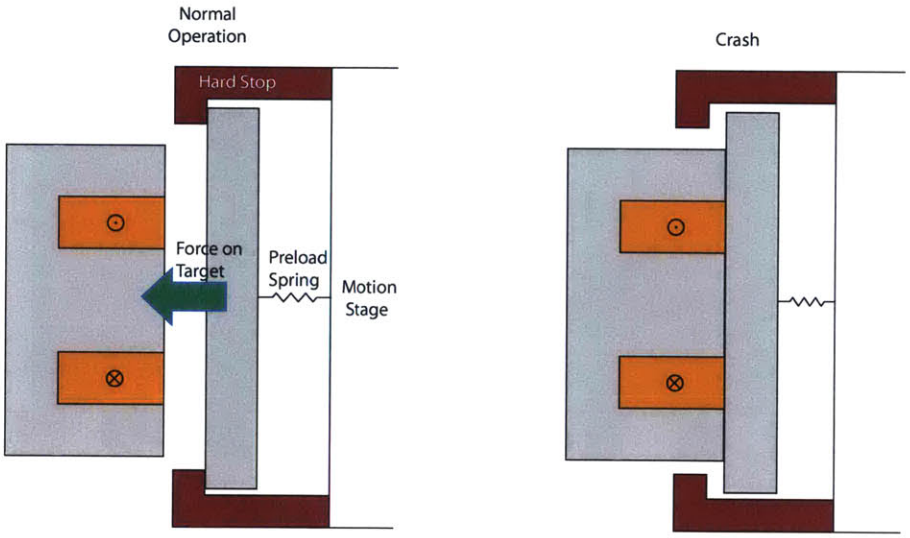

Figure 2-28: LEFT: Target is preloaded with spring against hard stops for normal operation. RIGHT: Spring allows target to function as soft stop in case of crash.

2.6.2 Multi-DoF Actuators

The actuator configurations shown thus far have only included one independent actuation coil per stator. This is the simplest configuration, but it only permits control of the force in the drive axis. Owing to stage rotation, asymmetry, and other non-idealities in the actuator, the actuator in practice will exhibit stray torques about both axes orthogonal to the drive axis. One way to mitigate these stray torques is to make the actuator as compact as possible in these axes. Another way is to design the actuator with multiple actuation coils and multiple sensors so that these stray torques can be measured and controlled independently of the force.

First, we qualitatively demonstrate why a three-pole actuator is more susceptible to parasitic torques than a two-pole actuator. Consider Figure 2-29. If there is a rotation of the target relative to the stator, the effective air gap on one side becomes smaller than the effective air gap on the other side. Since there are two separate flux paths, more flux travels through the path with the smaller air gap, generating more force on that side, and consequently, a torque. The relative sizes of the arrows in the figure qualitatively demonstrate the amount of flux going through each flux path. The air gaps in the two flux paths operate analogously to a parallel resistor circuit where the resistances are changing: as one resistance gets smaller than the other, more current will flow through that leg of the resistor network. Likewise, as one air gap gets smaller in the magnetic circuit of the stator core (and thus, the corresponding reluctance gets smaller), more flux will flow through that leg of the magnetic circuit.

A two-pole actuator does not have this problem since there is only one primary flux path. If there is a rotation of the target relative to the stator, all the flux must still go through the same path and so to a first-order approximation there are no parasitic torques produced.

If the three-pole actuator includes two independent actuator coils, this torque can be controlled. Figure 2-30 shows what this configuration might look like. The two independent flux paths are driven with amp-turns NI_1 and NI_2. The flux paths

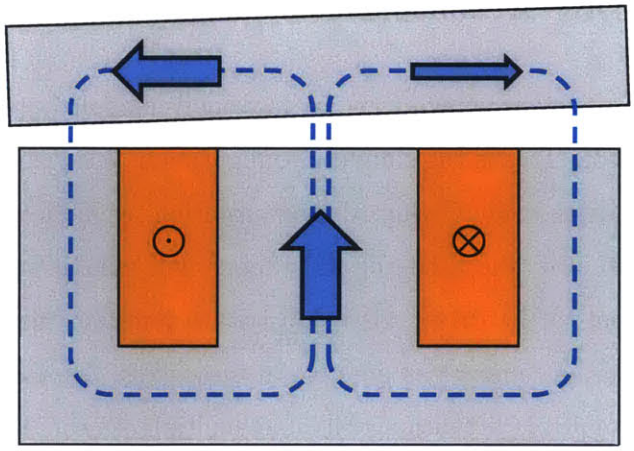

Figure 2-29: A three-pole actuator showing the effect on flux distribution of a relative rotation between the stator and target.

reinforce in the center leg. The flux in the left and right air gaps can be driven differentially to generate a torque to counteract any parasitic torque that arises. For this 2-DoF actuator to work effectively, both the force and torque must be sensed or estimated, thus requiring two independent sensors. This could take the form of two Hall-effect sensors or sense coils, one on the right pole and the other on the left pole, for example, or the stator could be mounted on two or more load cells. Another possibility would be to measure both the left and right air gaps and estimate the force and torque from the gap measurements and actuator currents. These sensor configurations are not shown in the figure.

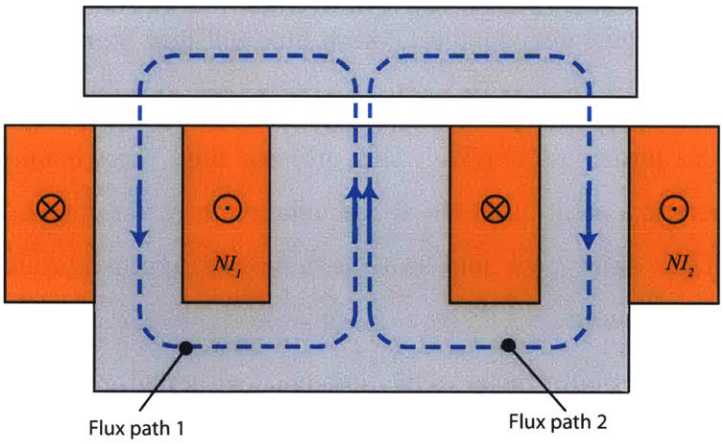

Figure 2-30: A three-pole actuator with two independent actuator coils.

Other multi-DoF actuator configurations are also possible. For example, the configuration presented above could be adapted also to control the torque about the x-axis by adding a second set of poles and actuator coils in the out-of-plane direction.

2.6.3 Multi-pole Actuators

An alternative to the two-pole or three-pole stator designS is a stator having additional poles. Additional poles allow for a smaller target mass and stator mass for the same force capability [56]. The reason for this is that by splitting the flux among additional poles, the minimum thickness of the target needed to prevent flux saturation can be made smaller. Likewise, the minimum thickness of the stator back leg can be made smaller.

For example, consider the case of a three-pole actuator versus a two-pole actuator. In the three-pole actuator, there are two primary flux paths as shown in Figure 2-30. The flux from the center pole face is split between the two sides. In contrast, in a two-pole actuator, all the flux travels in one path through the target. The upshot is that the target in the three-pole actuator will not saturate as quickly and can therefore be made thinner. Since force is proportional to pole face area, the three-pole actuator will have the same force capability as the two-pole actuator if the total pole face areas of each are identical. Thus, the target for a three-pole actuator with identical force-generating capability to a two-pole actuator can be made significantly lighter than the two-pole actuator target. This phenomenon can be adapted to multi-pole stator designs to decrease the target mass further if desired. Figure 2-31 shows a five-pole actuator.

Drawbacks of multi-pole actuators include increased complexity and reduced compactness in the horizontal direction, which can increase stray torques. However, the additional coil(s) in a multi-pole stator design permit the independent control of both force and stray torque.

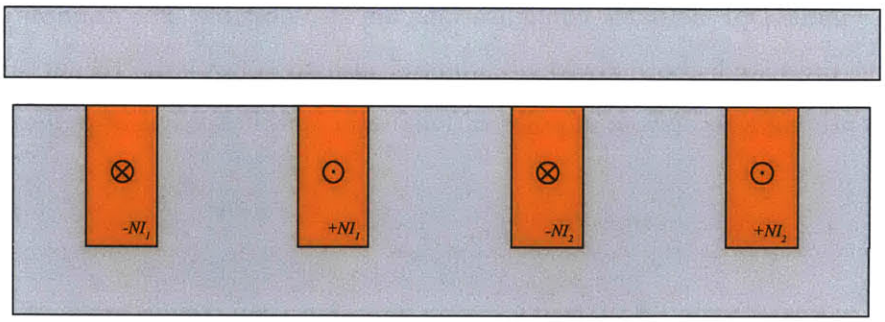

Figure 2-31: A five-pole actuator with two independent actuator coils.

2.7 Summary

In this chapter, we developed the fundamental electromagnetic theory underlying the reluctance actuator. By comparing the reluctance actuator operation with the Lorentz actuator operation, we learned that the reluctance actuator can generate higher forces at small air gaps, but that it suffers from higher stiffness. We gave an overview of core materials and learned that CoFe is likely the best candidate for a high-force-density actuator owing to its high saturation flux density. We presented an overview of the nonlinearities inherent to a reluctance actuator and reviewed techniques with which to linearize the actuator through actuator configuration and control. We learned that an air gap tends to linearize the actuator by 'shearing' the hysteresis curve. We will make use of this fact in Chapter 6. We determined that flux control is an attractive controller topology, as it eliminates a number of nonlinearities present with current control but does not suffer from the problems intrinsic to force sensing. Finally, we presented some variations on the basic reluctance actuator configuration.

In the next chapter, we focus on the reluctance actuator hysteresis. We present methods for modeling ferromagnetic hysteresis. These models will ultimately be used for real-time flux estimation and flux control to linearize the actuator.

Chapter 3

Hysteresis Modeling

In this chapter, we present approaches for modeling ferromagnetic hysteresis. The purpose of these models is to incorporate one of them into a full reluctance actuator model that can then be used both to predict and to investigate actuator behavior and to provide an accurate estimate of the air gap flux density for real-time control. In this chapter, we examine only the basic hysteresis model itself. Incorporation into a full actuator model will be investigated in subsequent chapters.

First, we present a general overview of hysteresis phenomena and review physical explanations for hysteresis in ferromagnetic materials. We then review the various types of hysteresis models in the literature.

Next, we examine the Classical Scalar Preisach hysteresis model in more detail. We first define the model in mathematical and in graphical terms. We then provide two alternative methods for identifying and implementing the Preisach model. We present simulation results showing hysteresis loops generated by the Preisach model.

Finally, we investigate an alternative model to the Preisach model: the Chua model. We show how to identify the Chua model and present simulation results of hysteresis loops generated by the Chua model. We identify drawbacks and benefits of the Chua model in comparison to the Preisach model.

3.1 Introduction to Hysteresis

Hysteresis is a nonlinear phenomenon in which the output of a system depends not only the present input, but also on the prior history of the input. This results in a lag between the input and output; unlike with dynamic systems, this lag persists even at quasi-static conditions. Hysteresis manifests itself in a wide variety of phenomena: these include ferromagnetism, piezoelectricity, friction, magnetoresistance, mechanical deformation, and many others.

Ferromagnetic hysteresis can be described at the molecular level [14] in the following way: when an external magnetic field is applied to a ferromagnetic material, the atomic magnetic dipoles will attempt to align themselves with this field; however, when the field is removed or reduced, some of the dipoles will retain their alignment. This results in the magnetization curve following a different path as the external field is reduced [14]. Figure 3-1 illustrates how this curve might look. As the applied magnetic field is increased from its initial state a, the magnetization follows path 1. As the applied magnetic field is decreased from state b, the magnetization follows path 2.

At the macroscale, the physics of ferromagnetic hysteresis is more complex [14]. A typical ferromagnet is comprised of a number of magnetic domains that interact. Within each of these domains, the magnetic dipoles are aligned and the domain has a uniform magnetization; however, the magnetization of each domain will vary in magnitude and direction. When the external field is varied, the domain walls separating adjacent domains move, causing the domains to change shape. Domains with a magnetization direction close to the direction of the external field expand while domains not aligned with the external field shrink and will ultimately disappear if the external field reaches sufficiently high values [14]. When the external field is reversed, domains with reversed magnetization will form. These will get larger and larger as the field continues to reverse [14].

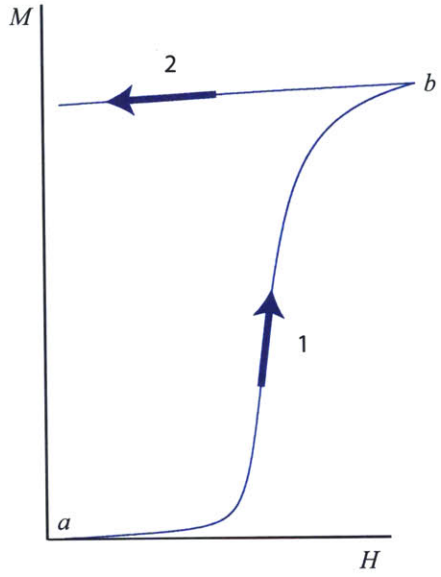

Figure 3-1: Hysteresis phenomenon, shown as magnetization versus applied field.

3.2 Prior Art

Much research has gone into modeling hysteresis. Hysteresis models can be classified as either physical models or phenomelogical models. Physical models are based on the underlying physical principles that give rise to the hysteresis. The most widely known example of a physics-based model applied to ferromagnetism is the Jiles-Atherton model [47]. Physics-based models applied to piezoelectric behavior are documented in [1, 51, 76]. One downside of physical hysteresis models is that they are specific to the type of hysteresis being modeled.

Phenomelogical models are models that attempt to model the hysteresis mathematically without regard to the underlying physical principles that give rise to the hysteresis. These types of models can be sub-classified into integral models and state-space models [49]. Integral models take a number of weighted fundamental operators (such as a relay) summed in parallel that each act on the input. As the number of these operators approaches infinity, the summation becomes an integration. The most widely used integral-type model is the Preisach model [61]. Other integral-type mod-

els include the Prandtl-Ishilinskii model [55] and the Generalized Maxwell-slip model [3]. State-space models use a set of differential equations with nonlinear functions to model the hysteresis. State-space models include the Chua model [25, 26, 23] and the Duhem model [88]. Other state-space models that are special cases of the Duhem model are the Bouc-Wen model [45, 77], the Dahl model [31], the LuGre model [32], and the Coleman-Hodgdon model [27, 87].

Phenemological models tend to be more generalizable than physical models. Among phenemological models, state-space models are simpler and more computationally efficient. Integral models are more computationally intensive, but have the advantage of greater capability for high accuracy.

3.3 The Classical Scalar Preisach Hysteresis Model

The Preisach hysteresis model is well known and is the model most commonly used to model ferromagnetic hysteresis. It is capable of high numerical accuracy and prediction [9]. Various modifications can be made to the basic Preisach model for improved accuracy. Some of these modified models have gained sufficient prominence to earn their own names: these include the Modified Preisach Model [20], the Moving Preisach Model [33], and the Product Preisach Model [33]. The basic scalar version of the Preisach model can also be generalized to vector models [61, 33]. The basic building block for the Preisach model is a non-ideal relay, called a 'hysteron' in the literature. Figure 3-2 is a graphical representation of one such hysteron. The input of the hysteron is u and the output is v. The output can take one of two values: 1 or -1. Switching occurs at the threshold values of u (α or β) depending on the state of the input.

This can be described mathematically as

$$v(u) = \begin{cases} 1, & \text{if } u \geq \alpha \\ -1, & \text{if } u \leq \beta \\ k, & \text{if } \beta < u < \alpha, \end{cases} \tag{3.1}$$

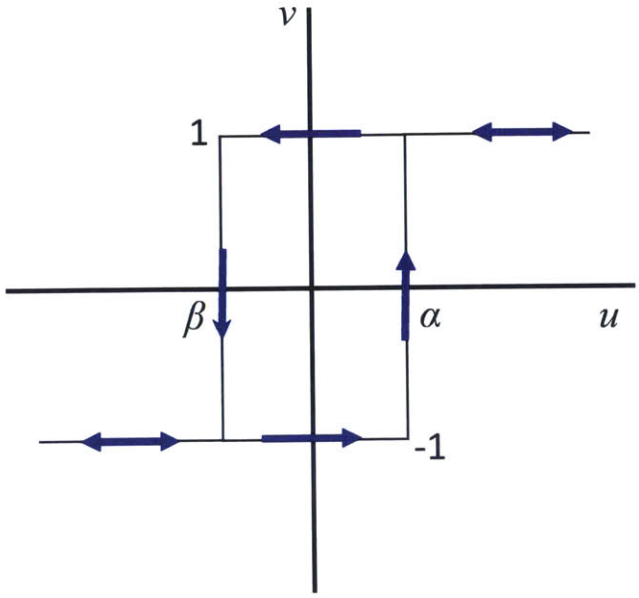

Figure 3-2: A Preisach hysteron with the threshold values α and β for switching output states.

where $k = -1$ if $u_T \leq \alpha$, and $k = 1$ otherwise, where u_T is defined as the value of u the last time that u was outside the thresholds (i.e., $u > \alpha$ or $u < \beta$).

Suppose we now have multiple hysterons connected in parallel, each one denoted by $R_{\alpha_i\beta_i}$. $R_{\alpha_i\beta_i}$ has threshold values α_i and β_i. Each hysteron is multiplied by a weight μ_i and the outputs are summed. Figure 3-3 illustrates this structure. The result is a discrete form of the Preisach model, and can be expressed as

$$v = \sum_i \mu_i R_{\alpha_i\beta_i}\left(u\left(t\right)\right). \tag{3.2}$$

As the number of hysterons approaches infinity, the Preisach model becomes continuous, and can be written as

$$v(t) = \iint_{\alpha\geq\beta} \mu_{\alpha\beta} R_{\alpha\beta}\left(u\left(t\right)\right) d\alpha d\beta. \tag{3.3}$$

The integration in (3.3) takes place over the space of α, β values. This way we account for the state of every hysteron, which is defined by its threshold values of α and β.

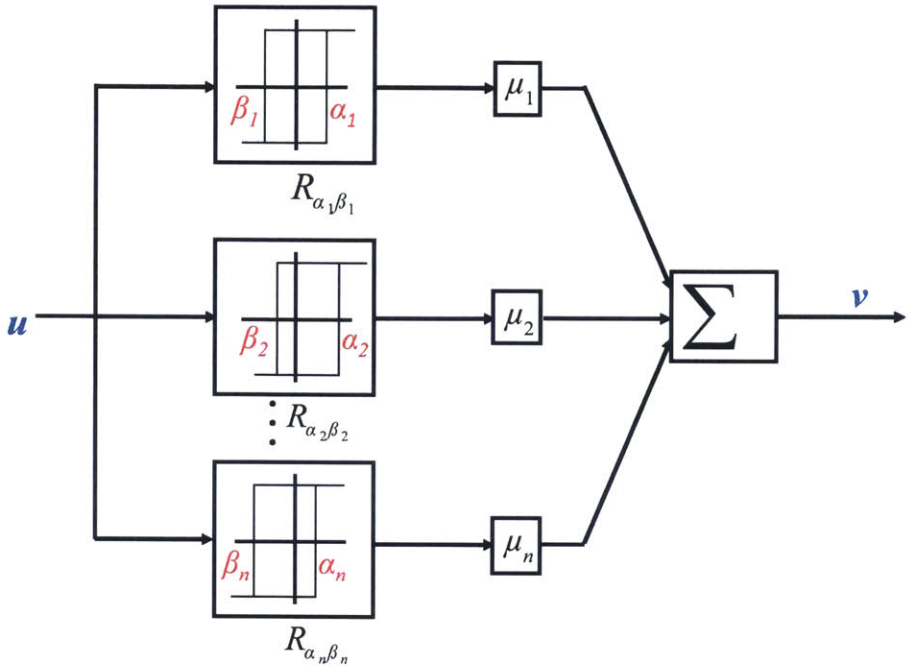

Figure 3-3: A parallel connection of weighted hysterons.

The integration is restricted to cases where $\alpha \geq \beta$ because $R_{\alpha\beta}$ is not defined for $\beta > \alpha$. This model is known as the Classical Scalar Preisach Model (CSPM). The weighting function $\mu_{\alpha\beta} = \mu(\alpha, \beta)$ is known as the Preisach density function (pdf). Setting up the Preisach model involves identifying and specifying this function. It can be specified with an analytic function (continuous model) or numerically with a lookup table (discrete model) and can be found experimentally.

While the Preisach model is a phenomenological model, the summing of hysterons in parallel with different switching levels bears resemblance to the macroscopic behavior of magnetic domains within a ferromagnetic material [61].

3.3.1 Graphical Interpretation of the CSPM

Details of a graphical perspective of the CSPM can be found in [61]. The CSPM can be interpreted graphically in the following way. Consider Figure 3-4, which shows the α-β plane, also known as the Preisach plane. The area over which the integration in 3.3 occurs is marked by the red triangle, defined by the lines $\alpha = \beta$, $\alpha = u_s$, and

$\beta = -u_s$. The variable u_s is the maximum value of the input. In a Preisach model of magnetic hysteresis, this would correspond to the largest magnetic field intensity expected, typically the magnetic field intensity H_s at which saturation occurs. The red triangle represents the pdf $\mu_{\alpha\beta}$. Each point (α_i, β_i) within the red triangle has a value μ_i. The pdf is assumed to have a value of zero for points (α, β) that lie outside the red triangle.

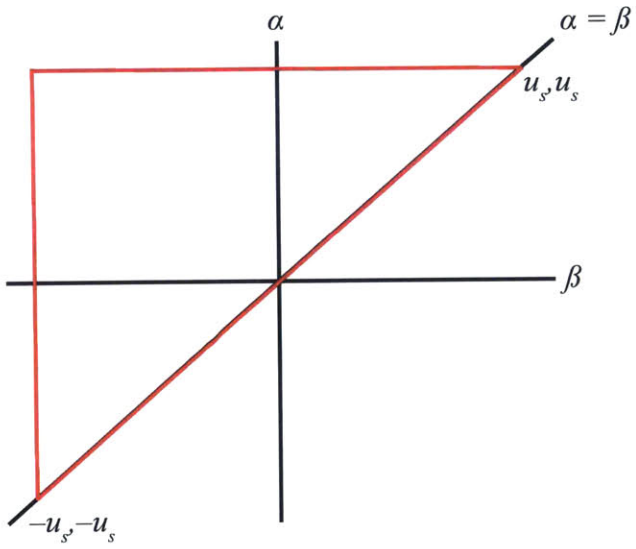

Figure 3-4: The Preisach plane.

Suppose now that the initial state of the CSPM is $-u_s, -v_s$, where v_s is the negative saturation value of the CSPM output. This state correpsonds to the lower-left vertex of the red triangle. As $u(t)$ is increased from u_s to some value u_1, all the hysteron operators $R_{\alpha\beta}$ with thresholds α less than u_1 are switched to $+1$. This subdivides the triangle into two areas, denoted by S^+ and S^- in Figure 3-5A. S^+ corresponds to the (α, β) points where the $R_{\alpha\beta}$ operaters have a $+1$ output, and S^- corresponds to the (α, β) points where the $R_{\alpha\beta}$ operators have a -1 output. This subdivision corresponds to the line $\alpha = u_1$.

Now suppose that we decrease the value of u from u_1 to u_2. All $R_{\alpha\beta}$ operators with thresholds β above u_2 will now switch to output -1. Note from Figure 3-5B that the subdivision between S^+ and S^- now has a vertical link corresponding to the line

$\beta = u_2$.

Next suppose we increase the value of u again from u_2 to u_3, where $u_3 < u_1$. Those $R_{\alpha\beta}$ operators with thresholds α less than u_3 will switch back to output $+1$. A new horizontal link in the subdivision between S^+ and S^- is formed corresponding to the line $\alpha = u_3$. See Figure 3-5C.

Finally, suppose that we increase u further to a value u_4, where $u_4 > u_1$. This is shown in Figure 3-5D. All $R_{\alpha\beta}$-operators with thresholds α less than u_4 will switch to output $+1$. Note that subdivision between S^+ and S^- is once again completely horizontal and now coincides with the line $\alpha = u_4$.

What the foregoing analysis demonstrates is that the Preisach plane is always subdivided into two regions: S^+ and S^-. In the S^+ region, all $R_{\alpha\beta}$ operators are switched to the $+1$ value; in the S^- region, all $R_{\alpha\beta}$ operators are switched to the -1 value. The line subdividing the two regions consists of vertices that correspond to the previous local minima and maxima of the input. When the input is increasing, the final link connecting the subdividing line to the $\alpha = \beta$ line is horizontal and coincides with the line $\alpha = u(t)$. When the input is decreasing, the final link connecting the subdividing line to the $\alpha = \beta$ line is vertical and coincides with the line $\beta = u(t)$.

The integral in (3.3) can be expressed in terms of S^+ and S^- as

$$v(t) = \iint_{S^+(t)} \mu_{\alpha\beta} R_{\alpha\beta}\left(u\left(t\right)\right) d\alpha d\beta + \iint_{S^-(t)} \mu_{\alpha\beta} R_{\alpha\beta}\left(u\left(t\right)\right) d\alpha d\beta. \tag{3.4}$$

Since $R_{\alpha\beta}\left(u\left(t\right)\right) = 1$ in the region S^+ and $R_{\alpha\beta}\left(u\left(t\right)\right) = -1$ on the region S^-, we can write (3.4) as

$$v(t) = \iint_{S^+(t)} \mu_{\alpha\beta} d\alpha d\beta - \iint_{S^-(t)} \mu_{\alpha\beta} d\alpha d\beta. \tag{3.5}$$

It is clear then that $v(t)$ depends on the particular subdividing line between S^+ and S^-. In particular, it will depend on the past local minima and maxima of the input that define the vertices of the subdividing line. In this way, we see graphically how the Preisach model output depends on the input's history. The output v can thus

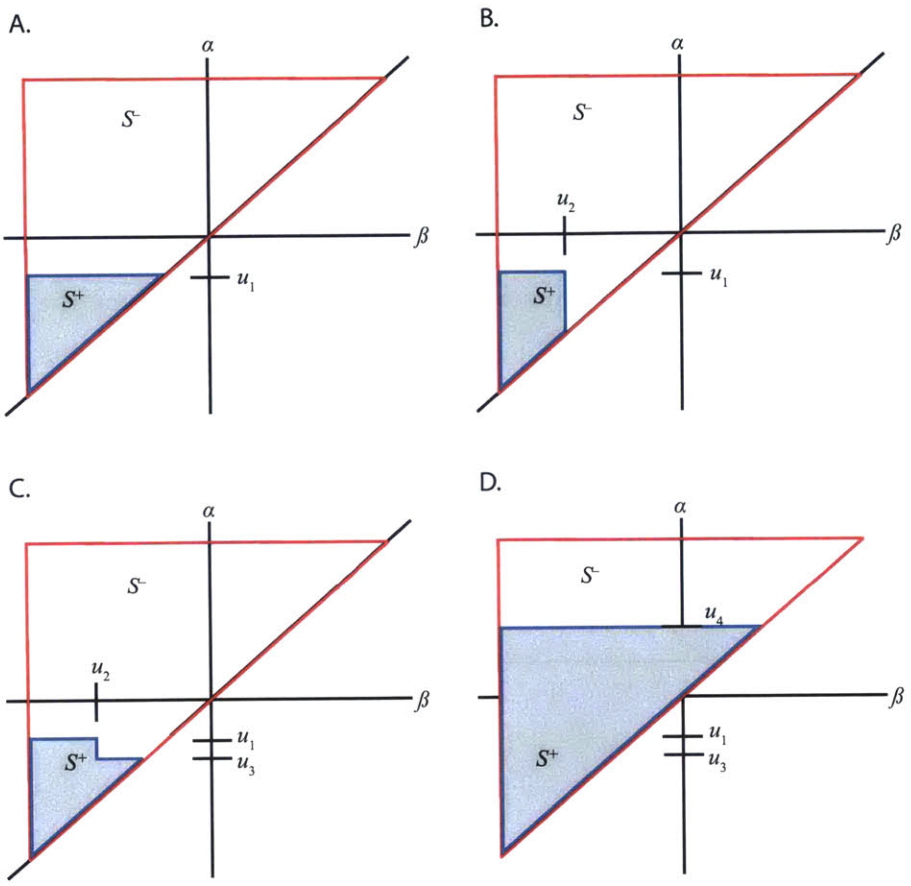

Figure 3-5: A: Input $u(t)$ increased $-u_s$ to u_1. B: Input $u(t)$ decreased from u_1 to u_2. C: Input $u(t)$ increased from u_2 to u_3. D: Input $u(t)$ increased from u_3 to u_4.

have different values for the same input value u because the subdividing line is not unique for a given u. Graphically, the non-unique subdividing line is the result of the two different rules that govern the subdividing line's progression: when the input is increasing, the subdividing line is characterized by a final link that is horizontal and moving upwards. When the input is decreasing, the subdividing line is characterized by a final link that is vertical and moving leftward.

Finally, note from Figure 3-5D that once the input increased beyond u_1, the vertex in the subdividing line at (u_2, u_1) was wiped out. This is a general property of the Preisach model, and is aptly named the 'wiping-out' property. The wiping-out property results in the removal of every vertex on the subdividing line that has an α-coordinate below the current input or a β-coordinate above the current input. One

implication of this fact is that in a subdividing line with multiple vertices, any particular vertex will always have an α-coordinate less than that of the vertex immediately to the left of it and a β-coordinate greater than that of the vertex immediately above it. Graphically, this means that the 'staircase' that the vertices form on the Preisach plane will always descend from left to right and never from right to left. See Figure 3-6 for an illustration. A further implication is that when implementing the Preisach model, only those local minima and maxima that have not been wiped out must be stored in memory.

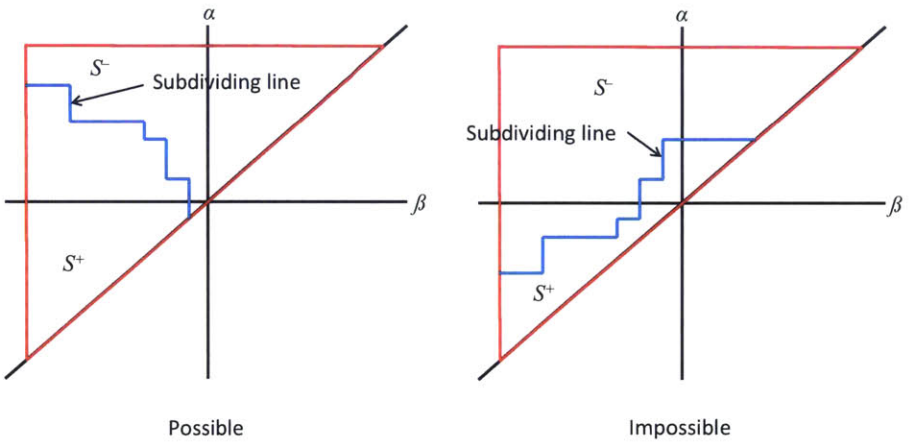

Figure 3-6: LEFT: A possible instantiation of the Preisach plane subdividing line. RIGHT: An impossible instantiation of the Preisach plane subdividing line.

3.3.2 Identification and Implementation of the CSPM

Now that the CSPM theory has been developed and explained, the next step is to find methods for identifying the model and implementing it. What this boils down to is identifying $u_{\alpha\beta}$. There are various methods for doing this, and in this section, we will briefly review some of these methods in the literature before giving more detailed presentations of two of them.

In [61], $\mu_{\alpha\beta}$ is identified by using the first-order reversal curve method. A first-order reversal curve is obtained by increasing the input u from negative saturation u_s to some value α before then reversing the input and decreasing u to some value β. The

values α and β define the first-order reversal curve, so-called because it corresponds to the first reversal of the input. This process is repeated for different values of α and β until we have a series of first-order reversal curves ranging between $-u_s < \alpha < u_s$ and $-u_s < \beta < \alpha$. The output values v are recorded for each first-order reversal curve, each corresponding to a different state on the Preisach plane. We can then apply an algorithm to populate the Preisach plane with $u_{\alpha\beta}$ values at discrete points using the data obtained from the first-order reversal curves. Interpolation is used to determine $\mu_{\alpha\beta}$ values that lie between the discrete points. One downside of the first-order reversal curve method is that the most straightforward algorithm to populate the Preisach plane requires taking second differences of the measured data. However, in [61] an alternative algorithm is developed that avoids this. In [12, 11], $\mu_{\alpha\beta}$ is identified by using the centered cycles method. Here, a series of B-H loops each with different amplitudes is experimentally recorded where H and B are odd-symmetric about the origin. This can be done for instance by driving H with a sine wave centered around zero. From this data, we can populate the Preisach plane. Two benefits of this method over the reversal curve method are: 1) the tests required (symmetric B-H loops) are easier to obtain experimentally; 2) the algorithm used to populate the Preisach plane is less sensitive to measurement noise because it does not require computing second differences of the data. Cardelli in [20] uses a similar method of symmetric minor loops to identify $\mu_{\alpha\beta}$. In [7], $\mu_{\alpha\beta}$ is assumed to be identical to the product of two single-variable functions. This simplifies the analysis, and allows the use of only the virgin curve and the major loop for identification of $\mu_{\alpha\beta}$. The virgin curve is the path followed by the magnetization when it starts from the demagnetized state [16]. The major loop is the M-H or B-H loop traversed when M is cycled between negative saturation and positive saturation. The virgin curve and the major loop are indicated in Figure 3-7.

Della Torre Implementation

Rather than explore the entire Preisach plane experimentally, which can be tedious, Della Torre noted that in many magnetic materials, $\mu_{\alpha\beta}$ can be approximated with

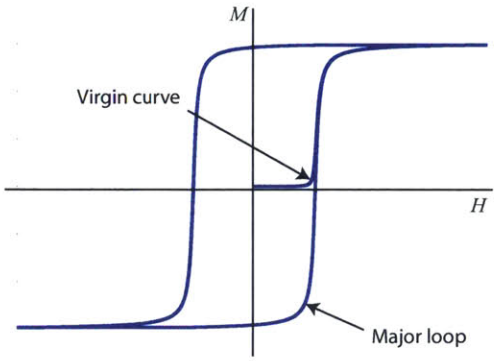

Figure 3-7: Virgin curve and major loop of the hysteresis curve.

a simple function. In hard magnetic materials, this function often takes a Gaussian form [33]. In soft magnetic materials, this function is better approximated with a Lorentzian function [9]. In soft materials, magnetization is mainly determined by domain wall motion, and this motion is typically unidirectional with a monotonically increasing or decreasing applied magnetic field. This means that we can model the probability distributions of α and β as statistically independent. This permits us to write $\mu_{\alpha\beta}$ as the product of two identical single variable functions [9], or

$$\mu(\alpha, \beta) = \mu_s(\alpha)\,\mu_s(-\beta) \tag{3.6}$$

Switching the input variable from u to H in order to represent applied magnetic field, we can write $\mu_s(H)$ as a Lorentzian function,

$$\mu_s(H) = \frac{A_d}{1 + \left(\frac{H - H_c}{H_c}\sigma\right)^2}, \tag{3.7}$$

where A_d, H_c, and σ are the parameters to be identified. One advantage of the Della Torre implementation is that it only requires identifying five parameters (in addition to the three parameters above, the magnetic field at which saturation occurs, H_s, and saturation magnetization, M_s must be identified). If we replace the output variable v with M to represent magnetization, we can differentiate (3.3) with respect to H and,

making use of (3.6), write

$$\frac{dM}{dH}(H) = \begin{cases} 2\mu_s(H) \displaystyle\int_{H_0}^{H} u_s(-\beta)\, d\beta, & \text{if } \frac{dH}{dt} \geq 0 \\ 2\mu_s(-H) \displaystyle\int_{H}^{H_0} u_s(\alpha)\, d\alpha, & \text{if } \frac{dH}{dt} < 0. \end{cases} \tag{3.8}$$

Here, H_0 is the last reversal point. The first equation applies to the case when the input H is increasing, while the second equation applies to the case when the input H is decreasing. The factor of 2 arises from the fact that the change in magnetization when a hysteron switches from its negative value to its positive value is twice its magnitude.

Substituting (3.7) into (3.8) for the case of an increasing field, we write

$$\begin{aligned} \frac{dM}{dH}(H) &= \frac{2A_d}{1+\left(\frac{H-H_c}{H_c}\sigma\right)^2} \int_{H_0}^{H} \frac{A_d}{1+\left(\frac{-\beta-H_c}{H_c}\sigma\right)^2}\, d\beta, \\ &= \frac{2A_d}{1+\left(\frac{H-H_c}{H_c}\sigma\right)^2} \left[-\frac{A_d H_c}{\sigma} \arctan\left(\frac{-\beta-H_c}{H_c}\sigma\right)\right]\Bigg|_{H_0}^{H}, \\ &= \frac{2A_d^2}{1+\left(\frac{H-H_c}{H_c}\sigma\right)^2} \frac{H_c}{\sigma} \left[-\arctan\left(\frac{-H-H_c}{H_c}\sigma\right) + \arctan\left(\frac{-H_0-H_c}{H_c}\sigma\right)\right], \\ \frac{dM}{dH}(H) &= \frac{2A_d^2}{1+\left(\frac{H-H_c}{H_c}\sigma\right)^2} \frac{H_c}{\sigma} \left[\arctan\left(\frac{H+H_c}{H_c}\sigma\right) - \arctan\left(\frac{H_0+H_c}{H_c}\sigma\right)\right]. \end{aligned} \tag{3.9}$$

Similarly, for a decreasing field, we derive

$$\frac{dM}{dH}(H) = \frac{2A_d^2}{1+\left(\frac{H+H_c}{H_c}\sigma\right)^2} \frac{H_c}{\sigma} \left[\arctan\left(\frac{H_0-H_c}{H_c}\sigma\right) - \arctan\left(\frac{H-H_c}{H_c}\sigma\right)\right]. \tag{3.10}$$

Here we make a quick aside to discuss a subtlety with the Preisach model that occurs when rather than traversing the Preisach plane from a reversal point, we traverse it from the demagnetized state. In this case, assuming that the hysteresis function is symmetric, the subdividing line between S^+ and S^- is no longer a staircase-

like structure comprised of vertical and horizontal links, but is rather a line coinciding with the line $\alpha = -\beta$. The reason for this is that when the hysteresis function is symmetric, $\mu(\alpha, \beta) = \mu(-\beta, -\alpha)$, so that the pdf above the subdividing line is identical the pdf below the subdividing line. From (3.5), the output $v(t)$ will thus be equal to zero. Because of the symmetry of $\mu_{\alpha\beta}$ about the $\alpha = -\beta$ line, the output for a decreasing input from the demagnetized state will be equal and opposite to the output for an increasing input from the demagnetized state. This matches expected behavior for traversal from the demagnetized state for a symmetric hysteresis function. Figure 3-8 shows the Preisach plane in the demagnetized state.

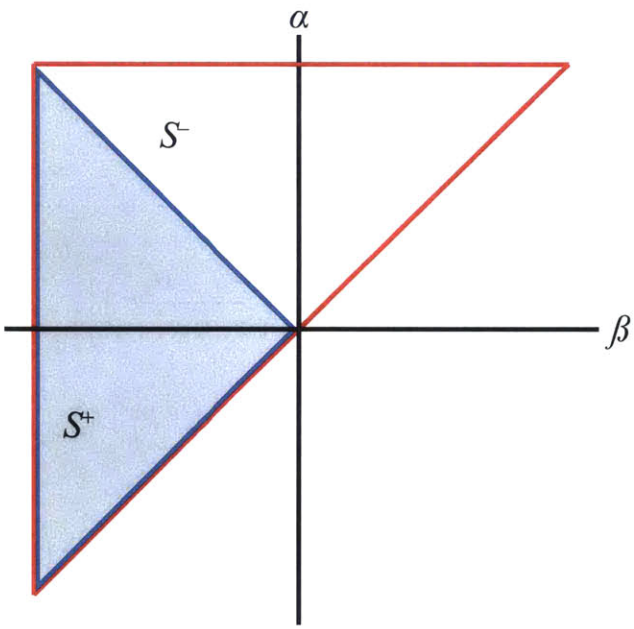

Figure 3-8: The Preisach plane showing the demagnetized state.

Increasing the input from the demagnetized state now results in a subdividing line that looks like the one shown in the left illustration of Figure 3-9. Decreasing the input from the demagnetized state results in a subdividing line that looks like the one shown in the right illustration of Figure 3-9. As before, the last links of the subdividing line in the increasing and decreasing cases are horizontal and vertical, respectively; however, the rest of the subdividing line remains coincident with the $\alpha = -\beta$ line.

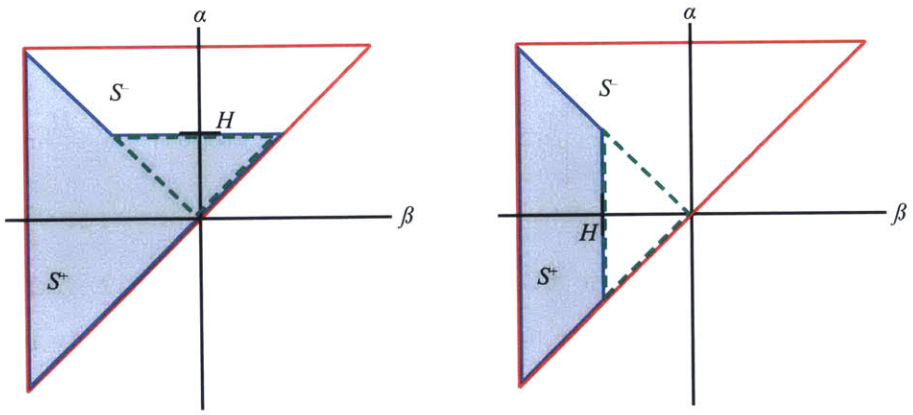

Figure 3-9: LEFT: Preisach plane with H increased from the demagnetized state. RIGHT: Preisach plane with H decreased from the demagnetized state.

The different structure of the subdividing line changes the integration limits in 3.8. Instead of the last reversal point H_0 as one of the limits, the corresponding limit is replaced with $-H$. This can be understood graphically by reference to Figure 3-9. In the left-side figure when H is increasing, the new area (marked by the dashed green triangle) added to S^+ is limited along the β-axis by the lines $\alpha = -\beta$ and $\alpha = \beta$. Since α equals the current input H, the lower and upper limits when integrating along β are therefore $-H$ and H, respectively. Likewise, in the right-side figure when H is decreasing, the new area (marked by the dashed green triangle) added to S^- is limited along the α-axis by the lines $\alpha = \beta$ and $\alpha = -\beta$. This corresponds to lower and upper limits when integrating along α of H and $-H$, respectively. When beginning from the demagnetized state, (3.8) thus becomes

$$\frac{dM}{dH}(H) = \begin{cases} 2\mu_s(H) \displaystyle\int_{-H}^{H} u_s(-\beta)\, d\beta, & \text{if } \frac{dH}{dt} \geq 0 \\ 2\mu_s(-H) \displaystyle\int_{H}^{-H} u_s(\alpha)\, d\alpha, & \text{if } \frac{dH}{dt} < 0. \end{cases} \tag{3.11}$$

Equation (3.9) becomes

$$\frac{dM}{dH}(H) = \frac{2A_d^2}{1 + \left(\frac{H-H_c}{H_c}\sigma\right)^2} \frac{H_c}{\sigma} \left[\arctan\left(\frac{H+H_c}{H_c}\sigma\right) - \arctan\left(\frac{-H+H_c}{H_c}\sigma\right) \right], \tag{3.12}$$

and (3.10) becomes

$$\frac{dM}{dH}(H) = \frac{2A_d^2}{1+\left(\frac{H+H_c}{H_c}\sigma\right)^2}\frac{H_c}{\sigma}\left[\arctan\left(\frac{-H-H_c}{H_c}\sigma\right) - \arctan\left(\frac{H-H_c}{H_c}\sigma\right)\right]. \tag{3.13}$$

To implement the Della Torre model, we use (3.9)–(3.10) and (3.12)–(3.13). One way to implement the Della Torre model for M as a function of H is to integrate these equations analytically with respect to H. This integral can be solved in closed-form [9]. However, the equations that result are very lengthy and unwieldy. More importantly, the evaluation is no longer accurate once the last extrema H_0 is wiped out.

Another way to implement the Della Torre model—and the one pursued here—is to evaluate dM/dH rather than M directly and then to integrate numerically. The advantage of implementing the Preisach model in this way is that this evaluation involves only one computation, whereas implementing the Preisach model in double integral form involves on the order of $N^2/2$ computations, where N is the number of vertices of local extrema in the subdividing line [86].

We implemented the Della Torre model using a MATLAB function we wrote. Values for H_c, σ, A_d, H_s, and M_s are specified within the function. The function takes as inputs the current value of H, the previous value of H, a variable indicating whether the input is increasing or decreasing, a stack that stores the previous local minima and maxima, and a variable indicating whether or not the initial state of M is the demagnetized state. We create a vector of the input signal H and then loop through this vector, computing dM/dH for each value of H using the MATLAB function. The value of M is then computed by integrating dM/dH numerically after each step and adding the result to the previous computed value of M. Besides the current value of dM/dH, the function also outputs an updated stack of the previous minima and maxima and the updated variable indicating whether the input is increasing or decreasing.

When the inputs are passed into the MATLAB function, the function first de-

termines whether the input is increasing or decreasing and whether or not we are traversing from the demagnetized state. Based on this evaluation, it determines which equation among (3.9)-(3.10) and (3.12)-(3.13) to use. The function then updates the stack of previous minima or maxima. If the current input is increasing and larger than the previous maximum or decreasing and less than the previous minimum, the function removes the last two extrema from the stack. The function continues to go through the stack to remove any other extrema that should be 'wiped-out'. If the input has just reversed direction, the function adds the last reversal point to the stack. The function then sets H_0 equal to the last reversal point of the updated stack if (3.9) or (3.10) are being used to evaluate dM/dH. It evaluates the appropriate equation and then outputs dM/dH.

Identifying the Parameters of the Della Torre Model

Identifying A_d, H_c, and σ is straightforward. The variable H_c is related to the width of the hysteresis loop and for many materials is very close in value to the coercivity of the material H_c. If we inspect (3.9) for the major ascending branch of the hysteresis loop (where H_0 is replaced with $-H_s$, the negative saturation input), we can reason that for values of $\sigma > 0.5$, the maximum value of dM/dH occurs close to $H = H_c$. It is easy to see that maximum value of the term outside the brackets occurs at $H = H_c$. The bracketed term will asymptote toward the constant maximum value of π as the value of σ is increased. Therefore, for values of σ large enough, the maximum dM/dH will occur near $H = H_c$. We can thus often approximate H_c either from the coercivity of the material, or, if we have the M-H data for the major hysteresis loop, with [9]

$$\left(\frac{dM}{dH}\right)^a_{H=H_c} = \max\left(\frac{dM}{dH}\right)^a, \tag{3.14}$$

where the superscript a denotes the ascending branch of the major hysteresis loop. In other words, if we compute dM/dH from the M-H data, then we can identify H_c by locating the value of H where the maximum dM/dH occurs. Figure 3-10 shows three hysteresis loops constructed from the Della Torre implementation, each with

different values of H_c. For each loop, $\sigma = 20$ and $\mu_0 M_s = 1.5\,\mathrm{T}$. It can be seen that $M = 0$ occurs at $H \approx H_c$.

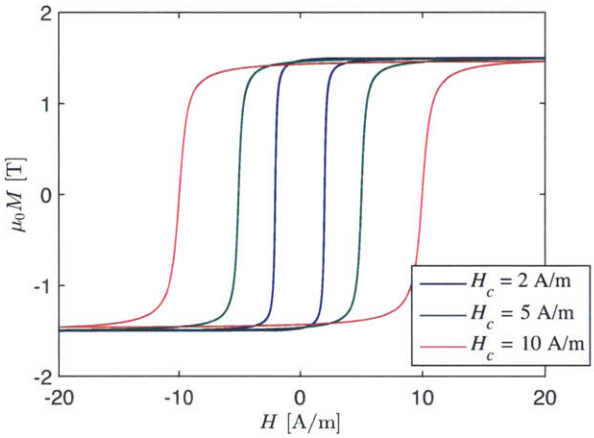

Figure 3-10: Three hysteresis loops constructed from the Della Torre CSPM with different values of H_c.

The parameter σ is related to the slope of the major hysteresis loop at $H = H_c$. From [9], σ can be calculated from

$$\frac{\left(\frac{dM}{dH}\right)^a_{H=H_c}}{\left(\frac{dM}{dH}\right)^d_{H=H_c}} = \frac{\arctan(2\sigma) - \arctan\left(\frac{-H_s+H_c}{H_c}\sigma\right)}{\arctan\left(\frac{H_s-H_c}{H_c}\sigma\right)}\left[1+(2\sigma)^2\right], \tag{3.15}$$

where the superscript d refers the descending branch of the major hysteresis loop. We can solve for σ for instance by plotting the right-hand side as a function of σ and locating the value of σ where the graph equals the value of left-hand side. The points on the major loop needed to evaluate the left-hand side are shown in Figure 3-11. Because $(dM/dH)^a_{H=H_c} >> (dM/dH)^d_{H=H_c}$, the left-hand side will be much greater than 1.

If $\sigma >> 0.5$, we can approximate (3.15) as

$$r \approx 2\left[1+(2\sigma)^2\right], \tag{3.16}$$

where r is the value of the left-hand side from (3.15). We can solve this equation

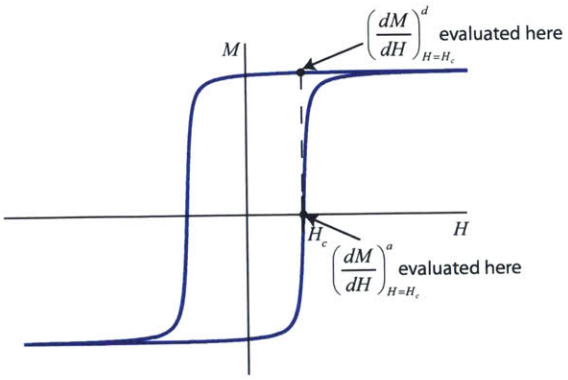

Figure 3-11: The dM/dH values needed to evaluate σ.

explicitly for σ as

$$\sigma \approx \frac{1}{2}\sqrt{\frac{r}{2} - 1}. \tag{3.17}$$

Figure 3-12 shows three hysteresis loops constructed from the Della Torre implementation of the CSPM, each with different values of σ. For each loop, $H_c = 5$ A/m and $\mu_0 M_s = 1.5$ T.

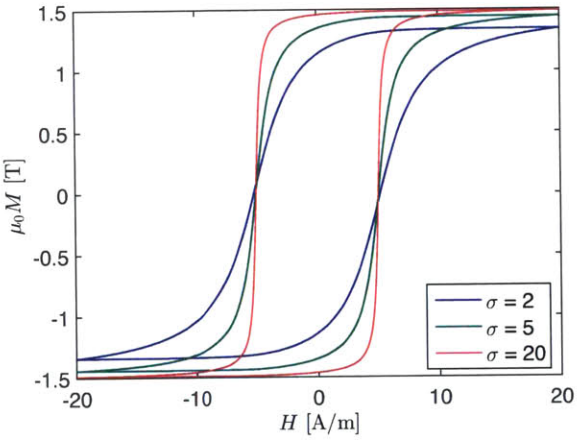

Figure 3-12: Three hysteresis loops constructed from the Della Torre CSPM with different values of σ.

Finally, the value of A_d can be calculated using results from [9] via

$$A_d = \sqrt{\frac{M_s}{\int_{-H_s}^{H_s} \left(\frac{1}{1+\left(\frac{\alpha - H_c}{H_c}\sigma\right)^2} \int_{-H_s}^{\alpha} \frac{d\beta}{1+\left(\frac{\beta + H_c}{H_c}\sigma\right)^2} \right) d\alpha}}. \tag{3.18}$$

Figure 3-13 shows the minor loops that the Della Torre implementation can produce. These plots were simulated using the MATLAB function described earlier. We used input H vectors with smaller amplitudes to simulate the minor loops.

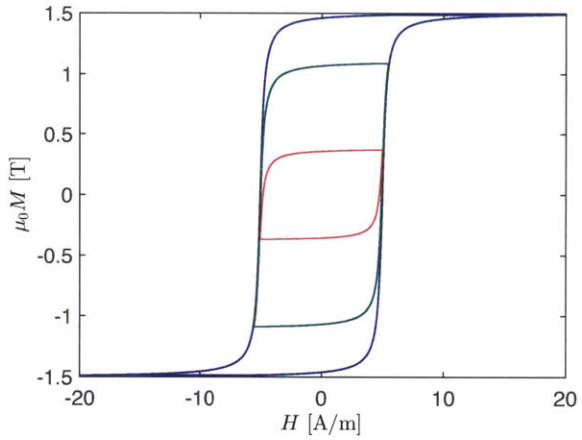

Figure 3-13: Minor loops constructed from the Della Torre implementation of the CSPM with parameters $H_c = 5\,\text{A/m}$, $\sigma = 20$, $\mu_0 M_s = 1.5\,\text{T}$.

Hui Implementation

In [44], a method for identifying and implementing the CSPM based on data obtained from the major hysteresis loop is presented. Here, the output is flux density, B, rather than M, so this terminology is followed in the subsequent discussion.

First, the function $T(H_1, H_2)$ is defined as

$$T(H_1, H_2) = \int_{H_2}^{H_1} \int_{\beta}^{H_1} \mu(\alpha, \beta) d\alpha d\beta. \tag{3.19}$$

In the Preisach plane, this corresponds to integrating over the right triangle with vertex corresponding to $\alpha = H_1$ and $\beta = H_2$. See Figure 3-14.

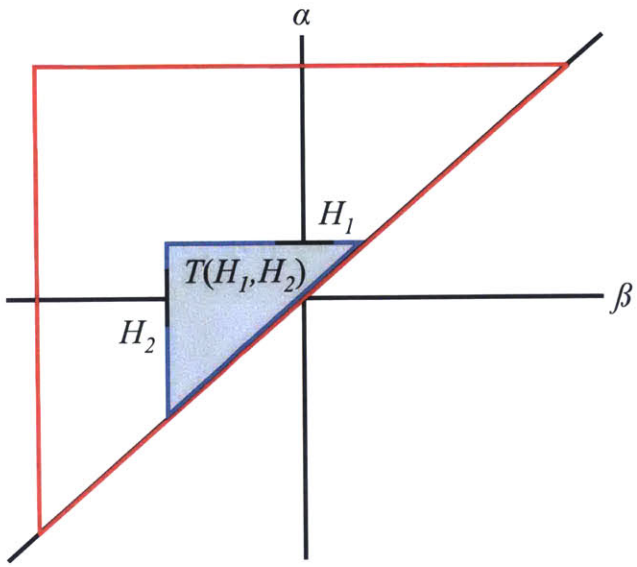

Figure 3-14: The area of the Preisach plane corresponding to $T(H_1, H_2)$.

Suppose now that we have reached positive saturation (H_s, B_s) and now decrease the magnetic field to some value H. This corresponds to traveling along the descending branch on the major hysteresis loop. The Preisach plane corresponds to that shown in the left illustration of Figure 3-15.

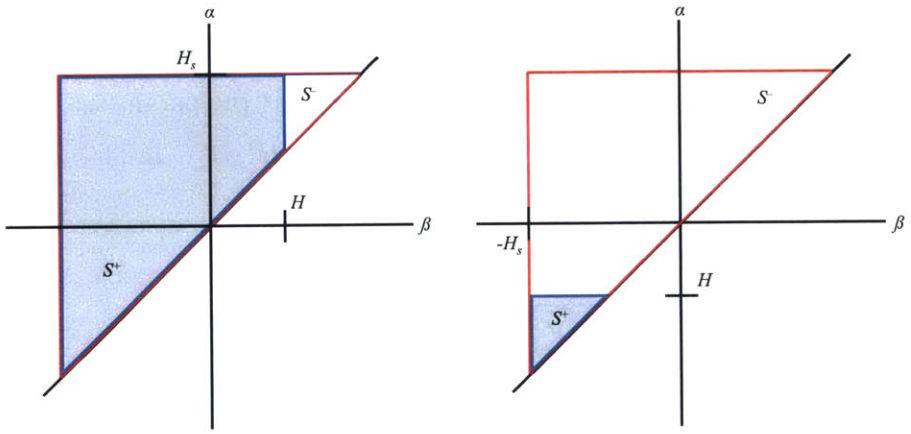

Figure 3-15: LEFT: Preisach plane corresponding to the descending branch of major hysteresis loop. RIGHT: Preisach plane corresponding the ascending branch of the major hysteresis loop.

The flux density corresponding to this state can be written as

$$\begin{aligned} B^d(H) &= \iint_{S^+} \mu_{\alpha\beta} d\alpha d\beta - \iint_{S^-} \mu_{\alpha\beta} d\alpha d\beta, \\ &= \big(B_s - T(H_s, H)\big) - T(H_s, H), \\ B^d(H) &= B_s - 2T(H_s, H). \end{aligned} \tag{3.20}$$

Likewise if we start from negative saturation and increase the magnetic field to some value H, the Preisach plane configuration depicted in the right illustration of Figure 3-15 obtains. We can write $B^a(H)$ as

$$B^a(H) = -B_s + 2T(H, -H_s). \tag{3.21}$$

We can generalize this analysis to determine the flux density for a magnetization curve that has n reversal points:

$$B(H) = \begin{cases} B_n + 2T(H, H_n), & \text{if } \dfrac{dH}{dt} \geq 0 \\ B_n - 2T(H_n, H), & \text{if } \dfrac{dH}{dt} < 0. \end{cases} \tag{3.22}$$

The variables H_n and B_n are the magnetic field and magnetic flux density, respectively, of the last reversal point. From (3.22), we see that the parameter we need to identify in order to implement the Preisach model is $T(H_1, H_2)$. In [44], it is shown that $T(H_1, H_2)$ can be written as

$$T(H_1, H_2) = \frac{B^a(H_1) - B^d(H_2)}{2} + F(H_1)F(-H_2), \tag{3.23}$$

where

$$F(\alpha) = \int_{\alpha}^{H_s} \mu_s(\alpha) d\alpha. \tag{3.24}$$

Here we have again assumed that $\mu_{\alpha\beta}$ is separable into two identical single variable

functions as was done for the Della Torre implementation.

The function $F(\alpha)$ can be expressed in terms of the ascending and descending branches of the major hysteresis loop as

$$F(\alpha) = \begin{cases} \dfrac{B^d(\alpha) - B^a(\alpha)}{2\sqrt{B^d(\alpha)}}, & \text{if } \alpha \geq 0 \\ \sqrt{B^d(-\alpha)}, & \text{if } \alpha < 0. \end{cases} \tag{3.25}$$

Finally, in [44] the initial flux density curve is derived in terms of $F(H)$ and $F(-H)$ as

$$B^i(H) = \left[F(-H) - F(H)\right]^2, \tag{3.26}$$

where the superscript i denotes the initial curve.

We can see then that (3.22) and (3.26) are ultimately reducible to terms that involve only the ascending and descending branches of the major hysteresis loop. To identify the CSPM using this method then, we need only experimentally to determine the major hysteresis loop. This data can then be implemented as a lookup table for real-time operation, or an analytic function can be fitted to the ascending and descending branches of the major loop.

The algorithm for implementing this form of the CSPM is simple. We create a stack for storing the previous minima and maxima. We update the stack by checking the stack against the current input and removing any previous extrema that should be wiped out. If the input has just reversed, we add the new reversal point to the stack. After updating the stack, we check the last reversal point. If the stack is empty, we use (3.26) to calculate B. Otherwise, we use (3.22) with the last reversal point for H_n. Figure 3-16 shows the major loop as well as minor loops constructed with the Hui implementation.

Accounting for Assymetry in the Hui Implementation

The foregoing analysis assumed that the hysteretic behavior is symmetric with respect to the origin of the B-H plane. In reality, this will not always be the case.

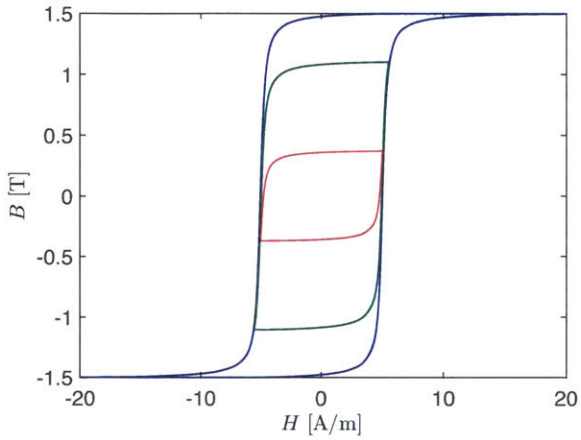

Figure 3-16: Major loop and minor loops constructed from the Hui implementation of the CSPM.

The equations used to implement the CSPM can be modified to account for asymmetry. We replace the function $F(\alpha)$ with two functions $F^+(\alpha)$ and $F^-(\alpha)$. $F_1(\alpha)$ is identical to $F(\alpha)$ given in 3.25. $F^-(\alpha)$ can be written as

$$F^-(\alpha) = \begin{cases} \dfrac{-B^a(\alpha) + B^d(\alpha)}{2\sqrt{-B^a(-\alpha)}}, & \text{if } \alpha \geq 0 \\ \sqrt{-B^a(\alpha)}, & \text{if } \alpha < 0. \end{cases} \tag{3.27}$$

$T(H_1, H_2)$ is modified as to

$$T(H_1, H_2) = \begin{cases} \dfrac{B^a(H_1) - B^d(H_2)}{2} + F^+(H_1)F^+(-H_2), & \text{if } H \geq 0 \\ \dfrac{B^a(H_2) - B^d(H_1)}{2} + F^-(H_1)F^-(-H_2), & \text{if } H < 0. \end{cases} \tag{3.28}$$

Finally, the equations for calculating $B(H)$ are modified as follows. For increasing H, we write

$$B(H) = \begin{cases} B_n + 2T(H, H_n), & \text{if } H \geq 0 \\ B_n + 2T(H_n, H), & \text{if } H < 0. \end{cases} \tag{3.29}$$

For decreasing H, we write

$$B(H) = \begin{cases} B_n - 2T(H_n, H), & \text{if } H \geq 0 \\ B_n - 2T(H, H_n), & \text{if } H < 0. \end{cases} \tag{3.30}$$

And finally, for the virgin curve, we write

$$B^i(H) = \begin{cases} \left[F^+(-H) - F^+(H)\right]^2, & \text{if } H \geq 0 \\ -\left[F^-(-H) - F^-(H)\right]^2, & \text{if } H < 0. \end{cases} \tag{3.31}$$

3.4 The Chua Hysteresis Model

The Chua hysteresis model belongs to the subset of state-space hysteresis models. It is described in detail in [25, 26, 23] and an implementation of it is detailed in [46]. The benefit of such a state-space model is that it is easy to implement for real-time operation and is less computationally intensive than the Preisach model. A further benefit of the Chua model is that its standard implementation captures the phenomenon of loop widening, that is, the widening of the hysteresis loop with increasing frequency. However, the simplicity of the Chua model comes at a cost: as we will see later, it cannot model minor loops as accurately as the Preisach model.

The Chua model [23] can be described by the differential equation

$$\frac{dv(t)}{dt} = w\left(\frac{du(t)}{dt}\right) \times h(v(t)) \times g\left[u(t) - f(v(t))\right]. \tag{3.32}$$

The functions f, g, h, and w are the functions to be identified: f is the described in the literature as the *restoring function* and g as the *dissipation function.* The w function models the frequency dependence of the hysteresis and h is a weighting function. In this thesis, $h = 1$. Note that with the Chua model, there is no need to store previous local minima and maxima.

3.4.1 Identification and Implementation of the Chua Model

Identifying f and g are straightforward. The function f can be determined from the curve consisting of the midpoints between the ascending and descending branches of the major hysteresis loop for equal values of B, where we have switched the input and output variables u and v with H and B, respectively. Mathematically, we can write

$$B^a(H_1) = B^d(H_2) = f^{-1}(H_m), \tag{3.33}$$

where H_m is the mean value of H_1 and H_2, expressed as

$$H_m = \frac{H_1 + H_2}{2}. \tag{3.34}$$

Graphically, f^{-1} is illustrated in Figure 3-17.

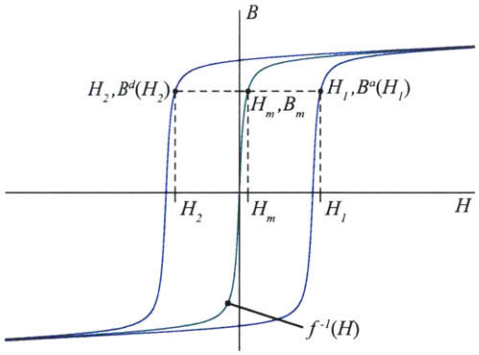

Figure 3-17: Identification of f for the Chua model.

The function g is determined by the width of the major hysteresis loop. Mathematically, we can write

$$g^{-1}\left(\frac{dB(t)}{dt}\right) = d(t). \tag{3.35}$$

Here $d(t)$ is half the width of the major hysteresis loop at time t when $B(t)$ is driven with a cosine wave with zero offset. Graphically, g^{-1} is illustrated in Figure 3-18. The functions f and g can be implemented as lookup tables or as analytic functions fit to the data.

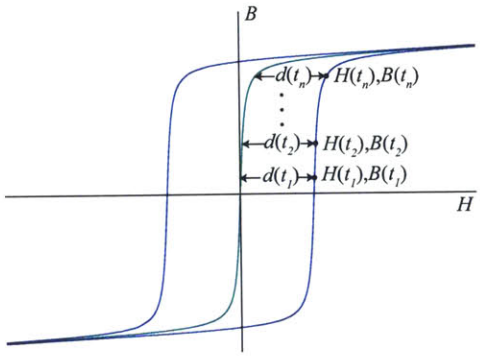

Figure 3-18: Identification of g for the Chua model.

The final function to determine is w. For frequency independence, we set w as

$$w\left(\frac{dH}{dt}\right) = \frac{1}{2\pi f_0 H_{\max}}\left|\frac{dH}{dt}\right|, \tag{3.36}$$

where f_0 is the frequency of the cosine wave that was used to identify g. The parameter $H_{\max}$ is the maximum value of H reached with the cosine wave.

Figure 3-19 shows the major loop as well as minor loops constructed with the frequency-independent Chua model. Note that the major loop looks reasonable. However, the minor loops show that the relationship between B and H is no longer monotonic. This does not accurately model real materials. This is a major disadvantage of the Chua model compared to the Preisach model. This limitation is discussed further in [27].

3.5 Summary

From a literature review, we learned that there are two general approaches to modeling hysteresis: physical modeling and phenomelogical modeling. We presented two phenomelogical models for modeling ferromagnetic hysteresis. The first is the Preisach model, an integral model that is capable of high accuracy. We learned that the graphical representation of the Preisach model provides insight into how the model works. We presented two methods for implementing the Preisach model, the Della Torre

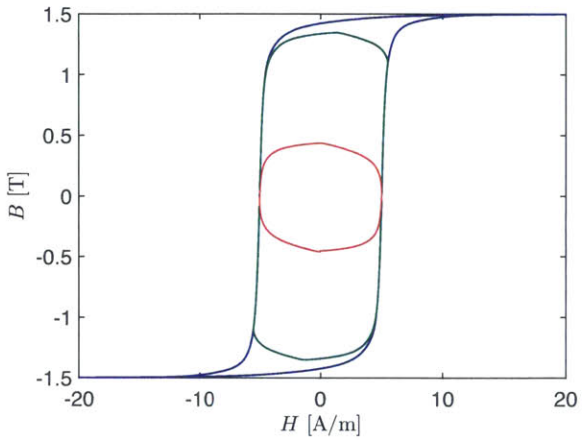

Figure 3-19: Major loop and minor loops constructed from the frequency-independent Chua model.

implementation and the Hui implementation. We learned that both these methods are both relatively straightforward to identify and yet are still capable of producing realistic minor loops. With the Hui implementation, we developed a way to account for asymmetry in the hysteresis loop. The second model we presented is the Chua model, a state-space model that is simple to implement with a single first-order differential equation. We learned that the Chua model produces minor loops that do not realistically model real materials.

In the next chapter, we develop a simulation model for the reluctance actuator that incorporates the Preisach model. With this model, we investigate force errors from hysteresis as well as other error sources.

Chapter 4

Reluctance Actuator Hysteresis Modeling

In this chapter, we present a method for incorporating the hysteresis models presented in the previous chapter into a full actuator model for simulation. This model can then be used to predict and investigate actuator behavior. It can also be used as a design tool to provide insight into how different actuator parameters affect results.

We first present the basic reluctance actuator model, where we implement Ampere's Law for the reluctance actuator and incorporate the Della Torre Preisach hysteresis model for the material B-H relationship.

We then use this model to investigate errors from hysteresis and gap disturbances. We also develop theory for characterizing the errors from these sources. This results in simplified formulas that can be used to approximate expected errors. We also show that the predictions from theory match up well with simulated results.

Next we augment the reluctance actuator model with a flux feedback controller. We develop theory for predicting the stiffness of the flux-controlled actuator with a current drive and with a voltage drive. In the case of the current-driven compensated actuator, we simulate the flux-controlled actuator model and show how the simulated stiffness matches the theoretical stiffness. Finally, we present an overview of how one might augment the basic actuator model in order to capture other phenomena and to improve the model's accuracy.

4.1 Basic Reluctance Actuator Model

We begin with the lumped parameter model described by (2.7), rewritten here with time dependence shown explicitly as

$$l_{Fe}H(t) + \frac{2g(t)}{\mu_0}B(H(t)) = NI(t), \tag{4.1}$$

where we have replaced B_g/μ with $H(t)$, the magnetic field in the core material, and where we have dropped the subscript from B_g. We write B as a function of H in order to highlight the fact that it is a nonlinear function of H that includes hysteresis.

The difficulty in creating a model of the actuator that captures the hysteretic behavior is that even if we have a model for the B-H relationship, we have no direct access to H. We only have access to the input I. And because of the nonlinear relationship between H and B, there is no straightforward way to solve for H explicitly as a function of I.

Instead, we implement (4.1) in MATLAB Simulink and use a numeric solver to solve it. In block diagram form, (4.1) can be represented as shown in Figure 4-1.

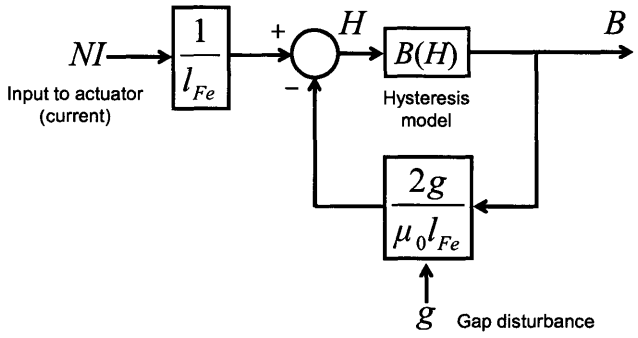

Figure 4-1: Block diagram for actuator model.

This gives us a model framework for simulating $B(t)$ without having explicitly to solve for H in terms of I or B. We will use this model to gain insight into the actuator behavior. For real-time prediction, however, there is no guarantee that the feedback loop in Figure 4-1 will be stable. We will address real-time prediction issues in Chapter 6.

4.1.1 Incorporating the Hysteresis Model into the Actuator Model

With the model framework described above, we can investigate the effect of magnetic hysteresis in the reluctance actuator. To do so, we first need to choose an appropriate hysteresis model and replace the $B(H)$ block in Figure 4-1 with this model. We selected the Della Torre implementation of the Preisach model described in the previous chapter. We chose this model because it can model minor loops well, unlike the Chua model, and because it is relatively easy to implement compared to other methods of implementing the Preisach model.

The output of the Della Torre model is dM/dH. To express the output in terms of dB/dH rather than dM/dH, we note that B in the magnetic material can be expressed as [16]

$$B = \mu_0(H + M). \tag{4.2}$$

Differentiating B with respect to H, we write

$$\frac{dB}{dH} = \mu_0(1 + \frac{dM}{dH}). \tag{4.3}$$

Therefore, to obtain dB/dH from the Della Torre model, we add 1 to the output dM/dH and multiply it by μ_0. Since our Della Torre model output now is dB/dH rather than B, however, we need to modify the actuator model to account for this. To do this, we take the derivative of (4.1) as

$$l_{Fe}\frac{dH}{dt} + \frac{2g}{\mu_0}\frac{dB}{dt} + \frac{2B}{\mu_0}\frac{dg}{dt} = N\frac{dI}{dt}. \tag{4.4}$$

We then use the chain rule to express dB/dt in terms of dB/dH as

$$l_{Fe}\frac{dH}{dt} + \frac{2g}{\mu_0}\frac{dB}{dH}\frac{dH}{dt} + \frac{2B}{\mu_0}\frac{dg}{dt} = N\frac{dI}{dt}. \tag{4.5}$$

The resulting block diagram implementing (4.5) with the Della Torre model is shown in Figure 4-2. This model takes dI/dt as its input rather than I. Integration is

then required to obtain B. For simulation, we took the desired current profile and differentiated it numerically in pre-processing to obtain the desired dI/dt profile. This dI/dt profile was then used as the input to the simulation model.

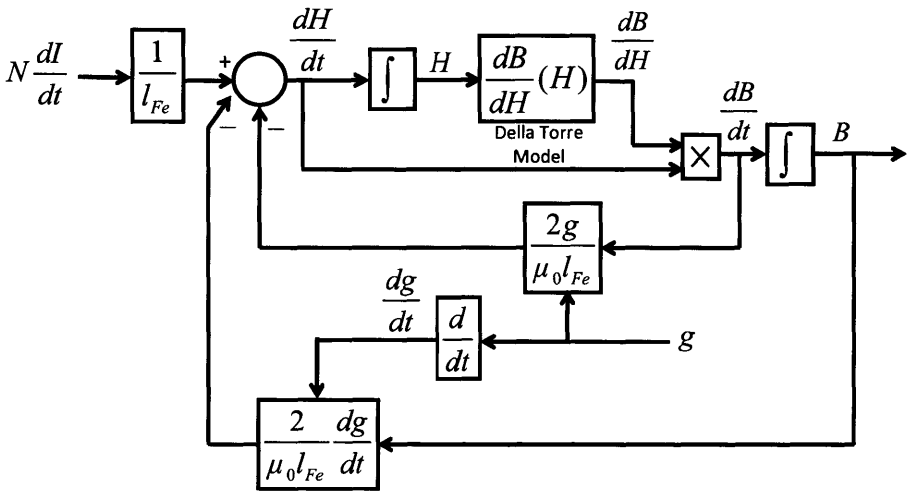

Figure 4-2: Block diagram for actuator model with Della Torre hysteresis model.

4.1.2 Hysteresis Model Parameters

For simulation purposes, we chose to model a reluctance actuator prototype that we designed for experiments in lab. The prototype actuator is a three-pole actuator with nickel-iron laminated cut-cores. The actuator parameters and design details can be found in Chapter 8.

The Della Torre parameters H_c, σ, A_d, H_s, and B_s, as defined in Section 3.3.2 (with B_s replacing M_s), were set to the values shown in Table 4.1.

Table 4.1: Della Torre model parameters

Parameter	Value
H_c	$4\,\mathrm{A/m}$
σ	20.4
H_s	$1 \times 10^4\,\mathrm{A/m}$
B_s	$1.215\,\mathrm{T}$
A_d	$1.807\,\sqrt{\mathrm{T}}/(\mathrm{A/m})$

Here, H_c was chosen to be the coercivity of the nickel-iron material as specified by Magnetic Metals [57], the company that supplied the cut-cores for the actuator prototype we designed. The saturation flux density was specified by Magnetic Metals to be $\sim$1.5 T. We then chose $B_s = (0.9)^2 \times 1.5\,\mathrm{T} = 1.215\,\mathrm{T}$. The first factor of 0.9 reflects the lamination stacking factor, which is given by Magnetic metals as 0.9 for our lamination thickness of 0.004" ($\sim$100 μm). The second 0.9 factor is a fudge factor intended to reflect the fact that fringing fields in the air gap and leakage flux will reduce the average flux density in the air gap. Since this model does not explicitly model fringing fields or leakage flux, we chose to account for these effects on the force by simply reducing the saturation flux density. The value for σ was chosen to be a value close to that found in the literature [9]. The variable H_s was chosen to be a large value so that the simulated H is guaranteed to remain between $-H_s$ and H_s. The value of A_d results directly from (3.18) as a consequence of setting the other parameters. Figure 4-3 shows the major loop as generated by this hysteresis model.

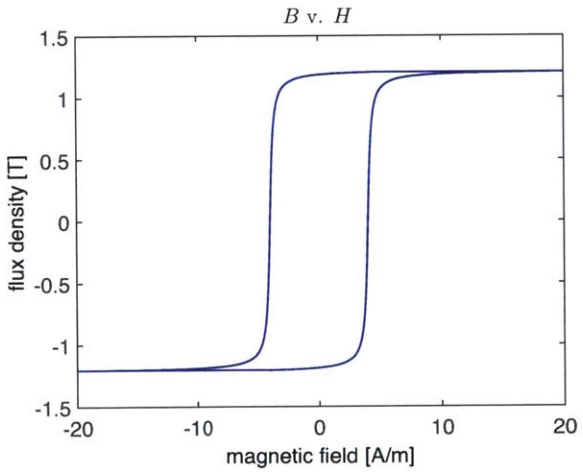

Figure 4-3: Major loop of hysteresis model used for simulation.

Note that these values were chosen *a priori* , without any experimental verification. For present purposes, this is acceptable since we are attempting to gain insight into general behavior rather than accurately predict a particular actuator's performance.

4.1.3 Current Profile

The current profile used to drive the actuator simulation was chosen to approximate a scaled version of an actual scanning profile. We started with a 2^{nd}-order acceleration setpoint profile with the following parameters: $a_{\max} = 225\,\text{m/s}^2$, $j_{\max} = 22500\,\text{m/s}^3$, $s_{\max} = 4.5 \times 10^6\,\text{m/s}^4$. These refer to the maximum acceleration magnitude, maximum jerk magnitude, and maximum snap magnitude, respectively. For a profile to be 2^{nd}-order means that its first two derivatives are finite. A 2^{nd}-order acceleration profile corresponds to a 4^{th}-order position profile. The top plot in Figure 4-4 shows the constructed acceleration profile.

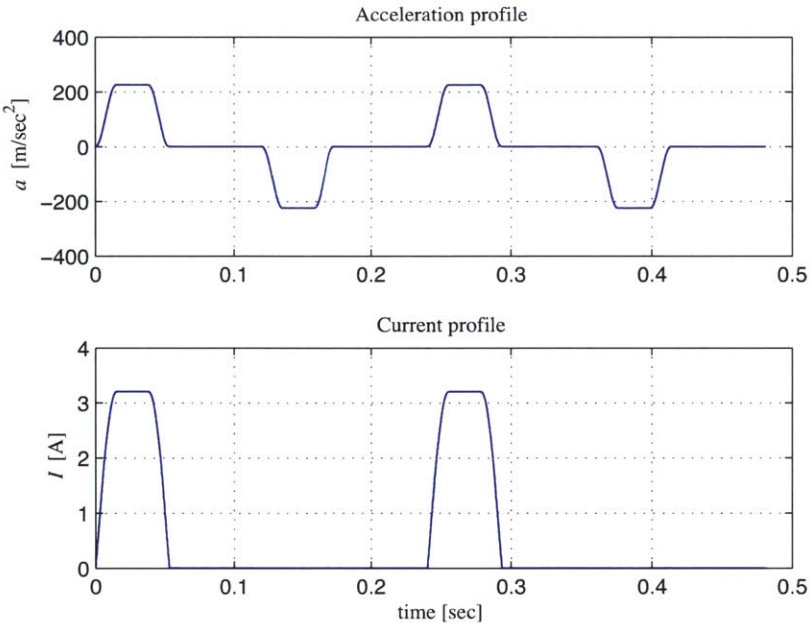

Figure 4-4: TOP: Acceleration profile for simulation. BOTTOM: Associated current profile for simulation of single reluctance actuator.

Based on the acceleration profile, we then derived a feedforward force profile scaled to the maximum force output of one prototype actuator. From this force profile, we then derived a current profile for the reluctance actuator using (2.14). The bottom plot in Figure 4-4 shows the current profile used for simulation. The current profile shows pulses corresponding only to the positive acceleration pulses: this is because

we are simulating only one reluctance actuator, which can generate force in only one direction. The opposing actuator is not simulated here.

4.2 Analysis of Errors from Hysteresis

We can use our simulation model to investigate the effects of hysteresis on accuracy. There are two types of errors associated with hysteresis. The first is offset error: this occurs when the current is driven to zero after the acceleration phase. Because of hysteresis, the actuator core will not fully demagnetize in this state. If not compensated, this will result in a residual force and a residual negative stiffness acting on the short-stroke stage during exposure, which can result in additional disturbances.

The second hysteresis error we are concerned with is the deviation in force between the increasing portion and the decreasing portion of the current pulse. This deviation will result in larger moving-average (MA) errors at the beginning of exposure if left uncompensated. We denote this error simply as the hysteresis error, as distinct from the offset error, although both are the result of hysteresis.

In this section we derive simple theoretical formulas that provide approximations for the force error due to offset and to hysteresis. These formulas are useful both for designing a reluctance actuator to minimize hysteresis error and for predicting expected order-of-magnitude errors from hysteresis. We then simulate the reluctance actuator and show how the errors from simulation compare with the theoretical approximations.

4.2.1 Offset Error

In this analysis, we have assumed that the actuator was driven into or near saturation before the drive current was returned to zero. When the actuator current returns to zero after the actuator core has been magnetized, there remains a residual flux density, ΔB_{off}, in the core and air gap. This residual flux density can be thought of as the 'remanence' of the sheared hysteresis curve. This is illustrated by point a in Figure 4-5.

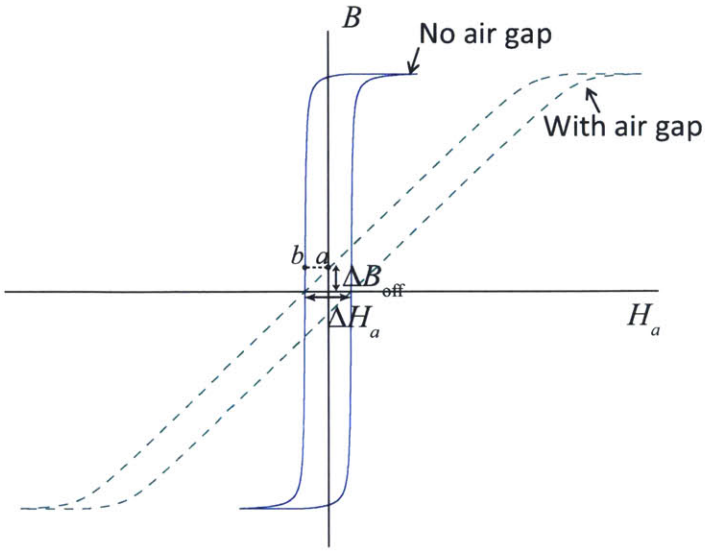

Figure 4-5: Hysteresis offset error ΔB_{off}.

The residual flux density can be estimated from (2.30). We note that the core magnetic field H_{Fe} corresponding to point a on the sheared hysteresis curve is located at point b on the unsheared hysteresis curve. At this point, $H_{Fe} \approx -H_c$. We can rewrite (2.30) as

$$-H_c + \frac{n\Delta B_{\text{off}}}{\mu_0} \approx H_a, \tag{4.6}$$

where we recall from Section 2.4.4 that $n = 2g/l_{Fe}$ and $H_a = NI/l_{Fe}$. The applied magnetic field H_a at point a is zero, so solving for ΔB_{off}, we write

$$\Delta B_{\text{off}} \approx \frac{\mu_0 H_c}{n},$$

$$\Delta B_{\text{off}} \approx \frac{l_{Fe}}{2g}\mu_0 H_c. \tag{4.7}$$

The offset error is proportional to the material coercivity and is inversely proportional to the air gap. Therefore, choosing a core material with low coercivity and increasing the actuator air gap will decrease the offset error.

An alternative way to derive this result is to consider the width of the B-I major

hysteresis loop at $B = 0$, which we denote as $\Delta I|_{B=0}$. From the definition of H_a, we can write

$$\Delta I|_{B=0} = \frac{l_{Fe}}{N} \Delta H_a|_{B=0}. \tag{4.8}$$

From Figure 4-5, we see that $\Delta H_a|_{B=0} = 2H_c$, so we can express (4.8) as

$$\Delta I|_{B=0} = \frac{2 l_{Fe} H_c}{N} \tag{4.9}$$

This gives us the maximum width of the B-I hysteresis loop. We now want to determine the maximum height of the B-I loop, $\Delta B_{\max}$. Since the ascending and descending branches of the B-I curve are approximately linear at the zero-flux crossings, we can say that $\Delta B_{\max}$ between the two branches will be approximately equal to the change in B that corresponds to $\Delta I = \Delta I|_{B=0}$ or $\Delta H_a = \Delta H_a|_{B=0}$ along either the ascending curve or descending curve. We denote this change of B as ΔB^a or ΔB^d, where the superscripts a and d refer to the ascending and descending branches, respectively. See Figure 4-6 for an illustration. We can then approximate ΔB^a from the relation given by (2.8), where we substitute $\Delta I|_{B=0}$ for I, shown here as

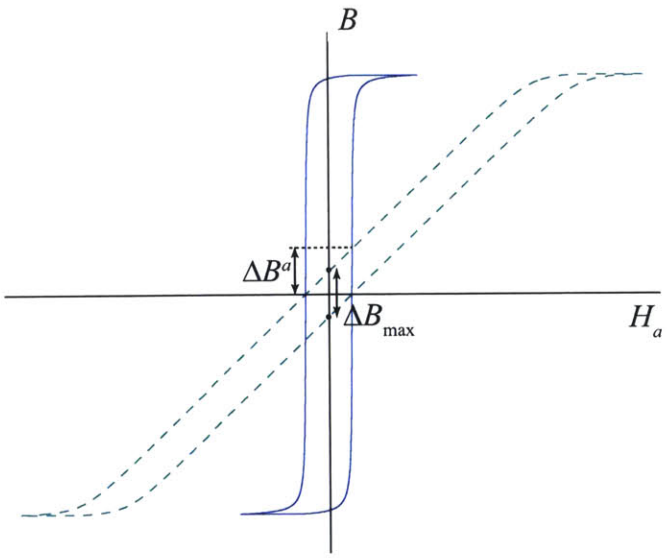

Figure 4-6: $\Delta B_{\max}$ is approximately equal to ΔB^a.

$$\Delta B_{\max} \approx \Delta B^a \approx \frac{\mu_0 N \Delta I|_{B=0}}{2g}. \tag{4.10}$$

Substituting (4.9), we can write

$$\Delta B_{\max} \approx \frac{l_{Fe}}{g}\mu_0 H_c. \tag{4.11}$$

Noting that ΔB_{off} is half $\Delta B_{\max}$, we arrive at the same result as (4.7).

We next want to determine the force error resulting from the offset (ΔF_{off}). This can be approximated in a straightforward manner by substituting ΔB_{off} for B_g in (2.13), shown here as

$$\Delta F_{\text{off}} \approx \frac{B_{\text{off}}^2 A}{2\mu_0}. \tag{4.12}$$

In terms of the material coercivity and actuator air gap, we can write

$$\Delta F_{\text{off}} \approx \frac{\mu_0 l_{Fe}^2 A H_c^2}{8g^2} \tag{4.13}$$

We can express A in terms of the maximum F and maximum B, $F_{\max}$ and $B_{\max}$, respectively, by noting that $F_{\max} = B_{\max}^2/(2\mu_0)A$. We write A as

$$A = \frac{2\mu_0 F_{\max}}{B_{\max}^2}. \tag{4.14}$$

If $B_{\max}$ is close to the saturation flux density, B_s, we can substitute B_s for $B_{\max}$ and then write ΔF_{off} as

$$\begin{aligned} \Delta F_{\text{off}} &\approx \frac{\mu_0 l_{Fe}^2 H_c^2}{8g^2}\left(\frac{2\mu_0 F_{\max}}{B_s^2}\right), \\ \Delta F_{\text{off}} &\approx \left(\frac{\mu_0 l_{Fe} H_c}{2gB_s}\right)^2 F_{\max}. \end{aligned} \tag{4.15}$$

If we stipulate a particular value for the l_{Fe}/g ratio, this form allows us easily to compare the expected offset errors among different materials for the same $F_{\max}$. Alternatively, if instead of stipulating a particular l_{Fe}/g ratio, we stipulate a particular

g, we can express l_{Fe} as a function of $F_{\max}$ and B_s if we make some assumptions about the actuator geometry. Figure 4-7 shows the flux path on an actuator with dimensions marked for calculating l_{Fe}.

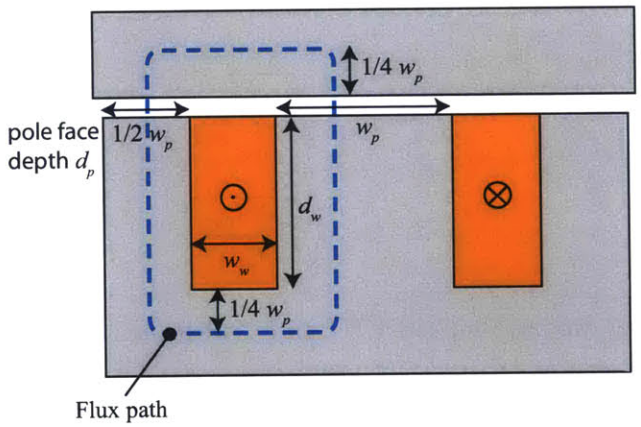

Figure 4-7: Actuator with flux path shown and dimensions marked.

We can express the average flux path length in the core l_{Fe} as

$$l_{Fe} = 2\left(d_w + \frac{1}{2}w_p\right) + 2\left(w_w + \frac{1}{2}w_p\right),$$

$$l_{Fe} = 2d_w + 2w_w + 2w_p. \tag{4.16}$$

We define the aspect ratios of the coil window and pole face as $\alpha = d_w/w_w$ and $\beta = d_p/w_p$, respectively. The amp-turns NI is equal to JA_w, where J is the current density and $A_w = w_w d_w$ is the coil window area. We can therefore derive an expression

for d_w in terms of these parameters as

$$\begin{aligned} w_w d_w &= A_w, \\ \frac{d_w^2}{\alpha} &= A_w, \\ d_w &= \sqrt{\alpha A_w}, \\ d_w &= \sqrt{\frac{\alpha N I}{J}}, \\ d_w &= \sqrt{\frac{\alpha N I_{\max}}{J_{\max}}}, \end{aligned} \tag{4.17}$$

where in the last line we have replaced NI and J with their maximum values, $NI_{\max}$ and $J_{\max}$, respectively. We can express $NI_{\max}$ using (2.8) as $NI_{\max} = 2gB_s/\mu_0$. If we substitute this into (4.17), we can write d_w as

$$d_w = \sqrt{\frac{2\alpha g B_s}{\mu_0 J_{\max}}}. \tag{4.18}$$

Likewise, for w_w, we can write

$$w_w = \sqrt{\frac{2gB_s}{\alpha \mu_0 J_{\max}}}. \tag{4.19}$$

We recognize that the center pole face area A_p is half the total pole face area and can be expressed using (4.14) as $A_p = 1/2A = \mu_0 F_{\max}/B_s^2$. Using this relation, we

can derive an expression for w_p in terms of these parameters as

$$\begin{aligned} w_p d_p &= A_p, \\ \beta w_p^2 &= A_p, \\ w_p &= \sqrt{\frac{A_p}{\beta}}, \\ w_p &= \frac{1}{B_s}\sqrt{\frac{\mu_0 F_{\max}}{\beta}}. \end{aligned} \tag{4.20}$$

Substituting (4.18-4.20) into (4.16), we write

$$\begin{aligned} l_{Fe} &= 2\sqrt{\frac{2\alpha g B_s}{\mu_0 J_{\max}}} + 2\sqrt{\frac{2gB_s}{\alpha\mu_0 J_{\max}}} + 2\frac{1}{B_s}\sqrt{\frac{\mu_0 F_{\max}}{\beta}}, \\ &= 2\sqrt{\frac{2g}{\mu_0 J_{\max}}}\left(\frac{\alpha+1}{\sqrt{\alpha}}\right)\sqrt{B_s} + 2\sqrt{\frac{\mu_0}{\beta}}\frac{\sqrt{F_{\max}}}{B_s}, \\ l_{Fe} &= C_1\sqrt{B_s} + C_2\frac{\sqrt{F_{\max}}}{B_s}, \end{aligned} \tag{4.21}$$

where C_1 and C_2 are constants that depend on actuator geometry, air gap, and maximum current density. Crucially, C_1 and C_2 do not depend on specific dimensions, but rather on the aspect ratio of the pole face and the aspect ratio of the coil window. In this way, scaled versions of the same actuator for different materials can be compared easily if we stipulate $J_{\max}$ and g.

We can use (4.13) to predict the force offset error and compare this with simulation results. At a nominal gap of $g = 500\,\mu\text{m}$, (4.13) predicts $\Delta F_{\text{off}} = 0.0730\,\text{mN}$. Simulation of the reluctance actuator using the current profile shown in Figure 4-4 results in $\Delta F_{\text{off}} = 0.0726\,\text{mN}$, showing a very close match to theory. The simulated force is shown in Figure 4-8. This error is only 2×10^{-5} percent of the full-scale force.

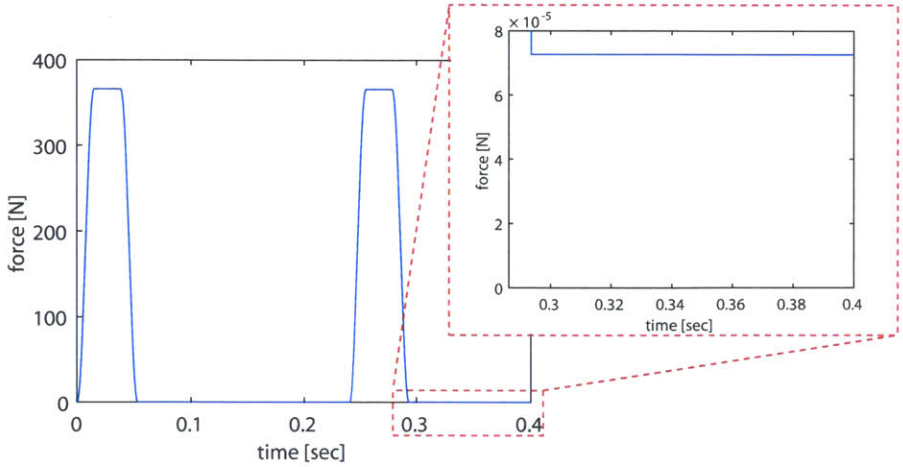

Figure 4-8: Simulation of a reluctance actuator showing the offset force due to hysteresis.

4.2.2 Hysteresis Error

To derive an expression for the force deviation due to hysteresis, we first solve (2.2) for B_g (dropping the subscript), where we have substituted B_g/μ_0 for H_{g_1} and H_{g_2}, and write

$$B = \frac{\mu_0 NI}{2g} - \frac{\mu_0 l_{Fe}}{2g} H_{Fe}. \tag{4.22}$$

We substitute this result into (2.13) to yield

$$\begin{aligned} F &= \frac{A}{2\mu_0}\left(\frac{\mu_0 NI}{2g} - \frac{\mu_0 l_{Fe}}{2g} H_{Fe}\right)^2, \\ &= \frac{A}{2\mu_0}\left(\frac{\mu_0^2}{4g^2} N^2 I^2 - \frac{\mu_0^2 l_{Fe}}{2g^2} NIH_{Fe} + \frac{\mu_0^2 l_{Fe}^2}{4g^2} H_{Fe}^2\right). \end{aligned} \tag{4.23}$$

Now consider the force-current hysteresis loop shown in Figure 4-9. We want to determine $\Delta F_h(I) = F^d(I) - F^a(I)$, the difference in force between the ascending and descending curves for the same current value.

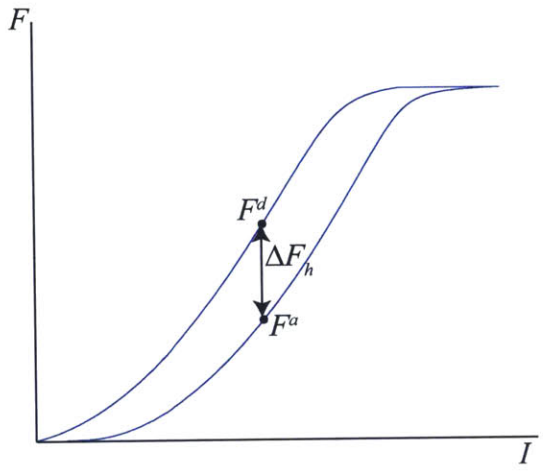

Figure 4-9: ΔF_h between the ascending and descending branches.

We can use (4.23) to write ΔF_h in terms of I^a, I^d, H^a_{Fe}, and H^d_{Fe} as

$$\begin{aligned}\Delta F_h = \frac{A}{2\mu_0}\Bigg(&\frac{\mu_0^2}{4g^2}N^2(I^d)^2 - \frac{\mu_0^2 l_{Fe}}{2g^2}NI^dH^d_{Fe} \\ &+ \frac{\mu_0^2 l_{Fe}^2}{4g^2}(H^d_{Fe})^2 - \frac{\mu_0^2}{4g^2}N^2(I^a)^2 + \frac{\mu_0^2 l_{Fe}}{2g^2}NI^aH^a_{Fe} - \frac{\mu_0^2 l_{Fe}^2}{4g^2}(H^a_{Fe})^2\Bigg).\end{aligned} \tag{4.24}$$

Noting that $I^d = I^a = I$ and dropping the subscript on H_{Fe} for simplicity, we can simplify this to

$$\begin{aligned}\Delta F_h &= \frac{A}{2\mu_0}\left[\frac{\mu_0 l_{Fe}N}{2g^2}I\left(H^d - H^a\right) + \frac{\mu_0 l_{Fe}^2}{4g^2}\left((H^d)^2 - (H^a)^2\right)\right], \\ &= \frac{\mu_0^2 l_{Fe}^2}{4g^2}\frac{A}{2\mu_0}\left[\frac{2N}{l_{Fe}}I\left(H^d - H^a\right) + \left((H^d)^2 - (H^a)^2\right)\right], \\ &= \frac{\mu_0^2 l_{Fe}^2}{4g^2}\frac{A}{2\mu_0}\left[\frac{2N}{l_{Fe}}I\left(H^d - H^a\right) + \left(H^d + H^a\right)\left(H^d - H^a\right)\right], \\ \Delta F_h &= \frac{\mu_0^2 l_{Fe}^2}{4g^2}\frac{A}{2\mu_0}\left[\frac{2N}{l_{Fe}}I\left(H^d - H^a\right) + 2\bar{H}\left(H^d - H^a\right)\right],\end{aligned} \tag{4.25}$$

where in the last line, we have used the mean value of H^a and H^d, $\bar{H} = \left(H^d + H^a\right)/2$. Except at well into saturation and near $I = 0$, NI/l_{Fe} will dominate over $\bar{H}$, so we

can approximate (4.25) as

$$\Delta F_h \approx \frac{\mu_0 l_{Fe}^2 A}{8g^2}\left[\frac{2N}{l_{Fe}} I\left(H^d - H^a\right)\right],$$

$$\Delta F_h \approx \frac{\mu_0 l_{Fe} AN}{4g^2} I\left(H^d - H^a\right). \tag{4.26}$$

We now have a simplified relation between the hysteretic force error on one hand and the current and magnetic field on the other. For this relation to be useful in predicting expected force deviation, H^d and H^a need to be related to I. This can be done for instance by noting the relation between the sheared hysteresis curve and the material hysteresis curve and using (2.30). See Figure 4-10 for a graphical representation of how H^d and H^a are related to I. For a particular value of I on the sheared hystersis curve (dotted green curve), we note the value of B on the ascending branch, B^a. Using (2.30), we calculate the core magnetic field H_{Fe} on the ascending branch of the blue curve by subtracting nB^a/μ_0 from $H_a = NI/l_{Fe}$, recalling that $n = 2g/l_{Fe}$. This gives us H^a. Likewise, we can determine the H^d associated with I by noting the value of B on the descending branch of the sheared curve, B^d, and subtracting the quantity nB^d/μ_0 from NI/l_{Fe}.

If the hysteresis loop is relatively square, we can further simplify the approximation in (4.26) by noting from Figure 4-10 that $H^d - H^a \approx 2H_c$ until very close to saturation. Substituting this into (4.26) we write

$$\Delta F_h \approx \frac{\mu_0 l_{Fe} ANIH_c}{2g^2}. \tag{4.27}$$

Using (2.8) and (2.13), we can express (4.27) in terms of B or F as

$$\Delta F_h \approx \frac{l_{Fe} ABH_c}{g} \approx \frac{l_{Fe} H_c}{g}\sqrt{2\mu_0 AF}. \tag{4.28}$$

If we want quickly to compare actuators of different materials capable of the same $F_{\max}$, we express A in terms of $F_{\max}$ and B_s using (4.14) with B_s substituted for $B_{\max}$.

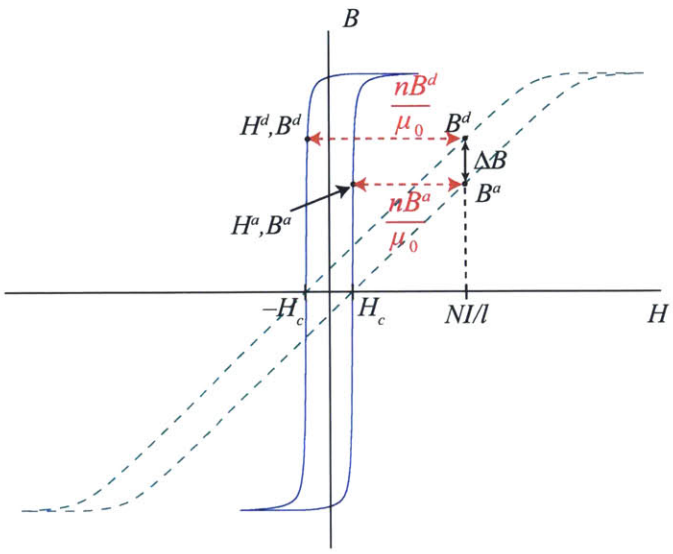

Figure 4-10: A graphical representation of the relation between the B-I curve and H_a and H_d.

We write

$$\Delta F_h \approx \approx \frac{l_{Fe}H_c}{g}\sqrt{\frac{4\mu_0^2 F_{\max}F}{B_s^2}},$$

$$\Delta F_h \approx \frac{2\mu_0 l_{Fe}H_c}{gB_s}\sqrt{F_{\max}F}, \tag{4.29}$$

where l_{Fe} can be expressed in terms of $F_{\max}$ using (4.21) if desired.

Equations (4.27)–(4.29) allow us to estimate the expected hysteresis error in terms of actuator parameters that can be approximated early in the design process. If we know the maximum force required for a single actuator, we can estimate the maximum hysteresis error by substituting $F_{\max}$ for F in (4.29). This will give an overestimate for the maximum hysteresis error, because the actual maximum will occur at some value less than $F_{\max}$ (intuitively, this makes sense, since we know that the hysteresis loop must close eventually, so that ΔF_h must start decreasing at some point before $F_{\max}$). As with the offset error, choosing a material with low coercivity and increasing

the actuator air gap will decrease the hysteresis error.

The accuracy of the approximations given in (4.27-4.29) will degrade if the shape of the hysteresis loop deviates significantly from the square shape because the range for which it is valid to approximate $H^d - H^a$ as $2H_c$ is much smaller. In such cases, if some knowledge of the shape of the hysteresis loop is known, then (4.26) can be applied, which is a more general version of the hysteresis error approximation.

As was done with the offset error, we want to compare the hysteresis error predicted from theory with that predicted by simulation. Using (4.28) with $F = F_{\max}$, we predict the maximum force hysteresis error, $\Delta F_{h,\max}$, to be 0.65 N. Simulation results in $\Delta F_{h,\max} = 0.56\,\text{N}$ maximum force error. This is 0.15 percent of full-scale force. The simplified formula shows reasonable agreement with simulation. Figure 4-11 shows the maximum hysteresis error from the simulation. The maximum error occurs at $I = 2.92\,\text{A}$ and $F \approx 307\,\text{N}$, slightly lower than the 3.2 A and 367 N corresponding to $I_{\max}$ and $F_{\max}$ used in (4.27) and (4.28), respectively.

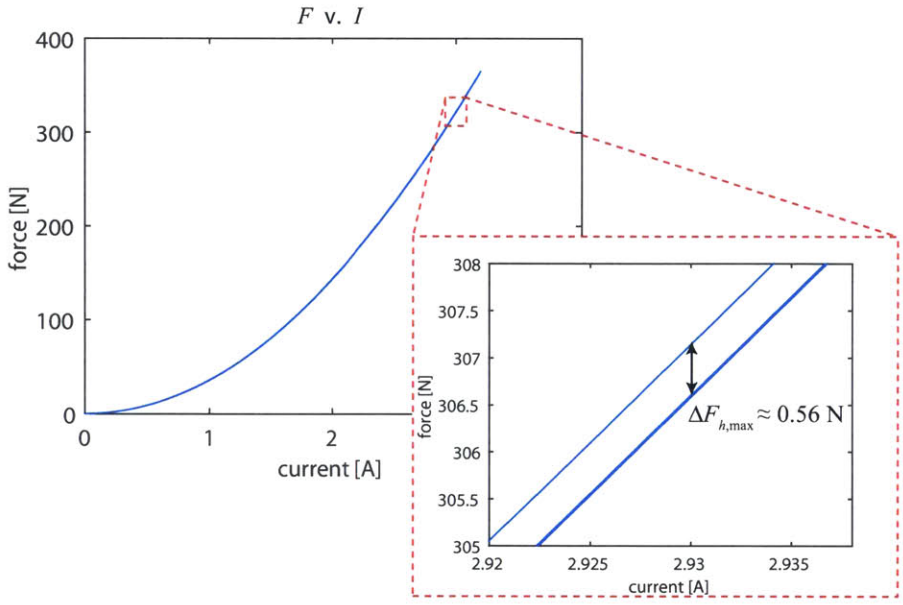

Figure 4-11: Simulated force versus current showing the maximum force error from hysteresis.

Figure 4-12 plots (4.27) and (4.28) for the second pulse in the current profile and compares them with the simulated force error. The approximations show a good

match with the simulated error except at high values of I and F.

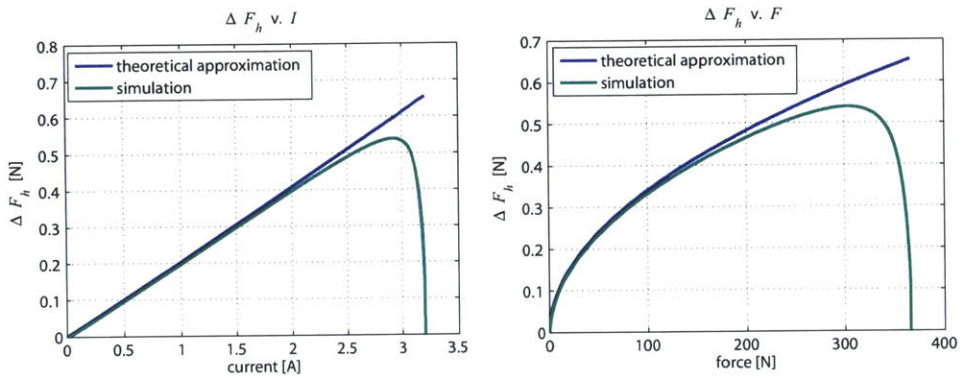

Figure 4-12: LEFT: Comparison of ΔF_h from (4.27) with ΔF_h from simulation. RIGHT: Comparison of ΔF_h from (4.28) with ΔF_h from simulation.

4.3 Analysis of Error from Gap Disturbance

We can also use our simulation model to investigate the effects of a gap disturbance on force accuracy. As was done in the previous section, we first derive a simple theoretical formula for approximating the error from a gap disturbance. We then simulate the gap disturbance and show how the simulation results compare with theory.

We start from the approximation given by (2.8), reproduced here and solved for NI as

$$NI \approx \frac{2g}{\mu_0} B. \tag{4.30}$$

We want to determine the change in flux density, ΔB_d, resulting from a gap disturbance, Δg. To do this, we define two different states (denoted with the subscripts 1 and 2) of the actuator with identical currents but with a difference in gap between them. We define $I_1 = I_2 = I_0$, and we define $g_1 = g_0$ and $g_2 = g_0 + \Delta g$, where g_0 is the nominal gap. Likewise, we define $B_1 = B_0$ and $B_2 = B_0 + \Delta B_d$, where B_0 is the

air gap flux density at $I = I_0$ and $g = g_0$. We rewrite (4.30) for states 1 and 2 as

$$NI_1 \approx \frac{2g_1}{\mu_0} B_1, \tag{4.31}$$

$$NI_2 \approx \frac{2g_2}{\mu_0} B_2. \tag{4.32}$$

If we subtract (4.31) from (4.32) and expand the terms for g_2 and B_2, we can write

$$\begin{aligned} \frac{2}{\mu_0}(g_0 + \Delta g)(B_0 + \Delta B_d) - \frac{2}{\mu_0} g_0 B_0 &\approx 0, \\ g_0 B_0 + B_0 \Delta g + g_0 \Delta B_d + \Delta g \Delta B_d - g_0 B_0 &\approx 0, \\ B_0 \Delta g + g_0 \Delta B_d + \Delta g \Delta B_d &\approx 0. \end{aligned} \tag{4.33}$$

Assuming small perturbations, we can remove the second-order term $\Delta g \Delta B_d$ and solve for ΔB_d as

$$\Delta B_d = -\frac{B_0}{g_0} \Delta g. \tag{4.34}$$

The change in flux density ΔB_d is thus proportional the gap deviation and the nominal flux density level and inversely proportional to the nominal gap. Thus, gap disturbances have a larger effect at high flux density levels.

A second way to derive the result in (4.34) is by substituting $B_0 + \Delta B_d$ for B and $g_0 + \Delta g$ for g directly into (2.8) as

$$\begin{aligned} B + \Delta B_d &\approx \frac{\mu_0 NI}{2(g_0 + \Delta g)}, \\ B + \Delta B_d &\approx \frac{\mu_0 NI / g_0}{2\left(1 + \Delta g / g_0\right)}. \end{aligned} \tag{4.35}$$

Recognizing that $\Delta g / g_0 << 1$, we can expand the left-hand side of (4.35) into a

Taylor series, truncating it after the first-order terms. We write

$$B_0 + \Delta B_d \approx \frac{\mu_0 NI}{2g_0}\left(1 - \frac{\Delta g}{g_0}\right). \tag{4.36}$$

Noting that $\mu_0 NI/(2g_0) = B_0$, we can solve (4.36) for ΔB_d as

$$\Delta B_d \approx -\frac{B_0}{g_0}\Delta g, \tag{4.37}$$

the same result we arrived at before.

We next want to determine the effect of the gap disturbance on force. We can linearize (2.13) in terms of ΔB_d around an operating point F_0, B_0

$$F = F_0 + \Delta F_d \approx \frac{B_0^2 A}{2\mu_0} + \frac{B_0 A}{\mu_0}\Delta B. \tag{4.38}$$

Noting that $F_0 = B_0^2 A/(2\mu_0)$, we can solve for ΔF_d

$$\Delta F_d \approx \frac{B_0 A}{\mu_0}\Delta B. \tag{4.39}$$

Substituting (4.34), we write

$$\Delta F_d \approx -\frac{B_0^2 A}{\mu_0 g_0}\Delta g. \tag{4.40}$$

Alternatively, expressing ΔF_d in terms of F_0, we write

$$\Delta F_d \approx -\frac{2F_0}{g_0}\Delta g. \tag{4.41}$$

If we divide both sides of (4.41) by Δg and take the limit as Δg approaches zero, we derive the stiffness of an uncompensated reluctance actuator, k_r

$$k_r = \frac{\partial F}{\partial g} = -\frac{2F_0}{g_0}. \tag{4.42}$$

We see that the stiffness is negative and that its magnitude increases with force and

decreases with operating gap.

We can set an upper limit to the expected force disturbance by stipulating that the maximum gap disturbance, $\Delta g_{\max}$, occurs at $F_{\max}$. Then

$$\Delta F_{d,\max} \approx -\frac{2F_{\max}}{g_0}\Delta g_{\max}. \tag{4.43}$$

For simulating the gap disturbance, we adapted a gap profile from data taken from the long-stroke error on a lithography machine. The simulated gap disturbance is shown in Figure 4-13. This gap disturbance is added to the nominal gap during simulation.

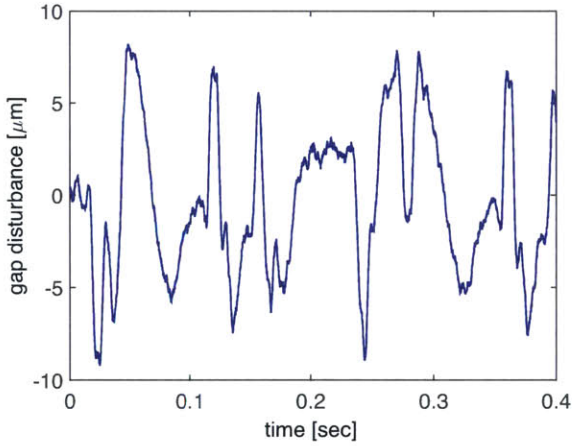

Figure 4-13: Simulated gap disturbance.

Since the exact gap disturbance profile is unlikely to be known before designing and implementing the reluctance actuator on a real stage, for comparing theory with simulation, we replaced $\Delta g_{\max}$ in (4.43) with an order-of-magnitude estimate of the maximum gap disturbance rather than the exact maximum gap disturbance from Figure 4-13. In this case, we estimated $\Delta g_{\max}$ as 10 µm. The actual maximum magnitude of the simulated gap disturbance is 9.2 µm.

Using this estimated $\Delta g_{\max}$, we approximated the maximum ΔF_d to be 14.6 N. The simulated force with gap disturbance is compared to the simulated force with no gap disturbance in the top plot of Figure 4-14. Below it is a graph showing the force error between the two cases. The maximum simulated ΔF_d is 13.8 N, showing good

agreement with theory. This error is 3.8 percent of full-scale force. Errors from gap disturbance are thus expected to dominate over errors from hysteresis or offset.

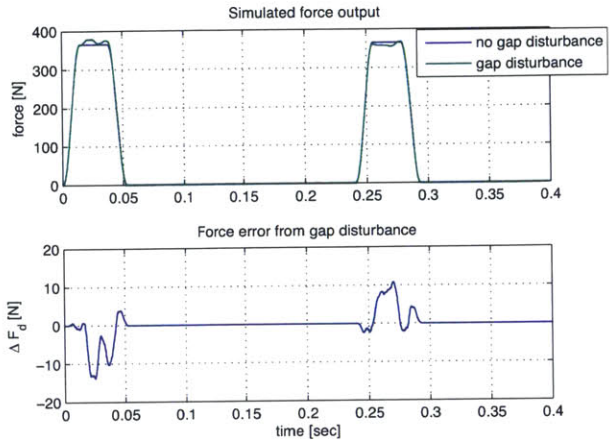

Figure 4-14: TOP: Simulated actuator force output with and without gap disturbance; BOTTOM: Simulated force error generated by gap disturbance.

4.4 Reluctance Actuator Model with Flux Feedback

We can use our model to investigate the effectiveness of flux feedback. Flux feedback in block diagram form is represented in Figure 4-15. The block labeled 'Actuator Model' represents the model developed in this chapter, B represents the actuator air gap flux density, and B_m represents the measured air gap flux density.

Simulating a flux feedback loop with the nonlinear actuator model permits us to investigate how well feedback control can linearize the actuator. We can explore the effect of controller bandwidth on force accuracy and stiffness as well as the effect of feedforward control. The sensor block represents the flux sensor. We can analyze the effects of such things as sensor noise, sensor nonlinearities, and sensor offset on force accuracy. We can compare and contrast different types of sensors. In the remainder of this section, we investigate the effect of flux feedback on actuator stiffness. We derive theoretical approximations for the compensated stiffness when the flux loop

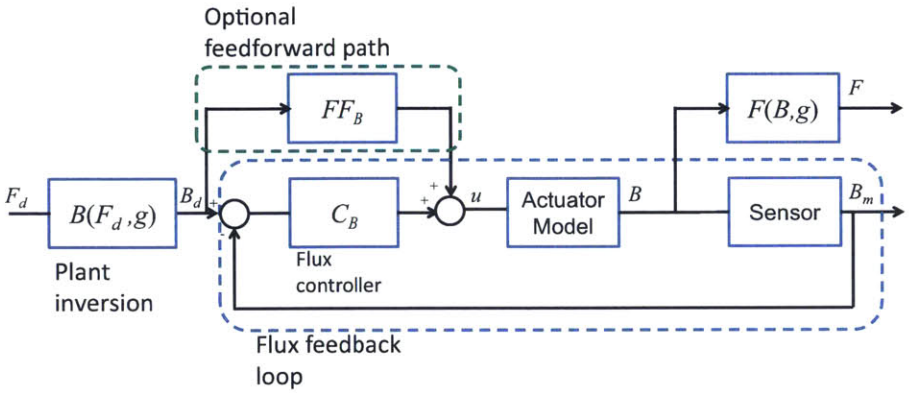

Figure 4-15: Block diagram of a reluctance actuator model with flux feedback.

includes a high-bandwidth inner current loop and when it does not. For the flux loop with current loop, we compare the theoretical approximation of the disturbance rejection with simulation results.

4.4.1 Stiffness with Flux and Current Control

We first analyzed the expected change in flux density ΔB resulting from a gap disturbance Δg when the flux is being controlled with a feedback loop that includes a high-bandwidth current loop. From this result, we then determined the expected stiffness $\Delta F/\Delta g$. A block diagram of a linearized flux control loop with a gap disturbance is shown in Figure 4-16.

The disturbance feedthrough transfer function $D(s)$ can be approximated from (4.34) as $D(s) = -B_0/g_0$, where B_0 is the nominal flux density level and g_0 is the nominal air gap. The plant $P(s)$ can be approximated as $P(s) = \mu_0 N/(2g_0)$, where we have linearized (2.8) about the nominal operating gap. This plant takes current as its input. Thus, this analysis ignores the electrical dynamics of the reluctance actuator. Such an analysis is representative of a flux loop that includes a high-bandwidth inner current loop (see Figure 2-17E).

The disturbance rejection transfer function $B(s)/g(s)$ can be expressed as

$$\frac{B(s)}{g(s)} = \frac{D(s)}{1 + C(s)P(s)} = -\frac{1}{1 + LT(s)}\frac{B_0}{g_0}, \tag{4.44}$$

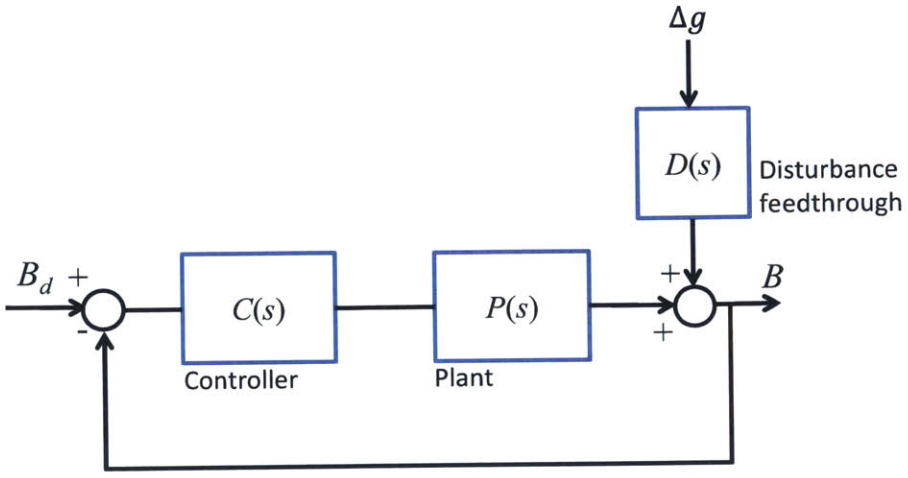

Figure 4-16: Block diagram of reluctance actuator flux control loop with gap disturbance.

where $LT(s) = C(s)P(s)$ is the negative of the loop transmission. At frequencies below the crossover frequency, $LT(s)$ will dominate the denominator, and we can approximate $B(s)/g(s)$ as

$$\frac{B(s)}{g(s)} \approx -\frac{1}{LT(s)}\frac{B_0}{g_0}. \tag{4.45}$$

We can replace $LT(s)$ with $C(s)\mu_0 N/(2g_0)$ and write

$$\begin{aligned} \frac{B(s)}{g(s)} &\approx -\frac{1}{C(s)\frac{\mu_0 N}{2g_0}}\frac{B_0}{g_0}, \\ \frac{B(s)}{g(s)} &\approx -\frac{2B_0}{C(s)\mu_0 N}. \end{aligned} \tag{4.46}$$

With current and flux control, the flux loop disturbance rejection is independent of gap. We also see that it is proportional to B_0, so the disturbance rejection will deteriorate as the flux increases. Assuming that $C(s)$ includes an integrator, the loop disturbance rejection transfer function will increase with ω at low frequencies.

We simulated a flux feedback loop using the model we developed earlier in this chapter. Our controller was $C(s) = 8.95 \times 10^4/s$, which was designed to achieve an approximate crossover frequency of 5 kHz. To determine the simulated actuator disturbance rejection, we generated a frequency sweep of the model where the controller

maintained a constant reference B_0 and the gap was given a sinusoidal disturbance about the nominal operating gap. Figure 4-17 shows the simulated actuator gap disturbance rejection frequency responses for different levels of B_0 when $g_0 = 500\,\mu\text{m}$. The simulations had some difficulties at some of the low frequencies, which accounts for the discrepancies in the phase plots. Otherwise, the simulated frequency responses confirm theory: the disturbance rejection magnitude increases with B_0 and increases linearly with ω at low frequencies.

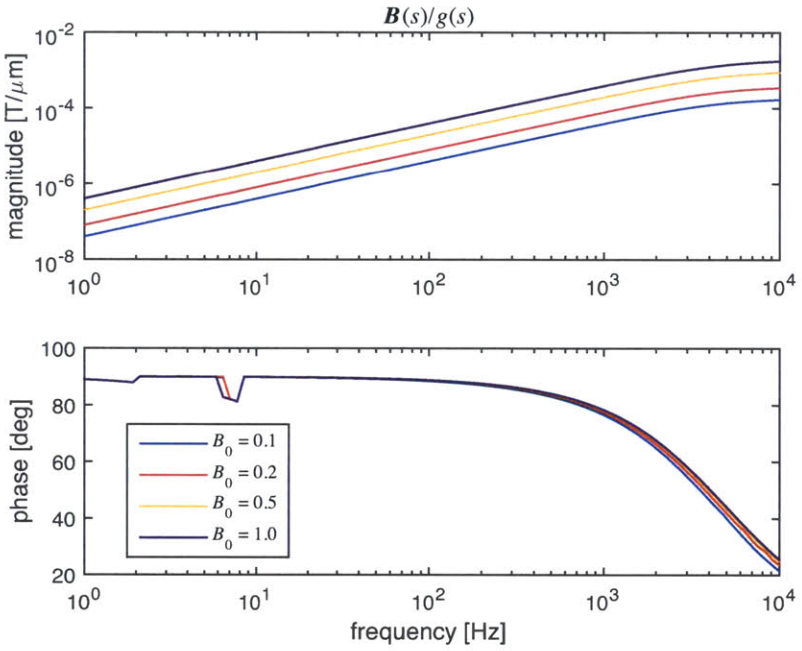

Figure 4-17: Simulated frequency responses of reluctance actuator gap disturbance rejection with flux and current control for varying flux levels.

Figure 4-18 shows the simulated gap disturbance rejection frequency responses for different nominal air gaps. As predicted by theory, the nominal gap has a negligible effect on disturbance rejection.

In Figure 4-19, we compare a simulated gap disturbance rejection frequency response with the theoretical approximations given by (4.44) and (4.45). Both approximations match the simulated frequency response closely for frequencies below the controller bandwidth.

From the disturbance rejection approximation, we can calculate the expected com-

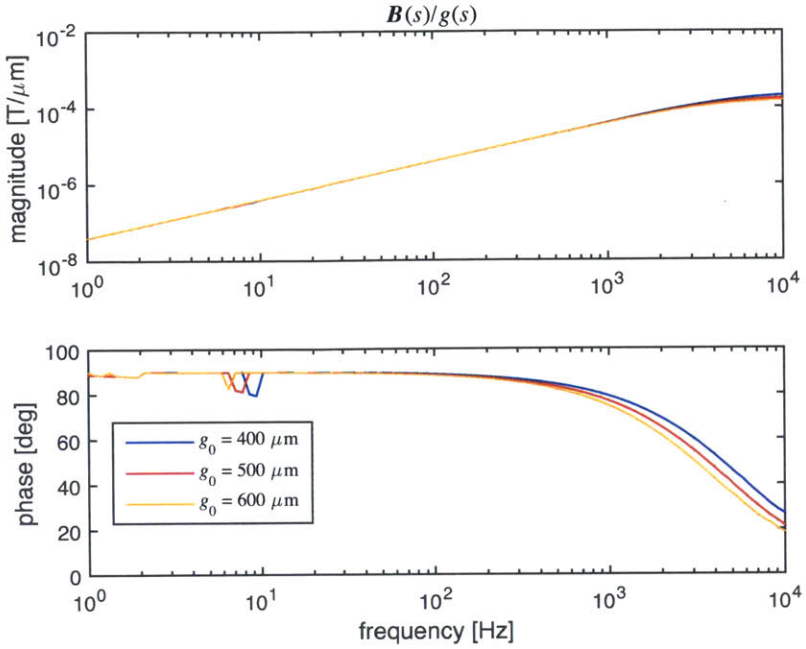

Figure 4-18: Simulated frequency responses of reluctance actuator gap disturbance rejection with flux and current control for different nominal air gaps.

pensated actuator stiffness. Expressing (4.45) in terms of ΔB and Δg and then substituting into (4.39), we write

$$\begin{aligned}
\Delta F &\approx \frac{B_0 A}{\mu_0}\left(-\frac{1}{LT(s)}\right)\frac{B_0}{g_0}\Delta g, \\
&\approx -\frac{B_0^2 A}{\mu_0 LT(s) g_0}\Delta g, \\
&\approx -\frac{2F_0}{LT(s) g_0}\Delta g, \qquad (4.47)
\end{aligned}$$

where in the last line, we have used (2.13) to express the result in terms of F_0. The expected stiffness of the compensated actuator, k_{rc}, is thus

$$k_{rc} = \frac{\partial F}{\partial g} = -\frac{2F_0}{LT(s) g_0}. \qquad (4.48)$$

By comparing this result with the stiffness for the uncompensated reluctance

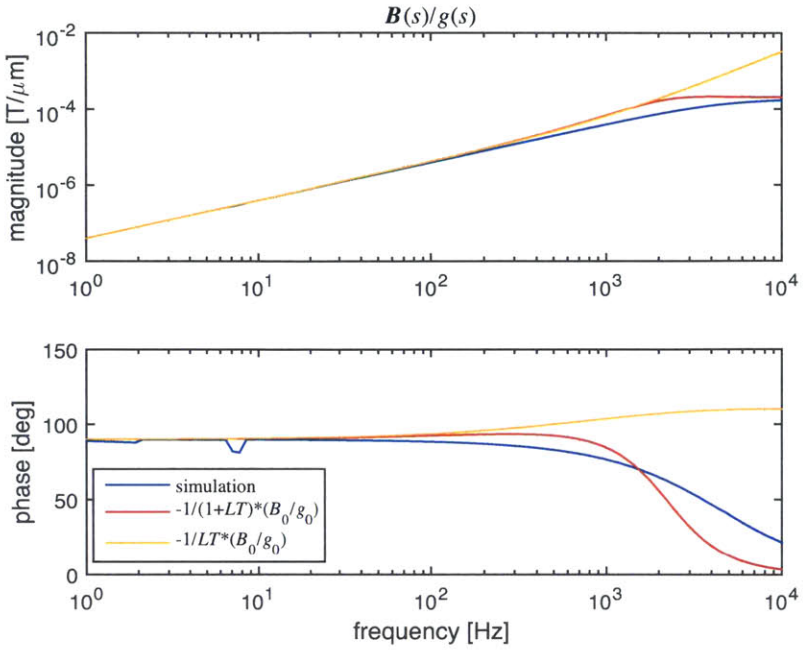

Figure 4-19: Simulated frequency response of reluctance actuator gap disturbance rejection compared with theoretical approximations.

actuator, k_r in (4.42), we see that k_{rc} is equal to

$$k_{rc} = \frac{1}{LT(s)} k_r. \tag{4.49}$$

We can replace $LT(s)$ in (4.48) with $C(s)P(s)$, and express k_{rc} as

$$k_{rc} = -\frac{2F_0}{C(s)\frac{\mu_0 N}{2g_0} g_0},$$

$$k_{rc} = -\frac{4F_0}{\mu_0 N C(s)}. \tag{4.50}$$

The compensated stiffness is proportional to the force level and independent of gap. The stiffness will increase with ω if the controller includes an integrator.

4.4.2 Stiffness with Flux Control and Voltage Drive

When we actuate the reluctance actuator with a voltage drive rather than with a current drive, the flux dependency on gap changes. In the basic actuator model, we assumed a perfect current source as the input. A more realistic model would include a model of the electrical domain of the actuator as well. We first derive the uncompensated disturbance stiffness for the actuator when driven with a voltage source. We then derive the stiffness for the voltage-driven actuator when compensated with a flux controller.

Uncompensated Stiffness

Suppose we have a voltage drive, V_S, applied to the actuator coil terminals. Then Kirchhoff's voltage law applied to the reluctance actuator is

$$V_S = IR + \frac{d\lambda}{dt}, \tag{4.51}$$

where I is the actuator current, R is the coil resistance, and λ is the flux linked by the actuator coil. The $d\lambda/dt$ term accounts for the actuator inductance and any speed voltage from the changing gap.

The flux linked by the actuator coil is $N\Phi$, where N is the number of coil turns and Φ is the magnetic flux through the center pole. If we ignore fringing and leakage flux, we can write that $\Phi = BA_p$, where A_p is the center pole face area. Substituting these relations into (4.51), we write

$$V_S = IR + NA_p\frac{dB}{dt}. \tag{4.52}$$

If we solve (2.8) for I and substitute the result into (4.52), we can write

$$V_S = \frac{2gR}{\mu_0 N}B + NA_p\frac{dB}{dt}. \tag{4.53}$$

Assuming a constant gap g_0, we can derive the transfer function from V_s to B as

$$\frac{B(s)}{V_s(s)} = \frac{\mu_0 N}{2g_0} \frac{1/R}{\frac{\mu_0 A_p N^2}{2Rg_0}s + 1} = \frac{\mu_0 N}{2g_0} \frac{1/R}{\frac{L}{R}s + 1}, \tag{4.54}$$

where $L = \mu_0 A_p N^2/(2g_0)$ is the actuator inductance. This is the open-loop transfer function from voltage input to flux density output, so in the block diagram of Figure 4-16, we set $P(s) = B(s)/V_s(s)$.

To determine $B(s)/g(s)$, we assume a state where $g = g_0$ and $B = B_0$. We then peturb g by an amount Δg, so that in the new state $B = B_0 + \Delta B$ and $g = g_0 + \Delta g$ in (4.53). If V_s is held constant between the two states, we can write

$$\begin{aligned} V_s &= \frac{2\left(g_0 + \Delta g\right) R}{\mu_0 N}\left(B_0 + \Delta B\right) + N A_p \frac{d\left(B_0 + \Delta B\right)}{dt}, \\ &= \frac{2g_0 R B_0}{\mu_0 N} + \frac{2g_0 R}{\mu_0 N}\Delta B + \frac{2RB_0}{\mu_0 N}\Delta g + \frac{2R}{\mu_0 N}\Delta g \Delta B + N A_p \Delta \dot{B}. \end{aligned} \tag{4.55}$$

Noting that the first term on the right-hand side is equal to V_s and ignoring the second-order term $\Delta g \Delta B$ under the assumption of small perturbations, we can write

$$0 = \frac{2g_0 R}{\mu_0 N}\Delta B + \frac{2RB_0}{\mu_0 N}\Delta g + N A_p \Delta \dot{B}. \tag{4.56}$$

Taking the Laplace transform of the above equation, we can solve for $B(s)/g(s)$ as

$$\begin{aligned} \left[N A_p s + \frac{2g_0 R}{\mu_0 N}\right] B(s) &= -\frac{2RB_0}{\mu_0 N} g(s), \\ \frac{B(s)}{g(s)} &= -\frac{\frac{2RB_0}{\mu_0 N}}{N A_p s + \frac{2g_0 R}{\mu_0 N}}, \\ &= -\frac{\mu_0 N}{2g_0 R} \frac{\frac{2RB_0}{\mu_0 N}}{\frac{\mu_0 A_p N^2}{2g_0 R}s + 1}, \\ \frac{B(s)}{g(s)} &= -\frac{B_0}{g_0} \frac{1}{\frac{L}{R}s + 1}. \end{aligned} \tag{4.57}$$

Compared to the uncompensated disturbance rejection of a reluctance actuator driven with a current (4.34), the voltage-driven uncompensated disturbance rejection is low-pass filtered by the transfer function $1/\big((L/R)s+1\big)$. A gap disturbance will thus have less effect on the flux when the actuator is driven with a voltage source. We can determine the uncompensated stiffness when the actuator is driven with a voltage by expressing (4.57) in terms of ΔB and Δg and substituting this into (4.39). This yields

$$\begin{aligned}\Delta F &\approx \frac{B_0 A}{\mu_0}\left(-\frac{B_0}{g_0}\frac{1}{\frac{L}{R}s+1}\right)\Delta g,\\ &\approx -\frac{B_0^2 A}{\mu_0 g_0}\frac{1}{\frac{L}{R}s+1}\Delta g,\\ &\approx -\frac{2F_0}{g_0}\frac{1}{\frac{L}{R}s+1}\Delta g. \end{aligned} \tag{4.58}$$

The stiffness is then

$$k_r = -\frac{2F_0}{g_0}\frac{1}{\frac{L}{R}s+1}. \tag{4.59}$$

Compensated Stiffness

To determine the compensated disturbance rejection when the flux loop does not include a high-bandwidth inner current loop, we apply (4.44) using (4.57) for $D(s)$. We write

$$\begin{aligned}\frac{B(s)}{g(s)} = \frac{D(s)}{1+C(s)P(s)} &= -\left(\frac{1}{1+LT(s)}\right)\left(\frac{B_0}{g_0}\frac{1}{\frac{L}{R}s+1}\right),\\ &\approx -\frac{1}{LT(s)}\frac{B_0}{g_0}\frac{1}{\frac{L}{R}s+1}, \end{aligned} \tag{4.60}$$

where in the second line, we have approximated $1/\big(1+LT(s)\big)$ as $1/LT(s)$, which is valid for frequencies below the loop crossover frequency. We can replace $LT(s)$ with

$C(s)B(s)/V_s(s)$ and write

$$\begin{aligned}
\frac{B(s)}{g(s)} &\approx -\left(\frac{1}{C(s)\frac{B(s)}{V_s(s)}}\right)\left(\frac{B_0}{g_0}\frac{1}{\frac{L}{R}s+1}\right), \\
&\approx -\left(\frac{1}{C(s)\frac{\mu_0 N}{2g_0}\frac{1/R}{\frac{L}{R}s+1}}\right)\left(\frac{B_0}{g_0}\frac{1}{\frac{L}{R}s+1}\right), \\
\frac{B(s)}{g(s)} &\approx -\frac{2RB_0}{\mu_0 NC(s)}.
\end{aligned} \tag{4.61}$$

This result is similar to (4.46) for flux control with current loop. Note that the controllers $C(s)$ will not be the same in the two cases. The disturbance rejection is proportional to B_0 and is independent of the operating gap g_0.

We can apply a similar analysis that we did for the flux loop with current control to determine the compensated stiffness. We express (4.60) in terms of ΔB and Δg and substitute it into (4.39) to yield

$$\begin{aligned}
\Delta F &\approx \frac{B_0 A}{\mu_0}\left(-\frac{1}{LT(s)}\right)\left(\frac{B_0}{g_0}\frac{1}{\frac{L}{R}s+1}\right)\Delta g, \\
&\approx -\frac{B_0^2 A}{\mu_0 LT(s) g_0}\left(\frac{1}{\frac{L}{R}s+1}\right)\Delta g, \\
&\approx \frac{2F_0}{LT(s)g_0}\left(\frac{1}{\frac{L}{R}s+1}\right)\Delta g.
\end{aligned} \tag{4.62}$$

The compensated stiffness k_{rc} is

$$k_{rc} = -\frac{2F_0}{g_0 LT(s)}\left(\frac{1}{\frac{L}{R}s+1}\right). \tag{4.63}$$

Substituting $C(s)B(s)/V_s(s)$ for $LT(s)$ yields

$$\begin{aligned} k_{rc} &= -\frac{2F_0}{C(s)\frac{\mu_0 N}{2g_0}\frac{1/R}{\frac{L}{R}s+1}g_0}\left(\frac{1}{\frac{L}{R}s+1}\right), \\ &\approx -\frac{4RF_0}{\mu_0 NC(s)}. \end{aligned} \tag{4.64}$$

4.4.3 Comparison between Compensated Stiffness with and without Current Control

It is useful to compare the compensated stiffness of the reluctance actuator with and without a high-bandwidth current control loop. In order properly to compare the two, we stipulate an identical flux loop crossover frequency for the two cases. In the current-controlled case, we can achieve a high crossover frequency with an integral controller K/s since the high-bandwidth current loop will have reduced most of the phase loss in the plant. Our loop transmission can then be expressed as

$$LT(s) = \frac{K}{s}\frac{\mu_0 N}{2g_0}. \tag{4.65}$$

To achieve the desired crossover frequency f_c, we set $\left|LT(s)\right| = 1$ and substitute $2\pi f_c$ for s. We then solve for K as

$$K = \frac{4\pi f_c g_0}{\mu_0 N}. \tag{4.66}$$

Substituting K/s for $C(s)$ in (4.50), we can write the compensated stiffness under current control, k_{rc}^I, as

$$\begin{aligned} k_{rc}^I &= -\frac{4F_0}{\mu_0 N}\frac{\mu_0 N s}{4\pi f_c g_0}, \\ k_{rc}^I &= -\frac{F_0}{\pi f_c g_0}s. \end{aligned} \tag{4.67}$$

For a flux loop with voltage drive, our loop transmission is $C(s)B(s)/V_s(s)$, which

we write as

$$LT(s) = C(s)\frac{\mu_0 N}{2g_0}\frac{1/R}{\frac{L}{R}s+1} = C(s)\frac{1}{NA_p}\frac{L/R}{\frac{L}{R}s+1}. \tag{4.68}$$

Because of the pole from the inductance, we cannot use a simple integrator as the controller because there will be too much phase loss at the crossover frequency. Instead, we use a proportional-integral (PI) controller of the form

$$C(s) = K\frac{\tau s+1}{\tau s}. \tag{4.69}$$

We can then write (4.68) as

$$LT(s) = K\frac{\tau s+1}{\tau s}\frac{1}{NA_p}\frac{L/R}{\frac{L}{R}s+1}. \tag{4.70}$$

If the PI zero is placed much lower than the crossover frequency, we can approximate $C(s)$ as K at f_c. To solve for K, we set $\left|LT(s)\right| = 1$ at $s = 2\pi f_c j$. We write

$$\begin{aligned} K\left|\frac{\tau 2\pi f_c j+1}{\tau 2\pi f_c j}\right|\left|\frac{1}{NA_p}\right|\left|\frac{L/R}{\frac{L2\pi f_c}{R}j+1}\right| &= 1, \\ K\frac{1}{NA_p}\frac{1}{2\pi f_c} &\approx 1. \end{aligned} \tag{4.71}$$

The second line is a valid approximation if the PI zero and the pole from the inductance are both well below f_c.

Solving for K, we write

$$K = 2\pi f_c NA_p. \tag{4.72}$$

Our controller is therefore

$$C(s) = 2\pi f_c NA_p\frac{\tau s+1}{\tau s}. \tag{4.73}$$

Substituting this result into (4.64), we can write the compensated stiffness with volt-

age drive, k_{rc}^V, as

$$\begin{aligned} k_{rc}^V &= -\left(\frac{4RF_0}{\mu_0 N}\right)\left(\frac{1}{2\pi f_c N A_p}\right)\left(\frac{\tau s}{\tau s+1}\right), \\ k_{rc}^V &= -\frac{2RF_0}{\pi f_c \mu_0 A_p N^2}\left(\frac{\tau s}{\tau s+1}\right). \end{aligned} \tag{4.74}$$

Noting that $L = \mu_0 A_p N^2/(2g_0)$, we can write k_{rc}^V as

$$k_{rc}^V = -\frac{RF_0}{\pi f_c L g_0}\left(\frac{\tau s}{\tau s+1}\right). \tag{4.75}$$

The zero of the PI controller occurs at a frequency $f_z = 1/(2\pi\tau)$. If we define α as the ratio of f_c to f_z, then we can write that $\tau = \alpha/(2\pi f_c)$. Then we can write k_{rc}^V as

$$k_{rc}^V = -\frac{RF_0}{\pi f_c L g_0}\left(\frac{\frac{\alpha}{2\pi f_c}s}{\frac{\alpha}{2\pi f_c}s+1}\right). \tag{4.76}$$

At the low frequency limit ($f << f_c/\alpha$), we can approximate k_{rc}^V as

$$\begin{aligned} k_{rc}^V &= -\frac{\alpha}{2\pi f_c}\frac{R}{L}\frac{F_0}{\pi f_c g_0}s, \\ &= \frac{\alpha}{2\pi f_c}\frac{R}{L}k_{rc}^I, \\ k_{rc}^V &= \frac{\alpha f_L}{f_c}k_{rc}^I, \end{aligned} \tag{4.77}$$

where in the second line, we have substituted (4.50), and in the last line, we have substituted the frequency of the inductive pole, $f_L = R/(2\pi L)$. A conservative value for α is 10. For our actuator, the inductive pole occurs at approximately 5.5 Hz at a nominal gap of 500 µm (see Chapter 8). If we select a crossover frequency of say, 5 kHz, then for these values, $k_{rc}^V \approx 0.01 k_{vc}^I$. Our low-frequency stiffness is a factor of 100 lower with a voltage drive compared to a current drive.

At the high frequency limit ($f >> f_c/\alpha$), we can approximate k_{rc}^V as

$$k_{rc}^V = -\frac{RF_0}{\pi f_c L g_0}. \tag{4.78}$$

The stiffness reaches a constant value at high frequencies. This is in contrast to the compensated stiffness when using a high-bandwidth current loop (4.67), where the stiffness continues to increase linearly with frequency. We thus see that one advantage of not using a current loop in conjunction with the flux controller is that we can achieve much lower stiffness at both low frequencies and high frequencies.

4.5 Augmenting the Reluctance Actuator Model

There are various ways in which we might augment the basic reluctance actuator model in order to investigate other phenomena or to make the model more accurate. In this section, we give a brief overview of some possible modifications to the model.

4.5.1 Angle Disturbance

The basic model permitted only a gap disturbance. If we model both halves of the three-pole reluctance actuator, we can simulate both gap disturbances and angle disturbances simultaneously and determine not only resulting force disturbances but also torque disturbances. This phenomenon was discussed qualitatively in Section 2.6.2.

If we consider Figure 4-20, assuming small angles, we can write the gaps at each pole face as

$$g_L \approx g - (L + w)\,\theta, \tag{4.79}$$

$$g_C \approx g - L\theta, \tag{4.80}$$

$$g_R \approx g - (L - w)\,\theta, \tag{4.81}$$

where g is the actuator gap without any angle disturbance, θ is the angle of rotation of the stage relative to the reluctance actuator stator and L is the distance from the

center of rotation to the center of the actuator target.

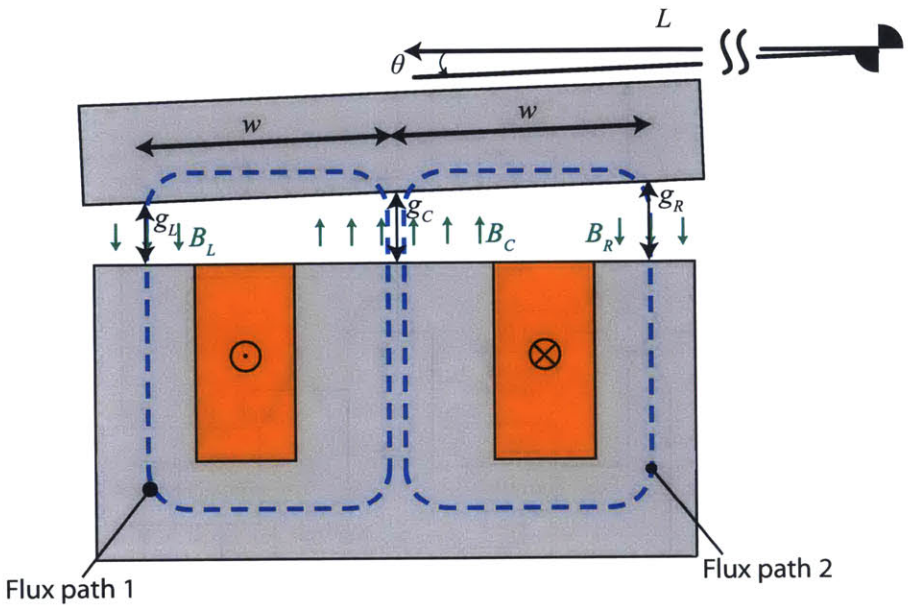

Figure 4-20: Reluctance actuator with angle disturbance.

For the left and right flux paths shown in Figure 4-20, we can write Ampere's Law as

$$\text{Flux path 1: } NI = \frac{B_C g_C}{\mu_0} + \frac{B_L g_L}{\mu_0} + H_L l_{Fe}, \tag{4.82}$$

$$\text{Flux path 2: } NI = \frac{B_C g_C}{\mu_0} + \frac{B_R g_R}{\mu_0} + H_R l_{Fe}. \tag{4.83}$$

Here, H_L and H_R are lumped parameters representing the average magnetic fields in the core and target material for path 1 and path 2, respectively. From Gauss's Law, we can express B_L and B_R as material hysteresis functions of H_L and H_R, respectively. Also using Gauss's Law, we can write $B_C = (B_L + B_R)/2$. With this in mind, we can draw the block diagram of (4.82) and (4.83) as shown in Figure 4-21. The dotted blue upper box encompasses the portion of the block diagram representing Ampere's Law for flux path 1 and the dotted green lower box encompasses the portion of the block diagram representing Ampere's Law for flux path 2. The coordinate transformation block represents (4.79-4.81). The outputs of the model are B_L, B_C, and B_R.

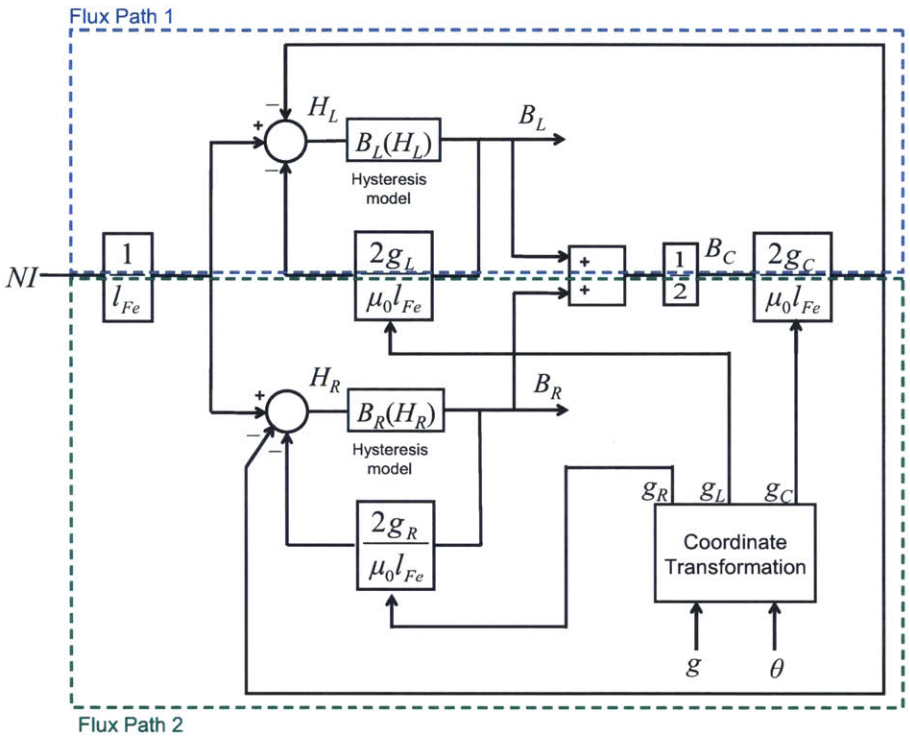

Figure 4-21: Block diagram of a reluctance actuator with angle disturbance.

The force (F) and torque (τ) output of the actuator can then be approximated as

$$F = \frac{1}{2\mu_0}\left(B_L^2 A_L + B_C^2 A_C + B_R^2 A_R\right), \tag{4.84}$$

$$\tau = \frac{wA_p}{4\mu_0}\left(B_L^2 - B_R^2\right), \tag{4.85}$$

where $A_p = 2A_L = 2A_R$. In the case where $\theta = 0$, (4.84) reduces to (2.13) and (4.85) reduces to zero.

4.5.2 Fringing Flux

As mentioned earlier, our basic reluctance actuator model does not account for fringing flux. Perhaps the simplest method for modeling fringing flux is to make the area associated with the air gap reluctance a function of gap, reflecting the fact that the flux will spread out more in the air gap as the air gap increases. The mapping between

this effective area, A_{eff}, could be determined from finite element analysis (FEA) for example. We can apply (2.4) with A_{g1} replaced with $A_{eff}(g)$ and solve for the air gap flux density, B_g

$$B_g = \frac{A_{Fe}}{A_{eff}(g)} B_{Fe}, \tag{4.86}$$

where we replaced the subscript C in (2.4) with the subscript Fe for the sake of generality. This gives us the average flux density in the air gap.

Fringing also affects the force generation: (2.13) does not account for fringing because it assumes that B_g is perfectly uniform. One way to model the effect of fringing on force generation is with a lookup table using average gap flux density and gap as inputs, and with the force as the output. This lookup table could be obtained via FEA or with experimental results. A block diagram with fringing effects accounted for is shown in Figure 4-22. The elements used to model the effect of fringing are outlined in blue.

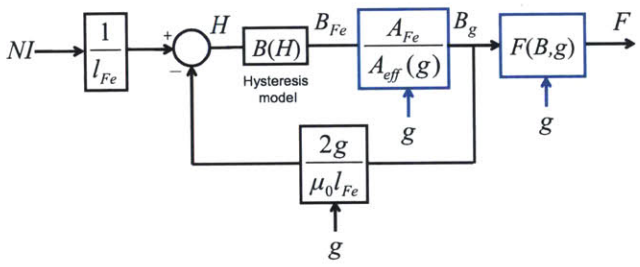

Figure 4-22: Block diagram of a reluctance actuator with fringing fields modeled.

Another way to model the fringing fields is to apply the flux tube method discussed in Chapter 7. By applying the magnetic circuit techniques analyzed there, we can further augment the model to account for leakage flux. Finally, we can apply these same techniques to discretize the single hysteretic lumped parameter core and target reluctance into multiple hysteretic lumped parameters. We can do likewise with the amp-turns in order to distribute the magnetomotive force spatially in a more realistic manner. This permits us to represent local variations in the magnetic field within the core and target and to explore which parts of the core and target saturate first.

4.5.3 Electrical Modeling

If we solve (4.52) for I, we can write

$$I = \frac{1}{R}\left(V_S - NA_p\frac{dB}{dt}\right). \tag{4.87}$$

We now have expressed the input of our actuator model (I) in terms of its output (B) and V_S. We can implement (4.87) in block diagram form as shown in Figure 4-23. The block labeled 'Actuator Model' represents the basic reluctance actuator model developed earlier in this chapter.

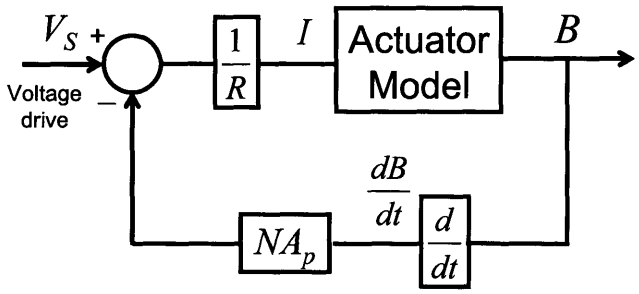

Figure 4-23: Block diagram of a reluctance actuator model with the electrical domain modeled.

Modeling the electrical domain allows us to investigate the effects of having a non-ideal current source. We can achieve the desired input current with a current feedback controller and explore the effect of the actuator inductance and resistance on the controlled current and output flux density and force. Alternatively, we can plug this model into a flux feedback loop and investigate controlling the flux directly sans current control.

4.5.4 Position Control

We can supplement the actuator model with a model of the actuated plant, i.e., the short-stroke stage. This allows us to investigate the actuator force accuracy required to maintain the required stage position accuracy, and to investigate the effect position feedback control has on actuator force accuracy.

The simplest model would include a single actuator pair that can actuate a single-DoF stage. A more comprehensive model could include four reluctance actuators acting on a 2-DoF stage (y and θ). This schematic is shown in Figure 4-24. Each actuator block has two outputs, a force (F) and torque (τ). The variables g_d and θ_d are the gap disturbance and angle disturbance from the long-stroke stage tracking error. The position controller and any flux controllers are not shown in the figure.

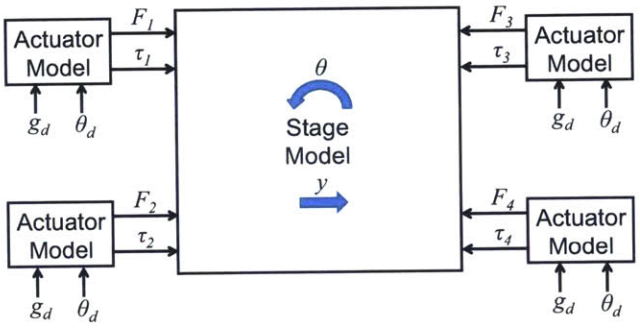

Figure 4-24: A 2-DoF model of the short-stroke stage with four reluctance actuator models and gap and angle disturbances.

Additional augmentations to the stage model can be easily envisioned. For example, we could add a model of the long-stroke stage, or we could include additional degrees-of-freedom to the model.

4.6 Summary

In this chapter, we have developed a reluctance actuator model that incorporates ferromagnetic hysteresis and air gap disturbances. We have developed simple formulas that allow the designer to estimate expected force errors from hysteresis and gap disturbances. We have also listed some ways in which the model could be improved.

Table 4.2 lists the formulas for approximating errors from offset, hysteresis, and gap disturbance. The formulas are expressed as functions of force rather than as functions of flux density or current. The reason for this is that the required force is more likely to be known in advance than either the required actuator flux density or current, which are typically determined later in the design process. For the lab pro-

totype actuator that we simulated, the maximum errors as percentages of maximum force are also listed for each error source. Both the theoretical and simulated maximum error percentages are listed. We learned that gap disturbances will generate the largest errors for the uncompensated reluctance actuator.

Table 4.2: Error sources for a reluctance actuator

Error source	**Theoretical approximation**	**Max error as % of $F_{\max}$ (theory)**	**Max error as % of $F_{\max}$ (sim)**
Offset	$\Delta F_{\text{off}} = \left(\frac{\mu_0 l_{Fe} H_c}{2gB_s}\right)^2 F_{\max}$	2.0×10^{-5}	2.0×10^{-5}
Hysteresis	$\Delta F_h = \frac{2\mu_0 l_{Fe} H_c}{gB_s}\sqrt{F_{\max} F}$	0.18	0.15
Gap disturbance	$\Delta F_d = -\frac{2F}{g}\Delta g$	3.68	3.77

In Table 4.3, we list formulas for approximating the reluctance actuator stiffness for several scenarios. These scenarios include an uncompensated actuator driven with a current source, an uncompensated actuator driven with a voltage source, an actuator compensated with a flux controller and driven with a current source (e.g., the flux loop includes an inner high-bandwidth current loop), and an actuator compensated with a flux controller and driven with a voltage source. Note that $C_I(s)$ and $C_V(s)$ refer to the different controller transfer functions required for a current-driven actuator and a voltage-driven actuator, respectively. We discovered that for flux loop bandwidths that would be typical for our application (i.e., several kHz), the flux-controlled actuator with voltage drive is likely to result in a much lower stiffness than a flux-controlled actuator with current drive. The reason for this is that in the voltage-driven case, the effect of a gap disturbance will be further filtered by the actuator inductive pole.

Table 4.3: Reluctance actuator stiffnesses

Controller topology	**Theoretical approximation**
Uncompensated, current drive	$k_r^I = -\frac{2F}{g_0}$
Uncompensated, voltage drive	$k_r^V = -\frac{2F}{g_0}\frac{1}{\frac{L}{R}s+1}$
Flux control, current drive	$k_{rc}^I = -\frac{4F}{\mu_0 N C_I(s)}$
Flux control, voltage drive	$k_{rc}^V = -\frac{4RF}{\mu_0 N C_V(s)}$

Chapter 5

Eddy Current and Power Dissipation Modeling

In this chapter, we augment the basic reluctance actuator model presented in Chapter 4 to account for eddy currents. We can use this augmented model to determine the effect of eddy currents on force generation and to select appropriate values for key design parameters, such as lamination thickness.

We begin by presenting the theory behind eddy current generation. We distinguish between two sources of eddy currents: classical eddy currents and excess eddy currents. We then develop lumped parameter models for approximating the average magnetic fields produced by these eddy current sources. These models are valid for frequencies well below the skin frequency of the material. We develop theory to approximate force errors generated by eddy currents and compare these errors to those obtained from simulation with the augmented actuator model. Finally, we investigate the power dissipated from hysteresis and from eddy currents. We develop approximate formulas for predicting the dissipated power and compare the results with simulation.

5.1 Diffusion Equation

Eddy currents arise in conducting material owing to the changing magnetic flux in the actuator core and target. These eddy currents result in an internal magnetic field that opposes the applied magnetic field, thus reducing the overall magnetic flux in the material. This phenomenon can be derived from Faraday's Law (2.32) and Ampere's Law (2.1). Applying these equations and Ohm's Law, we derive the diffusion equation [39] as

$$\nabla^2 \mathbf{H} = \sigma_e \frac{\partial \mathbf{B}}{\partial t}, \tag{5.1}$$

where σ_e is the electrical conductivity of the ferromagnetic material. If we can solve the diffusion equation for $\mathbf{H}$ or approximate it, we can add these terms to (2.2) and then determine the effect of eddy currents on the air gap flux density.

Solving (5.1) explicitly is often not possible. Instead, we employ a concept known as loss separation as presented in more detail in [14]. Loss separation takes into account the fact that for a wide range of ferromagnetic behavior, the total loss in the material can be decomposed into the sum of three contributions: hysteresis loss, classical eddy current loss, and excess eddy current loss. We can often approximate a lumped-parameter value of H associated with each contribution. Since we have already derived a lumped-parameter model of the material hysteresis, we focus our efforts here on classical eddy currents and excess eddy currents. Before discussing classical and excess eddy currents, however, we give a brief overview of the concepts of skin frequency and skin depth.

5.2 Skin Frequency and Skin Depth

As part of the design iteration process, calculating the expected skin frequency and skin depth aids in choosing the core material and lamination thickness. The skin depth is a measure of how far an applied magnetic field will penetrate a ferromagnetic material at a given frequency [39]. It is defined as the distance from the surface of the conductive material at which the flux density has decreased to $1/e$ of its surface value.

Alternatively, for a given thickness of material, the skin frequency is the frequency at which the skin depth is half the material thickness, thus indicating that the magnetic field no longer fully penetrates the material at this frequency.

For a lamination with thin rectangular shape, the skin frequency, f_s, can be derived from the 1-D diffusion equation and is given by [56]

$$f_s = \frac{4}{\pi \mu_r \mu_0 \sigma_e d^2}, \tag{5.2}$$

where μ_r is the relative permeability of the material and d is the lamination thickness.

The maximum relative permeability μ_r of NiFe is listed by Magnetic Metals as about 60,000. We use the maximum value to determine a worst-case skin frequency. The conductivity of NiFe is listed by Magnetice Metals as $2.22 \times 10^6\,\mathrm{S/m}$, and d for our prototype actuator is $100\,\mu\mathrm{m}$. Using these values, we calculate f_s to be 736 Hz, well above the main frequency content of the force profile.

The skin depth, δ, for a given frequency, f, is given by [39]

$$\delta = 2\sqrt{\frac{\pi}{\mu_r \mu_0 \sigma_e f}}. \tag{5.3}$$

We can approximate the maximum frequency, $f_{\max}$, in our simulated B-profile as

$$f_{\max} \approx \max\left(\frac{dB}{dt}\right) \cdot \frac{1}{2\pi B_{\max}}. \tag{5.4}$$

For our profile, the maximum dB/dt is $112\,\mathrm{T/s}$ and $B_{\max} = 1.12\,\mathrm{T}$. This results in an $f_{\max}$ of about 16 Hz. Substituting this into (5.3), we calculate $\delta = 2.2\,\mathrm{mm}$, over 20 times greater than the lamination thickness. These calculations suggest that classical eddy currents should have only a small effect at the frequencies of interest in our prototype actuator.

5.3 Classical Eddy Currents

The classical eddy current loss is the loss associated with the scale of the actuator geometry. It is derived from the diffusion equation applied to the ferromagnetic material assuming that it is perfectly homogeneous and consists of a single magnetic domain. In this section we follow the analysis presented in [14] in deriving the field associated with classical eddy currents.

If the frequency of the drive signal is well below the skin frequency of a core lamination, then the applied magnetic field will almost fully penetrate the material and we can approximate the internal magnetic field as being uniform within the material. Figure 5-1 demonstrates this graphically in one dimension for a single lamination. The variable H_a is the applied magnetic field and $H(x)$ is the internal magnetic field as a function of x. The variable $\bar{H}$ is the spatial average of $H(x)$. The spatial dimension x is defined as equal to zero at the center of the lamination.

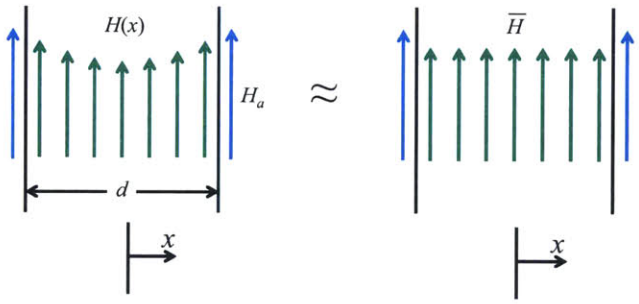

Figure 5-1: Magnetic field distribution within a single lamination (left) and approximation with uniform $\bar{H}$ (right).

For the 1-D case, (5.1) simplifies to

$$\frac{\partial^2 H}{\partial x^2} = \sigma_e \frac{\partial B}{\partial t}. \tag{5.5}$$

Because we are approximating the internal B as spatially uniform, we can integrate

(5.5) and write

$$\frac{\partial H}{\partial x} \approx \int \sigma_e \frac{d\bar{B}}{dt} dx,$$

$$\frac{\partial H}{\partial x} \approx \sigma_e \frac{d\bar{B}}{dt} x + C_1(t), \tag{5.6}$$

where $\bar{B}$ represents the spatial average of the internal B and $C_1(t)$ is the constant of integration. We can integrate a second time to solve for $H(t)$ as

$$H(t) \approx \int \left(\sigma_e \frac{d\bar{B}}{dt} x + C_1(t) \right) dx$$

$$H(t) \approx \sigma_e \frac{d\bar{B}}{dt} \frac{x^2}{2} + C_1(t)x + C_2(t), \tag{5.7}$$

where $C_2(t)$ is a second constant of integration. If we assume no skin current, then $H(x) = H_a$ at the boundaries $x = d/2$ and $x = -d/2$. We can substitute these values of x into (5.7) and write

$$x = \frac{d}{2}\colon\ H(t) = \sigma_e \frac{d\bar{B}}{dt} \frac{d^2}{8} + C_1(t)\frac{d}{2} + C_2(t), \tag{5.8}$$

$$x = -\frac{d}{2}\colon\ H(t) = \sigma_e \frac{d\bar{B}}{dt} \frac{d^2}{8} - C_1(t)\frac{d}{2} + C_2(t). \tag{5.9}$$

If we subtract (5.9) from (5.8), we find that $C_1(t) = 0$. Using $C_1 = 0$ in (5.8) we solve for $C_2(t)$ as

$$C_2(t) = H(t) - \sigma_e \frac{d\bar{B}}{dt} \frac{d^2}{8}. \tag{5.10}$$

Substituting the results for $C_1(t)$ and $C_2(t)$ into (5.7), we write

$$H(t) \approx H_a(t) - \frac{\sigma_e}{2} \frac{d\bar{B}}{dt} \left(\frac{d^2}{4} - x^2 \right). \tag{5.11}$$

We want now to determine the spatial average of $H(t)$, $\bar{H}(t)$. We do this by taking

the x-average of (5.11). We arrive at

$$\bar{H}(t) \approx H_a(t) - \frac{\sigma_e d^2}{12}\frac{d\bar{B}}{dt}. \tag{5.12}$$

The last term in (5.12) is the average magnetic field resulting from classical eddy currents. We denote this as H_{cl}, and we write

$$H_{cl}(t) = \frac{\sigma_e d^2}{12}\frac{dB}{dt}, \tag{5.13}$$

where we have replaced the $\bar{B}$ notation with B for simplicity. We can see from this equation how the lamination thickness can have a large effect on reducing eddy currents since H_{cl} increases as d^2. We can replace the magnetic field H_{Fe} in (2.2) with $H_{Fe} = H_h + H_{cl}$, where H_h is the field associated with hysteresis and is approximated by the average internal magnetic field $\bar{H}$. The modified version of (2.2) is therefore

$$(H_h + H_{cl})\, l_{Fe} + H_{g_1} g + H_{g_2} g = NI, \tag{5.14}$$

or

$$H_h l_{Fe} + \frac{\sigma_e d^2}{12}\frac{dB}{dt} l_{Fe} + \frac{2g}{\mu_0} B = NI. \tag{5.15}$$

We can then modify our basic actuator model with an additional feedback path that represents the classical eddy current term. This is shown in Figure 5-2, where the new feedback path is represented in blue. For the sake of simplicity, we have represented the hysteresis model as having the output of B directly rather than dB/dH as was done in Figure 4-2.

As was done with hysteresis and gap disturbances, we would like to estimate the expected error resulting from classical eddy currents. We define state 1 as the actuator model without classical eddy current effects (2.2) and state 2 as the actuator model with classical eddy current effects (5.15). For identical NI for the two models, we define $B_1 = B$ and $B_2 = B + \Delta B_{cl}$, where ΔB_{cl} is the the deviation in flux density

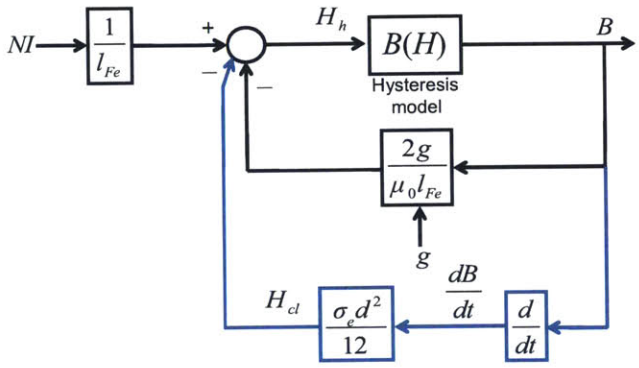

Figure 5-2: Block diagram for actuator model including the classical eddy current term.

resulting from classical eddy currents. We can write the two models as

$$H_{h1} l_{Fe} + \frac{2g}{\mu_0} B = NI \tag{5.16}$$

$$H_{h2} l_{Fe} + \frac{\sigma_e d^2}{12} \frac{dB}{dt} l_{Fe} + \frac{2g}{\mu_0} (B + \Delta B_{cl}) = NI. \tag{5.17}$$

If we assume that H_{cl} is small relative to H_a, then H_{cl} will not have a large effect on H_h, and $H_{h1} \approx H_{h2}$. If we subtract (5.16) from (5.17), we can solve for ΔB_{cl} as

$$\Delta B_{cl} \approx -\frac{\mu_0 \sigma_e d^2 l_{Fe}}{24g} \frac{dB}{dt}. \tag{5.18}$$

To determine the corresponding deviation in force, ΔF_{cl}, we can write

$$\begin{aligned} \Delta F_{cl} = F_2 - F_1 &= \frac{B_2^2 A}{2\mu_0} - \frac{B_1^2 A}{2\mu_0}, \\ &= \frac{A}{2\mu_0} \left[(B + \Delta B_{cl})^2 - B^2 \right], \\ &= \frac{A}{2\mu_0} \left[2B\Delta B_{cl} + (\Delta B_{cl})^2 \right], \\ \Delta F_{cl} &\approx \frac{A}{\mu_0} B \Delta B_{cl}, \end{aligned} \tag{5.19}$$

where in the last line, we removed the second-order term: $(\Delta B_{cl})^2$. Substituting (5.18), we derive

$$\Delta F_{cl} \approx -\frac{\sigma_e d^2 l_{Fe} A}{24g} B \frac{dB}{dt}. \tag{5.20}$$

We can write ΔF_{cl} in terms of I, where we approximate dB/dt using (2.8) and assume that g is constant,

$$\Delta F_{cl} \approx -\frac{\mu_0^2 \sigma_e d^2 l_{Fe} A N^2}{96 g^3} I \frac{dI}{dt}. \tag{5.21}$$

Finally, in order to express (5.20) in terms of F, we first solve (2.13) for B

$$B = \sqrt{\frac{2\mu_0 F}{A}}. \tag{5.22}$$

We then differentiate this equation with respect to t and express dB/dt as

$$\frac{dB}{dt} = \sqrt{\frac{\mu_0}{2AF}} \frac{dF}{dt}, \tag{5.23}$$

for $F \neq 0$. Substituting (5.22) and (5.23) into (5.20) and restricting ourselves to single-sided operation ($B \geq 0$), we obtain

$$\begin{aligned} \Delta F_{cl} &\approx -\frac{\sigma_e d^2 l_{Fe} A}{24g} \sqrt{\frac{2\mu_0 F}{A}} \sqrt{\frac{\mu_0}{2AF}} \frac{dF}{dt}, \\ \Delta F_{cl} &\approx -\frac{\mu_0 \sigma_e d^2 l_{Fe}}{24g} \frac{dF}{dt}. \end{aligned} \tag{5.24}$$

Force deviations from classical eddy currents will increase with lamination thickness and force slew rate (dF/dt) and inversely with air gap. Figure 5-3 shows the theoretical approximation of force deviation from (5.21) compared to the deviation shown by simulation. For the simulation we used the current profile from Figure 4-4 as the input to a Simulink implementation of the augmented model of Figure 5-2. The scaled force profile is also shown. The match between the theoretical approximation and simulation is very close. The maximum force deviation predicted by (5.21) is 8.80 mN and the maximum force deviation predicted from simulation is 8.86 mN. This amounts to 0.0024 percent of full-scale force, indicating that classical eddy currents

are expected to have negligible effect for this particular actuator design.

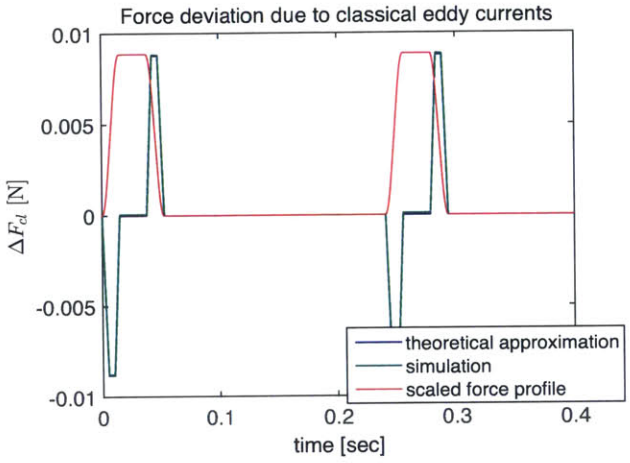

Figure 5-3: Comparison of ΔF_{cl} from (5.21) with ΔF_{cl} from simulation. Red line is a scaled force profile to provide a time reference.

Note that the maximum force deviation from eddy currents occurs during the high dF/dt portions of the force profile, as predicted by (5.24). Another feature to note is the small offset that can be observed during portions of zero dF/dt in the simulated force deviation. This is the result of numerical inaccuracies in the simulation solver: as the simulation time step is decreased, this offset is reduced.

We would like to determine whether our assumption that the internal H can be approximated as uniform is reasonable. In Figure 5-4, we plot the simulated applied magnetic field, H_a, the simulated average internal magnetic field, H_h, and the simulated average classical eddy current field, H_{cl}. H_h shows only a small deviation from H_a and $H_{cl} << H_a$, verifying our assumption.

5.3.1 Effect of Gap Disturbances on Classical Eddy Currents

Suppose we are driving the reluctance actuator with a known current profile (e.g., suppose that no flux feedback is being used). We can augment (5.21) to account for gap disturbances. In this case, (5.19) becomes

$$\Delta F_{cl} \approx -\frac{\mu_0^2 \sigma_e d^2 l_{Fe} A N^2}{96 g^3} \left(I \frac{dI}{dt} - \frac{I^2}{g} \frac{dg}{dt} \right). \tag{5.25}$$

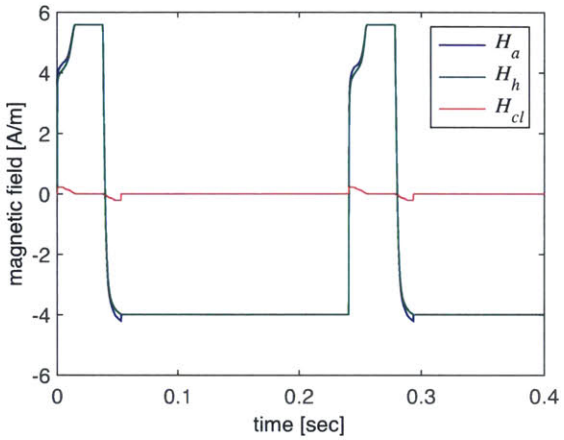

Figure 5-4: Simulated H_a, H_h, and H_{cl}.

If $\Delta g << g_0$, the nominal gap, we can approximate g as g_0 and write

$$\Delta F_{cl} \approx -\frac{\mu_0^2 \sigma_e d^2 l_{Fe} A N^2}{96 g_0^3} \left(I \frac{dI}{dt} - \frac{1}{g_0} I^2 \frac{dg}{dt} \right). \tag{5.26}$$

While the gap disturbance profile in a lithography application is unlikely to be known ahead of time, if the expected range of dg/dt can be estimated *a priori*, we can postulate an upper bound for (5.26).

Suppose we estimate that the maximum dg/dt will be approximately 10 mm/s. This is roughly the maximum dg/dt from the gap disturbance profile shown in Figure 4-13. For our simulated current profile, the $I \cdot dI/dt$ term has a maximum value of 512 A^2/s. The second term, assuming that I and dg/dt are uncorrelated, has an upper bound of 198 A^2/s. The first term dominates, but the second term could contribute nearly 40% additional error. It should also be noted, however, that $\max(I \cdot dI/dt)$ does not necessarily occur at the same time as $\max(I)$, so that the second term will not reach its maximum at the same time that the first does.

5.4 Excess Eddy Currents

If the ferromagnetic material under consideration were perfectly homogeneous and consisted of only a single magnetic domain, classical eddy currents would be the end

of the story as far as eddy current phenomena are concerned. In the real world, however, materials are not perfectly homogeneous and consist of multiple magnetic domains. This gives rise to additional eddy currents known as excess eddy currents [14]. Excess eddy currents result from domain walls undergoing motion from the externally applied field.

Because the magnetic domain structure of a material is often very complex and not known precisely, it is typically difficult to model excess eddy currents from first principles. Nevertheless, Bertotti in [14] has done an admirable job of deriving a plausible model for excess eddy currents that fits a wide variety of materials. His final result [14, p. 425] for the excess field, H_{exc}, is

$$H_{exc}(t) = \operatorname{sgn}\left(\frac{dB}{dt}\right)\frac{n_0 V_0}{2}\left(\sqrt{1+\frac{4\sigma_e G A_l}{n_0^2 V_0}\left|\frac{dB}{dt}\right|}-1\right), \tag{5.27}$$

where n_0 and V_0 are phenomenological parameters that characterize the material. The parameter G is a dimensionless constant approximately equal to 0.1356. The variable A_l is the cross-sectional area of a single lamination. The details of this derivation can be found in [14]. Here as with the derivation for H_{cl}, H_{exc} is assumed to be small relative to H_a, such that the internal magnetic field can be approximated as uniform.

The parameters n_0 and V_0 depend on the microstructure of the material and are related to features such as grain size and the number of correlation regions[1]. Bertotti provides some theoretical equations for approximating V_0 and n_0. Normally, however, these values are found by empirical curve fitting.

We can augment (5.14) to include H_{exc} as

$$\left(H_h + H_{cl} + H_{exc}\right) l_{Fe} + H_{g_1} g + H_{g_2} g = NI. \tag{5.28}$$

[1]Correlation regions describe the number of internal degrees of freedom in the magnetization process of a material. Bertotti [14] describes it thus: "Certain aspects of the magnetization process turn out to be describable by a small number of independent degrees of freedom, each degree of freedom corresponding to the magnetic flux linked to some *correlation region* of the material." [emphasis in the original]

Substituting (5.13) and (5.27) for H_{cl} and H_{exc}, respectively, we write

$$H_h l_{Fe} + \frac{\sigma_e d^2}{12}\frac{dB}{dt} l_{Fe} + \text{sgn}\left(\frac{dB}{dt}\right)\frac{n_0 V_0}{2}\left(\sqrt{1 + \frac{4\sigma_e G A_l}{n_0^2 V_0}\left|\frac{dB}{dt}\right|} - 1\right) l_{Fe} + \frac{2g}{\mu_0} B = NI. \tag{5.29}$$

We can include an additional feedback path in Figure 5-2 to account for the excess eddy currents. The modified block diagram in shown in Figure 5-5. Both eddy current paths (classical and excess) are shown in blue.

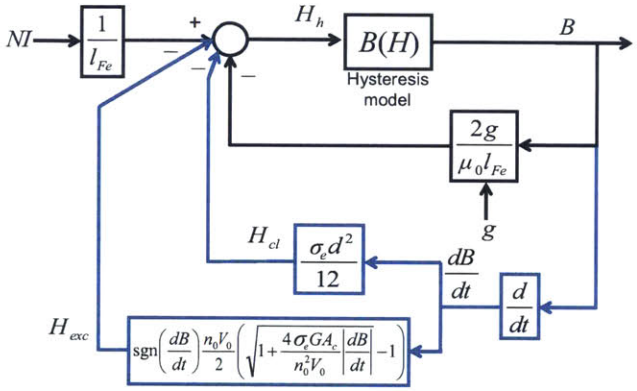

Figure 5-5: Block diagram for actuator model including excess eddy current term.

Of interest is to explore the low- and high-frequency limits on the behavior of H_{exc}. For the low-frequency limit, i.e., $dB/dt << (n_0^2 V_0)/(4\sigma_e G A_l)$, we can expand H_{exc} using a Taylor series applied to a function in the form of $(1+x)^{1/2}$ for $x << 1$, where in this case $x = 4\sigma_e G A_l/(n_0^2 V_0)\left|dB/dt\right|$. We write

$$\begin{aligned} H_{exc} &\approx \text{sgn}\left(\frac{dB}{dt}\right)\frac{n_0 V_0}{2}\left(1 + \frac{1}{2}\frac{4\sigma_e G A_l}{n_0^2 V_0}\left|\frac{dB}{dt}\right| - 1\right), \\ &\approx \text{sgn}\left(\frac{dB}{dt}\right)\frac{n_0 V_0}{2}\left(\frac{1}{2}\frac{4\sigma_e G A_l}{n_0^2 V_0}\left|\frac{dB}{dt}\right|\right), \\ H_{exc} &\approx \frac{\sigma_e G A_l}{n_0}\frac{dB}{dt}. \end{aligned} \tag{5.30}$$

In the last line, we have used the fact that $\text{sgn}(x)|x| = x$. For the high-frequency limit, i.e., $dB/dt >> (n_0^2 V_0)/(4\sigma_e G A_l)$, the second term underneath the square root

will dominate the other terms, so we can write

$$H_{exc} \approx \operatorname{sgn}\left(\frac{dB}{dt}\right)\sqrt{\sigma_e V_0 G A_l \left|\frac{dB}{dt}\right|}. \tag{5.31}$$

We see then that for low frequencies, like the classical eddy current field, the excess eddy current field increases linearly with frequency. At higher frequencies, however, the excess eddy current field follows a square root dependency on frequency. We see also that excess eddy currents are much less dependent on lamination thickness, d, than classical eddy currents are. Classical eddy currents vary with the square of lamination thickness. However, with excess eddy currents, A_l is proportional to d, not d^2. Therefore, at low frequencies, the excess eddy current field increases with d, and at high frequencies, it increases with $\sqrt{d}$. Decreasing lamination thickness will still help reduce excess eddy currents, but not to the same extent that it will with classical eddy currents.

To predict the force errors expected from the excess field, we follow a similar procedure to that used for the classical field. We first derive the change in flux density due to excess eddy currents, ΔB_{exc}, from (5.29) as

$$\Delta B_{exc} \approx -\operatorname{sgn}\left(\frac{dB}{dt}\right)\frac{\mu_0 l_{Fe} n_0 V_0}{4g}\left(\sqrt{1+\frac{4\sigma_e G A_l}{n_0^2 V_0}\left|\frac{dB}{dt}\right|}-1\right). \tag{5.32}$$

Following the analysis used to derive (5.19) and applying it to the excess field, we can write

$$\Delta F_{exc} \approx \frac{A}{\mu_0} B \Delta B_{exc}. \tag{5.33}$$

Substituting (5.32), we write

$$\Delta F_{exc} \approx \frac{A}{\mu_0} B \left[-\operatorname{sgn}\left(\frac{dB}{dt}\right) \frac{\mu_0 l_{Fe} n_0 V_0}{4g} \left(\sqrt{1 + \frac{4\sigma_e G A_l}{n_0^2 V_0} \left| \frac{dB}{dt} \right|} - 1 \right) \right],$$

$$\Delta F_{exc} \approx -\operatorname{sgn}\left(\frac{dB}{dt}\right) \frac{A l_{Fe} n_0 V_0}{4g} B \left(\sqrt{1 + \frac{4\sigma_e G A_l}{n_0^2 V_0} \left| \frac{dB}{dt} \right|} - 1 \right). \quad (5.34)$$

We can express (5.34) in terms of I for a constant gap by substituting (2.8) and its derivative for B and dB/dt, respectively,

$$\Delta F_{exc} \approx -\operatorname{sgn}\left(\frac{\mu_0 N}{2g}\frac{dI}{dt}\right) \frac{A l_{Fe} n_0 V_0}{4g} \frac{\mu_0 N I}{2g} \left(\sqrt{1 + \frac{4\sigma_e G A_l}{n_0^2 V_0} \left| \frac{\mu_0 N}{2g}\frac{dI}{dt} \right|} - 1 \right),$$

$$\Delta F_{exc} \approx -\operatorname{sgn}\left(\frac{dI}{dt}\right) \frac{\mu_0 A l_{Fe} N n_0 V_0}{8g^2} I \left(\sqrt{1 + \frac{2\mu_0 \sigma_e G A_l N}{n_0^2 V_0 g} \left| \frac{dI}{dt} \right|} - 1 \right). \quad (5.35)$$

Expressed in terms of F for $F \neq 0$ by substituting (5.22) and (5.23) into (5.34), we write

$$\Delta F_{exc} \approx -\operatorname{sgn}\left(\frac{dF}{dt}\right) \frac{A l_{Fe} n_0 V_0}{4g} \sqrt{\frac{2\mu_0 F}{A}} \left(\sqrt{1 + \frac{4\sigma_e G A_l}{n_0^2 V_0} \left| \sqrt{\frac{\mu_0}{2AF}}\frac{dF}{dt} \right|} - 1 \right),$$

$$\Delta F_{exc} \approx -\operatorname{sgn}\left(\frac{dF}{dt}\right) \frac{l_{Fe} n_0 V_0}{4g} \sqrt{2\mu_0 A F} \left(\sqrt{1 + \frac{4\sigma_e G A_l}{n_0^2 V_0} \sqrt{\frac{\mu_0}{2AF}} \left| \frac{dF}{dt} \right|} - 1 \right). \quad (5.36)$$

Expressing A in terms of $F_{\max}$ and B_s using (4.14) with B_s in place of $B_{\max}$, we write

$$\Delta F_{exc} \approx -\operatorname{sgn}\left(\frac{dF}{dt}\right) \frac{l_{Fe} n_0 V_0}{4g} \sqrt{\frac{4\mu_0^2 F_{\max} F}{B_s^2}} \left(\sqrt{1 + \frac{4\sigma_e G A_l}{n_0^2 V_0} \sqrt{\frac{B_s^2}{4F_{\max} F}} \left| \frac{dF}{dt} \right|} - 1 \right),$$

$$\Delta F_{exc} \approx -\operatorname{sgn}\left(\frac{dF}{dt}\right) \frac{\mu_0 l_{Fe} n_0 V_0}{2gB_s} \sqrt{F_{\max} F} \left(\sqrt{1 + \frac{2\sigma_e G A_l B_s}{n_0^2 V_0 \sqrt{F_{\max} F}} \left| \frac{dF}{dt} \right|} - 1 \right). \quad (5.37)$$

For simulation purposes, we selected values of $n_0 = 125$ and $V_0 = 0.472\,\mathrm{A/m}$.

These values were adapted from values documented in [14] for a silicon-iron specimen, accounting for the effect of differences in lamination cross-sectional area. These values are used to get a general idea of the behavior of excess eddy currents. For accurate prediction, experimental verification of n_0 and V_0 would be required.

Figure 5-6 shows the theoretical approximation of force deviation from both classical eddy currents and excess eddy currents compared to the deviation shown by simulation. The scaled force profile is also shown. The match between the theoretical approximation and simulation is very close. The maximum force deviation predicted by theory is 30.3 mN and the maximum force deviation predicted from simulation is 30.9 mN. This amounts to 0.008 percent of full-scale force. Excess eddy currents contribute about 22 mN to this error. For this particular actuator geometry and for the chosen values of n_0 and V_0, excess eddy currents play a larger role than classical eddy currents for the force profile simulated. However, the overall effect is still minuscule compared to errors from gap disturbances and hysteresis.

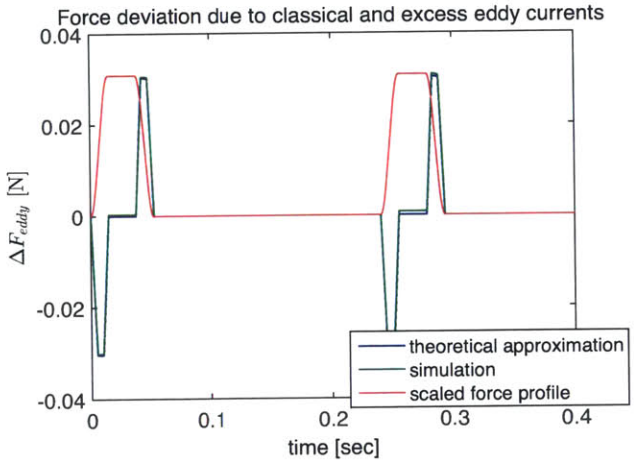

Figure 5-6: Comparison of $\Delta F_{eddy} = \Delta F_{cl} + \Delta F_{exc}$ from (5.21) and (5.35) with ΔF_{eddy} from simulation.

Figure 5-7 shows the simulated applied magnetic field, H_a, the simulated average internal magnetic field, H_h, the simulated average classical eddy current field, H_{cl}, and the simulated average excess eddy current field, H_{exc}. We can see that $H_{exc} << H_a$, again demonstrating that approximating the internal field as uniform is a reasonable assumption.

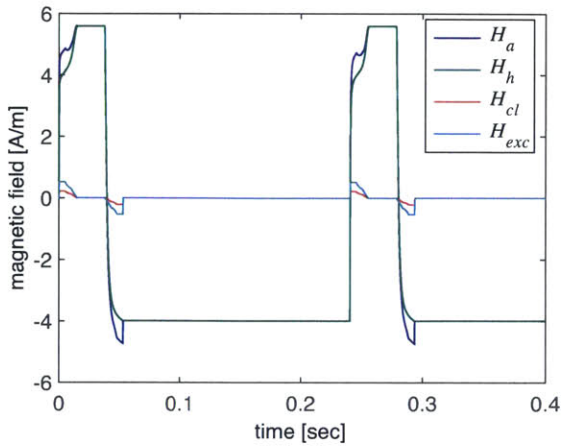

Figure 5-7: Simulated H_a, H_h, H_{cl}, and H_{exc} using (5.27) for H_{exc}.

Figure 5-8 illustrates the loop widening that results from eddy currents for one pulse of the simulated force profile. The inner loop is the B-H_a curve when no eddy currents are present. The middle loop is the B-H_a curve when accounting for only classical eddy currents. The outer loop is the B-H_a curve when accounting for both classical and excess eddy currents. The figure shows that the presence of eddy currents requires a larger applied field in order to reach a particular flux density. The 'kinks' in the two outer loops are the result of the shape of the force profile. Specifically, it is caused by the transition from the zero-snap phase to the non-zero constant snap phase of the force profile, which results in 'kinks' in the dB/dt profile.

Because of the linearizing effect that comes from shearing the material B-H curve, this loop widening of the material B-H curve has a much reduced effect when viewed from the perspective of the B-I domain. Figure 5-9 shows the loop widening in the B-I domain.

5.4.1 Excess Eddy Currents in 50%Ni-50%Fe Laminations

It was later discovered that while a wide variety of ferromagnetic materials follow the square-root dependency for H_{exc} given by (5.27), this is not true of 50%Ni-50%Fe. Instead, the field associated with excess eddy currents in nickel-iron have been found

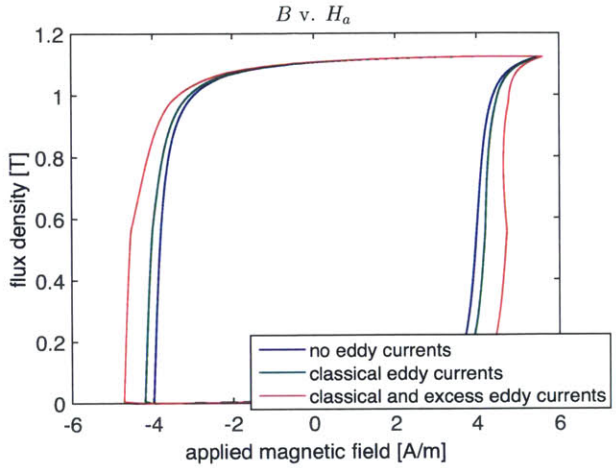

Figure 5-8: Loop widening from eddy currents for the simulated B-H_a curve.

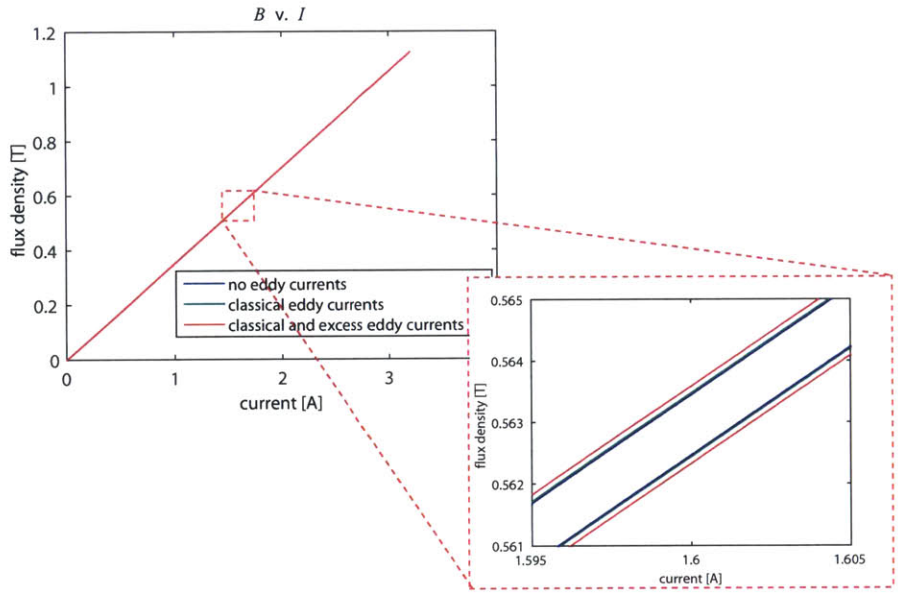

Figure 5-9: Loop widening from eddy currents for simulated B-I curve.

to follow a relationship given by [13]

$$H_{exc} \approx \frac{\sigma_e G A_l}{1 + \left(\frac{H_{exc}}{V_0}\right)^4} \frac{dB}{dt}. \tag{5.38}$$

Since a quintic equation is not generally solvable, we apply numeric methods instead to solve for H_{exc}. Our lab prototype actuator has nearly the same lamination cross-

sectional area as the specimen investigated in [13], so we use the same V_0 determined there, $V_0 = 3.8\,\mathrm{A/m}$. One advantage of (5.38) is that only one parameter needs to be determined.

For simulation, we did not use the augmented model shown in Figure 5-5 because the numeric solver had difficulty solving the algebraic loop with (5.38) in place of (5.27), even with time delays inserted. Instead, we used the real-time model described in Section 6.6.

Figure 5-10 shows the simulated deviation in force due to both classical eddy currents and excess eddy currents, with the excess field described by (5.38). The maximum force deviation predicted from simulation is 0.426 N. This amounts to 0.12 percent of full-scale force. We see then that excess eddy currents play a much larger role in nickel-iron than was originally predicted with the square-root dependence given by (5.27). This agrees with the findings in [13], where the 50 Hz losses due to excess eddy currents took up a much larger proportion of the total losses compared to most other materials tested.

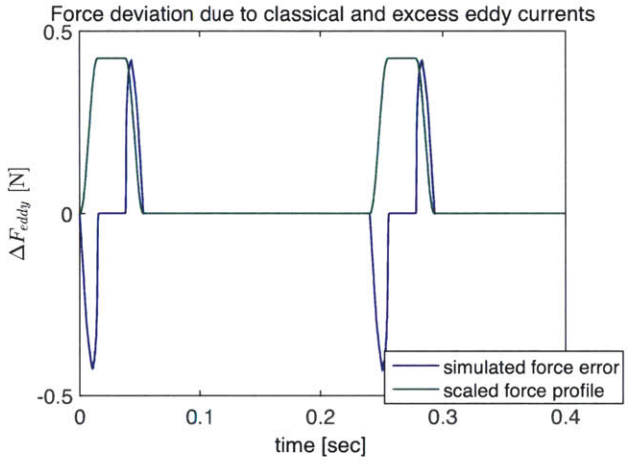

Figure 5-10: Simulation of $\Delta F_{eddy} = \Delta F_{cl} + \Delta F_{exc}$ using (5.38) for the excess eddy currents.

If we plot the simulated H_{exc} along with H_a in Figure 5-11, we see that the peak H_{exc} is on the same order of magnitude as the peak H_a. Approximating the internal field as uniform is therefore not a justified assumption in this case, so we should take the simulation results for ΔF_{eddy} in Figure 5-10 with a grain of salt. This also suggests

that NiFe is not the best core material to use in applications where minimizing eddy current effects is important.

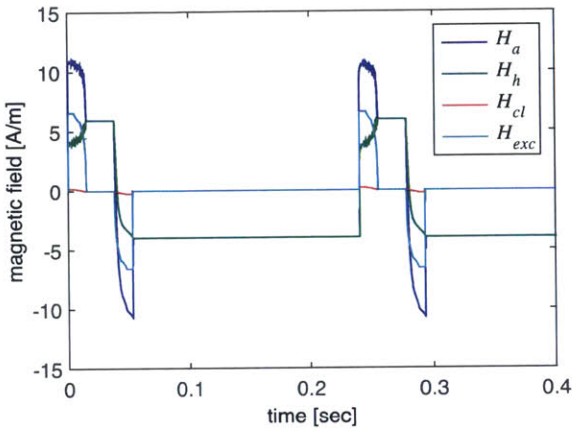

Figure 5-11: Simulated H_a, H_h, H_{cl}, and H_{exc} using (5.38) for H_{exc}.

5.5 Power Dissipation

Power is dissipated within the ferromagnetic core and target from hysteresis losses and eddy current losses. This dissipated power will cause heat generation in the stator and target. There are multiple drawbacks to heat generation. Ferromagnetic properties have some dependence on temperature, so a calibration done at one temperature will not necessarily be accurate at another temperature. Hall sensors have a temperature dependency, so if the pole face is heating up, this will affect a Hall sensor measurement. Temperature rises also cause the stator and target to expand: this can cause an unmeasured gap change and can also cause distortion to the chuck.

We would thus like to be able to estimate the expected magnitude of the power dissipated from hysteresis and eddy currents. These estimates can be used in a thermal model to estimate expected temperature rise and thermal distortion. Making use of the loss separation concept mentioned earlier, we treat hysteresis loss, classical eddy current loss, and excess eddy current loss separately. This allows us to write

the total internal power loss, P, as

$$P = P_h + P_{cl} + P_{exc}, \tag{5.39}$$

where P_h is the loss associated with hysteresis, P_{cl} is the loss associated with classical eddy currents, and P_{exc} is the loss associated with excess eddy currents.

For many materials, the total loss per cycle can be expressed as a function of frequency, f, as [14, 70]

$$\frac{P}{f} = C_0 + C_1 f + C_2 \sqrt{f}, \tag{5.40}$$

where C_0, C_1, and C_2 are constants. The hysteresis loss per cycle is constant, while the classical eddy current loss per cycle varies linearly with frequency. The excess eddy current loss per cycle often follows a square-root dependency on frequency.

The energy per volume, e, in a magnetic body is given by [14, 70]

$$e = \int H dB. \tag{5.41}$$

The energy lost while traversing a B-H loop is thus given by the area enclosed by the loop. The power dissipated per unit volume, p, can then be written as

$$p = H \frac{dB}{dt}. \tag{5.42}$$

5.5.1 Hysteresis Loss

Figure 5-12 shows a generic acceleration profile for a scanning stage. The duration of a single pulse is T and the period of the entire scan is T_s.

If we consider a single pulse, we can estimate the energy per volume lost owing to hysteresis (e_h) as

$$e_h \approx 2 H_c B_{\max}, \tag{5.43}$$

where H_c is the coercive field and $B_{\max}$ is the maximum flux density reached. This approximation is shown graphically in Figure 5-13. The area enclosed by the hystere-

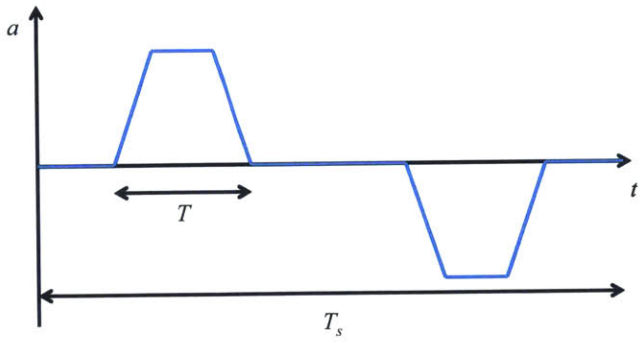

Figure 5-12: A generic acceleration profile for a scanning lithography stage.

sis loop (shown in blue) is approximated with a rectangle of width $2H_c$ and height $B_{\max}$ (shown in green). This approximation will improve the more square the material hysteresis loop is.

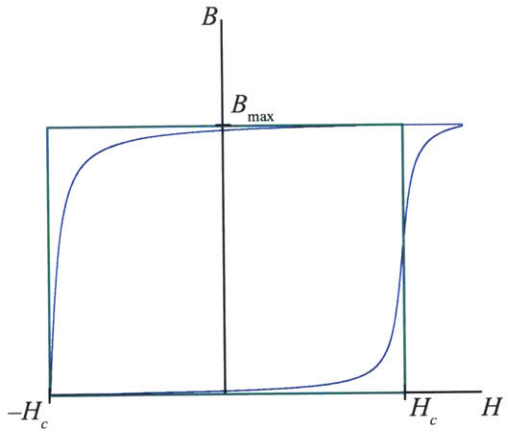

Figure 5-13: A rectangle of width $2H_c$ and height $B_{\max}$ approximates the energy per volume lost from hysteresis.

The average hysteretic power per volume dissipated during the pulse is then

$$\langle p_h \rangle_p \approx \frac{2H_c B_{\max}}{T}. \tag{5.44}$$

The $\langle\rangle$ denotes the *average* power per volume and the subscript p denotes that we are referring to the average power of a single pulse.

If we consider the entire scan cycle, then the duty cycle is defined as $D = 2T/T_s$,

i.e., the fraction of the entire scan during which the stage is accelerating. The average power per volume dissipated over the entire scan for a single actuator is

$$\langle p_h \rangle \approx \langle p_h \rangle_p \frac{1}{2} D,$$

$$\langle p_h \rangle \approx \frac{2DH_c B_{\max}}{T}. \tag{5.45}$$

The reason for the factor of $1/2$ in the first line is that since a reluctance actuator can only pull, any single actuator will only be on during one acceleration pulse per scan cycle rather than during both.

We can express (5.45) in terms of $F_{\max}$

$$\langle p_h \rangle \approx \frac{2DH_c}{T} \sqrt{\frac{2\mu_0 F_{\max}}{A}}. \tag{5.46}$$

We adapt (5.45) to our simulated profile in Figure 4-4 and predict $\langle p_h \rangle$ to be $45\,\mathrm{W/m^3}$. To determine the actual simulated power per volume dissipated from hysteresis, we use

$$\langle p_h \rangle = \langle H_h \frac{dB}{dt} \rangle, \tag{5.47}$$

which results in a value of $42.6\,\mathrm{W/m^3}$, a close match to the theoretical approximation.

5.5.2 Classical Eddy Current Loss

Based on (5.42), the instantaneous power loss per volume from classical eddy currents, p_{cl}, is $H_{cl} \cdot dB/dt$. Substituting (5.13), we can write

$$p_{cl} = \frac{\sigma_e d^2}{12} \left(\frac{dB}{dt} \right)^2. \tag{5.48}$$

Or in terms of F for $F \neq 0$, we can write

$$p_{cl} \approx \frac{\mu_0 \sigma_e d^2}{24AF} \left(\frac{dF}{dt} \right)^2 \approx \frac{\sigma_e d^2 B_s^2}{48 F_{\max} F} \left(\frac{dF}{dt} \right)^2. \tag{5.49}$$

Suppose that the exact force or flux profile is unknown ahead of time, but we know the approximate peak force or peak flux and the pulse width, and we want to estimate the average power per volume dissipated from classical eddy currents. We can estimate the force pulse with its first Fourier component (assuming a square wave for the force pulse, which should bias the result toward a conservative one, i.e., an overestimate). The average power dissipated per volume for a sine wave of amplitude B_0 and frequency f is given by [14]

$$\langle p_{cl} \rangle_{\sin} = \frac{\pi^2}{6} \sigma_e d^2 B_0^2 f^2, \tag{5.50}$$

where the sin subscript denotes that we are taking the average power per volume for a sine wave.

We note that for a square wave with amplitude $B_{\max}$, the fundamental component will have an amplitude of $4/\pi \cdot B_{\max}$. We can substitute this for B_0 into (5.50) to derive an approximate value for the average power dissipated per volume for a single pulse

$$\langle p_{cl} \rangle_p \approx \frac{8}{3} \sigma_e d^2 B_{\max}^2 f^2. \tag{5.51}$$

The frequency f of the fundamental component has a value of $f = 1/(2T)$. Multiplying (5.51) by $D/2$, we derive an approximation for the average power per volume dissipated from classical eddy currents over the entire scan cycle as

$$\langle p_{cl} \rangle \approx \frac{D \sigma_e d^2}{3T^2} B_{\max}^2. \tag{5.52}$$

In terms of $F_{\max}$, we can write

$$\langle p_{cl} \rangle \approx \frac{2D \mu_0 \sigma_e d^2}{3AT^2} F_{\max}. \tag{5.53}$$

Applying this formula to our simulated force profile, we predict $\langle p_{cl} \rangle$ to be $1.83\,\mathrm{W/m^3}$. To calculate the exact value $\langle p_{cl} \rangle$ for simulation, we use

$$\langle p_{cl} \rangle = \langle H_{cl} \frac{dB}{dt} \rangle. \tag{5.54}$$

This results in $1.99\,\mathrm{W/m^3}$, again a close match to the theoretical approximation.

5.5.3 Excess Eddy Current Loss

The instantaneous power loss per volume from excess eddy currents, p_{exc}, is $H_{exc} \cdot dB/dt$. If H_{exc} can be expressed by (5.27), then we can express p_{exc} as

$$p_{exc}(t) = \frac{n_0 V_0}{2}\left(\sqrt{\left(\frac{dB}{dt}\right)^2 + \frac{4\sigma_e G A_l}{n_0^2 V_0}\left|\frac{dB}{dt}\right|^3} - \left|\frac{dB}{dt}\right|\right). \tag{5.55}$$

Assuming that the low-frequency content will not contribute significantly to power loss because of the dependency on dB/dt, we can use the high-frequency limit of H_{exc} in (5.31) to approximate $p_{exc}(t)$ as

$$p_{exc}(t) \approx \sqrt{\sigma_e G A_l V_0}\left|\frac{dB}{dt}\right|^{3/2}. \tag{5.56}$$

In terms of F for $F \neq 0$, we write

$$p_{exc}(t) \approx \sqrt{\sigma_e G A_l V_0}\left|\frac{\mu_0}{2AF}\right|^{3/4}\left|\frac{dF}{dt}\right|^{3/2}. \tag{5.57}$$

If the force or flux profile is not known exactly ahead of time, using (5.56) or (5.57) to approximate the average power per volume dissipated during a scan is not as straightforward as was done for $\langle p_{cl}\rangle$ because of the $(dB/dt)^{3/2}$ term. Suppose though that we have an idea what the maximum dB/dt ($(dB/dt)_{\max}$) will be and approximate the jerk phase of the acceleration profile as having a constant dB/dt equal to this maximum. We can then write the average power dissipation per volume for a single acceleration pulse as

$$\langle p_{exc}\rangle_p \approx \frac{2a_{\max}}{j_{\max}T}\sqrt{\sigma_e G A_l V_0}\left(\frac{dB}{dt}\right)_{\max}^{3/2}. \tag{5.58}$$

Here $2a_{\max}/(j_{\max}T)$ is approximately the fraction of the acceleration pulse with non-zero jerk. We can further approximate $(dB/dt)_{\max}$ as $B_{\max}j_{\max}/a_{\max}$. Making this

substitution, we write

$$\langle p_{exc} \rangle_p \approx \frac{2}{T} \sqrt{\frac{a_{\max} \sigma_e G A_l V_0}{j_{\max}}} B_{\max}^{3/2}. \tag{5.59}$$

Finally, for the average power dissipated per volume for the entire scan cycle, we multiply by $D/2$

$$\langle p_{exc} \rangle \approx \frac{D}{T} \sqrt{\frac{j_{\max} \sigma_e G A_l V_0}{a_{\max}}} B_{\max}^{3/2}. \tag{5.60}$$

Or, in terms of $F_{\max}$, we write

$$\langle p_{exc} \rangle \approx \frac{D}{T} \sqrt{\frac{j_{\max} \sigma_e G A_l V_0}{a_{\max}}} \left(\frac{2\mu_0 F_{\max}}{A} \right)^{3/4}. \tag{5.61}$$

With this formula, we predict $\langle p_{exc} \rangle$ to be $7.7\,\mathrm{W/m^3}$ for our simulated profile. To calculate the exact value $\langle p_{cl} \rangle$ we use

$$\langle p_{exc} \rangle = \langle H_{exc} \frac{dB}{dt} \rangle. \tag{5.62}$$

This results in $6.6\,\mathrm{W/m^3}$, a reasonably close match to the theoretical approximation.

It should be noted that a number of approximations have gone into estimating power dissipation from eddy currents, particularly in regards to the excess eddy current calculation. The numbers calculated here should not be expected to have high-precision predictive power and may become less accurate with different force profiles. However, the order of magnitude of these numbers gives us confidence that power dissipation due to eddy currents should be negligible compared to that from hysteresis and from resistive loss in the coils.

5.6 Summary

In this chapter, we have augmented the basic reluctance actuator model introduced in Chapter 4 to include eddy current effects. We have presented models for classical eddy currents and for excess eddy currents valid for frequencies below the skin frequency.

From these models, we have developed formulas for approximating force errors due to eddy currents. These formulas are listed in Table 5.1. We learned that for our profile, excess eddy currents are likely to dominate over classical eddy currents. However, both of these are expected to contribute negligible force errors compared to errors from hysteresis or from gap disturbances. We also learned that excess eddy currents in 50%-50% NiFe follow a different law from that followed by excess eddy currents in many other ferromagnetic materials.

Table 5.1: Errors from eddy currents in a reluctance actuator

Error source	**Theoretical approximation**
Classical eddy currents	$\Delta F_{cl} = -\frac{\sqrt{2}\mu_0\sigma_e d^2 l_{Fe}}{24g}\frac{dF}{dt}$
Excess eddy currents	$\Delta F_{exc} = -\operatorname{sgn}\left(\frac{dF}{dt}\right)\frac{\mu_0 l_{Fe} n_0 V_0}{2gB_s}\sqrt{F_{\max}F}\left(\sqrt{1+\frac{2\sigma_e G A_l B_s}{n_0^2 V_0 \sqrt{F_{\max}F}}\left\lvert\frac{dF}{dt}\right\rvert}-1\right)$

We also developed formulas for approximating the average power per volume dissipated in the reluctance actuator core and target during scanning. This dissipated power was comprised of contributions from hysteresis loss, classical eddy current loss, and excess eddy current loss. Table 5.2 list the approximate formula for each contribution. Also listed are the theoretical and simulated numeric values for the average power dissipation per volume for the simulated prototype actuator. We learned that hysteresis loss will dominate eddy current loss for our application. However, we expect the both the hysteresis loss and eddy current loss to be small compared to the resistive loss in the coil.

In the next chapter we investigate methods for implementing the actuator model for real-time flux estimation and control. These real-time techniques can also be used as alternate methods for simulating the results presented in this chapter and the previous chapter.

Table 5.2: Reluctance actuator ferromagnetic power dissipation sources

Power dissipation source	**Theoretical approximation**	**Theoretical value** [W/m^3]	**Simulated value** [W/m^3]
Hysteresis loss	$\langle p_h \rangle = \frac{2DH_c B_{\max}}{T}$	45.0	42.6
Classical loss	$\langle p_{cl} \rangle = \frac{D\sigma_e d^2}{3T^2} B_{\max}^2$	1.8	2.0
Excess loss	$\langle p_{exc} \rangle = \frac{D}{T}\sqrt{\frac{j_{\max}\sigma_e G A_l V_0}{a_{\max}}} B_{\max}^{3/2}$	7.7	6.6

Chapter 6

Reluctance Actuator Modeling for Real-Time Flux Estimation

The actuator model presented in Chapter 4 cannot be used for real-time estimation as presented because it includes an algebraic loop. If time delays are added to break the algebraic loop, there is still no guarantee that the loop will be stable in real-time. Thus, real-time model implementation is a significant challenge. In this chapter, we present several model implementations for real-time estimation that incorporate hysteresis and gap disturbances. We discuss advantages and drawbacks of each.

Among the different implementations presented in this chapter are two novel techniques for estimating the actuator flux. The first, introduced in Section 6.4, is to use an observer with an adaptive controller gain. The observer permits us to estimate flux from the actuator current and gap measurements without having explicitly to solve for the magnetic field in the actuator core. The adaptive controller gain linearizes the observer loop gain even with the presence of the highly nonlinear material hysteresis model within the loop. This adaptation performs a similar function to feedback linearization. This feature allows us to maintain accurate flux estimation over the entire B-H plane.

The second novel technique, introduced in Section 6.6, is to introduce a change of variables into the reluctance actuator model that allows us to model a sheared version of the B-H hysteresis relationship. This shearing makes the plant model seen

by the observer much less nonlinear. The observer structure with sheared hysteresis model (SHM) is shown to be much more robust to large gap disturbances than the observer using the original unsheared hysteresis model. We present simulation results for each implementation. For a couple implementations, we also present preliminary experimental results. Finally, we present a conceptual analysis of the error behavior of the different observer implementations for real-time flux estimation.

Except for the implementation discussed in Section 6.7, which uses the Chua model, all the real-time flux estimation schemes presented in this chapter use the Preisach model for modeling the hysteresis. However, the methods presented in this chapter are all general enough that other hysteresis models could be used in place of the Preisach model.

6.1 Motivation

As discussed in Section 2.5, one way to linearize the reluctance actuator is by feedback control of the actuator flux (see Figures 2-16 and 2-17). In this thesis, we use a sense coil as the flux feedback sensor. However, this requires that we have a way to estimate the actuator flux at low frequencies since a sense coil is AC-coupled. Developing a real-time model that takes as its inputs the actuator current and air gap can provide this flux estimate without requiring the use of any additional feedback sensors. Additional details on the overall feedback scheme using this low-frequency model in tandem with a sense coil can be found in Chapter 10. In this chapter, we focus only on developing the real-time model for the low-frequency flux estimate.

6.2 Original Model with Stabilizing Filter

If the original model used for simulation in Chapter 4 and shown in Figure 4-1 is stable or can be made stable, then it may be possible to use this model for real-time estimation. We first fit the Della Torre hysteresis model to experimental data. We then analyze the loop transmission of the resulting estimation loop for stability and

find it wanting. We then add a filter to stabilize the loop and simulate the resulting model reliably.

6.2.1 Hysteresis Model Identification

To determine the parameters for the hysteresis model, we used experimental data from the reluctance actuator prototype on the air bearing testbed described in Chapter 8 and then fit the Della Torre Preisach hysteresis model to it. Figure 6-1 shows an experimental B-I curve taken from the reluctance actuator at a nominal gap of $g = 500\,\mu\text{m}$ and driven with a 10 Hz sine wave. The current was measured using a sense resistor tied to the low end of the actuator coil and the flux linkage derivative was obtained from a measurement taken from a sense coil wound around the center pole face. The sense coil measurement was numerically integrated in post-processing to obtain an estimate of the flux density. The target was attached to the testbed motion stage. The gap was maintained at $g = 500\,\mu\text{m}$ using position feedback on the motion stage. See Chapter 10 for details.

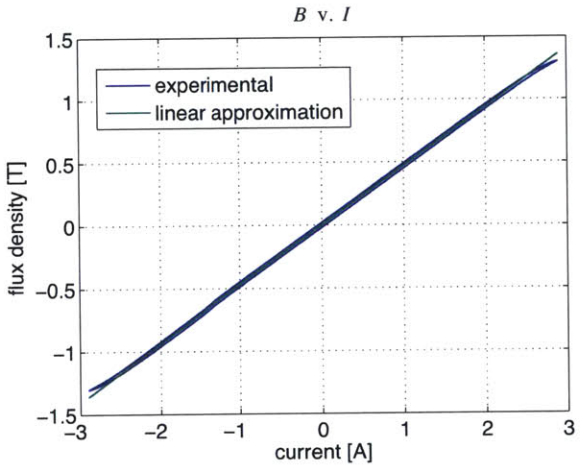

Figure 6-1: Experimental B-I curve and its linear approximation for an actuator gap of 500 µm.

A fit to the linear portion of the B-I curve is also shown. The slope m of this line is 0.47 T/A. From (2.8), we can replace $\mu_0 N/(2g)$ with m. We can use (2.30) to determine the material B-H curve for the actuator. We rewrite (2.30) in terms of I

and solve for H_{Fe}, the core material magnetic field as

$$H_{Fe} = \frac{NI}{l_{Fe}} - \frac{2gB}{\mu_0 l_{Fe}}, \tag{6.1}$$

or

$$H_{Fe} = \frac{N}{l_{Fe}} \left(I - \frac{1}{m} B \right). \tag{6.2}$$

Using this equation, we can solve for H_{Fe} from the experimental B-I data and plot the B-H curve as shown in Figure 6-2. We fit the Della Torre model introduced in Chapter 3 to this data. We set $H_c = 120\,\mathrm{A/m}$, $\sigma = 20.4$, and $B_s = 1.2\,\mathrm{T}$. We also add a linear part to the model, $dB/dH_{\mathrm{lin}} = 250\mu_0$, to improve the fit. The output of the hysteresis model is therefore $dB/dH = dB/dH_{\mathrm{DT}} + dB/dH_{\mathrm{lin}}$, where dB/dH_{DT} is the output of the unmodified Della Torre model. Figure 6-2 shows the fit of the Della Torre model to the experimental major loop. The fit is imperfect and could be improved, but for our present purposes of developing an operational real-time flux estimator, it is sufficient.

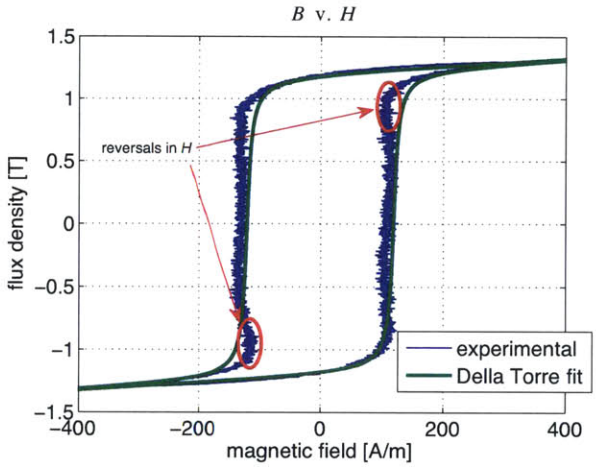

Figure 6-2: B-H major loop derived from experimental data and Della Torre model fit.

We note that the experimental data shows that B is not monotonic with H. This is indicated by the red circles in the figure. This is believed to be the result of the position controller not maintaining a perfectly constant air gap. The measured gap

data is shown in Figure 6-3. The air gap shows a peak fluctuation of approximately $\pm 4\,\mu m$ about the nominal. We attempted to compensate for this in the B data plotted in Figure 6-2 by multiplying the integrated sense coil data by g/g_0, so that the compensated flux density, B_c, is equal to $B \cdot g/g_0$. This compensation is based on (2.8), where $B \propto I/g$. We can express B_c at $g = g_0$ as

$$B_c = \frac{\mu_0 N I}{2 g_0}. \tag{6.3}$$

Likewise, we can express B in the general case as

$$B = \frac{\mu_0 N I}{2 g}. \tag{6.4}$$

If we solve for I in both equations and set them equal to each other, we can write

$$I = \frac{2 g_0 B_c}{\mu_0 N} = \frac{2 g B}{\mu_0 N}. \tag{6.5}$$

If we then solve for B_c, we can write

$$B_c = B \frac{g}{g_0}. \tag{6.6}$$

Therefore, to determine the B-I relationship at a particular constant gap from data in which the gap is changing, we multiply the measured B by g/g_0. This B_c variable is what is plotted in Figure 6-2. This is an improvement upon the uncompensated B, which is plotted in Figure 6-4.

The compensated B_c-H data from Figure 6-2 is likely still imperfect because the approximations in (6.3) and (6.4) do not take into account saturation. They assume a perfect inverse relationship between B and g throughout the entire range of B. In Figure 6-5, we plot the experimental B-H data from an actuator that was clamped with $500\,\mu m$ plastic shims between the stator and target. Clamping the actuator avoids the air gap fluctuation that occurs using the air bearing setup. The clamped actuator setup can be seen in Figure 6-18. The B-H data looks much improved,

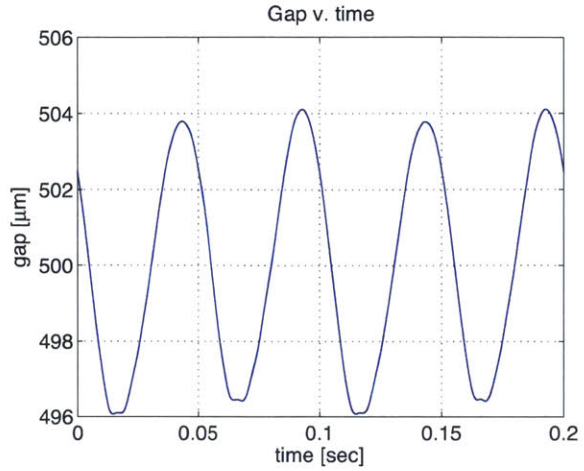

Figure 6-3: Air gap data for experimental B-H data from Figure 6-2.

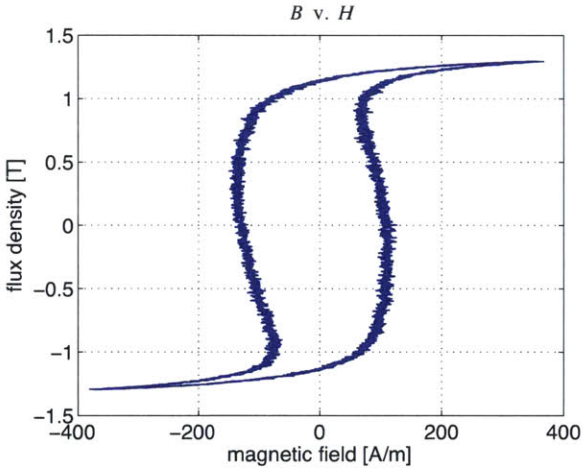

Figure 6-4: B-H experimental major loop with no compensation for changing gap.

indicating that the changing air gap is indeed the culprit for the non-monotonic relationship between B and H in Figure 6-2.

This procedure for finding the B-H curve highlights one of the drawbacks of this method of estimating flux: since we do not have direct access to H in the steel, we have to construct H from the original B-I experimental data.

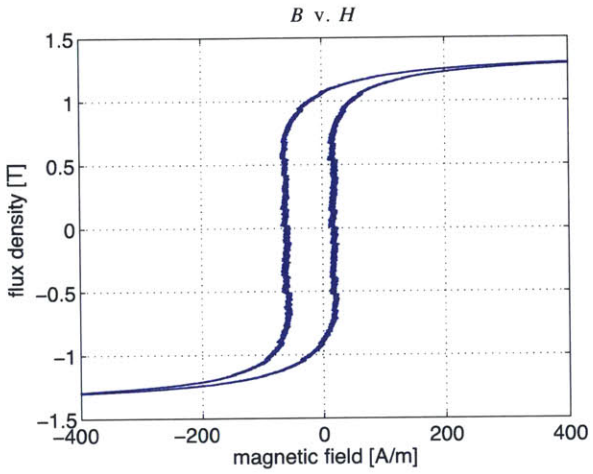

Figure 6-5: B-H major loop derived from experimental data and Della Torre model fit.

6.2.2 Analysis of Loop Stability

To determine whether the loop illustrated by the block diagram of Figure 4-1 is stable or not, we need to estimate the loop gain and phase shift. The loop gain, $|LT|$, is

$$|LT| = \left|\frac{B}{H}\right| \frac{2g}{\mu_0 l_{Fe}}, \tag{6.7}$$

where $\left|B/H\right|$ is the gain of the $B(H)$ block in Figure 4-1 at any relevant operating point.

The $2g/(\mu_0 l_{Fe})$ block will not contribute any phase loss to the loop, so the loop return ratio phase, $\angle LT$, is

$$\angle LT = \angle B/H, \tag{6.8}$$

where $\angle B/H$ is the phase of the $B(H)$ block at any relevant operating point. Therefore, determining the loop gain and phase comes down to estimating the gain and phase of the hysteresis block.

Since hysteresis is a nonlinear phenomenon, we must linearize the hysteresis operator in some way in order to estimate its gain and phase. Here we opt to use a describing function analysis to do so [72, Chapter 6].

We begin by approximating the hysteresis operator as simple non-ideal relay with

a lower output value of $-B_{\max}$ and an upper value of $B_{\max}$ and input switching thresholds of H_c and $-H_c$. See Figure 6-6.

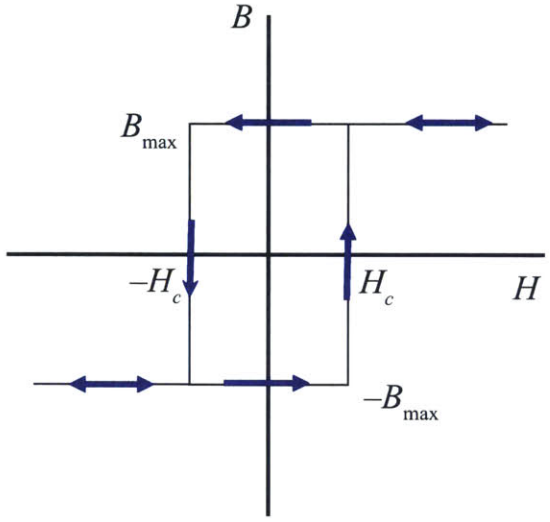

Figure 6-6: A simple relay as an approximation for the hysteresis operator.

We denote the describing function for such a relay as $B_D(H)$, which is given by [72] as

$$B_D(H) = \frac{4B_{\max}}{\pi H_0} \angle -\sin^{-1}\left(\frac{H_c}{H_0}\right), \tag{6.9}$$

where H_0 is the amplitude of the assumed sinusoidal input signal. As an initial test, we would like to see if our real-time flux estimator can recreate the experimental B-I curve shown in Figure 6-1. Therefore, we set $B_{\max}$ in (6.9) to the maximum experimental B, $B_{\max} = 1.3\,\mathrm{T}$, and H_0 to the maximum H, $H_0 = 360\,\mathrm{A/m}$, both taken from Figure 6-2. These values result in a gain for $B_D(H)$ of $0.0046\,\mathrm{T}\cdot\mathrm{m/A}$ and a phase of $-19.5°$. Note, however, that the gain and phase are both highly dependent on the input signal amplitude.

We can approximate the loop transmission as

$$\begin{aligned} LT &= \left|\frac{B}{H}\right| \frac{2g}{\mu_0 l_{Fe}} \angle B/H, \\ &\approx \frac{4B_{\max}}{\pi H_0}\frac{N}{m l_{Fe}} \angle -\sin^{-1}\left(\frac{H_c}{H_0}\right) = 27.4\angle -19.5°, \end{aligned} \tag{6.10}$$

where in the second line we have substituted N/m for $2g/\mu_0$ based on (6.2).

In addition to the phase loss from hysteresis, we will have phase loss from the time delay associated with sampling. For example, we will have an additional $-90°$ of phase loss at a frequency of $f_s/4$, where f_s is our sampling frequency. For stability, the loop gain must be less than 1 when the total loop phase reaches $-180°$. Since our loop gain is constant at 27.4 at all frequencies and there is no defined loop crossover frequency, we expect our model to be unstable for real-time operation.

6.2.3 Stabilizing Filter Design

We can add a low-pass filter in the loop to stabilize it. This low-pass filter must meet two criteria: 1) for stability, it must reduce the loop gain to below 1 before the loop phase reaches $-180°$; 2) it must have a low-frequency gain of 1 so as not to affect the model accuracy at low frequencies. Note the contrast between this filter and a controller in a typical feedback loop: in a typical feedback loop, we want a high gain on the controller filter within the loop bandwidth, while here we ideally want a gain of 1 within the loop bandwidth. The reason for this difference is that in a typical feedback loop we want the output to track the input, which requires a high controller gain, whereas in our loop, we want to keep the loop as unaffected as possible while at the same time stabilizing it.

Figure 6-7 shows the model with a stabilizing low-pass filter in the loop. The variable B_e is the estimated flux density after the filter.

Our new loop transmission, denoted as LT_2, now includes the stabilizing filter. The new loop gain magnitude can be expressed as

$$|LT_2| = |LT||F(s)| = \left|\frac{B}{H}\right| \frac{N}{ml_{Fe}} |F(s)|, \tag{6.11}$$

where $F(s)$ is the stabilizing filter transfer function. The phase of the loop transmission, denoted by ϕ_{LT_2}, is

$$\phi_{LT_2} = \phi_{BH} + \phi_F + \phi_T, \tag{6.12}$$

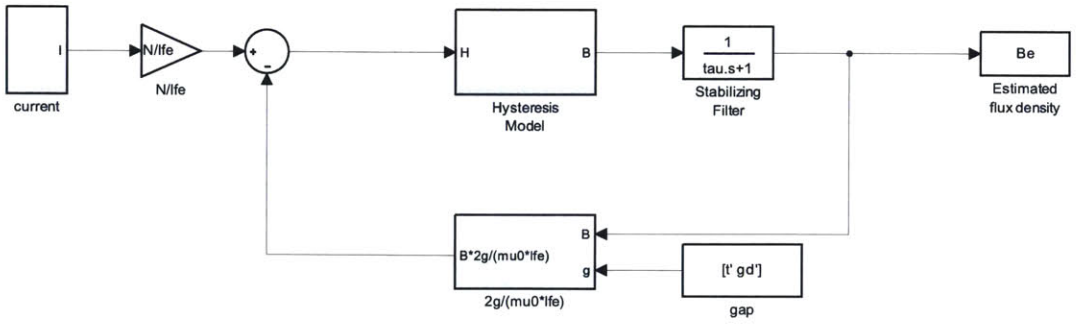

Figure 6-7: Reluctance actuator model with stabilizing filter for real-time.

where ϕ_{BH} is the phase associated with the hysteresis model, ϕ_F is the phase of the stabilizing filter, and ϕ_T is the phase of the time delay from sampling. The phase margin, ϕ_m, is defined as $\phi_m = 180 + \phi_{LT_2}$ at $f = f_c$, where f_c is the crossover frequency, the frequency where $|LT_2| = 1$. A positive phase margin is required for stability.

Suppose $f_s = 20\,\text{kHz}$. Then, if we set our crossover frequency, f_c, to be at 2 kHz, ϕ_T will contribute 36° of phase loss at f_c. If our stabilizing filter is a one-pole filter, this will add an additional 90° of phase loss at crossover. With ϕ_{BH} estimated as $-19.5°$, this gives us a nominal phase margin of $\phi_m = 35°$.

It remains to design $F(s)$ so that the loop gain is 1 at $f = f_c$. If $F(s)$ is a one-pole filter with DC gain of 1, we can write it as

$$F(s) = \frac{1}{\tau s + 1}. \tag{6.13}$$

The gain of $F(s)$ must be equal to $1/|LT|$ at $f = f_c$ to force crossover at f_c. The gain of $F(s)$ as a function of f for frequencies well above its corner frequency is $\sim 1/(2\pi f\tau)$. Solving for τ gives

$$\tau = \frac{|LT|}{2\pi f_c}. \tag{6.14}$$

This results in $\tau = 2.2\,\text{ms}$. This corresponds to a corner frequency of 73 Hz. We

implemented this filter in the loop and simulated the resulting model. However, we discovered the loop to be unstable. The reason posited for this is that the gain associated with the hysteresis model, $|B/H|$, is dynamic: it changes substantially depending on where on the hysteresis loop one is. The maximum occurs near $H = H_c$ and is $0.142\,\mathrm{T}\cdot\mathrm{m/A}$. This is 30 times greater than the gain obtained from the describing function analysis. The upshot is that the original loop gain will at times be much larger than that indicated by (6.10). This will result in a much higher crossover frequency and danger of instability.

A new filter design was based on this maximum gain of $|B/H| = dB/dH|_{\max}$, resulting in a much more conservative design. The maximum loop gain, $|LT|_{\max}$, without the filter is

$$|LT|_{\max} = \left.\frac{dB}{dH}\right|_{\max} \frac{N}{ml_{Fe}} = 850. \tag{6.15}$$

Using this value for $|LT|$ in (6.14), we calculate a value of 0.0675 s for τ. This corresponds to a corner frequency of 2.35 Hz for $F(s)$. From this result, we can anticipate that achieving an accurate flux estimate will be difficult since the corner frequency is so low. This means that our stabilizing filter will affect our loop even at very low frequencies.

The simulated estimated B-I curve using this stabilizing filter is shown on the left plot of Figure 6-8, where the input was a 1 Hz sine wave. We have included the experimental B-I curve from Figure 6-1 for reference. We can see that even at the low frequency of 1 Hz, the estimated B shows significant distortion. This distortion is even more apparent when plotting the simulated B-H curve, which is shown on the right plot.

One thing to note is that the distortion is greater near saturation. The reason for this can be understood by considering the model from the 'closed-loop' perspective. If we were to assume a linear model, the closed-loop transfer function from I to B_e is given by

$$\frac{B_e(s)}{I(s)} = \frac{N}{l_{Fe}} \frac{G(s)F(s)}{1 + G(s)H(s)F(s)}, \tag{6.16}$$

where $G(s)$ represents the linear transfer function approximation of the hysteresis

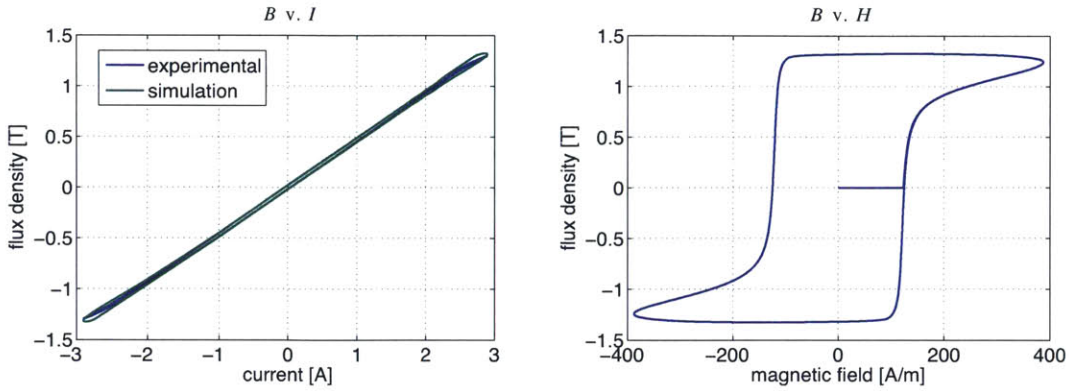

Figure 6-8: LEFT: Simulated B-I curve from Figure 6-7 model compared with experimental B-I curve; RIGHT: Corresponding simulated B-H curve.

model and $H(s)$ is the feedback gain $N/(ml_{Fe})$. When $\left|G(s)\right|$ is very large, e.g. near $H = H_c$, and we are operating at a frequency below $1/(2\pi\tau)$, then $G(s)H(s)F(s)$ will dominate in the denominator, and so $F(s)$ in the numerator will cancel with $F(s)$ in the denominator, and the distortion from $F(s)$ will be negligible.

On the other hand, when $\left|G(s)\right|$ is very small, for instance near saturation, then the 1 in the denominator will dominate, and $B_e(s)/I(s)$ can be approximated as

$$\frac{B_e(s)}{I(s)} \approx \frac{N}{l_{Fe}} G(s)F(s). \tag{6.17}$$

The filter $F(s)$ therefore will contribute significant distortion near saturation. Figure 6-9 shows the Bode plot of the stabilizing filter. At 1 Hz, we see a phase lag from the filter of 23°.

6.3 Flux Estimation Using an Observer

Another way to provide a real-time estimate of the flux is to design an observer to model the actuator. If we can estimate the current using a model of (4.1), we can compare this estimated current, $\hat{I}$, with the actual measured current, I. We can then design a feedback controller to drive the error between the estimated and measured currents to zero. This controller thereby forces the model to estimate the H and B

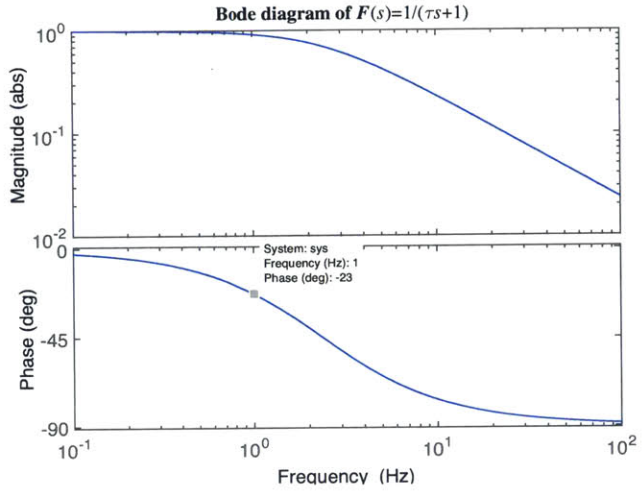

Figure 6-9: Bode plot of stabilizing filter $F(s)$.

that will solve (4.1). Figure 6-10 shows the block diagram of such an observer. The hat notation ($\hat{}$) used in this section and subsequent sections denotes an estimated variable.

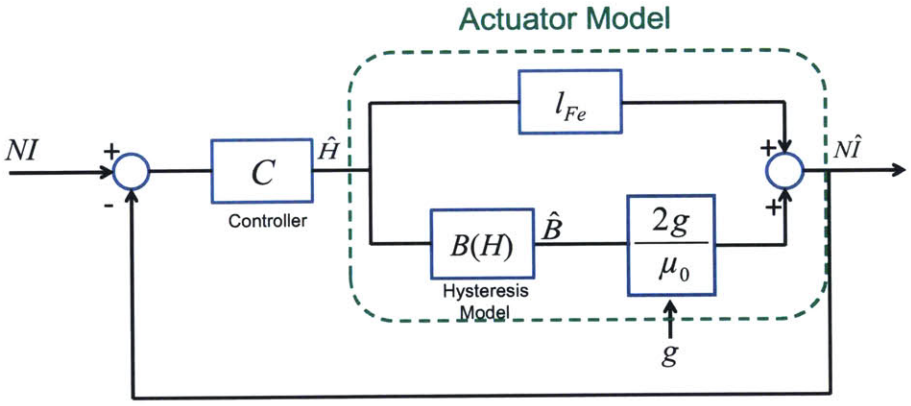

Figure 6-10: Block diagram of observer for estimating actuator flux density.

The changing gap can be treated as a disturbance to the plant model. The controller ideally will drive the model to the correct $\hat{H}$ and $\hat{B}$ even with this gap disturbance. The major advantage of using an observer to model (4.1) is that we do not need explicitly to solve for H in terms of I: the controller 'automatically' finds the correct input to the model that solves (4.1) if the estimation loop is stable.

One potential concern is that because of the hysteresis nonlinearity, (4.1) will

not necessarily always have a unique solution. However, because of the 'wiping-out' property of the Preisach model [61], we expect the observer to converge to the correct solution. The wiping-out property entails that previous local extrema in the input to the hysteresis model are removed from memory when they are exceeded by the current input. This memory is used to compute the current Preisach output. Thus, as the input continues to increase or decrease and previous extrema are wiped out, the Preisach model history will be erased and the output will converge to a unique solution, even if the initial output was inaccurate.

The benefit to this method compared to the previous method of using a stabilizing filter is that since the controller is separate from the plant, we can design the controller to have high gain over a large range of frequencies in order to drive $\hat{B}$ to the correct value. In contrast, the stabilizing filter method required that the stabilizing filter effectively become part of the plant model itself, which resulted in inaccuracies in the estimated flux density even at very low frequencies.

6.3.1 Controller Design

To design the controller for the observer, we first need to approximate the plant model. Rather than using the describing function analysis from Section 6.2.2 to approximate the hysteresis gain, we instead approximate it with the maximum dB/dH as was done in (6.15). This will bias the controller design toward a conservative one for a better guarantee of stability. The plant gain, $|P|$, can then be approximated as

$$|P| \approx \left.\frac{dB}{dH}\right|_{\max} \frac{2g}{\mu_0} + l_{Fe}. \tag{6.18}$$

For initial investigation, we implemented the Della Torre model for the hysteresis relationship, using the parameters given in Section 4.1.2 from the simulation model used in Chapter 4. The value of $dB/dH|_{\max}$ with these parameters is $3.98\,\mathrm{T}\cdot\mathrm{m/A}$. This results in $|P| = 3164\,\mathrm{m}$ at a nominal gap of $g = 500\,\mu\mathrm{m}$. Note that the units of the plant gain are length (m). This can be seen by inspecting (6.18): the parameter l_{Fe} for instance has units of meters. This is likewise true of the first term: dB/dH

has units of $\mathrm{T} \cdot \mathrm{m/A}$ and μ_0 has units that are the reciprocal of this. This leaves the variable g, which again has units of meters.

We choose as our controller a simple integrator, $C(s) = K/s$. This will add 90° of phase loss to the loop. Provided that our loop crossover is sufficiently lower than the sampling frequency, we should have enough phase margin for stability, since the only additional phase loss comes from the hysteresis.

We set the nominal crossover f_c to 2 kHz. The gain K is then set to

$$K = \frac{2\pi f_c}{|P|} = 3.97\,\mathrm{m}^{-1}\mathrm{s}^{-1}. \tag{6.19}$$

Our initial controller is therefore

$$C(s) = \frac{K}{s} = \frac{3.97}{s}. \tag{6.20}$$

6.3.2 Simulation Results and Analysis

Using the controller in (6.20), we simulated the observer with a 1 Hz sine wave with 3.2 A amplitude as the current input. Figure 6-11 shows the resulting $\hat{B}$-I curve along with the corresponding $\hat{B}$-$\hat{H}$ curve. We see that the observer flux density estimate is poor near saturation and when traversing from the demagnetized state. The reason for this is because in these regions, dB/dH is very low, which results in a low plant gain and consequently a low loop gain. Thus, we have low control authority in these regions and poor following error.

The low control authority also manifests itself when plotting the estimated current. Figure 6-12 plots the estimated current along with the input current. The controller is unable consistently to drive the error between the two to zero.

The minimum dB/dH, denoted $dB/dH|_{\mathrm{min}}$, is equal to μ_0. This can be seen from (4.3) when dM/dH approaches zero. This occurs at saturation for instance, since all the magnetic dipoles are already aligned with the external magnetic field, and so no additional magnetization can occur. For the Della Torre model, this also occurs at the demagnetized state: substituting zero for H in (3.12) and (3.13) results in

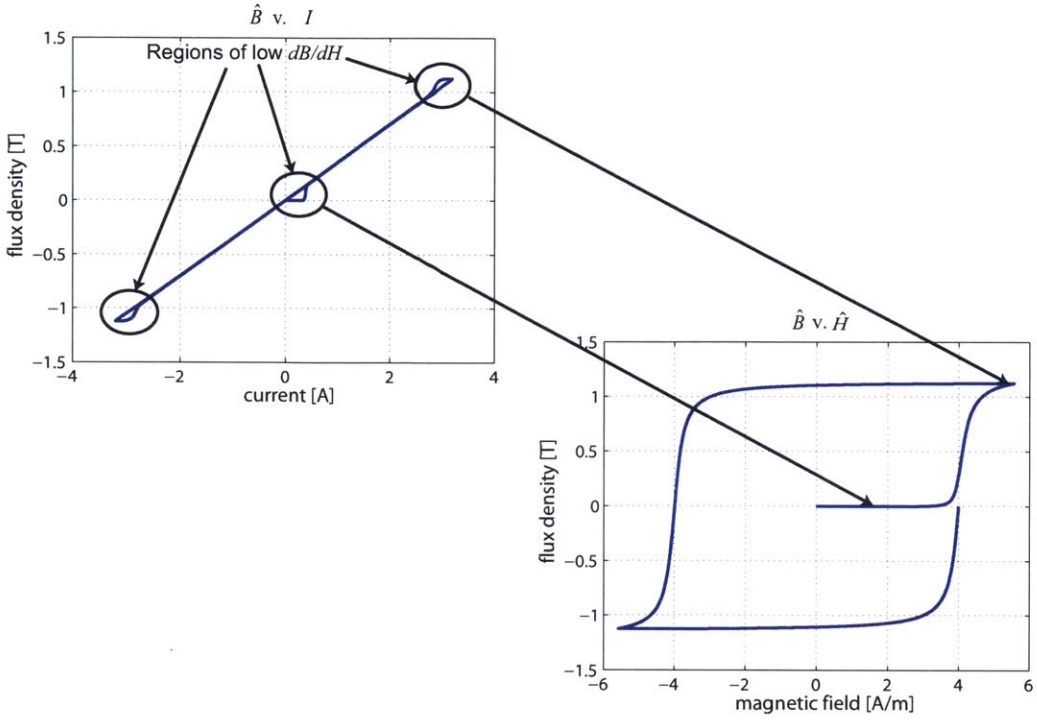

Figure 6-11: Simulated $\hat{B}$-I curve from observer with controller $C(s) = \frac{3.97}{s}$. Note errors where dB/dH is small.

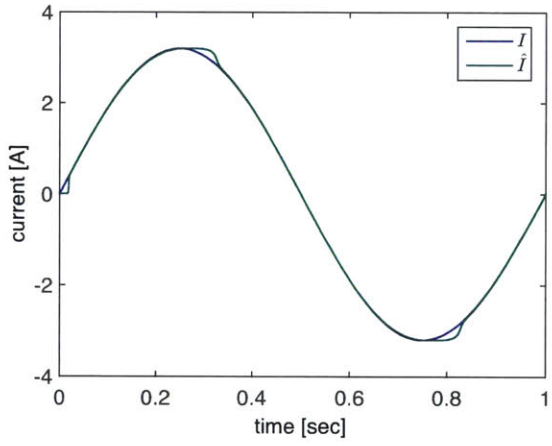

Figure 6-12: Simulated input current (I) and estimated output current ($\hat{I}$) from observer with controller $C(s) = \frac{3.97}{s}$.

$dM/dH = 0$. In real materials, however, $dM/dH \neq 0$ at the demagnetized state. This can be accounted for in the Della Torre model by adding a reversible or anhysteretic

component to the magnetization [8, 33]. Reversible magnetization accounts for the fact that some of the energy transferred by an applied field is stored and can be completely recovered when the applied field is returned to its original value [33]. There are different ways in which the reversible component can be implemented: it can be implemented as a single-valued function of the applied field [33], or it can be implemented as a single-valued function of the magnetization [8, 21, 33], for example.

Revising (6.18), we can write the minimum plant gain, $|P|_{\min}$, as

$$|P|_{\min} = \left.\frac{dB}{dH}\right|_{\min} \frac{2g}{\mu_0} + l_{Fe} = 2g + l_{Fe}. \tag{6.21}$$

The minimum plant gain is 0.101 m at a nominal gap of $g = 500\,\mu\text{m}$. This is a factor of 30,000 less than the maximum plant gain! The upshot is that the minimum loop gain will likewise be a factor of 30,000 less than the maximum loop gain. The cutoff frequency at the minimum loop gain is estimated to be

$$f_c = \frac{K|P|_{\min}}{2\pi} = 0.0638\,\text{Hz}. \tag{6.22}$$

As this is well below the signal frequency of 1 Hz, our controller will have limited effectiveness and our observer performance will suffer when dB/dH is low. We will revisit this topic in Section 6.8.

6.3.3 Controller Design with Higher Gain

We can attempt to increase the controller gain so that we have more control authority when the plant gain is low. We must be cautious that we do not increase the controller gain too much lest we compromise stability.

We increased K by a factor of 20, so that our updated controller, $C_2(s)$, is

$$C_2(s) = \frac{K_2}{s} = \frac{79.4}{s}. \tag{6.23}$$

The resulting $\hat{B}$-I curve of the observer for the 1 Hz sine wave input is shown in Figure 6-13. The observer shows much better performance than with the original

controller. However, one can still see that performance is degraded at the demagnetized state and at saturation.

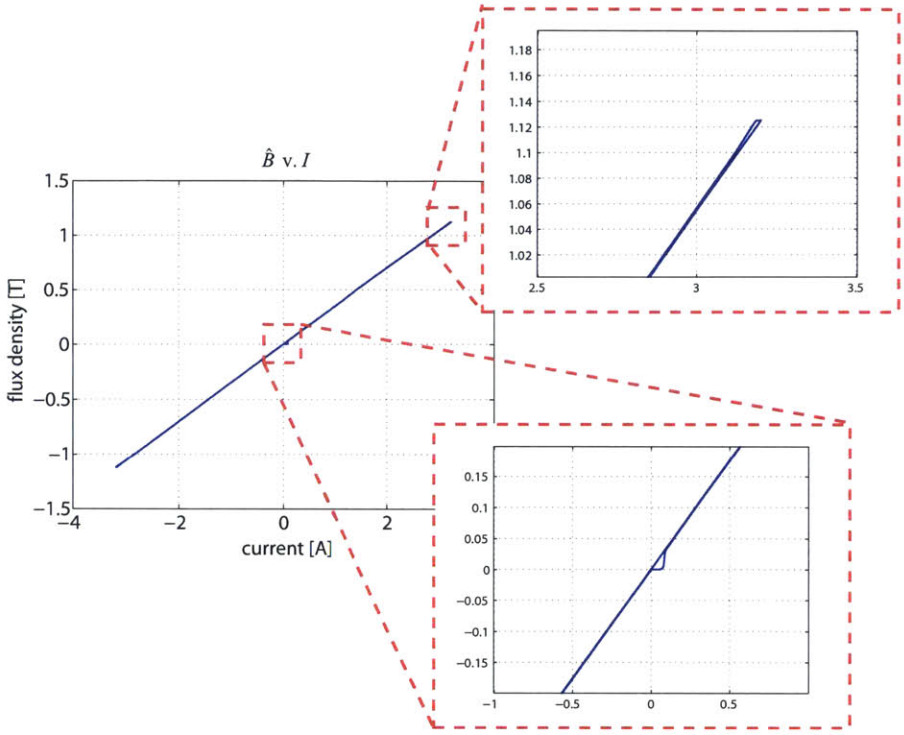

Figure 6-13: Simulated $\hat{B}$-I curve from observer with controller $C(s) = \frac{79.4}{s}$.

Figure 6-14 shows the input current and estimated observer output current in the top graph. The estimated output current tracks the input current more accurately with the higher-gain controller. The bottom graph shows the error between the two. The error can be seen to be larger at the initial state (65 mA error) and at saturation (14 mA error). This error will increase further as the input frequency increases and the control authority deteriorates. Increasing the controller gain much beyond a factor of 20 of the original gain led to stability problems.

6.4 Observer with Adaptive Controller Gain

To resolve the difficulty of providing an accurate flux estimate in the face of a wide-ranging plant gain, we designed a controller with an adaptive gain dependent on the

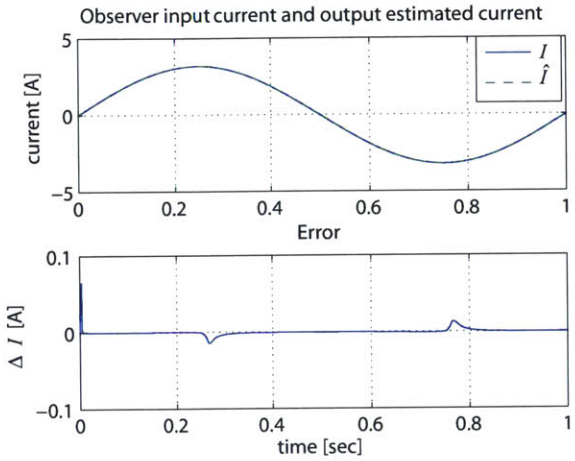

Figure 6-14: TOP: Simulated input current (I) and estimated output current ($\hat{I}$) from observer with controller $C(s) = \frac{79.4}{s}$; BOTTOM: Error between I and $\hat{I}$.

plant gain.

The Della Torre Preisach model implementation outputs dB/dH directly, which makes it particularly well-suited for implementing a dynamic gain controller. We can design our adaptive controller, $C_a(s)$, such that the gain is inversely proportional to dB/dH, to wit,

$$C_a(s) = \frac{K_d}{s} = \frac{K_s/\frac{dB}{dH}}{s}, \tag{6.24}$$

where K_s is a static gain, and K_d is the dynamic gain equal to $K_s/(dB/dH)$. With the gain inversely proportional to dB/dH, we will have high controller gain when dB/dH is low, giving us more control authority when we need it most, and low controller gain when dB/dH is high, helping us to maintain stability. The loop gain should remain approximately constant even while the plant gain is changing.

The loop gain as a function of frequency, f, can be approximated as

$$\begin{aligned} |LT| &\approx \frac{K_s/\frac{dB}{dH}}{2\pi f}\left(\frac{dB}{dH}\frac{2g}{\mu_0}\right), \\ |LT| &\approx \frac{K_s}{\pi f}\frac{g}{\mu_0}. \end{aligned} \tag{6.25}$$

From this, we can solve for K_s by setting the loop gain to 1 at $f = f_c$,

$$K_s = \frac{\pi f_c \mu_0}{g}. \tag{6.26}$$

For a loop crossover frequency of $f_c = 2\,\text{kHz}$, $K_s = 15.8\,\text{T}/(\text{A}\cdot\text{s})$ at $g = 500\,\mu\text{m}$.

6.4.1 Simulation Results

The Simulink model of the adaptive gain observer is shown in Figure 6-15. The gain K_s gets divided by dB/dH, which is fed back from the Preisach model output. A delay of one time step is placed into this feedback path to break the algebraic loop.

For our hysteresis model, we used the model fitted to experimental data described in Section 6.2.1. In (6.26), we replace μ_0/g with $2m/N$, with the result that $K_s = 21.1$.

Figure 6-16 shows the observer estimated flux density plotted against input current for a 1 Hz sine wave with 2.9 A amplitude. Shown in the same plot is the experimental B-I data from Figure 6-1 that was used to fit the hysteresis model. The dynamic gain observer output matches the experimental data well. Also shown is a graph zoomed in on the B-I initial trajectory from the demagnetized state. The observer with adaptive controller gain is seen to have superior performance to the observer with static gain.

Figure 6-17 shows the input current and estimated observer output current in the top graph. The bottom graph shows the error between the two. The error has been much reduced: the maximum error is 1.4 mA. The largest errors no longer occur at the demagnetized state and at saturation, showing that the adaptive gain controller resolves this problem effectively.

6.4.2 Preliminary Experimental Results

We next implemented the adaptive gain observer in real-time using the measured current to the prototype reluctance actuator as the input current. We clamped the actuator target to the stator with 500 µm plastic shims between the target and stator. The actuator was driven with a Kepco BOP 36-12M amplifier [50] the current

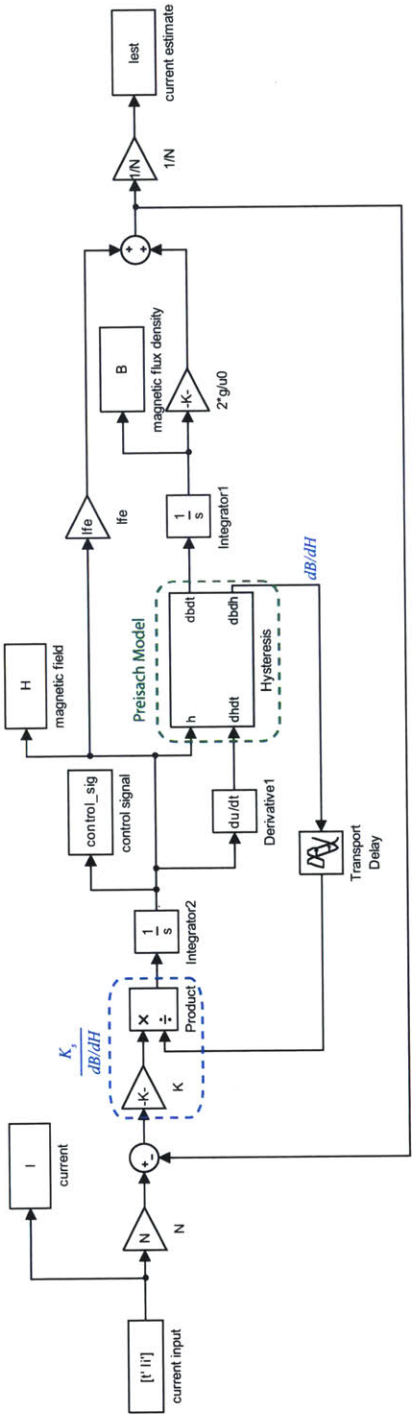

Figure 6-15: Simulink model of adaptive gain observer.

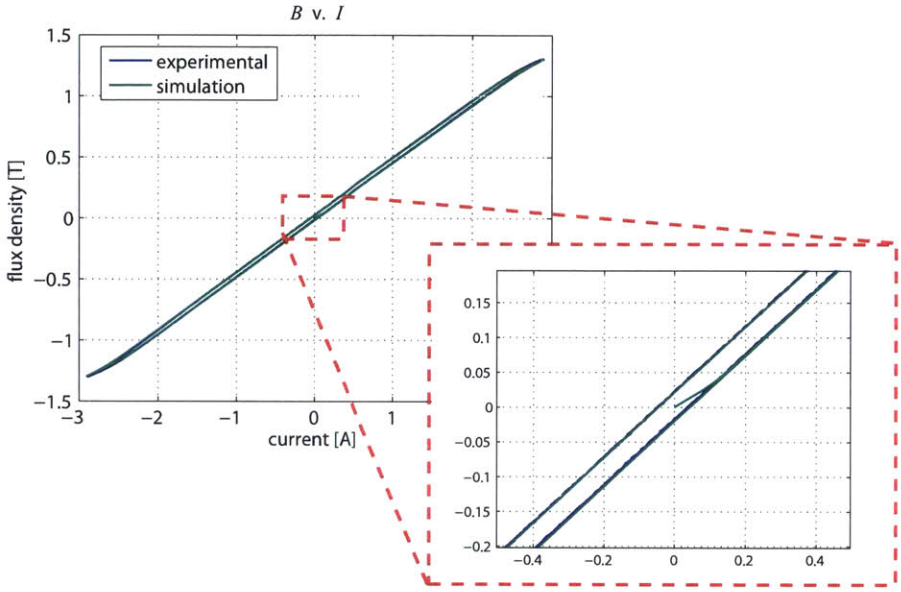

Figure 6-16: Simulated adaptive gain observer estimate of flux density versus input current.

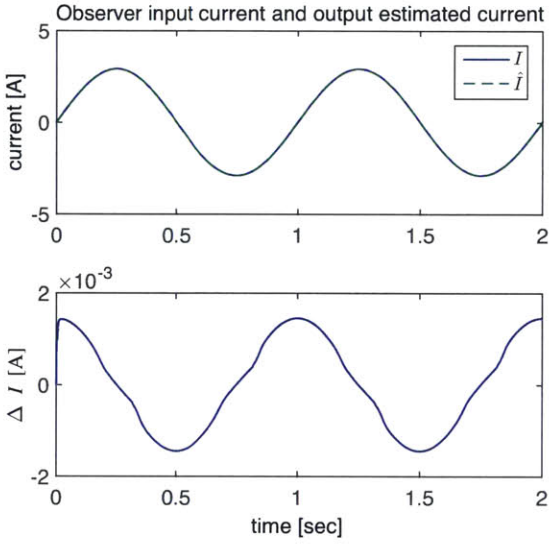

Figure 6-17: TOP: Simulated input current (I) and estimated output current ($\hat{I}$) from observer with adaptive gain controller; BOTTOM: Error between I and $\hat{I}$.

was measured with a sense resistor. A picture of the clamped actuator is shown in Figure 6-18.

Figure 6-19 shows the real-time estimated flux density, $\hat{B}$, of the observer for

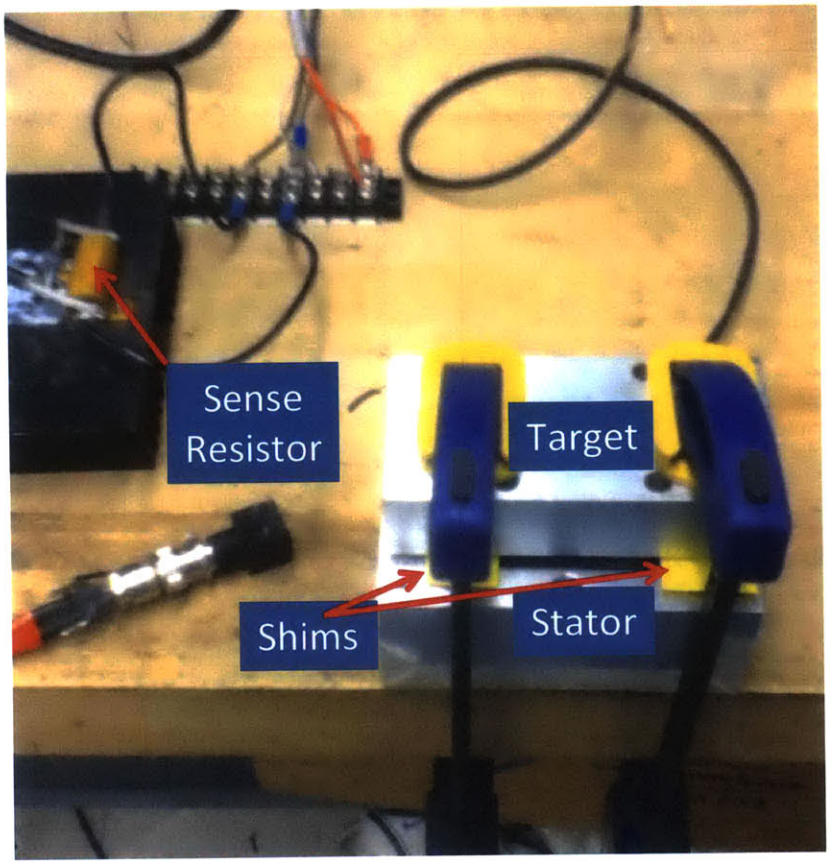

Figure 6-18: Clamped actuator with sense resistor shown.

a series of measured input current sine waves of varying amplitudes each driven at 1 Hz. The graph on the right shows the corresponding estimated $\hat{B}$-$\hat{H}$ curves from the observer.

If we take one of the estimated $\hat{B}$-$\hat{H}$ curves from Figure 6-19 and inspect it more closely, we see that there are 'whiskers' near the major reversal points, as shown in Figure 6-20.

These whiskers are the result of higher frequency variations in the measured current, e.g. from noise sources. These variations cause $\hat{H}$ to reverse direction, resulting in the traversal of tiny minor loops, giving the appearance of whiskers. Figure 6-21 shows the measured current that gave rise to the whiskers in Figure 6-20, filtered at 200 Hz. The inset graph shows the current zoomed in near the maximum current, showing that the higher-frequency variations cause the current to change direction.

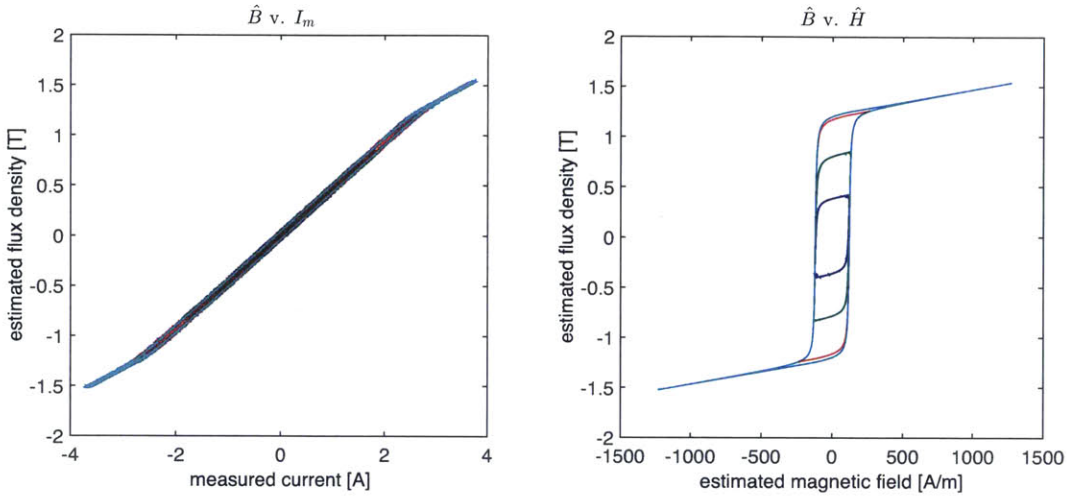

Figure 6-19: LEFT: Real-time observer estimates of flux density versus measured current; RIGHT: Real-time observer $\hat{B}$-$\hat{H}$ curves.

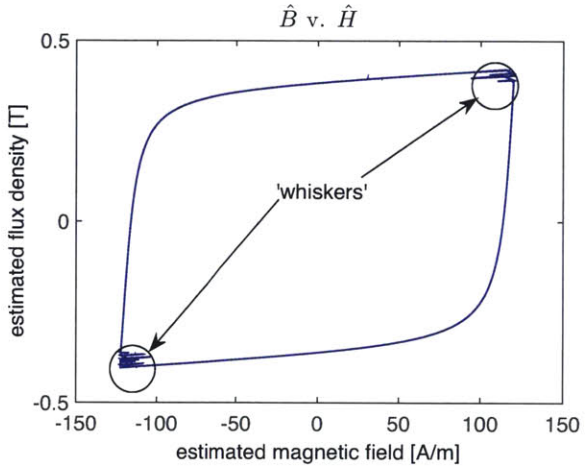

Figure 6-20: Real-time observer $\hat{B}$-$\hat{H}$ loop showing 'whiskers' near reversal points.

This explains why the minor loops only occur near the major reversal points of the B-H curve: since dI/dt of the fundamental frequency component is close to zero near the major reversal points, the higher-frequency variations cause tiny reversals in the direction of the current, and hence likewise in $\hat{H}$. In contrast, during the high dI/dt portions of the fundamental-frequency sine wave, the higher-frequency variations in current are not large enough to reverse the direction of the current.

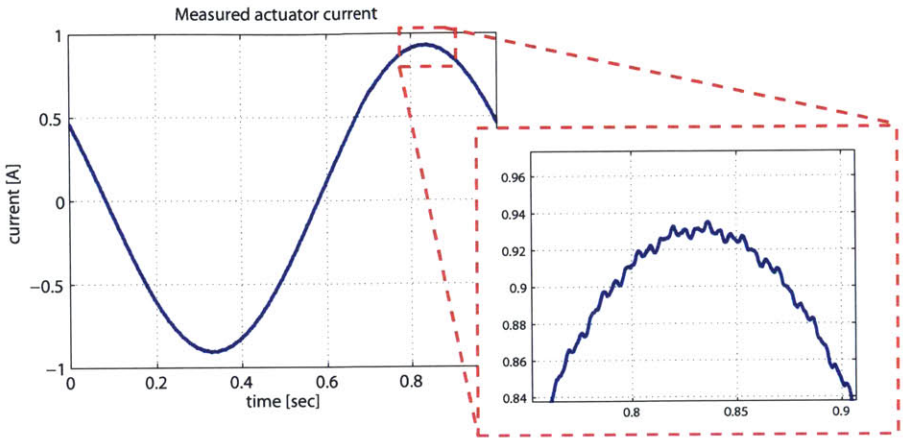

Figure 6-21: Measured actuator current filtered at 200 Hz showing high-frequency reversals.

6.4.3 Incorporating a Gap Disturbance

We next wanted to evaluate how our adaptive-gain observer handled gap disturbances. For a real-time hysteresis model to be effective for a motion control system, it must be able to estimate flux density accurately in the face of gap disturbances.

With our clamped actuator setup, we input a simulated gap disturbance to the observer model. The simulated gap disturbance is the same that was used for the simulations in Section 4.3 and that is shown in Figure 4-13. The observer was run in real-time and used the measured actuator current as its input.

Figure 6-22 shows the real-time estimated flux density of the observer for a series of measured input current sine waves of varying amplitudes each driven at 1 Hz and with the simulated gap disturbance input to the observer. The graph on the right shows the corresponding $\hat{B}$-$\hat{H}$ curves from the observer.

In Figure 6-23 we plot the outermost $\hat{B}$-I_m loop of Figure 6-22 zoomed in near the maximum flux density so that the effect of the gap disturbance can be more easily discerned. The gap disturbance effect is greater in this region because the flux density deviation from a gap disturbance increases with nominal flux density level (see (4.34)). Moreover, since dI/dt is lower near the maximum current, the flux density deviations from gap disturbances will appear more pronounced. In other words, $\partial B/\partial g \Delta g$ is not overwhelmed by $\partial B/\partial I \Delta I$ in this region.

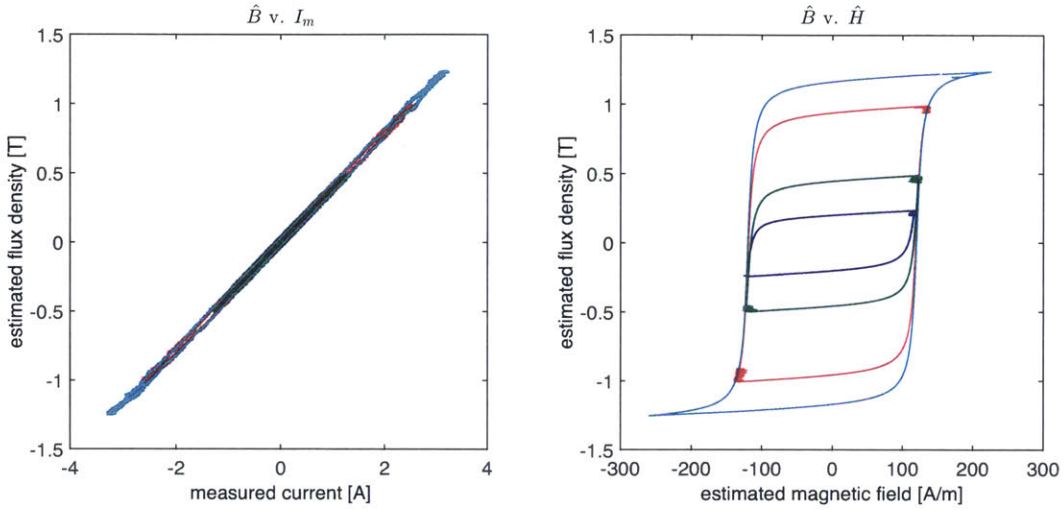

Figure 6-22: LEFT: Real-time observer estimate of flux density versus measured current with simulated gap disturbance; RIGHT: Real-time observer $\hat{B}$-$\hat{H}$ curves with simulated gap disturbance.

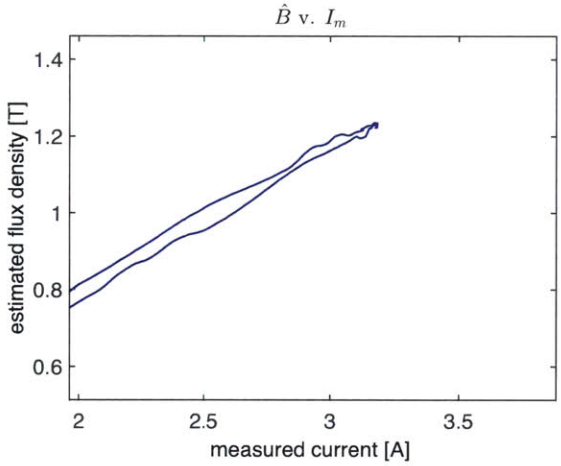

Figure 6-23: The effect of a gap disturbance on the observer estimated flux density.

6.4.4 Numeric Problems with the Della Torre Model

While the initial results for handling a gap disturbance looked promising, the observer had difficulty with larger gap disturbances. Figure 6-24 shows two $\hat{B}$-$\hat{H}$ curves with identical current inputs: the blue curve is the $\hat{B}$-$\hat{H}$ curve with the original gap disturbance; the green curve is the $\hat{B}$-$\hat{H}$ curve with twice the original gap disturbance. Since the current inputs were the same for both curves, we expect to trace the same

primary B-H loop in both cases. Instead, however, we see some discrepancy between the two. The whiskers on the B-H curve with twice the gap disturbance are also much more pronounced.

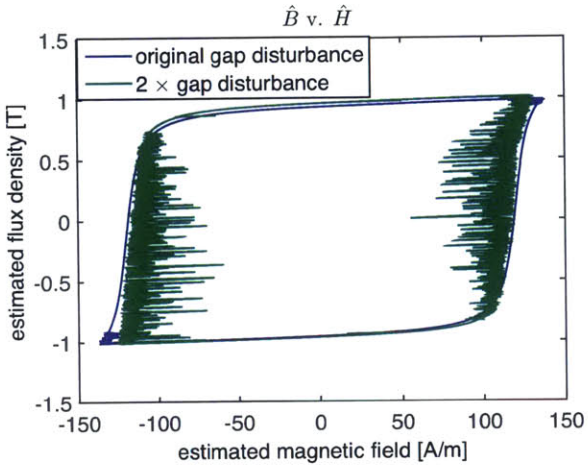

Figure 6-24: Comparison between observer B-H loops for different gap disturbances.

We suspected the culprit to be numeric problems with solving the Della Torre hysteresis model. To test this hypothesis, we ran simulations of just the hysteresis model without the observer using the H data from the green data set in Figure 6-24 as the input. We ran this simulation multiple times, using different numeric solvers. Figure 6-25 shows the resulting B-H curves for the solvers 'ode1', 'ode2', and 'ode3'. We see that the B-H loops depart significantly from one another, indicating that numeric problems are playing a role. We also found that changing the time step affected the hysteresis model output.

We posited that the reason the numeric solver had trouble accurately solving the Della Torre model is because the Della Torre model outputs dB/dH rather than outputting B directly. When the observer sees a relatively large gap change, this results in a large change in the value of H as input to the hysteresis model. Since dB/dH has a highly nonlinear dependence on H, this can result in an inaccurate path taken from the original value of B to the new value of B after the gap change. To demonstrate this, we ran a simulation with the model described in Chapter 4 where we ramped the input current to a constant level and then applied a $-200\,\mu$m step to

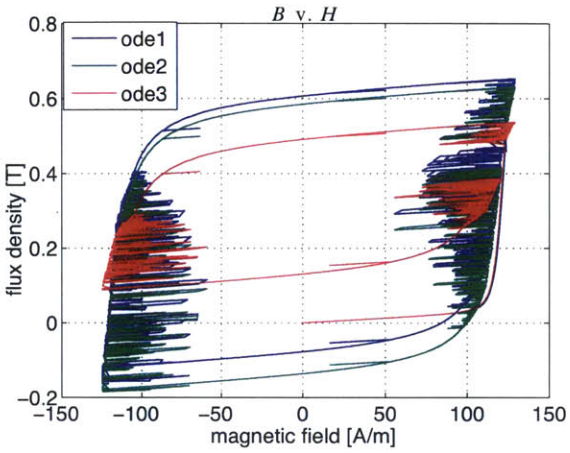

Figure 6-25: Comparison of different numeric solvers for Della Torre hysteresis model for same H input.

the gap. We used the Chapter 4 model instead of the observer model from this section so as to isolate actuator model effects from controller effects. Figure 6-26 shows the current profile and gap profile for the simulation.

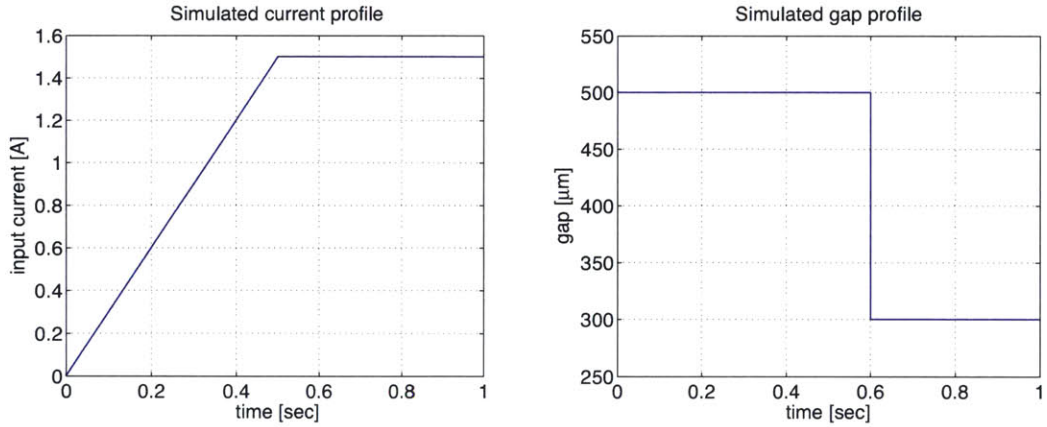

Figure 6-26: Simulated input current and gap step to actuator model.

Figure 6-27 shows the resulting B-H curve. The gap step results in a sharp increase in the value of H. This results in a sharp reduction in dB/dH, since at the new value of H the Della Torre model is in the saturation region where dB/dH is small. The integration routine for calculating B from dB/dH is unaware of the nonlinear nature of dB/dH and assumes that dB/dH is constant between the previous

value of H and the current value of H. This results in a large error in the resulting B. Note that while the Della Torre model thinks it is in the saturation region, the resulting B is about 0.7 T, which is far too low for the saturation region. We can see then how gap changes that result in large changes in the value of H can lead to errors in the estimate of B. Sudden large changes in current can produce the same phenomenon.

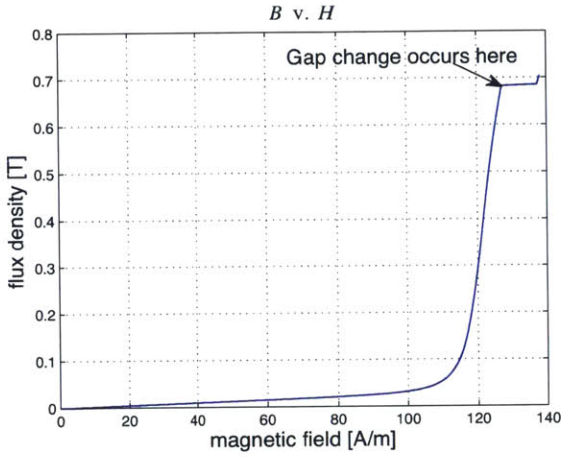

Figure 6-27: Simulated B-H curve showing the effect of a $-200\,\mu$m on the Della Torre hysteresis model.

One way to mitigate this problem is by reducing the controller gain of the observer. From the block diagram in Figure 6-10, we can write for a sudden change in gap

$$\Delta H = Ce = CN\left[I - \left(\hat{I} + \Delta\hat{I}\right)\right], \tag{6.27}$$

where $\hat{I}$ is the observer estimate of the current before the gap change occurs, $\Delta\hat{I}$ is the change in $\hat{I}$ resulting from the sudden gap change, and e is the error between the input current and observer estimated current. By reducing the gain of C, the error arising from a sudden gap change will translate into a smaller ΔH as input to the Della Torre model. A smaller ΔH will lead to a smaller error in the integration routine.

Simulations showed that reducing the controller gain was indeed effective in handling larger gap disturbances. However, a more robust solution is preferred.

6.4.5 Hui Hysteresis Model Implementation

The Hui implementation of the Preisach model as described in Section 3.3.2 has the advantage over the Della Torre implementation of having as its output $B(H)$ rather than $dB/dH(H)$. Using the Hui implementation should therefore avoid the numerical problems that come with integrating a nonlinear $dB/dH(H)$ relationship.

We implemented the Hui model into our adaptive observer. To do so, we implemented lookup tables for the ascending branch and the descending branch of the major B-H hysteresis loop. One downside of the Hui model compared to the Della Torre model is that we no longer get dB/dH for free, which we need for our adaptive controller gain. We compute dB/dH by differentiating (3.29-3.31) with respect to H. We also compute the derivatives of the functions T (3.28) and F^+ (3.25) and F^- (3.27) with respect to H. This allows us to express dB/dH in terms of dB^a/dH and dB^d/dH, the derivatives of the ascending and descending branches of the major loop with respect to H, respectively. We implement dB^a/dH and dB^d/dH as additional lookup tables.

We simulated the observer response with the Hui implementation of the Preisach model for a 1 Hz sine wave input current of 2.9 A amplitude and twice the original gap disturbance. Figure 6-28 shows the resulting $\hat{B}$-I and $\hat{B}$-$\hat{H}$ curves. These results look much more promising than those with the Della Torre model for the same gap disturbance. Compare the $\hat{B}$-$\hat{H}$ plot here with that shown in Figure 6-24 for instance (although note that the current inputs are different for the two cases).

We simulated with larger gap disturbances as well. Figure 6-29 shows the simulated $\hat{B}$-I and $\hat{B}$-$\hat{H}$ curves for a gap disturbance five times the original (this gives a peak gap disturbance of 41 µm, about 8% of the nominal operating gap). The plots look reasonable, although we note the spikes present in the $\hat{B}$-I curve. These are artifacts of the observer controller and are not genuine responses of the magnetic flux to the gap disturbances. When we are near the high-slope region of the B-H curve (H is near the coercive field), even a relatively small change in H from a gap disturbance can result in a large initial change in B. These large sudden changes

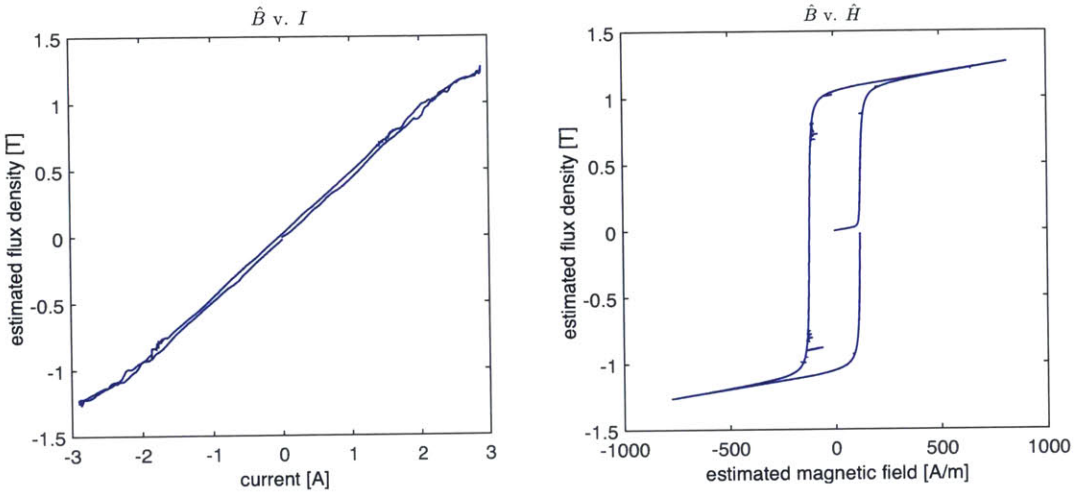

Figure 6-28: LEFT: Simulated Hui-model observer estimate of flux density versus input current with twice original gap disturbance; RIGHT: Simulated Hui-model observer $\hat{B}$-$\hat{H}$ curve with twice original gap disturbance.

in B result in the spikes seen in the $\hat{B}$-I curve. The controller eventually recovers and settles to the correct B-H operating point. However, these spikes will result in errors in the estimated flux density. We discuss this phenomenon in more detail in Section 6.8. One possible solution is either to filter $\hat{B}$ or to filter the gap measurement itself. Since the hysteresis model only needs to be accurate for low frequencies (the sense coil will measure the flux for higher frequencies), this may be an acceptable solution. Another possible solution is somehow to feedforward the gap measurement so that the observer can anticipate any sudden changes and react accordingly.

We found in simulation that if the gap disturbance becomes too large, the observer risks going unstable. Nevertheless, the Hui implementation performs significantly better than the Della Torre model in this regard, which had stability problems even at only twice the original gap disturbance. Lowering the controller gain can help avoid the problem of instability. While the Hui model implementation improved things, a more robust solution of dealing with gap disturbances is still desired.

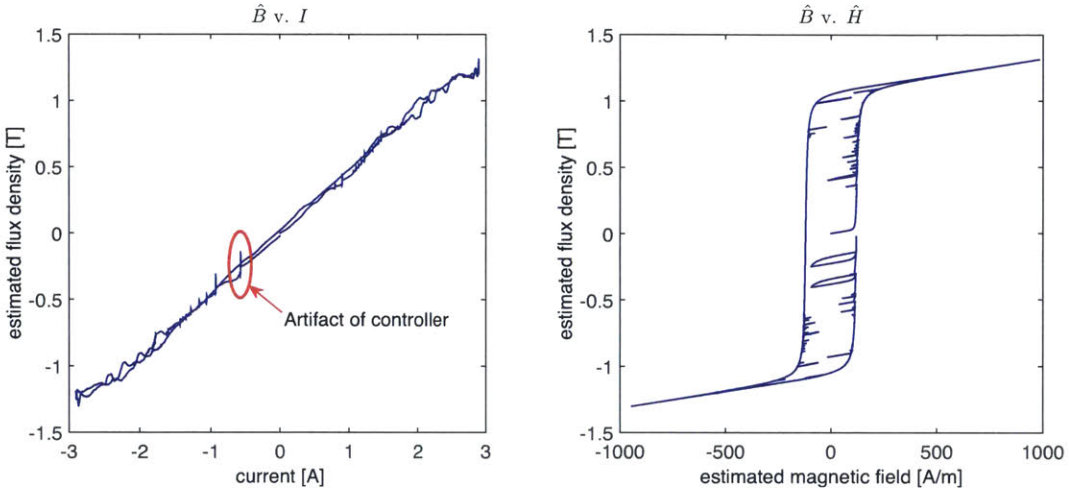

Figure 6-29: LEFT: Simulated Hui-model observer estimate of flux density versus input current with five times the original gap disturbance; RIGHT: Simulated Hui-model observer $\hat{B}$-$\hat{H}$ curve with five times the original gap disturbance.

6.5 Flux Estimation Using Interpolation

One way to avoid stability problems arising from the gap disturbance is to interpolate among different models at different nominal gaps rather than to input the gap directly as a disturbance to the model. Figure 6-30 shows the Simulink block diagram of an interpolation scheme we used for simulation. There are three observers, each with its own hysteresis model corresponding to a different nominal air gap. In this simulation model, the gaps for each model are 450 µm, 500 µm, and 550 µm, respectively. The simulated actuator current is the input to each of the three observers, so each observer estimates the appropriate flux density for that input current at its respective operating gap. The final estimate of flux density is then obtained by taking the simulated gap measurement and interpolating among the three observer models. We use a linear interpolation routine.

Figure 6-31 shows the flux density estimated by the interpolation scheme plotted against the input current and with the original gap disturbance. The input current was a 1 Hz sine wave with 2.9 A amplitude. The nominal gap was 500 µm. We also show the flux density estimated by the adaptive-gain observer using the Della Torre model from Section 6.4 for the sake of comparison. The two methods show good

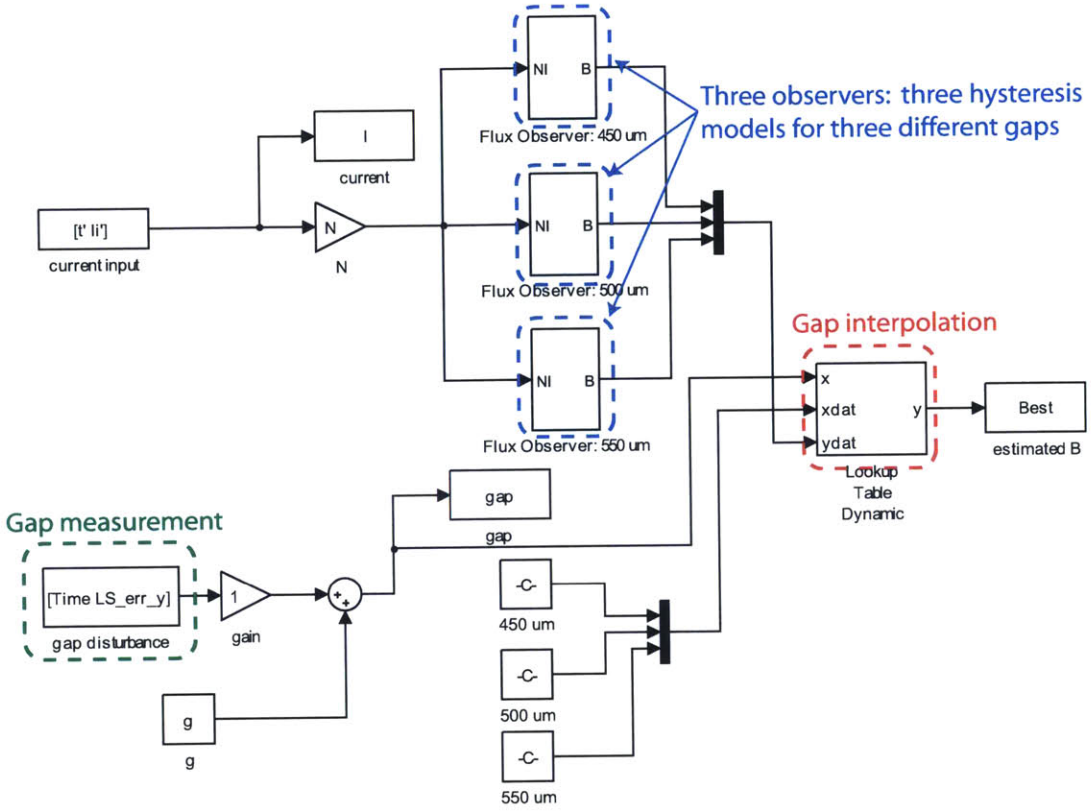

Figure 6-30: Interpolation scheme for estimating actuator flux density.

agreement.

Figure 6-32 shows the deviation in estimated flux density, $\Delta\hat{B}$, between the two methods. The maximum $\Delta\hat{B}$ is 1.5 mT.

Figure 6-33 shows the comparison of the two methods when the gap disturbance is twice the original gap disturbance and when the gap disturbance is five times the original gap disturbance. For the simulation results from the direct-gap observer method, the sampling rate was increased to 100 kHz and the controller gain was reduced to maintain stability. The $\hat{B}$-I curves are zoomed in near saturation to emphasize the effect of the gap disturbance and to highlight the discrepancies between the two methods. The bottom plots show the $\Delta\hat{B}$ between the two methods. For the simulations with twice the original gap disturbance, the maximum $\Delta\hat{B}$ between the two methods is 4.6 mT and for simulations with five times the original gap disturbance, the maximum $\Delta\hat{B}$ between the two methods is 19.6 mT.

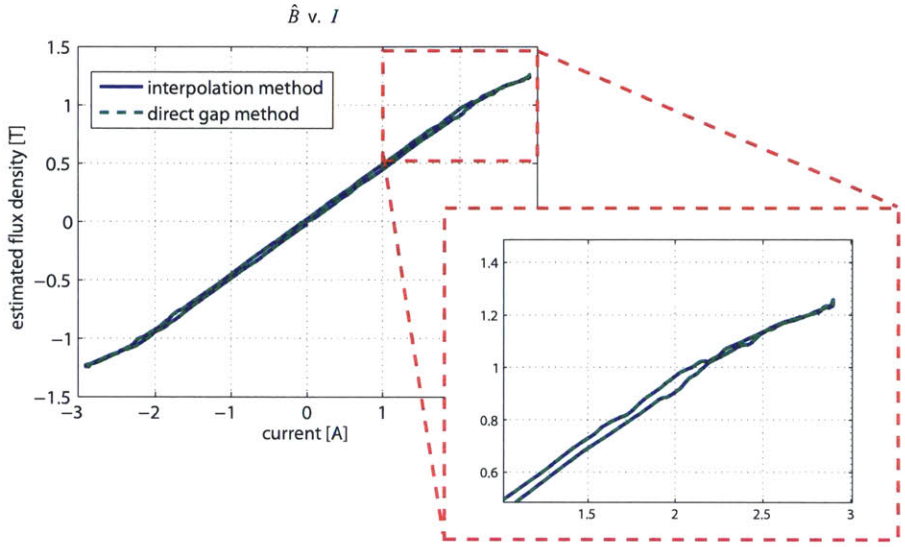

Figure 6-31: Simulation with gap disturbance: comparison of $\hat{B}$-I curves using gap interpolation scheme (blue) and adaptive-gain observer with gap disturbance applied directly (green).

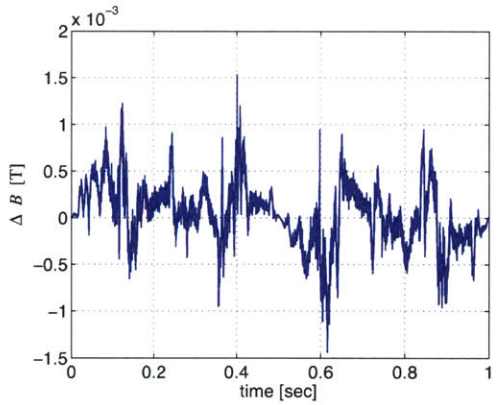

Figure 6-32: $\Delta\hat{B}$ between interpolation model simulation and direct gap model simulation both with original gap disturbance.

The foregoing simulation results suggest that interpolation may be a reasonable way to deal with the gap disturbance while avoiding instability. The primary downside is that it requires additional models operating in parallel, which reduces the computational efficiency compared to the direct gap method. If we require a larger operating range or additional accuracy, models for additional operating gaps must be added, further reducing the computational efficiency.

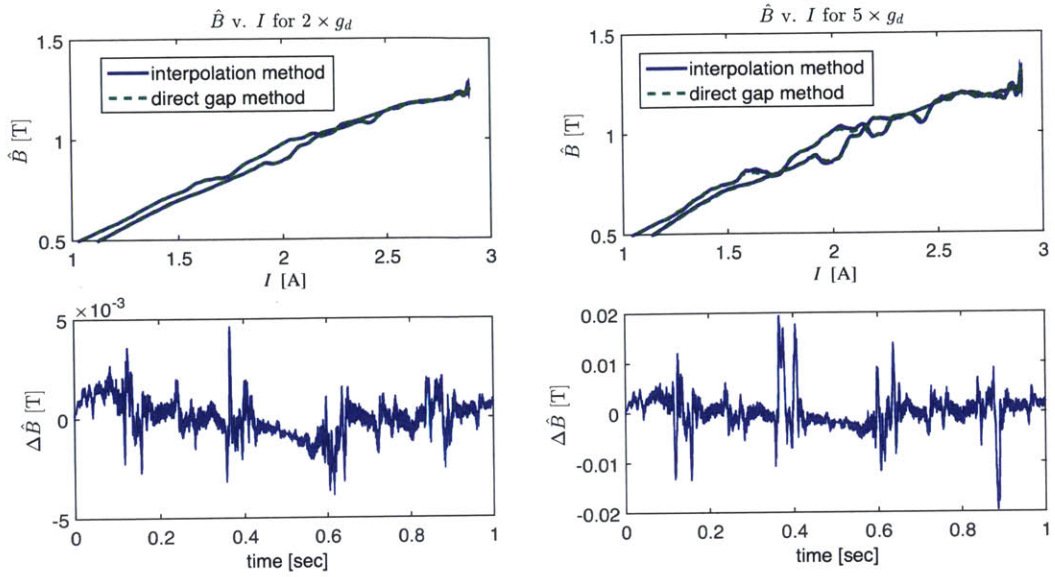

Figure 6-33: Comparison between interpolation method and direct gap method. (Simulation). LEFT: twice the original gap disturbance; RIGHT: five times the original gap disturbance.

Another disadvantage of interpolation is that it does not capture the hysteretic behavior that results from a changing gap. Since a gap disturbance will change the material (H, B) operating point needed to solve Ampere's Law, the relationship between B and g is ultimately hysteretic. However, the close match between the interpolation simulations and the direct gap method simulations suggest that this hysteretic relationship may be negligible, at least for the scale of gap disturbances with which we are concerned and for the material hysteresis we are modeling.

We recommend that if the interpolation method is selected to handle gap disturbances, the hysteresis relationship between B and I be modeled directly for each operating gap rather than modeling the hysteresis relationship between B and H and using an observer to obtain the B-I relationship at each gap. The observer structure becomes superfluous in such a case, since with no gap disturbance there is a one-to-one relationship between the B-I curve and the B-H curve. Moreover, since the B-I curves can be measured directly unlike the B-H curves, the potential for accurate calibration and accurate model-fitting is much greater.

6.6 Observer with Sheared Hysteresis Model

In this section, we present a novel way for designing an observer structure that can handle the gap disturbance while avoiding the stability problems discussed in Section 6.4. Instead of modeling the material B-H relationship directly, we model a sheared version of the B-H relationship. The sheared model does not have the sharp changes in dB/dH that the material B-H relationship has. This makes the observer's estimation problem much easier.

We begin with a change of variables in the model given by (4.1). We define the variables

$$g_2 = g - g_{\text{off}}, \tag{6.28}$$

and

$$H_2 = H + \frac{2g_{\text{off}}B(H)}{\mu_0 l_{Fe}}, \tag{6.29}$$

where g_{off} is some constant offset. It can be chosen to be g_0 for example. Figure 6-34 shows how g_2 is related to g and g_{off}, where g_{off} is arbitrarily chosen for the sake of illustration.

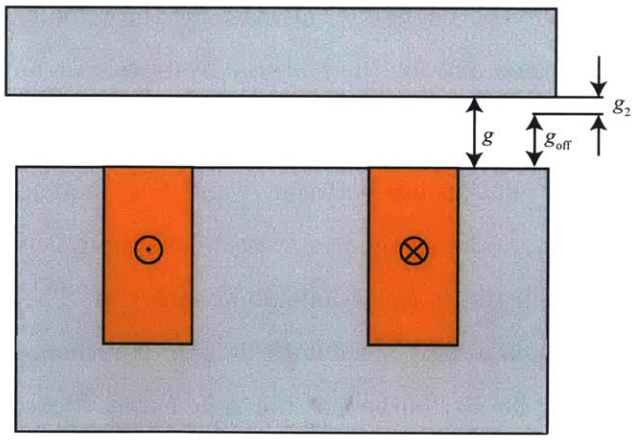

Figure 6-34: The relationship between g_2, g and g_{off} is shown on the reluctance actuator.

The variable H_2 is offset from H by the quantity $2g_{\text{off}}B(H)/(\mu_0 l_{Fe})$. The relationship between H and H_2 is demonstrated in Figure 6-35. For example, if we take a particular test point H_p, B_p from the $B(H)$ curve, we obtain H_{2p} by adding $2g_{\text{off}}B_p/(\mu_0 l_{Fe})$ to H_p. The green curve is the $B(H_2)$ major loop obtained in this way. The parameter g_{off} will determine the slope of the $B(H_2)$ curve.

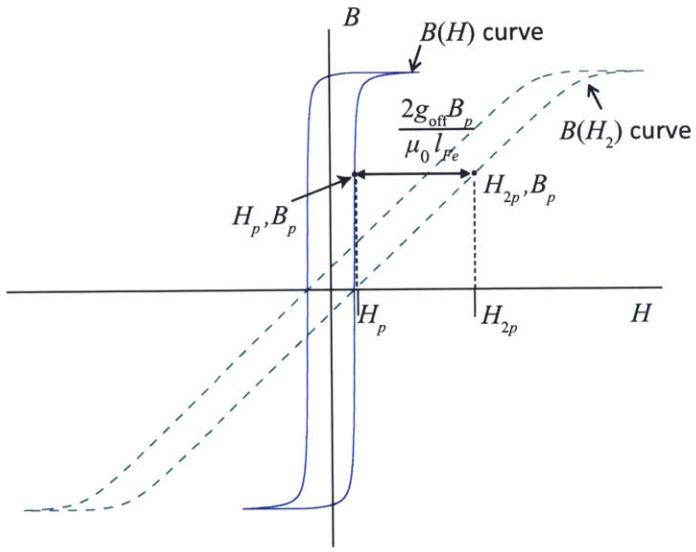

Figure 6-35: The variable H_2 is obtained by adding $\frac{2g_{\text{off}}B}{\mu_0 l_{Fe}}$ to H.

If we substitute the definitions of g_2 and H_2 into (4.1), we can write

$$\begin{aligned} l_{Fe}\left(H_2 - \frac{2g_{\text{off}}}{\mu_0 l_{Fe}}B\right) + \frac{2\left(g_2 + g_{\text{off}}\right)}{\mu_0}B &= NI, \\ l_{Fe}H_2 - \frac{2g_{\text{off}}}{\mu_0}B + \frac{2g_2}{\mu_0}B + \frac{2g_{\text{off}}}{\mu_0}B &= NI, \\ l_{Fe}H_2 + \frac{2g_2}{\mu_0}B &= NI. \end{aligned} \tag{6.30}$$

Equation (6.30) is equivalent to (4.1) except that instead of the being expressed in terms of the variables g and H, we have expressed it in terms of the variables g_2

and H_2. The problem of identification is now to identify the hysteresis model $B(H_2)$ rather than $B(H)$.

Suppose we choose $g_{\text{off}} = g_0$. Then at the nominal gap, $g_2 = 0$, and we can write (6.30) as

$$l_{Fe}H_2 = NI, \tag{6.31}$$

or

$$H_2 = \frac{NI}{l_{Fe}}. \tag{6.32}$$

At $g = g_0$ then, H_2 is proportional to the current, and we can identify the B-H_2 relationship simply by identifying the B-I relationship at g_0. This is one advantage of this method: we are able to identify the hysteresis model directly from the measured B-I data rather than having to estimate the material B-H relationship.

As we demonstrated in Section 2.4.4, the B-H_a relationship is a sheared version of the material B-H relationship, where H_a is the applied magnetic field and is equal to NI/l_{Fe}. We note from (6.31) that this is identical to the expression for H_2 at $g = g_0$. The B-H_2 relationship is thus a sheared version of the B-H relationship. Consequently, the hysteresis model of B-H_2 will be much more linear than a model of B-H and will have less drastic changes in slope.

6.6.1 Controller Design

Figure 6-36 shows a block diagram of the observer structure with the sheared hysteresis model (SHM), denoted as $B(H_2)$. The variables $\hat{I}$ and $\hat{B}$ are the estimated current and estimated flux density from the observer, respectively. Likewise, the variable $\hat{H}_2$ is the value of H_2 estimated by the observer.

Our plant now takes as its input the variable H_2 rather than H. Our plant gain is

$$|P| = \frac{dB}{dH_2}\frac{2g_2}{\mu_0} + l_{Fe}. \tag{6.33}$$

If we design our controller around the nominal operating gap, then $g_2 = 0$ and $|P| = l_{Fe}$. If we keep our controller as an integrator, we can use (6.19) to solve for

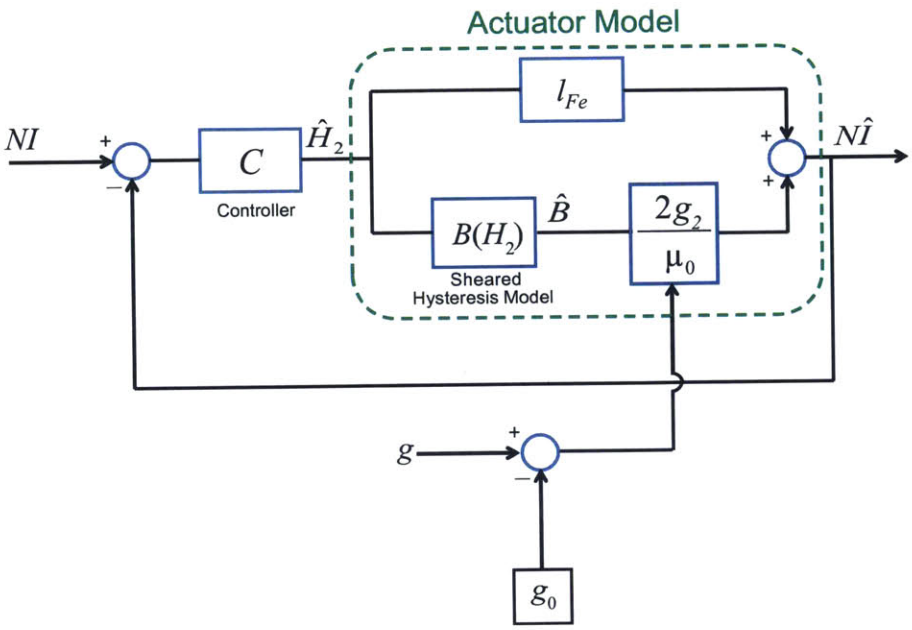

Figure 6-36: Observer block diagram with SHM.

the integrator gain, K, as

$$K = \frac{2\pi f_c}{l_{Fe}}, \tag{6.34}$$

where f_c is a desired crossover frequency. For $f_c = 2\,\text{kHz}$, $K = 1.26 \times 10^5\,\text{m}^{-1}\text{s}^{-1}$, and our controller is

$$C(s) = \frac{K}{s} = \frac{1.26 \times 10^5}{s}. \tag{6.35}$$

6.6.2 Simulation Results

For simulation, we fitted the Hui Preisach model to the B-I curve generated by the adaptive-gain observer in Section 6.4 and represented by the green curve in Figure 6-16. We used the simulated curve for fitting rather than the experimental data so that we could attempt to reproduce the simulation results of the adaptive-gain observer with the SHM observer and compare the two methods directly. Figure 6-37 shows the simulated flux density estimated by the SHM observer plotted against the input current with the original gap disturbance present. For comparison, the simulated $\hat{B}$-I curve from the adaptive-gain observer is also shown. The match between the two is

very close. The maximum deviation is less than 3 mT.

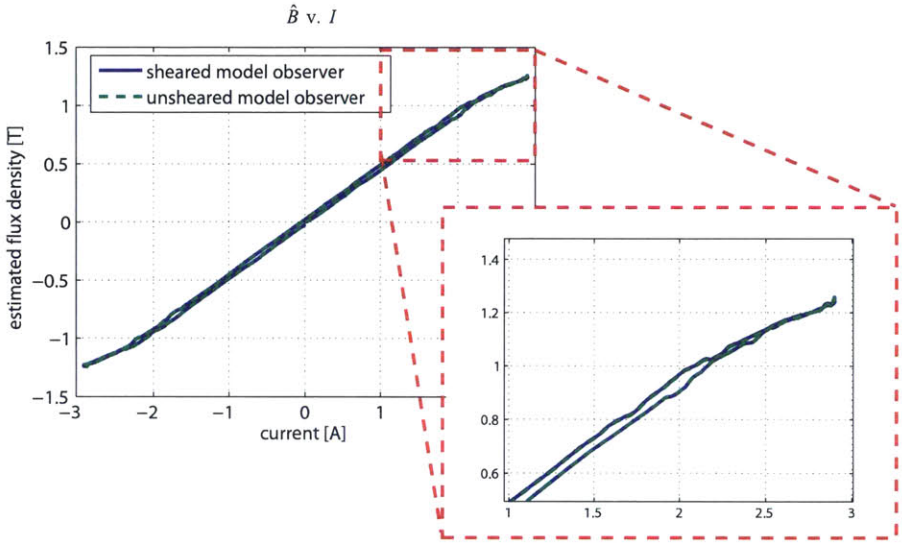

Figure 6-37: Simulation with gap disturbance: comparison of $\hat{B}$-I curves using sheared-model observer (blue) and adaptive-gain observer (green).

Figure 6-38 shows the simulated $\hat{B}$-I curves generated by the SHM observer for the original gap disturbance and for gap disturbances of two times, five times, and ten times the original gap disturbance. We note that the SHM observer did not run into any stability problems in generating these curves: we did not have to lower the controller gain or increase the sampling rate to maintain stability. We also note that there are no sharp spikes evident in the $\hat{B}$-I curves as there were for the Hui implementation of the adaptive-gain observer shown in Figure 6-29. Experimental results with our testbed for the SHM observer will be presented in Chapter 10.

6.6.3 Incorporating Eddy Currents and Feedforward Control

We can use the observer to model the effect of eddy currents as well. We use (5.28) as the new actuator model we want to estimate. For H_{cl} we use (5.13), and for H_{exc} we use (5.38). As both of these equations take dB/dt as their input, we differentiate the hysteresis model output. Figure 6-39 shows a Simulink block diagram that includes eddy current effects. There are now two new paths from the hysteresis model output to the summing junction of the NI estimate representing the classical and excess eddy

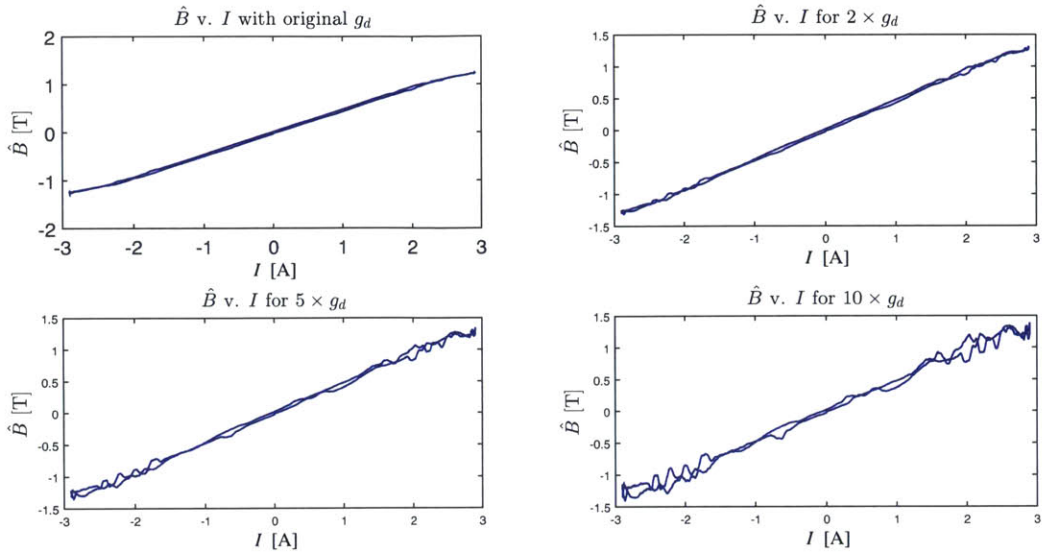

Figure 6-38: Estimated flux density versus input current simulated for SHM observer with different gap disturbances (1×, 2×, 5×, and 10× original gap disturbance).

currents. The classical eddy current path is shown in blue. The excess eddy current path is shown in red. The classical eddy current path is straightforward: dB/dt is simply multiplied by the constant $\sigma_e d^2 l_{Fe}/12$. For the excess eddy current path, we use an embedded Matlab function routine to solve the quintic equation of (5.38).

We also add a feedforward path to the input of the hysteresis model for improved performance. This path is shown in green in the figure. At the nominal gap, H_2 is equal to NI/l_{Fe}, so we can simply feedforward the input signal I multiplied by N/l_{Fe}. This is another advantage to using the SHM over the unsheared hysteresis model: it is more difficult to add an effective feedforward path to the unsheared-model observers since the relationship between the observer input I and the hysteresis model input H is highly nonlinear. A feedforward path with a simple gain is in that case insufficient. Simulation results for the SHM observer with eddy current effects included were already presented in Section 5.4.1, so they are omitted here.

6.7 Flux Estimation Using the Chua Model

The Chua model was not investigated in depth for the purpose of real-time estimation owing to its inability to track minor loops accurately (see discussion in Chapter 3). For the sake of completeness however, we include some brief remarks here.

6.7.1 Hysteresis Model Identification

We fitted the Chua model to experimental B-I data taken from the reluctance actuator driven with a 10 Hz sine wave with 2.9 A amplitude. We defined the functions f and g needed to identify the Chua model in Section 3.4. Here we rename g as G to avoid confusion with the gap variable. Figure 6-40 shows the f^{-1} and G^{-1} functions we extracted from the data. The w function, also defined in Section 3.4, is set to $\left|dI/dt\right| / (2\pi f_0 I_0)$ for frequency-independence, where $f_0 = 10\,\text{Hz}$ and $I_0 = 2.9\,\text{A}$.

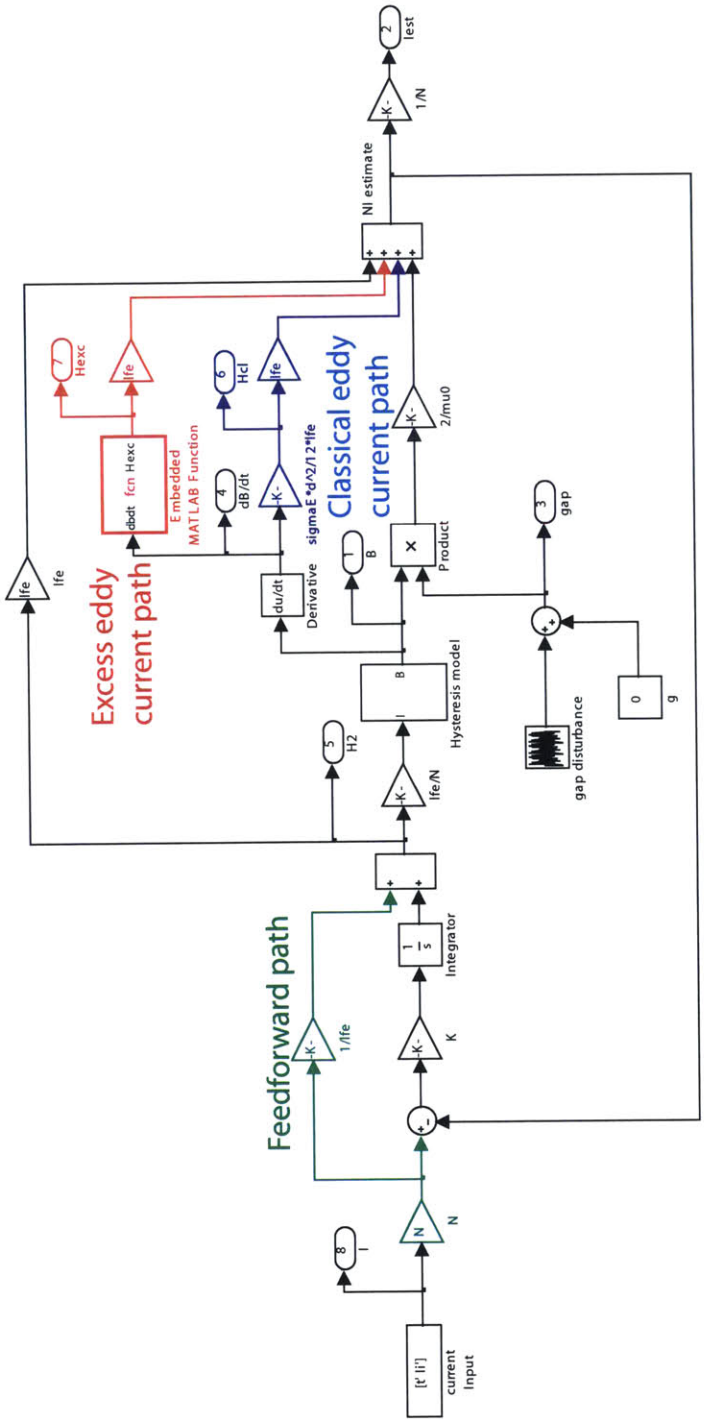

Figure 6-39: Simulink model of sheared-model observer with eddy current effects and feedforward path included.

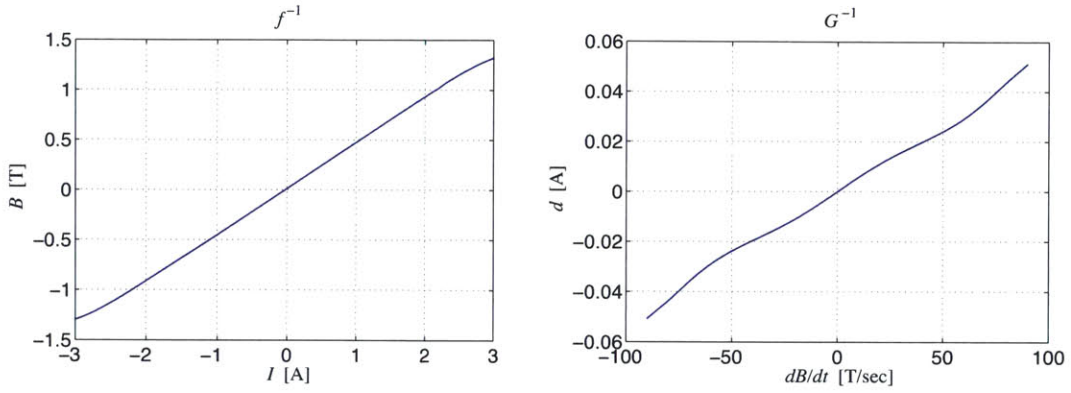

Figure 6-40: f^{-1} and G^{-1} functions for Chua model.

6.7.2 Experimental Results

Figure 6-41 shows the flux density estimated by the Chua model when driven with a sine wave of the same amplitude and frequency as that used to identify the Chua model. The Chua model output shows reasonable agreement with the experimental data. However, the match suffers somewhat near saturation. The reason for this is because the nonlinear relationship between I and B results in the output signal having a different frequency content from the input signal. This results in dB/dt not being perfectly proportional to dI/dt in the measured data. However, the choice of the w function in the Chua model forces the model dB/dt output to be proportional to dI/dt. As a result, the Chua model output deviates from the measured data.

Figure 6-42 shows a minor loop from the Chua model compared to experimental B-I data. We can see that the match is significantly worse than for the major loop. From the discussion in Section 3.4, this was expected.

For the sake of comparison, we investigated the Chua model performance when the w function was chosen to be equal to 1. This results in a model that is frequency-dependent: it will exhibit loop-widening with increasing frequency. Figure 6-43 shows the Chua model output for the major loop compared to the measured data. The actuator was driven at 10 Hz. By comparing this figure to Figure 6-41, we see that we now get a much better fit between the experimental data and the Chua model

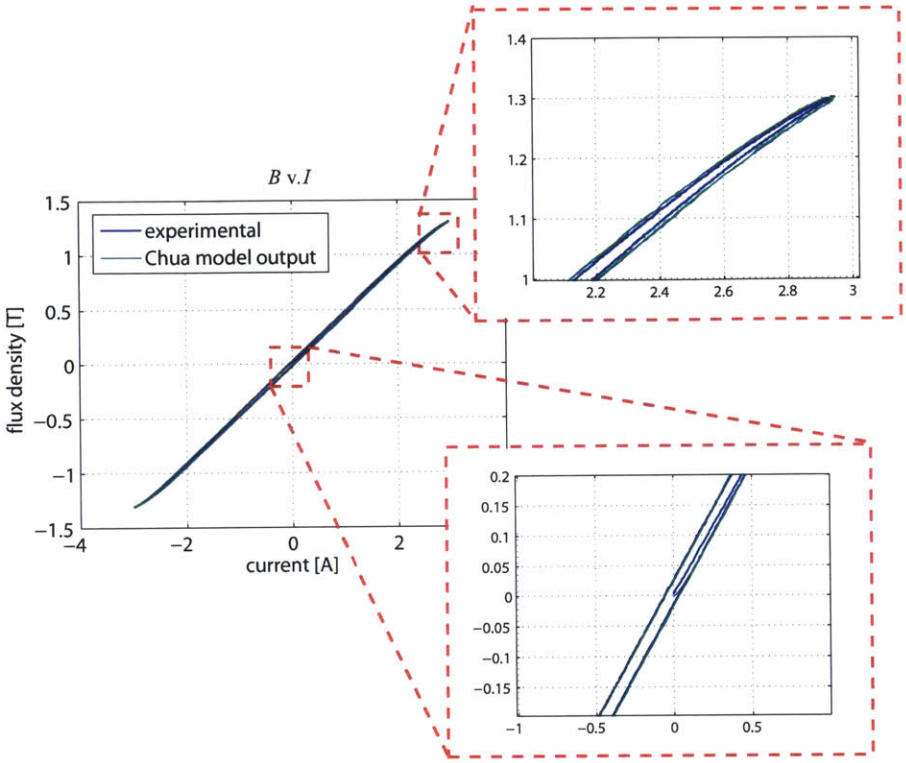

Figure 6-41: Frequency-independent Chua model B-I major loop output compared to measured B-I data.

output near saturation.

The frequency-dependent Chua model is also better at matching the minor loops when driven at the same frequency that was used to identify the model. Figure 6-44 shows a minor loop output of the frequency-dependent Chua model compared to the experimental data. The input signal was 10 Hz. The fit near the minimum flux density is very good. The fit near the maximum flux density shows some discrepancy, but the experimental loop and Chua-estimated loop still exhibit the same general shape, unlike with the frequency-independent Chua model that was shown in Figure 6-42.

The reason the minor loops show a better fit when w is set to 1 is because the Chua model cannot distinguish between a change in frequency and a change in amplitude. Both result in decreased dI/dt. Therefore, for the frequency-dependent Chua model, an input signal of the same frequency but lower amplitude than the signal used to identify the Chua model will exhibit 'loop narrowing'. However, because minor loops

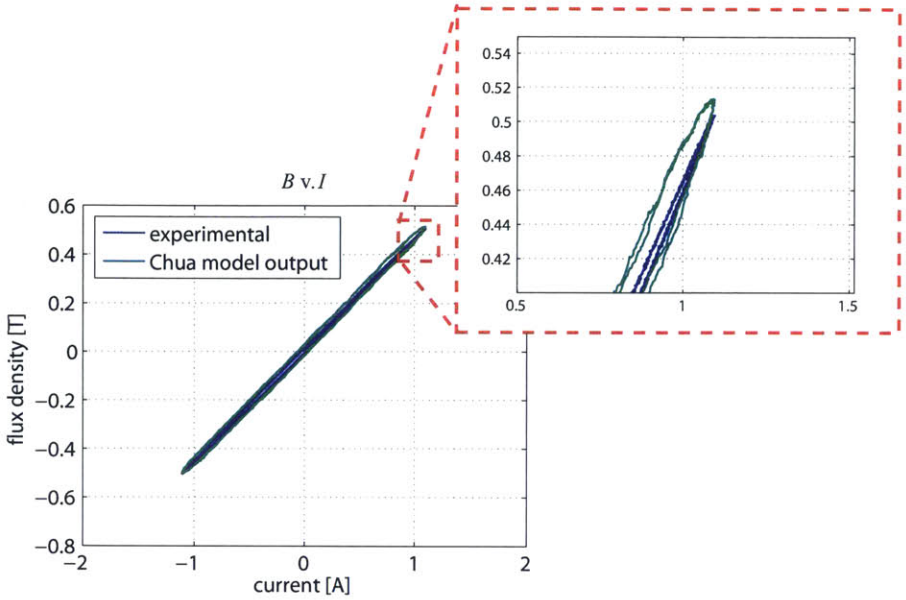

Figure 6-42: Frequency-independent Chua model B-I minor loop output compared to measured B-I data.

are typically thinner than the major loop, this is a case where the loop narrowing of the frequency-dependent model results in a better fit.

The problem with setting $w = 1$ is that our model output is now frequency dependent and will exhibit loop widening or loop narrowing as the frequency increases or decreases, respectively. Choosing $w = 1$ only makes sense in applications where the frequency content is fixed or if we desire the frequency dependence.

6.7.3 Gap Incorporation

One advantage that the Chua model offers is that if the w function described in Section 3.4 is equal to 1, then the Chua model is capable of incorporating the gap directly. This obviates the need for an observer. To see how, consider again the differential equation from (3.32), repeated here as

$$\frac{dB(t)}{dt} = G\left[H(t) - f(B(t))\right], \tag{6.36}$$

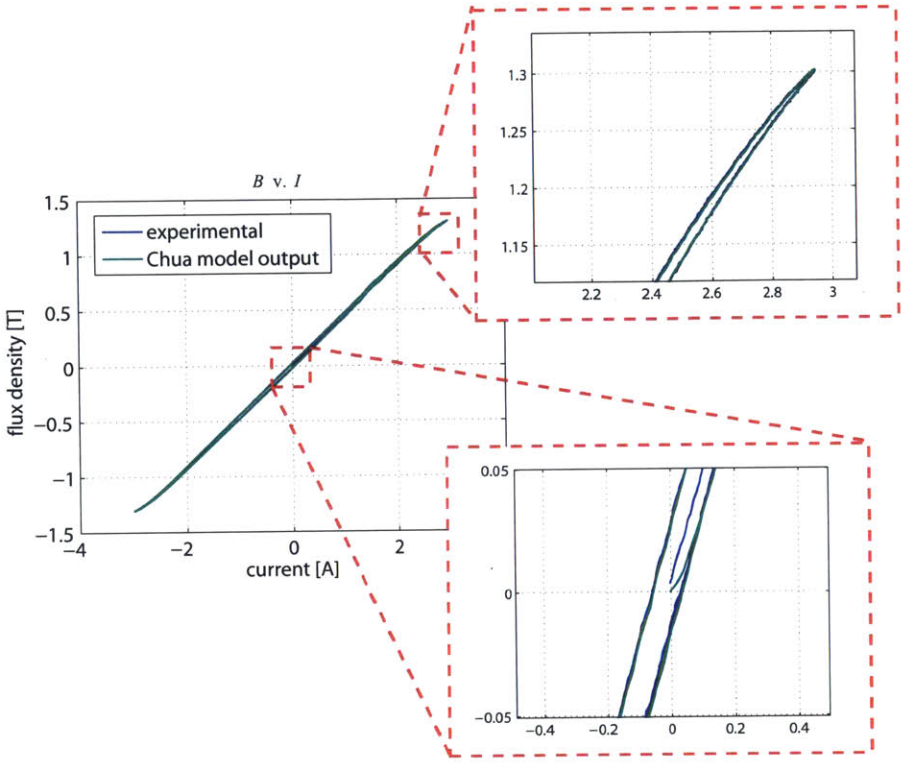

Figure 6-43: Frequency-dependent Chua model B-I major loop output compared to measured B-I data.

where we have set the functions w and h both equal to 1. We have replaced the variables u and v with H and B, respectively. If we solve (4.1) for H, we can substitute the result into (6.36) as

$$\frac{dB(t)}{dt} = G\left[\frac{N}{l_{Fe}}I - \frac{2g}{\mu_0 l_{Fe}}B - f(B(t))\right]. \tag{6.37}$$

We now have a state-space equation for B where we can input I and g directly. The caveat that $w = 1$ is a significant restriction, however: our model will exhibit loop widening whether we want it to or not.

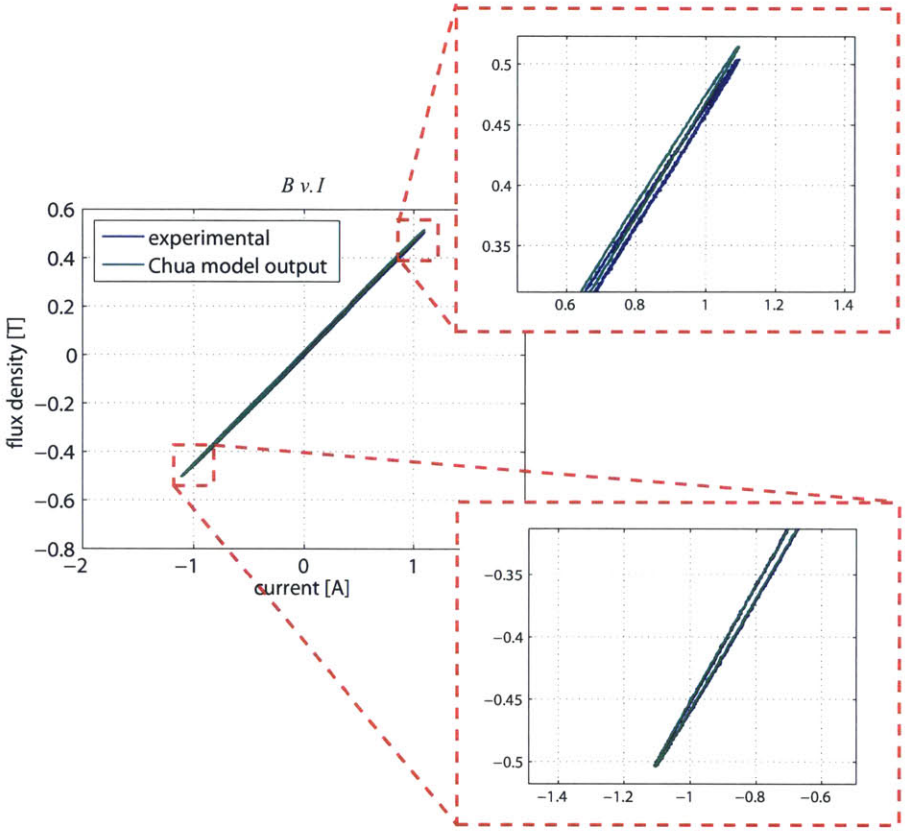

Figure 6-44: Frequency-dependent Chua model B-I minor loop output compared to measured B-I data.

6.7.4 Chua Model Inversion

We can also show that (6.37) is invertible and can be solved for I. We apply G^{-1} to both sides

$$G^{-1}\left(\frac{dB(t)}{dt}\right) = G^{-1}\left[G\left[\frac{N}{l_{Fe}}I - \frac{2g}{\mu_0 l_{Fe}}B - f(B(t))\right]\right],$$

or

$$G^{-1}\left(\frac{dB(t)}{dt}\right) = \frac{N}{l_{Fe}}I - \frac{2g}{\mu_0 l_{Fe}}B - f(B(t)). \tag{6.38}$$

Solving for I gives

$$I(t) = \frac{2g}{\mu_0 N} B + \frac{l_{Fe}}{N} f(B(t)) + G^{-1}\left(\frac{dB}{dt}\right), \tag{6.39}$$

where G^{-1} is given by (3.35). Equation (6.37) allows for a straightforward implementation of feedforward inverse hysteresis control: if the desired flux profile is known *a priori*, we can use this as the input to (6.37) to determine the appropriate current to the actuator. Again, note that this result is restricted to the case where $w = 1$.

6.8 Error Analysis

In this section, we investigate why the SHM observer performs better than both the adaptive-gain observer from Section 6.4 and the original observer without adaptive gain from Section 6.3. We show that in the linear case, both the SHM observer and the adaptive-gain observer respond identically to a gap disturbance. This is done to demonstrate that the difference between these two observer structures is not the result of unintentionally designing a better controller for the SHM observer. We then show conceptually how the hysteresis nonlinearity can easily lead to instability from large gap disturbances for the adaptive-gain observer. We next analyze the original observer without adaptive gain from Section 6.3 and show why it leads to poor performance. Finally, we analyze the SHM observer and examine why the SHM observer performs better than both the adaptive-gain observer and the original observer.

6.8.1 Linear Analysis of Observer Response to Gap Disturbance

Assume that we have a step change in gap, which we denote as Δg. If the input current to the observer is constant and the error between I and $\hat{I}$ before the gap step change was zero, then the error, e, immediately after the gap step change is

$$e = -\frac{2B\Delta g}{\mu_0}. \tag{6.40}$$

This can be understood by reference to the block diagrams of Figure 6-15 and Figure 6-36. We want to determine how this error propagates to the output of the hysteresis model. In the case of the adaptive-gain observer with the original B-H hysteresis model, we can write the change in H, ΔH, as

$$\Delta H = K_d \int e dt = -\frac{K_s}{dB/dH} \int \frac{2B\Delta g}{\mu_0} dt, \tag{6.41}$$

where we have introduced the controller from (6.24) in its time-domain form. We next carry out the integration in (6.41) over one time step. With reference to Figure 6-45, we see that the integration of the error over one time step is $2B\Delta g/\mu_0 \cdot T_s/2$ if we assume a trapezoidal integration, where T_s is the time step. After also substituting the expression for K_s from (6.26), we write ΔH as

$$\Delta H = -\frac{\pi f_c B T_s \Delta g}{g_0 \left(dB/dH\right)}. \tag{6.42}$$

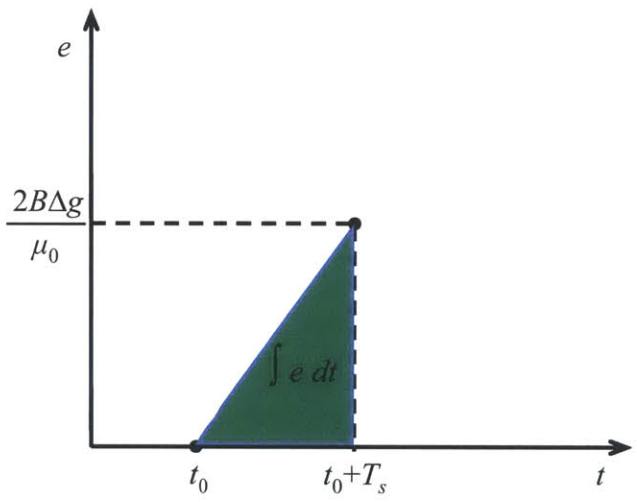

Figure 6-45: Error integration over one time step.

For the SHM observer, we can follow the same procedure to derive ΔH_2 from a step in gap. For this case, we substitute K from (6.34) to give

$$\Delta H_2 = -\frac{2\pi f_c B T_s \Delta g}{\mu_0 l_{Fe}}. \tag{6.43}$$

We next want to determine the resulting ΔB in both cases. Since $\Delta B_u = {}^{dB}/_{dH}\Delta H$, where the subscript u refers to the unsheared model of the adaptive-gain observer, we can write ΔB_u for the adaptive-gain observer as

$$\Delta B_u = -\frac{\pi f_c B T_s \Delta g}{g_0}. \tag{6.44}$$

For the sheared case, we note that $dB/dH_2 = (\mu_0 l_{Fe})/(2g_0)$. This can be derived from (6.29) if we assume that H is negligible. Since $\Delta B_s = {}^{dB}/_{dH_2}\Delta H_2$, where the subscript s denotes the sheared case, we can write ΔB_s for the SHM observer as

$$\Delta B_s = -\frac{2\pi f_c B T_s \Delta g}{\mu_0 l_{Fe}} \frac{\mu_0 l_{Fe}}{2g_0} = -\frac{\pi f_c B T_s \Delta g}{g_0}. \tag{6.45}$$

This is the same result as for the unsheared case, showing that in the linear case, both the sheared and unsheared models respond identically.

6.8.2 Analysis of Adaptive Gain Observer

Because of the nonlinearity, however, the observers can respond very differently in reality. We can see how there is a risk of instability in the adaptive gain observer by viewing it from a loop gain perspective. The loop gain of the adaptive gain observer at time $t = t_0 + T_s$ is

$$|LT| = \frac{f_c}{g_0 \frac{dB}{dH}(t_0) s} \left(\frac{dB}{dH}(t_0 + T_s) g \right). \tag{6.46}$$

The reason for the different values of dB/dH in (6.46) is that the value of dB/dH used for the adaptive gain lags one time step behind the current value of dB/dH. Because the value of $dB/dH(t_0 + T_s)$ can be much larger than $dB/dH(t_0)$, the loop gain can be very large at $t = t_0 + T_s$. If the ratio between $dB/dH(t_0 + T_s)$ and $dB/dH(t_0)$ is large enough, instability can result. Larger gap changes can result in larger changes in dB/dH from one time step to the next, increasing the risk of instability.

It is perhaps easiest to see this qualitatively. Suppose we are operating at point a on the B-H hysteresis loop shown in Figure 6-46. The value of dB/dH here is

relatively low. Now suppose we have a gap change in the positive direction. Because of the low value of dB/dH, the resulting ΔH for the adaptive gain observer calculated from (6.42) will be large: since the controller assumes the original low value of dB/dH for the entire time step, this leads to a large 'overshoot' from point a on the hysteresis loop to point b in the figure. The value of B calculated by the hysteresis model corresponding to the new value of H will be an overestimate. This is the phenomenon that gives rise to the 'spikes' seen in Figure 6-29. If the gap changes become too large, the controller is at risk of going unstable. The effect can be reduced by decreasing the sample time. Another possibility is perhaps to make the adaptive gain somehow dependent on the gap measurement as well.

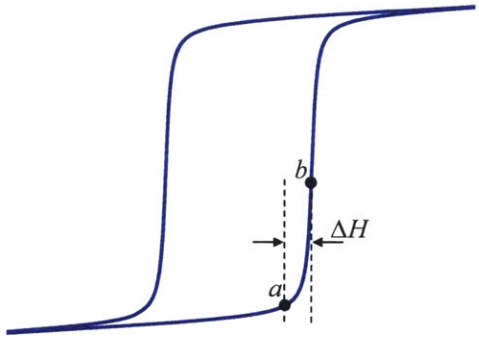

Figure 6-46: ΔH going from low-dB/dH region to high-dB/dH region.

6.8.3 Analysis of Original Observer

What about the original observer without the adaptive gain described in Section 6.3? We might wonder why the SHM observer performs so much better than this original model: after all, the original model did not have a controller gain dependent on dB/dH, so we should not have to worry about 'overshooting' on the B-H loop.

The reason for the difference is because of how we defined the plant in the two cases. In our original model, the plant input is H. The plant gain is

$$|P| = \frac{dB}{dH}\frac{2g}{\mu_0} + l_{Fe}. \tag{6.47}$$

The plant gain is dominated by the dB/dH term. Since this term varies so widely, we get a large range in plant gain, making good control authority over the entire range of inputs very difficult. For the hysteresis model identified in Figure 6-2, the plant gain varies from a minimum of 0.287 m to a maximum of 84.7 m for the range of inputs simulated, a ratio of nearly 300:1. While the adaptive-gain observer suffers from stability risks owing to the rapidly changing dB/dH in the controller structure, the original observer suffers from poor peformance because of the rapidly changing dB/dH in the plant.

6.8.4 Analysis of SHM Observer

In contrast, with the sheared model the plant gain is much more stable. The plant gain is given by (6.33). If there is no gap disturbance or gap offset from the nominal, the plant gain is the constant l_{Fe}. Let us consider the case of how the plant gain changes if there is a gap offset from the nominal. First, we need to determine dB/dH_2. We can differentiate (6.29) with respect to B as

$$\frac{dH_2}{dB} = \frac{dH}{dB} + \frac{2g_{\text{off}}}{\mu_0} l_{Fe}. \tag{6.48}$$

The expression for dB/dH_2 is then just the inverse of this, expressed here as

$$\frac{dB}{dH_2} = \frac{1}{\frac{dH}{dB} + \frac{2g_{\text{off}}}{\mu_0 l_{Fe}}}. \tag{6.49}$$

The term dH/dB is the inverse of dB/dH. For our range of operation, the value of dB/dH ranges from $3.14 \times 10^{-4}\,\text{T} \cdot \text{m/A}$ to $0.142\,\text{T} \cdot \text{m/A}$. The second term in the denominator is a constant and has a value of $5957\,\text{A}/(\text{T} \cdot \text{m})$, where we substituted N/m for $2g_{\text{off}}/\mu_0$ (see Section 6.2.1). Substituting these values into (6.49), we find that dB/dH_2 ranges from a minimum of $1.09 \times 10^{-4}\,\text{T} \cdot \text{m/A}$ near saturation to a maximumm of $1.67 \times 10^{-4}\,\text{T} \cdot \text{m/A}$.

Suppose we have a gap offset of 50 µm from the nominal gap. Substituting this for g_2 in (6.33) and using the maximum dB/dH_2 found above, we calculate a plant

gain of 0.113 m, a deviation of only 13.3% from the nominal plant gain.

In addition, the SHM observer sees a much more consistent loop gain from one time step to the next compared to the adaptive gain observer because the controller is not dependent on a widely varying dB/dH term. Any changes in loop gain come from changes in the plant gain, which we just showed to be minimal. This stability of loop gain accounts both for why the SHM observer does not risk instability for large gap changes in constrast to the adaptive-gain observer and for why the SHM observer shows good performance over the entire input range in contrast to the original observer without adaptive gain.

6.9 Summary

In this chapter we developed several methods for modeling the hysteretic behavior of a reluctance actuator for real-time flux estimation. We designed an observer to generate an estimate of the flux density without having to solve for the magnetic field in the steel. However, the flux estimation of the original observer suffered at saturation and at other regions with low dB/dH because of low control authority in these regions. To resolve this, we developed an observer with an adaptive gain controller that linearized the plant over the full B-H region of operation. However, the adaptive gain observer had numeric stability problems when subjected to dynamic gap disturbances.

We then designed an observer that used a sheared model of the hysteresis relationship. By taking advantage of the linearizing effect of the actuator operating gap, we were able to design an observer that can accurately capture hysteretic behavior and is robust to large gap disturbances. The main advantages offered by the SHM observer over the other flux estimation methods presented in this chapter are summarized below:

- The hysteresis model can be identified directly from the measured B-I data.
- The model exhibits good performance even into the saturation region of the

material.

- The model is capable of estimating flux density in the face of large gap disturbances.
- A feedforward path can be easily added for improved performance.
- The SHM observer is less computationally intensive than a flux estimation scheme that uses interpolation to estimate the effect of a gap disturbance; it also captures the hysteretic behavior resulting from a gap change, while an interpolation scheme cannot.
- The SHM observer is numerically stable in the presence of gap changes.

In the next chapter, we present alternative techniques for modeling the reluctance actuator, including magnetic circuit modeling and Finite Element Modeling (FEM). The magnetic circuit models can be supplemented with the hysteresis models developed in this thesis to generate an augmented model of the reluctance actuator.

Chapter 7

Magnetic Circuit Modeling of Reluctance Actuators

In this chapter, we present an alternative way of modeling a reluctance actuator using magnetic circuits. Magnetic circuit techniques provide an intuitive method for modeling and analyzing electromagnetic devices. By analogizing magnetic reluctance to electrical resistance, magnetomotive force to voltage, and magnetic flux to current, one can utilize standard electrical circuit techniques (e.g., Kirchoff's Voltage Law and Kirchoff's Current Law) to solve magnetic circuits. Good references for magnetic circuit theory and application include [68, 91, 53, 66, 70, 56].

We apply these magnetic circuit techniques to a standard three-pole reluctance actuator. We first model the three-pole actuator by selecting an appropriate magnetic circuit network consisting of a magnetomotive force (MMF) source and various reluctances. We then set up the circuit equations via linear network theory. Values for the reluctances are calculated based on material properties and actuator geometry. Flux tube methods [74, 59] are used to model fringing field reluctances and leakage field reluctances. Next we present a method for setting up the circuit equations when the circuit includes nonlinear elements.

Once the magnetic circuit is specified, we solve the circuit for the air gap flux density and the corresponding actuator force. This is analogous to solving an electrical circuit for the current through a particular resistor in the network. We then compare

this simulated force to experimental data measured on electromagnetic actuators, and thus verify the magnetic circuit model and augment it where necessary. We also present some simulation results using Finite Element Analysis.

7.1 Three-pole Actuator Magnetic Circuit Network

We refer to Figure 2-1 for an illustration of the reluctance actuator stator and target. By exploiting symmetry between the left and right halves of the actuator, we can model just one half of the actuator without loss of accuracy. Figure 7-1 shows a half-actuator overlayed with a corresponding magnetic circuit.

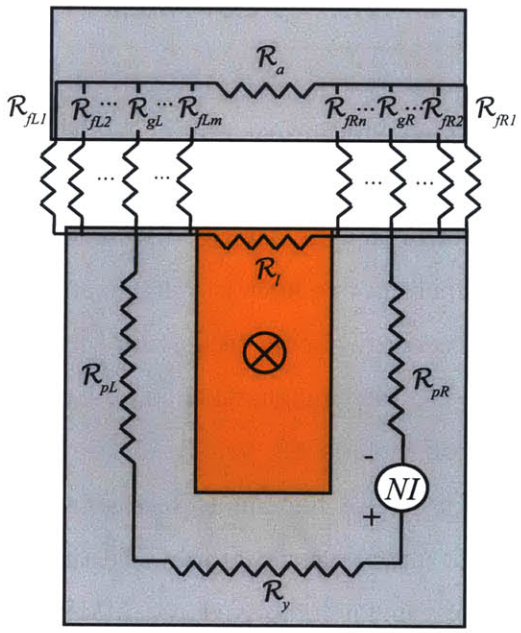

Figure 7-1: Magnetic circuit for the half-actuator.

The coil windings are idealized as a lumped MMF source with an MMF value of NI amp-turns[1]. The reluctances shown in the figure correspond to the following:

- $\mathcal{R}_y$: yoke reluctance

[1]Since the coil windings are equally spaced along the vertical length of the center pole and not concentrated in one location, a more realistic model of the source would consist of a series of MMF sources distributed along the center pole instead of a single lumped parameter MMF source. A single lumped parameter source is used at this point to simplify the analysis.

- $\mathcal{R}_{pL}$: left pole reluctance
- $\mathcal{R}_{pR}$: right pole[2] reluctance
- $\mathcal{R}_l$: leakage reluctance (cross-slot)
- $\mathcal{R}_{gL}$: left air gap reluctance
- $\mathcal{R}_{gR}$: right air gap reluctance
- $\mathcal{R}_{fL1}...R_{fLm}$: m fringing field reluctances from the left pole face to the armature
- $\mathcal{R}_{fR1}...R_{fRn}$: n fringing field reluctances from the right pole face to the armature
- $\mathcal{R}_a$: armature reluctance

The magnetic circuit is shown in a standard circuit diagram form in Figure 7-2.

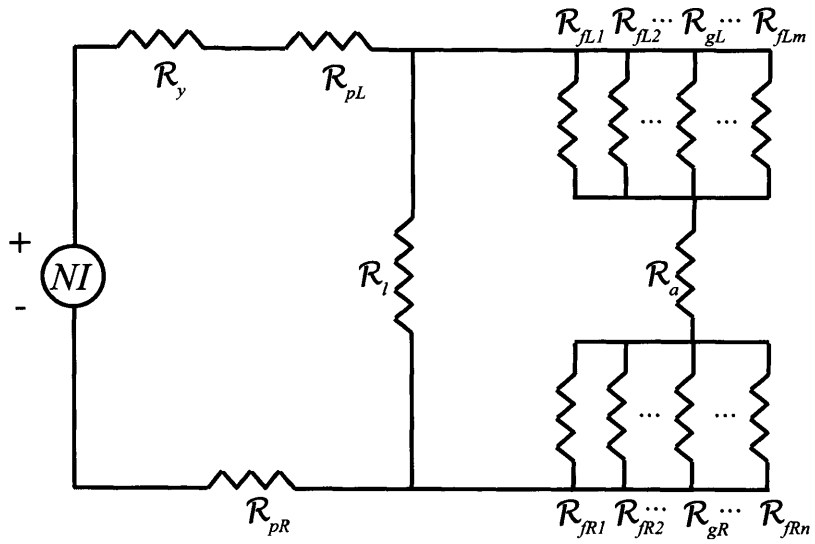

Figure 7-2: Magnetic circuit for the half-actuator in standard form.

[2]Note that 'right pole' here refers to the right pole of the *half* actuator in Figure 7-1. With respect to the *full* actuator, this corresponds to the *left* half of the *center* pole.

7.2 Solving the Magnetic Circuit via Linear Network Theory

Figure 7-3 shows the magnetic circuit with the MMF's and fluxes labeled. The node MMF's ($\Psi_{i's}$), or magnetic potentials, are analogous to node voltages in an electrical circuit. Note that we arbitrarily set $\Psi_5 = 0$ as the reference node. In a similar manner, the magnetic fluxes ($\Phi_{i's}$), are analogous to currents in an electrical circuit. The force on the electromagnet target is generated by the gap flux density. Consequently, the magnetic fluxes of primary interest are Φ_{gL} and Φ_{gR}.

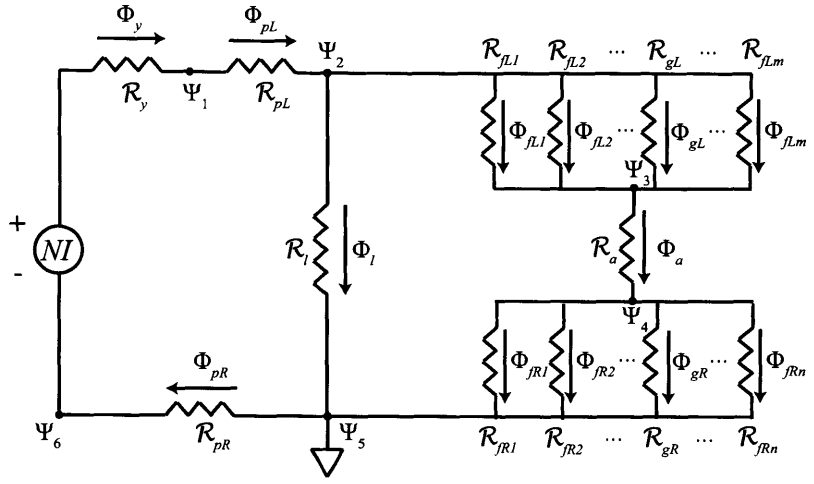

Figure 7-3: The magnetic circuit with the magnetic potentials ($\Psi_{i's}$) at each node and the magnetic fluxes ($\Phi_{i's}$) through each reluctance.

Following the linear network theory procedure outlined in [79] and [66], we can solve for the flux through each reluctance and for the MMF at each node. Using Kirchoff's Voltage Law (KVL) and Kirchoff's Current Law (KCL), we can write the network equations in general form as

$$\begin{bmatrix} \mathbf{P}^{-1} & \mathbf{A} \\ \mathbf{A}^T & \mathbf{0} \end{bmatrix} \begin{bmatrix} \mathbf{\Phi} \\ \mathbf{\Psi} \end{bmatrix} = \begin{bmatrix} \mathbf{\Psi}_s \\ \mathbf{\Phi}_s \end{bmatrix}. \tag{7.1}$$

Here, $\mathbf{P}$ is a permeance matrix, consisting of the permeances of each reluctance path,

where $P_i \triangleq 1/\mathcal{R}_i$. The matrix $\mathbf{A}$ is an incidence matrix that represents the flux into or out of each node. The vectors $\mathbf{\Phi}$ and $\mathbf{\Psi}$ consist of the fluxes through each reluctance and the MMF at each node (except for node 5), respectively. Finally, $\mathbf{\Phi}_s$ and $\mathbf{\Psi}_s$ are vectors corresponding to any MMF or flux sources, respectively.

To understand the relation expressed in (7.1) more clearly, we derive it for the circuit in Figure 7-3 in the following steps. For the sake of simplicity, we have assumed only two fringing field reluctances in the following derivation ($\mathcal{R}_{fL}$ and $\mathcal{R}_{fR}$).

1. Write the MMF drop across each reluctance as a function of node MMF's:

$$\begin{aligned}
\Psi_y &= NI + \Psi_6 - \Psi_1, \\
\Psi_{pL} &= \Psi_1 - \Psi_2, \\
\Psi_l &= \Psi_2 - \Psi_5, \\
\Psi_{fL} &= \Psi_2 - \Psi_3, \\
\Psi_{gL} &= \Psi_2 - \Psi_3, \\
\Psi_a &= \Psi_3 - \Psi_4, \\
\Psi_{fR} &= \Psi_4 - \Psi_5, \\
\Psi_{gR} &= \Psi_4 - \Psi_5, \\
\Psi_{pR} &= \Psi_5 - \Psi_6.
\end{aligned} \tag{7.2}$$

2. Write (7.2) in matrix form:

$$\begin{bmatrix} \Psi_y \\ \Psi_{pL} \\ \Psi_l \\ \Psi_{fL} \\ \Psi_{gL} \\ \Psi_a \\ \Psi_{fR} \\ \Psi_{gR} \\ \Psi_{pR} \end{bmatrix} = \begin{bmatrix} NI \\ 0 \\ 0 \\ 0 \\ 0 \\ 0 \\ 0 \\ 0 \\ 0 \end{bmatrix} - \begin{bmatrix} 1 & 0 & 0 & 0 & 0 & -1 \\ -1 & 1 & 0 & 0 & 0 & 0 \\ 0 & -1 & 0 & 0 & 1 & 0 \\ 0 & -1 & 1 & 0 & 0 & 0 \\ 0 & -1 & 1 & 0 & 0 & 0 \\ 0 & 0 & -1 & 1 & 0 & 0 \\ 0 & 0 & 0 & -1 & 1 & 0 \\ 0 & 0 & 0 & -1 & 1 & 0 \\ 0 & 0 & 0 & 0 & -1 & 1 \end{bmatrix} \begin{bmatrix} \Psi_1 \\ \Psi_2 \\ \Psi_3 \\ \Psi_4 \\ \Psi_5 \\ \Psi_6 \end{bmatrix}. \tag{7.3}$$

In matrix notation, we write

$$\mathbf{\Psi}_r = \mathbf{\Psi}_s - \mathbf{A}_0 \mathbf{\Psi}_f. \tag{7.4}$$

3. By noting that Ψ_5 has been selected as the reference (ground) potential, i.e., $\Psi_5 = 0$, we can remove the 5^{th} column from $\mathbf{A_0}$ and write

$$\begin{bmatrix} \Psi_y \\ \Psi_{pL} \\ \Psi_l \\ \Psi_{fL} \\ \Psi_{gL} \\ \Psi_a \\ \Psi_{fR} \\ \Psi_{gR} \\ \Psi_{pR} \end{bmatrix} = \begin{bmatrix} NI \\ 0 \\ 0 \\ 0 \\ 0 \\ 0 \\ 0 \\ 0 \\ 0 \end{bmatrix} - \begin{bmatrix} 1 & 0 & 0 & 0 & -1 \\ -1 & 1 & 0 & 0 & 0 \\ 0 & -1 & 0 & 0 & 0 \\ 0 & -1 & 1 & 0 & 0 \\ 0 & -1 & 1 & 0 & 0 \\ 0 & 0 & -1 & 1 & 0 \\ 0 & 0 & 0 & -1 & 0 \\ 0 & 0 & 0 & -1 & 0 \\ 0 & 0 & 0 & 0 & 1 \end{bmatrix} \begin{bmatrix} \Psi_1 \\ \Psi_2 \\ \Psi_3 \\ \Psi_4 \\ \Psi_6 \end{bmatrix}. \tag{7.5}$$

In matrix notation, we write

$$\boldsymbol{\Psi}_r = \boldsymbol{\Psi}_s - \mathbf{A}\boldsymbol{\Psi}. \tag{7.6}$$

4. Write the constitutive relations between each reluctance MMF and the flux flowing through it. This is analogous to Ohm's Law. Then write these constitutive relations in matrix form:

$$\begin{bmatrix} \Phi_y \\ \Phi_{pL} \\ \Phi_l \\ \Phi_{fL} \\ \Phi_{gL} \\ \Phi_a \\ \Phi_{fR} \\ \Phi_{gR} \\ \Phi_{pR} \end{bmatrix} = \begin{bmatrix} P_y & 0 & 0 & 0 & 0 & 0 & 0 & 0 & 0 \\ 0 & P_{pL} & 0 & 0 & 0 & 0 & 0 & 0 & 0 \\ 0 & 0 & P_l & 0 & 0 & 0 & 0 & 0 & 0 \\ 0 & 0 & 0 & P_{fL} & 0 & 0 & 0 & 0 & 0 \\ 0 & 0 & 0 & 0 & P_{gL} & 0 & 0 & 0 & 0 \\ 0 & 0 & 0 & 0 & 0 & P_a & 0 & 0 & 0 \\ 0 & 0 & 0 & 0 & 0 & 0 & P_{fR} & 0 & 0 \\ 0 & 0 & 0 & 0 & 0 & 0 & 0 & P_{gR} & 0 \\ 0 & 0 & 0 & 0 & 0 & 0 & 0 & 0 & P_{pR} \end{bmatrix} \begin{bmatrix} \Psi_y \\ \Psi_{pL} \\ \Psi_l \\ \Psi_{fL} \\ \Psi_{gL} \\ \Psi_a \\ \Psi_{fR} \\ \Psi_{gR} \\ \Psi_{pR} \end{bmatrix}. \tag{7.7}$$

In matrix notation, we write

$$\boldsymbol{\Phi} = \mathbf{P}\boldsymbol{\Psi}_r. \tag{7.8}$$

In general, provided there is no coupling between reluctance elements, $\mathbf{P}$ will always be a diagonal matrix.

5. Combine (7.6) and (7.8) to form the matrix equation $\boldsymbol{\Phi} = \mathbf{P}(\boldsymbol{\Psi}_\mathbf{s} - \mathbf{A}\boldsymbol{\Psi})$. Then

multiply both sides by $\mathbf{P}^{-1}$, recalling that $P_i \triangleq 1/\mathcal{R}_i$:

$$\begin{bmatrix} \mathcal{R}_y & 0 & 0 & 0 & 0 & 0 & 0 & 0 & 0 \\ 0 & \mathcal{R}_{pL} & 0 & 0 & 0 & 0 & 0 & 0 & 0 \\ 0 & 0 & \mathcal{R}_l & 0 & 0 & 0 & 0 & 0 & 0 \\ 0 & 0 & 0 & \mathcal{R}_{fL} & 0 & 0 & 0 & 0 & 0 \\ 0 & 0 & 0 & 0 & \mathcal{R}_{gL} & 0 & 0 & 0 & 0 \\ 0 & 0 & 0 & 0 & 0 & \mathcal{R}_a & 0 & 0 & 0 \\ 0 & 0 & 0 & 0 & 0 & 0 & \mathcal{R}_{fR} & 0 & 0 \\ 0 & 0 & 0 & 0 & 0 & 0 & 0 & \mathcal{R}_{gR} & 0 \\ 0 & 0 & 0 & 0 & 0 & 0 & 0 & 0 & \mathcal{R}_{pR} \end{bmatrix} \begin{bmatrix} \Phi_y \\ \Phi_{pL} \\ \Phi_l \\ \Phi_{fL} \\ \Phi_{gL} \\ \Phi_a \\ \Phi_{fR} \\ \Phi_{gR} \\ \Phi_{pR} \end{bmatrix} =$$

$$\begin{bmatrix} NI \\ 0 \\ 0 \\ 0 \\ 0 \\ 0 \\ 0 \\ 0 \\ 0 \end{bmatrix} - \begin{bmatrix} 1 & 0 & 0 & 0 & -1 \\ -1 & 1 & 0 & 0 & 0 \\ 0 & -1 & 0 & 0 & 0 \\ 0 & -1 & 1 & 0 & 0 \\ 0 & -1 & 1 & 0 & 0 \\ 0 & 0 & -1 & 1 & 0 \\ 0 & 0 & 0 & -1 & 0 \\ 0 & 0 & 0 & -1 & 0 \\ 0 & 0 & 0 & 0 & 1 \end{bmatrix} \begin{bmatrix} \Psi_1 \\ \Psi_2 \\ \Psi_3 \\ \Psi_4 \\ \Psi_6 \end{bmatrix}. \tag{7.9}$$

In matrix notation, we write

$$\mathbf{P}^{-1}\mathbf{\Phi} = \mathbf{\Psi}_s - \mathbf{A}\mathbf{\Psi},$$

or

$$\mathbf{P}^{-1}\mathbf{\Phi} + \mathbf{A}\mathbf{\Psi} = \mathbf{\Psi}_s. \tag{7.10}$$

6. Write the fluxes entering and exiting each node. This is analogous to Kirchoff's

Current Law:

$$\begin{aligned}
\Phi_y - \Phi_{pL} &= 0, \\
\Phi_{pL} - \Phi_l - \Phi_{fL} - \Phi_{gL} &= 0, \\
\Phi_{fL} + \Phi_{gL} - \Phi_a &= 0, \\
\Phi_a - \Phi_{fL} - \Phi_{gR} &= 0, \\
\Phi_l - \Phi_{fR} - \Phi_{gR} - \Phi_{pR} &= 0, \\
\Phi_{pR} - \Phi_y &= 0.
\end{aligned} \tag{7.11}$$

.

7. Write (7.11) in matrix form as

$$\begin{bmatrix}
1 & -1 & 0 & 0 & 0 & 0 & 0 & 0 & 0 \\
0 & 1 & -1 & -1 & -1 & 0 & 0 & 0 & 0 \\
0 & 0 & 0 & 1 & 1 & -1 & 0 & 0 & 0 \\
0 & 0 & 0 & 0 & 0 & 1 & -1 & -1 & 0 \\
0 & 0 & 1 & 0 & 0 & 0 & 1 & 1 & -1 \\
-1 & 0 & 0 & 0 & 0 & 0 & 0 & 0 & 1
\end{bmatrix}
\begin{bmatrix}
\Phi_y \\ \Phi_{pL} \\ \Phi_l \\ \Phi_{fL} \\ \Phi_{gL} \\ \Phi_a \\ \Phi_{fR} \\ \Phi_{gR} \\ \Phi_{pR}
\end{bmatrix} =
\begin{bmatrix}
0 \\ 0 \\ 0 \\ 0 \\ 0 \\ 0
\end{bmatrix}. \tag{7.12}$$

In matrix notation, we write

$$\mathbf{B}\boldsymbol{\Phi} = \boldsymbol{\Phi}_s. \tag{7.13}$$

Note that $\mathbf{B}$ is the transpose of $\mathbf{A}_0$ in (7.4). Consequently, we can eliminate

the 5^{th} row in (7.12), as the dual of step 3. We write the result as

$$\begin{bmatrix} 1 & -1 & 0 & 0 & 0 & 0 & 0 & 0 & 0 \\ 0 & 1 & -1 & -1 & -1 & 0 & 0 & 0 & 0 \\ 0 & 0 & 0 & 1 & 1 & -1 & 0 & 0 & 0 \\ 0 & 0 & 0 & 0 & 0 & 1 & -1 & -1 & 0 \\ -1 & 0 & 0 & 0 & 0 & 0 & 0 & 0 & 1 \end{bmatrix} \begin{bmatrix} \Phi_y \\ \Phi_{pL} \\ \Phi_l \\ \Phi_{fL} \\ \Phi_{gL} \\ \Phi_a \\ \Phi_{fR} \\ \Phi_{gR} \\ \Phi_{pR} \end{bmatrix} = \begin{bmatrix} 0 \\ 0 \\ 0 \\ 0 \\ 0 \end{bmatrix}. \tag{7.14}$$

In matrix notation, we write

$$\mathbf{A}^T \mathbf{\Phi} = \mathbf{\Phi}_s. \tag{7.15}$$

8. Finally, combine (7.10) and (7.15) to form (7.1):

$$\begin{bmatrix} \mathcal{R}_y & 0 & 0 & 0 & 0 & 0 & 0 & 0 & 0 & 1 & 0 & 0 & 0 & -1 \\ 0 & \mathcal{R}_{pL} & 0 & 0 & 0 & 0 & 0 & 0 & 0 & -1 & 1 & 0 & 0 & 0 \\ 0 & 0 & \mathcal{R}_l & 0 & 0 & 0 & 0 & 0 & 0 & 0 & -1 & 0 & 0 & 0 \\ 0 & 0 & 0 & \mathcal{R}_{fL} & 0 & 0 & 0 & 0 & 0 & 0 & -1 & 1 & 0 & 0 \\ 0 & 0 & 0 & 0 & \mathcal{R}_{gL} & 0 & 0 & 0 & 0 & 0 & -1 & 1 & 0 & 0 \\ 0 & 0 & 0 & 0 & 0 & \mathcal{R}_a & 0 & 0 & 0 & 0 & 0 & 0 & -1 & 0 \\ 0 & 0 & 0 & 0 & 0 & 0 & \mathcal{R}_{fR} & 0 & 0 & 0 & 0 & 0 & -1 & 0 \\ 0 & 0 & 0 & 0 & 0 & 0 & 0 & \mathcal{R}_{gR} & 0 & 0 & 0 & 0 & -1 & 0 \\ 0 & 0 & 0 & 0 & 0 & 0 & 0 & 0 & \mathcal{R}_{pR} & 0 & 0 & 0 & 0 & 1 \\ 1 & -1 & 0 & 0 & 0 & 0 & 0 & 0 & 0 & 0 & 0 & 0 & 0 & 0 \\ 0 & 1 & -1 & -1 & -1 & 0 & 0 & 0 & 0 & 0 & 0 & 0 & 0 & 0 \\ 0 & 0 & 0 & 1 & 1 & -1 & 0 & 0 & 0 & 0 & 0 & 0 & 0 & 0 \\ 0 & 0 & 0 & 0 & 0 & 1 & -1 & -1 & 0 & 0 & 0 & 0 & 0 & 0 \\ -1 & 0 & 0 & 0 & 0 & 0 & 0 & 0 & 1 & 0 & 0 & 0 & 0 & 0 \end{bmatrix} \begin{bmatrix} \Phi_y \\ \Phi_{pL} \\ \Phi_l \\ \Phi_{fL} \\ \Phi_{gL} \\ \Phi_{fR} \\ \Phi_a \\ \Phi_{gR} \\ \Phi_{pR} \\ \Psi_1 \\ \Psi_2 \\ \Psi_3 \\ \Psi_4 \\ \Psi_6 \end{bmatrix} = \begin{bmatrix} NI \\ 0 \\ 0 \\ 0 \\ 0 \\ 0 \\ 0 \\ 0 \\ 0 \\ 0 \\ 0 \\ 0 \\ 0 \\ 0 \end{bmatrix}. \tag{7.16}$$

To summarize, the matrix and vector elements from (7.1) are

$$\mathbf{P}^{-1} = \begin{bmatrix} \mathcal{R}_y & 0 & 0 & 0 & 0 & 0 & 0 & 0 & 0 \\ 0 & \mathcal{R}_{pL} & 0 & 0 & 0 & 0 & 0 & 0 & 0 \\ 0 & 0 & \mathcal{R}_l & 0 & 0 & 0 & 0 & 0 & 0 \\ 0 & 0 & 0 & \mathcal{R}_{fL} & 0 & 0 & 0 & 0 & 0 \\ 0 & 0 & 0 & 0 & \mathcal{R}_{gL} & 0 & 0 & 0 & 0 \\ 0 & 0 & 0 & 0 & 0 & \mathcal{R}_a & 0 & 0 & 0 \\ 0 & 0 & 0 & 0 & 0 & 0 & \mathcal{R}_{fR} & 0 & 0 \\ 0 & 0 & 0 & 0 & 0 & 0 & 0 & \mathcal{R}_{gR} & 0 \\ 0 & 0 & 0 & 0 & 0 & 0 & 0 & 0 & \mathcal{R}_{pR} \end{bmatrix}, \tag{7.17}$$

$$\mathbf{A} = \begin{bmatrix} 1 & 0 & 0 & 0 & -1 \\ -1 & 1 & 0 & 0 & 0 \\ 0 & -1 & 0 & 0 & 0 \\ 0 & -1 & 1 & 0 & 0 \\ 0 & -1 & 1 & 0 & 0 \\ 0 & 0 & -1 & 1 & 0 \\ 0 & 0 & 0 & -1 & 0 \\ 0 & 0 & 0 & -1 & 0 \\ 0 & 0 & 0 & 0 & 1 \end{bmatrix}, \tag{7.18}$$

$$\begin{bmatrix} \mathbf{\Phi} \\ \mathbf{\Psi} \end{bmatrix} = \begin{bmatrix} \Phi_y & \Phi_{pL} & \Phi_l & \Phi_{fL} & \Phi_{gL} & \Phi_a & \Phi_{fR} & \Phi_{gR} & \Phi_{pR} & \Psi_1 & \Psi_2 & \Psi_3 & \Psi_4 & \Psi_6 \end{bmatrix}^T, \tag{7.19}$$

$$\begin{bmatrix} \mathbf{\Phi_s} \\ \mathbf{\Psi_s} \end{bmatrix} = \begin{bmatrix} NI & 0 & 0 & 0 & 0 & 0 & 0 & 0 & 0 & 0 & 0 & 0 & 0 & 0 \end{bmatrix}^T. \tag{7.20}$$

Note that Ψ_5 does not appear in the network equations because node 5 has been arbitrarily selected as the reference potential, $\Psi_5 = 0$. Using linear algebra techniques, we can readily solve (7.16) for Φ_{gL} and Φ_{gR}, given the assumptions of linear permeances.

We can then solve for the actuator force using (2.13). We can also solve for the fringing field flux densities and compute the force contributions from these fields. The flux for each fringing field path is calculated by solving (7.16) for the appropriate fringing field flux variable, Φ_f. The mean flux density at the target interface, B_f, is then calculated by dividing the fringing field flux by the cross-sectional area of the flux tube at the target interface, A_f. The force contribution from the fringing field path is then given by[3]

$$F_f = 2\left(\left(\frac{\Phi_f}{A_f}\right)^2 \frac{A_f}{2\mu_0}\right) = \frac{{B_f}^2 A_f}{\mu_0}. \tag{7.21}$$

The total force on the target is then the sum of the force contributions from the working air gaps and from the various fringing fields, expressed below as

$$\begin{aligned} F &= F_{gL} + F_{gR} + F_{fL1} + ... + F_{fLm} + F_{fR1} + ... + F_{fRn}, \\ &= \frac{{B_{gL}}^2 A_{gL}}{\mu_0} + \frac{{B_{gR}}^2 A_{gR}}{\mu_0} + \frac{{B_{fL1}}^2 A_{fL1}}{\mu_0} + ... \\ &\quad + \frac{{B_{fLm}}^2 A_{fLm}}{\mu_0} + \frac{{B_{fR1}}^2 A_{fR1}}{\mu_0} + ... + \frac{{B_{fRn}}^2 A_{fRn}}{\mu_0}. \end{aligned} \tag{7.22}$$

In contrast, a lumped parameter model that does not include the fringing fields uses only the first two contributions (the contributions from the working air gaps) from the right-hand side to compute the force. Moreover, these flux densities B_{gL} and B_{gR} have a greater magnitude when fringing and leakage fields are not included, because all the flux exiting or entering the pole faces will contribute to B_{gL} and B_{gR} rather than to any fringing fields.

7.3 Reluctance Calculations

The next step for solving the magnetic circuit model is to calculate reluctance values for each of the reluctances in the circuit. The reluctances can be separated into

[3]The factor of 2 in (7.21) corresponds to the fact that the magnetic circuit only models *one-half* of the total actuator.

four main groups: the working air gap reluctances, the core material reluctances, the fringing field reluctances, and the leakage field reluctances.

7.3.1 Reluctance Calculations for the Air Gap and Core

Calculating the values for most of the reluctances in Figure 7-3 is straightforward. The general linear reluctance formula is

$$\mathcal{R} = \frac{l}{\mu_r \mu_0 A}, \tag{7.23}$$

where l is the length of the reluctance path and A is the cross-sectional area of the reluctance path.

Figure 7-4 shows the half-actuator with dimensions labeled. With these dimensions, reluctances $\mathcal{R}_y, R_{pL}, R_{pR}, R_{gL}, R_{gR}$, and $\mathcal{R}_a$ are calculated below. The path length for each reluctance is taken as the approximate *average* length of the path the flux will follow. The reluctances are

$$\mathcal{R}_y = \frac{w}{\mu_r \mu_0 d_s b}, \tag{7.24}$$

$$\mathcal{R}_{pL} = \mathcal{R}_{pR} = \frac{h + \frac{b}{2}}{\mu_r \mu_0 d_s f}, \tag{7.25}$$

$$\mathcal{R}_{gL} = \mathcal{R}_{gR} = \frac{g}{\mu_0 d_s f}, \tag{7.26}$$

$$\mathcal{R}_a = \frac{w}{\mu_r \mu_0 d_a f}. \tag{7.27}$$

Note that in calculating $\mathcal{R}_{gL}$ and $\mathcal{R}_{gR}$, the pole face area $d_s f$ is used as the relevant area.

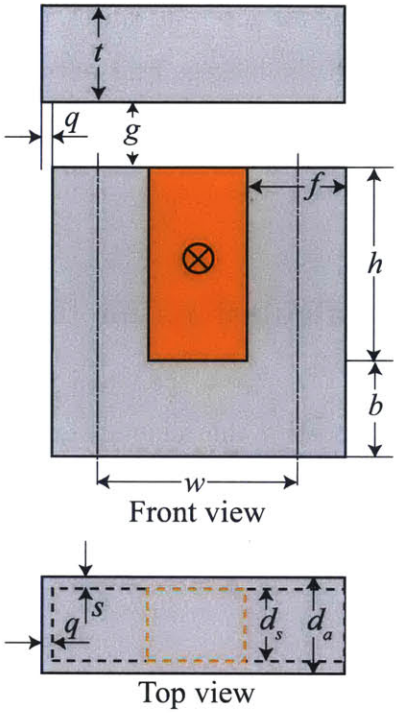

Figure 7-4: The half-actuator with dimensions labeled. The actuator core has a depth d_s into the paper. The target has a depth d_a into the paper.

7.3.2 Reluctance Calculations for Fringing Fields and Leakage Fields

Calculating the fringing field and leakage field reluctances is not as straightforward because the paths that the actual field follows can be quite complex. To aid in this calculation, we follow the flux tube procedure outlined in [74, 59]. As Roters explains in [74], the flux tube method consists of breaking the field up into "flux paths which are of simple shape and still probable." A 'probable' path is one that is similar to the true flux path, in the sense that the lumped permeance of the probable path will be close to the lumped permeance of the true path.

Figure 7-5 shows some of the flux tubes used to represent probable flux paths for the fringing and leakage fields.[4] The subscripts indicate the following: the first letter in the subscript indicates whether the fringing flux tube belongs to the left pole face

[4]Note that not all the flux tubes are shown in this 2-D figure.

(L) or the right pole face (R); second and optionally third letters indicate from which location of the given pole face the flux tube originates (L, R, F, B for left, right, front, or back, respectively; and FL, FR, BL, BR for front left corner, front right corner, back left corner, or back right corner, respectively). The lowercase l in the coil window slot indicates the flux tube associated with the leakage flux.

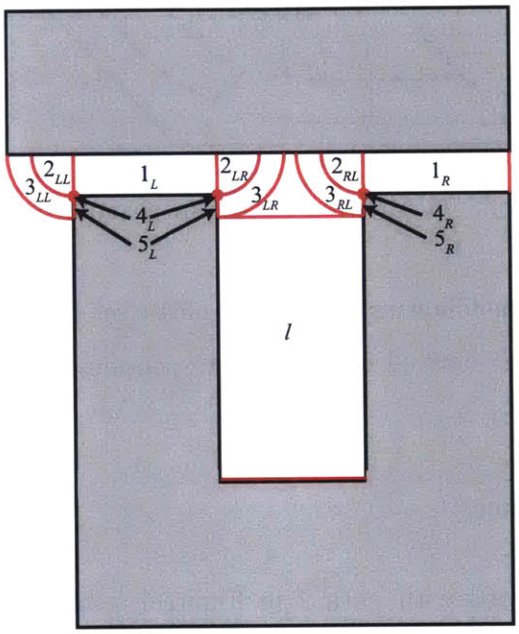

Figure 7-5: Numbered flux tubes are shown representing probable flux paths for the electromagnet.

Figure 7-6 is a figure taken from [74] showing a 3-D view of the characteristic shapes of some of the flux tubes used in the flux tube analysis. In the figure, the faces marked A and B correspond to the pole face sides in Figure 7-5. Surface D corresponds to the underside of the electromagnet target. Flux tubes in Figure 7-5 correspond to flux tubes in Figure 7-6 in the following way: path 2 corresponds to path 11; path 3 corresponds to path 12; path 4 corresponds to path 13; path 5 corresponds to path 14.

The flux tubes denoted by path 1 in the Figure 7-5 represent the working air gap flux, the reluctance of which has already been calculated in (7.26). Note also that this reluctance is not part of the fringing field, and so will not figure into the calculations

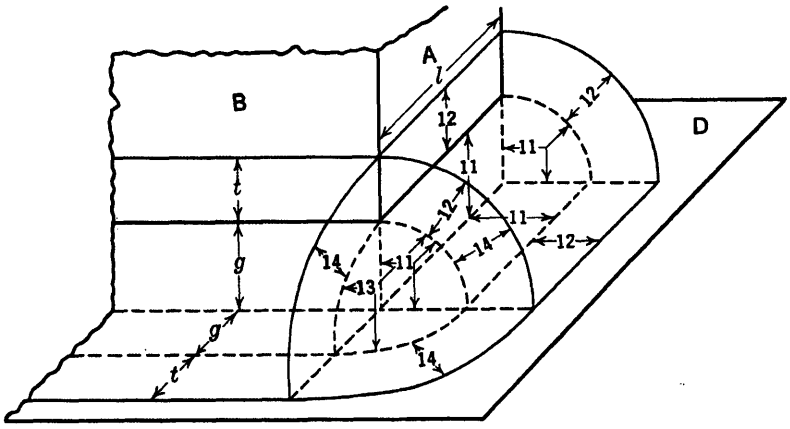

Figure 7-6: Figure from [74] showing the 3-dimensional shapes of the flux tubes.

for $\mathcal{R}_{fL}$ and $\mathcal{R}_{fR}$. In the following discussion, please see [74] for more details on how the reluctance values are derived from the corresponding flux tube shapes.

Flux path 2 reluctance

The flux tubes associated with path 2 in Figure 7-5 are shown in more detail in Figure 7-7. The characteristic dimensions of flux tubes 2_{LB}, 2_{LF}, 2_{RB}, and 2_{RF} are g and f. The characteristic dimensions of flux tubes 2_{LL}, 2_{LR}, and 2_{RL} are g and d_s. In both cases, g figures in both the characteristic length and the characteristic area, resulting in a cancelation in the final reluctance calculations.

Since the flux tubes represent reluctances in parallel, we can find the permeance of each flux tube and sum them to find the total path 2 permeance associated with each pole face. Inverting this total permeance will give us the lumped total path 2 reluctance associated with the pole face. For the total path 2 permeance of the left pole face and right pole face, we have, respectively,

$$P_{2L} = P_{2LL} + P_{2LR} + P_{2LF} + P_{2LB} = 2 \times 0.52\mu_0 f + 2 \times 0.52\mu_0 d_s, \quad (7.28)$$

$$P_{2R} = P_{2RL} + P_{2RF} + P_{2RB} = 2 \times 0.52\mu_0 f + 0.52\mu_0 d_s. \quad (7.29)$$

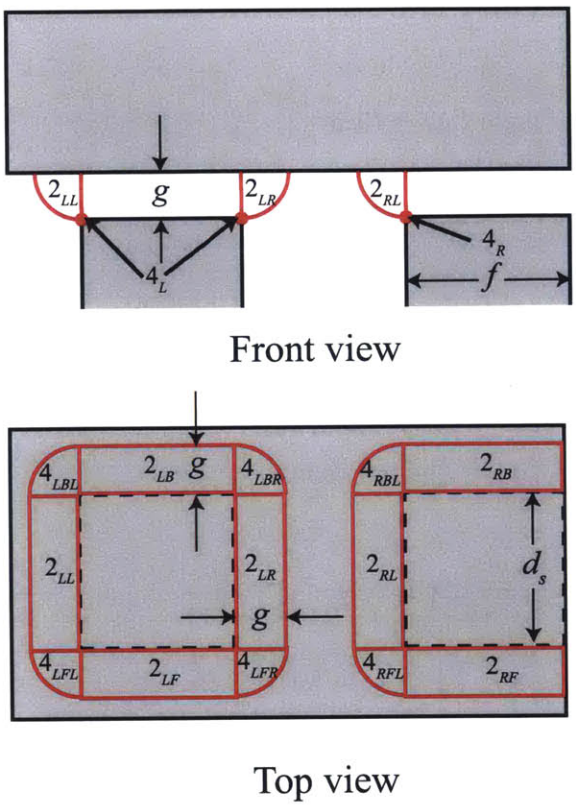

Figure 7-7: Flux paths 2 and 4 showing characteristic dimensions.

Then we can write

$$\mathcal{R}_{2L} = \frac{1}{P_{2L}}, \tag{7.30}$$

$$\mathcal{R}_{2R} = \frac{1}{P_{2R}}. \tag{7.31}$$

Flux path 3 reluctance

The flux tubes associated with path 3 are shown in Figure 7-8. The characteristic dimensions of flux tubes 3_{LL} and 3_{RL} are g, d_s, and q. The characteristic dimensions of 3_{LR} are g, d_s, and p (p has not yet been determined). The characteristic dimensions of 3_{LF}, 3_{LB}, 3_{RF}, and 3_{RB} are g, f, and s. The flux tube permeance of path 3 for the

left pole face is

$$\begin{aligned} P_{3L} &= P_{3LL} + P_{3LR} + P_{3LF} + P_{3LB}, \\ &= \frac{2\mu_0 d_s}{\pi} \ln\left(1 + \frac{q-g}{g}\right) + \frac{2\mu_0 d_s}{\pi} \ln\left(1 + \frac{p-g}{g}\right) + \frac{4\mu_0 f}{\pi} \ln\left(1 + \frac{s-g}{g}\right), \end{aligned} \tag{7.32}$$

and the flux tube permeance of path 3 for the right pole face is

$$\begin{aligned} P_{3R} &= P_{3RL} + P_{3RF} + P_{3RB}, \\ &= \frac{2\mu_0 d_s}{\pi} \ln\left(1 + \frac{p-g}{g}\right) + \frac{4\mu_0 f}{\pi} \ln\left(1 + \frac{s-g}{g}\right). \end{aligned} \tag{7.33}$$

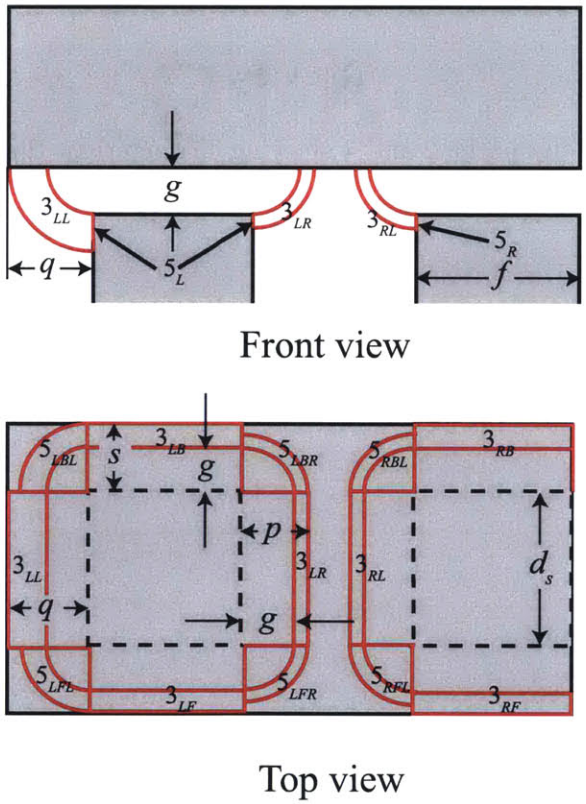

Figure 7-8: Flux paths 3 and 5 showing characteristic dimensions.

Flux path 4 reluctance

For the flux tubes associated with path 4, refer back to Figure 7-7. The only characteristic dimension associated with this flux tube is g since the mean reluctance path length and the mean reluctance path area are proportional to g and g^2, respectively. Therefore, the path 4 permeances for the left and right pole faces are, respectively,

$$P_{4L} = P_{4LBL} + P_{4LBR} + P_{4LFL} + P_{4LFR} = 4 \times 0.308\mu_0 g, \tag{7.34}$$

$$P_{4R} = P_{4RBL} + P_{4RFL} = 2 \times 0.308\mu_0 g. \tag{7.35}$$

Flux path 5 reluctance

For the flux tubes associated with path 5, refer back to Figure 7-8. For paths 5_{LBL} and 5_{LFL}, the characteristic dimensions are g and x, where $x = \min(q, s)$. In the figure, s is shown to be the smaller dimension, and so $x = s$ in this particular case. For paths 5_{LBR}, 5_{LFR}, 5_{RBL}, and 5_{RFL}, the characteristic dimensions are g and y, where $y = \min(p, s)$. In the figure, $y = p$. The path 5 permeance for the left pole face is

$$\begin{aligned} P_{5L} &= P_{5LBL} + P_{5LFL} + P_{5LBR} + P_{5LFR}, \\ &= 2 \times 0.5\mu_0(x - g) + 2 \times 0.5\mu_0(y - g), \end{aligned} \tag{7.36}$$

and the path 5 permeance for the right pole face is

$$\begin{aligned} P_{4R} &= P_{5RBL} + P_{5RFL}, \\ &= 2 \times 0.5\mu_0(y - g). \end{aligned} \tag{7.37}$$

Leakage reluctance

The only remaining reluctance to be calculated is the leakage reluctance between the left and right poles. This flux tube is shown in Figure 7-9. A typical leakage flux path is shown in the dotted blue line, while a typical flux path through flux tube 3 is shown in the dotted black line.

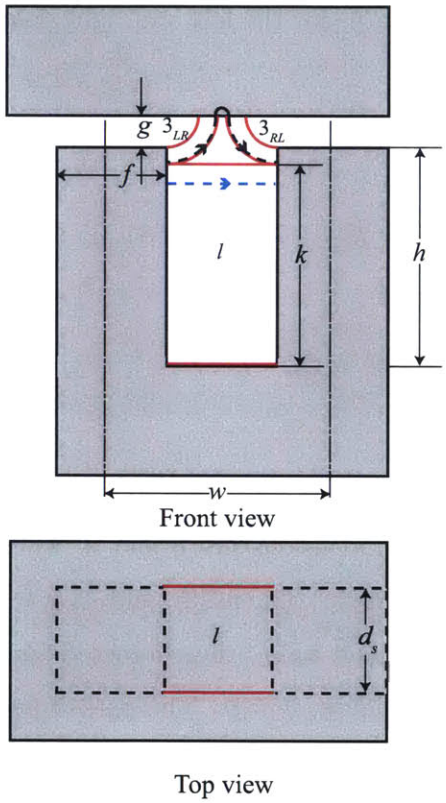

Figure 7-9: The leakage flux tube showing characteristic dimensions.

The dimension $w - f$ is the reluctance path length, and d_s and k are used to calculate the reluctance path area. The leakage reluctance is then given by

$$\mathcal{R}_l = \frac{w - f}{\mu_0 d_s k}. \tag{7.38}$$

It remains to find k. The dimension k is chosen such that the black dotted path in Figure 7-9 is equal in length to that of the blue dotted line, $w - f$, the leakage reluctance path length. The reasoning for this is that flux will want to flow through

the lowest reluctance path available. If the black dotted path is longer than $w - f$, the flux will be more likely to travel through the blue dotted path instead. If the black dotted path is shorter than $w - f$, the flux will be more likely to travel from the left pole through the left black dotted path, then through the armature, then through the right black dotted path, into the right pole. Thus, we set the length of the black dotted path (denoted l_3) equal to that of the blue dotted path (denoted l_l) to give an approximate boundary between flux tubes 3 and the leakage reluctance path,

$$l_3 = \frac{2\pi\,(g + h - k)}{4} \times 2 = w - f \;\; = \;\; l_l. \tag{7.39}$$

Solving for k yields

$$k \;\; = \;\; h - \frac{w - f}{\pi} - g. \tag{7.40}$$

Substituting this value for k into (7.38), we can write $\mathcal{R}_l$ as

$$\mathcal{R}_l = \frac{w - f}{\mu_0 d_s \left(h - \frac{w-f}{\pi} - g\right)}. \tag{7.41}$$

Now that k is determined, we can calculate p (see Figure 7-8) for (7.32) and (7.33),

$$p = h - k + g = \frac{w - f}{\pi}. \tag{7.42}$$

7.4 Solving the Magnetic Circuit via Nonlinear Network Theory

In the real magnetic circuit, the reluctances will not all be linear. That is, all reluctances associated with the core material will have nonlinear B-H characteristics. In Figure 7-3, these reluctances are $\mathcal{R}_y$, $\mathcal{R}_{pL}$, $\mathcal{R}_{PR}$, and $\mathcal{R}_a$. Consequently, if we want to capture the nonlinear behavior of the circuit, the linear network theory presented in the previous section will not suffice. Instead, we turn to a procedure outlined in [24]

called Tableau analysis. This method is capable of handling such nonlinear circuits.

We present this analysis by way of example for the circuit in Figure 7-10. This circuit is identical to that in Figure 7-3, except we have three more variables labeled: Ψ_0, the potential at the node between the source and $\mathcal{R}_y$, Φ_s, the flux associated with the flux through the MMF source, and Ψ_s, the potential drop associated with the source. As with the linear analysis, we assume only two fringing field reluctances ($\mathcal{R}_{fL}$ and $\mathcal{R}_{fR}$) for now. The analysis can be extended to incorporate additional fringing field reluctances.

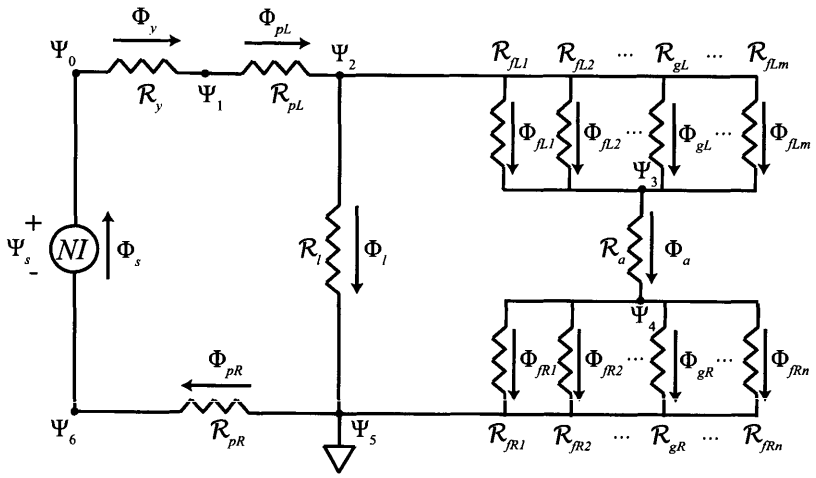

Figure 7-10: Magnetic circuit for example Tableau analysis.

The steps that comprise the Tableau analysis are as follows:

1. Write the fluxes entering and exiting each node. This is the same as Step 6 in

Section 7.2, except we must also include the flux entering and exiting node 0:

$$\begin{aligned}
\Phi_s - \Phi_y &= 0, \\
\Phi_y - \Phi_{pL} &= 0, \\
\Phi_{pL} - \Phi_l - \Phi_{fL} - \Phi_{gL} &= 0, \\
\Phi_{fL} + \Phi_{gL} - \Phi_a &= 0, \\
\Phi_a - \Phi_{fL} - \Phi_{gR} &= 0, \\
\Phi_l - \Phi_{fR} - \Phi_{gR} - \Phi_{pR} &= 0, \\
\Phi_{pR} - \Phi_y &= 0.
\end{aligned} \tag{7.43}$$

In matrix form, after eliminating the equation associated with node 5, we write

$$\begin{bmatrix}
1 & -1 & 0 & 0 & 0 & 0 & 0 & 0 & 0 & 0 \\
0 & 1 & -1 & 0 & 0 & 0 & 0 & 0 & 0 & 0 \\
0 & 0 & 1 & -1 & -1 & -1 & 0 & 0 & 0 & 0 \\
0 & 0 & 0 & 0 & 1 & 1 & -1 & 0 & 0 & 0 \\
0 & 0 & 0 & 0 & 0 & 0 & 1 & -1 & -1 & 0 \\
-1 & 0 & 0 & 0 & 0 & 0 & 0 & 0 & 0 & 1
\end{bmatrix}
\begin{bmatrix}
\Phi_y \\ \Phi_{pL} \\ \Phi_l \\ \Phi_{fL} \\ \Phi_{gL} \\ \Phi_a \\ \Phi_{fR} \\ \Phi_{gR} \\ \Phi_{pR}
\end{bmatrix}
=
\begin{bmatrix}
0 \\ 0 \\ 0 \\ 0 \\ 0 \\ 0
\end{bmatrix}. \tag{7.44}$$

In matrix notation, this is equivalent to

$$\mathbf{A}^T \mathbf{\Phi} = \mathbf{0}. \tag{7.45}$$

Note that $\mathbf{A}$ here is not identical to $\mathbf{A}$ in the linear analysis: $\mathbf{A}$ in the nonlinear analysis has an additional column corresponding to node 0.

2. Write the MMF drop across each reluctance as a function of node MMF's. This

is analogous to Steps 1 and 2 in the linear analysis:

$$\begin{aligned}
\Psi_s &= \Psi_6 - \Psi_0, \\
\Psi_y &= \Psi_0 - \Psi_1, \\
\Psi_{pL} &= \Psi_1 - \Psi_2, \\
\Psi_l &= \Psi_2 - \Psi_5, \\
\Psi_{fL} &= \Psi_2 - \Psi_3, \\
\Psi_{gL} &= \Psi_2 - \Psi_3, \\
\Psi_a &= \Psi_3 - \Psi_4, \\
\Psi_{fR} &= \Psi_4 - \Psi_5, \\
\Psi_{gR} &= \Psi_4 - \Psi_5, \\
\Psi_{pR} &= \Psi_5 - \Psi_6.
\end{aligned} \tag{7.46}$$

In matrix form, after the column associated with node 5 has been eliminated, we write

$$\begin{bmatrix} \Psi_s \\ \Psi_y \\ \Psi_{pL} \\ \Psi_l \\ \Psi_{fL} \\ \Psi_{gL} \\ \Psi_a \\ \Psi_{fR} \\ \Psi_{gR} \\ \Psi_{pR} \end{bmatrix} + \begin{bmatrix} 1 & 0 & 0 & 0 & 0 & -1 \\ -1 & 1 & 0 & 0 & 0 & 0 \\ 0 & -1 & 1 & 0 & 0 & 0 \\ 0 & 0 & -1 & 0 & 0 & 0 \\ 0 & 0 & -1 & 1 & 0 & 0 \\ 0 & 0 & -1 & 1 & 0 & 0 \\ 0 & 0 & 0 & -1 & 1 & 0 \\ 0 & 0 & 0 & 0 & -1 & 0 \\ 0 & 0 & 0 & 0 & -1 & 0 \\ 0 & 0 & 0 & 0 & 0 & 1 \end{bmatrix} \begin{bmatrix} \Psi_0 \\ \Psi_1 \\ \Psi_2 \\ \Psi_3 \\ \Psi_4 \\ \Psi_5 \\ \Psi_6 \end{bmatrix} = \begin{bmatrix} 0 \\ 0 \\ 0 \\ 0 \\ 0 \\ 0 \\ 0 \\ 0 \\ 0 \\ 0 \end{bmatrix}. \tag{7.47}$$

In matrix notation, we write

$$\boldsymbol{\Psi}_r + \mathbf{A}\boldsymbol{\Psi} = \mathbf{0}. \tag{7.48}$$

Here also, $\mathbf{\Psi}_r$ and $\mathbf{\Psi}$ are not identical to the similarly-named vectors in the linear analysis: in the nonlinear analysis, these vectors include the elements Ψ_s and Ψ_0, respectively, which are absent from the linear analysis.

3. Write the constitutive relations for each reluctance and for each MMF or flux source. This is similar to Step 4 in the linear analysis, except we include sources as well as reluctances.

   The nonlinear reluctances are characterized by the B-H relationship of the ferromagnetic material. In order to manipulate the B-H relationships to involve the circuit variables, Ψ_i and Φ_i[5], we note first that Ψ_i is related to H_i by $\Psi_i = H_i l_i$, where l_i is the length of the reluctance path of interest. We also note that Φ_i is related to B_i by $\Phi_i = B_i A_i$, where A_i is the cross-sectional area of the reluctance path of interest. Writing the B-H relationship as $B(H)$, we can then express the general form of the constitutive relation for a nonlinear reluctance as

$$\Phi_i = A_i B_i = B\left(H_i\right) = B\left(\frac{\Psi_i}{l_i}\right), \tag{7.49}$$

   where $B(\Psi_i/l_i)$ denotes the B-H relationship in terms of Ψ_i. The exact B-H relationship will depend on the particular ferromagnetic material used in the actuator. It can include hysteresis; however, for the simulation results presented later in this chapter, we use a nonlinear function that includes saturation but does not include hysteresis.

   For each constitutive relationship, we subtract the quantity on the right-hand side from both sides so that the resulting quantity on the left-hand side is equal to zero. The parameters A_y, A_{pL}, A_a, and A_{pR} are the cross-sectional areas associated with the core material reluctances. For our magnetic circuit, we

[5]The subscript i is a generic notation meant to signify any of the core material reluctance subscripts.

then write the constitutive relations as

$$
\begin{aligned}
&f_1(\Psi_s) = \Psi_s + NI = 0,\\
&f_2(\Psi_y, \Phi_y) = \Phi_y - A_y B\left(\frac{\Psi_y}{w}\right) = 0,\\
&f_3(\Psi_{pL}, \Phi_{pL}) = \Phi_{pL} - A_{pL} B\left(\frac{\Psi_{pL}}{h}\right) = 0,\\
&f_4(\Psi_l, \Phi_l) = \Psi_l - R_l \Phi_l = 0,\\
&f_5(\Psi_{fL}, \Phi_{fL}) = \Psi_{fL} - R_{fL}\Phi_{fL} = 0,\\
&f_6(\Psi_{gL}, \Psi_{gL}) = \Psi_{gL} - R_{gL}\Phi_{gL} = 0,\\
&f_7(\Psi_a, \Phi_a) = \Phi_a - A_a B\left(\frac{\Psi_a}{w}\right) = 0,\\
&f_8(\Psi_{fR}, \Phi_{fR}) = \Psi_{fR} - R_{fR}\Phi_{fR} = 0,\\
&f_9(\Psi_{gR}, \Phi_{gR}) = \Psi_{gR} - R_{gR}\Phi_{gR} = 0,\\
&f_{10}(\Psi_{pR}, \Phi_{pR}) = \Phi_{pR} - A_{pR} B\left(\frac{\Psi_{pR}}{h}\right) = 0.
\end{aligned}
\tag{7.50}
$$

4. We now have a system of nonlinear equations in the Tableau form, taken from (7.45),(7.48), and (7.50), written in matrix notation as

$$
\begin{aligned}
\mathbf{A}^T\boldsymbol{\Phi} &= \mathbf{0}\\
\boldsymbol{\Psi}_r - \mathbf{A}\boldsymbol{\Psi} &= \mathbf{0}\\
\mathbf{f}(\boldsymbol{\Psi}_r, \boldsymbol{\Phi}) &= \mathbf{0}.
\end{aligned}
\tag{7.51}
$$

This system consists of $(n-1)+2b$ nonlinear algebraic equations in $(n-1)+2b$ variables, where n is the number of nodes in the circuit and b is the number of branches in the circuit (one branch for each reluctance element and source element). We can solve this system of nonlinear equations using MATLAB's command 'fsolve' for instance.

7.5 Magnetic Circuit Simulations

In this section, we present simulation results using both the linear magnetic circuit and the nonlinear magnetic circuit. We also present simulation results using Finite Element Analysis (FEA). We compare the simulated actuator force to the experimentally measured force in lab. Matlab scripts were written to run the linear magnetic circuit simulations. For the nonlinear magnetic circuit simulations, we used a Matlab script initially and then switched to using Spice, a circuit simulation software.

7.5.1 Experimental Setup

To measure the actuator force, we used the test fixture shown in Figure 7-11. This test fixture was designed and built by Tony Poovey. More details on its design can be found in Poovey's Master's thesis [71]. The test fixture consists of a platen mounted on three load cells with kinematic mounts. An electromagnetic target is bolted to the underside of the platen. The load cells are mounted to three micrometers. These micrometers are used to set the air gap. Three capacitance probes measure the gap. Inside the test fixture cavity is an electromagnet stator that generates a force on the platen. Using this fixture, we can map the force-gap-current relationship for the actuator. The kinematic mounts are silicon-carbide and the force is measured by quartz load cells, which provide for a high-stiffness force loop. The first mechanical resonance of the structure is above of 1 kHz. A sample electromagnetic actuator that can be used with the test fixture is shown in Figure 7-12. The particular actuator shown has a silicon-iron core.

7.5.2 Linear Simulations

Figure 7-13 shows the experimentally measured force compared to the simulated force for a 50 µm gap, where we used the linear magnetic circuit to simulate the actuator. The linear simulation was run by increasing current until the flux density in the core reached its saturation value. The simulation shows a good fit at low currents, but departs from the measured data at high currents. A nonlinear simulation is needed

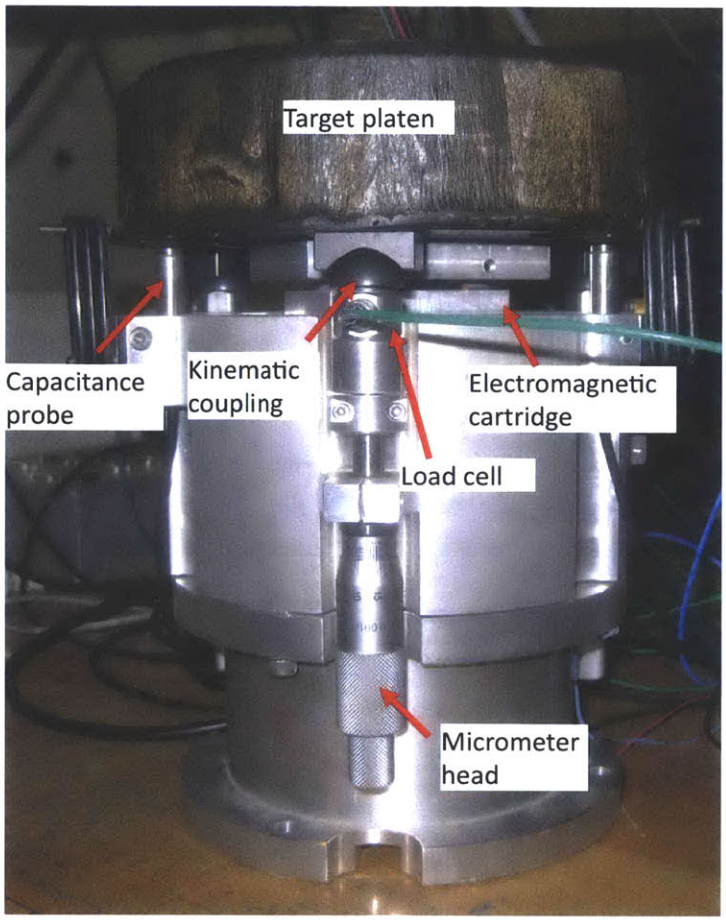

Figure 7-11: Test fixture for measuring electromagnetic actuator characteristics.

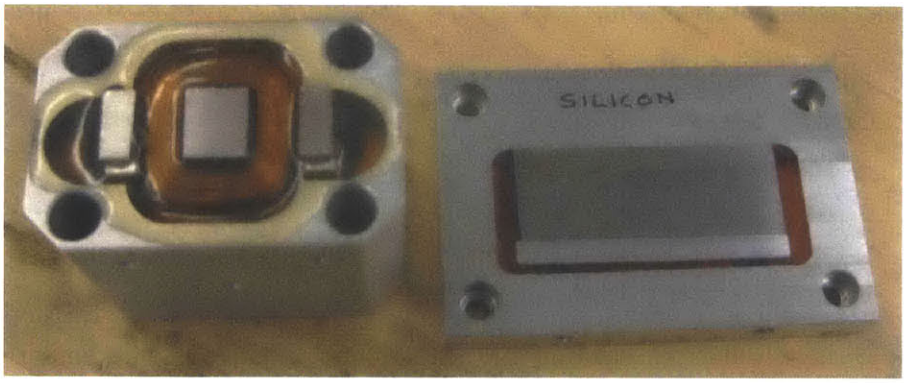

Figure 7-12: Sample electromagnet for testing.

to model the high-current behavior. For comparison, we also show a simulation that did not include the force contributions from fringing fields. We see that at a 50 µm

gap, the fringing fields have very little influence.

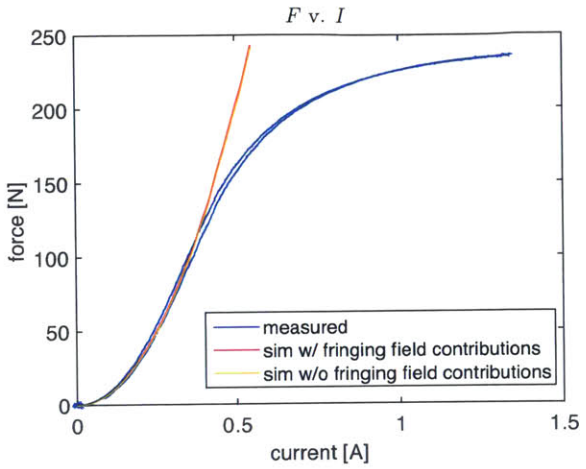

Figure 7-13: Simulated and measured force at 50 µm gap. Linear magnetic circuit used for simulation.

Figure 7-14 shows the experimentally measured force compared to the simulated force for a 450 µm gap. The power amplifier used in the experiments was only capable of providing up to 1.3 A, so force data up to saturation was not available. The simulated force does not fit quite as well with the measured force as it did at the 50 µm gap. This may be because the leakage flux dominates more at the larger gaps, so we may need to use a more spatially-distributed MMF source and multiple leakage reluctances to capture the leakage flux behavior more accurately. Moreover, the fringing fields dominate more at larger air gaps, so any inaccuracies in the flux tubes will have a more pronounced effect. However, we see that at this larger gap, including the fringing field contributions to the force generates a noticeably better fit than not including them.

7.5.3 Nonlinear Simulations

To provide a better model fit at high current levels, a nonlinear saturation model for the permeable material reluctances was developed. *B-H* measurements from a 50-50% NiFe toroidal core with tape-wound laminations of 50 µm thickness were used to create an empirically-based model. Figure 7-15 shows the measured data. The data

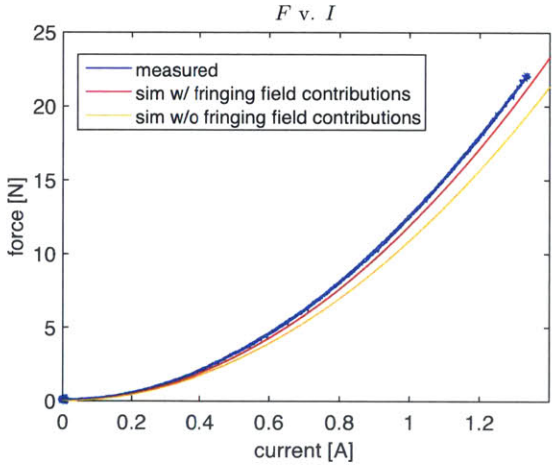

Figure 7-14: Simulated and measured force at 450 µm gap. Linear magnetic circuit used for simulation.

was obtained by exciting the drive coil with a 1 Hz voltage sine wave and measuring the current through the drive coil (proportional to H) and measuring the voltage on a secondary coil (proportional to dB/dt) and integrating it.

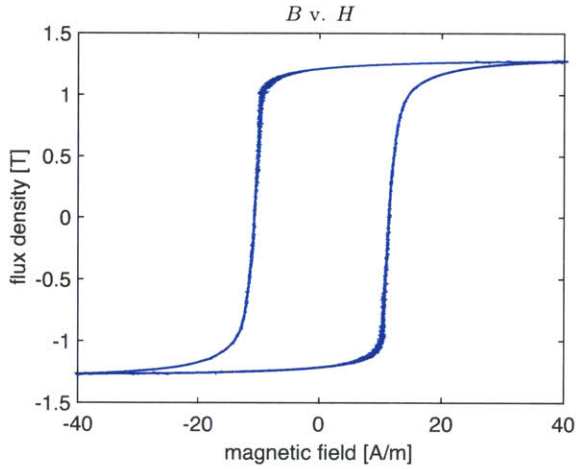

Figure 7-15: Experimentally measured B-H data for a 50-50% NiFe toroidal core.

Two vectors were created from the measured B-H data, one to represent the H data, and the other to represent the corresponding B data. These vectors represent the $B(H)$ function of the core material. Since we did not consider hysteresis nonlinearities in our magnetic circuit model at this point, we took an average between the two branches of the major B-H loop. The result of this method is shown graphically

in Figure 7-16.

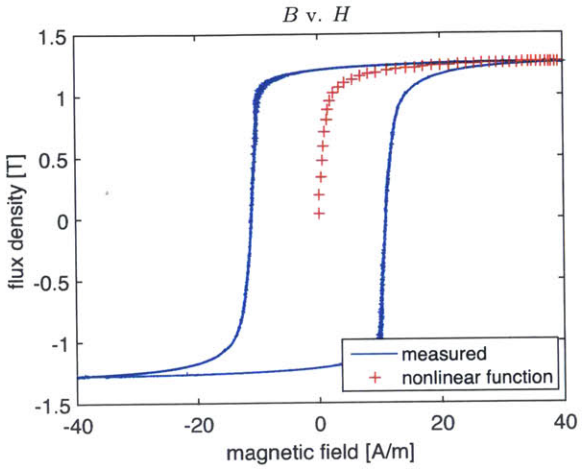

Figure 7-16: Single-valued B-H function (red) computed from measured B-H (blue).

This single-valued $B(H)$ function was then applied to all the core material reluctances in our magnetic circuit model, namely, $\mathcal{R}_{pL}$, $\mathcal{R}_{pR}$, $\mathcal{R}_y$, and $\mathcal{R}_a$. This results in a system of nonlinear equations as described in Section 7.4. Once this system of nonlinear equations is set up, a nonlinear solver, such as MATLAB's 'fsolve' command, is used to solve the circuit for a given current input (NI) trajectory.

Figure 7-17 shows a nonlinear simulation compared with measured data for a 50 µm gap. The simulation still does not accurately capture the actuator behavior at high currents. To rectify this situation, we posited that a more complex circuit network with additional reluctances and a distributed MMF source may be needed. Such a network with these additional elements will be better able to capture the fact that certain parts of the core will saturate earlier than others, which may lead to a more gradual transition to saturation as seen in the measured data.

7.5.4 Nonlinear Simulations with Additional Lumped-parameter Elements

In an effort to improve the accuracy of the magnetic circuit simulation, we augmented the magnetic circuit with additional elements. The modified circuit is shown in Fig-

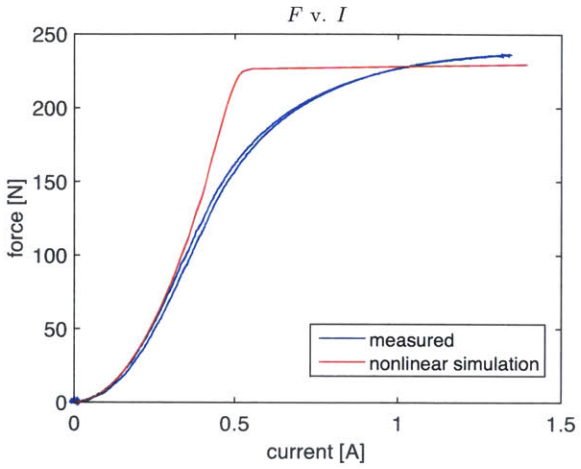

Figure 7-17: Simulated and measured force at 50 µm gap. Simulated force includes nonlinear core reluctance elements.

ure 7-18. We now have two MMF sources with the total amp-turns split evenly between the two. This better reflects the fact that the MMF from the actuator core is spatially distributed. We have also split the leakage reluctance into two separate reluctances. This is intended to capture the phenomenon that leakage flux will be concentrated near the bottom of the coil window because the MMF drop across the coil window is greater here.

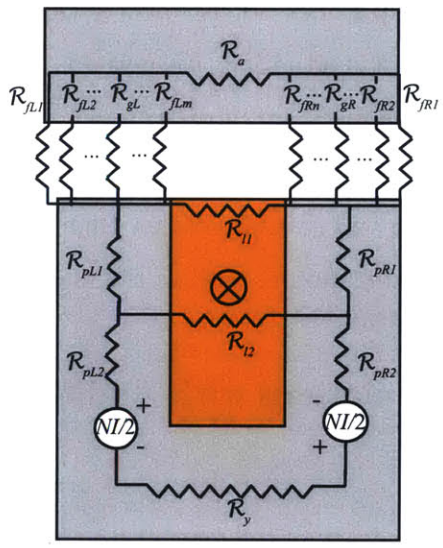

Figure 7-18: Augmented magnetic circuit.

For simulations with the modified circuit, we used the circuit software SPICE. Figure 7-19 shows a nonlinear simulation of the augmented circuit compared to measured data for a 50 µm gap. We have also included the nonlinear simulation using the original circuit. We see very little difference between the two simulations. The additional circuit elements did not seem to help much. As we will discuss later in this section, it turned out that the reason for the discrepancy is because the actuator core material was not identical to the toroid core material from which we obtained the B-H data for our magnetic circuit model.

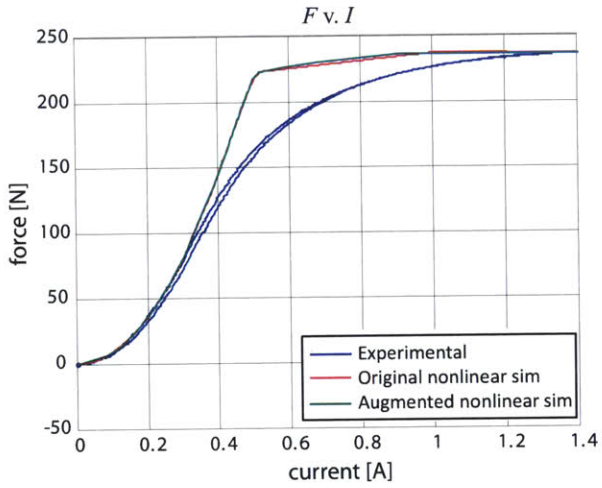

Figure 7-19: Simulated and measured force at 50 µm gap. Augmented nonlinear simulation (green) uses additional lumped parameters in model.

7.5.5 Nonlinear Simulations Using Finite Element Analysis

Since we seemed to be reaching the point of diminishing returns by adding more lumped parameter elements to the nonlinear magnetic circuit (the material discrepancy had not been discovered at this point), we switched our efforts to finite element modeling of the actuator. We used COMSOL Multyphysics software [28] for this analysis. COMSOL permits the user to enter nonlinear B-H functions for the material properties. Figure 7-20 shows a 2-D FEA model of the actuator under test. We used the data from Figure 7-16 for the material B-H relationship.

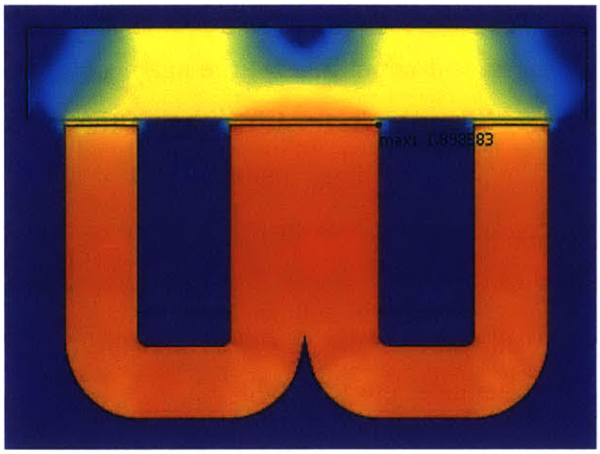

Figure 7-20: COMSOL FEA model of actuator.

Figure 7-21 shows the FEA simulated B-I curve compared to measured data for a 50 µm gap. We see a similar divergence of the simulated data from the measured data that we saw with the nonlinear magnetic circuit simulations. We also note that at saturation, the FEA had difficulty solving the model. As we discuss in the next subsection, the reason for this is because of the material discrepancy.

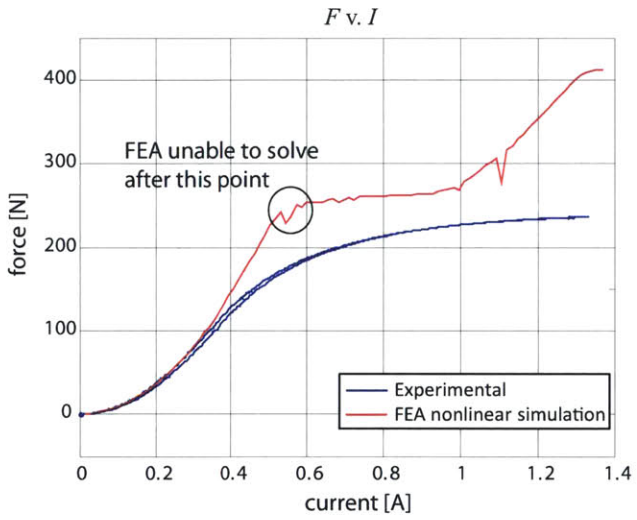

Figure 7-21: FEA simulation and measured force for 50% NiFe at 50 µm gap.

7.5.6 Finite Elemenent Analysis of 49% NiFe

We later discovered that the actuators we had been testing used 49% NiFe cores rather than 50% NiFe cores [58]. In our simulation models, we had used data from a 50% NiFe core. It turns out that there is a significant divergence between the two materials at higher magnetic fields: 50% NiFe has a much steeper B-H curve than 49% NiFe. We then measured the B-H curve on a 49% NiFe sample with laminations of 25 µm thickness. The sample is shown in Figure 7-22. The measured B-H curve is shown in Figure 7-23.

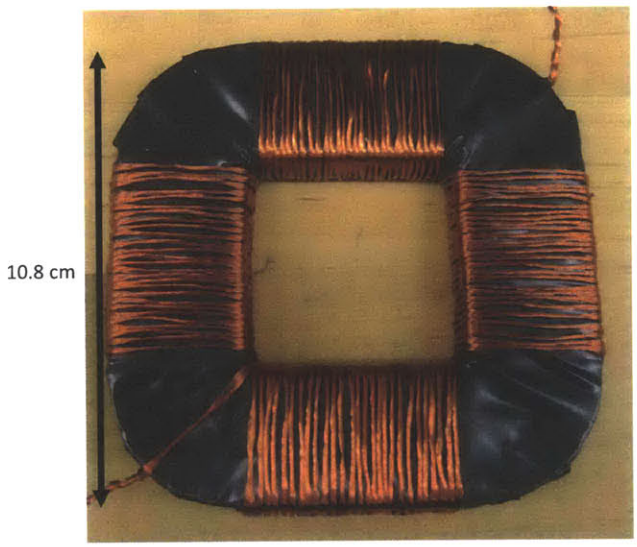

Figure 7-22: 49% NiFe sample used to measure B-H curve.

If we compare this graph to the 50% NiFe B-H curve from Figure 7-16, we see that B-H curve from the latter transitions to saturation much more rapidly. This is confirmed by B-H data from Vacuumschmelze [15], replotted below on a log-log plot. While the 49% NiFe has higher initial permeability, 50% NiFe has a steeper transition to saturation and reaches saturation first. Because of this, using 50% NiFe for the actuator cores could result in a more efficient actuator. However, because of the accuracy requirements of the lithography application, 49% NiFe is likely to be the better option for our purposes because the gentler transition to saturation will be easier to manage. Moreover, as we discuss in Chapter 9, eddy currents affect 50%

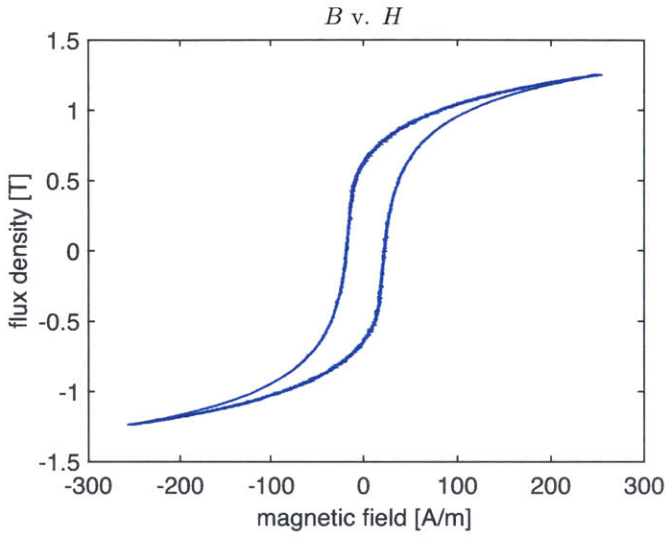

Figure 7-23: Experimentally measured B-H data for a 49% NiFe toroidal core.

NiFe at very low frequencies, complicating actuator linearization further. The 50% NiFe is typically used for switching applications rather than for actuator applications.

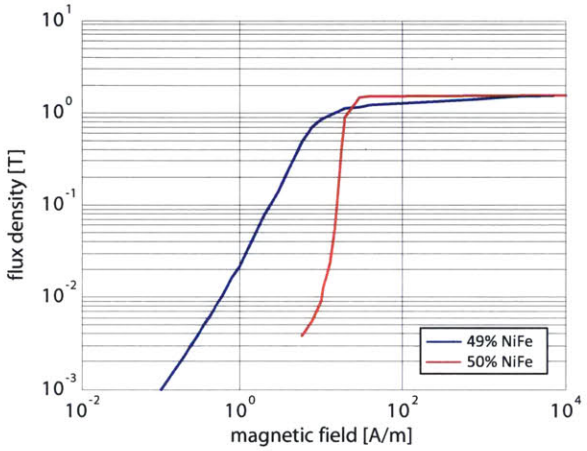

Figure 7-24: B-H data from Vacuumschmelze for 49% NiFe and 50% NiFe.

We used COMSOL software to run a 2-D FEA of the actuator, now using the nonlinear B-H data for 49% NiFe. Figure 7-25 shows the FEA simulated force of the actuator under test compared to measured data for a 50 µm gap. We see that the fit is much better than the magnetic circuit simulations that used 50% NiFe data.

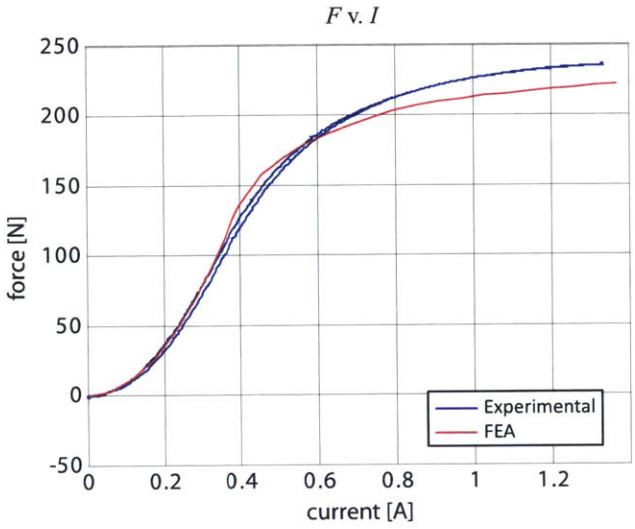

Figure 7-25: FEA and measured force at 50 µm gap. Simulated force used 49% NiFe *B-H* data.

7.6 Summary

We developed linear and nonlinear magnetic circuit techniques to model a reluctance actuator. We simulated these models and compared them to experimental measurements on an NiFe actuator we tested in lab. We also modeled the actuator using FEA. The models showed good agreement at low current levels but divergence at high current levels. This was because we had been simulating 50% NiFe while the actuators that were tested were 49% NiFe. From testing toroidal samples of the two materials, we learned that while the saturation flux density between the two materials is similar, there is a significant divergence between the two in how rapidly they transition to saturation. The FEA simulation showed much better agreement once we changed the material properties to those of 49% NiFe. We concluded that 49% NiFe is likely better for our actuator prototype.

In the nonlinear magnetic circuit simulations, the nonlinear elements representing the core reluctances were represented by single-valued functions. These reluctances could be replaced by hysteretic elements using the models developed in Chapter 3, but this has not been addressed in this thesis. This would allow the magnetic circuit model to capture the hysteretic behavior of the actuator.

We can adapt the magnetic circuit techniques developed in this chapter as a design tool used to size actuators. In the next chapter, we present a design for a 1-DoF testbed for testing reluctance actuators. We use the models presented in this chapter to size the reluctance actuator prototype.

Chapter 8

One-DoF Reluctance Actuator Testbed Design

In this chapter, we present the design of a 1-DoF testbed for testing a reluctance actuator prototype with flux feedback control. The testbed includes a moving mass on an air bearing setup and a high-resolution linear encoder for position sensing and control. Load cells provide a force measurement of the actuator. The reluctance actuator incorporates a sense coil for flux sensing and control.

We first present several alternative concepts we considered for testing reluctance actuator force accuracy. We then give an overview of the design of the 1-DoF testbed. Finally, we present the detailed design of a reluctance actuator prototype for use with the testbed.

8.1 Design Requirements

We require a design that can measure the force accuracy of a reluctance actuator prototype when a dynamic force profile is applied. We also require that we can change the actuator air gap dynamically so that we can evaluate the force accuracy of the reluctance actuator in the presence of a gap disturbance. Finally, we require a design that permits us to test the accuracy of our hysteresis models and flux control schemes. The following is a list of components and capabilities for the testbed needed

to satisfy these high-level requirements:

- Actuator force measurement
- Dynamic motion capability
- Position measurement
- Actuator flux measurement
- Actuator current measurement
- Real-time operating system for control
- Amplifiers to drive actuators

8.2 One-DoF Testbed Concepts

We present in this section several general concepts for testing the reluctance actuator force accuracy. We focused on 1-DoF designs. This constrains the design space and permits for relatively fast turnaround for the design and assembly phases. Thus, this actuator testbed cannot be used to explore effects of rotation, which will be relevant to the 6-DoF levitation case. While investigating off-axis effects is critically important for scanning lithography, the focus of this thesis is on modeling and control of the drive axis. Roberto Meléndez has investigated off-axis behavior of the reluctance actuator in his thesis [62].

For the main motion stage, we focused on concepts that used a linear air bearing. The reason for this is that an air bearing closely approximates the near-zero stiffness in the scan axis of the magnetically-levitated short-stroke stage in a lithography machine. This allows us to isolate the stiffness of the reluctance actuator from other sources of stiffness. Linear roller guides have friction and also exhibit non-zero stiffness for small motions. Flexures stages also have non-zero stiffness. Another reason for focusing on air bearing designs is that we had a linear air bearing in lab that we could adapt to our design requirements.

8.2.1 Differential-mode Actuation Configuration

Figure 8-1 is a 1-DoF testbed concept in which the moving mass is actuated differentially. The idea is that a common-mode force can be applied to the actuator on either side of the payload, thereby nulling the net force on the payload. The advantage of such a configuration is that we can utilize the full range of the reluctance actuator force capability without the actuated mass accelerating and traveling long distances. Since the payload will remain nominally at the same position, this obviates the need for a long-stroke stage. The position deviation from zero can be used to measure the force accuracy of the reluctance actuator. Load cells are mounted on the stator side of the actuators for force measurement. Locating them on the stator side avoids measurement errors resulting from acceleration of the payload. (Note we assume zero acceleration of the support structure.) A linear encoder is included on the air bearing payload for metrology. One actuator can be used to generate a gap disturbance while the other tries to maintain the desired force accuracy. One downside of this concept is that force control and position control cannot be maintained simultaneously using the same actuator if we want to apply a gap disturbance.

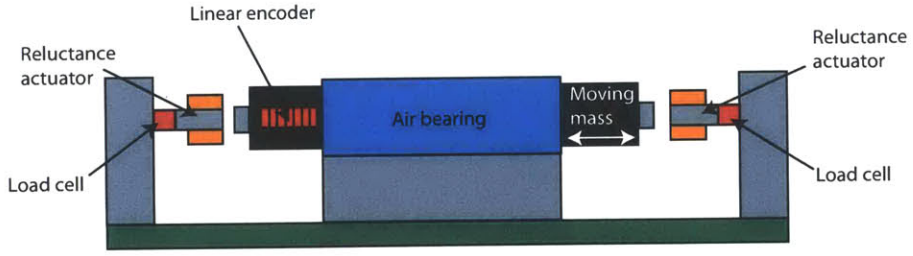

Figure 8-1: Testbed concept with differential-mode actuation.

8.2.2 Differential-mode Actuation Configuration with Gap Disturbance Stage

Figure 8-2 shows one of the reluctance actuator stators mounted on its own stage. This allows a gap disturbance to be directly applied to the stator, and in this way it emulates the long-stroke stage. This configuration is more true to the scanning system as now the reluctance actuator can be used for positioning control of the air bearing payload even while a gap disturbance is being applied to it.

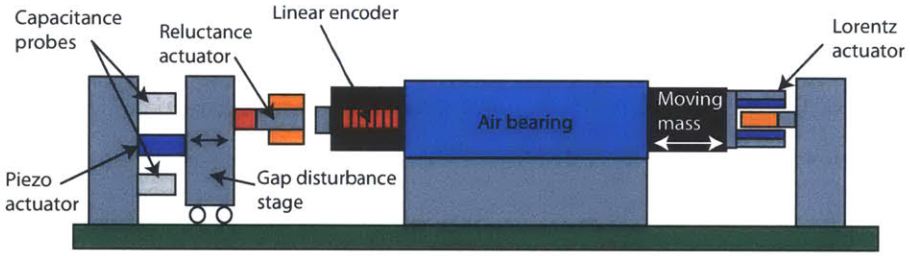

Figure 8-2: Testbed concept with differential-mode actuation and gap disturbance stage.

The gap disturbance stage actuator is shown as a piezo actuator. An advantage of a piezo stage is that piezo actuators are capable of high force and high stiffness and can therefore overcome the reaction force from the reluctance actuator stator. Other actuators are also possible, however. Gap metrology is shown being provided by capacitance probes. The gap disturbance stage can be mounted on linear guides for instance, since low friction and low stiffness are not as critical for the gap disturbance stage. Other possibilities include a flexure stage or another air bearing stage.

A modification of this idea is to use multiple piezo actuators to provide not only a gap disturbance but disturbances in other degrees of freedom as well. This would permit us to investigate the off-axis behavior of the reluctance actuator.

One downside of adding a gap disturbance stage is that now there is no direct way to measure the force of the reluctance actuator, since load cells mounted to the

stator will be affected by the gap disturbance stage acceleration. To rectify this, the other end of the air bearing slide is shown with a Lorentz actuator attached. When the air bearing slide is operated in nulling mode, the Lorentz actuator can provide another force measurement, since the Lorentz actuator current is proportional to the force applied by the actuator, assuming that the central mass is not moving.

8.2.3 Long-stroke Stage Configuration

Another potential configuration uses a long-stroke stage instead of a differential-mode configuration. Such a concept is shown in Figure 8-3. The main advantage here is that we can now command both the desired force profile to the reluctance actuator and the desired position profile. Since demonstrating accurate servo performance is the ultimate goal of using reluctance actuation for scanning lithography, this concept provides greater capabilities for testing the reluctance actuator. The primary downside is much greater complexity, cost, and testbed size requirements. A larger area is needed for the testbed since now the stage will be traveling large distances when the forces are applied. Another downside is that the large accelerations will introduce large reaction forces into the force frame. This is why a large reaction mass is shown in the concept. A drift motor is included to keep the position of the reaction mass centered. This reaction mass and drift motor increase the design complexity further.

8.3 Testbed Design

Ultimately, we chose the differential-mode configuration. It is the simplest configuration that still permits us to test the reluctance actuator force accuracy in the presence of a gap disturbance.

A CAD model of the testbed is shown in Figure 8-4 with a reluctance actuator on one end of the air bearing and a voice coil actuator (Lorentz actuator) on the other end of the air bearing. A photograph of the completed assembly is shown in Figure 8-5. We designed the testbed such that we could interchange a reluctance actuator with a voice coil actuator if so desired. The design of the testbed was a

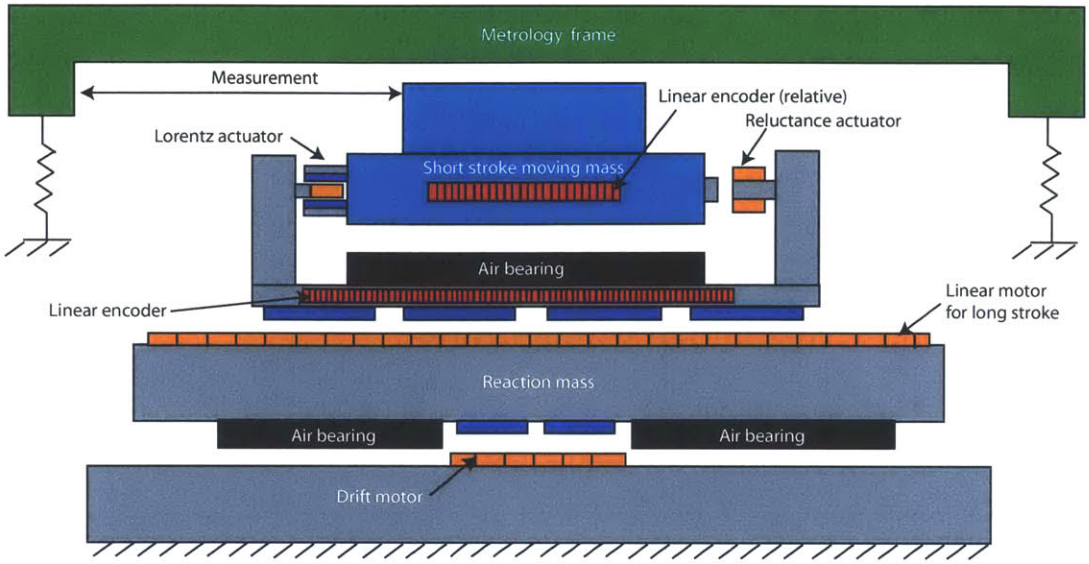

Figure 8-3: Testbed concept with long-stroke stage.

collaboration with Darya Amin-Shahidi. Many of the design details can be found in his thesis [4]. We here give a general overview of the design.

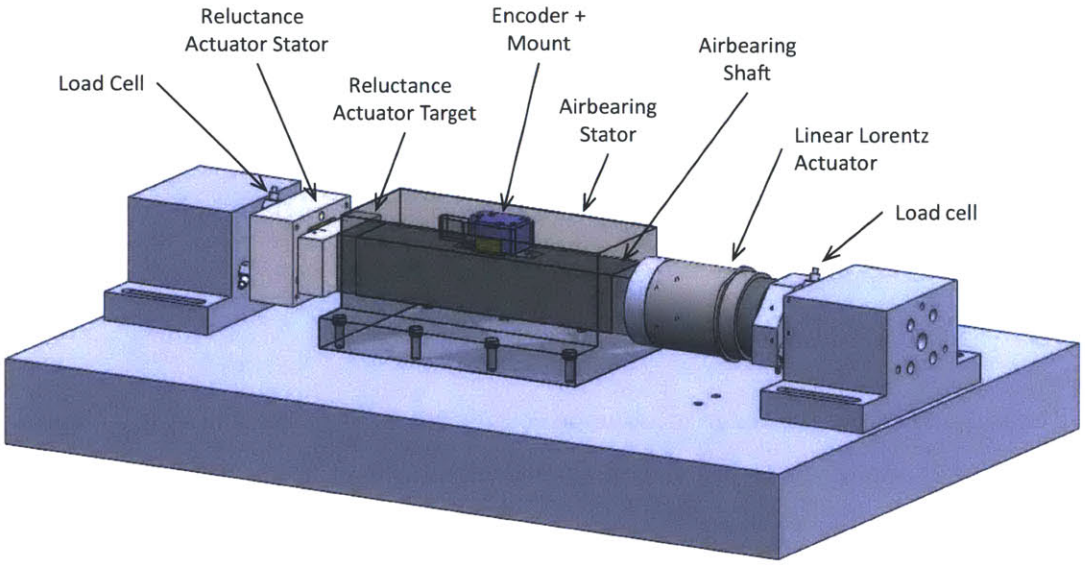

Figure 8-4: CAD model of 1-DoF testbed.

Figure 8-6 shows a cross-sectional view of the CAD model of the testbed. The testbed motion stage uses a linear air bearing from New Way [65]. Metrology is provided by a high-resolution linear encoder that we had custom-made by Sony [78]

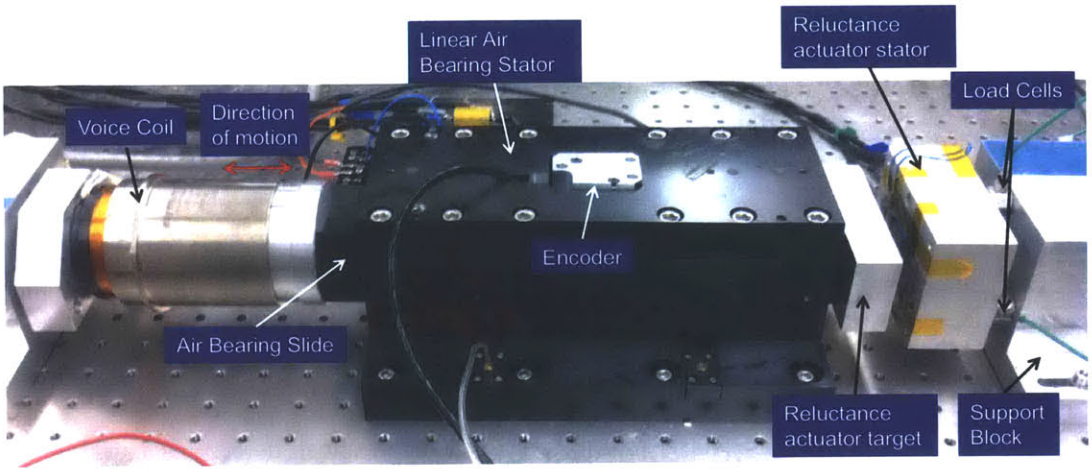

Figure 8-5: Photograph of 1-DoF testbed.

to fit with our air bearing. It is adapted from their BH20 model to use a short scale with a 7 mm length and with 1 µm grating pitch. It is capable of 0.25 nm resolution at 1000-times interpolation. The scale is mounted to the air bearing slide, and the encoder read head is mounted to the air bearing stator. In order for the air bearing to accommodate the encoder, we had to modify the air bearing. For details of these modifications, see [4].

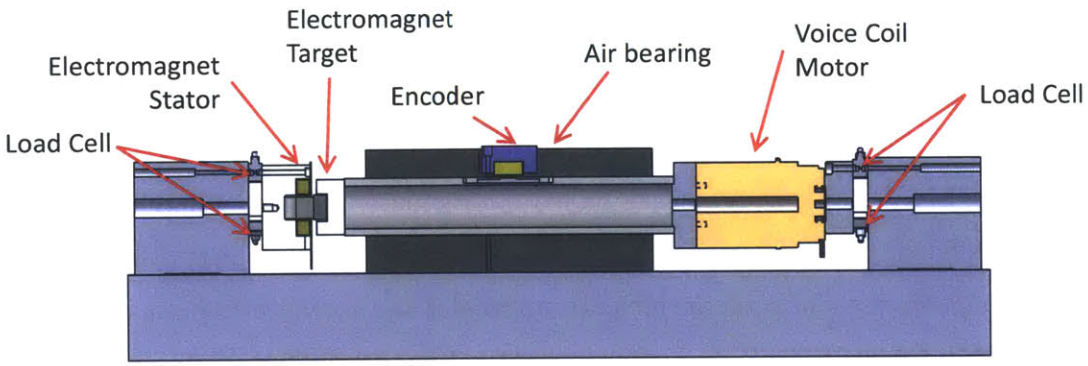

Figure 8-6: CAD model of cross-sectional view of 1-DoF testbed.

A reluctance actuator target is bolted to one side of the air bearing slide. The reluctance actuator stator is connected by three Kistler 9212 load cells [52] to the support block in the stationary frame. These load cells provide high-stiffness force measurements of the actuator force. However, because they are quartz piezo load

cells, they are AC-coupled and cannot measure a true static force. The three load cell outputs are tied together and input to a single Kistler 5010 charge amplifier. In this way, we obtain a sum of the three load cell charge outputs, proportional to the total actuator force.

On the other end of the air bearing is shown a voice coil linear actuator. This provides the nulling force that opposes the reluctance actuator force. It can also be used to generate a gap disturbance to the stage. The voice coil actuator is a BEI Kimco model LA30-46-000A [10]. Its specification sheet lists it as capable of generating a peak force of 445 N at 12.7 A. One reason a voice coil actuator was chosen is because the current is close to linear with the force generated. If we measure the voice coil current accurately, this gives us an estimate of the force. If the air bearing armature can be approximated as a pure mass, which is valid for low frequencies, the voice coil actuator gives us another measure of the reluctance actuator force when the position is nulled. Unlike the load cells, the voice coil can also give us a DC measurement of force.

Figure 8-7 shows a system diagram of the testbed. The encoder signal is sent to the interpolator and then brought into the dSPACE real-time controller (RTC) [35] via the digital I/O ports. The charge amplifier output for the load cells is brought into the RTC via an A/D input. The RTC sends a voltage drive signal to the power amplifier via dSPACE's D/A outputs to drive the actuators. Different amplifiers were used at different phases of testing. Kepco bipolar operational amplifiers (Model BOP 36-12) [50] were used for both the reluctance actuator and the voice coil actuator when the testbed setup was in Wilton, CT at ASML. When the setup was brought back to MIT, both actuators were driven with a dual-channel Crown DC300A amplifier [29]. Sense resistors are used to measure the actuator currents. These signals are sent to Tektronix AMD502 differential amplifier channels [80] to reduce common-mode noise before being passed into the dSPACE RTC. The signal from a sense coil on the reluctance actuator for estimating magnetic flux is sent to a separate AMD502 before being sent to the RTC.

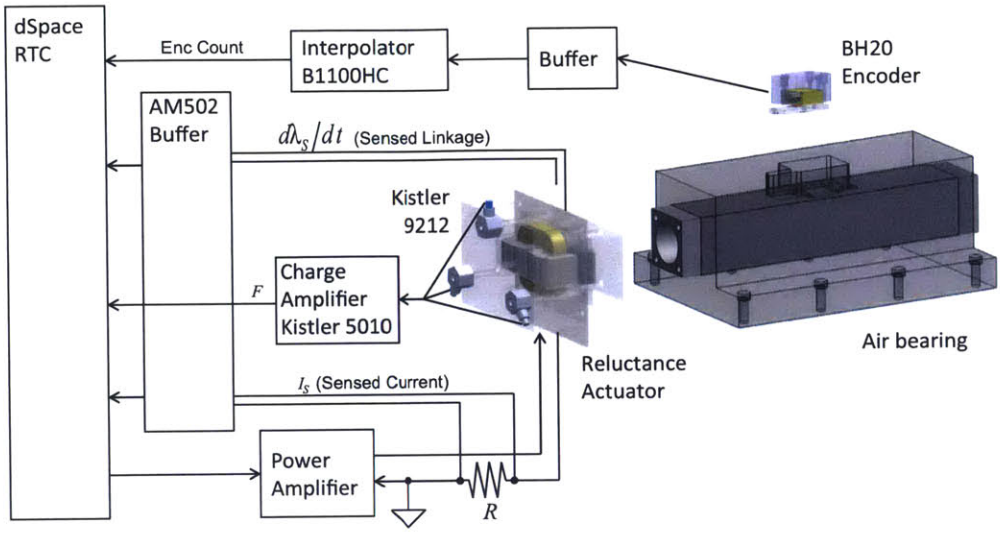

Figure 8-7: Testbed system diagram.

8.4 Reluctance Actuator Prototype Design

A photograph of the reluctance actuator prototype stator is shown in Figure 8-8. The reluctance actuator prototype was designed to be a scaled version of a full-size actuator. Each actuator designed for a lithography machine requires ~1500 N maximum force (assuming two actuators per side for the short-stroke stage). We designed our prototype to have a maximum force capability of roughly 25% of this, or about 300-400 N. This decision was made for several reasons. First, the voice coil actuator required can be much smaller; this adds less weight to the assembly and takes up less space. Second, the cut cores used for the reluctance actuator are generally less expensive if they are smaller. Finally, power management and amplifier selection are much more feasible when we do not have to worry about large voltages and currents resulting from high-force and high-inductance actuators.

We chose to design a three-pole actuator with a single actuator coil wound around the center pole face. One advantage of a three-pole actuator over a two-pole actuator is that only a single actuator coil is needed. A two-pole actuator normally would require two coils for the purposes of symmetry. However, a real device should probably use a two-pole actuator because it is less liable to parasitic moments (see

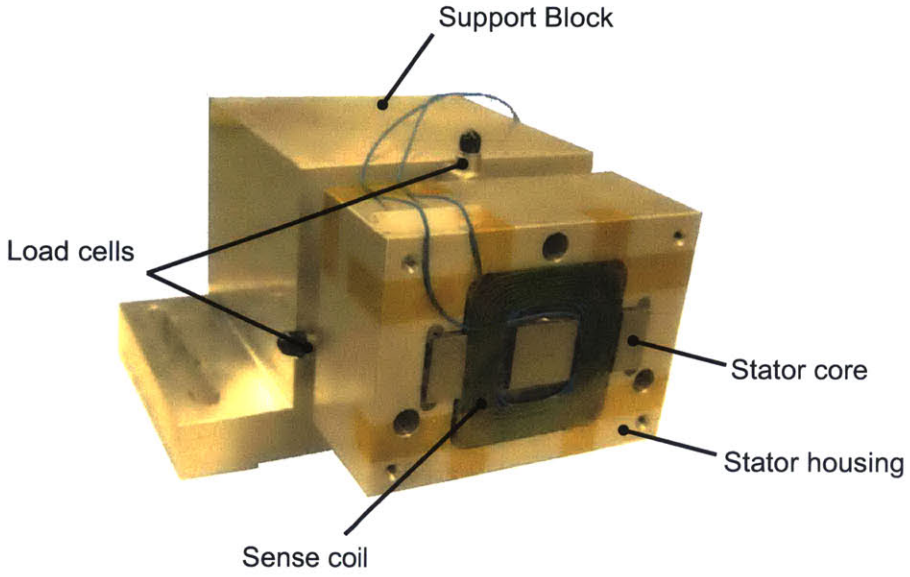

Figure 8-8: Reluctance actuator stator prototype.

Section 2.6.2). The target can also be made thinner for the same force capability with a three-pole actuator. The actuator stator consists of two tape-wound cut cores adjacent to each other as was shown in Figure 2-15. For the core material, we chose SuperPerm49 from Magnetic Metals. This is a nickel-iron alloy with 49% nickel. We chose NiFe over CoFe because it was less expensive. However, because CoFe has a higher saturation flux density and can generate higher forces, CoFe is probably the correct long-term solution.

The cut cores are laminated with 0.004"-thick (~100 μm) laminations. Magnetic Metals lists the stacking factor as 0.9. The actuator coil consists of 280 turns of AWG # 21 magnet wire. The coil resistance is $R = 1.5\,\Omega$ and the coil inductance at $g = 500\,\mu\text{m}$ is 46 mH. In the rest of this section, we present a more detailed analysis of the design procedure. The general procedure can be outlined as follows:

1. Size the actuator pole face area for the desired maximum force.

2. Determine number of amp-turns required to achieve maximum force at largest expected gap.

3. Size coil window area to prevent coil from overheating.

4. Determine number of turns based on constraints such as peak current.

5. Select wire gauge such that desired number of turns are met.

6. Select cut cores and I-bar with dimensions close to those needed for required pole face area and coil window area.

7. Iterate on design to finalize amp-turns and wire gauge.

8. Design housings for stator and target.

8.4.1 Actuator Pole Face Sizing

The first step in designing a reluctance actuator is to size the pole face area for the desired force. As a first iteration, we can use (2.13) to size the total pole face area A. We replace F with the maximum desired force, $F_{\max}$, and B_g with the maximum flux density, $B_{\max}$, and write

$$A = \frac{2\mu_0 F_{\max}}{B_{\max}^2}. \tag{8.1}$$

The variable $B_{\max}$ is limited by the saturation flux density, B_s, of the core material. The average flux density in the air gap will be further limited by the lamination stacking factor, which decreases the $B_{\max}$ by a factor of 0.9. We include an additional factor of 0.9 so as to bias toward a conservative design. The saturation flux density is listed as 1.5 T by the manufacturer, so we estimate $B_{\max}$ to be 1.215 T. If we set $F_{\max} = 400\,\text{N}$, then $A = 681\,\text{mm}^2$.

8.4.2 Coil Amp-turns

To estimate the number of amp-turns necessary, we use (2.8) solved for NI with $B_g = B_s$ and $g = g_{\max}$. We write

$$NI = \frac{2g_{\max} B_s}{\mu_0}. \tag{8.2}$$

Our nominal operating gap g_0 is 500 µm. A typical gap disturbance is tens of microns. As a conservative estimate then, we set $g_{\max} = 600\,\mu\text{m}$. This results in $NI = 1440$ A-turns as a starting point for our design.

8.4.3 Coil Window Area

We can write the amp-turns in terms of the coil window area, A_w, and the average current density, J, as

$$NI = JA_w. \tag{8.3}$$

The coil window area is indicated by the white dotted line in the half-actuator of Figure 8-9. A rule of thumb for current density is that an average current density of $1 \times 10^6\,\text{A/m}^2$ does not require any active cooling, while an average current density of $1 \times 10^7\,\text{A/m}^2$ requires water cooling. We stipulate a peak current density of $1 \times 10^7\,\text{A/m}^2$ at the nominal gap. This translates to $1.2 \times 10^7\,\text{A/m}^2$ at the maximum gap. Provided that we maintain a low duty cycle, this should be feasible without water cooling. With this peak current density, J_{pk}, we can solve for A_w by setting $J_{pk}A_w$ equal to the peak NI. This results in $A_w = 120\,\text{mm}^2$. However, this is without taking into account the wire packing factor.

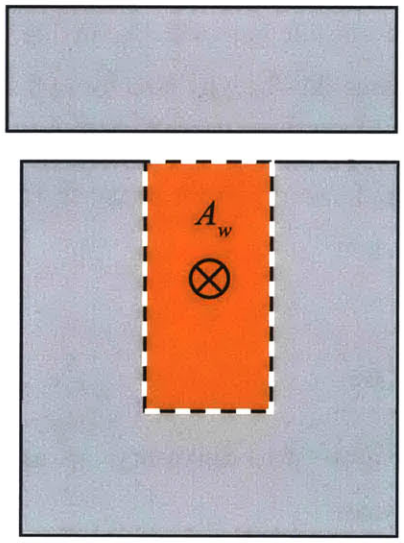

Figure 8-9: Coil window.

8.4.4 Wire Gauge

Suppose we want to limit ourselves to roughly a peak current of 5 A. This is well within the capability of several commercial amplifiers we have available in lab. From Section 20.3 of [48], AWG # 23 is listed as having a packing density of 237 turns/cm^2. Using this wire gauge, we should be able to fit an approximate 284 turns in our coil. With $N = 284$ turns, we expect a peak current of 8.46 A at $g_{\max}$ and a peak current of 5 A at the maximum gap.

8.4.5 Selecting Cut Cores and I-bar

Using the foregoing parameters of A and A_w as our starting point, we selected cut-cores from Magnetic Metals that would roughly match these parameters. The dimensions for the chosen cut core are shown in Figure 8-10. The dimensions A and G are set by the specified dimensions given in the figure. The strip width refers to the lamination width. The total pole face area (which includes two c-cores) for these dimensions is $A = 726\,\text{mm}^2$.

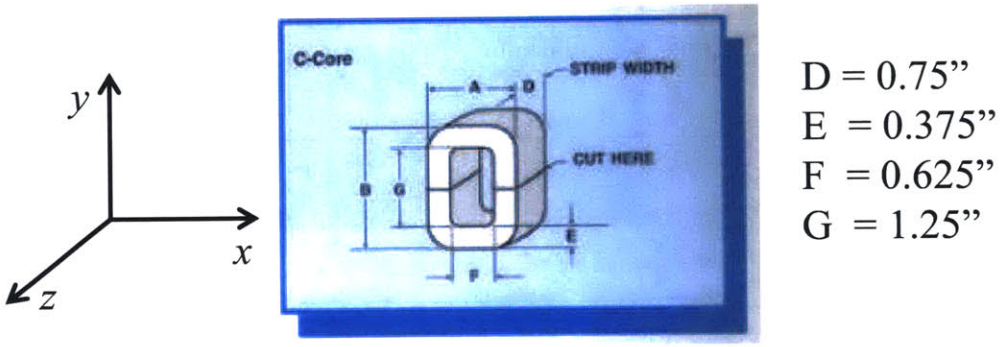

Figure 8-10: Dimensions of c-core. Figure taken from Magnetic Metals website.

The dimensions of the I-bar are shown in Figure 8-11. The x- and z-dimensions are oversized by 1/8” on each side relative to the c-core stator. These dimensions were oversized so that the actuator would be less sensitive to misalignment and to any off-axis motion. The I-bar y-dimension is oversized by 1/16”. This dimension was oversized because we wanted to ensure that target saturation was not what limited our maximum force.

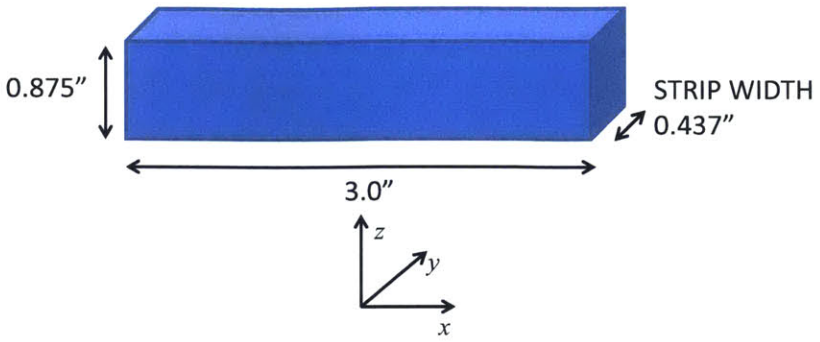

Figure 8-11: Dimensions of I-bar.

8.4.6 Simulations of Actuator Design

Using the c-core and I-bar dimensions, we simulated the actuator design using the linear magnetic circuit presented in Chapter 7. The simulated force is plotted against coil current density in Figure 8-12 for a 500 µm gap. The simulated actuator reaches a maximum force of 400 N at a current density of 7.5×10^6 A/m^2. This current density is based on the original coil window area from Section 8.4.3. In reality, it will take a higher current density to reach this force because the effect of saturation was not taken into account in the linear simulation.

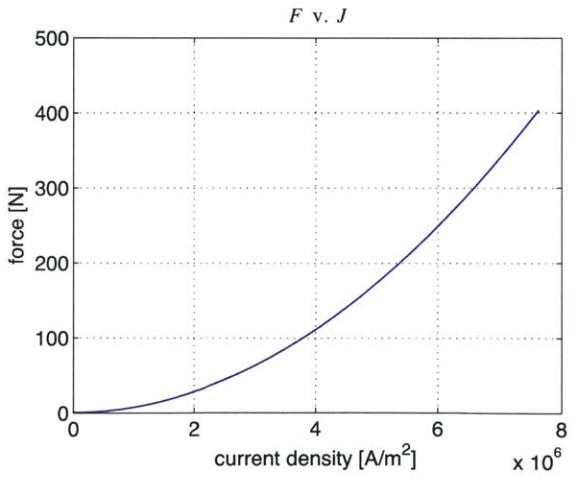

Figure 8-12: Magnetic circuit simulation of force versus current density for reluctance actuator design.

We ran a nonlinear 2-D FEA simulation of the actuator to take into account the

effect of saturation. We also increased the coil window area to $135\,\mathrm{mm}^2$ to make better use of the area available from the cut cores chosen. Figure 8-13 shows the FEA model at saturation. The stator cores are completely saturated. The target on the other hand has several areas with very low magnetic flux density. This suggests possibilities for optimizing the target shape: for instance, one could chamfer the top corners as shown in Figure 8-14 in an effort to save mass. The target height could also be reduced.

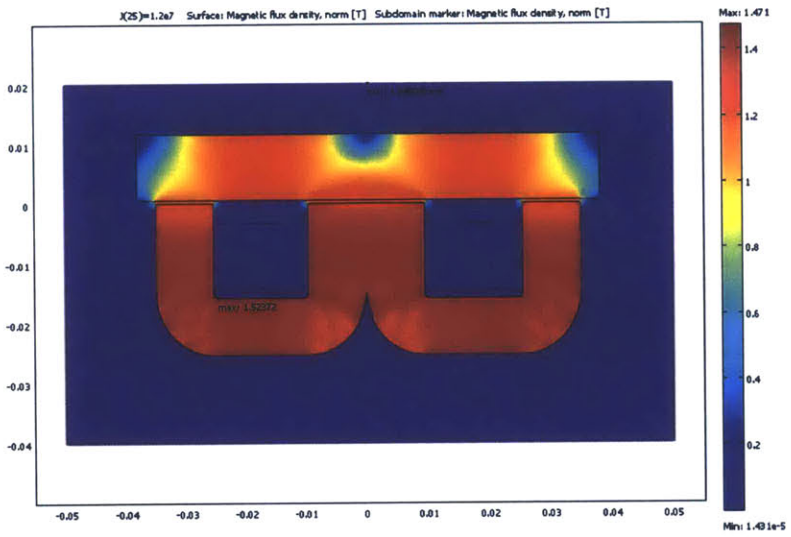

Figure 8-13: FEA model of reluctance actuator prototype at saturation.

Figure 8-14: Concept of target design with top corners chamfered to reduce mass.

Figure 8-15 shows the simulated force plotted against the coil current density from the FEA simulation. We reach 400 N at about $6.5 \times 10^6\,\mathrm{A/m}^2$. There are two caveats: 1) the actual force reached will likely be somewhat lower than the simulation indicates because the FEA model is 2-D and does not take into account the effect of fringing in the out-of-plane dimension; 2) the peak current density will be somewhat higher

than indicated because the packing factor of the coil turns within the coil window reduces the ratio of copper area to total coil window area.

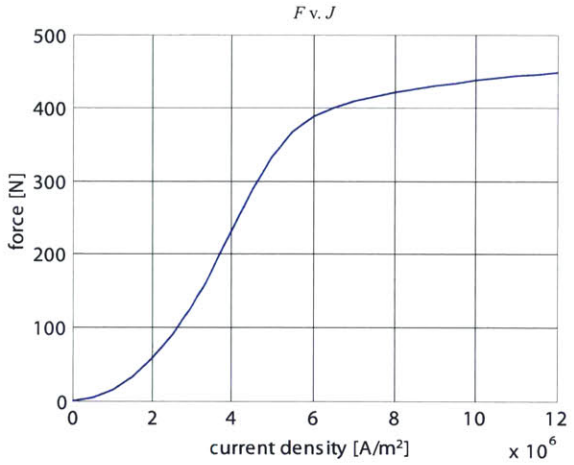

Figure 8-15: FEA simulation of force versus current density for reluctance actuator prototype.

8.4.7 Housing Assembly Design

A CAD model of the actuator housing assembly is shown in Figure 8-16 along with two cross-sectional views. We worked with Fred Sommerhalter, who provided inputs in finalizing the housing design. In the picture, a PCB is shown on the face of the stator housing. We originally intended to design our sense coil on a PCB that fit over the pole faces. We ended up winding the coil by hand instead using thin coaxial cable.

The stator housing includes a deep pocket to locate the c-cores and then a shallower pocket against which the coil sits. The hole in the center of the back of the stator housing is a 1/4"-20 tapped hole used to preload the stator against the load cells. The three counterbore through-holes are used to bolt the stator to the load cells. The c-core pole faces extend beyond the face of the housing so that there is room to place a sense coil after assembly.

The target housing has a pocket in which the I-bar resides. The I-bar rests against two flats on the bottom surface of the pocket. These flats allow a space for epoxy

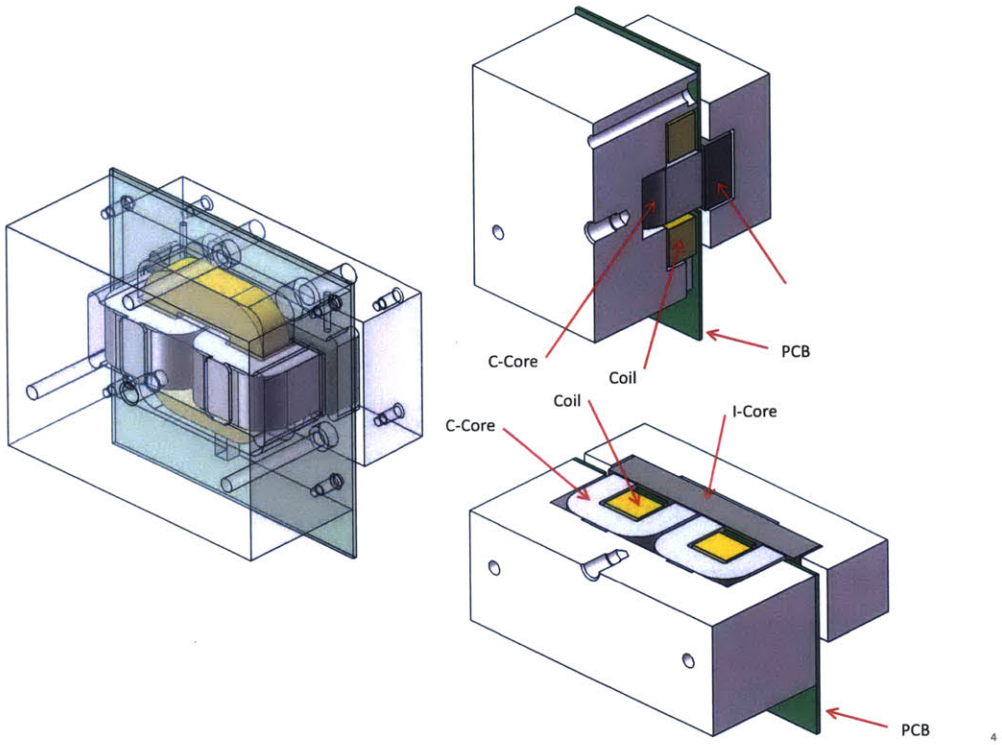

Figure 8-16: CAD model of reluctance actuator housing.

on the backside of the target. There are four counterbore clearance holes for 1/4"-20 screws to bolt the target to the air bearing slide. The housings were made of aluminum for ease of manufacturing, for its high thermal conductivity, and for its nonmagnetic properties.

8.4.8 Manufacture and Assembly

Fred Sommerhalter manufactured the housings, wound the coils, and assembled the completed actuators for us. Figure 8-17 is a photograph of the stator aluminum housing, and Figure 8-18 shows two photographs of the stator with c-cores and coil before potting. With the larger coil window area, we were able to specify a larger wire gauge and so we selected AWG #21. The coil consisted of 280 turns. Kapton insulating tape [36] is placed on the aluminum housing surfaces that come into contact with the coil and the cores.

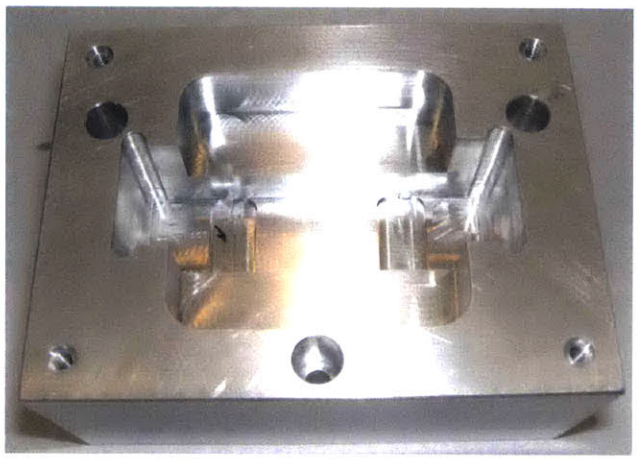

Figure 8-17: Stator housing.

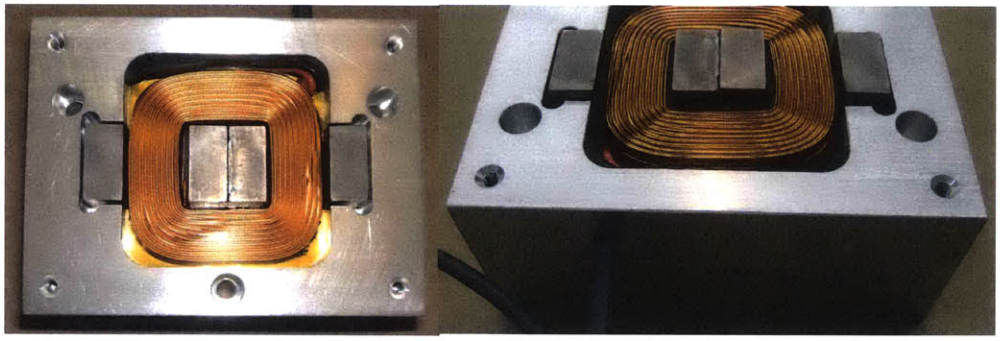

Figure 8-18: Actuator stator before potting.

The c-cores and coil were potted in place with EC-1012M/EH-20M potting compound [38], a thermally conductive epoxy. A type K thermocouple was also placed inside the housing next to the coil to permit temperature measurement. Figure 8-19 shows a set of potted actuators.

After potting, the cut-core pole faces were ground flat and parallel to the back face of the stator housing. The parallelism is important so that force applied by the reluctance actuator is in the direction of the air bearing slide and in the direction of the load cell sensing axes. Before grinding, hot melt glue was applied to the portion of the cores protruding from the housing. This was done with the intention to support the cores during grinding so that the laminations would not 'mushroom' outwards from the the grinding procedure. A photograph of the hot glue applied

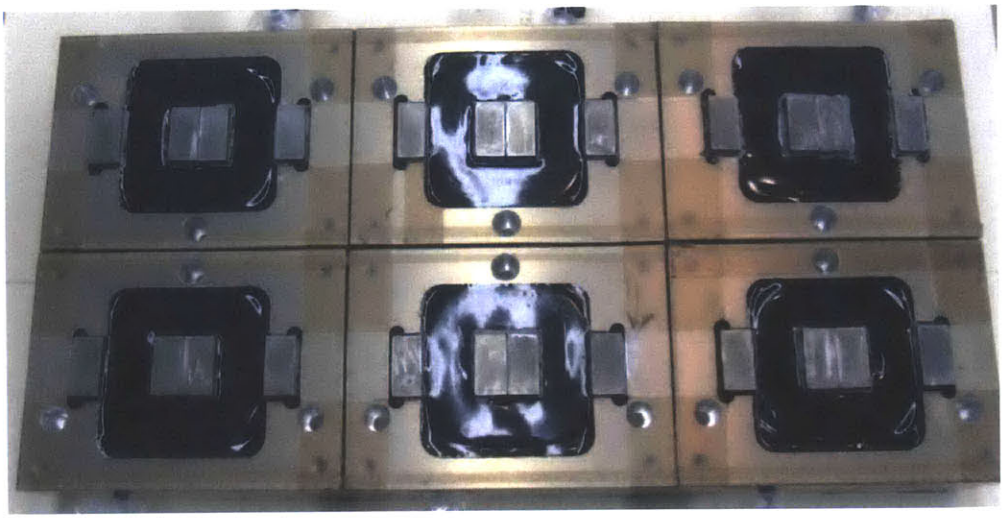

Figure 8-19: Potted actuators.

to the cut-cores is shown in Figure 8-20. Unfortunately, the c-core laminations still mushroomed out after grinding in spite of the presence of the hot glue. Figure 8-21 shows the laminations of the completed stator mushroomed out.

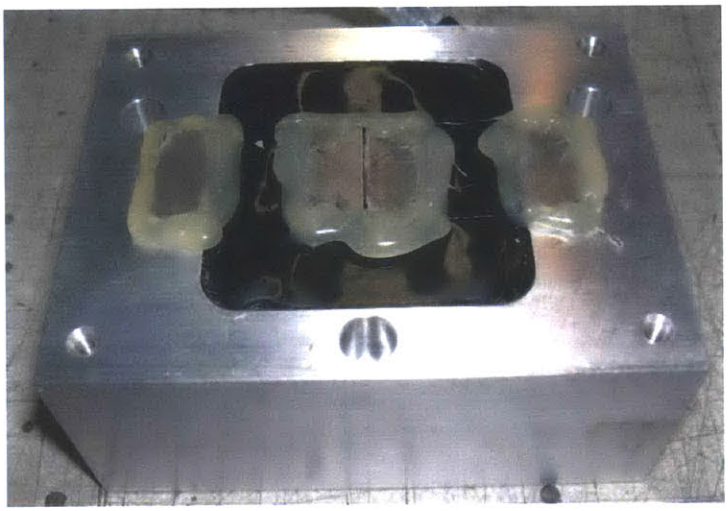

Figure 8-20: Hot melt glue applied to cut cores.

For a second batch of actuators, we decided not to grind the faces of the c-cores, as the c-core pole faces are already quite flat. The challenge then is ensuring that the pole faces are parallel to the back surface of the stator housing. To do this, Fred built a fixture with two sets of flat, parallel surfaces. A sketch of this fixture is shown in

Figure 8-21: Photograph of pole face laminations frayed outward from grinding.

Figure 8-22. The outer set of surfaces was placed against the front surface of the stator housing. The inner surface of the fixture is located above the c-core pole faces. Two permanent magnets are placed on the back side of the fixture to pull the cut-cores up against the fixture. The areas marked 'adhesive' are where Kapton insulating tape is located. Figure 8-23 shows a photograph of the stator with the fixture and permanent magnets in place. With the coil in place and the fixture locating the cut-cores, the cavity was filled with epoxy and then left to cure.

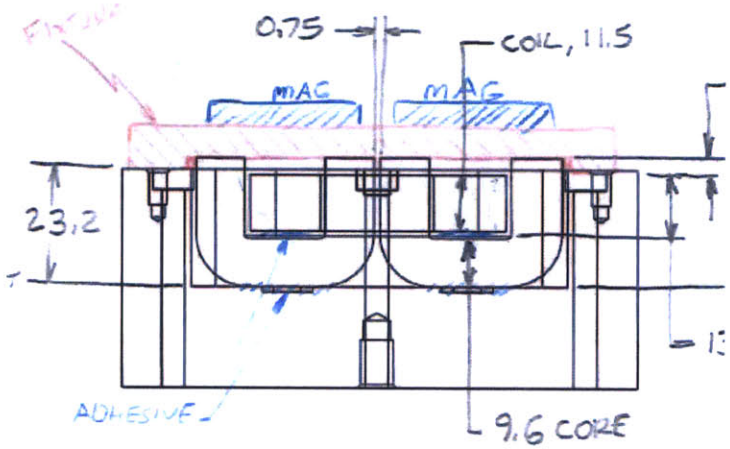

Figure 8-22: Fixture for making c-cores parallel to housing surface.

The targets were assembled by placing the I-bars in the target housing pockets and then using a mold for the epoxy that fit around the top surface of the I-bar. Kapton tape was placed on the surfaces of the housing pocket to insulate it from the target. Figure 8-24 shows the target housing and also shows the mold used for

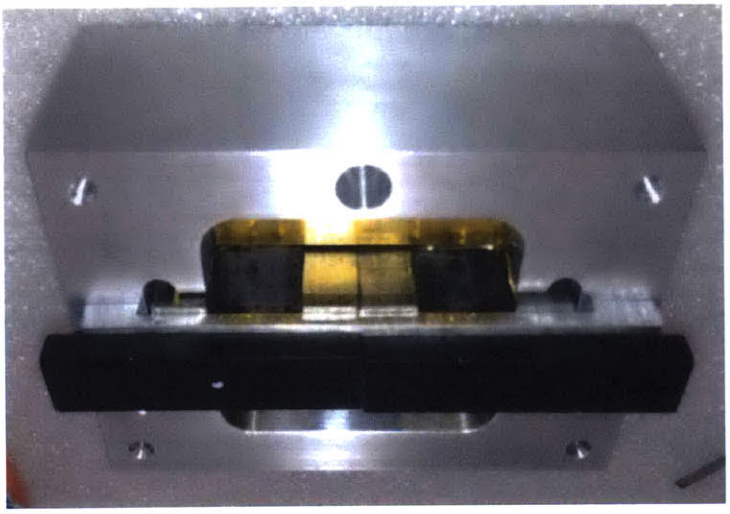

Figure 8-23: Photograph of fixture for making c-cores parallel to housing surface.

potting the target assembly.

Figure 8-24: LEFT: Target housing; CENTER: Housing with I-bar in pocket; RIGHT: Mold for potting target assembly.

Figure 8-25 shows the potting procedure. The leftmost assembly in the figure shows the target assembly with the mold in place and epoxy in the opening. The center assembly shows the target assembly after the epoxy has cured and the mold has been removed. After the mold has been removed, the cured excess epoxy and target face are machined down to size. This is shown in the rightmost assembly.

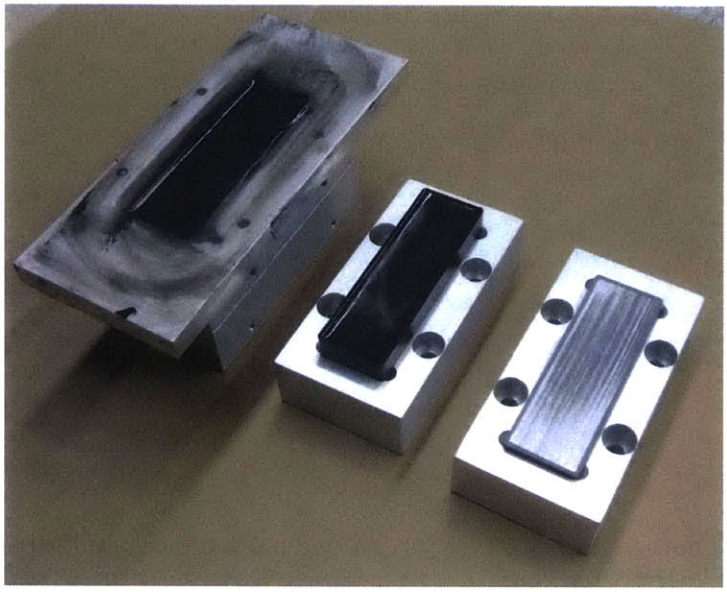

Figure 8-25: Target assembly showing potting procedure.

The target is then ground flat and parallel to the back surface of the housing. It is more critical to grind the I-bar surface than the c-core faces because the I-bar force-generating surface has greater surface roughness. The c-core pole faces are formed by cuts made in the original tape-wound core: this results in a flat surface where the cut is. The cuts in the I-bar are at the two ends of the I-bar, where flatness is not critical. In contrast, the force-generating face of the I-bar is formed by the edges of the laminations as they are wound, resulting in an uneven surface. The potting compound acts to support the laminated I-bar during grinding so that the laminations do not mushroom out. This worked much better than the hot glue method did for the c-core pole faces. The grinding direction may have also helped. Figure 8-26 shows a completed target assembly.

8.4.9 Sense Coil

For the sense coil, we used miniature coaxial shielded cable. The sense coil is shown in Figure 8-27. We placed kapton on the epoxy surface for additional insulation between the actuator coil and sense coil. We then placed double-sided tape on top of

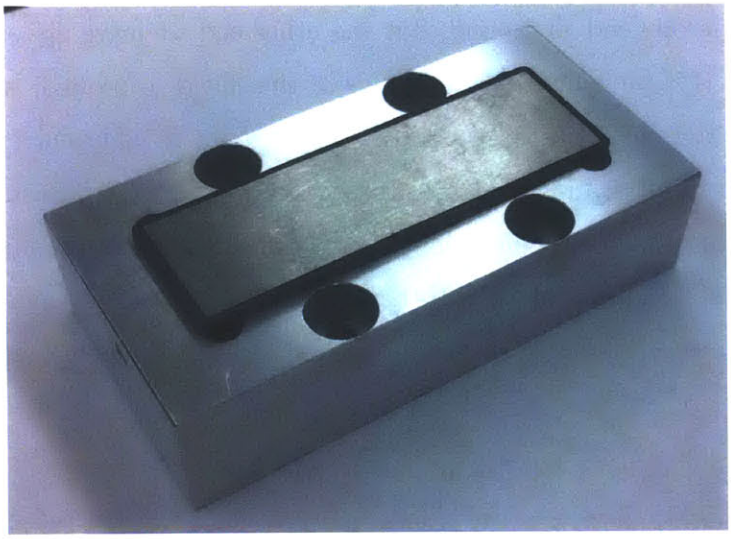

Figure 8-26: Completed target assembly.

the kapton. This kept the sense coil in place as we wound it. After winding the coil, we taped it down in place with more kapton. The sense coil has 13 turns.

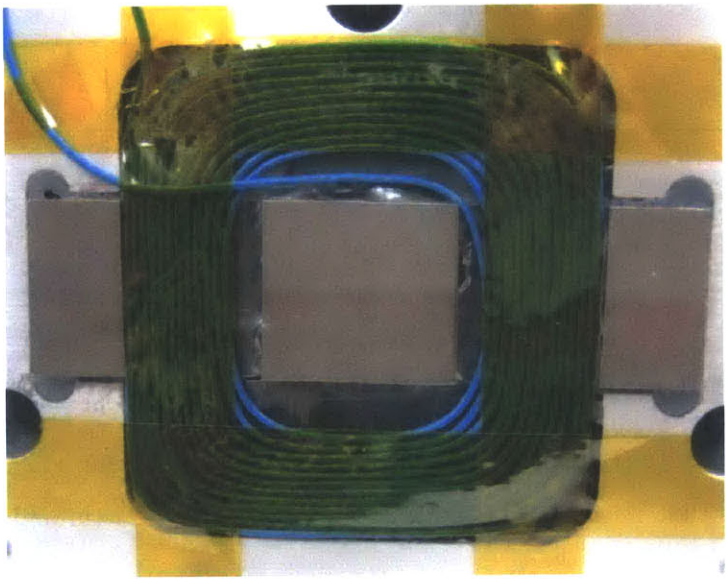

Figure 8-27: Hand-wound sense coil.

The shielding helps to reduce any capacitive coupling from the actuator coil and noise from other sources. A key subtlety to the shield is that it must be open-

circuited: we tie one end to ground, but the other end we leave disconnected. The reason for this is if we connected both ends of the shield to ground, we would have a shorted turn around the pole face. This would result in eddy currents flowing in the shorted turn and would affect our flux generation and flux measurement. This configuration also provides self-shielding: since both the cable center and the shield see the same potential induced by dB/dt, there will be no current in the cable center-to-shield capacitance. Figure 8-28 shows the circuit diagram with actuator and amplifier connections.

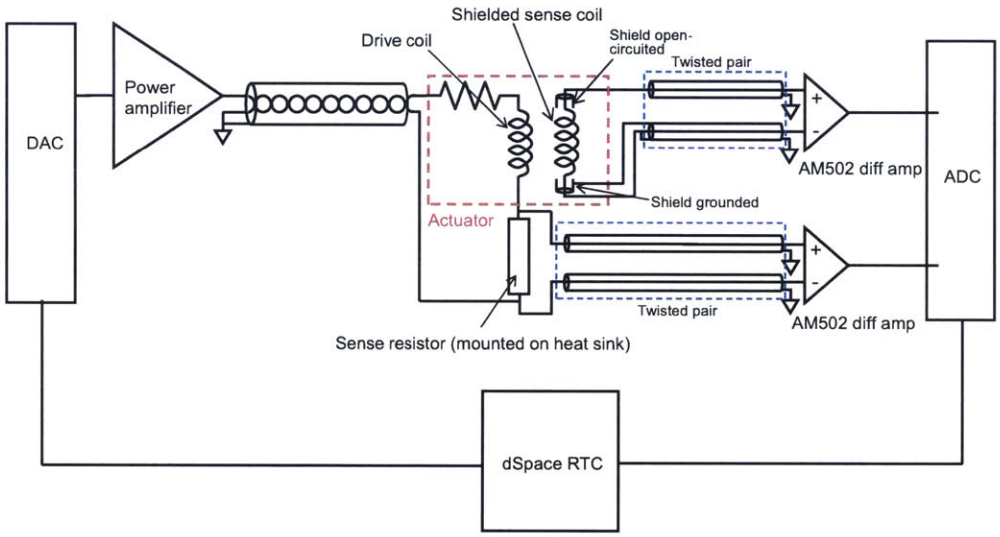

Figure 8-28: Circuit diagram of actuator setup.

8.4.10 Summary of Design Parameters

Table 8.1 lists some of the parameters of the finalized actuator design. These are also the parameters that were used in the simulations of Chapter 4 through Chapter 6.

8.5 Reluctance Actuator Electrical Characteristics

In this section we calculate the resistive voltage, the inductive voltage, the speed voltage, and maximum slew rate of the actuator to ensure that the amplifier is capable of driving the actuator. We also predict the power dissipation.

Table 8.1: Reluctance actuator prototype design parameters.

Parameter	Value
Core material	49% Ni-49% Fe
Pole face area	726 mm^2
Actuator coil turns	280
Coil window area	148 mm^2
Coil wire gauge	AWG #21
Sense coil turns	13

8.5.1 Resistive Voltage

We first calculate the coil resistance R. AWG #21 wire is listed in Section 20.3 of [48] as having a resistance per length of $r = 51\,\Omega/\text{km}$. The resistance R is then calculated as

$$R = rNl_{avg}, \tag{8.4}$$

where l_{avg} is average turn length. The average turn length is 127 mm and the number of turns is 280. This results in a predicted $R = 1.5\,\Omega$. This is what we measured as well. The resistive voltage, v_R, is given as

$$v_R = RI. \tag{8.5}$$

At a peak current (I_{pk}) of 5 A, we therefore expect the maximum v_R to be about 7.5 V.

The peak dissipated power in the coil is $I_{pk}^2 R$. We thus estimate a peak power of 37.5 W. Suppose we want to estimate how quickly the coil temperature will rise. As a worst-case scenario, we can assume that all the heat is stored in the copper (i.e., the thermal resistance of the actuator is infinite). The temperature rise ΔT is given by

$$\Delta T = \frac{Q}{C} = \frac{\bar{P}\Delta t}{C}, \tag{8.6}$$

where Q is the heat energy dissipated by the current through a time Δt, C is the thermal capacitance of the copper coil, and $\bar{P}$ is the average power dissipated. The

thermal capacitance is given by

$$C = m_{Cu}c, \tag{8.7}$$

where m_{Cu} is the copper mass and c is the specific heat capacity of copper. The specific heat capacity of copper is $385\,\mathrm{J/(kg \cdot K)}$. The copper mass is given by

$$m_{Cu} = \rho_{cu}V = \rho_{cu}\pi\frac{d^2}{4}Nl_{avg}, \tag{8.8}$$

where ρ_{cu} is the density of copper, V is the copper volume, d is the diameter of the coil wire, and l_{avg} is the average turn length. The copper density ρ_{cu} is $8960\,\mathrm{kg/m^3}$, d for AWG #21 is 0.7239 mm, and l_{avg} is 127 mm. This results in $m_{cu} = 0.131\,\mathrm{kg}$. If we assume a 50% duty cycle operating at peak power with a period of 0.1 seconds, then $\bar{P} = 19\,\mathrm{W}$ and for ten cycles (1 second duration), $\Delta T = 0.37\,\mathrm{K}$. This is a relatively low temperature change, and indicates that we can run a number of cycles on the actuator before having to worry about overheating. Suppose we want to maintain an average coil temperature below 80°C. Then we set ΔT in (8.6) to 55 K (the change in temperature from room temperature) and solve for Δt. This results in $\Delta t = 150\,\mathrm{s}$ for a duty cycle of 50%. In other words, we can run the actuator at peak power with a 50% duty cycle for two and a half minutes. This would give us over a thousand cycles.

A more accurate estimate would need to include a thermal model of the whole actuator, including the thermal resistance and the thermal capacitance of the housing and the epoxy. It should also include the effect of temperature rise on the resistance. This model was not computed herein. In any case, the actuator for a real device will likely require the addition of liquid cooling, which is not undertaken here.

8.5.2 Inductive Voltage

From the analysis of Section 4.4.2, we can write the voltage v_λ from the flux linked by the coil as

$$v_\lambda = NA_p\frac{dB}{dt}. \tag{8.9}$$

We can replace B with (2.8) and write

$$v_\lambda = \frac{\mu_0 A_p N^2}{2} \frac{d}{dt}\left(\frac{I}{g}\right),$$

$$v_\lambda = \frac{\mu_0 A_p N^2}{2}\left(\frac{1}{g}\frac{dI}{dt} - \frac{I}{g^2}\frac{dg}{dt}\right). \tag{8.10}$$

The first term is the inductive voltage v_L, which we write as

$$v_L = L\frac{dI}{dt} = \frac{\mu_0 A_p N^2}{2g}\frac{dI}{dt}, \tag{8.11}$$

where L is the inductance.

The foregoing analysis neglects the core reluctance. Thus, the analysis will not be accurate near saturation. For our prototype, if we assume an operating gap of $g_0 = 500\,\mu\text{m}$, we can calculate the nominal inductance at this gap. We calculate a value of 36 mH. A linearized circuit model of the actuator and amplifier at constant gap is shown in Figure 8-29.

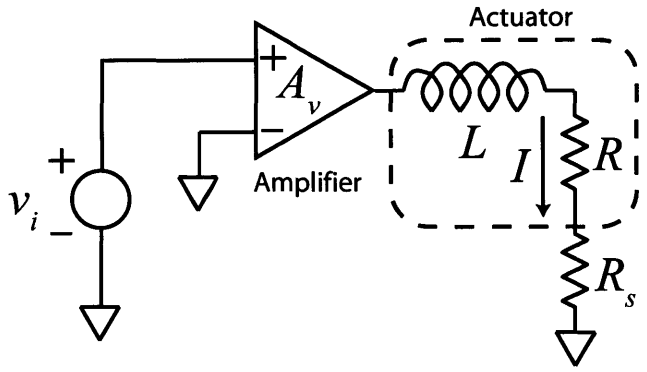

Figure 8-29: Circuit model of reluctance actuator.

The transfer function of the actuator circuit model is

$$\frac{I(s)}{V_i(s)} = \frac{A_v}{Ls + R + R_s}, \tag{8.12}$$

where R_s is the sense resistor ($0.1\,\Omega$ in our setup) and A_v the amplifier gain. The corner frequency of the transfer function will occur at $f = (R+R_s)/(2\pi L)$. We deter-

mined the actual actuator inductance by measuring the frequency response from input voltage (v_i) to output current (I) of the actuator with a 500 µm gap. The measured frequency response for several different current bias levels is shown in Figure 8-30. The phase reaches 45° degrees at 5.5 Hz, indicating the corner frequency. Calculating the inductance from this value, we find $L = 46\,\text{mH}$, higher than predicted. One possible reason for this is that our model does not take into account the leakage flux.

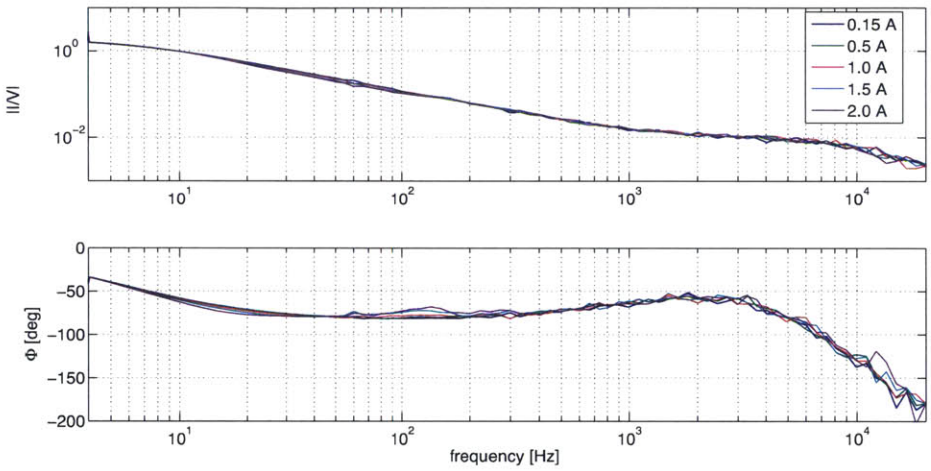

Figure 8-30: Frequency response of input amplifier voltage to reluctance actuator current for different bias currents.

To determine the peak inductive voltage expected, we need to determine the peak dI/dt. We can differentiate (2.8) and solve for dI/dt as

$$\frac{dI}{dt} = \frac{2g}{\mu_0 N}\frac{dB}{dt}. \tag{8.13}$$

We can substitute (5.23) for dB/dt and write

$$\frac{dI}{dt} = \frac{g}{N}\sqrt{\frac{2}{\mu_0 AF}}\frac{dF}{dt}. \tag{8.14}$$

As shown in (8.14), the slew rate is inversely proportional to the square root of the force. To avoid infinite slew rates, we must operate with some non-zero bias force F_0. If the force profile is known, this equation permits us to calculate the expected

profile of the slew rate. For a typical scanning profile, the maximum value of dF/dt is about 100 times greater than the numeric value of the maximum force, $F_{\max}$. If we take $F_{\max}$ for our prototype to be the maximum force simulated in Chapter 4, then $F_{\max} = 367\,\mathrm{N}$, and our maximum dF/dt will be approximately $3.67 \times 10^4\,\mathrm{N/s}$. If we use a 3rd-order position profile (i.e., finite jerk and infinite snap), then our maximum dI/dt will occur at the beginning of the jerk phase when $F = F_0$. We can write the maximum dI/dt as

$$\left.\frac{dI}{dt}\right|_{\max} = \frac{g}{N}\sqrt{\frac{2}{\mu_0 A F_0}}\left.\frac{dF}{dt}\right|_{\max}, \tag{8.15}$$

where $dF/dt_{\max}$ is the maximum force slew rate. Suppose that $F_0 = 1\,\mathrm{N}$, then $dI/dt_{\max}$ for our system will be $3.1\,\mathrm{A/ms}$. Our maximum inductive voltage, $v_{L,\max} = LdI/dt_{\max}$, will then be 140 V!

We can decrease the maximum inductive voltage by increasing F_0. We can also reduce v_L by using a 4th-order position profile (finite snap), even while maintaining equal or greater maximum dF/dt. The reason for this is that by using a 4th-order profile, $dF/dt_{\max}$ no longer occurs at the minimum force equal to F_0. The simulated profile from Chapter 4 is derived from a 4th-order position profile. It has the same $dF/dt_{\max} = 3.67 \times 10^4\,\mathrm{N/s}$ that we calculated above. If we substitute F and dF/dt from this profile into (8.14) and add a bias force of $F_0 = 1\,\mathrm{N}$, we find a $dI/dt_{\max}$ of $0.32\,\mathrm{A/ms}$, a factor of nearly 10 lower than when using a 3rd-order profile. We calculate an associated $v_{L,\max} = 14.5\,\mathrm{V}$.

8.5.3 Speed Voltage

The second term in (8.10) is the speed voltage, v_s, which we write as

$$v_s = -\frac{\mu_0 A_p N^2 I}{2g^2}\frac{dg}{dt}. \tag{8.16}$$

The motor constant K_{mr} is thus

$$K_{mr} = \frac{\mu_0 A_p N^2 I}{2g^2}. \tag{8.17}$$

We can double-check this motor constant by calculating $\partial F/\partial I$ by differentiating (2.14) with respect to I,

$$\frac{\partial F}{\partial I} = \frac{\mu_0 A N^2 I}{4g^2}. \tag{8.18}$$

If we note that $A = 2A_p$, we see that $\partial F/\partial I = K_{mr}$. The speed voltage is proportional to I, so we expect the maximum v_s to occur near the maximum current, $I_{\max}$. We also need to approximate the maximum speed, $dg/dt_{\max}$. In Chapter 5 we approximated $dg/dt_{\max}$ as 10 mm/s. Substituting this for dg/dt in (8.16) and 5 A for I, we estimate a maximum v_s of 3.6 V, which is small relative to the resistive and inductive terms.

8.5.4 Summary of Electrical Parameters

We summarize the lumped parameter electrical elements for the reluctance actuator in Table 8.2. For the coil inductance and resistance, we include predicted and measured values. We do not include values for the motor constant because it varies with current.

Table 8.2: Reluctance actuator prototype electrical parameters.

Parameter	**Formula**	**Predicted Value**	**Measured Value**
Resistance (R)	rNl_{avg}	1.5 Ω	1.5 Ω
Inductance (L)	$\frac{\mu_0 A_p N^2}{2g}$	36 mH	46 mH
Motor Constant (K_{mr})	$\frac{\mu_0 A_p N^2 I}{2g^2}$	N/A	N/A

Table 8.3 summarizes the voltages, slew rate, and dissipated power expected in the reluctance actuator. We have assumed a bias force of $F_0 = 1$ N and the force profile simulated in Chapter 4, which has a peak force of 367 N.

8.6 Voice Coil Actuator Electrical Parameters

Table 8.4 lists the electrical parameters of the voice coil actuator, as specified by BEI-Kimco. The measured inductance varies considerably from the specified inductance.

Table 8.3: Predicted peak electrical variables for reluctance actuator prototype.

Variable	Formula	Predicted Max Value
Resistive voltage (v_R)	RI	7.5 V
Inductive voltage (v_L)	$L\frac{dI}{dt}$	14.5 V
Speed voltage (v_s)	$-K\frac{dg}{dt}$	3.6 V
Slew rate ($\frac{dI}{dt}$)	$\frac{g}{N}\sqrt{\frac{2}{\mu_0 AF}}\frac{dF}{dt}$	0.32 A/ms
Dissipated power (P)	I^2R	37 W
Peak force (N)		367 N

This may be because the specified inductance was measured at 1 kHz, whereas we calculated the inductance by measuring the frequency response of the actuator and determining the corner frequency, as was done for the reluctance actuator.

Table 8.4: Voice coil actuator electrical parameters.

Parameter	Specified Value	Measured Value
Resistance (R)	2.6 Ω±12.5%	2.9 Ω
Inductance (L)	2.9 mH±30%	7.5 mH
Motor Constant (K_{mvc})	35.14 N/A±10%	30.7 N/A

From these parameters, we can calculate the expected peak electrical variables. For dI/dt, we write

$$\frac{dI}{dt} = \frac{1}{K_{mvc}}\frac{dF}{dt}. \tag{8.19}$$

Since K_{mvc} is constant, the peak dI/dt will occur at peak dF/dt. The peak electrical variables for the voice coil actuator are summarized in Table 8.5.

The 13 A listed as the peak current is slightly above the specified safe peak current from BEI-Kimco, which is 12.7 A. For this reason, we will test the prototype actuator at a maximum force level below 400 N. The dual channel Crown DC300A amplifier

Table 8.5: Predicted peak electrical variables for voice coil actuator.

Variable	**Formula**	**Predicted Max Value**
Peak current (I_{pk})	$\frac{F_{\max}}{K_{mvc}}$	13 A
Resistive voltage (v_R)	RI	37.7 V
Inductive voltage (v_L)	$L\frac{dI}{dt}$	9.0 V
Speed voltage (v_s)	$-K\frac{dg}{dt}$	0.3 V
Slew rate ($\frac{dI}{dt}$)	$\frac{1}{K_{mvc}}\frac{dF}{dt}$	1.2 A/ms
Dissipated power (P)	I^2R	490 W

we use to drive the actuators is capable of delivering a minimum of 155 W RMS per channel. Since our predicted peak power dissipated for the voice coil actuator is 490 W, we should run the actuator at a duty cyle of 30% or less. Figure 8-31 shows the VI limits for the Crown amplifier. The DC limits of the amplifier indicate that it can source sufficient current to the voice coil. The slew rate limit of the crown amplifier is 8 A/ms, so we have sufficient margin for both the voice coil actuator and reluctance actuator.

8.7 Summary

In this chapter we presented the design of a 1-DoF testbed for testing reluctance actuator force accuracy. The testbed incorporates an air bearing for the moving stage in order closely to approximate a zero-stiffness motion stage. We use a high-resolution encoder for accurate position sensing and control and high-stiffness load cells for force measurement.

We presented a detailed design of the reluctance actuator prototype. We learned that grinding the cut-core pole faces causes the laminations to 'mushroom' out despite

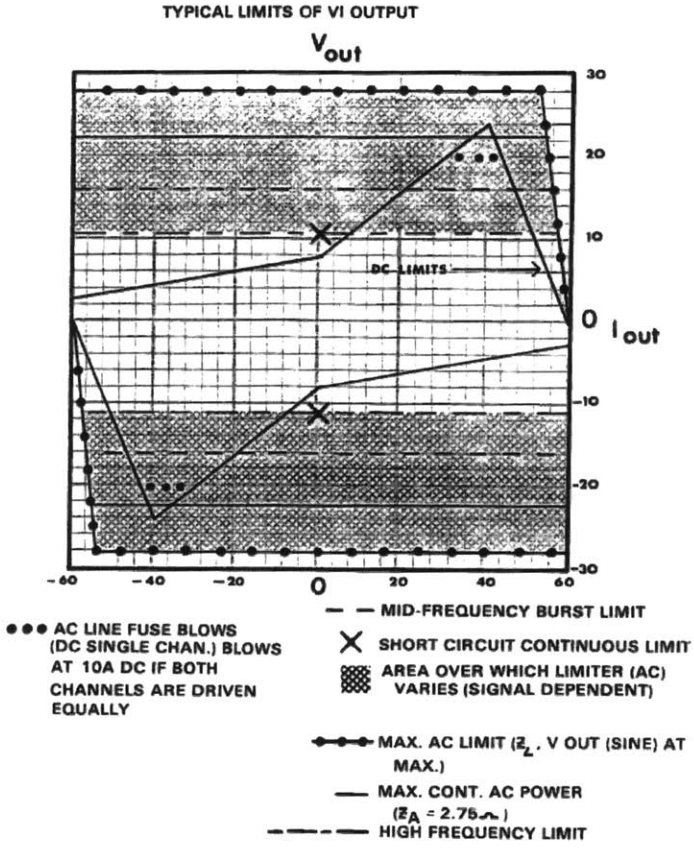

Figure 8-31: Crown amplifier VI limits. Figure taken from [30].

measures taken to prevent this. Moreover, it is not needed in order to ensure pole face flatness. We therefore recommend not grinding the faces. We also determined that the shield of the sense coil must be open-circuited to avoid eddy currents flowing in the shield. We calculated predicted peak electrical variables for both the reluctance actuator and voice coil actuator to ensure that our amplifier could drive the actuators. We learned that we can reduce the slew rate and inductive voltage by using a 4^{th}-order position profile rather than a 3^{rd}-order position profile. In the next chapter, we present experimental results from the reluctance actuator prototype using the 1-DoF testbed.

Chapter 9

Loop-Widening Phenomenon

In this chapter, we document an investigation into unexpected loop-widening behavior that the reluctance actuator prototype exhibited at low frequencies. In the course of measuring the actuator outputs on the 1-DoF air bearing setup, we discovered that the flux estimated from the sense coil exhibited a phase that lag relative to the actuator current that increased with frequency. This loop widening manifests itself when plotting the flux against the actuator current for different frequencies: the hysteresis loop widens with increasing frequency. While loop widening is expected at higher frequencies, we discovered the phenomenon at low frequencies ($< 10\,\text{Hz}$) where eddy currents should not affect the hysteresis loop. After discovering the loop widening phenomenon on the air bearing setup, we embarked upon a series of experiments in an effort to discover the root cause of the behavior.

This chapter is organized as follows. We first present a series of experiments performed on several actuator prototypes using both NiFe prototypes and CoFe prototypes. We then present experiments done on wound cut-cores. These were done in order to isolate any effects from the cores themselves from any effects that might arise from the actuator assembly process. Next we show the results of experiments that were performed on ferromagnetic toroidal specimens. In this section we demonstrate the difference in behavior between 49% NiFe and 50% NiFe. We then present a series of experiments designed to uncover any problems in the instrumentation chain. The outcome of our investigation was inconclusive and so we recommend further research

to uncover the root cause.

9.1 Actuator Experiments

To provide context, Figure 9-1 shows a representative series of B-I loops measured on the reluctance actuator prototype on the 1-DoF air bearing setup. The zoomed-in plot on the right clearly shows that the loops widen with increasing driving frequency.

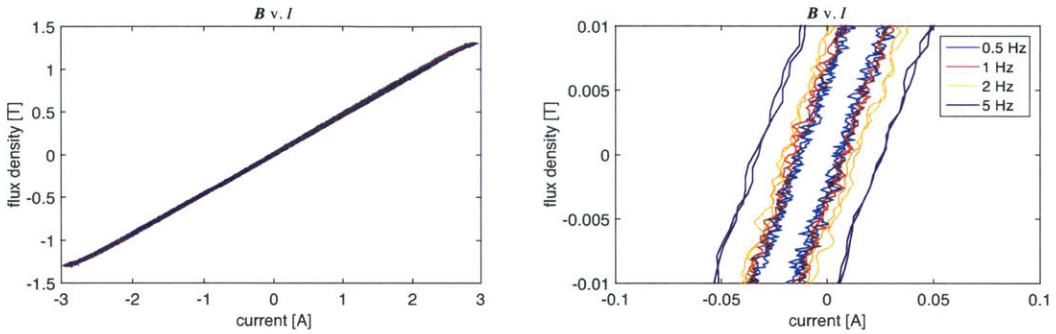

Figure 9-1: LEFT: B-I data measured on reluctance actuator demonstrating loop-widening phenomenon; RIGHT: zoomed in near origin.

Because the relationship between actuator force and air gap flux density is not a dynamic one (see (2.13)), we expected no phase lag between the measured force and flux. However, when plotting the force measured by the load cells mounted to the stator against the flux computed from the sense coil measurement, we found that the force *leads* the flux. Figure 9-2 shows a measured B-F curve that was driven with a 10 Hz voltage sine wave. The red arrows show the direction of the loop made by the B-F curve, indicating that the flux as measured by the sense coil lags the load cell force measurement.

Furthermore, when we plotted the measured force against the measured current, the loop width remained relatively constant with increasing frequency. Figure 9-3 shows a series of measured F-I curves at different frequencies. These plots are taken from the same data sets that were used in Figure 9-1. Any loop widening present appears much reduced compared to the B-I curves shown in Figure 9-1. Moreover, the direction of the F-I loop (counter-clockwise) indicates that the force lags the

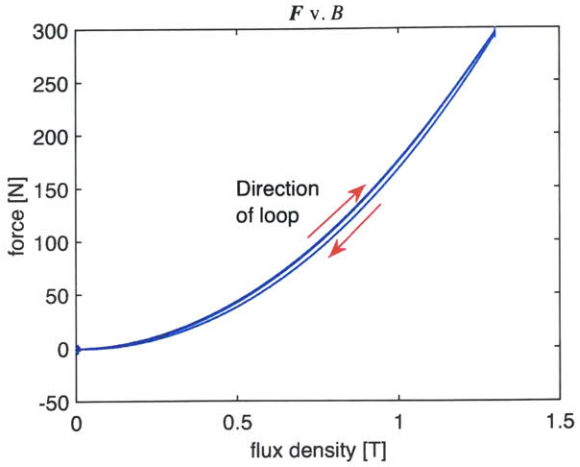

Figure 9-2: Measured B-F curve showing that the force leads the flux density.

current, as expected owing to hysteresis.

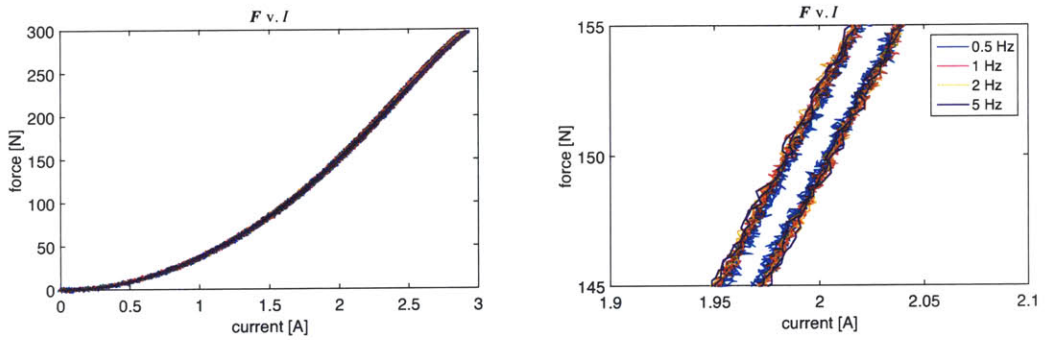

Figure 9-3: LEFT: F-I data measured on reluctance actuator; RIGHT: zoomed in near 2 A.

The problem that arises from loop widening is that it becomes much more challenging to generate accurate force control with the reluctance actuator. The purpose of using a high-bandwidth flux loop to control the actuator is that it ideally allows for accurate force control without having to resort to complex dynamic feedforward force models of the actuator. If the measured flux exhibits phase lag that is not present in the actual force, it becomes more difficult accurately to track a dynamically varying force since the mapping between the measured flux and force is no longer a static one.

The fact that the measured force leads the measured flux and that the loop widening is not apparent in the F-I data indicated that the problem was an instrumentation

problem. To investigate the cause of the loop widening, we took a reluctance actuator stator and clamped a target to it. This way we could isolate the actuator effects from any other effects caused by the air bearing setup. This clamped setup is shown in Figure 9-4.

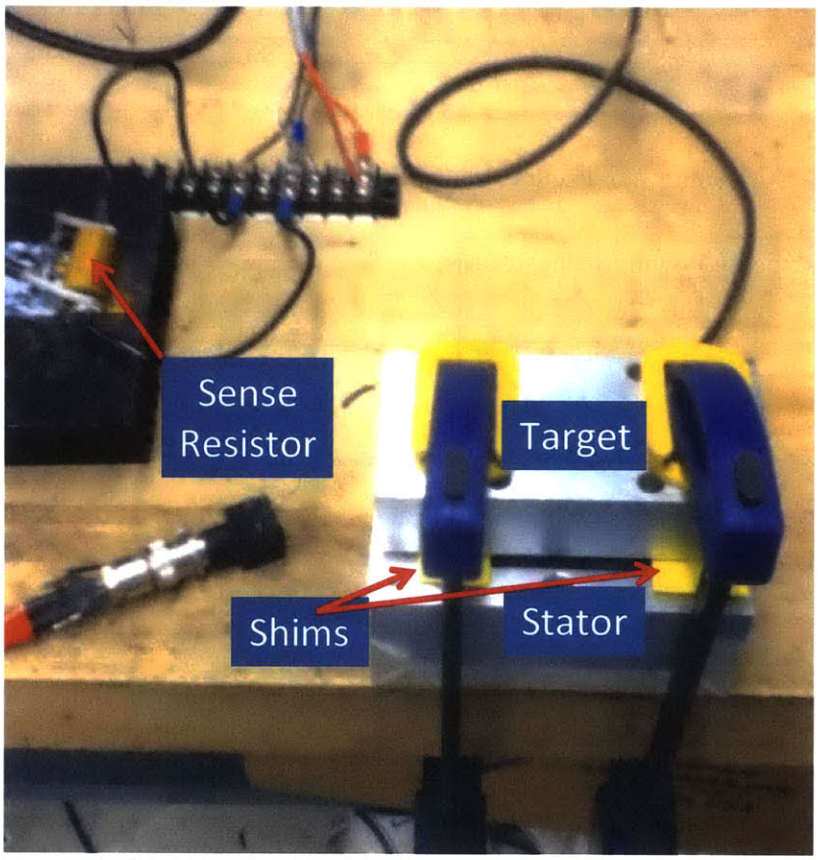

Figure 9-4: Clamped actuator setup.

The instrumentation diagram of our clamped setup is shown in Figure 9-5. The sense coil shield is tied to the cable shield on one end. On the other end, the sense coil shield is disconnected and left open-circuited to avoid external eddy current loss and for self-shielding from capacitance effects.

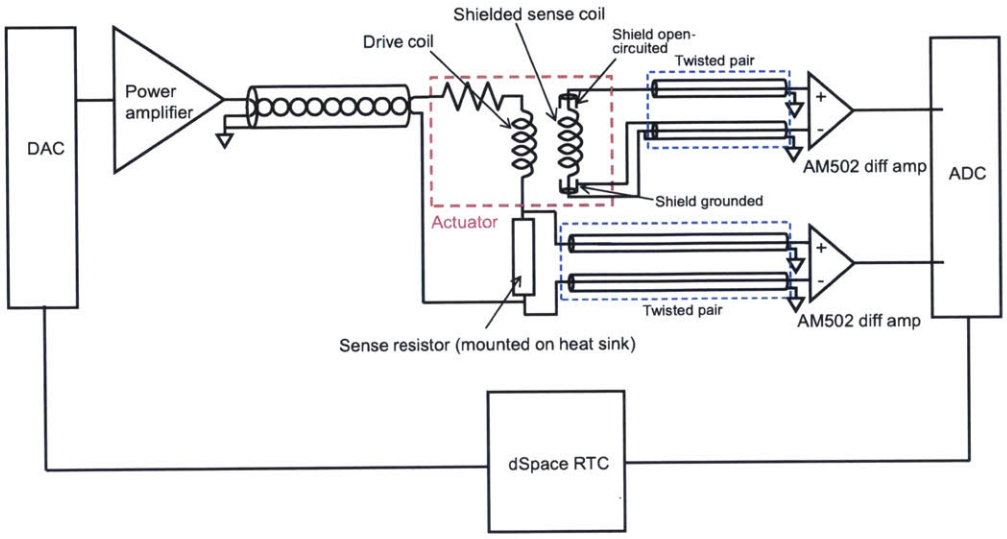

Figure 9-5: Instrumentation diagram for actuator experiments.

9.1.1 Gaussmeter Measurements

We used a Gaussmeter to measure the air gap flux independently. We placed the Gaussmeter probe in the center pole face air gap and taped it to the center pole face. We placed delrin spacers in the left and right air gaps and then clamped the target to the stator. The delrin spacers were slightly thicker than the Gaussmeter probe so that the probe itself was not clamped. The total air gap was about 1.55 mm. The Gaussmeter was an F.W. Bell 5180 model [69]. Figure 9-6 shows a series of B-I curves measured with both the sense coil (left plots) and the Gaussmeter (right plots). The Gaussmeter data is significantly noisier than the sense coil estimate; nevertheless, loop widening is still evident from the Gaussmeter data. This suggests that the cause of the loop widening is the actuator itself rather than the sense coil instrumentation chain.

9.1.2 Actuator Simulations

We ran a series of actuator simulations to see if eddy currents could account for the loop widening phenomenon. We used the model described in Section 6.6.3 for the simulations with (5.38) used to model the excess eddy currents. Equation (5.38)

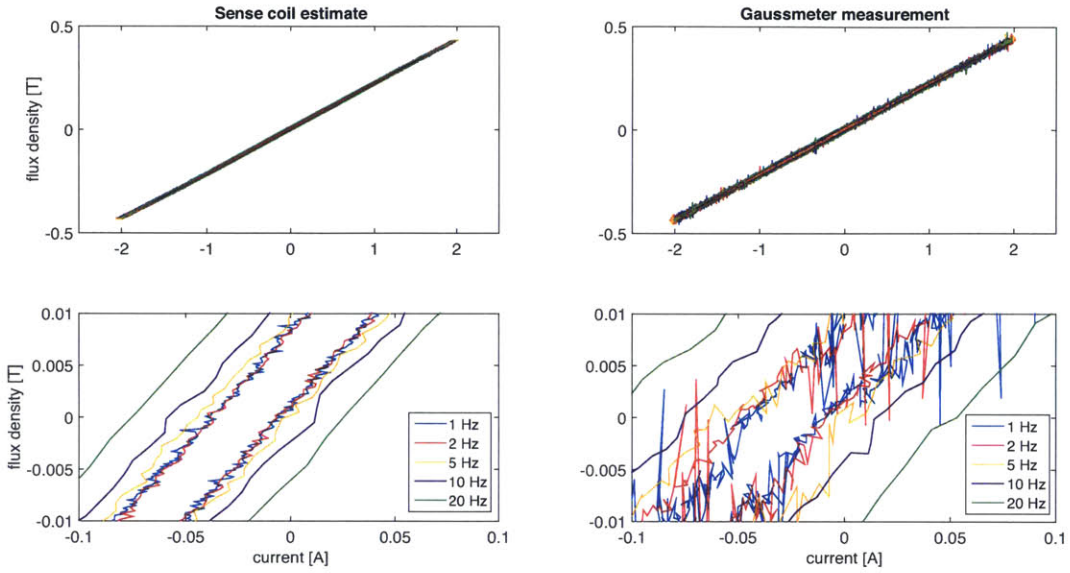

Figure 9-6: LEFT: Measured B-I curves with B estimated from sense coil; RIGHT: Measured B-I curves with B measured by Gaussmeter. Bottom plots are zoomed-in graphs of the top plots.

describes the behavior of excess eddy currents in 50% NiFe. Our prototype uses 49% NiFe. It is unknown whether 49% NiFe can be described by same model as 50% NiFe. However, since (5.38) resulted in simulations with larger excess eddy currents than the square root law of (5.27) that many other materials have been found to follow, we used (5.38) since it should result in more loop widening than (5.27).

Figure 9-7 shows the simulation results for the model when driven with a 1 A amplitude sine wave. There is some loop widening, but it is much less than what was measured in the experimental results.

We applied a Fast Fourier Transform (FFT) to the current and flux density simulated data sets to gain more insight. At the fundamental frequency of each data set, we computed the phase difference between the current and flux density FFT's. Table 9.1 summarizes the results of this analysis. The function $B(jw)/I(jw)$ refers to the FFT from the input current to the flux density output. The phase lag increases about 0.1° from 1 Hz to 20 Hz. In contrast, the measured data showed an increase of ∼0.8° from 1 to 20 Hz (see 'Center Coil' columns of Table 9.2). It therefore seems

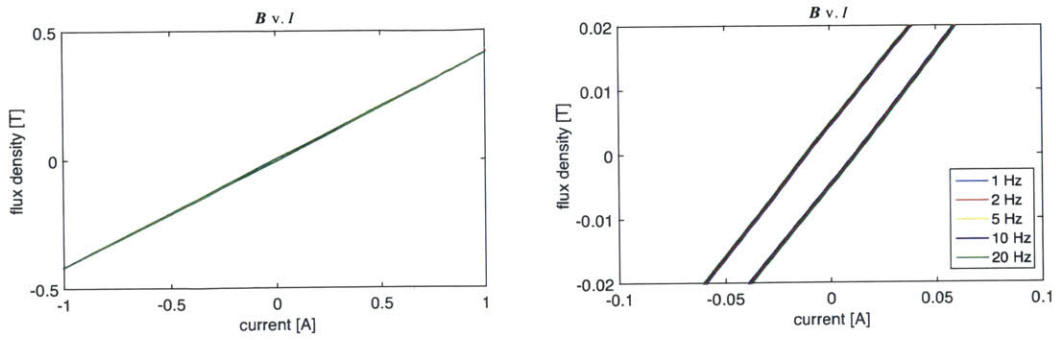

Figure 9-7: LEFT: Simulated B-I curves at different frequencies; RIGHT: zoomed in near origin.

unlikely that eddy currents account for all of the loop widening in the prototype. If we simulate the excess eddy currents with the square root dependency of (5.27), the loop widening from eddy currents is even more negligible: the increase in phase lag from 1 to 20 Hz is under 0.01°.

Table 9.1: Phase between simulated actuator current and flux density

Frequency [Hz]	$\angle \frac{B(j\omega)}{I(j\omega)}$ [°]
1	−0.30
2	−0.33
5	−0.36
10	−0.39
20	−0.41

9.1.3 Multiple-pole Sense Coil Measurements

We added an independent sense coil wrapped around one of the outer pole faces to compare with the center pole sense coil. We clamped the target to the stator with 500 µm plastic shims. We acquired the data using a LabVIEW data acquisition system with its own differential front ends [64] instead of the dSPACE RTC and AMD502 buffers (see Section 9.4.4 for more details on the LabVIEW acquisition system). Figure 9-8 shows the B-I curves estimated from the center sense coil and the outer sense coil. The bottom plots are zoomed in near the origin. While the flux

density estimated from the outer sense coil approximately reaches the same maximum flux density as center sense coil, the zoomed-in plots demonstrate that there is some discrepancies between the loop shapes. For example, from the center coil flux estimate, the 1 Hz loop the narrowest, while with the outer coil flux estimate, the 2 Hz loop is the narrowest.

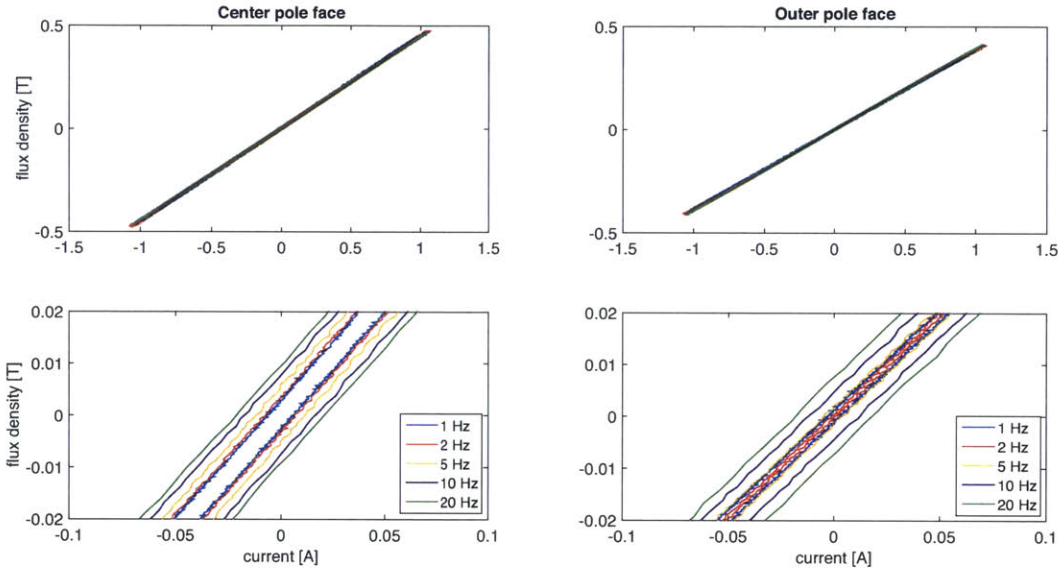

Figure 9-8: LEFT: Measured B-I curves estimated from center pole face sense coil; RIGHT: Measured B-I curves estimated from outer pole face sense coil. Bottom plots are zoomed-in graphs of the top plots.

We applied a Fast Fourier Transform (FFT) to the current and sense coil voltage data sets to gain more insight. At the fundamental frequency of each data set, we computed the phase difference between the current and sense coil voltage FFT's. Table 9.2 summarizes the results of this analysis. The function $V_{sc}(jw)/I(jw)$ refers to the FFT from the input current to the center sense coil voltage output. Likewise, $V_{so}(jw)/I(jw)$ refers to the FFT from the input current to the outer sense coil voltage output. In these columns are listed the FFT phases of the fundamental frequency component corresponding to the driving frequencies of the leftmost column. The functions $B_{sc}(jw)/I(jw)$ and $B_{so}(jw)/I(jw)$ are the respective center coil and outer coil FFT's from current input to flux density. The fundamental component phases

were computed by subtracting 90° from the fundamental frequency component phases of $V_{sc}(jw)/I_(jw)$ and $V_{so}(jw)/I_(jw)$.

Table 9.2: Phase between actuator current and sense coil voltage

	Center coil		Outer coil	
Frequency [Hz]	$\angle\frac{V_{sc}(j\omega)}{I(j\omega)}$ [°]	$\angle\frac{B_{sc}(j\omega)}{I(j\omega)}$ [°]	$\angle\frac{V_{so}(j\omega)}{I(j\omega)}$ [°]	$\angle\frac{B_{so}(j\omega)}{I(j\omega)}$ [°]
1	89.66	−0.34	89.84	−0.16
2	89.60	−0.40	89.96	−0.04
5	89.36	−0.64	90.25	0.25
10	89.06	−0.94	90.65	0.65
20	88.84	−1.16	91.02	1.02

From the $B_{sc}(jw)/I(jw)$ column, we see that the center coil flux lags the current and that this phase lag increases with frequency, confirming the conclusions drawn from the graphical analysis. The outer coil flux, however, tells a different story. Here, the flux lags the current at frequencies of 1 Hz and 2 Hz, but *leads* the current at 5 Hz and higher. In contrast to the center pole flux, the phase lag from the current to the flux *decreases* with frequency so that it actually becomes a phase lead at frequencies of 5 Hz and above. The center coil and outer coil thus show opposite loop-widening behavior. When we inspect the right-hand graph of Figure 9-8 more closely, we see that *B-I* loops corresponding to frequencies of 5 Hz and greater travel in a clockwise direction rather than in a counter-clockwise direction, graphically verifying that the flux leads the current at these frequencies.

9.1.4 CoFe Lab Prototype Actuator

We tested a CoFe actuator prototype designed and built by Roberto Meléndez [62]. Figure 9-9 is a photograph of the actuator stator in a test fixture that Roberto used for his thesis. The test fixture was not used for the loop-widening experiment, but rather the actuator was clamped in a similar fashion to the setup shown in Figure 9-4. The actuator is a two-pole actuator rather than a three-pole actuator. The target used was a NiFe target because CoFe targets were not available at the time of testing.

We wound a sense coil by hand around one of the actuator pole faces.

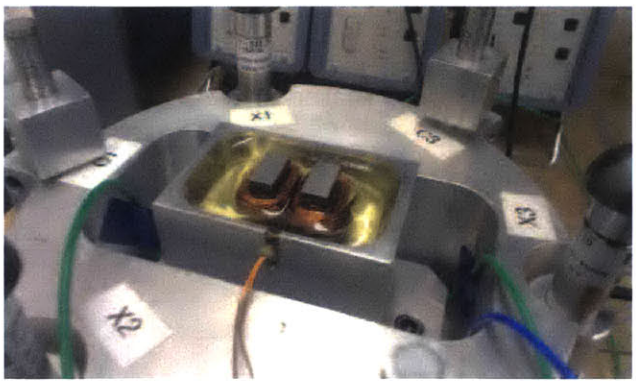

Figure 9-9: CoFe actuator prototype stator.

Figure 9-10 show the measured λ-I curves at a gap of 500 µm, where λ is the total flux linked by the sense coil. Loop widening appears to be less pronounced for frequencies 10 Hz and below, although some loop widening is apparent for the 20 Hz and 50 Hz curves.

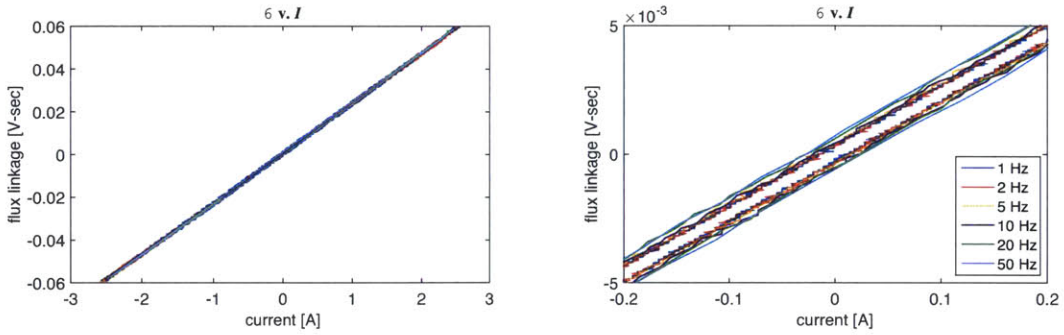

Figure 9-10: LEFT: Measured λ-I curves from CoFe lab prototype actuator; RIGHT: Zoomed in near origin.

Table 9.3 summarizes the FFT analysis of the data shown in Figure 9-10. The CoFe actuator shows less loop widening than the NiFe actuator.

9.1.5 CoFe ASML Prototype Actuator

We also tested a CoFe prototype actuator that we designed at ASML. This actuator is a two-pole actuator. It was designed for the full force capability required for the

Table 9.3: Phase between CoFe lab prototype actuator current and sense coil voltage

Frequency [Hz]	$\angle \frac{V_s(j\omega)}{I(j\omega)}$ [°]	$\angle \frac{\lambda(j\omega)}{I(j\omega)}$ [°]
1	89.72	−0.28
2	89.72	−0.28
5	89.66	−0.34
10	89.61	−0.39
20	89.49	−0.51
50	89.36	−0.64

reticle short-stroke stage and is capable of generating over 1000 N of force. For this actuator, we also had a CoFe target with which to test it. We tested it at both 500 µm gap and a 1 mm gaps. Figure 9-11 shows series of measured *B-I* curves at both of these gaps. The curves appear to show less loop widening than the NiFe actuator for frequencies 10 Hz and below, although some loop widening is apparent for the 20 Hz curve.

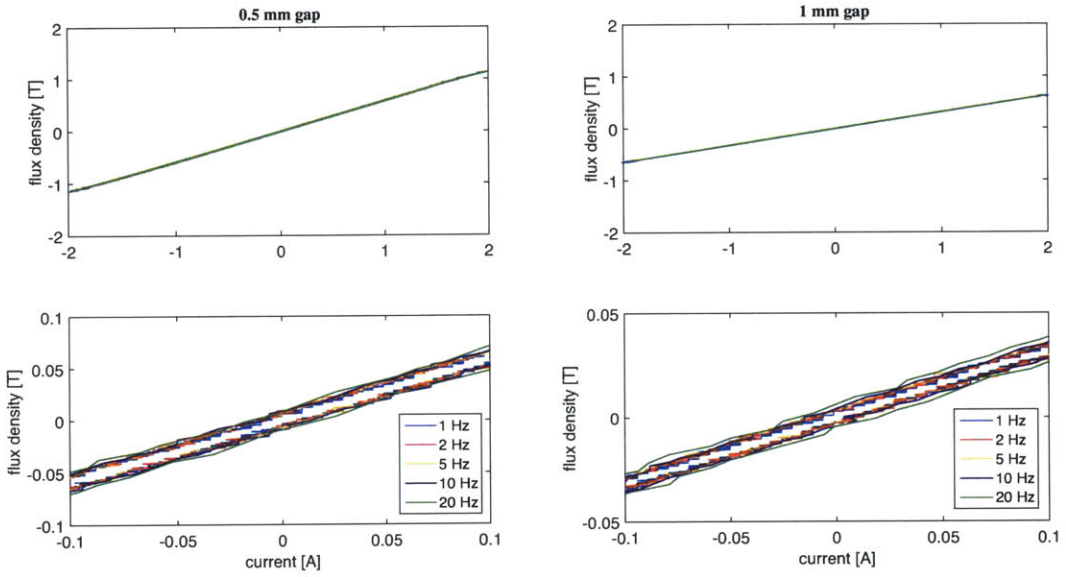

Figure 9-11: LEFT: Measured *B-I* curves from ASML CoFe prototype actuator at 500 µm gap; RIGHT: Measured *B-I* curves from ASML CoFe prototype actuator at 1 mm gap. Bottom plots are zoomed-in graphs of the top plots.

The FFT analysis results for the ASML prototype are presented in Table 9.4.

The results indicate the presence of loop widening; however, this loop widening is considerably less than the amount present in the NiFe actuator. For example, between 1 Hz and 10 Hz, there is an additional 0.14° of phase lag in the 500 µm gap case, whereas for the NiFe actuator, we see an additional 0.3° of phase lag (see 'Center coil' columnn in Table 9.2).

Table 9.4: Phase between actuator current and sense coil voltage for ASML CoFe prototype actuator.

	0.5 mm gap		**1 mm gap**	
Frequency [Hz]	$\angle\frac{V_{sc}(j\omega)}{I(j\omega)}$ [°]	$\angle\frac{B_{sc}(j\omega)}{I(j\omega)}$ [°]	$\angle\frac{V_{so}(j\omega)}{I(j\omega)}$ [°]	$\angle\frac{B_{oc}(j\omega)}{I(j\omega)}$ [°]
1	89.65	−0.35	89.75	−0.25
2	89.63	−0.37	89.72	−0.28
5	89.60	−0.40	89.66	−0.34
10	89.51	−0.49	89.62	−0.38
20	89.42	−0.58	89.46	−0.54

9.2 Cut-core Experiments

In an effort to isolate potential causes of the loop widening, we measured the flux-current relationship of cut-cores that were not potted and incorporated into a stator housing. We experimented on both a 49% NiFe cut-core and a CoFe cut-core.

9.2.1 49% NiFe Cut-core

Figure 9-12 shows the experimental setup for testing a 49% NiFe core. This core is identical to the ones used in our actuator prototype. Two coils are hand-wound around the full length of the cut-core in a bifilar fashion. The cut core is then clamped to an assembled target with 500 µm plastic shim between the core and the target. The primary coil is connected to the sense resistor on one end. The secondary coil is used as the sense coil. The inductance of the primary with a 500 µm gap was computed as 9.3 mH. The primary coil resistance was 1.5 Ω. These values correspond to a corner frequency between drive voltage and current of 26 Hz.

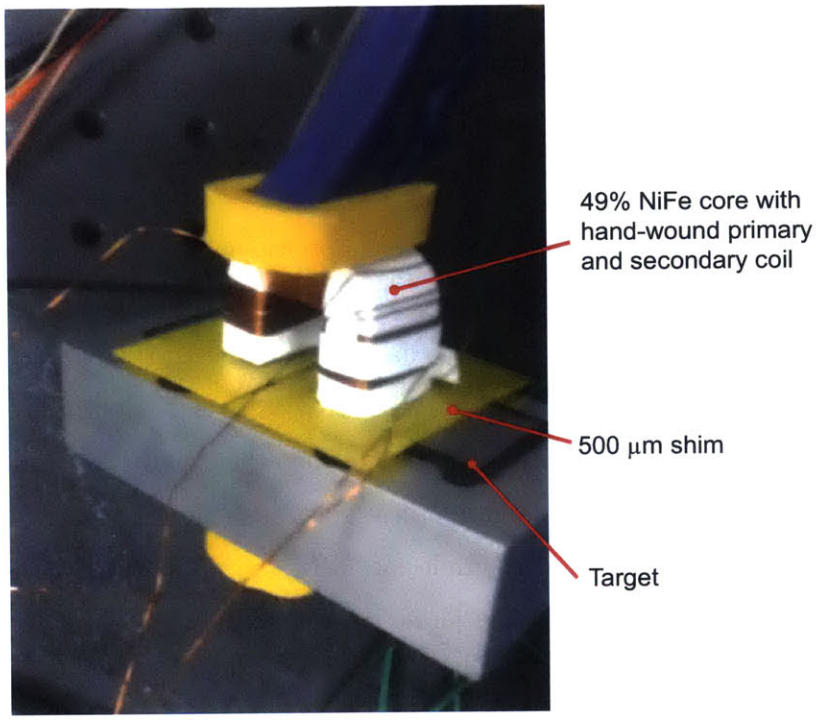

Figure 9-12: Experimental setup for measuring B-I characteristics of single 49% NiFe cut-core.

Figure 9-13 shows the λ-I loops measured on the cut-core when driven at different frequencies. The measured loops appear to show much less loop widening than the NiFe prototype actuator exhibited. The loops corresponding to frequencies 1-10 Hz are on top of one another. The 50 Hz loop is the first one to show noticeable loop widening.

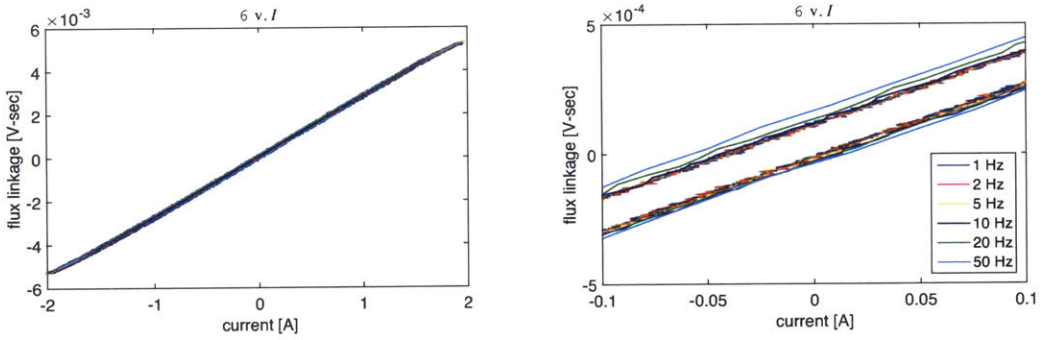

Figure 9-13: LEFT: Measured λ-I curves from 49% NiFe cut-core; RIGHT: Zoomed in near origin.

We applied an FFT analysis to this data. Table 9.5 summarizes the results of this analysis. The function $V_s(jw)/I(jw)$ refers to the FFT from the drive coil current to the secondary coil voltage output. The functions $\lambda(jw)/I(jw)$ is the FFT from drive coil current to secondary coil flux linkage. The FFT analysis confirms that for frequencies between 1-5 Hz, there is negligible loop widening. The 10 Hz loop shows an increase in phase lag of $\sim 0.1\,^\circ$ and the 20 Hz loop likewise shows an additional $\sim 0.1\,^\circ$ of phase lag. These are smaller changes than the corresponding phase lag changes in the actuator, where the phase lag increased by $0.3\,^\circ$ from 5 to 10 Hz and by $\sim 0.2\,^\circ$ from 10 to 20 Hz (see Table 9.2). On the other hand, the phase lag from the current to flux linkage in the cut-core is greater at low frequencies than that manifested by the actuator. For example, at 1 Hz, the phase lag measured in the actuator center pole is 0.34° while the phase lag measured in the cut-core is 0.72°.

Table 9.5: Phase between 49% NiFe cut-core current and sense coil voltage

Frequency [Hz]	$\angle \frac{V_s(j\omega)}{I(j\omega)}$ [°]	$\angle \frac{\lambda(j\omega)}{I(j\omega)}$ [°]
1	89.28	−0.72
2	89.29	−0.71
5	89.27	−0.73
10	89.15	−0.85
20	89.03	−0.97
50	88.88	−1.12

9.2.2 CoFe Cut-core

Figure 9-14 is a photograph of the CoFe cut-core that we tested. The details of this cut-core can be found in [62]. A machine-wound coil assembled by Roberto Melendez was used as the drive coil. A hand-wound coil was used as the secondary coil. Each coil was placed around separate poles. The setup for testing was otherwise identical to that shown in Figure 9-12. A 49% NiFe assembled target was used instead of a CoFe target because the CoFe I-bars had not arrived at the time of testing.

Figure 9-15 shows the measured λ-I curves at different frequencies. The CoFe core

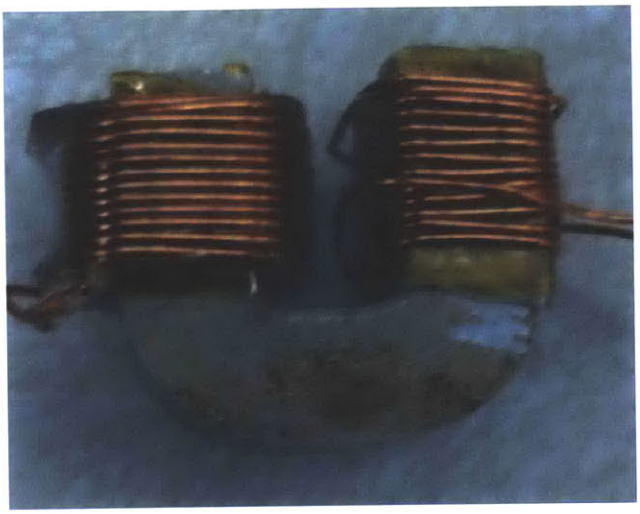

Figure 9-14: Photograph of CoFe cut-core with machine-wound primary coil on left and hand-wound secondary sense coil on right.

shows very little loop widening for the frequencies tested. An FFT analysis confirms that the phase lag variations at the different frequencies remain within 0.05° of one another.

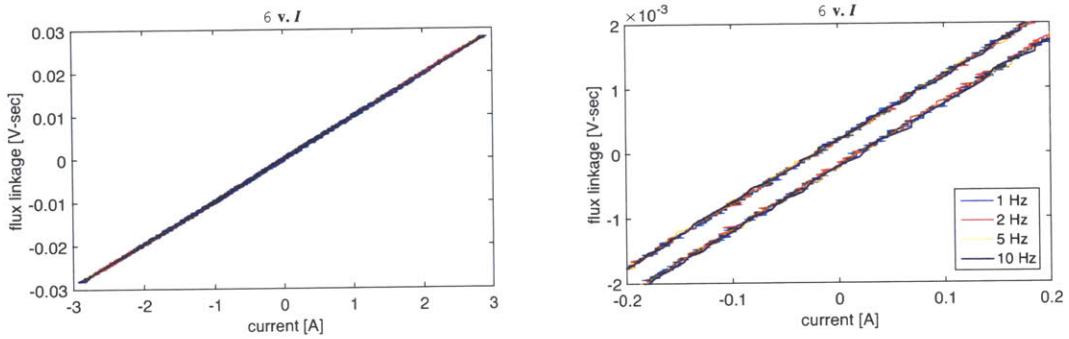

Figure 9-15: LEFT: Measured λ-I curves from CoFe cut-core; RIGHT: Zoomed in near origin.

9.3 Material B-H Experiments

In an earlier set of experiments, we tested the magnetic properties of several ferromagnetic materials. We discovered loop widening at low frequencies on a 50% NiFe specimen but not on a 49% NiFe specimen.

9.3.1 50% NiFe

Figure 9-16 is a photograph of a 50% NiFe toroidal specimen with bifilar windings. The lamination thickness is 0.002" (~50 µm). The inner diameter is 2", the outer diameter is 2.5", and the height is 0.5". The inner winding used as the drive coil has 150 turns and the outer coil used as the sense coil has 120 turns.

Figure 9-16: Photograph of 50% NiFe toroid with bifilar windings.

Figure 9-17 shows a series of B-H curves measured on the specimen at different frequencies. The primary coil was driven with a voltage sine wave. The magnetic field H was measured with a sense resistor connected to the drive coil and the magnetic flux density B was calculated in post-processing from numeric integration of the secondary coil voltage. The B-H curves show clear loop widening, even at low frequencies.

We discovered that the reason for this loop widening is because of the steep transition in the B-H loop near the coercive field. This results in B having a higher frequency content than the driving signal. Figure 9-18 demonstrates the sense coil voltage signal v_s when the primary coil is driven with a 1 Hz voltage sine wave. Note the high-frequency spikes in the v_s signal. These correspond to traversing the high dB/dH portions of the B-H loop.

We can also view this phenomenon from a mathematical perspective. Using the chain rule, we can express dB/dt as

$$\frac{dB}{dt} = \frac{dB}{dH}\frac{dH}{dt}. \tag{9.1}$$

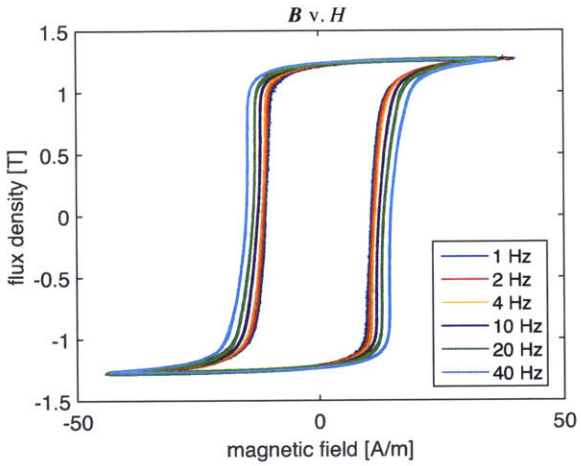

Figure 9-17: Measured B-H curves on 50% NiFe toroid specimen.

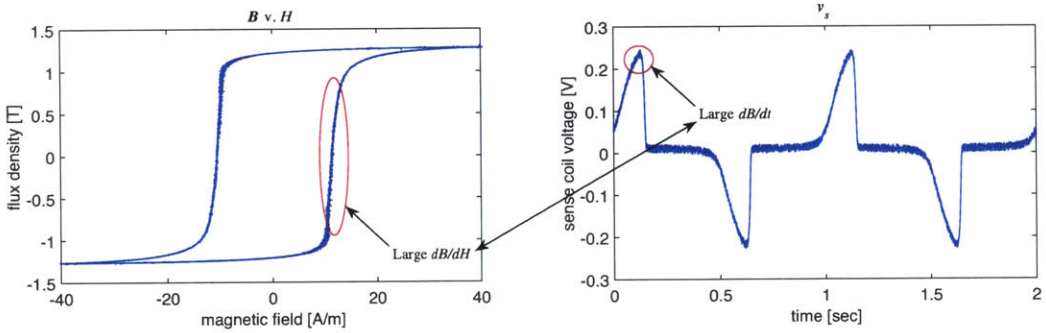

Figure 9-18: LEFT: Measured B-H loop on 50% NiFe toroid driven at 1 Hz; RIGHT: Measured sense coil voltage v_s.

From Ampere's Law, the magnetic field rate of change dH/dt is proportional to the current rate of change dI/dt. Because of the nonlinear nature of dB/dH, even if the current input is driven at a low frequency, the output dB/dt will have higher frequency content than the input signal. Exciting this high-frequency content can result in eddy currents reducing the flux measured by the sense coil. This is what we see in the B-H measurements on the 50% NiFe sample.

9.3.2 49% NiFe

We also measured the B-H characteristics of 49% NiFe. Some of the differences between 50% NiFe and 49% NiFe were previously discussed in Section 7.5.6. A pho-

tograph of the specimen is shown again in Figure 9-19. The specimen is wound with two coils in a bifilar fashion. The inner coil, used as the drive coil, has 116 turns and the outer coil, used as the sense coil, has 108 turns. The specimen is laminated with 0.001" (~25 µm) thick laminations.

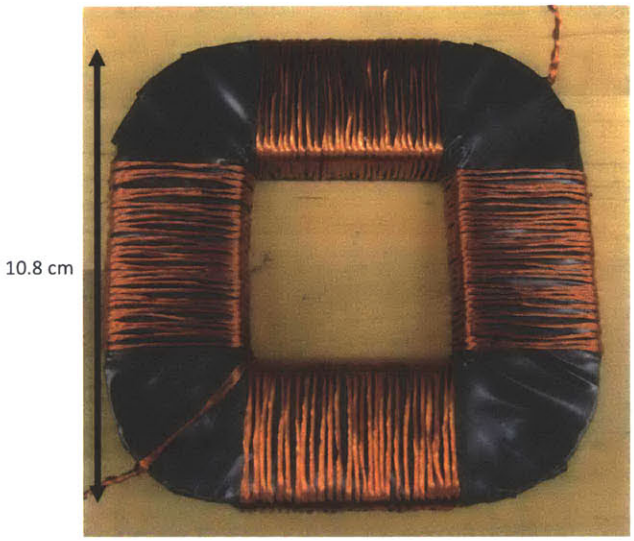

Figure 9-19: 49% NiFe sample used to measure B-H curves.

Figure 9-20 shows the measured B-H curves at three different frequencies of the 49% NiFe specimen. The primary coil was driven with voltage sine waves. The loops show negligible loop widening. Note that the B-H loop is much less steep at the transition region from negative saturation to positive saturation than the 50% NiFe B-H loop. This may account for why we see loop widening at low frequences in the 50% NiFe but not in the 49% NiFe.

We also measured two 49% NiFe cut-cores positioned face-to-face to approximate a toroidal shape. These cut-cores have a lamination thickness of 0.004" (~100 µm), identical to the lamination thickness in the NiFe actuator prototype. Testing these cut-cores helps us to determine whether the absence of loop widening at low frequencies for the 49% NiFe specimen shown in Figure 9-19 is due to the thinner laminations or to the relatively low dB/dH in the transition region from negative B to positive B. The cut-cores are smaller than the ones we used in the prototype actuators. The pole face dimensions of a single pole are 0.25"×0.5", compared to 0.375"×0.75" for

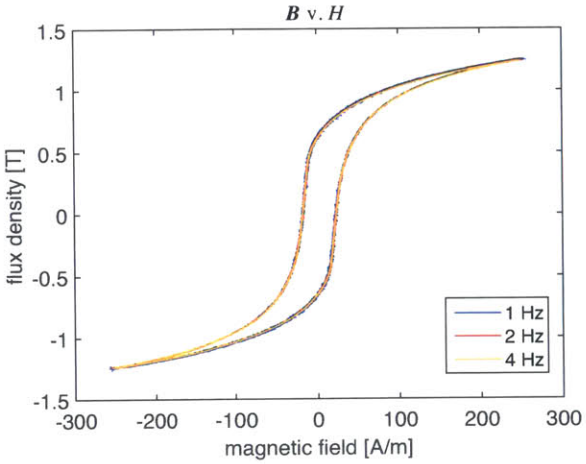

Figure 9-20: Measured B-H curves on 49% NiFe specimen.

the cut-core used for the prototype actuator. Figure 9-21 shows a photograph of one of the cut-cores and the setup used for clamping the two cut-cores together. The drive coil is wound with 25 turns on one cut-core, and the sense coil is wound with 85 turns on the other cut-core.

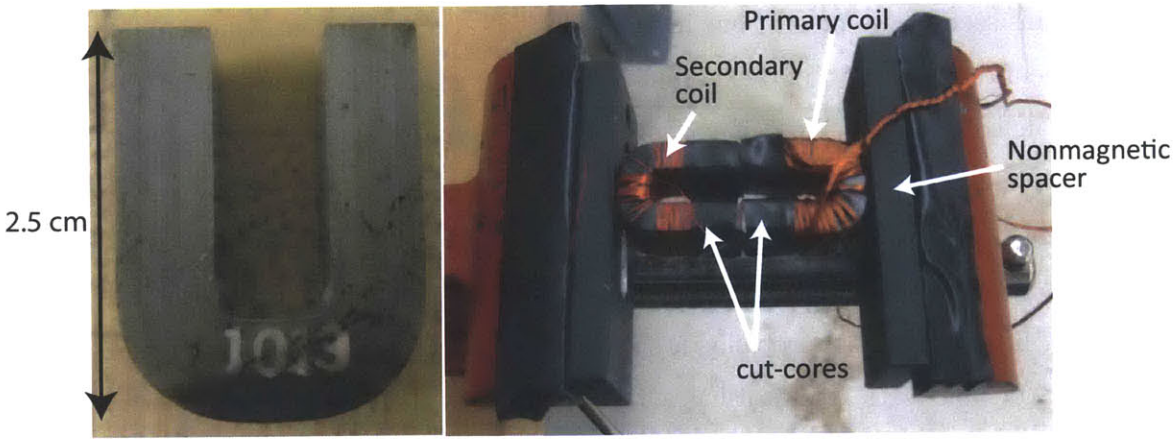

Figure 9-21: LEFT: 49% NiFe cut-core used for testing B-H properties; RIGHT: Experimental setup for testing B-H properties.

Figure 9-22 shows the measured B-H loops for three different frequencies on the clamped cut-core setup. We drove the primary coil with voltage sine waves. We see negligible loop widening at low frequencies, giving us further evidence that the lower dB/dH near the coercive field is what distinguishes the 49% NiFe behavior from the

50% NiFe behavior.

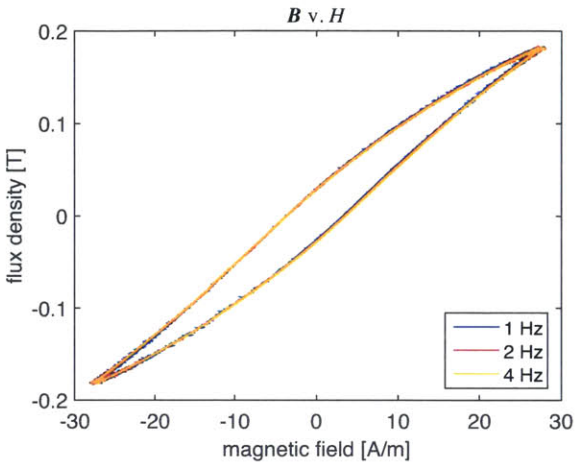

Figure 9-22: Measured B-H curves on 49% NiFe cut-cores.

9.4 Instrumentation

In this section, we present our investigation into the instrumentation chain to determine if this was causing the loop-widening behavior. We document experiments with an air core toroid. We demonstrate on the air core that the current sense resistor value affects the amount of loop widening. We then investigate the affect of the differential amplifier gain with the reluctance actuator prototype and discover that the amplifier gain also affects the amount of loop widening. These two results indicate that instrumentation problems are at least a partial cause of the loop widening. We then demonstrate results using a LabVIEW data acquisition system with its own differential front-end and our own instrumentation front-end built with AD620 differential amplifiers. Both of these options improve the results but do not completely eliminate the loop widening.

9.4.1 Air Core Test Setup

To debug the instrumentation chain, Professor Jeffrey Lang suggested that we test an air core. This way, we eliminate ferromagnetic effects from the test. The air core

should exhibit no phase lag between the drive current and the flux estimated from the sense coil. If phase lag persists, this indicates a problem with the instrumentation chain.

Figure 9-23 is a photograph of the air core with primary and secondary coils. A roll of electrical tape was used as the 'air core'. The coils were wound in a bifilar fashion, with the inner coil consisting of 150 turns and the outer coil consisting of 100 turns. The instrumentation chain was identical to that shown in Figure 9-5 except for the air core replacing the actuator. Additionally, the sense coil is not shielded. A photograph of the testing setup is shown in Figure 9-24.

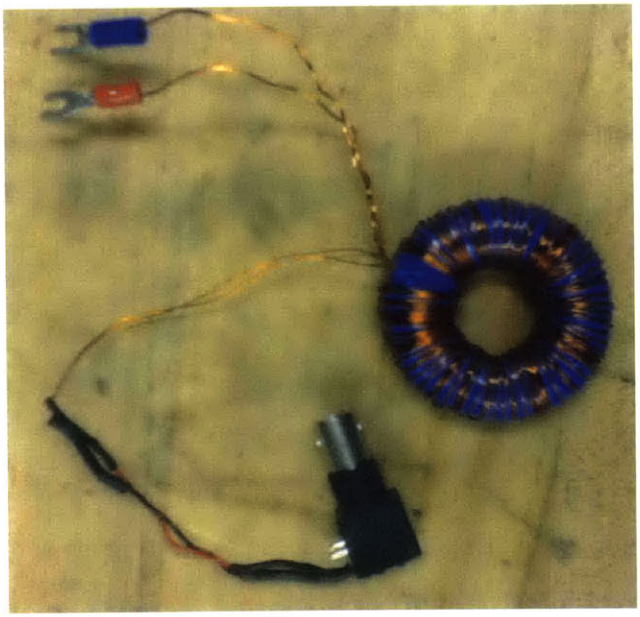

Figure 9-23: Photograph of 'air core' with primary and secondary coils.

9.4.2 Current Sense Resistor

One of the hypothesized causes of the loop widening was sense resistor heating: as the resistor heats up, the resistance increases and gives an erroneous current measurement. Because of the slow time constant associated with the temperature rise, this could result in a phase lag between the estimated flux and the measured current. To test this hypothesis, we switched the $0.1\,\Omega$ sense resistor with a $0.01\,\Omega$ sense resistor

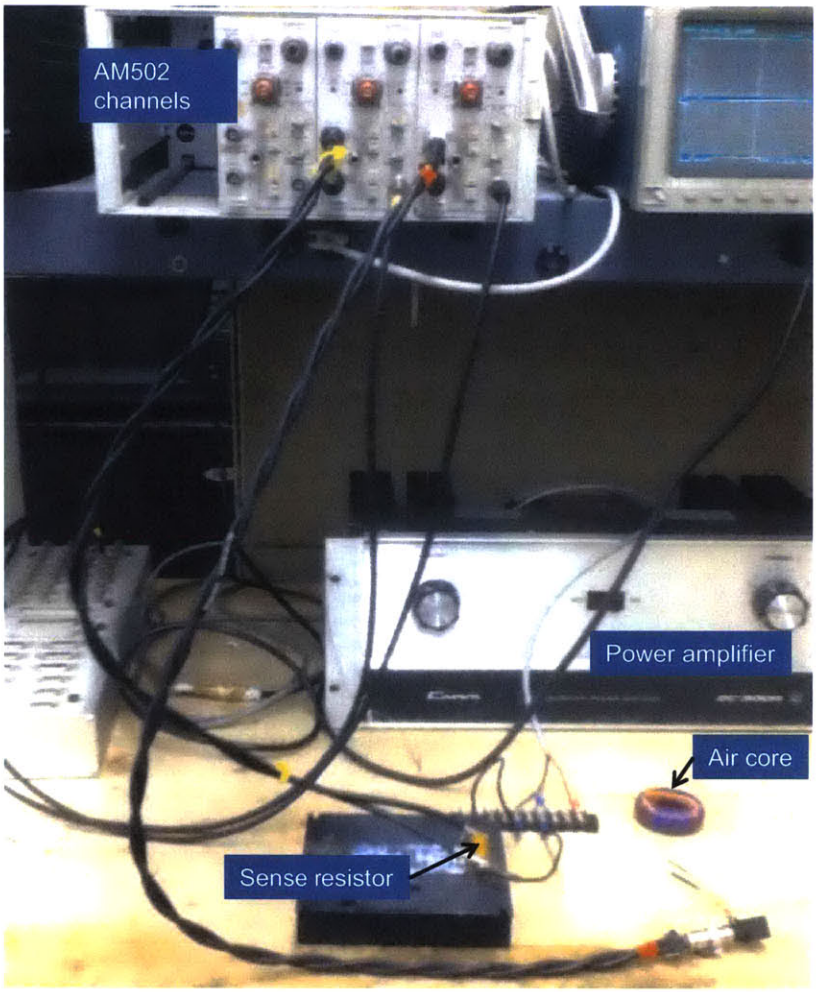

Figure 9-24: Experimental setup for testing air core.

with identical volume. The smaller sense resistor will nominally dissipate ten times less power for the same current, which will limit its temperature rise. Figure 9-25 compares the measured flux-current loops on the air core using the $0.01\,\Omega$ resistor with the measured flux-current loops using the $0.1\,\Omega$ resistor. In an effort to reduce noise, the plotted variables are cyclic averages of 10 to 20 cycles at each frequency. We also set the low-pass filters on the AM502 amplifier channels to a 1 kHz cutoff frequency. We set the gain on the AM502 sense coil channel to as high as possible while still avoiding saturation.

Contrary to expectations, the data obtained with the 0.1 Omega sense resistor

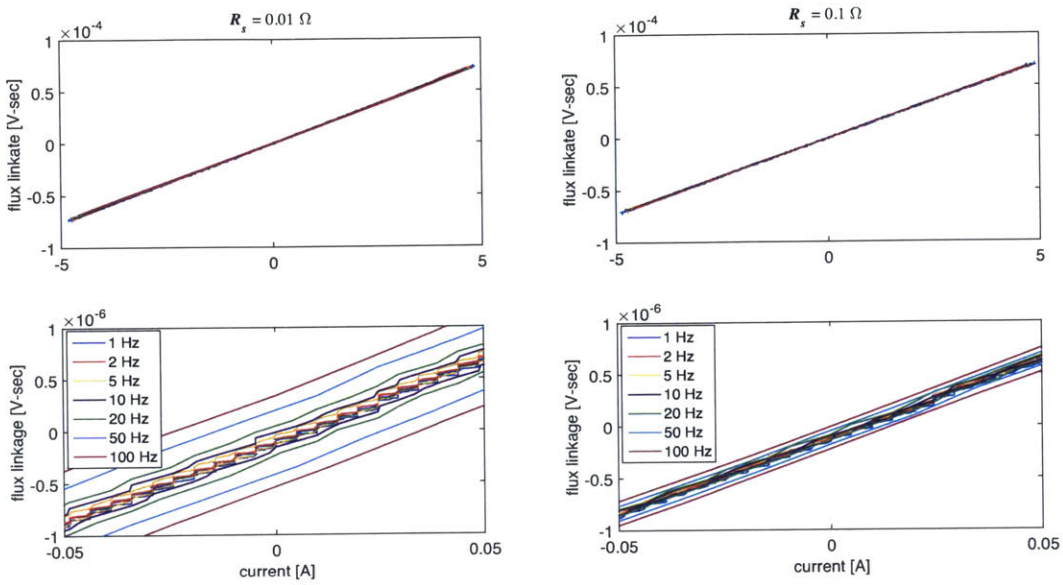

Figure 9-25: LEFT: Measured λ-I curves on air core with $0.01\,\Omega$ sense resistor; RIGHT: Measured λ-I curves on air core with $0.1\,\Omega$ sense resistor. Bottom plots are zoomed-in graphs of the top plots.

showed less loop widening than the data obtained with the 0.01 Omega sense resistor. Note that both data sets show much less loop widening than the actuator did: the bottom plots are significantly zoomed in order to show the loop widening that does exist. Applying an FFT analysis to the data sets generated the phase lag results summarized in Table 9.6. We see that the phase difference between current and estimated flux linkage remains within $0.1\,^\circ$ for frequencies up to 100 Hz when using a 0.1 Omega sense resistor. We hypothesized that the reason the smaller sense resistor fares worse is because the voltage drop across the sense resistor is smaller relative to the voltage drop in the power return line from the low end of the sense resistor to power ground. As a result, the common-mode voltage across the resistor is higher relative to the differential voltage. Since the AMD502 instrumentation amplifiers have finite CMRR, this could result in phase lag.

At a frequency of 100 Hz, we suspected that mismatches between the 1 kHz filters on the differential amplifier channels may be causing some of the small phase difference between the current and flux. To test this, we switched the channels so

Table 9.6: Phase between air core primary coil current and secondary sense coil voltage with different current sense resistors

	$R_s = 0.01\,\Omega$		$R_s = 0.1\,\Omega$	
Frequency [Hz]	$\angle \frac{V_s(j\omega)}{I(j\omega)}$ [°]	$\angle \frac{\lambda(j\omega)}{I(j\omega)}$ [°]	$\angle \frac{V_s(j\omega)}{I(j\omega)}$ [°]	$\angle \frac{\lambda(j\omega)}{I(j\omega)}$ [°]
1	90.002	0.002	90.005	0.005
2	89.992	−0.008	90.005	0.005
5	89.927	−0.073	89.998	−0.002
10	89.877	−0.123	90.009	0.009
20	89.777	−0.223	90.022	0.022
50	89.589	−0.411	90.047	0.047
100	89.445	−0.555	90.088	0.088

that the channel we had connected to the sense coil was now connected to the sense resistor and vice-versa. Figure 9-26 shows the measured λ-I loops for the two different configurations when driven at 100 Hz. The plots are zoomed in near the origin. The sense resistor value is 0.01 Ω. We see that in the configuration with the differential amplifier channels switched, the phase difference between the current and flux reverses, so that the loop now travels in a counter-clockwise direction rather than a clockwise direction. This suggests that the filter mismatch between the two channels does indeed account for some of the phase difference between the current and flux.

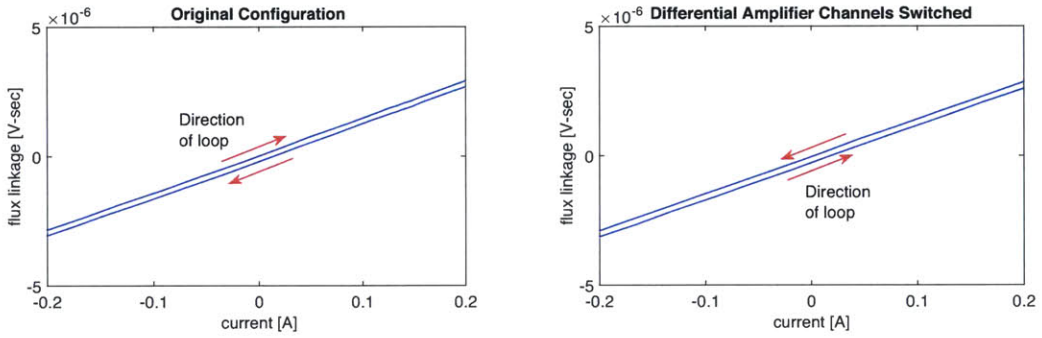

Figure 9-26: LEFT: Measured λ-I loop on air core; RIGHT: Measured λ-I loop on air core with AM502 differential amplifier channels switched.

We increased the sense resistor value to 0.2 Ω to see if we could further improve the results. We did not see any change from the 0.1 Ω case. We likewise tried a 0.2 Ω resistor with the reluctance actuator, but saw no change.

9.4.3 AM502 Differential Amplifiers

The AM502 instrumentation amplifiers have finite CMRR. This CMRR increases with amplifier gain. For example, the AM502 specifications list the CMRR as 100 dB for gains greater than or equal to 100, but 50 dB for gains less than 100 [81]. With the air core tests, we were able to set the amplifier gain on the sense coil channel to high values because the flux levels were so low, and thus we were able to take advantage of the high-gain CMRR. Up to this point, when testing the reluctance actuator, we had used a gain of ten on the sense coil differential amplifier channel to avoid saturation. We decided to investigate the effect that amplifier gain had on loop widening.

Table 9.7 compares the phase difference between B and I for the NiFe reluctance actuator prototype when the sense coil differential amplifier channel gain is set to different gains. The left columns show the results using a high gain on the differential amplifier channel: we selected the highest gain possible while still avoiding saturation. This is why the gain is lowered as the frequency is increases: dB/dt and therefore v_s increases with increasing frequency, so the amplifier gain must be decreased to prevent saturation. The right columns show the results using the original differential amplifier gain setting of ten. The table shows that high gain settings result in lower phase lags than the low gain setting. For example, a gain of 500 for a 1 Hz signal leads to a phase lag of roughly half that measured with a gain of ten.

Table 9.7: Comparison of phase between actuator current and sense coil voltage for different sense coil differential amplifier gain settings.

Frequency [Hz]	**High DA gain**			**Low DA gain**		
	DA gain	$\angle \frac{V_s(j\omega)}{I(j\omega)}$ [°]	$\angle \frac{B(j\omega)}{I(j\omega)}$ [°]	**DA gain**	$\angle \frac{V_s(j\omega)}{I(j\omega)}$ [°]	$\angle \frac{B(j\omega)}{I(j\omega)}$ [°]
1	500	89.64	−0.36	10	89.26	−0.74
2	200	89.56	−0.44	10	89.40	−0.60
5	100	89.34	−0.66	10	89.28	−0.72
10	50	89.02	−0.98	10	89.00	−1.00
20	20	88.73	−1.27	10	88.73	−1.27

These results motivated us to improve our instrumentation chain. We considered

two options. The first option was to use a LabVIEW high-resolution data acquisition system in place of the dSPACE DAQ and AM502 differential amplifiers. The dSPACE 1103 board that we had been using has 16-bit A/D boards with a mininum of 83 dB of signal-to-noise ratio. In contrast, the LabVIEW A/D has 18-bit resolution and its own differential front-end with a CMRR over 100 dB. The second option is to build our own differential front end with high CMRR and use this instead of the AM502 channels. We investigated both options.

9.4.4 LabVIEW Data Acquisition System

We first tested the LabVIEW Data Acquisition System (DAQ) with the air core to ensure that the instrumentation chain was working properly. We obtained similar results to those presented in Section 9.4.1 with the $0.1\,\Omega$ sense resistor, i.e., showing negligible phase lag between the current and flux.

When testing the reluctance actuator, we obtained similar results to those obtained using the AM502 high-gain setting. Table 9.8 summarizes the phase results using LabVIEW. Loop widening at low frequencies is still present.

Table 9.8: Phase between reluctance actuator current and sense coil voltage using LabVIEW DAQ

Frequency [Hz]	$\angle\frac{V_s(j\omega)}{I(j\omega)}$ [°]	$\angle\frac{\lambda(j\omega)}{I(j\omega)}$ [°]
1	89.65	−0.35
2	89.58	−0.42
5	89.35	−0.65
10	89.06	−0.94
20	88.83	−1.17

9.4.5 AD620 Instrumentation Amplifier Front-End

We breadboarded two AD620 IC's to use as our differential amplifier front-end to our data acquisition system. The AD620 is an instrumentation amplifier IC from Analog Devices [6] with adjustable gain. The gain is set with a single resistor. As with the

AM502 amplifiers, the CMRR degrades as the gain is decreased. The typical CMRR listed on the data sheet is 90 dB, 110 dB, and 130 dB for gains of for gains of 1, 10, and 100, respectively. Nevertheless, these CMRR values are still significantly higher than the AM502 CMRR at comparable gains. Figure 9-27 is a photograph of the breadboarded circuit. One AD620 chip is used to measure the voltage across the sense resistor and the other is used to measure the sense coil voltage.

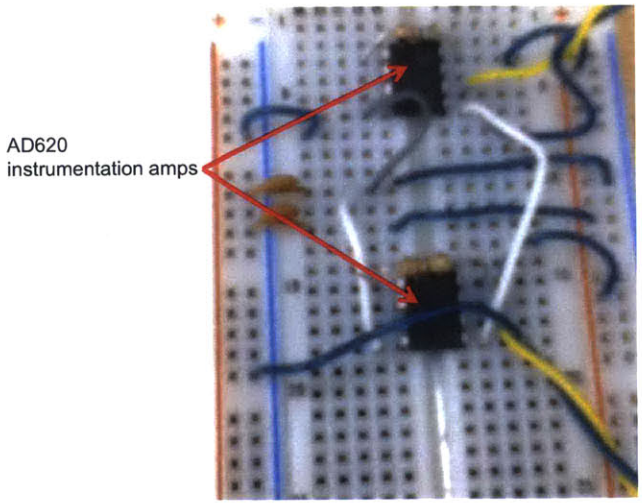

Figure 9-27: Experimental setup for testing air core.

As with the LabVIEW differential front-end, we first tested the AD620 front-end with the air core. We achieved negligible phase lag between the measured current and flux with the air core. With the reluctance actuator, we obtained similar results to the LabVIEW results. Table 9.9 summarizes the phase results with the AD620 front-end. A gain of 10 was used for the current measurement AD620 and a gain of 100 was used for the sense coil AD620.

We also found that the gain on the AD620 sense coil channel affected the amount of phase lag. For example, when we used a gain of 10, there was more phase lag from the measured current to the measured flux than when we used a gain of 100. Thus, the AD620 instrumentation amplifiers showed similar behavior to that of the AM502 amplifiers.

Table 9.9: Phase between reluctance actuator current and sense coil voltage using AD620 front-end.

Frequency [Hz]	$\angle \frac{V_s(j\omega)}{I(j\omega)}$ [°]	$\angle \frac{B(j\omega)}{I(j\omega)}$ [°]
1	89.67	−0.33
2	89.55	−0.45
5	89.32	−0.68
10	88.97	−1.03

9.5 Summary

We have documented a series of experiments undertaken to uncover the root cause of the loop widening phenomenon at low frequencies with the prototype reluctance actuator. Actuator simulations suggest that the amount of loop widening is too large to be explainable by eddy currents alone. This conclusion was confirmed by testing NiFe cut-cores and measuring the B-H properties of 49% NiFe, which showed negligible loop widening at low frequencies. Changing the gain on the differential amplifier and changing the sense resistor value both resulted in different results. This indicated that the instrumentation chain was part of the problem. To debug the instrumentation chain, we tested an air core. We were able to demonstrate negligible loop widening on the air core both with the AMD502 buffers using high gain settings and with the Labview high-resolution DAQ. However, the problem reappeared when testing the actuator with the Labview high-resolution DAQ, indicating that the problem is with the actuator itself.

On the other hand, the Gaussmeter measurements showed similar loop-widening behavior to that manifested by the sense coil measurements. This suggests that it is not a measurement problem but that the actuator flux is being affected. However, in that case, we would expect the measured force to show similar loop-widening behavior when plotted against the current, but we do not. Moreover, the sense coil measurements from the outer pole face showing phase *lead* with increasing frequency are inexplicable with this hypothesis.

We do not at present have a hypothesis that accounts for the apparent contra-

dictions among the different tests and simulations. Time did not permit for a more thorough investigation to uncover the root cause of the loop widening.

One crucial point that was driven home during this investigation is the importance of properly managing the electrical wires and connections, especially on the instrumentation side. Appropriate grounding and shielding can solve a host of problems and is necessary for achieving high precision control of a reluctance actuator. Moreover, as was demonstrated from the variation resulting from the choice of current sense resistor and differential amplifier gain, we learned that careful of selection of sensors and buffer amplifiers is critical to achieving high performance.

Another important insight gained during testing was the effect of the nonlinear B-H curve on loop widening in 50% NiFe. Because of the steep transition in the B-H loop near the coercive field, the flux density can have high-frequency content even when driven with a low-frequency magnetic field. This generates eddy currents that cause loop widening. Thus, we recommend that 50% NiFe not be used for a reluctance actuator in a lithography machine.

In the next chapter, we present experimental results from the reluctance actuator prototype using the 1-DoF testbed. We demonstrate the accuracy of the SHM, and we present results of a flux feedback controller that combines the SHM and sense coil estimates. We discuss the effects of the loop widening phenomenon on the force tracking experimental results using the flux feedback controller.

Chapter 10

One-DoF Testbed Experimental Results

In this chapter, we present experimental results for the reluctance actuator on the 1-DoF testbed. We first present the overall controller structure of the testbed and then present controller designs for the voice coil current controller and the air bearing position controller. We then demonstrate calibration results for the reluctance actuator from the 1-DoF testbed. We map current and gap to flux and map flux and gap to force.

We implement the SHM observer from Section 6.6 to provide a low-frequency estimate of the actuator flux. We compare the accuracy of the estimated output with the sense coil measurement for different inputs. We also demonstrate the accuracy of the hysteresis model when a gap disturbance is applied to the air bearing slide using the voice coil actuator.

We then incorporate this SHM observer into a flux estimator. For the flux estimator, we employ a novel technique for estimating the flux, whereby we combine the sense coil measurement with the SHM observer estimate using a complementary filter pair. This results in a flux estimate for frequencies from DC to several kHz that can be used as the feedback variable for the reluctance flux controller. This hybrid flux estimator is incorporated into a flux feedback controller. We use the calibration results to invert the desired force into a desired flux density that is used for the flux

loop command signal. We experimentally demonstrate the small-signal force tracking ability and the stiffness of the actuator with flux control. Finally, we demonstrate the force accuracy of the reluctance actuator with flux control for a force pulse similar to that used on a scanning lithography machine. We repeat this experiment in the presence of a gap disturbance.

10.1 Controller Structure

Figure 10-1 illustrates the overall controller structure of the testbed. The linear encoder signal x_m is used as the position feedback variable. The position controller (dotted blue box) tracks the desired reference position x_r. The voice coil actuator is used as the position feedback actuator and applies a force F_{vc} to the air bearing slide. Within the position loop, a inner current control loop (dotted green box) is used to achieve high actuator bandwidth for the voice coil. A flux control loop (dotted red box) is used to provide accurate force control for the reluctance actuator. An inverse actuator calibration $B(F_d, g)$ transforms the desired force F_d into a desired flux density B_d. This inverse calibration uses x_m as an input to account for the actuator dependency on operating gap. The flux estimation scheme is used to generate a flux density estimate $\hat{B}$ for the flux feedback variable. The reluctance actuator applies a force F_r to the air bearing stage. The desired force is also multiplied by $-1/\hat{K}_{mvc}$ to generate a feedforward current I_{FF} to the voice coil controller. The purpose of this is to help counteract the reluctance actuator force and achieve higher performance in maintaining the desired operating gap. The parameter $\hat{K}_{mvc}$ is the estimated motor constant of the voice coil actuator.

10.1.1 Voice Coil Current Controller

The measured frequency response of the uncompensated voice coil is shown in Figure 10-2. The input is the voltage to the amplifier and the output is the measured current across the sense resistor. The measurement chain thus includes the amplifier dynamics. The sense resistor voltage was sent to an AM502 differential amplifier

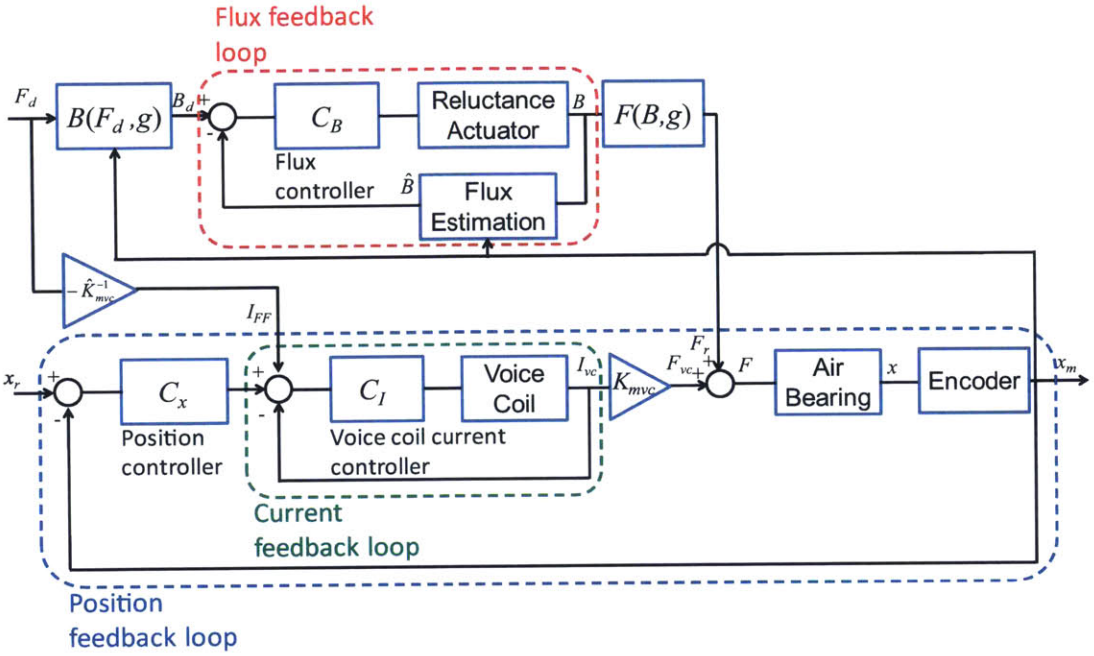

Figure 10-1: Controller configuration used for 1-DoF testbed.

channel with a low pass filter with cutoff frequency of 10 kHz. This signal was sent to a dSPACE A/D channel in order to capture the phase delay from sampling. The signal was sampled at 40 kHz.

We designed our voice coil controller to have a crossover frequency f_c of 5 kHz. The plant has a gain of 0.057 A/V and a phase of $-112°$ at 5 kHz. Our controller is a simple PI controller with the zero frequency set at a factor of five below f_c. The controller form is

$$C_I(s) = K_I \frac{\tau_I s + 1}{\tau_I s}. \tag{10.1}$$

We set $K_I = 17.2\,\mathrm{V/(A \cdot s)}$ and $\tau_I = 1.59 \times 10^{-4}\,\mathrm{s}$. The predicted and measured frequency responses of the voice coil loop transmission are shown in Figure 10-3. The crossover frequency of the measured loop transmission is ~6.3 kHz, slightly higher than predicted. The reason for this may be that the input voltage amplitude is different from that used to measure the plant frequency response from which the predicted loop transmission was derived. The phase margin is ~45°.

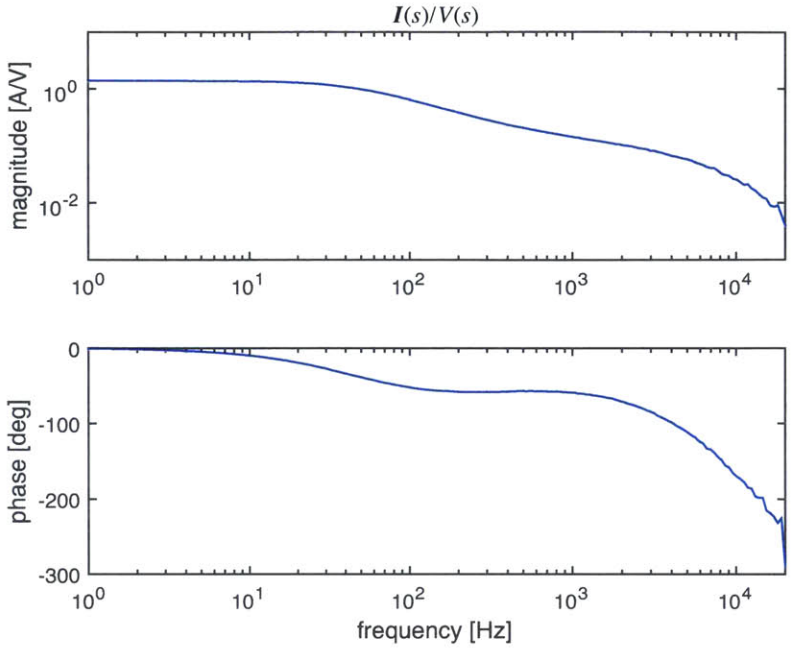

Figure 10-2: Measured frequency response for uncompensated voice coil actuator.

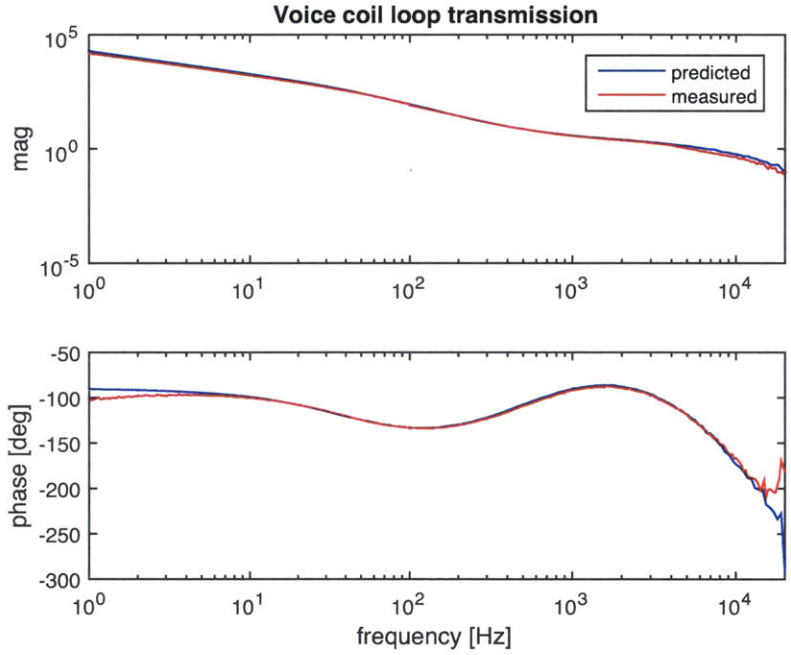

Figure 10-3: Predicted and measured frequency responses for voice coil loop transmission.

10.1.2 Position Controller

The measured frequency response of the air bearing slide is shown in Figure 10-4. The slide was driven with the voice coil actuator. The input for the measured frequency response is the voice coil current I_{vc} and the output is the encoder measurement x_m. Since the response was measured open-loop, we placed soft compression springs between the air bearing stator and the reluctance actuator target to ensure that the slide did not drift and cause the reluctance actuator target to hit the air bearing stator. A photograph of this setup is shown in Figure 10-5. A bias current was applied to the voice coil to preload the slide against the compression springs.

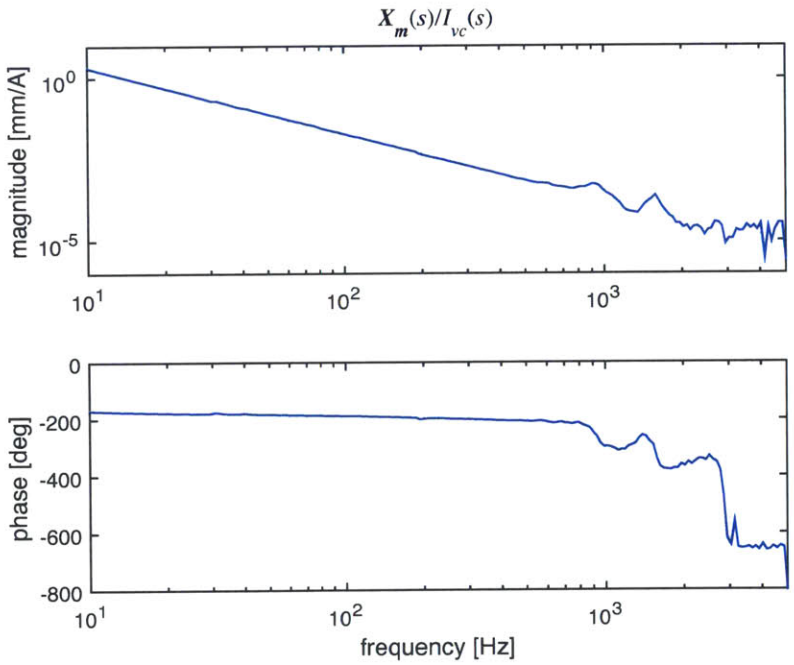

Figure 10-4: Measured frequency response from voice coil current to air bearing position.

We designed a lead-lag controller for the air bearing and targeted a crossover frequency f_c of 150 Hz. The lag compensator is a PI controller. We placed the PI zero at a factor of eight below f_c, or $f = 18.75$ Hz. We designed for a phase margin $\phi_m = 30°$. The plant has a phase of $-190.7°$ at 150 Hz. The PI controller contributes another 7.1° of phase lag at 150 Hz. Therefore, the lead controller must add 47.8°

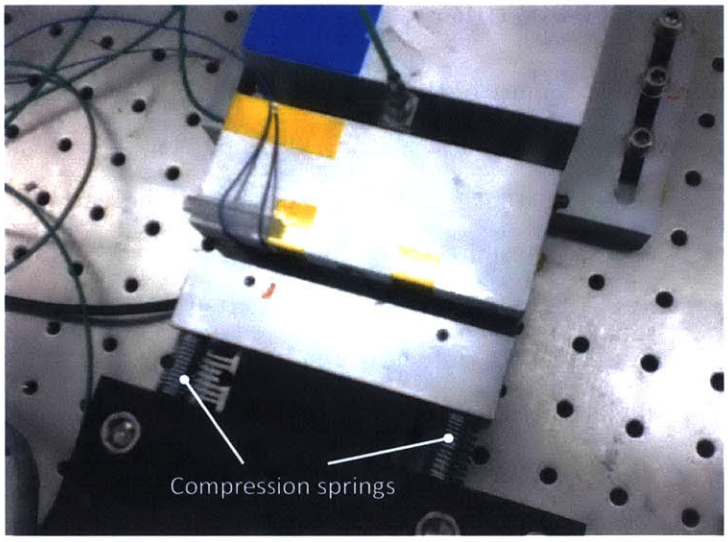

Figure 10-5: Air bearing setup with preload springs.

of phase to achieve the desired phase margin. If we place the maximum phase of the lead controller at the crossover frequency, we require a separation factor α between the lead compensator zero and lead compensator pole of $\alpha = 6.72$. This results in a lead zero at $f = 58.7\,\text{Hz}$ and a lead pole at $f = 389\,\text{Hz}$.

The gain of the plant at 150 Hz is $0.00868\,\text{mm/A}$. The gain of the lead compensator at 150 Hz is $\sqrt{\alpha} = 2.59$ and the gain of the PI compensator at 150 Hz is 1.0078. Therefore, to achieve unity gain at a crossover frequency of 150 Hz, we select $K = 1/(0.00868 \cdot 2.59 \cdot 1.0078) = 44.8\,\text{A/mm}$. The position feedback controller is

$$\begin{aligned} C_x(s) &= K_x \left(\frac{\tau_1 s + 1}{\tau_1 s}\right)\left(\frac{\alpha\tau_2 s + 1}{\tau_2 s + 1}\right) \\ &= 44.8 \left(\frac{8.488 \times 10^{-3} s + 1}{8.488 \times 10^{-3} s}\right)\left(\frac{2.752 \times 10^{-3} s + 1}{4.092 \times 10^{-4} s + 1}\right). \end{aligned} \tag{10.2}$$

The predicted controller and measured loop transmission frequency responses are shown in Figure 10-6.

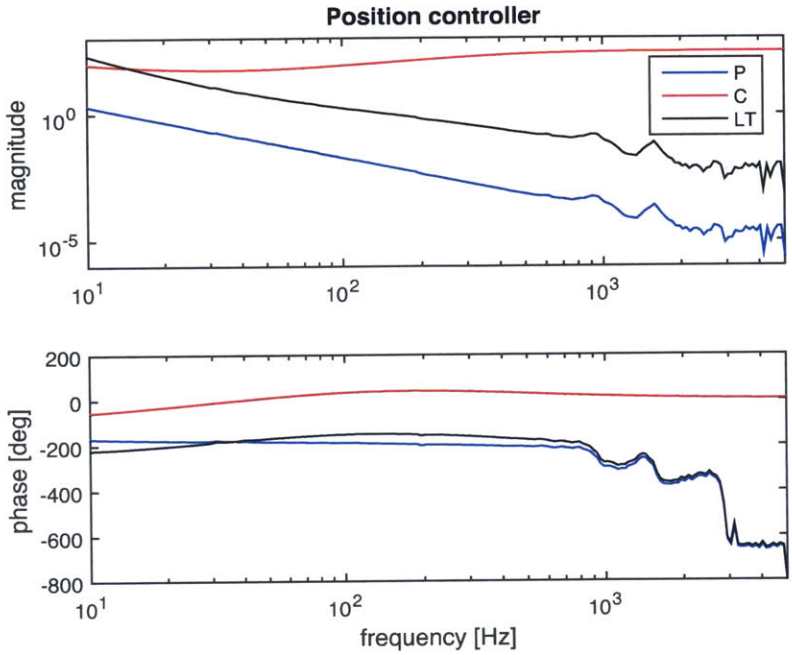

Figure 10-6: Air bearing frequency responses: P - plant (measured); C - controller (predicted); LT - loop transmission (measured).

10.2 Actuator Calibration

We calibrated the reluctance actuator by mapping the current-gap-flux relationship and force-gap-flux relationship. The position controller maintained a constant operating air gap during these calibrations. In the initial calibration routine, we drove the reluctance actuator into positive and negative saturation at several different operating gaps with a 1 Hz voltage sine wave. We recorded the following measurements: reluctance actuator current, sense coil voltage, load cell signal, air bearing position, and voice coil current. We recorded five to ten cycles of data. In post-processing, we took the cyclic average of each measurement in an effort to reduce noise. We integrated the sense coil voltage in post-processing to provide a flux estimate. In this initial calibration, we used only the position feedback controller to maintain the constant operating gap. The block diagram for this setup is shown in Figure 10-7. The variables highlighted in red are the recorded measurements. The variables I_r and v_s refer to the reluctance actuator current and sense coil voltage, respectively.

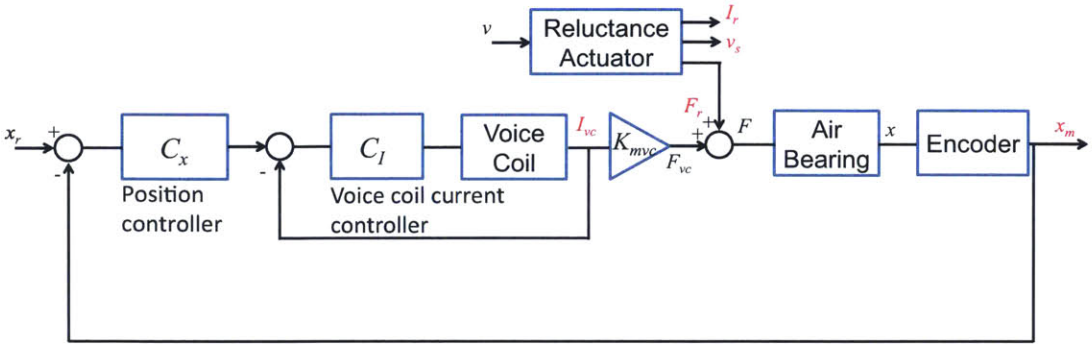

Figure 10-7: Controller configuration used for initial calibration of reluctance actuator.

Because the position feedback controller has finite bandwidth, there is some deviation from the nominal air gap during the calibration tests. Figure 10-8 shows the cyclic air gap position during a calibration test at a nominal air gap of 500 µm. The reluctance actuator current during this test reached a peak value of 1.9 A and the peak force as measured by the load cells was 150 N. The air gap is shown to have a peak fluctuation of about ±6 µm about the nominal. The peak gap fluctuation per peak force is therefore 0.04 µm/N.

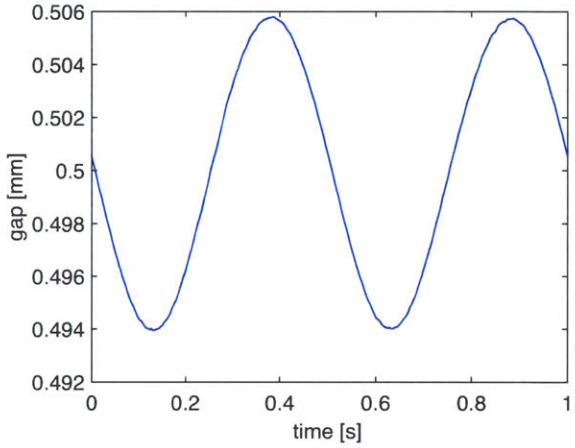

Figure 10-8: Air gap fluctuation during calibration at $g_0 = 500\,\mu\text{m}$.

After this first set of calibrations, we implemented two 2-D lookup tables (LUT). We used the current-gap-flux relationship to generate a 2-D lookup table that estimated the reluctance actuator flux based on the actuator current and air gap. We

then designed a simple flux feedback controller using this estimated flux as the feedback variable. This flux estimate does not incorporate hysteresis. We used a second 2-D LUT to estimate the reluctance actuator force from the desired flux and air gap. We used this predicted force to command a feedforward force to the voice coil actuator to improve the cancellation of the reluctance actuator force. This helped to reduce the position deviation during the second set of calibrations and allowed us to generate a more accurate reluctance actuator mapping. For this second set of calibrations, instead of commanding a sinusoidal voltage, we commanded a sinusoidal flux density. The block diagram for this setup is shown in Figure 10-9. After generating new calibration curves using this configuration, we could replace the $B(I_r, g)$ LUT and the $F(B_d, g)$ LUT with more accurate mappings and run the calibration routine again in an iterative process.

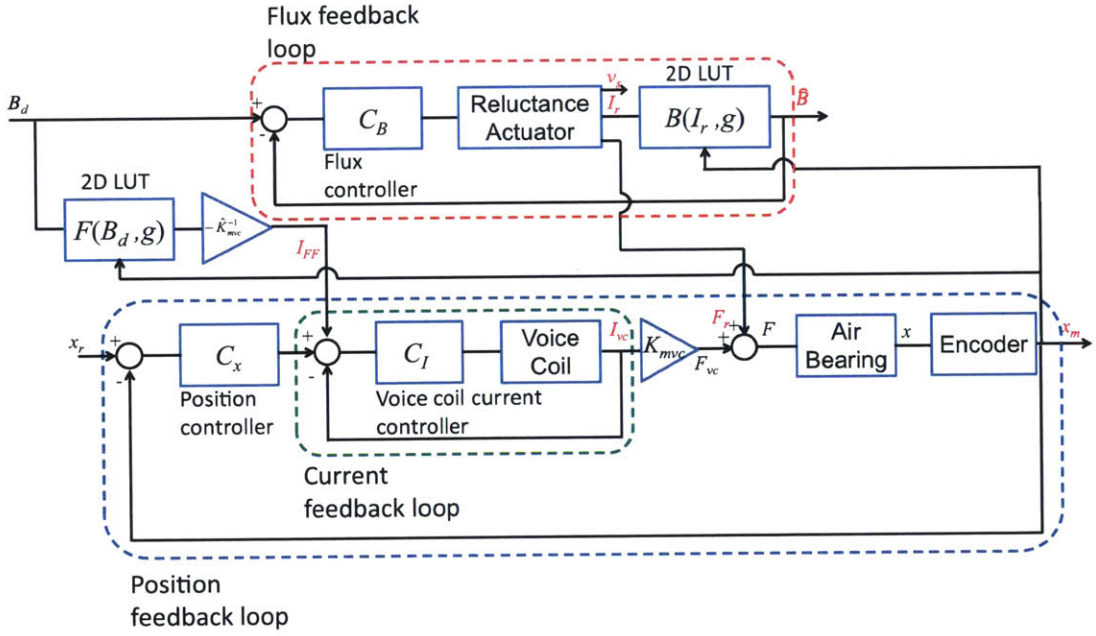

Figure 10-9: Controller configuration used for calibration of reluctance actuator with voice coil feedforward added.

Figure 10-10 shows the cyclic air gap position during a calibration test at a nominal air gap of 500 µm with feedforward force control implemented on the voice coil. The actuator current during this test reached a peak value of 2.9 A and the peak

measured force was 315 N. We were able to reach these higher force levels because of the improved position control from the feedforward force. The air gap has a peak fluctuation of about $\pm 1.6\,\mu$m about the nominal. The peak gap fluctuation per peak force is therefore $0.005\,\mu$m/N, an eight-fold improvement over the calibration done without feedforward.

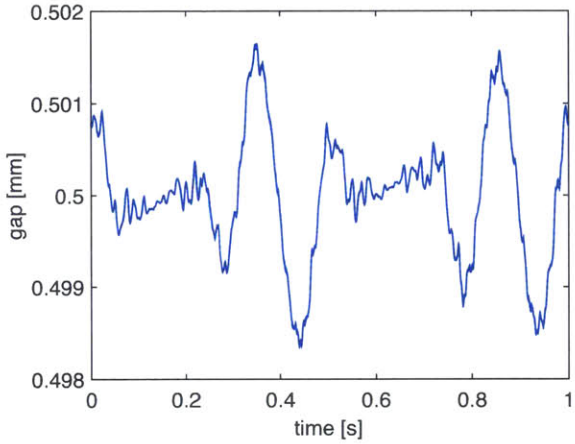

Figure 10-10: Air gap fluctuation during calibration with force feedforward at $g_0 = 500\,\mu$m.

10.2.1 Flux-Current-Gap Calibration

Figure 10-11 shows the reluctance actuator B-I curves recorded at different operating gaps using the calibration configuration of Figure 10-10. The operating gaps ranged from $300\,\mu$m to $700\,\mu$m in increments of $50\,\mu$m. The 2-D LUT map generated from these curves is shown in Figure 10-12. For current values beyond those measured in the calibration routine, we extrapolated linearly to estimate the corresponding flux density. At small air gaps, we could not drive the actuator very far into saturation because the voice coil and amplifier could not sufficiently counteract the reluctance actuator force. For the LUT at these air gaps, we extrapolated linearly from the measured current-flux points to generate missing table entries. This is why some of the flux density values at small gaps reach values greater than 2 T, which is not physically possible for NiFe.

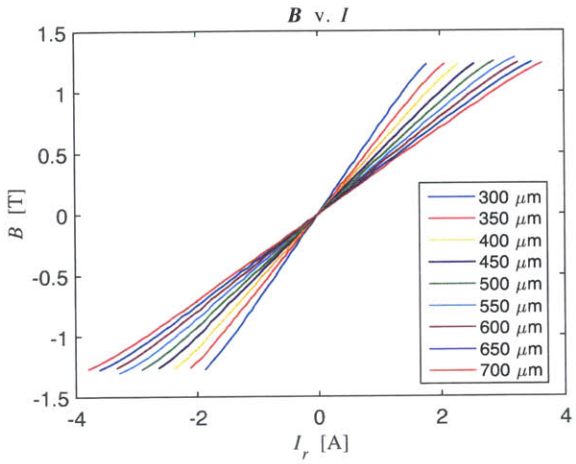

Figure 10-11: B-I curves at different operating gaps for reluctance actuator calibration.

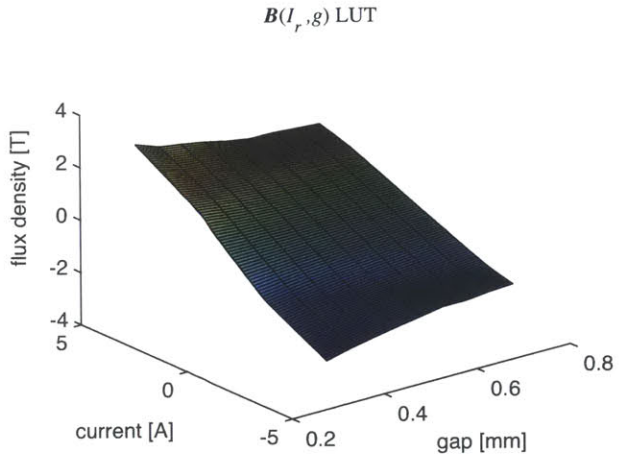

Figure 10-12: $B(I_r, g)$ lookup table.

Figure 10-13 shows the mutual inductance L_m of the reluctance actuator as a function of the gap g. The experimental data points were obtained by computing the slopes of the linear regions of the curves in Figure 10-11. A theoretical best-fit curve proportional to $1/g$ is shown in red. This $1/g$ relationship is derived from (2.8). Another fit is shown in blue, where we fit a function of the form

$$L_m(g) = \frac{a}{(g+b)^y} \tag{10.3}$$

to the experimental data, where a, b, and y are the fitting parameters. We found that the best fit for a function of this form to the experimental data was

$$L_m(g) = \frac{1.22 \times 10^{-3}}{(g - 0.0582)^{0.717}}, \tag{10.4}$$

where g is in units of mm.

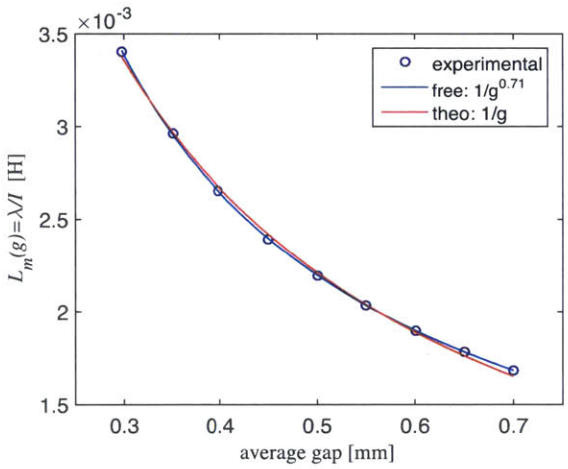

Figure 10-13: Mutual inductance L_m of reluctance actuator as a function of gap g.

10.2.2 Force-Flux-Gap Calibration

Figure 10-14 shows the force-flux curves for the different operating gaps obtained from the calibration routine. The force is measured by the load cells and the flux density is computed in post-processing from the recorded sense coil voltage. As expected, the relationship between the force and flux density is parabolic. The force decreases as a function of gap. This is in contrast to the prediction from (2.13). The reason for the difference is that (2.13) does not take into account fringing fields. As the air gap changes, the fringing field patterns change. For example, as the air gap gets larger, the fringing fields will take up a greater proportion of the total flux measured by the sense coil. As a result, the force-to-measured-flux ratio will reduce.

The 2-D LUT generated from these curves is shown in Figure 10-15. The mapping from flux density and gap to force is shown in the left plot. We also created the inverse

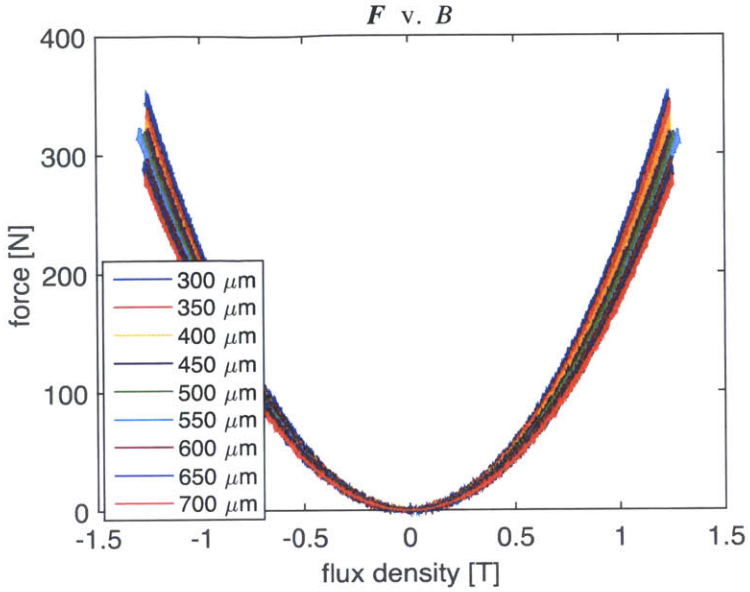

Figure 10-14: F-B curves at different operating gaps for reluctance actuator calibration.

2-D LUT from these curves in order to generate a desired flux density from a desired force. This inverse LUT is represented as the $B(F_d, g)$ block in Figure 10-1. The inverse map is shown in the right plot of Figure 10-15.

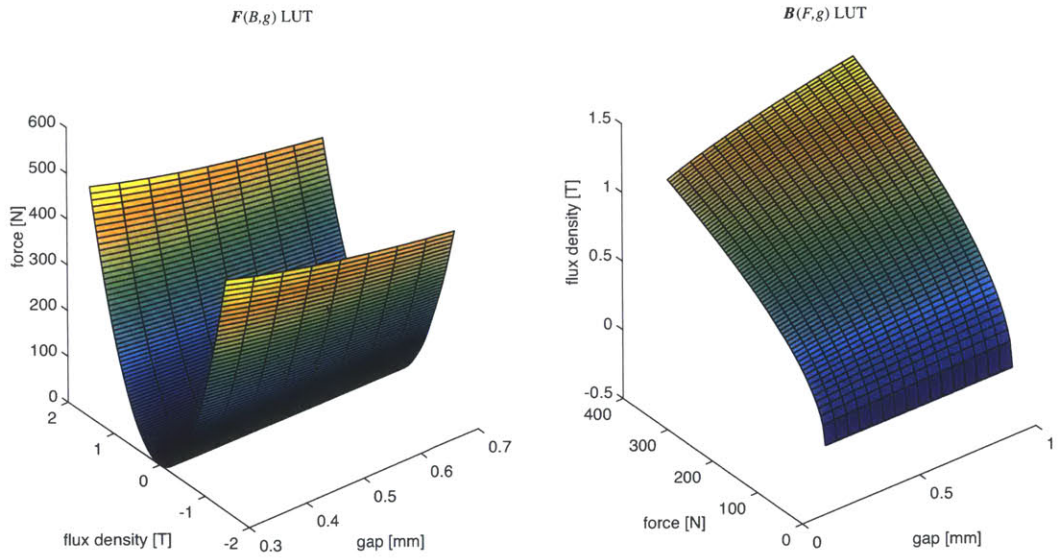

Figure 10-15: LEFT: $F(B, g)$ lookup table; RIGHT: Inverse $B(F, g)$ lookup table.

The force can be expressed as a function of the flux density in the form of

$$F = k(g)B^2, \tag{10.5}$$

where $k(g)$ is called the k-factor and is a function of g. The k-factor thus captures the gap dependency that is absent from (2.13). In Figure 10-16, we plot the k-factor as a function of gap as determined from the calibration data. From (2.13), the predicted k-factor (gap-independent) is $k = A/(2\mu_0) = 289\,\mathrm{N/T^2}$. The measured k is lower than the predicted value because of the effect of fringing fields. If we fit a function to the measured k values, we find that

$$k(g) = \frac{179}{(g + 0.32)^{0.48}}\mathrm{N/T^2}, \tag{10.6}$$

where g is in units of mm. We find that the gap dependency of the k-factor follows an approximately inverse square-root law. We use this function to extend the $F(B, g)$ LUT and $B(F, g)$ LUT shown in Figure 10-15 beyond the range of the data we collected.

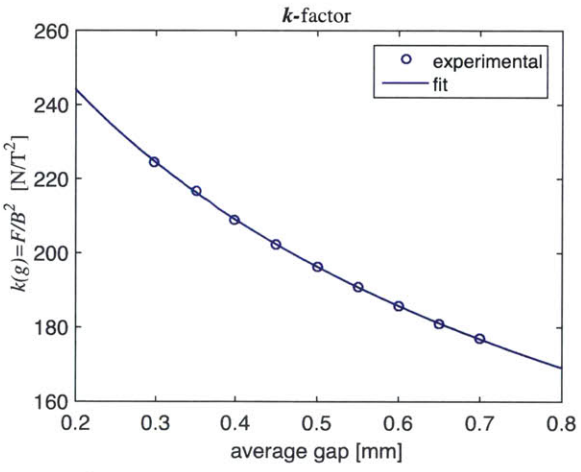

Figure 10-16: Reluctance actuator k-factor.

10.2.3 Voice Coil Calibration

We calibrated the voice coil current against the load cell measurements in order to generate the voice coil feedforward current. The voice coil current I_{vc} is plotted against the reluctance actuator load cell force measurement F_r in Figure 10-17. The data is taken from the calibration test done at $g_0 = 500\,\mu\text{m}$. A linear fit reveals the slope to be $0.0329\,\text{A/N}$. This is the value used for the $\hat{K}_{mvc}^{-1}$ block in Figure 10-1 and Figure 10-9. The motor constant K_{mvc} is the inverse of this and is estimated to be $30.4\,\text{N/A}$. The specification sheet lists the motor constant as $35.14 \pm 10\%\,\text{N/A}$ [10]. Our estimated motor constant is slightly below the minimum.

There is also a small offset of $-30\,\text{mA}$ in the voice coil current at zero reluctance actuator force. It is believed that there is a small attractive force between the voice coil magnet assembly and a long steel bolt used to attach the coil assembly to the mounting bracket. Further evidence for this hypothesis is that with power to the air bearing setup shut off, the air bearing slide moved toward the voice coil mounting bracket. The position controller compensates for this attractive force with a DC offset force. This accounts for the voice coil current offset. This offset was added to the feedforward control.

10.3 SHM Observer Implementation

With the actuator feedforward calibrations completed, we then implemented the SHM observer described in Section 6.6. The observer structure is shown again in block diagram form in Figure 10-18. In the block labeled 'cg_2', we have replaced $2/\mu_0$ with the constant c. This signifies that we can fit the constant c to experimental data to generate a better fit. We first fit the SHM to experimental data recorded at a single air gap. We then verified the SHM in real-time under several different testing conditions. We included the feedforward path in Figure 10-18 for better performance.

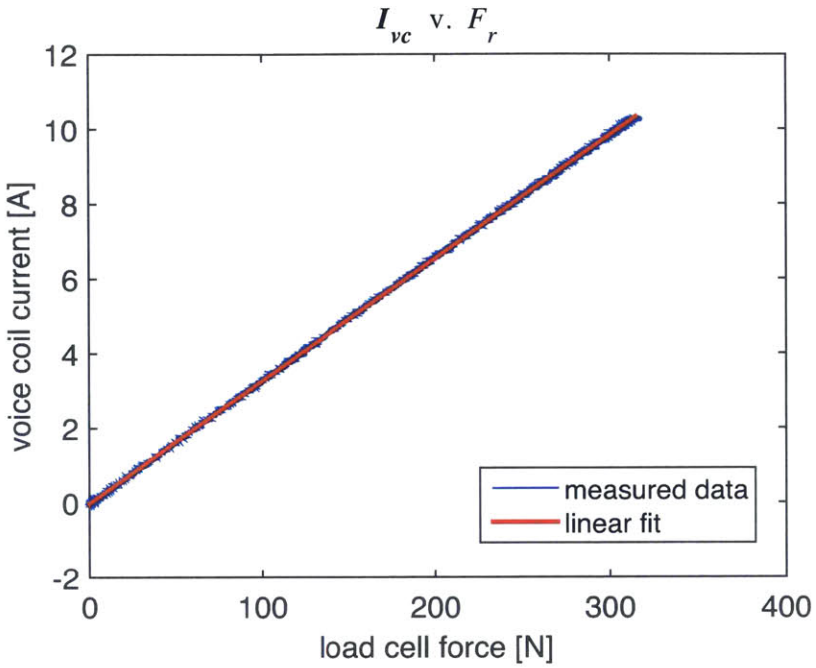

Figure 10-17: Plot of voice coil current versus reluctance actuator load cell measurements used to estimate K_{mvc}.

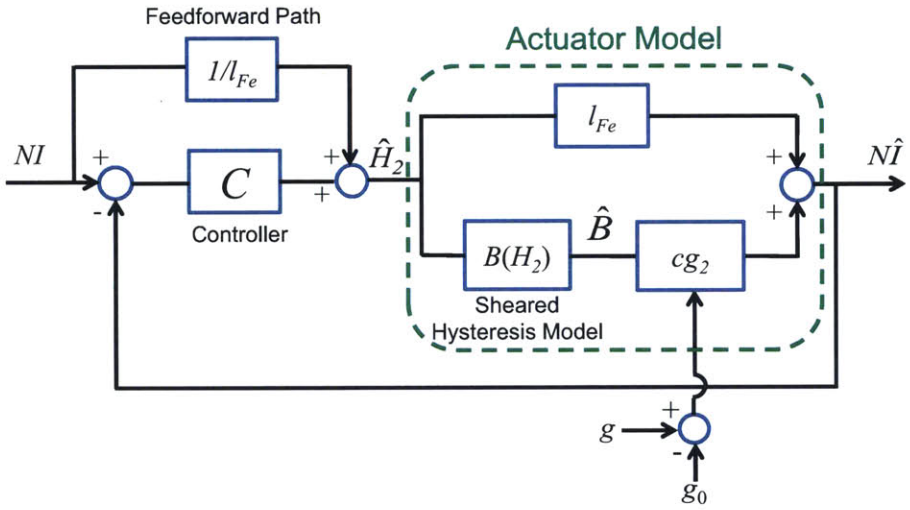

Figure 10-18: Observer block diagram with SHM.

10.3.1 Calibration

We calibrated the SHM at a nominal operating gap of 530 μm against the sense coil measurement. The reluctance actuator was driven into positive and negative

saturation with a 1 Hz voltage sine wave. The position feedback controller with voice coil actuator maintained the constant operating gap. Feedforward control with the voice coil actuator was included to reduce deviations from the nominal operating gap.

The reluctance actuator current and sense coil measurements were recorded. In postprocessing, cyclic averages over five cycles of the current and sense coil data were computed, and then based on (2.35) the averaged sense coil data was integrated and scaled by $1/(N_s A_p)$ to give a cyclic average of the flux density B. This data is shown in Figure 10-19. The Preisach model was fitted to the resulting B-I major loop data using the Hui method described in Section 3.3.2.

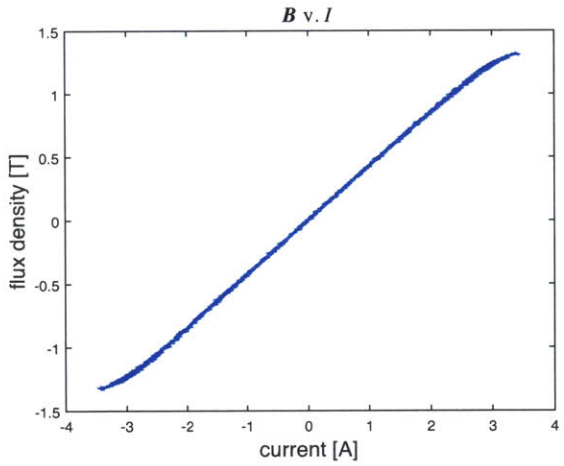

Figure 10-19: B-I data at 530 µm gap used to calibrate SHM.

The constant c in Figure 10-18 can be determined by inspecting the linear portion of the B-I curve. Since c replaces $2/\mu_0$ in the block diagram of Figure 10-18, we can substitute c for $2/\mu_0$ in (2.8) and write

$$B = \frac{NI}{cg}. \tag{10.7}$$

Solving for c, we write that

$$c = \frac{NI}{Bg}. \tag{10.8}$$

If we express B as $B = mI$, where m is the slope of the B-I curve when $g = g_0$, we

can write

$$c = \frac{N}{mg_0}. \tag{10.9}$$

The slope m of the linear portion of the B-I curve was found to be $0.427\,\mathrm{T/A}$. This results in $c = 1237\,\frac{\mathrm{A}}{\mathrm{T{\cdot}mm}}$. The parameter g_0 for the SHM is set to $g_0 = 0.530\,\mathrm{mm}$.

10.3.2 Observer Controller Design

We selected an integrator as our observer controller. The controller gain K_o was set such that the observer crossover frequency f_c would be $2\,\mathrm{kHz}$ at the nominal gap. From (6.34), we set

$$K_o = \frac{2\pi f_c}{l_{Fe}} = 1.26 \times 10^5\,\mathrm{m^{-1}s^{-1}}, \tag{10.10}$$

and our observer controller is

$$C_o(s) = \frac{1.26 \times 10^5}{s}. \tag{10.11}$$

10.3.3 Experimental Verification

To verify the SHM, we implemented the SHM observer in the dSPACE RTC. We used an embedded Matlab [60] code to implement the Preisach model.

For testing, we used the position feedback controller to keep the air gap at the desired gap, whether a constant gap or an applied gap disturbance. The reluctance actuator was then driven with a voltage profile, and the SHM observer estimated the flux density output in real-time from the current and encoder measurements. We integrated the sense coil measurement in post-processing to give us a flux density estimate from the sense coil and then compared this result to the real-time estimate from the SHM.

Major Loop at Nominal Gap

Figure 10-20 shows the B-I major loop at nominal gap of the observer real-time flux estimate compared to the integrated sense coil measurement. The sense coil

measurement is shown in blue and the observer estimate is shown in red. The fit between the two is excellent and shows good agreement both near the origin and near saturation.

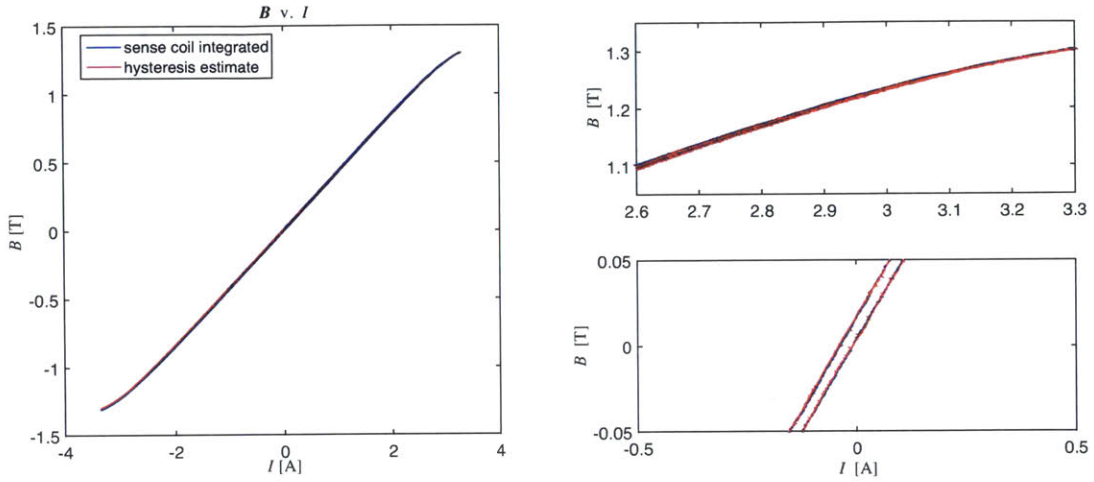

Figure 10-20: LEFT: major loop of SHM observer real-time flux estimate compared to sense coil measurement at nominal gap of 530 µm; TOP RIGHT: zoomed in at saturation; BOTTOM RIGHT: zoomed in at origin.

Minor Loop at Nominal Gap

Figure 10-21 shows the observer real-time flux estimate compared to the integrated sense coil measurement for a B-I minor loop centered about the origin at the nominal gap. The fit between the two is reasonable but is not as good as it was for the major loop. This is because in identifying the hysteresis model, only the major loop data was used. An implementation of the Preisach model that takes into account minor loop data during calibration could possibly provide a more accurate fit. Nevertheless, the hysteresis model still performs better than a single-valued nonlinear estimate. The single-valued flux density estimate $\tilde{B}$ is defined as

$$\tilde{B} = \frac{1}{2}\left[B^a(I) + B^d(I)\right], \tag{10.12}$$

where B^a is the flux density of the ascending branch of the major loop, and B^d is the flux density of the descending branch of the major loop. The RMS error between the

observer estimate and the sense coil measurement is 2.2 mT, compared to 12.6 mT for the single-valued estimate.

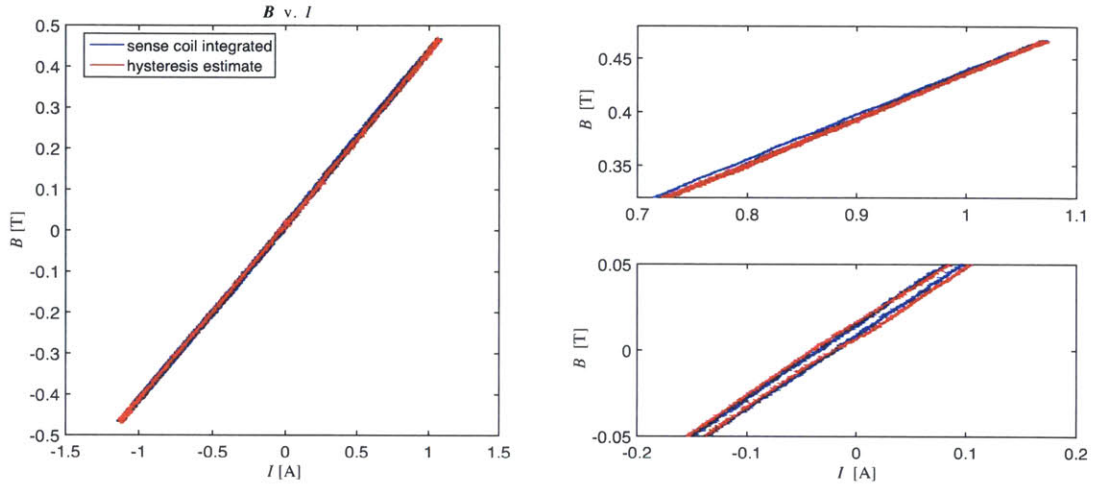

Figure 10-21: Left: minor loop of SHM observer real-time flux estimate compared to sense coil measurement at nominal gap of 530 µm; Top right: zoomed in at maximum flux density; Bottom right: zoomed in at origin.

Gap Offset from Nominal Gap

We next changed the air gap from 530 µm to 580 µm. Figure 10-22 shows the resulting B-I major loop of the observer real-time flux estimate compared to the integrated sense coil measurement. The observer flux estimate shows good agreement with the sense coil measurement. There is some discrepancy at saturation. The RMS error between the observer estimate and the sense coil measurement is 5.8 mT, while the RMS error between a single-valued estimate and the sense coil measurement is 18.6 mT.

One of the potential error sources is that our lumped parameter model does not take into account fringing flux, which will change with air gap. The fit could be improved by calibrating the actuator at multiple gaps, determining the relationship between B and g, and then changing the gap dependency in (6.30) accordingly. We can generalize the SHM to other gap dependencies. Suppose that we express (4.1) as

$$l_{Fe}H + f(g)B = NI, \tag{10.13}$$

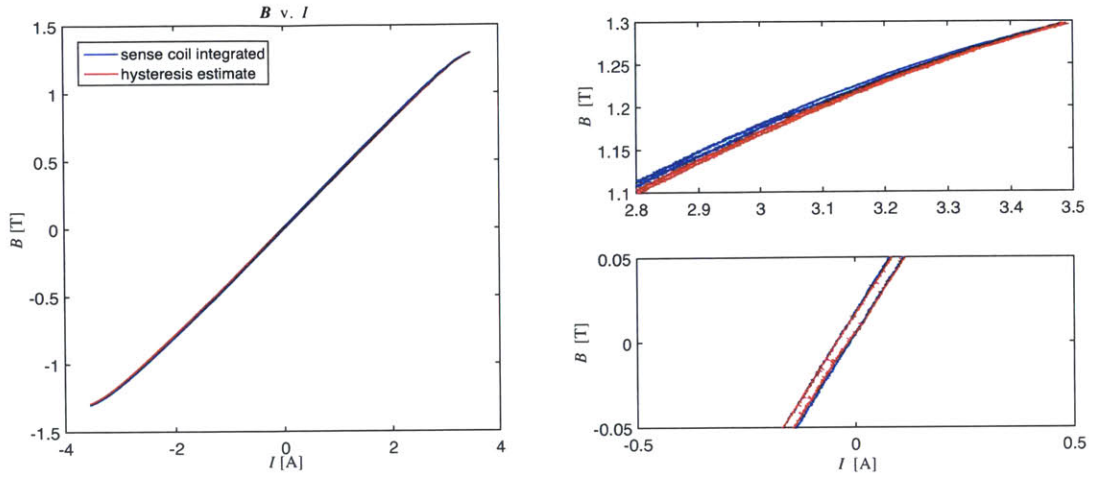

Figure 10-22: LEFT: SHM observer real-time flux estimate compared to sense coil measurement at gap of 580 µm; TOP RIGHT: zoomed in at saturation; BOTTOM RIGHT: zoomed in at origin.

where $f(g)$ is a function describing the gap dependency. We can follow a similar procedure to the change-of-variables procedure used in deriving the SHM in Section 6.6. However, we now define the variables f_2 and H_2 as

$$f_2 = f(g) - f(g_0), \tag{10.14}$$

and

$$H_2 = H + \frac{f(g_0)B}{l_{Fe}}. \tag{10.15}$$

We can then express (10.13) in terms of f_2 and H_2 as

$$\begin{aligned} l_{Fe}\left(H_2 - \frac{f(g_0)B}{l_{Fe}}\right) + \left(f_2 + f(g_0)\right)B &= NI, \\ l_{Fe}H_2 - f(g_0)B + f_2B + f(g_0)B &= NI, \\ l_{Fe}H_2 + f_2B &= NI. \end{aligned} \tag{10.16}$$

This is the same result that we obtained before in deriving (6.30), except that now we

use $f_2 = f(g) - f(g_0)$ instead of $g_2 = g - g_0$. The $B(H_2)$ hysteresis model is calibrated the same way as was done before: we measure the B-I relationship at the nominal gap where $f_2 = 0$. For $f(g)$, we implemented the relationship given in (10.4) in our SHM observer in an attempt more accurately to model the gap dependency of the reluctance actuator. However, while simulations indicated that the we were able to implement this relationship successfully, the dSPACE RTC would crash shortly after compiling. Time constraints precluded us from investigating this further.

Another possible error source is that the actuator stator heats up as current is driven through it. This causes the stator to expand, resulting in the air gap becoming smaller. This air gap change is invisible to the encoder, so the observer model will not accurately account for it. We discovered this by clamping the air bearing slide to the reluctance actuator stator with a plastic shim between the stator and target. We then drove the actuator with a 1 Hz voltage sine wave. The actuator current reached an amplitude of 3.2 A, so the RMS power dissipated is $1/2 \times (3.2\,\mathrm{A})^2 \times 1.5\,\Omega = 7.7\,\mathrm{W}$ for a $1.5\,\Omega$ coil resistance. The encoder measurement during this test is shown in Figure 10-23. We can see that the encoder measurement slowly increases over time. Over ten seconds, the average position changed by $\sim$100 nm.

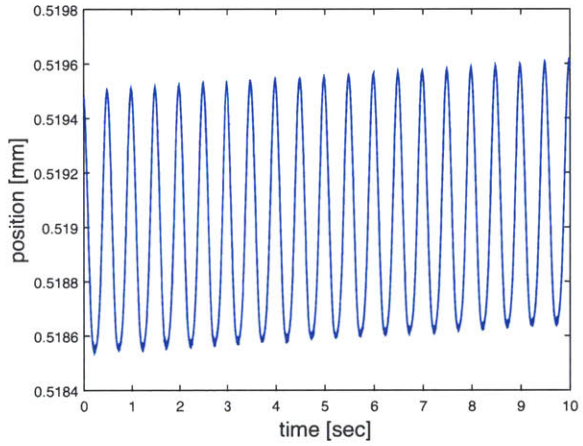

Figure 10-23: Encoder measurement showing reluctance actuator stator expansion due to actuator heating.

We ran a longer-term test where we drove the reluctance actuator with a con-

stant DC voltage with the stator clamped to the air bearing slide with a plastic shim between the target and stator. We measured the resulting current and encoder measurement. The current gradually decreases as the coil resistance increases owing to the coil heating. The current and encoder measurements are shown in Figure 10-24. The current measurement shows a sudden decrease around 1700 seconds. It is unclear what the cause of this is, although it is thought to be a problem with the measurement as there seems to be no effect on the position measurement at this time. The current measurement also becomes much noisier after this point. The encoder measurement shows an increase of over 20 µm during the test, demonstrating that actuator heating can have a significant effect on the air gap. The nominal power dissipation during this test was about $(3.2\,\mathrm{A})^2 \times 1.5\,\Omega = 15.4\,\mathrm{W}$. In the real application, the actuator will be water-cooled, so expansion from heating will be much less of a problem.

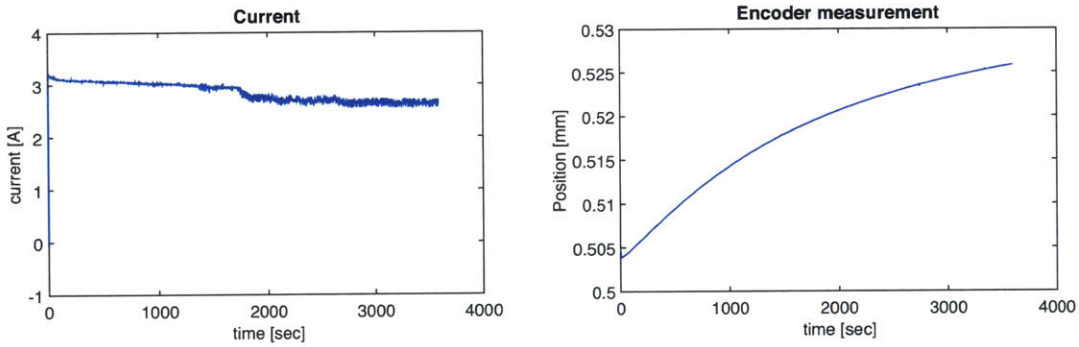

Figure 10-24: Reluctance actuator driven with constant voltage and air bearing slide clamped to stator. LEFT: reluctance actuator current measurement. RIGHT: encoder measurement.

Sinusoidal Gap Disturbance

We used the voice coil to apply a 4 Hz gap disturbance with 11 µm amplitude about the nominal operating gap of 530 µm. The reluctance actuator was driven with a 1 Hz voltage sine wave. Figure 10-25 shows the resulting B-I major loop of the observer real-time flux estimate compared to the integrated sense coil measurement. The observer estimate shows excellent tracking with the sense coil measurement in the presence of the sinusoidal gap disturbance.

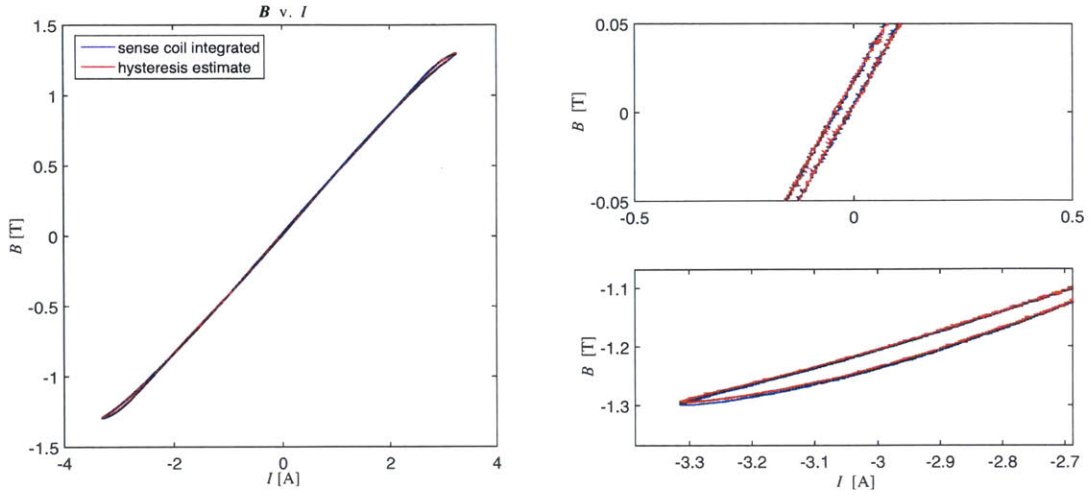

Figure 10-25: LEFT: SHM observer real-time flux estimate compared to sense coil measurement with sinusoidal gap disturbance about nominal gap of 530 µm; TOP RIGHT: zoomed in at origin; BOTTOM RIGHT: zoomed in at saturation.

Scanning Gap Disturbance

We applied a gap disturbance to the air bearing slide that was similar to a typical gap disturbance on a real lithography stage during scanning. Figure 10-26 shows the gap disturbance that was applied to the air bearing stage. The peak-to-peak amplitude is about 35 µm.

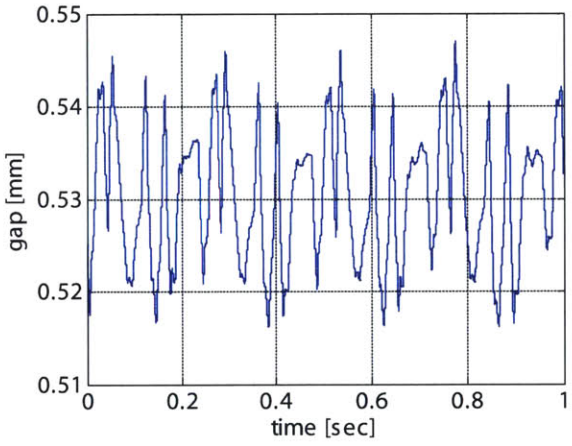

Figure 10-26: Gap disturbance applied to air bearing stage.

Figure 10-27 shows the B-I loop of the observer real-time flux estimate compared

to the integrated sense coil measurement in the presence of this gap disturbance. The reluctance actuator was driven with a 1 Hz voltage sine wave. The observer estimate shows good agreement with the sense coil measurement in the face of the dynamic gap disturbance.

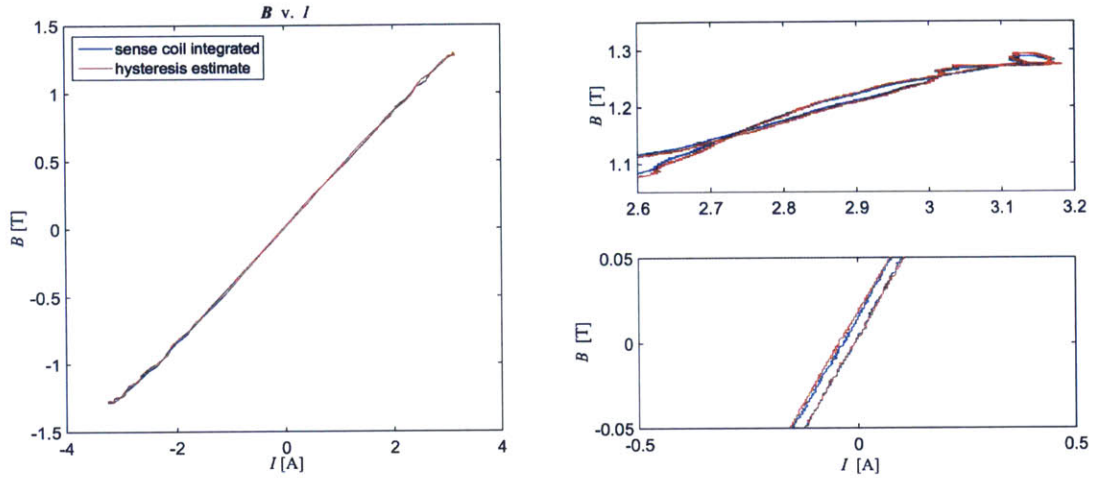

Figure 10-27: LEFT: SHM observer real-time flux estimate compared to sense coil measurement with scanning gap disturbance about nominal gap of 530 µm; TOP RIGHT: zoomed in at saturation; BOTTOM RIGHT: zoomed in at origin.

10.4 Hybrid Flux Estimator

For accurate high-bandwidth flux feedback control, we need a way to estimate the flux for frequencies from DC to several kHz or beyond. The flux estimation needed for the flux controller is represented by the 'Flux Estimation' block in Figure 10-1. For this flux estimation, we combined the sense coil measurement and the SHM approximation based on the current and gap measurements: the sense coil provides an accurate feedback signal at higher frequencies, while the current and gap measurements provide an accurate feedback signal at lower frequencies including true DC. Some preliminary results with this scheme using a lookup table instead of a hysteresis model can be found in [5, 4]. Figure 10-28 shows a complementary filter structure used for combining the two signals.

The sense coil measurement is passed through a second-order high-pass filter

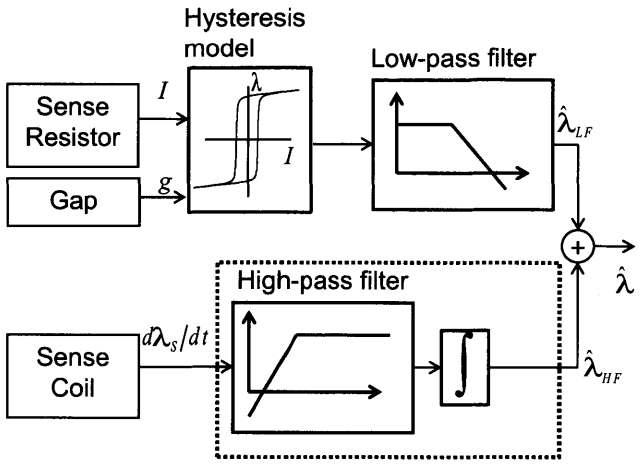

Figure 10-28: Complementary filter structure for estimating actuator flux.

(HPF) and then integrated, resulting in the signal $\hat{\lambda}_{HF}$. The filter is second-order rather than first-order so that any offset in the flux-rate measurement is not transferred to the high-frequency flux estimate after integration. To understand this, we write the transfer function from the sense coil measurement v_s to high-frequency flux estimate $\hat{\lambda}_{HF}$ using a first-order high-pass filter as

$$\begin{aligned} \frac{\hat{\lambda}_{HF}(s)}{V_s(s)} &= HPF(s) \cdot \frac{1}{s}, \\ &= \frac{s}{s+\omega_F}\frac{1}{s}, \\ \frac{\hat{\lambda}_{HF}(s)}{V_s(s)} &= \frac{1}{s+\omega_F}, \end{aligned} \tag{10.17}$$

where ω_F is the cutoff frequency of the filter. The transfer function has a DC gain of $1/\omega_F$, so any voltage offset from the sense coil buffer will result in a DC error in $\hat{\lambda}_{HF}$. If instead we use a second-order filter, we write

$$\begin{aligned} \frac{\hat{\lambda}_{HF}(s)}{V_s(s)} &= \frac{s^2}{(s+\omega_F)^2}\frac{1}{s}, \\ \frac{\hat{\lambda}_{HF}(s)}{V_s(s)} &= \frac{s}{(s+\omega_F)^2}. \end{aligned} \tag{10.18}$$

The resulting transfer function now has a DC gain of zero, so any voltage offset at the input will not propagate to the output. For our complementary filter pair, we set ω_F to 6.28 rad/s, which corresponds to a cutoff frequency of 1 Hz.

The current sense resistor and encoder measurements are passed into a hysteresis model that estimates the flux as its output. In our setup, the SHM observer described in the previous section is used as the hysteresis model. The output of the hysteresis model is passed through a complementary low-pass filter (LPF). The low-pass filter is defined as

$$LPF = 1 - HPF, \tag{10.19}$$

so that the resulting complementary filter pair sums to one. In our case, using (10.18) for the high-pass filter, we can write the low-pass filter transfer function as

$$\begin{aligned} LPF(s) &= 1 - \frac{s}{(s+\omega_F)^2}, \\ &= \frac{(s+\omega_F)^2}{(s+\omega_F)^2} - \frac{s}{(s^2+\omega_F)^2}, \\ &= \frac{s^2 + 2\omega_F s + \omega_F^2 - s^2}{(s+\omega_F)^2}, \\ LPF(s) &= \frac{2\omega_F s + \omega_F^2}{(s+\omega_F)^2}. \end{aligned} \tag{10.20}$$

We see then that the low-pass filter has a zero at $\omega_F/2$. The resulting low-pass signal $\hat{\lambda}_{LF}$ is summed with $\hat{\lambda}_{HF}$ to provide a flux estimate for feedback control that is accurate at both low and high frequencies. With this scheme, we take advantage of the benefits of a sense coil over other types of flux sensors, such as a Hall sensor, while the hysteresis model compensates for the sense coil's poor performance at low frequencies. Because the sense coil provides an accurate measurement at high frequencies, the hysteresis model only needs to be accurate at low frequencies. This gives us more flexibility. For example, we can separate the hysteresis model computation from the sense coil measurement: the computation of the hysteresis model could be done

with a real-time computer at a relatively low sample rate, but then we could use a high-bandwidth analog controller or FPGA to run the flux control loop.

10.5 Flux Control Loop Design

Using the calibration results and the hybrid flux estimator, we designed the flux controller represented by the dotted red box in Figure 10-1. A block diagram of the flux controller is shown in Figure 10-29.

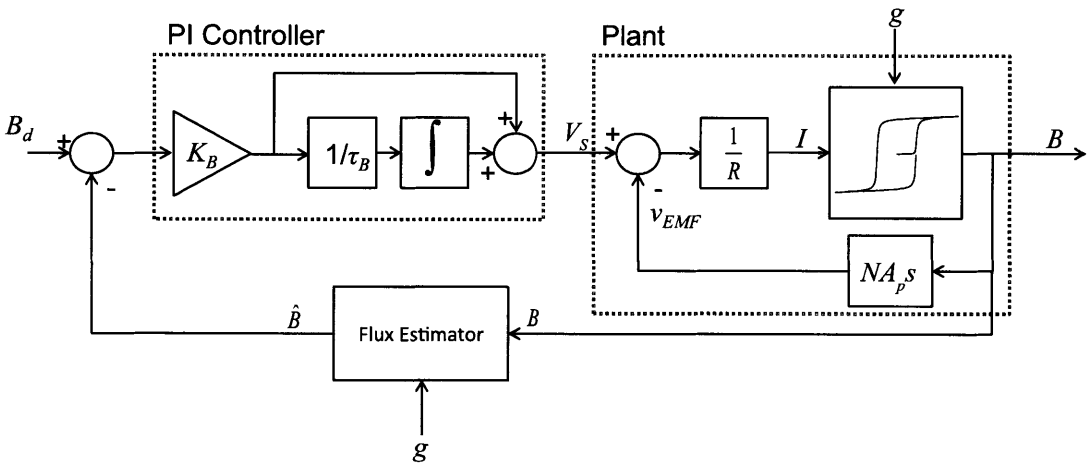

Figure 10-29: Block diagram of flux control loop.

The plant is described by (4.52), repeated here as

$$V_S = IR + NA_p \frac{dB}{dt}. \tag{10.21}$$

If we linearize the plant about an operating gap g_0 as was done in (4.54), we can write the transfer function from V_S to B as

$$\frac{B(s)}{V_S(s)} = \frac{\mu_0 N}{2g_0} \frac{1/R}{\frac{L}{R}s + 1} = \frac{1}{NA_p} \frac{L}{Ls + R}, \tag{10.22}$$

where L is the actuator inductance. At low frequencies, $B(s)/V_S(s) \approx L/(NA_pR)$. Because L depends on g, the DC gain of the transfer function will vary with nominal

gap. At high frequencies, $B(s)/V_S(s) \approx 1/(NA_p s)$, and there is no dependence on gap.

If we used a high-bandwidth current control inner loop instead of driving the reluctance actuator with a voltage, then our plant could be approximated from (2.8) as

$$B = \frac{\mu_0 NI}{2g}. \tag{10.23}$$

In this case our plant will depend on the operating gap at both low frequencies and high frequencies. Therefore, one benefit of driving the reluctance actuator with a voltage instead of a current is that if the flux loop crossover frequency is set much higher than $\omega = R/L$, the crossover frequency and phase margin will remain constant irrespective of gap, thereby ensuring stability over a wide range of gaps. This permits the reluctance actuator to be used for stable position control. Experiments demonstrating position control with the flux-controlled reluctance actuator are documented in [4].

Figure 10-30 shows the measured frequency response of the reluctance actuator from input amplifier voltage to output flux linkage as measured by the sense coil. The frequency response therefore includes any amplifier dynamics. We also had a 10 kHz low-pass filter on the sense coil differential amplifier channel, so the effect of this filter is also present in the frequency response. The air gap was set to 500 µm. The frequency response was acquired with the dSPACE DAQ, where we set the sampling frequency to 40 kHz. The variable λ is obtained in post-processing by multiplying the magnitude of the measured sense coil variable $d\lambda/dt$ by $1/\omega$, where ω is the frequency of the signal, and subtracting 90° from the phase of $d\lambda/dt$.

We designed our controller based on the actuator frequency response. To express the actuator plant in terms of B rather than λ, we divided the frequency response magnitude by $N_s A_p$, where N_s is the number of sense coil turns. We initially targeted a crossover frequency f_c of 3.65 kHz. At this frequency, the plant phase is $-143°$ and the gain (in terms of B rather than λ) is 0.001325 T/V. To achieve this crossover

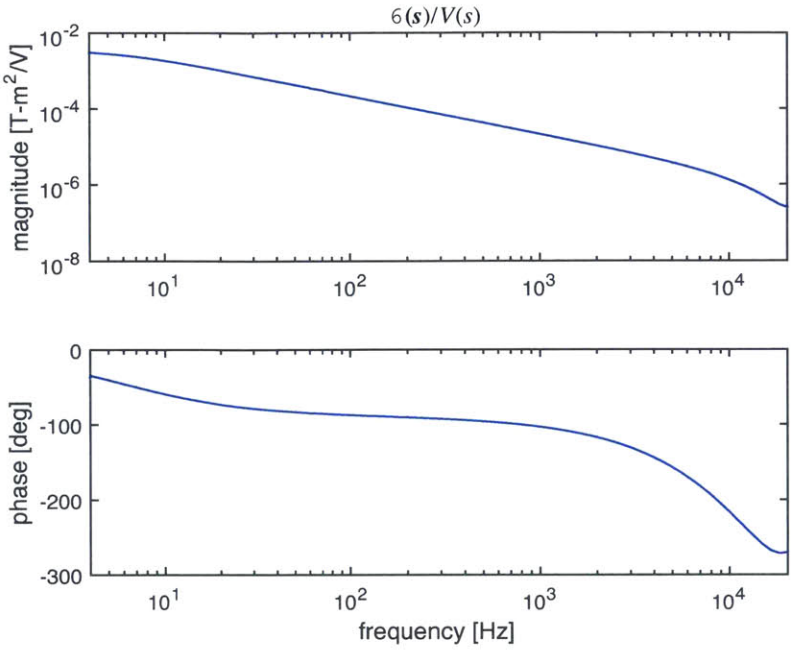

Figure 10-30: Measured frequency response for reluctance actuator.

frequency with sufficient phase margin, we use a PI controller of the form

$$C_B(s) = K_B \frac{\tau_B s + 1}{\tau_B s}. \tag{10.24}$$

We set the frequency of the zero to a decade below the intended crossover frequency, so that the zero frequency $f_z = 365\,\text{Hz}$. From this, we set $\tau_B = 1/(2\pi f_z) = 4.356\times10^{-4}\,\text{s}$. The gain of the PI compensator at 3.65 kHz is 1.005. To achieve a unity gain at 3.65 kHz, we set $K_B = 1/(0.001325 \cdot 1.005) = 750\,\text{V/T}$.

After implementing this controller and inspecting the experimental loop transmission, we modified our controller to be slightly more aggressive and targeted a crossover frequency of 4 Khz. We increased our controller gain to $K_B = 834\,\text{V/T}$. Our final controller is

$$C_B(s) = 834 \frac{4.356 \times 10^{-4} s + 1}{4.356 \times 10^{-4}}. \tag{10.25}$$

Figure 10-31 shows the measured loop transmission frequency response with this controller. The measured plant frequency response $B(s)/V(s)$ and the predicted

controller frequency response are also shown. The small 'blips' on the measured loop transmission are the result of the controller signal saturating. The input was then reduced at these frequencies and the frequency response was retaken from that point onward. The frequency responses with different input amplitudes were then concatenated together to cover the entire frequency range. The loop transmission shows a crossover frequency of 4 kHz with a phase margin of 30°.

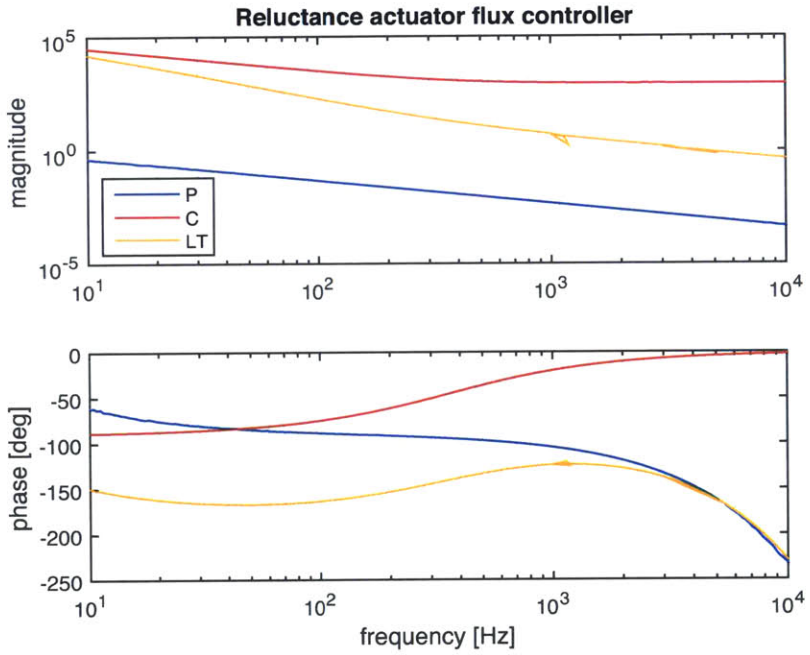

Figure 10-31: Reluctance actuator frequency responses: P - plant (measured); C - controller (predicted); LT - loop transmission (measured)

10.6 Force Control with Flux Feedback

We tested the reluctance actuator force accuracy with the flux feedback loop in place. We measured the force frequency response of the actuator and then measured the stiffness frequency response. We also measured the force accuracy of the actuator when trying to follow a desired force pulse profile. The block diagram for the reluctance actuator force controller is shown in Figure 10-32. A desired force F_d is sent to the inverse 2-D LUT described in Section 10.2.2 to generate a desired flux density B_d.

The flux control loop drives the reluctance actuator to generate a flux density B that tracks B_d. The resulting actuator force is measured by the load cells. The desired force is also fedforward to the voice coil actuator as shown in Figure 10-1.

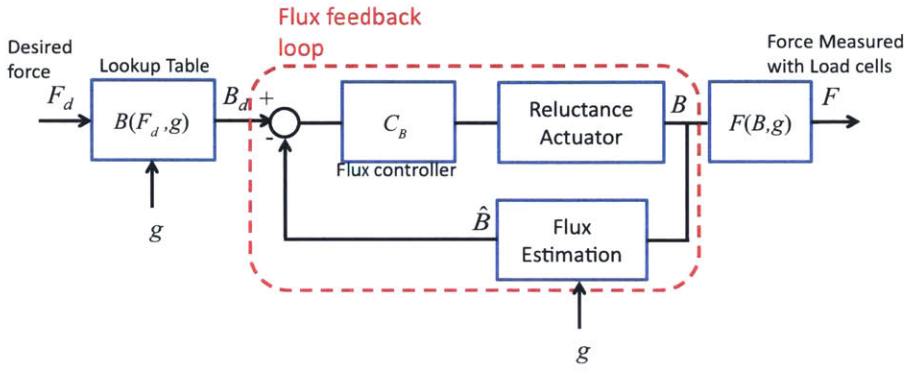

Figure 10-32: Block diagram for reluctance actuator force control.

10.6.1 Force Frequency Response

We measured the frequency response from F_d to F while the air gap was maintained at 530 µm with the position controller. We measured frequency responses for bias forces F_0 of 5 N, 25 N, and 50 N. Figure 10-33 shows the measured frequency responses of $F(s)/F_d(s)$. We were unable to measure frequency responses at higher bias forces near saturation because the voice coil actuator will overheat at the high continuous currents required to offset the reluctance actuator bias force. The amplifier is also limited in the amount of continuous power it can deliver to the voice coil.

The measured force tracks the desired force up to about 100 Hz. Beyond this frequency, the performance deteriorates and we see various resonances and anti-resonances. These are likely the result of structural resonances affecting the load cell measurement. Moreover, the air gap is not perfectly constant because of the finite bandwidth of the position controller. The position controller has a loop crossover of 150 Hz, so beyond this frequency, the imperfect gap disturbance rejection of the force controller will also affect our accuracy. Acceleration of the optical table will also result in errors in the load cell measurement. These errors become more pronounced at higher frequencies, owing to the ω^2 dependency of acceleration.

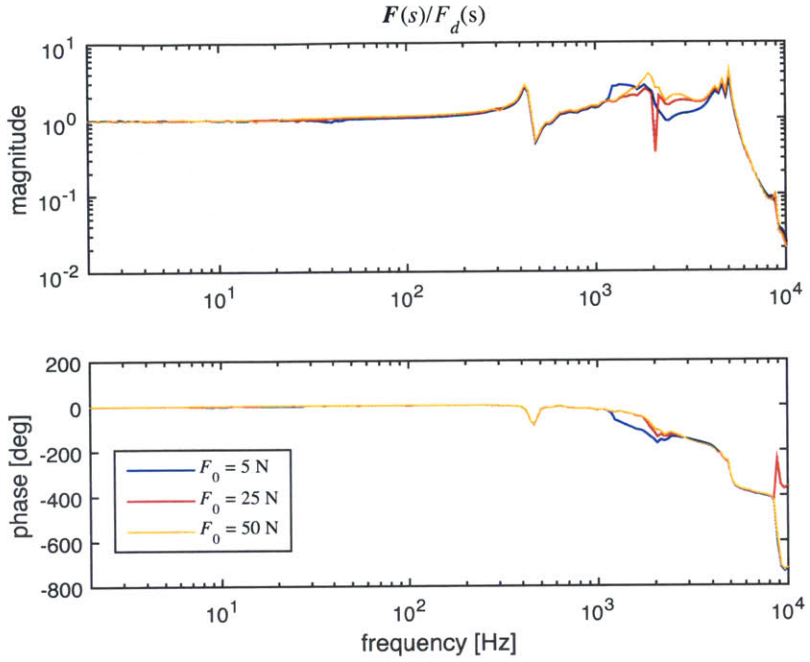

Figure 10-33: Measured flux-controlled reluctance actuator frequency responses from desired force to measured force.

Figure 10-34 shows the frequency responses for frequencies below 100 Hz. Up through 20 Hz, the measured force magnitude remains within ±2% of the desired force magnitude. Part of the inaccuracy may be the result of the limited load cell resolution. This resolution can be changed on the charge amplifier. However, when we used a higher resolution setting, the amplifier would quickly overload before much data could be captured. The spikes that are circled in the magnitude plot are artifacts: these occurred when the charge amplifier overloaded and had to be reset. The phase shows a gradual increase with frequency. Likewise the magnitude begins to increase after about 20 Hz. This is thought to be due to the loop-widening phenomenon present in the sense coil measurements, resulting in the phase of the measured force leading the phase of the measured flux.

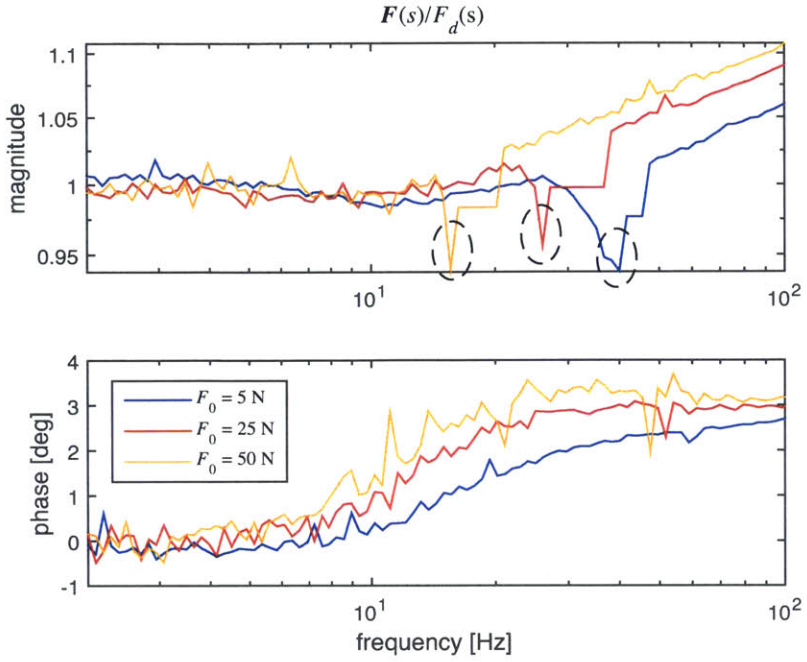

Figure 10-34: Measured flux-controlled reluctance actuator frequency responses from desired force to measured force for frequencies below 100 Hz.

10.6.2 Reluctance Actuator Stiffness

The reluctance actuator stiffness was measured by using the flux controller to maintain a constant force, applying a gap disturbance using the voice coil actuator, and measuring the resulting force disturbance. We first present stiffness results of the flux-controlled actuator with the SHM observer incorporated into the hybrid flux estimator. We then present the results of a previous set of experiments done with a flux-controlled actuator but using the Chua model instead of the SHM. We then present a theoretical analysis of the effect that imperfect feedforward and sampling delay have on stiffness.

Stiffness Results with SHM

Figure 10-35 shows the measured frequency responses of the reluctance actuator stiffness for bias force levels of 5 N and 35 N. The stiffness for both bias levels is shown to be well below the maximum allowable stiffness, demonstrating that the flux controller

is effective in rejecting gap disturbances. For example, the stiffness of the reluctance actuator at 10 Hz is 0.003 N/µm. This results in a force error of less than 0.01% of the full-scale force for a 10 µm air gap disturbance at this frequency. The maximum allowable stiffness is based on the 99.9% feedforward force accuracy specification for the reluctance actuators. For our prototype actuator, the maximum force is approximately 400 N. The maximum force error permitted is therefore $\Delta F = 0.4\,\mathrm{N}$. A typical gap disturbance is on the order of $\Delta g = 10\,\mu\mathrm{m}$. Therefore, the maximum allowable stiffness $k_{r,\max}$ is estimated to be

$$k_{r,\max} = \frac{\Delta g}{\Delta F} = \frac{0.4\,\mathrm{N}}{10\,\mu\mathrm{m}} = 0.04\,\mathrm{N}/\mu\mathrm{m}. \tag{10.26}$$

This value corresponds to the horizontal dotted green line in the figure. The majority

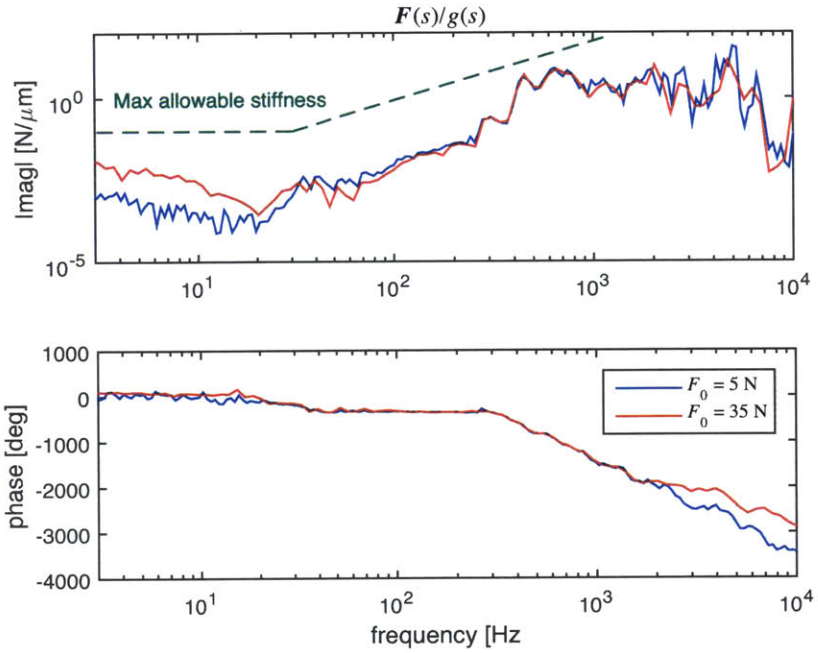

Figure 10-35: Measured frequency responses of flux-controlled reluctance actuator stiffness.

of the frequency content of a typical gap disturbance during scanning is below 30 Hz. Gap disturbance data from ASML was analyzed in [62], and the gap disturbance amplitude was found to fall off as approximately $1/\omega$ at higher frequencies. The max-

imum allowable stiffness requirement is therefore less stringent at higher frequencies, and is shown in the figure as the green dotted line with positive slope. This line has a slope of ω.

For frequencies below 20 Hz, the measured stiffness decreases with frequency. This may be because the signal-to-noise ratio from the load cell measurement is low at these frequencies. For frequencies beyond 20 Hz, the stiffness increases with approximately a slope of ω. This matches the the theoretical prediction of (4.64) with an integrator in the controller. At low frequencies, the stiffness also increased with bias force as expected. However, at higher frequencies, the bias force did not seem to have an effect. This may be the result of the force feedforward, which if imperfect will also introduce a stiffness. Using (4.64), we predict a stiffness of about 4×10^{-4} N/μm at 100 Hz for $F_0 = 35$ N. From the measured frequency response in Figure 10-35, we find a measured stiffness of 0.0065 N/μm, a factor of 16 greater than predicted. This supports the hypothesis that imperfect feedforward is dominating the actuator stiffness.

Stiffness Results with Chua Model

In a previous set of experiments before we had developed the SHM, we measured the stiffness of the flux-controlled actuator using the Chua model in the hybrid estimation scheme. The flux controller was nearly identical to the one that was described in Section 10.5, however, and we achieved a similar loop crossover frequency of 4 kHz. Figure 10-36 shows the measured disturbance rejection frequency responses ($B(s)/g(s)$) of the flux loop alone (without the force inversion) for different levels of bias flux density B_0 on the reluctance actuator prototype. The nominal air gap was 500 μm. The B_0 levels of 0.09 T, 0.28 T, and 0.62 T correspond to bias force levels of 1.5 N, 15 N, and 75 N, respectively. As predicted in (4.61), the magnitude of the frequency response increases with B_0.

Figure 10-37 shows the measured disturbance rejection frequency responses for different nominal air gaps. The bias force was 1.5 N. As predicted by theory (4.61), the frequency response does not depend on g_0.

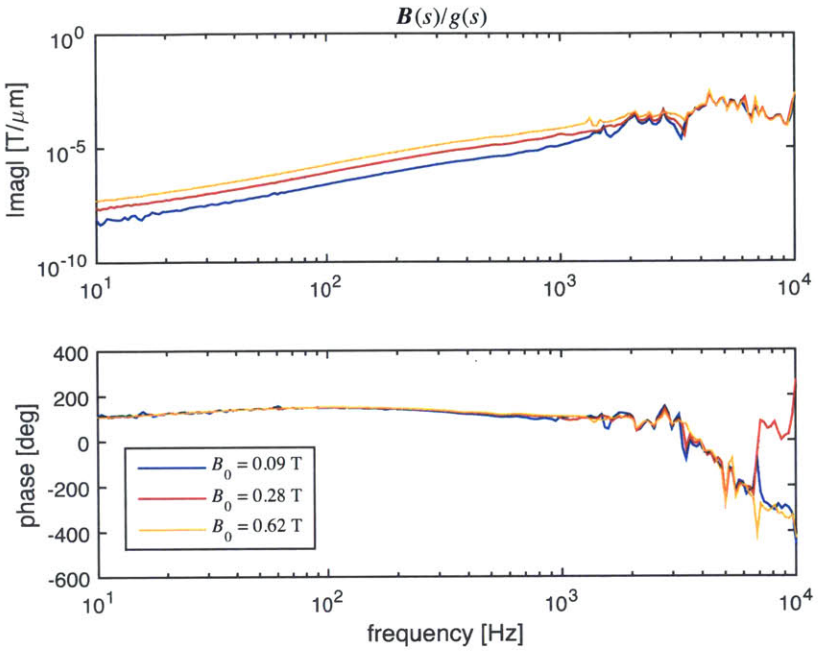

Figure 10-36: Measured frequency responses of flux-controlled reluctance actuator gap disturbance rejection at different flux levels.

Figure 10-38 shows the measured frequency responses for the compensated actuator stiffness at two different nominal operating air gaps. The bias force is 35 N in both cases. We can see that there is not much discrepancy between the two, illustrating that the nominal air gap does not have an effect on the stiffness. The break in the plots at 100 Hz is due to recording the frequency responses in two steps: at the lower frequencies, a higher gap displacement was used (25 µm amplitude), while at the higher frequencies, a lower gap displacement was used (5 µm amplitude). This was done to avoid overdriving the voice coil actuator. The stiffness is higher than what was shown for the $F_0 = 35$ N plot in Figure 10-35. This indicates that the SHM helps significantly in reducing the actuator stiffness.

Stiffness from Imperfect Feedforward

In this case of perfect inverse force-flux-gap modeling ($B(F_d, g)$) and no gap sampling delay, the only stiffness in the compensated actuator results from the finite bandwidth

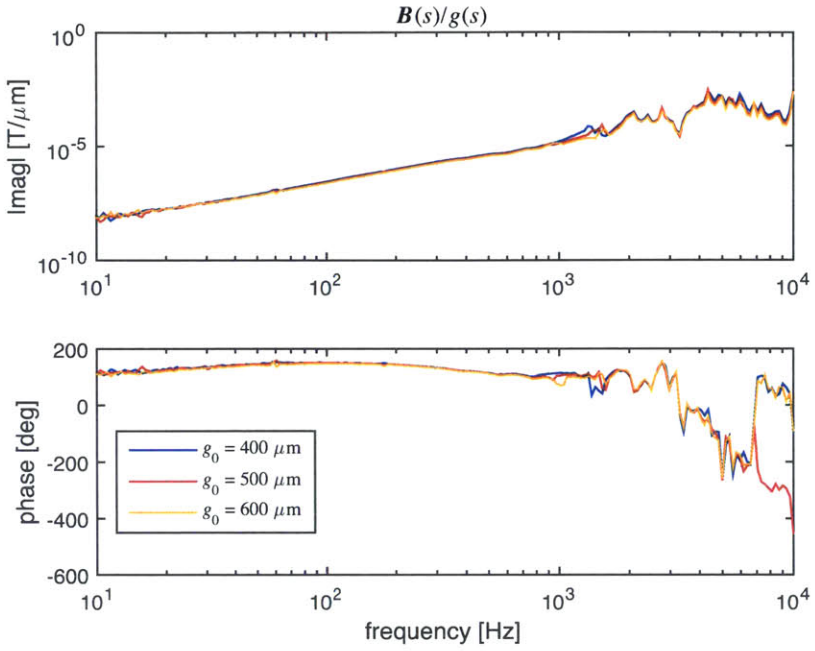

Figure 10-37: Measured frequency responses of flux-controlled reluctance actuator gap disturbance rejection for different nominal air gaps.

of the flux control loop. In reality, the force-flux-gap relationship will not be modeled perfectly. Since the compensated stiffness in Figure 10-35 is worse than we would have predicted if the flux loop finite bandwidth were the only contribution to stiffness, we expect that imperfect feedforward is dominating our stiffness. Using (10.5) to express the force, we can write the change in force ΔF about an operating point as

$$\Delta F \approx \frac{\partial F}{\partial B}\Delta B + \frac{\partial F}{\partial k}\Delta k(g) = 2k_0 B_0 \Delta B + \Delta k(g) B_0^2, \tag{10.27}$$

where B_0 and g_0 are the flux density and air gap at the operating point, respectively, and where $k_0 = k(g_0)$. With reference to the block diagram of Figure 4-16, we can approximate ΔB as

$$\Delta B \approx G_{cl}\Delta B_d + G_d \Delta g, \tag{10.28}$$

where G_{cl} is the closed-loop transfer function of the flux loop, equal to $C(s)P(s)/(1 + C(s)P(s))$, and G_d is the closed-loop disturbance rejection transfer function, equal to

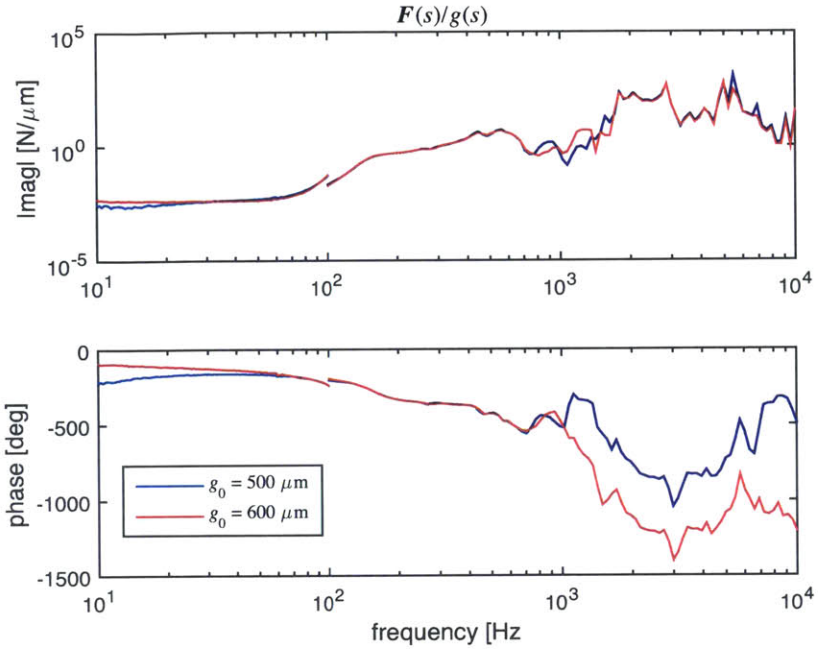

Figure 10-38: Measured frequency responses of flux-controlled reluctance actuator stiffness at different nominal air gaps.

$D(s)/(1 + C(s)P(s))$. We can related the desired force F_d to B_d as

$$F_d = \hat{k}(g)B_d^2, \tag{10.29}$$

where $\hat{k}(g)$ is the feedforward approximation of $k(g)$. Solving this for B_d, we write that

$$B_d = \sqrt{\frac{F_d}{\hat{k}(g)}}. \tag{10.30}$$

Taking partial derivatives again, we can approximate ΔB_d as

$$\Delta B_d \approx \frac{\partial B_d}{\partial \hat{k}} \Delta \hat{k}(g) = -\frac{1}{2}\frac{1}{\hat{k}_0}\sqrt{\frac{F_d}{\hat{k}_0}}\Delta \hat{k}(g), \tag{10.31}$$

where $\hat{k}_0 = \hat{k}(g_0)$. We have ignored any contribution from ΔF_d since we are concerned with the response in ΔF to a gap disturbance rather than a change in the desired

force. We substitute (10.31) and (10.28) into (10.27). We then write

$$\begin{aligned}\Delta F &\approx 2k_0B_0\left[G_{cl}\Delta B_d + G_d\Delta g\right] + \Delta k(g)B_0^2,\\ &\approx 2k_0B_0\left[-G_{cl}\frac{1}{2}\frac{1}{\hat{k}_0}\sqrt{\frac{F_d}{\hat{k}_0}}\Delta\hat{k}(g) + G_d\Delta g\right] + \Delta k(g)B_0^2. \qquad (10.32)\end{aligned}$$

If we divide both sides by Δg and take the limit as Δg approaches zero, we can derive an expression for the compensated stiffness $k_{rc} = \partial F/\partial g$. This yields

$$k_{rc} = 2k_0B_0\left[-G_{cl}\frac{1}{2}\frac{1}{\hat{k}_0}\sqrt{\frac{F_d}{\hat{k}_0}}\frac{\partial\hat{k}}{\partial g} + G_d\right] + \frac{\partial k}{\partial g}B_0^2. \qquad (10.33)$$

We can note from (10.5) that $B_0 = \sqrt{F_0/k_0}$, where F_0 is the force at the operating point. If $F_d = F_0$, we can simplify (10.33) to

$$\begin{aligned}k_{rc} &= -2k_0\sqrt{\frac{F_0}{k_0}}G_{cl}\frac{1}{2}\frac{1}{\hat{k}_0}\sqrt{\frac{F_0}{\hat{k}_0}}\frac{\partial\hat{k}}{\partial g} + 2k_0G_d\sqrt{\frac{F_0}{k_0}} + \frac{\partial k}{\partial g}\frac{F_0}{k_0},\\ k_{rc} &= -\frac{k_0}{\hat{k}_0}\frac{F_0}{\sqrt{k_0\hat{k}_0}}\frac{\partial\hat{k}}{\partial g} + 2G_d\sqrt{k_0F_0} + \frac{F_0}{k_0}\frac{\partial k}{\partial g}. \qquad (10.34)\end{aligned}$$

This is a general expression for the compensated stiffness that includes both the effects of imperfect feedforward and finite flux loop bandwidth. If $k_0 = \hat{k}_0$, we can further simplify this expression to

$$k_{rc} = \frac{F_0}{k_0}\left(\frac{\partial k}{\partial g} - \frac{\partial\hat{k}}{\partial g}\right) + 2G_d\sqrt{k_0F_0}. \qquad (10.35)$$

Thus, if the feedforward is perfect and $\partial k/\partial g = \partial\hat{k}/\partial g$, the compensated stiffness reduces to $2G_d\sqrt{k_0F_0}$. This result is consistent with the compensated stiffness derived in Chapter 4. We can use (10.35) to investigate the effect that different k-factors and different types of mismatches between k and $\hat{k}$ (e.g., offset error, gain error) have on the stiffness.

Effect of Sampling Rate on Stiffness

Suppose that our force feedforward is perfect, that is, $\hat{k}(g) = k(g)$. The fact that the gap measurement will be delayed by one time step will still introduce a stiffness into the system. Assuming that we have a perfect flux feedback loop ($B = B_d$), we can write F as

$$F = k(g)B^2 = k(g)B_d^2 = \frac{k(g)}{k(g - \Delta g)}F_d, \tag{10.36}$$

where Δg is the difference between the actual gap and the measured gap as a result of the sampling delay. The force error $\Delta F = F - F_d$ is

$$\begin{aligned} \Delta F &= \frac{k(g)}{k(g - \Delta g)}F_d - F_d, \\ &= F_d\left[\frac{k(g) - k(g - \Delta g)}{k(g - \Delta g)}\right]. \end{aligned} \tag{10.37}$$

Expanding $k(g - \Delta g)$ into a Taylor series, we can write

$$\begin{aligned} \Delta F &\approx F_d\left[\frac{k(g) - k(g) + \frac{\partial k}{\partial g}\Delta g}{k(g) - \frac{\partial k}{\partial g}\Delta g}\right], \\ &\approx F_d\left[\frac{\frac{\partial k}{\partial g}\Delta g}{k(g) - \frac{\partial k}{\partial g}\Delta g}\right], \\ \Delta F &\approx \frac{F_d}{k(g)}\frac{\frac{\partial k}{\partial g}\Delta g}{1 - \frac{1}{k(g)}\frac{\partial k}{\partial g}\Delta g}. \end{aligned} \tag{10.38}$$

Since the force-flux relationship dependency on gap is a second-order effect, then for small gap disturbances, we can say that $1/k(g)(\partial k/\partial g)\Delta g << 1$, and we can

further approximate (10.38) as

$$\begin{aligned}\Delta F &\approx \frac{F_d}{k(g)}\frac{\partial k}{\partial g}\Delta g\left(1+\frac{1}{k(g)}\frac{\partial k}{\partial g}\Delta g\right),\\ &\approx F_d\left[\frac{1}{k(g)}\frac{\partial k}{\partial g}\Delta g+\left(\frac{1}{k(g)}\frac{\partial k}{\partial g}\Delta g\right)^2\right],\\ &\approx \frac{F_d}{k(g)}\frac{\partial k}{\partial g}\Delta g. \end{aligned} \tag{10.39}$$

In the last line, we have ignored the second-order term. We can express Δg as $dg/dt\Delta t$, where $\Delta t = T_s$, the time step. We can then write that

$$\Delta F \approx \frac{F_d}{k(g)}\frac{\partial k}{\partial g}\frac{dg}{dt}T_s. \tag{10.40}$$

The Laplace Transform of dg/dt is $s\Delta g$. Substituting this for dg/dt and taking the limit as Δg approaches zero, we derive the stiffness due to sampling delay, denoted k_{rs}, as

$$k_{rs} = \frac{\partial F}{\partial g} = \frac{F_0}{k(g)}\frac{\partial k}{\partial g}T_s s. \tag{10.41}$$

We have replaced F_d with F_0 for consistency with the other stiffness results. We therefore see that if the force-flux relationship depends on gap, we will have a resulting stiffness that increases with frequency even if our force feedforward is perfect and our flux loop has infinite bandwidth. For our prototype actuator, if we use the $k(g)$ function described by (10.6), we derive a maximum k_{rs} equal to $6.4\times10^{-6}s$ in units of N/μm. This is computed at the maximum actuator force $F_0 = 400\,\text{N}$ and a sampling rate of 20 kHz. This is well below the maximum allowable stiffness.

10.6.3 Force Pulse Experiments

To demonstrate the force accuracy of the reluctance actuator with flux control and force-flux inversion, we attempted to have the reluctance actuator follow a desired force pulse waveform. This force pulse waveform is a scaled version of the force wave-

form used for simulation in Chapter 4. It is therefore similar to the force feedforward that would be used on a scanning lithography machine. This force waveform was set as F_d in the block diagram of Figure 10-1. The same force was fedforward to the voice coil actuator to aid in maintaining the desired air gap. The nominal air gap during the experiment was 530 µm. The hybrid flux estimation scheme included the SHM observer. The reluctance actuator force was measured with the load cells and then compared to the reference force.

Initial Force Pulse Results

Figure 10-39 shows the initial results of the force pulse experiment. We see that the maximum error between the reference force and measured force is 11.8 N. This is 3.7% of full-scale force. The largest errors occur during the portions of the force profile with high dF/dt. One unexpected result was the overshoot that occurs at the end of the positive dF/dt portion of the force pulse. This overshoot is followed by a slow decay to the correct force value. The time constant associated with this decay is much slower than the time constant associated with the flux loop bandwidth.

We hypothesized that the cause of this overshoot and slow decay is the loop-widening phenomenon associated with the sense coil measurement documented in Chapter 9. Because of the phase lag that was discovered in the sense coil measurement, the flux controller will drive the actuator harder (i.e., larger currents) to compensate for the measured flux lag. This lag will be the most pronounced during the high dF/dt portions of the force pulse because this is the portion of the force pulse with the highest frequency content. Because the measured force was not found to exhibit this same phase lag, the force will feature an overshoot. After the high dF/dt portion of the pulse has completed, the flux controller transitions to using the hysteresis model to estimate the flux rather than the sense coil measurement. This is a result of the complementary filter structure. Because the hysteresis model does not include any loop-widening phenomenon, the flux controller reduces the actuator current until the hysteresis model output matches the desired flux. The measured force is likewise reduced.

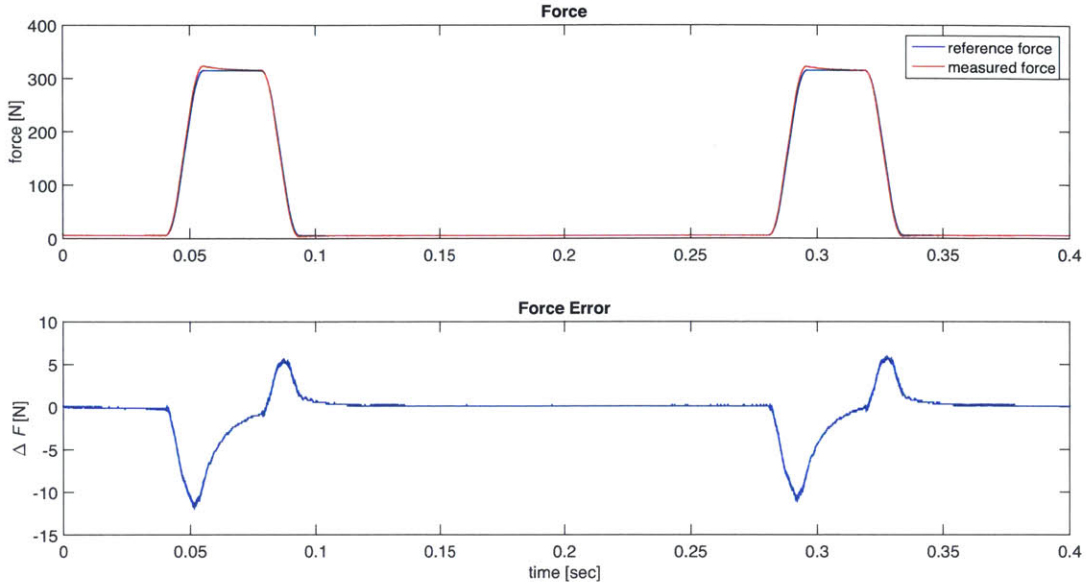

Figure 10-39: Force pulse experimental results with flux feedback and force-flux inversion. TOP: reference force profile and measured force profile. BOTTOM: error between reference force and measured force.

Figure 10-40 shows the position error during the force pulse experiment. The air gap changes by over 10 µm during the experiment. The voice coil feedforward assumes that the air bearing slide is a pure mass. However, because of the high frequency content of the reluctance actuator force pulse, this is no longer a good approximation and the dynamics of the air bearing slide affect the results. The position error could be reduced by including feedforward that takes into account the plant dynamics. Another possibility would be to use iterative learning control to improve the voice coil feedforward signal over multiple trials.

Force Pulse Results with Increased Complementary Filter Pair Cutoff Frequency

To test the hypothesis that the overshoot and slow decay in the force measurement were the result of the sense coil loop widening, we changed the cutoff frequency for the complementary filter pair from 1 Hz to 10 Hz. This will cause the hybrid flux estimator to rely mainly on the hysteresis model instead of the sense coil measurement over a

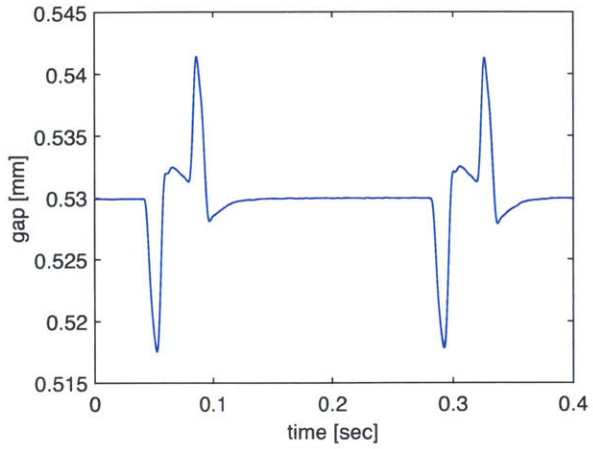

Figure 10-40: Air gap measurement during force pulse experiment.

larger frequency range (up to 10 Hz instead of 1 Hz). Doing this should reduce the dependency of the flux estimate on the sense coil during the high dF/dt portion of the force pulse, and so we expect to see a reduced overshoot. Figure 10-41 shows the results of this experiment. The overshoot decreases from the previous results. The maximum error is now 8.6 N, or 2.7% of full-scale force. Moreover, the time constant associated with the overshoot decay is faster. These results provide confirmation that the loop widening is the cause of the force overshoot.

One potential solution to the overshoot problem is to increase the complementary filter pair cutoff frequency until the flux estimator's reliance on the sense coil is sufficiently reduced such that the overshoot reaches acceptable levels. However, this defeats the very purpose of having the sense coil in the first place. Moreover, with the SHM observer having a crossover frequency of 2 kHz, the accuracy of the SHM estimate will suffer at higher frequencies. Another alternative solution is to calibrate the phase lag between the sense coil measurement and force measurement and then incorporate this dynamic mapping into the force inversion. A third alternative is to use iterative learning control to find the correct signal with which to drive the reluctance actuator to achieve the desired force. One challenge to this is that ILC requires a repeatable signal, but the gap disturbance will not necessarily be repeatable. Thus, the signal required to drive the reluctance actuator will change between

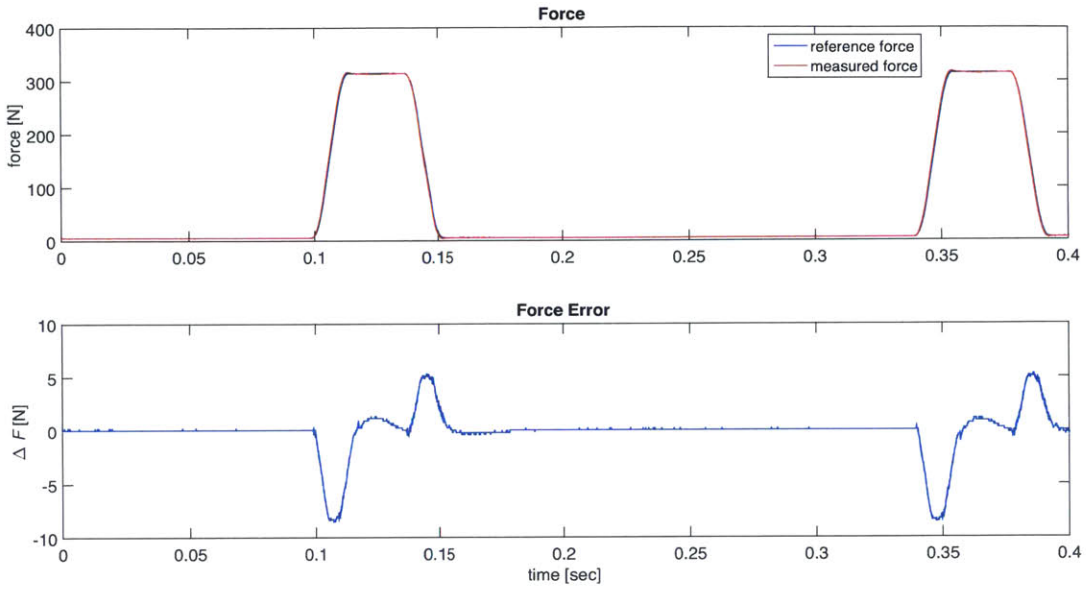

Figure 10-41: Force pulse experimental results with complementary filter pair cutoff frequency set to 10 Hz. TOP: reference force profile and measured force profile. BOTTOM: error between reference force and measured force.

trials. However, since we attained acceptable levels for the flux-controlled reluctance actuator stiffness using the sense coil, it is possible that the flux controller will be able to compensate for the gap disturbance in spite of the loop-widening problem. The best solution is of course to solve the loop-widening problem so that there is no phase lag between the flux measured by the sense coil and the measured force.

Force Pulse Results with Applied Gap Disturbance

We tested the compensated reluctance actuator's ability to track a force pulse in the presence of a gap disturbance similar to a gap disturbance on a scanning lithography stage. The measured gap disturbance is shown in Figure 10-42. The peak-to-peak amplitude of the disturbance has a maximum of about 30 µm.

The measured force pulse and the associated force error are shown in Figure 10-43. The complementary filter pair cutoff frequency was 10 Hz. The error looks very similar to the error without the applied gap disturbance from Figure 10-41, indicating that the flux loop and force inversion are able to reject the gap disturbance. However,

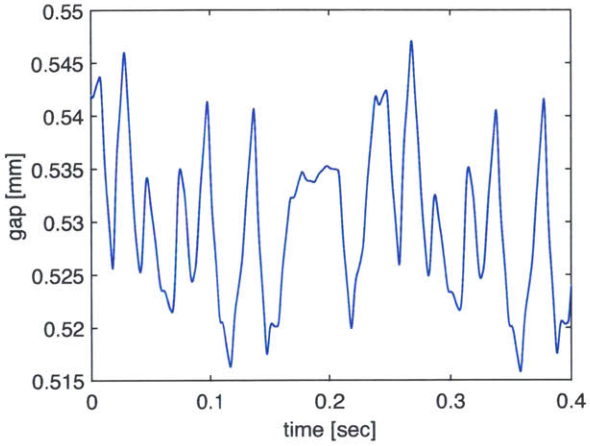

Figure 10-42: Gap disturbance during force pulse experiment.

because there is still a sizable position error even when not intentionally applying a gap disturbance (see Figure 10-40), we are not truly comparing the force accuracy with and without gap disturbances. Nevertheless, the fact that there is not much change in the force error is a promising result. Another difficulty with this measurement is that we are limited by the load cell charge amplifier: since we are measuring large dynamic forces in the force pulse test, the charge amplifier sensitivity must be lowered to avoid overloading. This limits the minimum force change we are able to detect.

10.7 Summary

In this chapter, we presented experimental results of our reluctance actuator prototype on the 1-DoF air bearing testbed. We tested the SHM observer as well as flux feedback loop that incorporated it. For the flux feedback loop, we designed a complementary filter pair that permitted us to take advantage of the benefits of both a sense coil measurement and the hysteresis model estimate. One subtlety we discovered is that the complementary filter pair must be at least second-order to avoid offsets in the sense coil measurement translating into flux estimation errors. We tested the force accuracy of the reluctance actuator using the flux feedback loop and a force-flux-gap model inversion implemented as a lookup table.

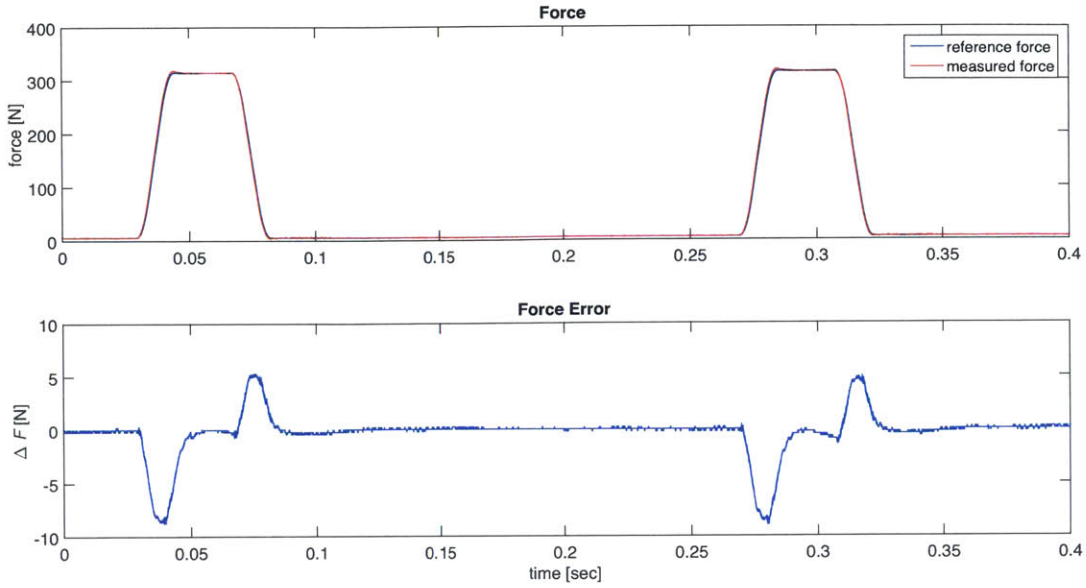

Figure 10-43: Force pulse experimental results with gap disturbance applied. TOP: reference force profile and measured force profile. BOTTOM: error between reference force and measured force.

We demonstrated that the SHM observer worked in real-time operation and could accurately estimate the actuator flux. We calibrated the SHM at a gap of 530 µm. We demonstrated that the SHM was capable of estimating the flux when we offset the nominal gap by 50 µm to 580 µm. The SHM was also shown accurately to predict the flux in the face of a dynamically varying gap with a peak-to-peak amplitude of 35 µm and was demonstrated to be numerically stable in real-time in the face of such a gap disturbance.

We experimentally demonstrated a flux control loop crossover frequency of 4 kHz that was capable of reducing the stiffness of the reluctance actuator to well below the maximum allowable stiffness. For example, at 10 Hz, the flux-controlled actuator exhibited a stiffness of 0.003 N/µm at a bias force of 35 N, which is an order of magnitude below the maximum stiffness specification of 0.04 N/µm. We also showed that using the SHM observer in our hybrid estimation scheme results in lower stiffness than using the Chua model.

The dynamic force tracking capability of the flux loop was demonstrated via a

measured frequency response and via force pulse experiments in the time domain. The force tracking capability did not meet the required 99.9% accuracy requirement. We determined that one of the likely reasons for this is the loop-widening phenomenon exhibited by the sense coil measurement. Resolving this problem would result in more accurate force tracking. We learned that one way to improve the force tracking in the face of the loop widening behavior was to increase the complementary filter pair cutoff frequency so that the flux estimator would rely more on the hysteresis model estimate than on the sense coil measurement.

In the next chapter, we will present our thesis conclusions and recommendations for future work. Included in our recommendations are suggestions for how to improve the force tracking capabilities of the reluctance actuator.

Chapter 11

Conclusion and Future Work

11.1 Conclusion

This thesis develops control and modeling techniques for a reluctance actuator in order to achieve high-dynamic-force accuracy on a scanning photolithography stage. The primary contributions of this thesis include:

1. Designed and experimentally demonstrated a flux controller for a reluctance actuator that utilizes a sense coil for the feedback measurement.

2. Experimentally investigated the high-force-accuracy capability of a reluctance actuator using flux control.

3. Experimentally demonstrated the low stiffness of a reluctance actuator using flux control.

4. Designed and experimentally demonstrated a low-frequency flux hysteresis estimate based on the actuator current and air gap to compensate for the poor performance of the sense coil at low frequencies. This low-frequency estimate was combined with the sense coil estimate using a hybrid estimation scheme.

5. Developed a novel way to model actuator hysteresis, the sheared hysteresis model (SHM), that takes advantage of the linearizing effect of the air gap.

6. Developed an actuator hysteresis model that can incorporate the effect of eddy currents.

7. Designed an adaptive gain observer that accurately models actuator hysteresis over the entire B-H plane into saturation.

8. Investigated electromagnetic hysteresis dependence on frequency.

9. Developed simple approximate formulas for predicting reluctance actuator force errors from hysteresis, eddy currents, and gap disturbances; for predicting actuator uncompensated stiffness and compensated stiffness; and for predicting power dissipation from hysteresis and eddy currents.

11.2 Future Work

In this section, we outline suggestions for future work.

11.2.1 Further Investigation into Force Accuracy

Because of the sense coil loop-widening phenomenon, we were unable to achieve 99.9% force accuracy with the prototype reluctance actuator. For a sense coil to be a viable feedback sensor for the reluctance actuator, this problem must be better understood and resolved.

Other ways to improve the force accuracy were not investigated owing to time constraints. ILC could be used to find the optimal force command that achieves the best force accuracy for the desired profile. ILC could potentially also be used to find the hysteresis model parameters in an automatic way.

Flux feedforward could be added to the flux feedback loop to improve the flux estimation accuracy, and thus, the force accuracy. This feedforward could be as simple as adding resistance compensation, whereby the voltage required to drive the actuator resistance is fedforward to the actuator, or as complex as a full inverse hysteresis model. One possibility for an inverse hysteresis model is to use the observer

structure developed in this thesis, but modifying it so that the reference signal is the desired flux density rather than the measured current and placing the hysteresis model in the observer feedback path. An advantage of this is that an inverse hysteresis model does not have to be directly modeled. An alternative possibility is to use an inverse hysteresis model that is simpler than the one used for the low-frequency flux estimation for the flux feedback. Since the high-bandwidth flux feedback loop should be designed such that it will not be the limiting factor in achieving the force accuracy and stiffness specifications, any flux feedforward does not need to be highly accurate, as its function is simply to give incremental improvements.

11.2.2 Analog or FPGA Flux Control Loop

On our testbed, we were limited in the flux loop bandwidth we could achieve by the sampling rate of the dSPACE RTC. Our accuracy was also limited by the resolution and noise of the ADC. Designing an analog control loop or a controller implemented in an FPGA could easily permit loop bandwidths into the tens of kHz. Designing an amplifier tailored to driving the reluctance actuator rather than a commercial amplifier could also increase bandwidth and accuracy. A hybrid scheme could also be pursued: the low-frequency hysteresis model estimate could be computed on a slow RTC while the controller, sense coil integration, and complementary filter pair are implemented in the analog domain or on a high-speed FPGA.

11.2.3 Optimized Actuator Design

For incorporation into an actual lithography stage, it is important to optimize the actuator for high force-to-mass ratio in order to achieve the required accelerations and servo bandwidths. One straightforward way toward reducing the actuator mass is to use CoFe as the core and target material rather than NiFe, because CoFe has a much higher saturation flux density. Incorporating an efficient water-cooling jacket would allow the actuator to run much higher current densities and would permit a much more compact design. Using a double-sided actuator, described in Section 2.6.1,

could allow for half the total target mass on the moving stage since each target now only needs to transfer half the force compared to the equivalent single-sided design. Geometric optimization also should be considered. We briefly remarked on a couple possibilities for geometric optimization in Section 8.4.6. Other possibilities in addition to these should also be investigated.

11.2.4 Cross-Coupling

With our testbed we were only capable of characterizing the actuator in the driving direction. Investigation into the other degrees-of-freedom should also be analyzed and tested. These include parasitic torques and forces and cross-axis stiffnesses. In [62], which supplements the work of this thesis, the parasitic torques resulting from angle disturbances have been investigated.

11.2.5 Integration into 6-DoF Stage

To prove the reluctance actuator fully for scanning lithography applications, the actuator must be integrated into a full magnetically-levitated 6-DoF stage and used for position control for scanning profiles. Key issues that need to be addressed include calibration on the 6-DoF stage, achieving small operating gaps given assembly and crash tolerances, determining whether a 'pull-only' design is acceptable or whether a 'push-pull' design is needed, and managing the additional sensor wires when mounted on a high-acceleration stage.

11.2.6 Other Applications

We briefly mention how a couple of the concepts presented in this thesis might be applied to other applications.

Hybrid Estimation Scheme

The hybrid flux estimation scheme detailed in Chapter 10 could be applied to other applications in which it would be advantageous to combine the benefits of a sensor or

estimation method suited to low frequencies with the benefits of a sensor or estimation method suited to high frequencies. In [4], such a scheme is applied to a piezoelectric actuator, combining a hysteresis model with charge control. On the reluctance actuator, we could combine a Hall sensor with the sense coil using this scheme. If force sensing were considered instead of flux sensing, the AC-coupled quartz piezo load cells could be combined with a force-current hysteresis model based on the current and gap measurements. We can also think of applications such as those involving a rotating mechanical system that includes a transmission between the drive motor and the load. Suppose the output is measured by a tachometer, but we want to control the position. We can use a hybrid estimation scheme to combine the integral of the tachometer signal with an estimate of the position based on the input signal and a model of the transmission.

Observer Structure

We used an observer to estimate the flux of the actuator in the presence of a gap disturbance. One of the benefits of this method is that by treating the gap variation as a disturbance to the observer loop, we were able to estimate the flux without having to resort to a more complex two-input hysteresis model. This idea can be extended to other nonlinear phenomena with more than one input. Remaining within the domain of reluctance actuators, the flux dependency on temperature could possibly be modeled in this way. For piezoelectric actuators, if both the electric field and applied stress levels are changing, the voltage-strain relationship could be modeled with a hysteresis model, and the stress variation could be handled as a disturbance to an observer loop. Similarly, the dependence of magnetostriction on both magnetic field and stress could possibly be modeled in this way. Shape memory alloy's dual dependence on temperature and stress could also potentially be modeled in this way.

Bibliography

[1] HJMTS Adriaens, W De Koning, and Reinder Banning. Modeling piezoelectric actuators. *Mechatronics, IEEE/ASME Transactions on*, 5(4):331–341, 2000.

[2] Hyo-Sung Ahn, YangQuan Chen, and Kevin L Moore. Iterative learning control: brief survey and categorization. *IEEE TRANSACTIONS ON SYSTEMS MAN AND CYBERNETICS PART C APPLICATIONS AND REVIEWS*, 37(6):1099, 2007.

[3] Farid Al-Bender, Vincent Lampaert, and Jan Swevers. The generalized maxwell-slip model: a novel model for friction simulation and compensation. *Automatic Control, IEEE Transactions on*, 50(11):1883–1887, 2005.

[4] Darya Amin-Shahidi. *Design and control of a self-sensing piezoelectric reticle assist device.* PhD thesis, Mechanical Engineering, Massachusetts Institute of Technology, 2013.

[5] Darya Amin-Shahidi, Ian MacKenzie, and David L Trumper. Magnetic flux linkage estimation and control for a reluctance actuator. In *Proc. of 2013 ASPE Spring Topical Meeting.*

[6] Analog Devices. `http://www.analog.com/en/index.html`.

[7] M Angeli, E Cardelli, and E Della Torre. Modelling of magnetic cores for power electronics applications. *Physica B: Condensed Matter*, 275(1):154–158, 2000.

[8] B Azzerboni, E Cardelli, E Della Torre, and G Finocchio. Reversible magnetization and lorentzian function approximation. *Journal of applied physics*, 93(10):6635–6637, 2003.

[9] B Azzerboni, E Cardelli, G Finocchio, and F La Foresta. Remarks about Preisach function approximation using lorentzian function and its identification for nonoriented steels. *IEEE transactions on magnetics*, 39(5):3028–3030, 2003.

[10] BEI Kimco Magnetics. `www.beikimco.com`.

[11] Y Bernard, E Mendes, and F Bouillault. Dynamic hysteresis modeling based on Preisach model. *Magnetics, IEEE Transactions on*, 38(2):885–888, 2002.

[12] Y Bernard, E Mendes, and Z Ren. Determination of the distribution function of Preisach's model using centred cycles. *COMPEL: The International Journal for Computation and Mathematics in Electrical and Electronic Engineering*, 19(4):997–1006, 2000.

[13] Giorgio Bertotti. General properties of power losses in soft ferromagnetic materials. *Magnetics, IEEE Transactions on*, 24(1):621–630, 1988.

[14] Giorgio Bertotti. *Hysteresis in magnetism: for physicists, materials scientists, and engineers.* Gulf Professional Publishing, 1998.

[15] Richard Boll. *Soft Magnetic Materials: fundamentals, alloys, properties, products, applications.* Heyden, 1979.

[16] Richard Boll, editor. *Soft magnetic materials: fundamentals, alloys, properties, products, applications / The Vacuumschmelze Handbook.* Heyden, London, 1979.

[17] Douglas A Bristow, Marina Tharayil, and Andrew G Alleyne. A survey of iterative learning control. *Control Systems, IEEE*, 26(3):96–114, 2006.

[18] Hans Butler. Position control in lithographic equipment. *IEEE Control Systems Magazine*, 31(5):28–47, 2011.

[19] Hans Butler and Franciscus Adrianus Gerardus Klaassen. Method for controlling the position of a movable object, a positioning system, and a lithographic apparatus, 2008. US Patent 7,352,149.

[20] E Cardelli, F Bertoncini, S Di Fraia, and B Tellini. Implementation of the modified Preisach scalar model in the finite difference–time-domain numerical modeling. *Physica B: Condensed Matter*, 306(1):126–131, 2001.

[21] Ermanno Cardelli, Edward Della Torre, and Enrico Pinzaglia. Identifying the preisach function for soft magnetic materials. *IEEE transactions on magnetics*, 39(3):1341–1344, 2003.

[22] Ping-Wei Chang, Kazuhiro Hirano, Tim Teng, Pai-Hsueh Yang, and Bausan Yuan. E/i core actuator commutation formula and control method, August 7 2007. US Patent 7,253,576.

[23] L Chua and Steven C Bass. A generalized hysteresis model. *Circuit Theory, IEEE Transactions on*, 19(1):36–48, 1972.

[24] Leon O Chua, Charles A Desoer, and Ernest S Kuh. *Linear and nonlinear circuits.* McGraw-Hill New York, 1987.

[25] Leon O Chua and Keith A Stromsmoe. Lumped-circuit models for nonlinear inductors exhibiting hysteresis loops. *Circuit Theory, IEEE Transactions on*, 17(4):564–574, 1970.

[26] Leon O Chua and Keith A Stromsmoe. Mathematical model for dynamic hysteresis loops. *International Journal of Engineering Science*, 9(5):435–450, 1971.

[27] Bernard D Coleman and Marion L Hodgdon. A constitutive relation for rate-independent hysteresis in ferromagnetically soft materials. *International journal of engineering science*, 24(6):897–919, 1986.

[28] COMSOL Multiphysics Modeling Software. `http://www.comsol.com/`.

[29] Crown International, Inc. `http://www.crownaudio.com/`.

[30] Crown International, Inc. *Instruction Manual: DC-300A Dual Channel Laboratory Amplifier.*

[31] Philip R Dahl. Solid friction damping of mechanical vibrations. *AIAA Journal*, 14(12):1675–1682, 1976.

[32] C Canudas De Wit, Hans Olsson, Karl Johan Aström, and Pablo Lischinsky. A new model for control of systems with friction. *Automatic Control, IEEE Transactions on*, 40(3):419–425, 1995.

[33] Edward Della Torre. *Magnetic hysteresis.* IEEE press New York, 1999.

[34] B.G. Dijkstra. *Iterative learning control, with applications to a wafer stage.* PhD dissertation, Delft University of Technology, Mechanical Engineering Systems and Control Group, September 2004.

[35] dSPACE Inc. `www.dspace.com/en/inc/home.cfm`.

[36] DuPont. `http://www.dupont.com/`.

[37] Michel Dussaux. The industrial applications of the active magnetic bearings technology. In *Proc. 2nd Int. Symp. Magn. Bearings*, pages 33–38, 1990.

[38] EpoxySet, Inc. `http://www.epoxysetinc.com/`.

[39] Hermann A Haus and James R Melcher. *Electromagnetic fields and energy.* Prentice Hall Englewood Cliffs, 1989.

[40] Kazuhiro Hirano, Tim Teng, Pai Hsueh Yang, and Bausan Yuan. Auto-calibration of attraction-only type actuator commutations, April 25 2006. US Patent 7,034,474.

[41] Sven Antoin Johan Hol, Antonius Franciscus Johannes De Groot, Theodorus Petrus Maria Cadee, Marijn Kessels, and Daniël Godfried Emma Hobbelen. Actuator, positioning system and lithographic apparatus, June 25 2013. US Patent 8,472,010.

[42] Sven Antoin Johan Hol, Jan Van Eijk, Johannes Petrus Martinus Bernardus Vermeulen, Gerard Johannes Pieter Nijsse, Simon Bernardus Cornelis Maria Martens, Yang-Shan Huang, Michael Wilhelmus Theodorus Koot, Jeroen De Boeij, Maarten Hartger Kimman, Wei Zhou, et al. Electromagnetic actuator, stage apparatus and lithographic apparatus, April 1 2014. US Patent 8,687,171.

[43] Yi-Ping Hsin. Adaptive gain adjustment for electromagnetic devices, May 16 2006. US Patent 7,046,496.

[44] SYR Hui and J Zhu. Numerical modelling and simulation of hysteresis effects in magnetic cores using transmission-line modelling and the Preisach theory. In *Electric Power Applications, IEE Proceedings-*, volume 142, pages 57–62. IET, 1995.

[45] Fayçal Ikhouane, Víctor Mañosa, and José Rodellar. Dynamic properties of the hysteretic bouc-wen model. *Systems & control letters*, 56(3):197–205, 2007.

[46] Mohammad Imani Nejad. *Self-bearing motor design & control.* PhD thesis, Mechanical Engineering, Massachusetts Institute of Technology, 2013.

[47] DC Jiles and DL Atherton. Theory of ferromagnetic hysteresis. *Journal of magnetism and magnetic materials*, 61(1):48–60, 1986.

[48] John G Kassakian, Martin F Schlecht, and George C Verghese. *Principles of power electronics.* Addison-Wesley Reading, USA, 1991.

[49] Andelko Katalenić. *Control of reluctance actuators for high-precision positioning.* PhD dissertation, Eindhoven University of Technology, 2013.

[50] Kepco, Inc. `http://www.kepcopower.com/`.

[51] Byeongil Kim and Gregory N Washington. Nonlinear position control of smart actuators using model predictive sliding mode control. In *ASME 2008 Conference on Smart Materials, Adaptive Structures and Intelligent Systems*, pages 511–522. American Society of Mechanical Engineers, 2008.

[52] Kistler. `www.kistler.com`.

[53] Daniel Joseph Kluk. An advanced fast steering mirror for optical communication. Master's thesis, Massachusetts Institute of Technology, 2007.

[54] Stephan Kotyczka. Manufacturing and control of a single degree of freedom stage. Visiting student at MIT.

[55] Klaus Kuhnen and Hartmut Janocha. Adaptive inverse control of piezoelectric actuators with hysteresis operators. In *Proceedings of European Control Conference (ECC)*, 1999.

[56] Xiaodong Lu. *Electromagnetically-driven ultra-fast tool servos for diamond turning.* PhD thesis, Mechanical Engineering, Massachusetts Institute of Technology, 2005.

[57] Magnetic Metals. Tape wound core design manual. `www.magmet.com`.

[58] Magnetic Metals. Transformer lamination catalog. `www.magmet.com/lamination/materials.php`.

[59] H Malsky. Printed winding DC torque motor. Technical report, Charles Stark Draper Laboratory, Inc., 1976.

[60] MathWorks. `www.mathworks.com/products/matlab/`.

[61] Isaak D Mayergoyz. *Mathematical models of hysteresis and their applications.* Academic Press, 2003.

[62] Roberto Meléndez. A reluctance actuator gap disturbance testbed. Master's thesis, Massachusetts Institute of Technology, 2014.

[63] Kevin L Moore. *Iterative learning control for deterministic systems.* Springer, 1993.

[64] National Instruments. `http://www.ni.com/labview/`.

[65] New Way Air Bearings. `www.newwayairbearings.com`.

[66] Donald Richard Nohavec. Magnetic bearing design for interferometric mirror-scanning mechanisms. Master's thesis, Massachusetts Institute of Technology, 1997.

[67] Kazuya Ono. Curved i-core, June 14 2005. US Patent 6,906,334.

[68] Vlado Ostovic. *Dynamics of saturated electric machines*, volume 2. Springer-Verlag New York, 1989.

[69] Pacific Scientific-OECO. `http://fwbell.com/default.aspx`.

[70] David J Perreault and Khurram Afridi. *6.332 Advanced Topics in Power Electronics.* Fall 2013. MIT.

[71] Tony Poovey. A kinematically coupled magnetic bearing test fixture. Master's thesis, University of North Carolina at Charlotte, 1992.

[72] James K Roberge. Operational amplifiers: Theory and practice john wiley and sons. *Inc., New York, London, Sydney, Toronto*, 1975.

[73] Iuliana Rotariu, Branko Dijkstra, and Maarten Steinbuch. Standard and lifted approaches of iterative learning control applied on a motion system. In *Proceedings of The International Symposium on the Mathematical Theory of Networks and Systems (MTNS 2004)*, 2004.

[74] HC Roters. Electromagnetic devices, 1941.

[75] Stephen Roux, Frederick Michael Carter, and Ross Ian Mackenzie. Method for controlling the position of a movable object, a control system for controlling a positioning device, and a lithographic apparatus, October 8 2013. US Patent 8,553,205.

[76] Ralph C Smith. *Smart material systems: model development*, volume 32. Siam, 2005.

[77] Mohammad Sheikh Sofla, Seyed Mehdi Rezaei, and Mohammad Zareinejad. Adaptive trajectory tracking control of nanopositioning stage under dynamic load condition. In *ASME 2009 International Mechanical Engineering Congress and Exposition*, pages 315–320. American Society of Mechanical Engineers, 2009.

[78] Sony Precision Technology, Inc. `sony-magnescale.com`.

[79] Gilbert Strang and Kaija Aarikka. *Introduction to applied mathematics*, volume 16. Wellesley-Cambridge Press Wellesley, MA, 1986.

[80] Tektronix, Inc. `www.tek.com`.

[81] Tektronix, Inc. *AM502 Differential Amplifier Instruction Manual*, 1986.

[82] Ting-Chien Teng and Bausan Yuan. Magnetic actuator producing large acceleration on fine stage and low rms power gain, October 10 2000. US Patent 6,130,517.

[83] Ting-Chien Teng and Bausan Yuan. Stage having paired e/i core actuator control, May 30 2000. US Patent 6,069,417.

[84] David L Trumper. Nonlinear compensation techniques for magnetic suspension systems. In *NASA Workshop on Aerospace Applications of Magnetic Suspension Technology*, 1990.

[85] David L Trumper, Sean M Olson, and Pradeep K Subrahmanyan. Linearizing control of magnetic suspension systems. *Control Systems Technology, IEEE Transactions on*, 5(4):427–438, 1997.

[86] Ferenc Vajda and Edward Della Torre. Efficient numerical implementation of complete-moving-hysteresis models. *Magnetics, IEEE Transactions on*, 29(2):1532–1537, 1993.

[87] Jozef Vörös. Modeling and identification of hysteresis using special forms of the coleman-hodgdon model. *Journal of Electric Engineering*, 60(2):100–105, 2009.

[88] Wen-Fang Xie, Jun Fu, Han Yao, and C-Y Su. Neural network-based adaptive control of piezoelectric actuators with unknown hysteresis. *International Journal of Adaptive Control and Signal Processing*, 23(1):30–54, 2009.

[89] Jian-Xin Xu, Sanjib K Panda, and Tong Heng Lee. *Real-time iterative learning control: design and applications.* Springer, 2008.

[90] Markus Zahn. *6.641 Electromagnetic Fields, Forces, and Motion.* Spring 2008. MIT.

[91] Markus Zahn. *Electromagnetic field theory: a problem solving approach.* Krieger Pub. Co., Malabar, 2003.